Nanostructure Science and Technology
Series Editor: David J. Lockwood

Teruyuki Nakato
Jun Kawamata
Shinsuke Takagi *Editors*

Inorganic Nanosheets and Nanosheet-Based Materials

Fundamentals and Applications of Two-Dimensional Systems

Springer

Nanostructure Science and Technology

Series editor

David J. Lockwood, FRSC
National Research Council of Canada
Ottawa, Ontario, Canada

More information about this series at http://www.springer.com/series/6331

Teruyuki Nakato · Jun Kawamata
Shinsuke Takagi
Editors

Inorganic Nanosheets and Nanosheet-Based Materials

Fundamentals and Applications of Two-Dimensional Systems

Springer

Editors
Teruyuki Nakato
Kyushu Institute of Technology
Kitakyushu
Japan

Shinsuke Takagi
Tokyo Metropolitan University
Hachioji
Japan

Jun Kawamata
Yamaguchi University
Yamaguchi
Japan

ISSN 1571-5744 ISSN 2197-7976 (electronic)
Nanostructure Science and Technology
ISBN 978-4-431-56494-2 ISBN 978-4-431-56496-6 (eBook)
DOI 10.1007/978-4-431-56496-6

Library of Congress Control Number: 2017932786

Printed on acid-free paper

This Springer imprint is published by Springer Nature
The registered company is Springer Japan KK
The registered company address is: Chiyoda First Bldg. East, 3-8-1 Nishi-Kanda, Chiyoda-ku, Tokyo 101-0065, Japan

Preface

Zhuangzi (Chaung Tzu), a philosopher of ancient China, wrote "looking at the sky through a tube" as a metaphor for shortsighted recognition (in *Autumn Floods*, an outer chapter of *Zhuangzi*). As seen in children's games, however, "looking through a tube" often gives attractive and stimulating landscapes. The restricted and low-dimensional sight can clarify unusual aspects of the scenery hidden in an ordinary view. Does it hold for materials chemistry? The answer is yes.

From the last quarter of the twentieth century, chemical science has discovered structural design at nanometer scales, being larger than the size of single molecules but much smaller than that of practical materials, as an important key for developing novel advanced materials. Shape anisotropy has also been found as another key that facilitates gradient functions in a system by asymmetric location of functional moieties. Research interests have created various nano-objects and nanospaces in the materials world. Today, they are recognized as important building blocks or matrixes for constructing advanced materials with the integration of plural functional moieties.

Inorganic nanosheets are two-dimensional particles with nm-level thickness. In particular, they mean crystalline inorganic monolayers provided by exfoliation of inorganic layered crystals. The exfoliation has been developed as an extension of intercalation phenomena that are the events in the two-dimensional interlayer spaces of the layered crystals. In fact, the exfoliated inorganic nanosheets and the interlayer spaces, being two sides of the same coin, have contributed as anisotropic nano-objects or nanospaces to developing nanostructured materials. Various nanosheet-based architectures have been constructed often with immobilizing functional molecules in the nanospaces or on the nanosheets themselves. Recently, the research field has been progressing and expanding more and more as stimulated by the Nobel Prize for graphene in 2010. Publications including the word "nanosheet" exceeded 2,800 in 2015, although they were fewer than 10 in 2000 (by SciFinder).

Based on such research development, we decided to summarize current materials chemistry of the inorganic nanosheets in this book. We aimed at bundling diverse aspects of inorganic nanosheets, e.g., nanosheet preparation, hybridization with

other materials, and various applications, to give a concise summary of the inorganic nanosheets and nanosheet-based materials. Fortunately, we succeeded in collecting contributions from many leading researchers involved in this area.

This book is composed of two parts. Part I provides fundamental aspects. The research area is overviewed, and preparation, properties, and fabrications of representative inorganic nanosheets, i.e., clay minerals, oxometallates, graphene, metal dichalcogenides, are summarized. Interactions of the nanosheets and their 2D interlayer spaces with organic and polymer species, which are the critical basis of fabricating nanosheet-based assemblies, are described. Moreover, colloidal properties of the nanosheets are also depicted, exploring their utilization in the field of soft matter.

Part II collects applications of the nanosheet-based materials. They are extended to various fields: adsorption, sensing, electric, optic, energy conversion, and biological functions, covering broad state-of-the-art research topics. Among them, photochemical and electrochemical functions related to energy conversion and storage are described in detail because these functions are highly sensitive to microenvironments and hierarchical arrangements of the reaction molecules as seen in natural photosynthetic systems.

Finally, we express our sincere thanks to all the authors who contributed to this book with their deep insights into this field.

Kitakyushu, Japan Teruyuki Nakato
Yamaguchi, Japan Jun Kawamata
Hachioji, Japan Shinsuke Takagi

Contents

Part I
Fundamental Aspects of Inorganic Nanosheets

Chapter 1
Materials Chemistry of Inorganic Nanosheets—Overview and History

Teruyuki Nakato, Jun Kawamata and Shinsuke Takagi

1.1 Introduction—What Are Inorganic Nanosheets?

Inorganic nanosheets are inorganic plate-like particles with thickness at the nm-level and lateral length in the range of several to thousands of times greater than their thickness. The term *nanosheets* can essentially be applied to any particle with thickness in the range of a 1 nm to sub-μm, and a wide range of materials from graphene to plate-like polymers can satisfy this requirement. However, the term *inorganic nanosheets* is generally reserved for thin layers or monolayers, with thickness less than several nanometers, obtained by exfoliation of inorganic layered crystals (Fig. 1.1). In this book, we consider *inorganic nanosheets* in this narrow sense.

Exfoliated inorganic nanosheets obtained from inorganic layered crystals have characteristics distinguishable from those of typical inorganic particles. Nanosheets are ideally monolayers, or a few layers, of a mother layered crystal. Monolayers are yielded by complete exfoliation of the mother crystals to achieve highly anisotropic layers with thickness around 1 nm. Significance of the monolayer nanosheets is their ultimate thinness as inorganic crystallites. In other words, nanosheets are the

T. Nakato (✉)
Department of Applied Chemistry, Kyushu Institute of Technology,
1-1 Sensui-cho, Tobata-ku, Kitakyushu, Fukuoka 804-8550, Japan
e-mail: nakato@che.kyutech.ac.jp

J. Kawamata
School of Chemistry, Faculty of Science, Yamaguchi University,
Yoshida, Yamaguchi 753-8512, Japan
e-mail: j_kawa@yamaguchi-u.ac.jp

S. Takagi
Department of Applied Chemistry, Graduate School of Urban Environmental Sciences,
Tokyo Metropolitan University, 1-1 Minami-Ohsawa, Hachioji, Tokyo 192-0397, Japan
e-mail: takagi-shinsuke@tmu.ac.jp

T. Nakato et al. (eds.), *Inorganic Nanosheets and Nanosheet-Based Materials*,
Nanostructure Science and Technology, DOI 10.1007/978-4-431-56496-6_1

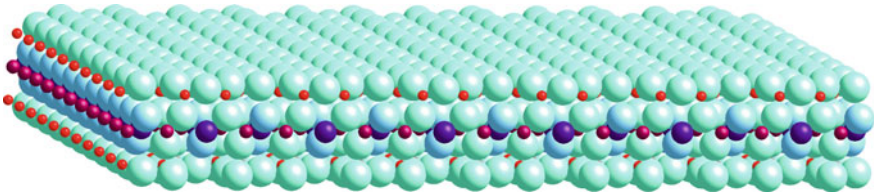

Fig. 1.1 Inorganic nanosheet obtained by exfoliation of montmorillonite (layered clay mineral), indicating the 2:1-type single layer of the clay mineral. *Red* Si^{4+}, *brown* Al^{3+}, *purple* Mg^{2+}, *blue-green* O^{2-} or OH^{-}

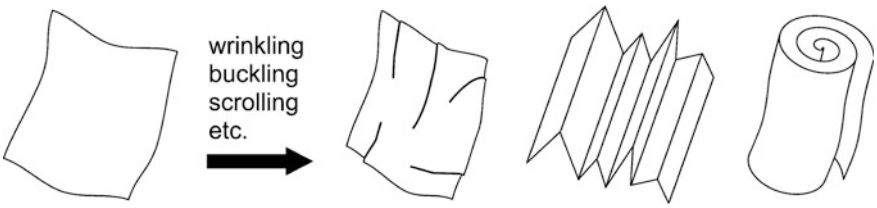

Fig. 1.2 Schematic representation of the possible deformations of a nanosheet

smallest units of inorganic crystals that can be manipulated, in analogy with monomolecular layers of organic solids. The thinness of inorganic nanosheets also endows macroscopic softness as nanosheets undergo wrinkling, buckling, and scrolling (Fig. 1.2). Most exfoliated nanosheets retain crystallinity that reflects the crystalline structure of the mother compounds. This contrasts with conventional inorganic nanosheets that are often amorphous or poorly crystalline. These morphological features of the inorganic nanosheets facilitate construction of macroscopic structures by manipulation at the nanoscale and have stimulated development of a wide range of new materials.

The broad range of layered materials that can be exfoliated gives us a rich library of inorganic nanosheets. These materials span elementary substances, such as carbon and phosphorus, to oxides and chalcogenides; inorganic compounds of almost all categories can form nanosheets. The crystal structures of nanosheets also have a broad diversity, which reflects their composition. It is possible to obtain nanosheets with electrical characters ranging from dielectric to semiconducting and conducting properties. Such variation of the electric properties leads to differences in optical, photochemical, and magnetic properties. Similarly, nanosheet surface properties show behavior that ranges from hydrophilic (polar) to hydrophobic (nonpolar). Surface functionalities also show a wide variation, and many nanosheets can undergo surface chemical modifications to control their properties.

Because of the above-mentioned characteristics, inorganic nanosheets are now recognized as an important class of materials that offer novel advanced functionalities. Such materials have been developed, not only by fabrication of nanosheets, but also through fusion of nanosheets with other inorganic and organic substances.

Thus, in this book we describe the preparation, structure, and functions of inorganic nanosheets themselves and various hybrid systems constructed by assembling them, as the materials chemistry of nanosheets. Applications of these materials have expanded in a range of the fields including various electronic, optic, and photochemical functions, adsorption and materials transportation, catalysis, and bio-related functions for medicine and pharmacy. The broadness of this range of applications reflects the diversity of compositions and properties of nanosheets.

1.2 Inorganic Nanosheets and Chemistry of Nanomaterials

Along with developments in nanotechnology, various inorganic particle systems possessing nm-level dimensions have drawn increasing interest. These materials have been investigated as functional fine particles that exhibit specific properties due to their nm-level size, and as building blocks for constructing higher order structures. Inorganic particles can be classified into 0D (nanodots, nanospheres), 1D (nanorods, nanowires, nanotubes), and 2D (nanosheets, nanoplates) particles based on their shape. Among these structures, considerable attention was initially been paid to isotropic 0D nanoparticles, which has expanded to anisotropic particles. In terms of anisotropic nanoparticles, many investigations into 1D matter have been performed and 2D nanoparticles have become an active area of study in the last decade. This situation is typically found in the trend shift of carbon allotrope research from fullerene to carbon nanotubes and most recently to graphenes.

Using anisotropic nanoparticles as building blocks, we can develop novel functionally graded materials [1] characterized by gradient functions based on structural asymmetry. It is difficult to realize such materials from isotropic building blocks. Shape anisotropy of building blocks induces anisotropic compositions and structures in the final material. Low-dimensionality allows anisotropic transportation of electrons and/or molecules on a material's surface or in its internal spaces, which can realize graded functions. Among anisotropic building blocks, 2D matter has specific microenvironments characterized by both confinement and freedom (Fig. 1.3). The surfaces of 2D particles are larger than those of 0D and 1D particles, and 2D surfaces can feature degrees of freedom within the plane, i.e., in both the x and y directions. Such structures allow for freer movement of electrons and molecules compared with 1D matter. Conversely, the freedom of assemblage of 2D particles is more restricted than those of the 0D and 1D particles, as a trade-off between the large freedoms of their surface morphology. Although 0D and 1D nanoparticles can organize into many types of structures, 2D nanoparticles basically assemble into layered structures. The layered structures provide 2D microspaces, restricted in the z (interlayer) direction but open in the x and y directions. Nevertheless, the interlayer spacing is often expandable to gain an additional degree of freedom in the z direction.

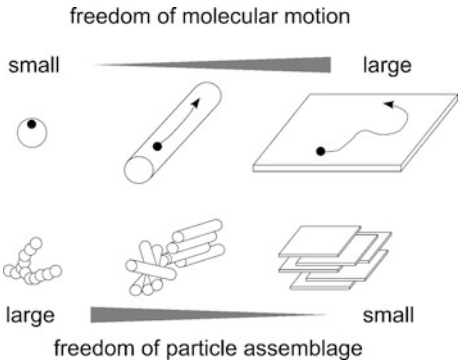

Fig. 1.3 Schematic representation of the characteristics of 0D (*dot*), 1D (*rod*), 2D (*plate*) particles. *Circles* and *arrows* indicate electrons or molecules and their transportation

Because of these morphological characteristics, materials design with inorganic nanosheets depends on what types of 2D surfaces or spaces are constructed with the nanosheets, and how the 2D structures are used. Nanosheet-based structures will merit applications if they hold advantages over structures prepared from other building blocks. Such advantages should be related to the two-dimensionality of the nanosheets. Although the final structures in which the nanosheets are involved are 1D or 3D, the effects of the local two-dimensionality provided by nanosheets in the whole structures should be evaluated. This has been conversely exemplified by that simple transformation of the layered structures to 3D structures, typically found in pillaring of layered crystals, has not been paid attention for a long time in most cases even though shed light temporally. To date a wide variety of the nanosheet-based assembled structures have been proposed in the past few decades, which will be described in the following chapters of this book.

1.3 Intercalation Chemistry and Nanosheets

Materials chemistry of the inorganic nanosheets is deeply connected with the intercalation chemistry of layered crystals [2]. This is because exfoliation of the layered crystals, by which the nanosheets are obtained, is an extension of intercalation (Fig. 1.4). Many layered crystals capable of intercalating other molecules or ions can be swollen through solvation of their interlayer spaces. Layered crystals with polar interlayer spaces are swollen with water and polar solvents, whereas nonpolar molecules can be incorporated into nonpolar solids. When a very large amount of solvent is intercalated, the interlayer spaces become infinitely swollen. Some layered crystals can retain layer stacking with interlayer spacing of up to several tens of nanometers, accommodated by solvent [3]. In the infinitely swollen state, stacking of the inorganic layers is no longer retained and individual layers are exfoliated [4].

Exfoliation through the ion-exchange routes facilitates the formation of single nanosheets. As seen in many cation-exchangeable layered solids, this is guaranteed

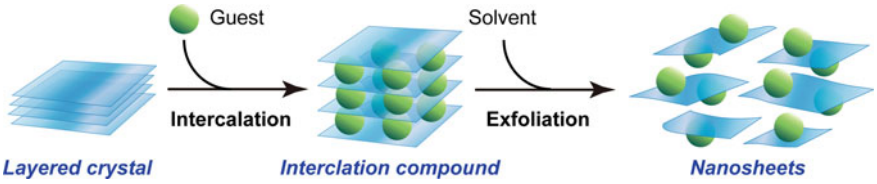

Fig. 1.4 Schematic representation of the exfoliation of a layered crystal as an extension of intercalation

by that the interlayer exchangeable cations are located in all the interlayer spaces possessing identical microenvironments determined by the crystalline inorganic layers and the stoichiometric occurrence of the layer charges. One known exception is hexaniobate ($Nb_6O_{17}^{4-}$) nanosheets as described later [5]. The incorporated exfoliating reagents attract solvent molecules equally into all of the interlayer spaces to infinitely swell the interlayer spaces. The driving force for swelling is solvation of the exfoliating reagents by dipole interactions with water and other polar solvent molecules. As a result of infinite swelling, individual layers of the mother crystals become exfoliated to form the nanosheets. The obtained nanosheets bear negative charges so that exfoliating reagents such as tetrabutylammonium (TBA^+) ions are attached to the nanosheets to compensate for the layer charge.

Intercalation reactions have also been used as a method to build up nanohybrid materials through incorporation of functional molecules into the interlayer nanospaces of the layered crystals. These nanohybrids, or intercalation compounds, are 2D nanostructured materials, which have been studied for many years before the concept of nanohybrids materials was established [6]. The exploration and application of exfoliated layered crystals is thus an important extension of progress in intercalation chemistry. The development of new synthesis for exfoliated nanosheets has greatly enriched the variety of nanosheet-based materials available in terms of their compositions and functions.

However, this shifting research trend, toward nanosheets, does not detract from the importance of conventional intercalation chemistry approaches in nanoscience. Intercalation chemistry is a well-grown field of research that has accumulated a broad knowledge base that is indispensable for developing novel nanosheet-based materials. The importance of intercalation chemistry is exemplified by studies of the effects of confined molecules and nanoparticles, in the 2D spaces between nanosheets, on the structures and properties of the resulting materials [7, 8]. The materials chemistry of inorganic nanosheets will continue to develop based on the unique 2D properties found in intercalation compounds in conjunction with many unique intrinsic properties of nanosheets such as indistinguishable internal and external surfaces owing to the loss of stacked structures, deformation of the liberated nanosheets, quantum confinement caused by the nm-level thickness, and soft-matter-like behavior seen in colloidal systems. Furthermore, depending on the target structure and function, appropriate materials design may be better achieved by conventional intercalation reactions rather than exfoliation.

1.4 History of Nanosheet Research

1.4.1 Paradigm of Chemistry Researches Related to Nanosheets

Inorganic nanosheets are not newly synthesized materials. These materials have been discovered in the course of investigations over more than hundred years on intercalation compounds of inorganic layered crystals. For some layered compounds, the phenomenon of exfoliation was first discovered more than a half century ago [9, 10], although it was not unambiguously confirmed until recently with modern analytical instruments [11]. However, the understanding of the nanosheets and their great potential for contributions to advanced materials has deepened only in the past few decades.

Nanosheet chemistry is connected to the general paradigm of chemistry. In the twentieth century, the establishment of quantum mechanics and rapid progress in spectroscopic analyses guided the development of mainstream of chemistry. This led to a paradigm shift from holistic chemistry, or synthetic chemistry in an etymological sense, which originated from alchemy, to a reductionist approach to chemistry, or analytical chemistry in etymological sense [12]. Investigations in materials chemistry were conducted following the reductionist ideology, under which materials design has been directed by composition and structure at the molecular level. However, together with a deeper understanding of living things, chemistry has again returned from a reductionist to a holistic paradigm. This second paradigm shift began in the final quarter of the last century, and has opened fields of research relating to supramolecular systems inspired by biological systems. This movement has provided strategies for forming hierarchical materials design with multiple constituents by recognizing the limitations of single compounds. These developments have led to the current "era of nanotechnology."

In the twentieth century, which is the period corresponding to the golden age of reductionist chemistry, inorganic nanosheets remained outside of mainstream research with their recognition as colloidal particles, i.e., matter of neglected dimension. However, the current revolution toward holistic chemistry has changed the position of nanosheets. They are now recognized as important materials to support nanotechnology as building blocks of the supramolecualr systems together with other nanomaterials. Among these building blocks, inorganic nanosheets are characterized by their high anisotropy, dimensionality, softness, and crystallinity accompanied by the broad range of compositions.

1.4.2 Progress in Intercalation Chemistry

As described in Sect. 1.3, research of inorganic nanosheets started from studies of the intercalation chemistry of layered crystals. On this basis, we have divided the

progress of nanosheet research from early studies to the current time into three periods, as shown in Fig. 1.5. During the pre-intercalation period, intercalation phenomena had been investigated separately for individual layered materials. In the intercalation period, the intercalation research was integrated. In the most recent nanosheet period, exfoliation of layered crystals has developed from the intercalation research.

Inclusion phenomena in inorganic layered crystals, which allow accommodation of guest molecules in interlayer spaces of the crystals, have been known of since the nineteenth century. At that time, graphite and transition metal dichalcogenides were found to form complexes that can be understood today as intercalation compounds [13, 14]. After these compounds were discovered, investigations into clay–organic complexes started from the middle of the twentieth century. This was likely because of a delay in the establishment of clay mineralogy, a prerequisite for intercalation research, in the twentieth century because of the complicated isomorphic substitutions in clay minerals [15]. Intercalation research was performed mainly for these three groups of compounds separately. Knowledge accumulated based on these investigations was summarized into textbooks for individual layered compounds, such as graphite [13], metal dichalcogenides [14], clay minerals [15], until the middle of the 1970s, which marked the end of the pre-intercalation period.

Research on individual layered compounds led to integration of knowledge to establish a field of general intercalation chemistry that considered the behavior of different layered crystals. This research started at the beginning of the 1980s, opening the door to the intercalation period. Textbook summaries by Whittingham and Jacobson were one of the first achievements of this period [6].

In the intercalation period, the variety of layered host crystals for intercalation compounds was expanded. This extension of the host materials directed exploration of layered oxides and oxometallates, which have intercalating reactivity similarly to that of clay minerals. This direction was rationalized by the physicochemical inertness of clay minerals. Clay minerals, classified as aluminosilicates, are usually

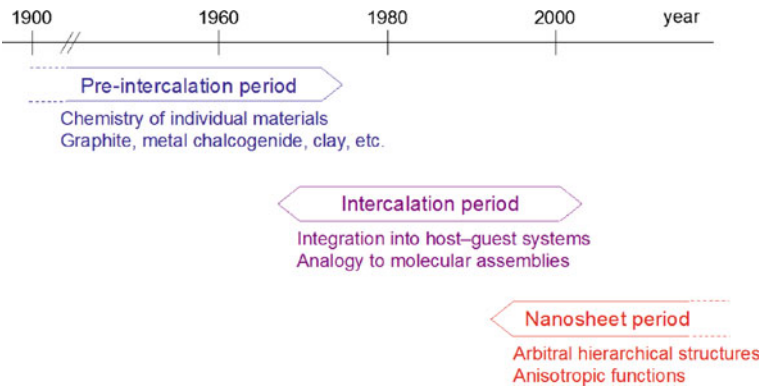

Fig. 1.5 History of the intercalation and nanosheet chemistry

electrically insulating and optically transparent, and have very different properties from graphite and metal dichalcogenides. These properties allow clay minerals to be used as stable matrixes that do not disrupt the properties of guest species. However, these materials do not feature unusual functions caused by synergistic host–guest interactions. Thus, layered crystals that intercalate guest molecules with cation exchange like clay minerals but exhibit specific physicochemical properties absent in clay minerals have been explored as host materials of intercalation compounds. Some examples of these compounds include layered silicates and zirconium phosphates that can covalently attach guest organic moieties, and layered transition element oxometallates, including titanates and niobates, which show semiconducting/conducting properties. Layered double hydroxides (LDHs), which are characterized by exchangeable anions, in contrast to cation-exchangeable clay minerals, were also studied over this period.

At this time, the concepts of supramolecules (by Lehn) [16] and molecular assemblies (by Kunitake) [17, 18] were generalized in the chemical research community, and induced a movement from molecular to supramolecular chemistry, in accordance with the paradigm shift from reductionism to holism. This trend has extended the size range targeted in chemistry from the molecular level ($\sim$1 nm) to larger ones at higher structure hierarchies. Nanoparticles, clusters, and organic polymers became important areas of materials chemistry research. The era of nanotechnology in chemistry began under the influence of this movement, and was accelerated by the National Nanotechnology Initiative, which started in the United States of America at the beginning of the 21st century [19]. This initiative spurred chemical design of nm-scale materials via bottom–up routes, where previously such materials were provided by physical top–down methods.

The integration of intercalation chemistry of individual materials in the intercalation period has synchronized with the growth of supramolecular chemistry. The intercalation chemistry has occupied an important position that supports developments in nanotechnology. Intercalation compounds are an important class of molecular assembly characterized by the involvement of inorganic building blocks. Intercalation compounds have also been reconsidered as useful nanohybrid and nanocomposites rather than peculiar complexes of inorganic layered crystals. The cover graphic of *Chemistry of Materials*, at its launch in 1989, symbolized intercalation and reflected the importance of intercalation compounds in materials chemistry. In fact, clay–polymer nanocomposites [20] and mesoporous silica from layered silicates [21] produced in this period stand among the most important achievements of intercalation chemistry.

Another important finding of the intercalation period was recognition of the similarities between intercalation compounds and organic molecular assemblies, such as bilayers and Langmuir–Blodgett (LB) films, based on their 2D structures. While structural similarity between alkylammonium ions in layered crystals and lipid bilayer films was pointed out in the 1970s [17], this knowledge was not used to produce new materials until the late 1980s. Materials research has progressed rapidly through the use of organic layered structures, with reference to the principles of functional bilayer films in biological systems. Along these lines, inclusion of

functional molecules in the interlayer spaces of layered crystals has been used to generate a variety of advanced materials; in particular, electro- and photofunctional materials have demonstrated characteristic features of intercalation compounds, and also shown features of organic layered molecular assemblies in various aspects. These developments ushered in the period of nanosheet research.

1.4.3 Development of Nanosheet Chemistry

In 1994, two research groups independently reported alternating assembly of exfoliated inorganic nanosheets and organic species [22, 23], which initiated the nanosheet period of research and resulted in development of new materials chemistry relating to inorganic nanosheets. The studies presented the concept of inorganic nanosheets prepared by exfoliation of layered crystals as the thinnest possible subunit of inorganic crystals. The 1994 papers used aluminosilicate (clay mineral), zirconium phosphate, and niobate nanosheets. However, among these, only clay nanosheets can be obtained spontaneously in water. Exfoliation of the clay minerals through osmotic swelling was first suggested in 1934, as described in Chap. 3 [9]. Exfoliation of the other layered crystals proceeds with the aid of appropriate organic cations, which are often called exfoliating reagents. Thus, studies were performed to evaluate intercalation processes based on exfoliating reagents, which draw solvent molecules into the interlayer spacing to induce swelling. These researches established the universality of the osmotic swelling mechanism for all layered solids, and not just clay minerals [24].

Nanosheets have been found as inorganic building blocks of the thinnest possible layers with considerable anisotropy. They have been applied to create hierarchically structured nanomaterials through alternate electrostatic stacking of anionic oxide nanosheets with organic polycations as described in Chaps. 2 and 13. Today, this technique is called the layer-by-layer (LbL) method. This method was used for the first time to fabricate multilayer films of charged colloidal particles [25], and later extended to multilayers of organic polyions and nanosheets. The development of the LbL method has enabled fabrication of various inorganic and organic nanomaterials with a broad range of compositions and scales [26]. Although the LbL method was developed as an alternative of the LB method [27], the LbL method does not require the tedious procedures used by the LB method. Hence, the LbL method has become a key technique for preparing functional multilayer films. These developments have cemented the importance of inorganic nanosheets in materials chemistry, from their limited roles as host materials in intercalation compounds to their current use as general building blocks of 2D nanostructured materials.

In parallel with these investigations, exfoliation techniques for nanosheets have been extended to a broad range of inorganic layered solids. Before 1994, exfoliation (and related phenomena) had been reported for only a few layered solids including clay minerals [9], graphite [28], transition metal dichalcogenides [29], zirconium

phosphate $Zr(HPO_4)_2$ [30], and perovskite-type niobate $HCa_2Nb_3O_{10}$ [31]. After the 1994 papers, exfoliation of other ion-exchangeable layered solids was explored, and nanosheets became available for many other layered crystals that possessed intercalation abilities. LbL film fabrication of nanosheets has also been examined.

The discovery of almost perfect graphene in 2004 [32] resulted in an explosion in publications on graphenes and related materials. These studies have also made a great impact on the materials chemistry of inorganic nanosheets. From a synthetic point of view, available target materials for exfoliation were extended from polar solids, represented by ion-exchangeable crystals, to nonpolar materials such as graphenes. These nonpolar inorganic nanosheets feature stacking mediated by van der Waals interactions rather than electrostatic attractions. More recently, nanosheets of metal chalcogenides, boron nitride, and phosphorene have been explored as "post graphenes" [33, 34]. Graphene and "post graphene" nanosheets have since attracted great attention from physicists and materials chemists, for their unique properties and potential for various device applications. The rapid development of these materials has also stimulated research on nanosheets obtained from ion-exchangeable layered solids, which have been investigated from a chemical point of view, to spur device fabrication [35, 36].

The colloidal liquid crystallinity of exfoliated nanosheets obtained from the layered metal phosphate $H_3Sb_3P_2O_{14}$, reported in 2001, clarified the soft matter behavior of inorganic nanosheets [37]. Although this system is known as an example of nanosheet liquid crystals today and can go back to 1938 [38], it has not been unambiguously established until the twenty-first century as a state of the nanosheet-based materials. Nanosheet colloids had been recognized only as reservoirs of nanosheets that are obtained as colloids through exfoliation processes in solvents. However, these nanosheet liquid crystals indicate the importance of considering nanosheets in their colloidal states. Moreover, nanosheet liquid crystals are a type of soft matter and their materials chemistry is closely related to that of organic materials and polymers. Thus, the materials science of inorganic nanosheets has expanded from pure inorganic solid-state chemistry, which is their "place of birth," into various organic and bio-related materials chemistry and physics.

1.5 Classification and Preparation of Exfoliated Nanosheets

Inorganic nanosheets prepared by exfoliation of layered solids can be classified based on the intercalation behavior of the mother layered crystals because exfoliation is an extension of intercalation. Table 1.1 lists representative layered crystals, whose exfoliation and nanosheet formation were reported. Layered crystals that can be exfoliated are categorized as ion-exchangeable and non-ion-exchangeable crystals. Ion-exchangeable crystals can be further classified into cation- and anion-exchangeable solids, where the former case occurs more widely. Non-ion-exchangeable crystals can

be classified into nonpolar and polar solids. Nonpolar layered solids are often called van der Waals (vdW) solids, where the inorganic layers are bound to each other by van der Waals interactions.

1.5.1 Nanosheets of Ion-Exchangeable Layered Solids

Ion-exchangeable layered solids are built up from electrically charged nanosheets (polyions) that are electrostatically bound through interlayer counterions. These interlayer ions can be exchanged with other ions. Further details of these exchange reactions will be described in Chaps. 2 and 3. The majority of ion-exchangeable layered solids are cation-exchangeable, i.e., constructed from negatively charged nanosheets and interlayer cations.

Among nanosheets prepared by exfoliating ion-exchangeable layered solids, those obtained from the smectite group of clay minerals have been known for a long time. Clay minerals consist of aluminosilicate layers and interlayer exchangeable cations [15]. Exchangeable cations are easily hydrated when they are small inorganic cations such as Na^+ ions. Thus, if clay powders are dispersed in water, a large amount of water molecules can be intercalated into the interlayer spaces to solvate the interlayer cations. The solvation causes infinite swelling of the interlayer spaces and exfoliates individual aluminosilicate nanosheets [10]. Such facile spontaneous exfoliation distinguishes clay minerals from other layered materials. Thus, clay scientists have handled the nanosheet colloids of clay minerals for several decades. Today, clay colloids remain an important area of clay science, as summarized in a number of textbooks [10, 11, 39].

Cation-exchangeable layered solids, other than the clay minerals, include transition element oxometallates, such as niobates, titanates, perovskite-type

Table 1.1 Classification of inorganic layered crystals that form nanosheets through exfoliation

Group	Subgroup	Example
Ion-exchangeable	Cation-exchageable	Clay minerals (montmorillonite, hectorite) Metal phosphates (α-$Zr(HPO_4)_2$) Niobates and titanates ($K_4Nb_6O_{17}$, $H_xTi_{2-x/4\cdot x/4}O_4$) Manganates ($K_xMnO_2{\cdot}nH_2O$)
	Anion-exchangeable	Layered double hydroxide [LDH; $[Mg_{1/3}Al_{2/3}(OH)_2](NO_3)_{1/3})$] Hydroxide salt ($La(OH)_2NO_3$)
Non-ion-exchangeable	Nonpolar	Graphite Metal dichalcogenides (MoS_2) Black phosphorus
	Polar	Metal carbides/nitrides (MXene; Ti_2C, Ti_3C_2) Metal phosphate ($VOPO_4{\cdot}2H_2O$)

oxometallates, and manganates, as well as metal phosphates. These systems have been investigated as mother crystals of exfoliated nanosheets [24, 40]. Anion-exchangeable layered double hydroxides (LDHs) have been used for preparing positively charged nanosheets [41]. Among these materials, clay minerals are exfoliated spontaneously. However, most of ion-exchangeable layered crystals are not spontaneously exfoliated in contrast to the clay minerals. This is ascribed to strong electrostatic binding between the layers because of their higher layer charge density. This energetic barrier can be overcome by incorporating exfoliating reagents into the interlayer space. Exfoliating reagents expand the interlayer spacing and draw solvent molecules into the interlayer space to wedge open the stacked nanosheets. All ion-exchangeable layered solids can be exfoliated if appropriate exfoliating reagents are found.

An important characteristic of nanosheet formation from ion-exchangeable layered solids is that, in principle, they can easily be exfoliated into monolayers. This is rationalized by the presence of interlayer exchangeable ions that allow for exfoliation when exchanged for appropriate exfoliating reagents. In most ion-exchangeable layered solids, the exchangeable ions are evenly distributed over the interlayer spaces at crystallographically determined positions with a fixed stoichiometry. Hence, exfoliating reagents insert into interlayers and cause successive interlayer swelling uniformly for all the interlayer spaces to exfoliate the layered crystals into monolayers. The homogeneity of interlayer reactions in ion-exchangeable layered solids is supported by the absence of higher stage structures, which are often observed in graphite intercalation compounds.

1.5.2 Nanosheets of Non-ion-Exchangeable Layered Solids

Non-ion-exchangeable layered solids used as a source of nanosheets are exemplified by graphite and transition metal dichalcogenides, which are typical vdW solids. These materials consist of nonpolar inorganic layers stacked through interlayer vdW interactions. Non-ion-exchangeable layered solids cannot be exfoliated easily because the interlayer interactions are strong, preventing penetration of solvent molecules into the interlayer spaces.

Historically, exfoliation of vdW solids has been enabled by their partial oxidation or reduction, which introduces hydrophilic moieties that can allow solvent molecules to penetrate between layers. Today, this strategy is known as chemical exfoliation. Graphite is oxidized to graphite oxide by Brodie [42] and Hummers [43] methods, which have been discovered long time ago. Because graphite oxide has polar functional groups and defects on its surfaces, it can be swollen and exfoliated in water to form graphene oxide (GO) nanosheets. Formation of colloidal GO dispersions has been known for more than 70 years [28, 44]. Conversely, metal chalcogenides have been exfoliated through partial reduction, in which small cations such as H^+ and Li^+ are incorporated into interlayer spaces to compensate for the negative charge of the reduced chalcogenides layers [29, 45, 46]. Hydration of the

interlayer cations leads to exfoliation. Although chemically exfoliated nanosheets of vdW solids had been investigated sporadically for many years, these materials were highlighted by the discovery of LbL assemblies for nanosheets of ion-exchangeable layered solids in 1994 [22, 23]. In fact, LbL assemblies of GO and metal dichalcogenide nanosheets were reported at the end of 20th century [47–50]. After the discovery of single layer graphene in 2004 [32], chemically exfoliated nanosheets of vdW solids, in particular GO, have received great attention [51–55].

However, chemical exfoliation often suffers from deterioration of both the structural and functional characteristics of the mother vdW crystals. Graphite oxidation by the Hummers method generates numerous defects in the graphite layers by destroying the π-electron system. Thus, GO nanosheets show electronic properties different from those of authentic graphene nanosheets obtained by mechanical exfoliation. In addition, the oxidation process often generates "oxidative debris" as by-products, which attach to the GO nanosheets and affect their properties [56, 57]. For metal dichalcoegnides, the reduction of the chalcogenide layers by oxidative intercalation of alkali metals or hydrogen atoms alters the electronic structure of the chalcogenides. As an alternative to such harsh modification of the mother crystals, exfoliation under moderate conditions has been examined with organic species, such as surfactants and polymers, which behave as exfoliating reagents that do not react with the layers [53]. However, these species tend to cover the nanosheet surfaces and inhibit physicochemical interactions with molecules surrounding the nanosheets.

To overcome these disadvantages, direct exfoliation of the vdW solids in solvents without exfoliating reagents has been developed recently [58, 59]. This strategy is called liquid phase exfoliation [60]. Liquid phase exfoliation is possible if the vdW interactions between the stacked nanosheets can be overwhelmed by the nanosheet–solvent interactions. Thus, selection of appropriate solvents is a key, and the Hansen solubility parameter is often used as a measure for this purpose. The exfoliated nanosheets are usually obtained by ultrasonication. However, this technique is inappropriate for preparing nanosheets with large lateral sizes because ultrasonication often crushes the nanosheets. Liquid phase exfoliation was first used for graphite, and then extended to other vdW solids such as boron nitride [61], graphitic carbon nitride [62], molybdenum oxide [63], and black phosphorus [64, 65], to provide many post graphene nanosheets.

Some post graphene nanosheets have also been obtained by chemical interlayer etching of the mother layered crystals. Silicon nanosheets can be prepared from $CaSi_2$ by selective leaching of Ca with an acid treatment. This technique was originally developed for preparing the layered siloxane polymer $Si_6H_3(OH)_3$ or layered polysilane Si_6H_6; however, careful termination of the Si–H bonds yields organically modified silicon nanosheets dispersed in nonpolar solvents [66, 67]. Another example has been reported for exfoliated nanosheets of transition metal carbides/nitrides, designated as MXene [68, 69]. The mother crystals of these materials are ternary layered metal carbides and nitrides known as MAX phases, where M is transition metal, A is group 13 or 14 element, and X is C or N [70, 71]. An MXene can be obtained by acid leaching of the A element from the MAX phase, followed by exfoliation to form nanosheets in water (Fig. 1.6).

Non-ion-exchangeable layered materials, other than the vdW solids, have also been exfoliated. Typical examples are layered metal phosphates and phosphonates. These nanosheets have been investigated along with those of ion-exchangeable metal phosphates. Vanadyl phosphate $VOPO_4 \cdot 2H_2O$ has been exfoliated via exchange of interlayer water molecules, which attach to the oxide layers by hydrogen bonding, for polar organic molecules and subsequent swelling in polar organic solvents [72, 73]. Another recent study has reported direct liquid phase exfoliation of this compound [74]. Lanthanide organophosphonates have been exfoliated directly in organic solvents through interactions between organic moieties on the layer surfaces and solvent molecules [75]. The exfoliated nanosheets are porous and form a type of metal-organic framework (MOF) because their structure is built from coordination of organophosphate ligands to the lanthanide cations. MOF nanosheets have also been prepared by exfoliation of a layered MOF, constructed from copper coordinated by bipyridine-based ligands (Fig. 1.7) [76]. Porous nanosheets have also been reported for exfoliation of layered aluminosilicates that can be used as precursors for zeolites [60, 77]. The exfoliation proceeds in organic solvents through incorporation of melt polymers.

For the exfoliation of non-ion-exchangeable solids, it should be noted that complete exfoliation into monolayers is rather difficult. The exfoliated nanosheets usually have a distribution of thickness as well as a range of lateral lengths. This tendency is particular serious for vdW solids that have a low driving force for intercalation. Such vdW solids lack mechanisms that allow stoichiometric intercalation of guest molecules equally into all the interlayer spaces, unlike ion-exchangeable layered solids. Ion-exchangeable solids generally incorporate guest molecules into all the interlayer spaces uniformly through exchange of ions

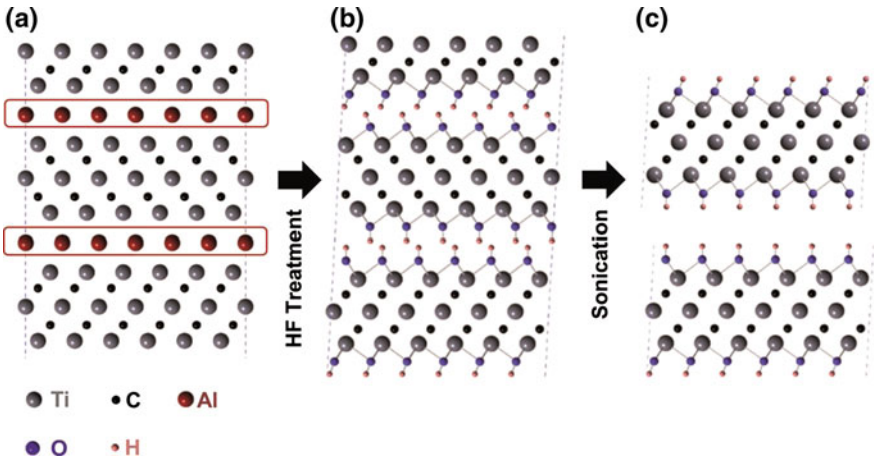

Fig. 1.6 Schematic of the exfoliation process for Ti_3AlC_2 (MAX phase). **a** Ti_3AlC_2 structure. **b** Al atoms replaced by OH after reaction with HF. **c** Formation of Ti_3C_2 (MXene) nanosheets by breakage of the hydrogen bonds and separation with sonication. Reprinted with permission from [69]. Copyright 2011 John Wiley & Sons, Inc

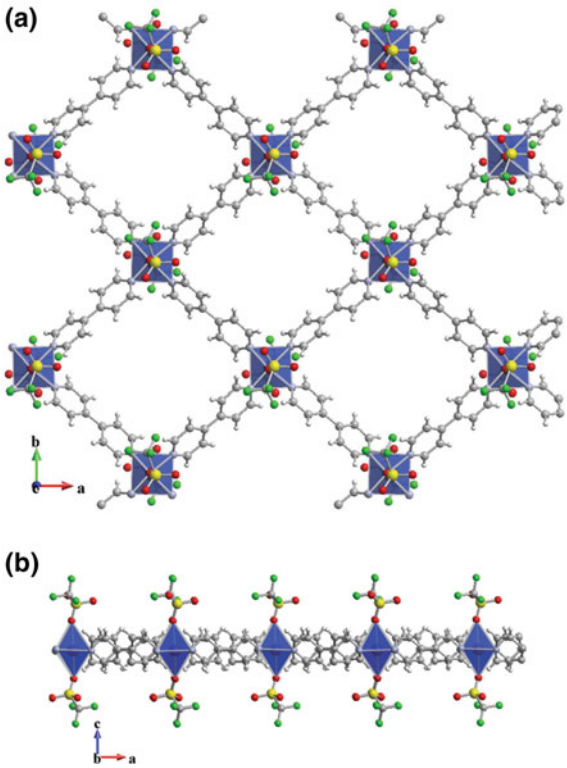

Fig. 1.7 Schematic representation of a nanosheet of CuMOF **a** along the *c* axis and **b** along the *b* axis. The coordination sphere of Cu(II) ions is shown as a *blue octahedron*. Reprinted with permission from [76]. Copyright 2013 Royal Society of Chemistry

stoichimetrically distributed between the charged inorganic layers. However, the structures of vdW solids do not permit insertion of guest molecules into all the interlayer spaces to the same degree. This effect is commonly seen in GO. During the oxidation of graphite, oxygen-containing groups such as epoxides and carboxylates become attached to the graphite surfaces [78]. However, these groups are not grafted with the same composition over all the graphite layers. As a result, the interlayer spaces of GO vary; some interlayer spaces allow for easy exfoliation while others can only be exfoliated with difficulty. For these reasons, monolayer exfoliation should not be assumed to occur in studies of these nanosheets. In fact, many recent papers use the term of "few-layer" nanosheets [79–81].

1.6 Nanosheet-Based Nanostructures

We can produce various nanostructured materials using exfoliated inorganic nanosheets as the building blocks. The 2D nature of nanosheets can be applied to obtain unusual nanostructures that are hardly organized from building blocks other than the nanosheets. Figure 1.8 gives an overview of typical nanosheet-based

structures with their preparation routes. Hierarchical structures can be organized if secondary building units are included, which interact with the crystallographically defined nanosheets, to create large-scale integrated structures.

One of the simplest organizations of nanosheets is reconstruction of the layered structures. Swelling and exfoliation of layered crystals has been recognized as a method to confine guest species that are difficult to be incorporated into interlayer spaces by direct intercalation reactions [22, 23]. In particular, intercalated structures of smectite-type clay minerals have been prepared via an exfoliation–reconstruction pathway with clay nanosheets and polymers. Direct intercalation of polymers into other layered solids is usually difficult if spontaneous exfoliation does not take place [82, 83]. Polymer–clay nanocomposites, where exfoliated clay nanosheets are randomly and almost homogeneously dispersed, in organic polymers has been innovated along this line [20].

Advances in LbL assembly of nanosheets have greatly extended the range of potential nanosheet-based layered structures. The LbL technique allows tailor-made stacking of more than two nanosheet species with arbitrary sequences as described in Chap. 2. This contrasts with the above-mentioned conventional restacking technique, which yields only one stacking sequence determined by the combination of nanosheets and interlayer species. With the electrostatic LbL assembly and the Langmuir–Blodgett (LB) methods, a number of nanosheet-based 2D structures have been organized, and various thin-film devices have been developed by controlling the stacking sequence of the nanosheets.

Integration of exfoliated nanosheets is possible not only in the interlayer direction (vertical to the layer surface) but also in the lateral one (parallel to the surface). On the basis of their 2D shape, exfoliated nanosheets deposited on flat substrates can be oriented parallel to the substrate surface. Various techniques such as drop-casting and spin-coating have been used for preparing high-quality films. Appropriate deposition of single nanosheets on a substrate provides inorganic

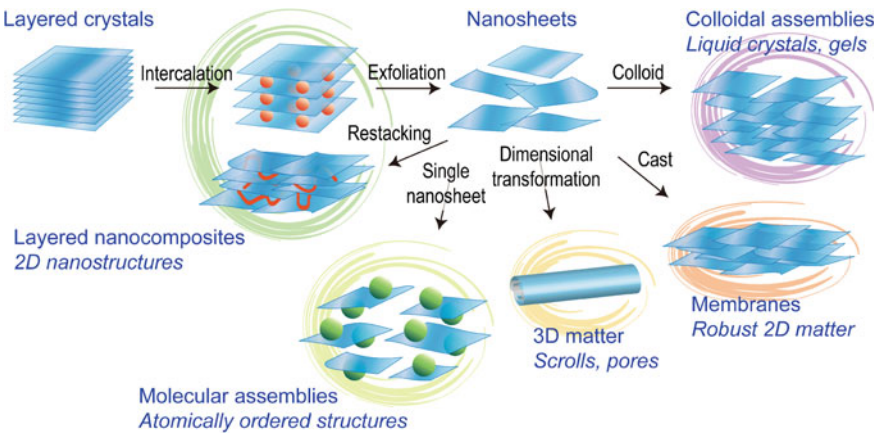

Fig. 1.8 Overview of typical nanosheet-based structures and their preparation routes

monolayers, which can be used, for example, to form a p–n junction of semiconducting nanosheets, as described in Chap. 17. Self-standing oriented nanosheet films can be prepared by peeling films from the substrate. While both supported and self-standing films have been routinely prepared with clay nanosheets for many years, those of other types of nanosheets have also only been developed in recent decades. Examples include photocatalytic and superhydrophilic TiO_2 coatings prepared from titanate nanosheets [84] and electrically conducting papers made of self-standing graphene nanosheets, which are also known as "graphene paper" [85]. Optically transparent membranes for use in optical devices have also been prepared by precisely controlled deposition of the clay nanosheets, as described in Chap. 19.

When solvent is removed from colloidal dispersions of exfoliated nanosheets by evaporation or freeze drying without any special care, the nanosheets form aggregates with a low degree of order. In these aggregates, the nanosheets are partly stacked to form secondary building blocks with low stacking regularity and broad size distributions. These secondary blocks are assembled, almost randomly, to form porous structures. These porous aggregates, characterized as "house-of-cards" structures, have long been known to occur for nanosheets of smectite-type clay minerals [10]. Similar structures have since been obtained for other nanosheets. This disordered aggregation is the most simple and effective protocol to take advantage of the large surface areas of nanosheets in the solid state and does not require precisely controlled architectures. In fact, aggregation of the nanosheets of vdW solids in a house-of-cards manner produces aerogels [86–88]. These are prepared by crosslinking chemically exfoliated nanosheets at functional groups introduced during the exfoliation. Pores are generated as internal voids between the nanosheets partly cross-linked in particular at their edges; honeycomb cellular structures are often observed based on these structures. The viscoelasticity and deformation at macroscopic scales observed for these aerogels manifest the high mechanical strength of the nanosheets. The void structures and properties are attributed to effective use of the nanosheets even though their manner of aggregation is almost random.

1.7 Application of the Nanosheets to Advanced Materials

Inorganic nanosheets have been used for a broad range of applications. As mentioned above, the characteristic properties of nanosheet-derived materials can be attributed to their low-dimensionality. The 2D nature is related to various features of nanosheets such as the crystalline surfaces, the anisotropically confined nanospaces, the layer thinness, and the colloidal properties. Although many examples of nanosheet-based advanced materials will be presented in the following Chapters, here we survey these applications in relation to the low-dimensionality of the nanosheets.

1.7.1 Applications of Single Nanosheets

Although nanosheets tend to stack intrinsically and exist in multilayer states in the solid states, the basic unit is single nanosheet. Thus, understanding the nature of individual nanosheets is important. In the case of clay–polymer nanocomposites, clay nanosheets are present as single or a few-layer stacks, which confer functionalities such as an enhancement of flame resistance and gas barrier abilities. In this case, the high aspect ratio of the nanosheet plays an important role for its functionality. Full details of clay–polymer nanocomposites will be described in Chaps. 7 and 21. Stacked nanosheet conditions are important for use in many applications; however, single nanosheets are unique and interesting from the perspective of basic research owing to their simplicity. From the viewpoint of host–guest chemistry, nanosheets can be considered as a unique type of host material, which possesses an atomically flat surface. Among various nanosheets, cation-exchangeable clay minerals can be exfoliated easily under aqueous conditions because of the repulsion of their electric double layer. The exfoliated state is stable and substantially transparent, and is thus suitable for basic scientific observations. Recently, research interest has increased with regards to complex formation behavior between exfoliated single nanosheets and guest molecules, such as simple organic molecules and dyes, as described in Chap. 14. Guest molecules interact with nanosheets through electrostatic, vdW, and hydrophobic interactions. Electrostatic interactions in particular can be intentionally modulated using various types of clay minerals. For smectite-type clay minerals, isomorphous substitution in the aluminosilicate layers, such as substitution of Si^{4+} in tetrahedral sheets by Al^{3+}, and substitution of Al^{3+} in octahedral sheets by Mg^{2+}, produces anionic charges in the structure (Fig. 1.9). It has been reported that the substitution ratio can be controlled and the charge density can be modulated [89]. For Li^{+}-type homoionic clay minerals, it is possible to control the charge density by chemical treatments [90, 91]. Modifications to the charge density of the layers directly affects the adsorption behavior of guest molecules, as described below.

Single molecules on nanosheet surfaces can feature molecular structures that differ from their most stable structure in solution. Nanosheets possess extremely flat surfaces, and the structure of the guest molecules should reflect these steric characteristics. Guest molecules on the nanosheets tend to be flatter and more rigid than when in solution. Some researchers have reported that photochemical properties,

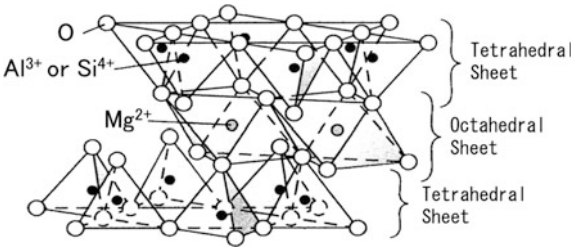

Fig. 1.9 Isomorphous substitution of Si^{4+} by Al^{3+} in the tetrahedral sheet of clay structure

such as absorption and emission, can be drastically modulated by complex formation with clays [92, 93]. These changes of photochemical properties can be explained by the above-mentioned mechanisms. For the case of methyl viologen, the fluorescence quantum yield increased by a several orders of magnitude when a complex was formed with clay [94, 95]. Adsorption behavior has been studied based on temperature and solvent effects, which can modulate the adsorption tilt angle of the adsorbate, with respect to the clay surface [96, 97].

From the viewpoint of assembling structures on nanosheet surfaces, the distribution and aggregation of adsorbed molecules depends on the charge density of nanosheets. For amorphous host materials, a precise analysis of the surface assembly is difficult. Thus, clay surfaces are valuable as an ideal inorganic surfaces for studies. Many researchers have reported the aggregation behavior of dyes on exfoliated single layer clay surfaces, as described in Chap. 14. Depending on the charge density of the nanosheet, various types of aggregates, such as J and H type aggregates can form [98]. Conversely, some types of dye molecules behave as single molecules even at high densities on clay surfaces under specific conditions. Achieving such a high density of chromophores, without any aggregation effects, is useful for constructing photofunctional materials, because they retain intrinsic lifetime of excited states. This effect is known as a size-matching effect [99] and the full details will be described in Chap. 14.

The fundamental understanding of single exfoliated nanosheets is also useful for understanding the precise stacking of layered systems.

1.7.2 Applications of Two-Dimensional Nanospaces

Materials that use specific features of three-dimensionally (3D) restricted spaces, such as the spaces provided by zeolites or MOFs, have attracted considerable interest. In these materials, restricted spaces are used for molecular recognition, as catalysts, and reaction sites. Two-dimensional (2D) nanospaces can also be constructed by stacking of nanosheets. These structures can be used for realizing specific functionalities and characteristics of restricted microenvironments. One advantage of 2D nanospaces compared with 3D spaces is the tunability of the microenvironment of the restricted space, as shown in Fig. 1.10. By incorporation of different chemical species, the height and/or polarity of the microenvironment can be flexibly tuned. Furthermore, anisotropic microenvironments can easily be constructed.

2D nanospaces are commonly applied as adsorbents. Full details of these applications are described in Chaps. 6 and 9. The interlayer distance of a hybrid material consisting of a nanosheet and an organic compound corresponds to the size of the intercalated compound. By selecting the size of the intercalated molecule, hybrid materials possessing nanospaces with a desirable size can be fabricated [100]. When an organic molecule that possesses the ability to form a supramolecular assembly has been incorporated into the hybrid materials that can

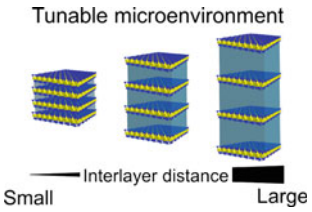

Fig. 1.10 Schematic representation of tunable interlayer distance of stacked nanosheets. For example, the interlayer distance of smectites varies depending on humidity. This is because the amount of water hydrated to the exchangeable interlayer cation varies

be used as an adsorbent capable of recognizing specific molecules with high selectivity [8].

The 2D interlayer space between nanosheets can also be used as a specific microenvironment for chemical reactions. In the 2D space, the direction of molecular motion of incorporated molecules is restricted in the in-plane direction. Therefore, reactions will preferentially occur with other chemical species that approach from the in-plane direction. These systems may allow selective synthesis of molecules with highly stereospecific structures [101] and control over the direction of energy transfer reactions [102].

Recently, it has been shown that a stress is imposed on molecules in 2D and 3D microspaces. For example, oxygen molecules confined to MOFs experience a high-pressure field that corresponds to a few GPa [103]. Although the 3D nanospaces provided by zeolites or MOFs can only confine molecules with sizes and structures that fit into the 3D space, 2D nanospaces can incorporate a wider range of chemical species owing to their flexible height and the additional degrees of freedom in the in-plane directions. In 2D nanospace, a uniaxial force is imposed on a confined molecule, which may enhance its planarity. When a molecule with a large π-electron system is confined, the π-conjugation is often extended in the 2D nanospace. The extension of π-conjugation results in larger nonlinear optical responses from the confined molecules [104, 105]. The uniaxial force also suppresses vibrational motion of the confined molecules. This suppression often enhances the luminescence quantum yields of confined molecules [93].

1.7.3 Applications Based on Thinness of the Nanosheets

The 2D planar shape of nanosheets and their extreme thinness of around 1 nm have inspired applications in nanofilm devices. The 2D morphology of nanosheets can regulate the direction of energy, electron, and molecular transfer. Anisotropic transfer on nanosheets can be used to create functionally graded devices, which are

not simple miniatures of commercially available devices and difficult to produce from assemblies of 3D nanoparticles. Various electronic, optic, and magnetic devices have been proposed through nanosheet organizations, such as the LbL assemblies, in the past decade.

For nanosheets prepared by exfoliation of ion-exchangeable layered solids, device preparation is mainly achieved by LbL organization of nanosheets that can be selected from a rich library of compounds. As described in Chap. 3, the nanosheet library of the ion-exchangeable layered solids involves numerous transition element oxometallates and hydroxides with a wide range of compositions. These include electrically conducting, semiconducting, and dielectric materials which exhibit various functions such as photocatalytic, magnetic, and electrochemical activities. Stacking such nanosheets in a desired sequence can yield a variety of functional superlattices. As a result, a number of functional nanofilms have been prepared for applications in ferroelectrics, rechargeable batteries, supercapacitors, field-effect transistors, ferromagnetics, and magneto-optics, as described in chapters in Part II.

Device organizations that use nanosheets of vdW solids tend to achieve the desired nanosheet function by adjusting the electronic properties of the nanosheet rather than by combination with other types of nanosheets. This tendency is related to the variability of the nanosheet's oxidation state in these applications. For example, the oxidation state of graphene nanosheets can be controlled by oxidation to GO and by re-reduction to reduced GO, which the processes can adjust the amounts of functional groups and defects present [106, 107]. Metal dichalcogenide nanosheets can also be modified to change their oxidation state [108]. Appropriately modified nanosheets with the desired electronic properties can be integrated with other building blocks to assemble various functional devices, such as electrodes for lithium-ion batteries, photovoltaic cells, composite photocatalysts, and fluorescence sensors [109–114].

Functional membranes are another application of stacked nanosheets. Deposition of nanosheets dispersed in a solvent on a substrate by coating methods or filtration induces stacking of nanosheets. These structures can yield supported or freestanding nanosheet membranes. The 2D morphology of nanosheets can stabilize the membranes, which results in a lower thickness than that possible from conventional 3D particles, allowing for efficient mass transfer with a high flux. Membranes of aluminosilicate nanosheets of zeolite precursors deposited by suction filtration can be converted to zeolite membranes after calcination, which exhibit molecular sieving effects [115]. Freestanding membranes prepared by deposition and subsequent reduction of GO nanosheets can produce conducting papers usable in electric devices [116, 117]. Selectively permeable reduced GO membranes (Fig. 1.11) [118] can also be used for separation of emulsified oil and water [119]. Metal dichalcogenide and LDH nanosheets have also been fabricated as selective permeation membranes [120–122].

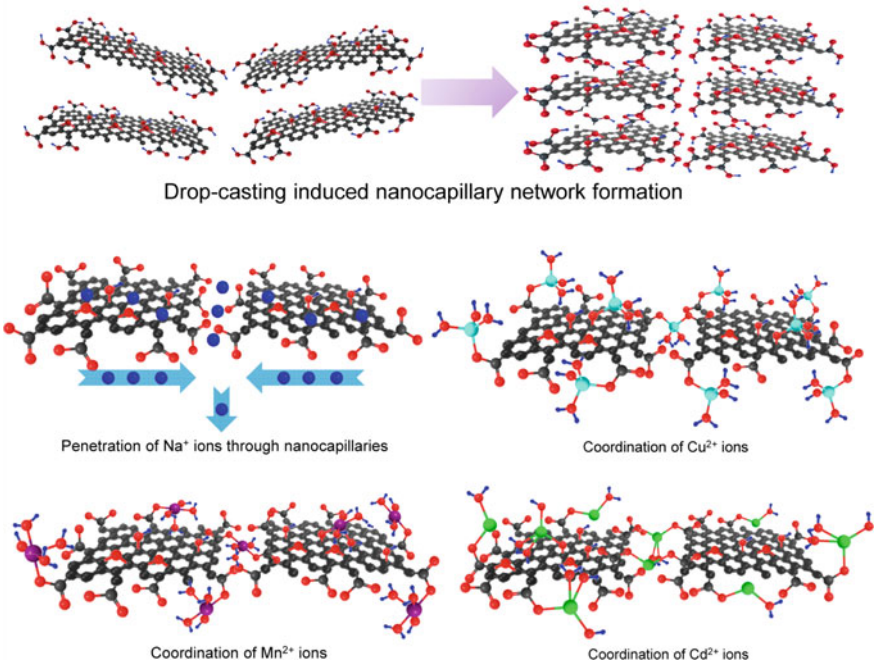

Fig. 1.11 Schematic diagrams of the structure of a GO membrane and interactions with different ions for the selective permeation. Reprinted with permission from [118]. Copyright 2013 American Chemical Society

1.7.4 Applications Based on the High Surface Area of the Nanosheets

An important characteristic of nanosheets is that "they are all surfaces." Exfoliation of layered solids exposes their internal spaces to the external atmosphere and greatly enlarges their surface area. In monoatomic-thick nanosheets, such as graphene, all the constituting atoms are surface atoms. Thus, these nanosheets have been applied in situations requiring materials with surface-area-dependent functions such as adsorbents, catalysts, and electrodes. The use of these nanosheets as biomaterials, exemplified by enzyme and drug carriers is also a growing area of research.

Adsorbents are a representative application of inorganic layered solids as described in Chap. 9. The surfaces and interlayer spaces of layered crystals function as adsorption sites. Their adsorption properties can be improved by various strategies: for example, enlargement of the external surfaces with house-of-cards structures [10] and modification of the interlayer spaces to alter their

hydrophobicity and molecular selectivity [8]. The most widely studied materials are smectite-type clay minerals, whose adsorption properties have been examined for a range of adsorbates including molecular organic pollutants and heavy metals [123, 124]. Clay adsorbents can be used practically as clay liners that act as leachate barriers for waste repositories [125]. Layered titanates and clay minerals are also applicable as adsorbents for radioactive nuclear waste [126, 127]. LDHs are promising adsorbents for pharmaceutical compounds because of their biocompatibility [128]. Graphenes are often applied as adsorbents in the form of aerogels that can be prepared by cross-linking GO nanosheets (see Sect. 1.6 of this chapter) [129]. The electrical conductivity of graphenes allows the aerogels to be used in electrochemical devices, with applications in energy storage and sensing. These materials can also function as easily reusable adsorbents that can release the adsorbed species by squeezing the aerogels [130].

Catalysts are another typical use of inorganic layered solids and their nanosheets. Clay minerals exhibit acidity which can catalyze various organic reactions [131, 132]. In fact, acidic clays were used industrially as catalysts for crude oil cracking. Although these materials have now been replaced by zeolites in industry, clay catalysis has been continuously investigated to develop many characteristic reactions [133]. Furthermore, layered niobates, tantalates, and titanates and their nanosheets, which are characterized by wide band-gap semiconducting nature, have been investigated as photocatalysts [134, 135]. Exfoliation of layered semiconductors into nanosheets can improve their photocatalytic activities because of the large surface area of the nanosheets. Applications to electrocatalysts, i.e., as electrode materials and photocatalysts, have been investigated, particularly for nanosheets of graphenes and metal dichalcogenides, based on their electronic properties [109, 111, 112].

1.7.5 Applications of Colloidally Dispersed State of the Nanosheets

As described above, the exfoliated nanosheets are usually obtained as colloids, which give applications impossible in the solid state. The use of colloidal nanosheets is related to organization of specific colloidal structures through cooperation of the nanosheets and solvent molecules. Colloids are a kind of soft matter. While nanosheets assemblies in the solid state are recognizable as a type of hard matter, colloidal nanosheets have soft structures by themselves and in composites with other organic soft matter such as polymers.

The liquid crystalline phases of colloidal nanosheets are a typical example of the soft matter properties of nanosheets [136, 137], as described in Chap. 8. The orientation and ordering of liquid crystalline nanosheets, accompanied by their

fluidity, endows nanosheet–polymer nanocomposites with anisotropic properties as represented by their mechanical and stimuli response behaviors [138, 139]. Liquid crystalline GO nanosheets yields fibers with improved mechanical strength [140]. Even when nanosheets do not form liquid crystalline structures, careful control of their colloidal state can facilitate the preparation of unusual nanosheet–polymer nanocomposites. Typical examples include clay–polymer hydrogels with large amounts of internal water and high elasticity [141, 142].

Agglomerated inorganic layered solids and their nanosheets have found characteristic applications in colloidal systems. Stabilization of interfaces in heterogeneous systems such as oil–water and air–water interfaces is one such application [143]. When the surfaces of inorganic powders are appropriately modified, they can be agglomerated at interfaces to stabilize liquid or air droplets in continuous phases. Examples include liquid droplets stabilized in nonmiscible liquids by solids, liquid droplets stabilized in air, and air droplets stabilized in liquids, which are called Pickering emulsions, liquid marbles, and foams, respectively [144, 145]. The plate-like morphology of inorganic particles is assumed to contribute the stability of such droplets [146–148]. Conversely, reversible agglomeration of the particles in nonpolar liquids under external electric fields can be used to control liquid fluidity. Such particle–liquid systems are called electrorheological fluids, and are expected to have applications in clutches, dampers, valves, and so forth [149]. GO nanosheets have also been investigated for these purposes [150, 151].

1.8 Outlook

The materials chemistry of inorganic nanosheets has been explored as an extension of intercalation chemistry, because exfoliation of layered crystals owes its fundamentals to intercalation phenomena. Today, we have a rich library of the inorganic nanosheets based on progress in intercalation chemistry on diverse inorganic layered crystals. However, the nanosheet-based materials are greatly expanded from conventional intercalation compounds, which means development from host–guest systems to nanointegrated systems. Exfoliated nanosheets can be assembled into a variety of nanostructured materials. These nanostructures are characterized by anisotropy or asymmetry based on the 2D nature of the nanosheets, which leads to unusual functions that cannot be attained in the mother layered crystals or conventional intercalation compounds. Nanosheet assemblage is not limited to the construction of nanometer-level structures but can also be employed for the organization of hierarchical structures: from multilayer films inspired by intercalated structures to macroscopic structures featuring 3D materials with a local 2D nature induced by nanosheets. Such developments suggest great potential for broad applications of inorganic nanosheets to composite, hybrid, multiscale, and functionally graded materials. The use of nanosheets with other moieties will continue to blur the boundaries of inorganic/organic, 1D/2D/3D, and hard/soft materials. The

following chapters of this book introduce a number of examples of nanosheet preparations, structural organizations, and chemical and physical functions.

References

1. Miyamoto Y (1999) Functionally graded materials: design, processing, and applications. Kluwer Academic Publishers, Boston
2. Auerbach SM, Carrado KA, Dutta PK (eds) (2004) Handbook of layered materials. Marcel Dekker, New York
3. Geng F, Ma R, Nakamura A, Akatsuka K, Ebina Y, Yamauchi Y, Miyamoto N, Tateyama Y, Sasaki T (2013) Nat Commun 4:1632
4. Sasaki T, Watanabe M, Hashizume H, Yamada H, Nakazawa H (1996) J Am Chem Soc 118:8329
5. Miyamoto N, Yamamoto H, Kaito R, Kuroda K (2002) Chem Commun 2378
6. Whittingham MS, Jacobson AJ (eds) (1982) Intercalation chemistry. Academic Press, New York
7. Ogawa M, Kuroda K (1995) Chem Rev 95:399
8. Okada T, Seki Y, Ogawa M (2014) J Nanosci Nanotechnol 14:2121
9. Barbier G (1934) Compt Rend 199:226
10. van Olphen H (1991) Clay colloid chemistry, reprinted edn. Krieger, Malabar
11. Smalley M (2006) Clay swelling and colloid stability. Taylor & Francis, Boca Raton
12. In ancient Greek, the term “synthesis” means “to put together” while “analysis” means “to dissolve”
13. Ubbelohde AR, Lewis FA (1960) Graphite and its crystal compounds. Clarendon Press, Oxford
14. Lévy FA (ed) (1979) Intercalated layered materials. D. Reidel, Dordrecht
15. Theng BKG (1974) The chemistry of clay-organic reactions. Wiley, New York
16. Lehn JM (1995) Supramolecular chemistry: concepts and perspectives. VCH, Weinheim
17. Kunitake T (1979) J Macromol Sci, Chem A13:587
18. Kunitake T (1992) Angew Chem Int Ed Engl 31:709
19. Nanotechnology Timeline. United States National nanotechnology initiative, http://www.nano.gov/timeline. Accessed 1 Aug 2016
20. Usuki A, Kojima Y, Kawasumi M, Okada A, Fukushima Y, Kurauchi T, Kamigaito O (1993) J Mater Res 8:1179
21. Yanagisawa T, Shimizu T, Kuroda K, Kato C (1990) Bull Chem Soc Jpn 63:988
22. Kleinfeld ER, Ferguson GS (1994) Science 265:370
23. Keller SW, Kim H-N, Mallouk TE (1994) J Am Chem Soc 116:8817
24. Ma R, Sasaki T (2010) Adv Mater 22:5082
25. Iler RK (1966) J Colloid Interface Sci 21:569
26. Decher G (1997) Science 277:1232
27. Blodgett KB (1935) J Am Chem Soc 57:1007
28. Hofmann U, Holst R (1939) Ber Dtsch Chem Ges 72:754
29. Murphy DW, Hull GW Jr (1975) J Chem Phys 62:973
30. Alberti G, Casciola M, Costantino U (1985) J Colloid Interface Sci 107:256
31. Treacy MMJ, Rice SB, Jacobson AJ, Lewandowski JT (1990) Chem Mater 2:279
32. Novoselov KS, Geim AK, Morozov SV, Jiang D, Zhang Y, Dubonos SV, Grigorieva IV, Firsov AA (2004) Science 306:666
33. Xu M, Liang T, Shi M, Chen H (2013) Chem Rev 113:3766
34. Bhimanapati GR, Lin Z, Meunier V, Jung Y, Cha J, Das S, Xiao D, Son Y, Strano MS, Cooper VR, Liang LB, Louie SG, Ringe E, Zhou W, Kim SS, Naik RR, Sumpter BG,

Terrones H, Xia FN, Wang YL, Zhu J, Akinwande D, Alem N, Schuller JA, Schaak RE, Terrones M, Robinson JA (2015) ACS Nano 9:11509
35. Osada M, Sasaki T (2012) Adv Mater 24:210
36. Kim IY, Jo YK, Lee JM, Wang L, Hwang S-J (2014) J Phys Chem Lett 5:4149
37. Gabriel J-CP, Camerel F, Lemaire BJ, Desvaux H, Davidson P, Batail P (2001) Nature 413:504
38. Langmuir I (1938) J. Chem. Phys. 6:873
39. Güven N, Pollastro RM (eds) (1992) Clay-water interface and its rhelogical implications. The Clay Minerals Society, Aurora
40. Gunjakar JL, Kim IY, Lee JM, Jo YK, Hwang S-J (2014) J Phys Chem C 118:3847
41. Duan X, Evans DG (2005) Layered double hydroxides. Springer, Berlin
42. Brodie BC (1859) Philos Trans 149:249
43. Hummers WS Jr, Offeman RE (1958) J Am Chem Soc 80:1339
44. Thiele H (1948) Kolloid-Z 111:15
45. Lerf A, Schöllhorn R (1977) Inorg Chem 16:2950
46. Clement R, Garnier O, Jegoudez J (1986) Inorg Chem 25:1404
47. Kotov NA, Dékány I, Fendler JH (1996) Adv Mater 8:637
48. Cassagneau T, Fendler JH (1998) Adv Mater 10:877
49. Kovtyukhova NI, Ollivier PJ, Martin BR, Mallouk TE, Chizhik SA, Buzaneva EV, Gorchinskiy AD (1999) Chem Mater 11:771
50. Tachibana H, Yamanaka Y, Sakai H, Abe M, Matsumoto M (2000) Chem Mater 12:854
51. Dreyer DR, Park S, Bielawski CW, Ruoff RS (2010) Chem Soc Rev 39:228
52. Eda G, Chhowalla M (2010) Adv Mater 22:2392
53. Georgakilas V, Otyepka M, Bourlinos AB, Chandra V, Kim N, Kemp KC, Hobza P, Zboril R, Kim KS (2012) Chem Rev 112:6156
54. Nicolosi V, Chhowalla M, Kanatzidis MG, Strano MS, Coleman JN (2013) Science 340:1226419
55. Zhang H (2015) ACS Nano 9:9451
56. Rourke JP, Pandey PA, Moore JJ, Bates M, Kinloch IA, Young RJ, Wilson NR (2011) Angew Chem Int Ed Engl 50:3173
57. Coluci VR, Martinez DST, Honório JG, de Faria AF, Morales DA, Skaf MS, Alves OL, Umbuzeiro GA (2014) J Phys Chem C 118:2187
58. Coleman JN, Lotya M, O'Neill A, Bergin SD, King PJ, Khan U, Young K, Gaucher A, De S, Smith RJ, Shvets IV, Arora SK, Stanton G, Kim HY, Lee K, Kim GT, Duesberg GS, Hallam T, Boland JJ, Wang JJ, Donegan JF, Grunlan JC, Moriarty G, Shmeliov A, Nicholls RJ, Perkins JM, Grieveson EM, Theuwissen K, McComb DW, Nellist PD, Nicolosi V (2011) Science 331:568
59. Valles C, Drummond C, Saadaoui H, Furtado CA, He M, Roubeau O, Ortolani L, Monthioux M, Penicaud A (2008) J Am Chem Soc 130:15802
60. Varoon K, Zhang X, Elyassi B, Brewer DD, Gettel M, Kumar S, Lee JA, Maheshwari S, Mittal A, Sung CY, Cococcioni M, Francis LF, McCormick AV, Mkhoyan KA, Tsapatsis M (2011) Science 334:72
61. Zhi C, Bando Y, Tang C, Kuwahara H, Golberg D (2009) Adv Mater 21:2889
62. Yang S, Gong Y, Zhang J, Zhan L, Ma L, Fang Z, Vajtai R, Wang X, Ajayan PM (2013) Adv Mater 25:2452
63. Alsaif MM, Latham K, Field MR, Yao DD, Medhekar NV, Beane GA, Kaner RB, Russo SP, Ou JZ, Kalantar-zadeh K (2014) Adv Mater 26:3931
64. Brent JR, Savjani N, Lewis EA, Haigh SJ, Lewis DJ, O'Brien P (2014) Chem Commun 50:13338
65. Hanlon D, Backes C, Doherty E, Cucinotta CS, Berner NC, Boland C, Lee K, Harvey A, Lynch P, Gholamvand Z, Zhang S, Wang K, Moynihan G, Pokle A, Ramasse QM, McEvoy N, Blau WJ, Wang J, Abellan G, Hauke F, Hirsch A, Sanvito S, O'Regan DD, Duesberg GS, Nicolosi V, Coleman JN (2015) Nat Commun 6:8563
66. Okamoto H, Sugiyama Y, Nakano H (2011) Chem Eur J 17:9864

67. Okamoto H, Kumai Y, Sugiyama Y, Mitsuoka T, Nakanishi K, Ohta T, Nozaki H, Yamaguchi S, Shirai S, Nakano H (2010) J Am Chem Soc 132:2710
68. Naguib M, Mochalin VN, Barsoum MW, Gogotsi Y (2014) Adv Mater 26:992
69. Naguib M, Kurtoglu M, Presser V, Lu J, Niu J, Heon M, Hultman L, Gogotsi Y, Barsoum MW (2011) Adv Mater 23:4248
70. Barsoum MW (2000) Prog Solid State Chem 28:201
71. Radovic M, Barsoum MW (2013) Am Ceram Soc Bull 92(3):20
72. Nakato T, Furumi Y, Okuhara T (1998) Chem Lett 611
73. Yamamoto N, Okuhara T, Nakato T (2001) J Mater Chem 11:1858
74. Wu C, Lu X, Peng L, Xu K, Peng X, Huang J, Yu G, Xie Y (2013) Nat Commun 4:2431
75. Araki T, Kondo A, Maeda K (2013) Chem Commun 49:552
76. Kondo A, Tiew CC, Moriguchi F, Maeda K (2013) Dalton Trans 42:15267
77. Maheshwari S, Jordan E, Kumar S, Bates FS, Penn RL, Shantz DF, Tsapatsis M (2008) J Am Chem Soc 130:1507
78. Lerf A, He HY, Forster M, Klinowski J (1998) J Phys Chem B 102:4477
79. Niyogi S, Bekyarova E, Itkis ME, McWilliams JL, Hamon MA, Haddon RC (2006) J Am Chem Soc 128:7720
80. Wei Y, Sun Z (2015) Curr Opin Colloid Interface Sci 20:311
81. Ganatra R, Zhang Q (2014) ACS Nano 8:4074
82. Enea O, Bard AJ (1986) J Phys Chem 90:301
83. Theng BKG (1982) Clays Clay Miner 30:1
84. Sasaki T, Ebina Y, Fukuda K, Tanaka T, Harada M, Watanabe M (2002) Chem Mater 14:3524
85. Chen H, Müller MB, Gilmore KJ, Wallace GG, Li D (2008) Adv Mater 20:3557
86. Worsley MA, Pauzauskie PJ, Olson TY, Biener J, Satcher JH, Baumann TF (2010) J Am Chem Soc 132:14067
87. Zeng X, Ye L, Sun R, Xu J, Wong CP (2015) Phys Chem Chem Phys 17:16709
88. Li C, Shi G (2014) Adv Mater 26:3992
89. Egawa T, Watanabe H, Fujimura T, Ishida Y, Yamato M, Masui D, Shimada T, Tachibana H, Yoshida H, Inoue H, Takagi S (2011) Langmuir 27:10722
90. Hofmann U, Klemen R (1950) Z Anorg Chem 262:95
91. Bujdák J, Komadel P (1997) J Phys Chem B 101:9065
92. Ishida Y, Masui D, Shimada T, Tachibana H, Inoue H, Takagi S (2012) J Phys Chem C 116:7879
93. Ishida Y, Shimada T, Takagi S (2014) J Phys Chem C 118:20466
94. Villemure G, Detellier C, Szabo AG (1986) J Am Chem Soc 108:4658
95. Villemure G, Detellier C, Szabo AG (1991) Langmuir 7:1215
96. Fujimura T, Shimada T, Hamatani S, Onodera S, Sasai R, Inoue H, Takagi S (2013) Langmuir 29:5060
97. Takagi S, Shimada T, Masui D, Tachibana H, Ishida Y, Tryk DA, Inoue H (2010) Langmuir 26:4639
98. Bujdák J, Iyi N, Fujita T (2002) Clay Miner 37:121
99. Takagi S, Shimada T, Ishida Y, Fujimura T, Masui D, Tachibana H, Eguchi M, Inoue H (2013) Langmuir 29:2108
100. Ogawa M, Kuroda K (1997) Bull Chem Soc Jpn 70:2593
101. Shichi T, Takagi K (2000) J Photochem Photobiol, C 1:113
102. Ohtani Y, Nishinaka H, Hoshino S, Shimada T, Takagi S (2015) J Photochem Photobiol, A 313:15
103. Kitaura R, Kitagawa S, Kubota Y, Kobayashi TC, Kindo K, Mita Y, Matsuo A, Kobayashi M, Chang HC, Ozawa TC, Suzuki M, Sakata M, Takata M (2002) Science 298:2358
104. Kamada K, Tanamura Y, Ueno K, Ohta K, Misawa H (2007) J Phys Chem C 111:11193
105. Suzuki Y, Tenma Y, Nishioka Y, Kamada K, Ohta K, Kawamata J (2011) J Phys Chem C 115:20653

106. Krishnamoorthy K, Veerapandian M, Yun K, Kim SJ (2013) Carbon 53:38
107. Ekiz OO, Urel M, Guner H, Mizrak AK, Dana A (2011) ACS Nano 5:2475
108. Muscuso L, Cravanzola S, Cesano F, Scarano D, Zecchina A (2015) J Phys Chem C 119:3791
109. Rao CNR, Gopalakrishnan K, Maitra U (2015) ACS Appl Mater Interfaces 7:7809
110. Yang J, Shin HS (2014) J Mater Chem A 2:5979
111. Xiang Q, Cheng B, Yu J (2015) Angew Chem Int Ed 54:11350
112. Ma Y, Chang H, Zhang M, Chen Y (2015) Adv Mater 27:5296
113. Roy-Mayhew JD, Aksay IA (2014) Chem Rev 114:6323
114. Yao J, Sun Y, Yang M, Duan Y (2012) J Mater Chem 22:14313
115. Agrawal KV, Topuz B, Jiang Z, Nguenkam K, Elyassi B, Francis LF, Tsapatsis M, Navarro M (2013) AIChE J 59:3458
116. Park S, An JH, Piner RD, Jung I, Yang DX, Velamakanni A, Nguyen ST, Ruoff RS (2008) Chem Mater 20:6592
117. Zhu YW, Stoller MD, Cai WW, Velamakanni A, Piner RD, Chen D, Ruoff RS (2010) ACS Nano 4:1227
118. Sun PZ, Zhu M, Wang KL, Zhong ML, Wei JQ, Wu DH, Xu ZP, Zhu HW (2013) ACS Nano 7:428
119. Gao P, Liu Z, Sun DD, Ng WJ (2014) J Mater Chem A 2:14082
120. Zhang Y, Evans JRG (2012) Colloids Surf A 408:71
121. Sun L, Huang H, Peng X (2013) Chem Commun 49:10718
122. Sun LW, Ying YL, Huang HB, Song ZG, Mao YY, Xu ZP, Peng XS (2014) ACS Nano 8:6304
123. Lagaly G (1994) Prog Colloid Polym Sci 95:61
124. Ruiz-Hitzky E, Aranda P, Darder M, Rytwo G (2010) J Mater Chem 20:9306
125. Gullick RW, Weber WJ Jr, Gray DH (1996) In: Sawhney BL (ed) Organic pollutants in the environment. The Clay Minerals Society, Aurora
126. Komatsu Y, Fujiki Y, Sasaki T (1983) Bunseki Kagaku 32:E33
127. Morimoto K, Tamura K, Umemura Y, Sato H, Yamagishi A (2011) Chem Lett 40:867
128. Costantino U, Ambrogi V, Nocchetti M, Perioli L (2008) Micropor Mesopor Mater 107:149
129. Wang H, Yuan X, Zeng G, Wu Y, Liu Y, Jiang Q, Gu S (2015) Adv Colloid Interface Sci 221:41
130. Li J, Li J, Meng H, Xie S, Zhang B, Li L, Ma H, Zhang J, Yu M (2014) J Mater Chem A 2:2934
131. McCabe RW (1992) In: Bruce DW, O'Hare D (eds) Inorganic Materials. Wiley, Chichester
132. Carrado KA (2004) In: Auerbach SM, Carrado KA, Dutta PK (eds) Handbook of layered materials. Marcel Dekker, New York
133. Kumar BS, Dhakshinamoorthy A, Pitchumani K (2014) Catal Sci Technol 4:2378
134. Osterloh FE (2008) Chem Mater 20:35
135. Kudo A, Miseki Y (2009) Chem Soc Rev 38:253
136. Gabriel J-CP, Davidson P (2003) Top Curr Chem 226:119
137. Nakato T, Miyamoto N (2009) Materials 2:1734
138. Inadomi T, Ikeda S, Okumura Y, Kikuchi H, Miyamoto N (2014) Macromol Rapid Commun 35:1741
139. Kim YS, Liu M, Ishida Y, Ebina Y, Osada M, Sasaki T, Hikima T, Takata M, Aida T (2015) Nat Mater 14:1002
140. Kim YS, Kang JH, Kim T, Jung Y, Lee K, Oh JY, Park J, Park CR (2014) Chem Mater 26:5549
141. Haraguchi K, Takehisa T (2002) Adv Mater 14:1120
142. Wang Q, Mynar JL, Yoshida M, Lee E, Lee M, Okuro K, Kinbara K, Aida T (2010) Nature 463:339
143. Booth SG, Dryfe RAW (2015) J Phys Chem C 119:23295
144. Aveyard R, Binks BP, Clint JH (2003) Adv Colloid Interface Sci 100–102:503
145. Fujii S, Murakami R (2008) KONA Powder Part J 26:153

146. Tsugita A, Takemoto S, Mori K, Yoneya T, Otani Y (1983) J Colloid Interface Sci 95:551
147. Nonomura Y, Kobayashi N (2009) J Colloid Interface Sci 330:463
148. Mejia AF, Diaz A, Pullela S, Chang Y-W, Simonetty M, Carpenter C, Batteas JD, Mannan MS, Clearfield A, Cheng Z (2012) Soft Matter 8:10245
149. Wen W, Huang X, Sheng P (2008) Soft Matter 4:200
150. Zhang WL, Liu YD, Choi HJ, Kim SG (2012) ACS Appl Mater Interfaces 4:2267
151. Zhang WL, Choi HJ (2014) Soft Matter 10:6601

Chapter 2
Clay Minerals as Natural Nanosheets

Robert A. Schoonheydt and Yasushi Umemura

2.1 Introduction

Particles with nanometer dimensions (nanoparticles) are all around us. The finest particles of sand are blown by the wind over thousands of kilometers. The finest particles of soils are either eroded by the wind in extremely dry conditions or by water under wet conditions and deposited hundreds of kilometers or more from the origin. The air contains nanoparticles of carbon, ice, and oxides and is often contaminated with organic and inorganic compounds. As natural layered silicates, clay minerals, are available everywhere and cheap, they have been mixed with organic polymers as bulking fillers in the industry. On the other hand, intercalated compounds of layered clay mineral, such as smectite, with organic molecules have been studied in the academia. The intercalated compounds are expecting to have hybridized characters and properties, which are something alike to those of the parent compounds; clay minerals and guest organic molecules, but something different from those of them.

Among these nanoparticles in nature, clay minerals take a unique position, not only because of their nanometer size but also because of their shape (clay minerals are layered materials or two-dimensional (2D) materials), ion exchange, and adsorption properties. These properties are the basis for intense research in the transformation of clay minerals into nanomaterials for a variety of technological application and in the incorporation of clay minerals in nanodevices. As clay minerals are natural materials that can be mined, they are cheap. But this comes at a

R.A. Schoonheydt (✉)
Department of Microbial and Molecular Systems, Kuleuven,
Kasteelpark Arenberg 23, 3001 Leuven, Belgium
e-mail: robert.schoonheydt@telenet.be

Y. Umemura
Department of Applied Chemistry, National Defense Academy,
Hashirimizu 1-10-20, Yokosuka, Kanagawa 239-8686, Japan

T. Nakato et al. (eds.), *Inorganic Nanosheets and Nanosheet-Based Materials*,
Nanostructure Science and Technology, DOI 10.1007/978-4-431-56496-6_2

price in which they invariably contain impurities that may be harmful for the technological application envisaged. Synthetic clay minerals of high purity are also available and deserve to be investigated for possible application in the nanotechnological area.

2.2 Clay Minerals

2.2.1 General

Clay minerals form a group of layered silicates or phyllosilicates. The elementary building unit is the layer. It consists of sheets of corner-shared SiO_4^{4-} tetrahedral and edge-shared Al or Mg, [Al, Mg O_{6-n} $(OH)_n$] octahedra. These sheets are joined by common O atoms. 1:1 clay minerals have a layer, which consists of one sheet of Si tetrahedral and one sheet of Al or Mg octahedra. 2:1 clay minerals consist of one sheet of Al or Mg octahedral sandwiched between two sheets of Si tetrahedral.

Isomorphous substitution is the partial replacement of Si^{4+} in the tetrahedral sheets by cations of about the same size and one unit of charge less. Examples are Al^{3+} and Fe^{3+}. Isomorphous substitution also occurs in the octahedral sheets. Thus, Al^{3+} can be substituted by Mg^{2+}, Fe^{3+} or Fe^{2+}, and Mg^{2+} by Li^{+}. As a result not all the negative charges of the O atoms are neutralized by the cations. The clay mineral layer carries a negative charge, which is compensated by cations at the surface of the layers, the exchangeable cations.

Clay minerals occur in nature, but may also be synthesized. Table 2.1 summarizes the most common 1:1 and 2:1 clay minerals. They are subdivided into dioctahedral and trioctahedral clay minerals, respectively, with an Al octahedral sheet and a Mg octahedral sheet in the layer. The table gives the common name of the clay mineral, the chemical formula of the pseudo-unit cell, and the degree of isomorphous substitution x.

When $x = 0$ there is no isomorphous substitution and there are no exchangeable cations. When $x = 0.2–0.6$, exchangeable cations compensate the negative layer charge. They are hydrated and located in the interlayer space. The distance between

Table 2.1 Clay minerals: structural formulae, degree of isomorphous substitution and names

Degree if isomorphous substitution, x	Structural formula	Name
$x = \approx 0$	$[Si_2Al_2O_5(OH)_4]$	Kaolinite
$x = \approx 0$	$[Si_2Mg_3O_5(OH)_4$	Serpentine
$x = \approx 0$	$[Si_4Al_2O_{10}(OH)_2]$	Pyrophillite
$x = \approx 0$	$[Si_4Mg_3O_{10}(OH)_2]$	Talc
$x = 0.2–0.6$	$[Si_4Al_{2-x}Mg_xO_{10}(OH)_2]xM^+$	Montmorillonite
$x = 0.2–0.6$	$[Si_{4-x}Al_xAl_2O_{10}(OH)_2]xM^+$	Beiddelite
$x = 0.2–0.6$	$[Si_4Mg_{3-x}Li_xO_{10}(OH)_2]xM^+$	Hectorite
$x = 0.2–0.6$	$[Si_{4-x}AlxMg_3O_{10}(OH)_2]xM^+$	Saponite

successive layers is then determined by the thickness of the layer, the exchangeable cation, and the amount of water in the interlayer space. The layer thickness is constant. It is 0.76 nm for 1:1 clay minerals and 0.96 nm for 2:1 clay minerals. The interlayer distance is however variable and depends on the amount of water in the interlayer space. In dilute aqueous dispersions, the amount of water taken up by the clay minerals is so large that the clay minerals layers are completely separated into individual layers, diffusing randomly and independently in water. One says that the clay mineral is completely dispersed. The increase of the interlayer distance with water content is called swelling and the clay minerals are called swelling clay minerals or smectites. This is the case for 2:1 clay minerals with x = 0.2–0.6. If the degree of isomorphous substitution x is in the range 0.6–0.9, the 2:1 clay minerals can take up one or two water layers in the interlayer space, but cannot reach the fully dispersed state. These clay minerals are called vermiculites. 2:1 Clay minerals with x = 0.9–1 are called micas. They do not take up water in the interlayer space. In this chapter, we concentrate our discussion on smectites.

2.2.2 Smectites

Figure 2.1 shows the structure of one layer of a dioctahedral smectite. The 2:1 clay mineral layer consists of four layers of O atoms with Si atoms between the first and second layer and between the third and fourth layer and Al atoms (Mg in the case of trioctahedral 2:1 clay minerals) between the second and third layer. The negative charge of the layer, due to isomorphous substitution, is compensated by exchangeable cations at the surface of the layer. Oxygen atoms at the edges may also carry a negative charge that is compensated by H atoms, thus giving Si–OH, Al–OH, or Mg–OH groups. These hydroxyl groups undergo acid–base equilibria in aqueous dispersion:

$$\mathrm{M{-}OH} + \mathrm{H_3O^+} \rightleftarrows \mathrm{M{-}OH_2^+} + \mathrm{H_2O}$$

$$\mathrm{M{-}OH} + \mathrm{H_2O} \rightleftarrows \mathrm{M{-}O^-} + \mathrm{H_3O^+} \quad (\mathrm{M{=}Si,\ Al,\ or\ Mg})$$

In acid medium they take up a proton, while in basic medium they release a proton in solution. Thus, edges may be positively charged or negatively charged depending on the pH conditions.

Smectites are extracted from clays by fractionation or a combination of mild acid treatment and fractionation. The size fraction less than 2 μm is considered as the pure smectite fraction. Figure 2.1 shows AFM pictures of Langmuir–Blodgett (LB) films of saponite, hectorite, and montmorillonite. One observes layers of different sizes and shapes. Hectorite consists of lath-like layers; montmorillonite has plate-like layers, while saponite has both types. The white spots might be clay mineral particles or impurities attached to the clay mineral layers.

Synthetic smectites are also available. One avoids impurities such as quartz or calcite. The particle size of synthetic smectites can be tuned by the synthesis conditions. The best known is probably Laponite, a synthetic hectorite. It consists of very small particles, 30–50 nm. Dispersions of Laponite easily form gels. F-hectorite is obtained by melt synthesis followed by annealing to improve charge homogeneity and phase purity [1, 2]. Table 2.2 gives the synthetic smectites most often encountered in the scientific literature.

Ion exchange is one of the most important properties of smectites. The reaction is usually performed in water and the smectite is swollen to a partially dispersed state. It is then possible to introduce almost any type of cation, organic or inorganic, irrespective of its size. In the case of alkylammonium cations, the surface of the smectite layers is fully covered with alkyl chains. The clay mineral layers adopt a hydrophobic character. The alkyl chains take a specific orientation depending on

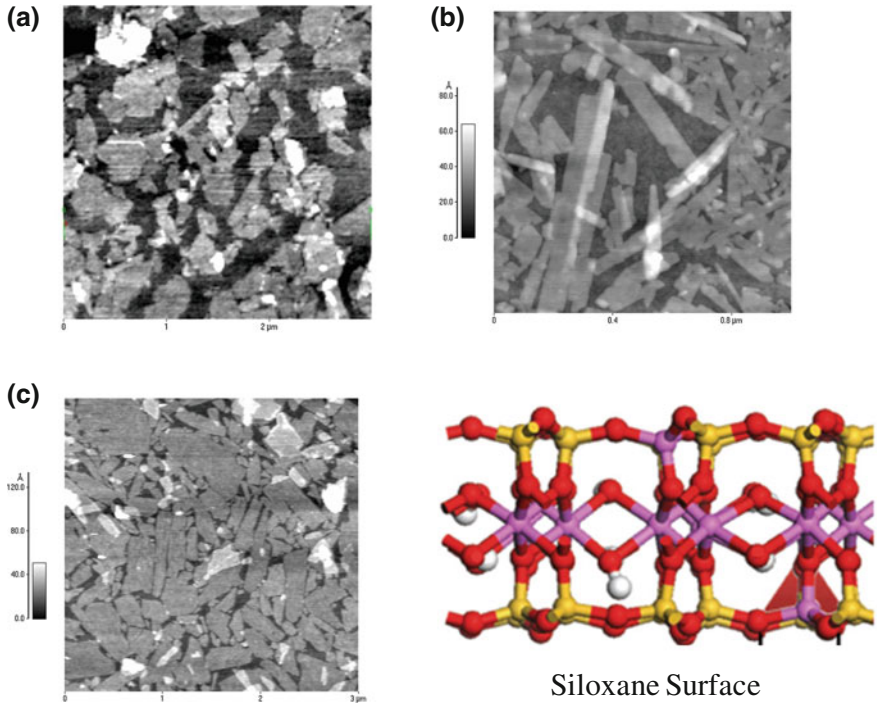

Fig. 2.1 Structure of one layer of a smectite: AFM pictures of single layers and particles (*white areas*) of **a** saponite, **b** hectorite, and **c** montmorillonite

Table 2.2 Examples of synthetic smectites

Name	Natural analog	Structural formula
Laponite	Hectorite	$[(Si_4)(Mg_{2.5}Li_{0.5})O_{10}(OH)_2]Na_{0.5}$
Fluor-hectorite	Hectorite	$[(Si_4)(Mg_{2.5}Li_{0.5})O_{10}(OH)_2]Na_{0.5}$
Smecton	Saponite	$[(Si_{3.6}Al_{0.4})(Mg_{2\cdot 99}Al_{0.01})O_{10}(OH)_2]Na0_{.25}Mg_{0\cdot 07}$

their length and on the charge density x of the layers. A schematic drawing is given in Fig. 2.2.

The lesson to be learnt is that molecules can be organized in the interlayer space of smectites. If these molecules carry a functionality such as a dipole moment, the resulting dipole moment of a single smectite layer may be zero or different from zero depending on the specific organization of the dipole moments in the interlayer

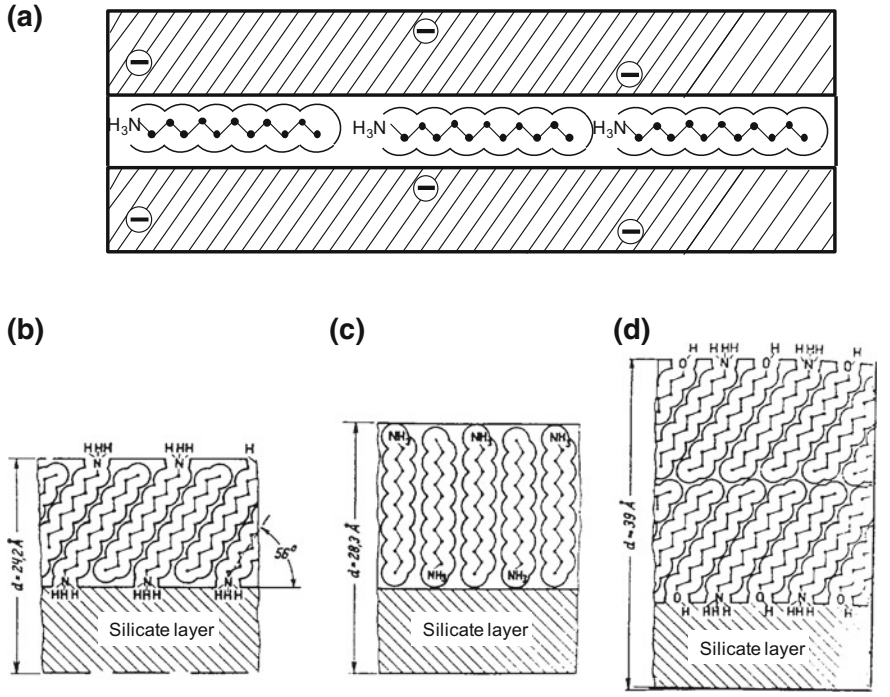

Fig. 2.2 Orientation of alkylammonium cations in the interlayer space of a smectite

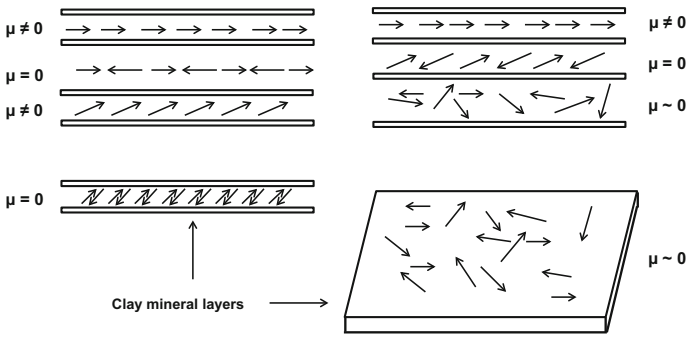

Fig. 2.3 Examples of arrangement of dipolar molecules in the interlayer space: ordered arrangements at the *left hand side*; disordered arrangements at the *right side*

space. If single layers each carrying a net dipole moment are organized in a film, the film may or may not have a dipole moment depending on the organization of the layers in the film (Fig. 2.3). Thus in order to prepare functional films, organization at two levels is required: (1) organization of the functional molecules at the surface of the clay mineral layers; (2) organization of the clay mineral layers themselves. There are four groups of methods to do so: casting, spin coating, layer-by-layer assembly, and Langmuir–Blodgett.

2.3 Film Formation Techniques

2.3.1 Casting

Casting is the deposition of an aqueous dispersion of clay minerals, followed by removal of excess water. It can be achieved in different ways, two of them are illustrated in Fig. 2.4. A few drops of the dispersion can be deposited on a hydrophobic surface. Upon slow drying in air at room temperature, a continuous film is formed with thickness in the mm range. While the dispersion is slowly drying, the clay mineral layers settle under the influence of gravitational forces with their surfaces parallel to the surface of the substrate. The result is a film with organized clay mineral layers. It can be used in X-ray diffraction (XRD) studies, Fourier Transform Infrared Spectroscopy (FTIR), electron paramagnetic resonance (EPR), and others. The orientation of structural OH groups of adsorbed molecules

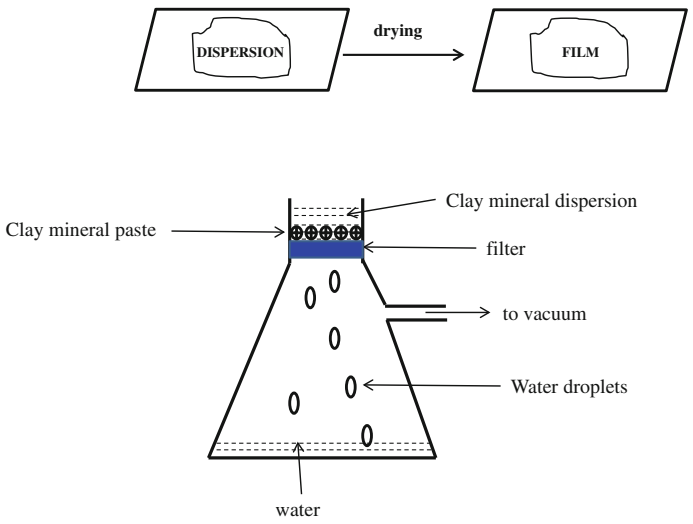

Fig. 2.4 Examples of film casting. *Upper part* Drying of a spread clay mineral dispersion. *Lower part* Suction of water out of a clay mineral dispersion

and of transition metal ion complexes at the interlayer surfaces can be studied with these films. The aqueous smectite dispersion can also be put on a filter paper with small pores and the excess water can be sucked away. What remains on the filter is a cake with oriented clay mineral layers and particles, which can be dried in air at room temperature.

2.3.2 *Spin Coating*

A few drops of the aqueous dispersion of a smectite are put on a disk, which is subsequently rotated. The dispersion is equally spread over the surface of the disk due to the centrifugal forces of the rotation. The solvent evaporates simultaneously, thus forming a film. The thickness of the film is dependent on the mass% of smectite in the aqueous dispersion and on the rotation speed. This is illustrated in Fig. 2.5 for Laponite. For 1 mass% dispersion, the film thickness decreases from ≈20 to ≈10 nm upon increasing the rotation speed from 400 to 1000 rpm (rounds per minute). For 2 mass% dispersions, the film thickness decreases from 60 to ≈30 nm with the rotation speed increasing from 400 to 1000 rpm.

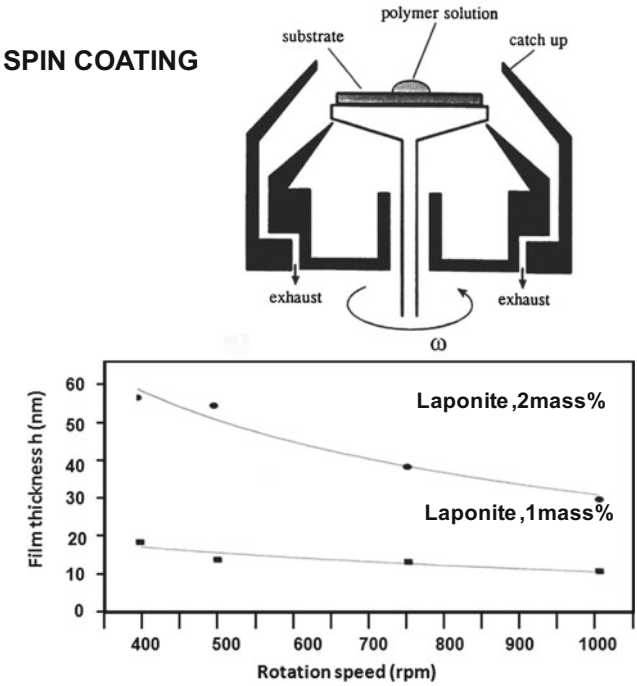

Fig. 2.5 *Upper part* Scheme of a spin coating apparatus. *Lower part* Film thickness as a function of the rotation speed for 2 mass% and 1 mass% Laponite dispersions

With spin coating one can also construct films, consisting of alternating layers of two different materials. Thus, alternating layers of Laponite and of a material with high refractive index such as TiO_2 result in a material with an optical band gap. As the Laponite layer is porous and the TiO_2 layer is not, the band gap properties can be influenced by adsorption of molecules in the Laponite layer. Such photonic band gap materials can then be used as sensors [3, 4].

2.3.3 *Layer-by-Layer (LbL) Assembling*

The principle of the technique is shown in Fig. 2.6. A substrate with a negatively charged surface is alternatively immersed in a solution of cationic polymers and in a dilute aqueous clay mineral dispersion. After each deposition the deposited layers are rinsed with water to remove excess material. This results in deposition of alternating layers of polymers and smectite layers and particles. One layer of polymer and one layer of clay mineral particles form a bilayer. These bilayers are held together mainly by electrostatic forces, as the polymer is positively charged and the clay mineral layers are negatively charged. The anions accompanying the cationic polymer and the exchangeable cations of the clay mineral layers and particles are free and are removed in the washing steps. The result is an ion exchange of a cationic polymer on the clay mineral surfaces.

The number of bilayers deposited can be increased, in principle infinitely, but not in practice. Indeed, the thickness of the films increases linearly with the number of bilayers, but this is not the case for the roughness of the films. Film roughness is defined as

$$\text{Roughness} = \left[\frac{\Sigma(h_i - h_a)^2}{n-1}\right]^{1/2},$$

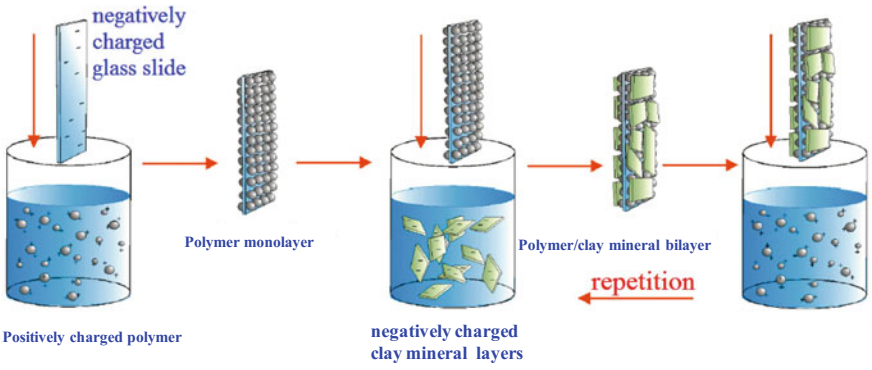

Fig. 2.6 The principle of layer-by-layer assembling

where h_i is the thickness of the film at point i, h_a is the average film thickness, and n is the number of datapoints.

It is observed that the roughness of the films increases with the concentration of poly(dialkyldimethylammonium) (PDDA) in solution and with the number of bilayers deposited. The roughness is also dependent on the particle size of the clay minerals [5]. For Laponite with particle sizes around 30 nm, the roughness is 4 nm or less after deposition of 20 bilayers, while it is 3–4 times higher for hectorite. After deposition of 20 bilayers the hectorite films are about 60 nm thick. A roughness of 12 nm is 20% of the film thickness. Thus hybrid LbL films of smectites and cationic polymers are not atomically smooth. The reasons for this are: (1) presence of clay mineral layers and particles; (2) sub-monolayer coverage for each deposition of clay mineral layers and particles; (3) overlap of clay mineral layers and particles in the film; (4) aggregation of clay mineral layers and particles in the PDDA matrix.

2.3.4 *Langmuir–Blodgett (LB) and Langmuir–Schaefer (LS) Technique*

The thickness of a 2:1 clay mineral layer is 0.96 nm and if a film is composed of these single clay mineral layers, it would be thin and smooth at the nanometer level. The LB and LS techniques have been applied to prepare such films. The procedures are illustrated in Fig. 2.7.

Clay mineral particles that are intercalated with amphiphilic cations such as alkylammonium cations are hydrophobic. They swell in organic solvents and form dilute dispersions of individual layers, analogously to the swelling of hydrophilic smectites in water. These dilute dispersions of hydrophobic smectite layers can be spread at the air–water interface. After evaporation of the solvent, the individual clay mineral layers are left at the interface. The floating individual layers can be gathered by barriers to form a film, as shown in Fig. 2.7a. The ultrathin film of packed clay mineral layers is then transferred to a substrate by vertical lifting (LB technique) or horizontal lifting (LS technique) [6, 7].

A second way of film preparation is spreading a solution of amphiphilic cations in a volatile organic solvent on a dilute aqueous clay mineral dispersion (Fig. 2.7b). The volatile solvent evaporates and the negatively charged smectite layers interact with the positively charged amphiphilic cations at the air–water interface. A floating hybrid monolayer is formed, consisting of clay mineral layers and amphiphilic cations. This floating monolayer is compressed and transferred on a substrate by vertical or horizontal lifting. Multilayers can be prepared by repeating the deposition procedure [8, 9]. This type of LB or LS film preparation is very versatile and therefore a promising technique for preparation of functional ultrathin films [10–12]. First, the layered structure of these hybrid multilayers is far more stable than those of conventional LB and LS films. Second, the density of amphiphilic cations on the clay mineral layers in the film is controlled by changing the clay

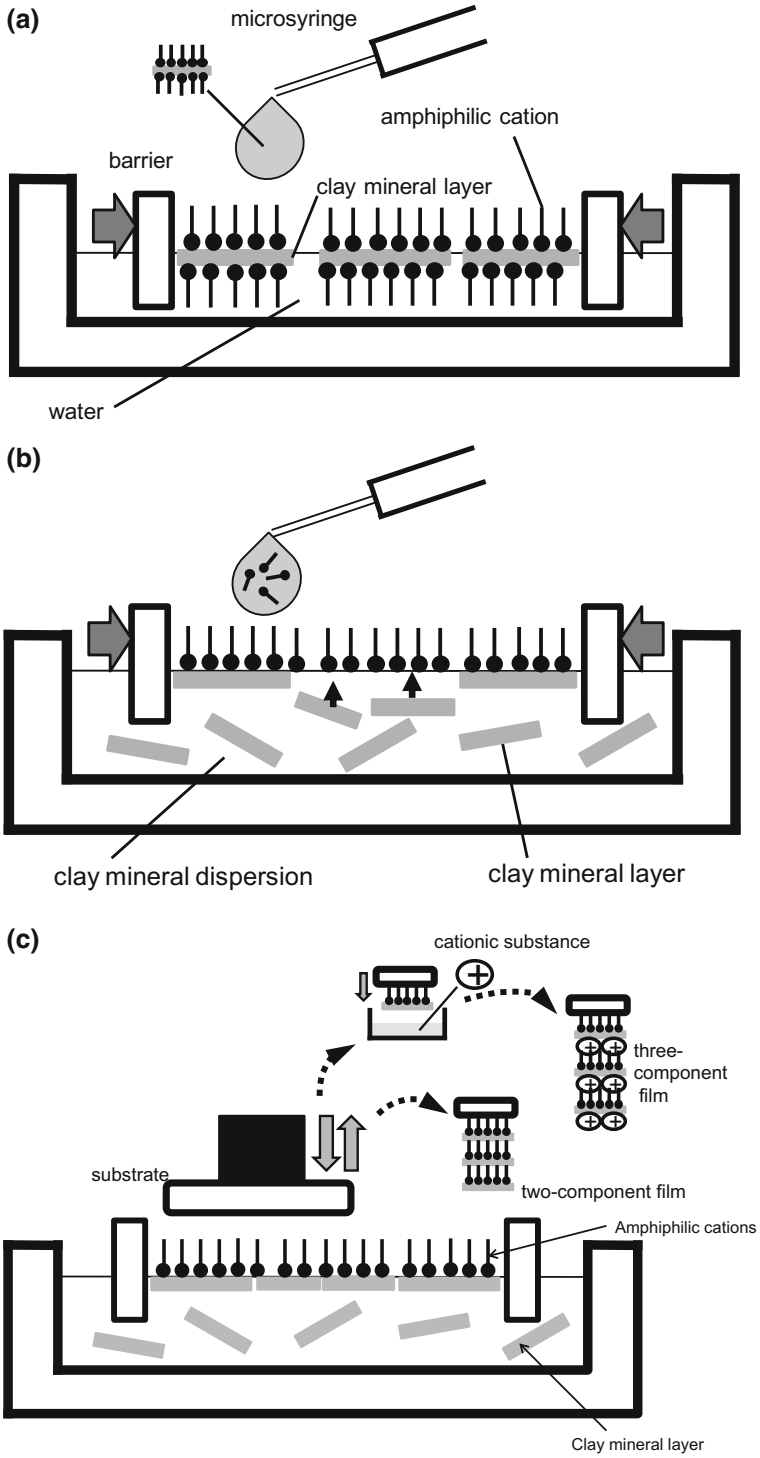
(a)
microsyringe
amphiphilic cation
barrier
clay mineral layer
water
(b)
clay mineral dispersion
clay mineral layer
(c)
cationic substance
three-
component
film
substrate
two-component film
Amphiphilic cations
Clay mineral layer

◀**Fig. 2.7** LB or LS technique for clay film preparation: **a** formation of a floating film of hydrophobic clay mineral particles at the air–water interface, **b** formation of a floating film of amphiphilic cations and clay mineral layers at the air–clay dispersion interface, and **c** deposition of a floating clay film (horizontal lifting) and multilayer fabrication

mineral concentration in the dispersion. If the clay mineral concentration is high, their adsorption rate at the air–water interface is high. Consequently, the individual clay mineral layers are adsorbed on the film of floating amphiphilic cations before evaporation of the solvent and aggregation of the amphiphilic cations. This brings about a low density of amphiphilic cations on the clay mineral layers in the film. Third, even if the amphiphilic cations are water soluble to some extent, a floating hybrid monolayer of clay mineral layers and amphiphilic cations is formed [13]. Fourth, another cationic substance can be deposited on the LB and LS film surfaces as a third component by dipping the surfaces of the films in a solution of the third component after every deposition of the floating hybrid monolayer from the air–water interface, as illustrated in Fig. 2.7c [10–12]. This is because the hybrid LB and LS films possess a cation exchange ability. In the hybrid films, the negative charge of the clay mineral layers is larger than the positive charge of the amphiphilic cations. The density of the third component is dependent on the clay mineral concentration in the dispersion. The three-component films have layered structures, as well as the two-component (clay mineral layers and amphiphilic cations) films.

Recently, formation of clay LB films with amphiphilic anions was reported [14]. A stearic acid solution was spread on the surface of the clay mineral dispersion including divalent cations such as Mg^{2+}. The films cannot be formed with monovalent cations. This suggest that an adduct of clay mineral layers—Mg^{2+} is formed with excess positive charge, which is adsorbed on the floating monolayer of amphiphilic anions.

2.4 Organization of Molecules in the Interlayer Space

Preparation of films is the realization of a two-level organization: that of the clay mineral layers and that of the molecules in the interlayer space. An adequate organization leads to functional films and ultimately to incorporation of these films in devices. Organization of molecules in the interlayer space is a subject with a long history, going back to the pioneering research of Weiss in the 1960s and Lagaly in the 1970s and 1980s, summarized in the Handbook of Clay Science [15].

2.4.1 Alkylammonium Cations

The exchange of alkylammonium cations leads to well organized two-dimensional arrays of alkyl chains in the interlayer space. Monolayers and bilayers can be

obtained depending on the length of the alkyl chain and the charge density of the clay minerals. Idealized pictures are shown in Fig. 2.2. At low charge density, the alkylammonium cations have enough space to lie flat on the siloxane surface, that is to maximize the interaction between the surface and the alkyl ammonium cations. The alkyl chains are positioned with their long axis parallel to the surface. As the charge density increases, the average surface area per charge e is insufficient for such an organization and the alkyl chains are tilted with respect to the surface or they can form a bilayer. These idealized pictures can be perturbed: (1) by thermal motion of the alkyl chains, inducing disorder in their organization; (2) hindered rotations around C–C bonds; (3) the presence of C=C bonds, which prohibit rotation.

2.4.2 *Cationic Organic Dyes*

Cationic organic dyes have some hydrophobic character, limited solubility in water and easily form dimers and aggregates:

$$\begin{aligned} &2\text{dye} \rightleftarrows (\text{dye})_2 \\ &(\text{dye})_2 + \text{dye} \rightleftarrows (\text{dye})_3 \\ &\cdots \\ &(\text{dye})_{n-1} + \text{dye} \rightleftarrows (\text{dye})_n \end{aligned}$$

These reactions are characterized by thermodynamic equilibrium constants, such as

$$K_2 = \frac{[(\text{dye})_2]}{[\text{dye}]^2},$$

$$K_n = \frac{[(\text{dye})_n]}{(\text{dye})^n},$$

where K_n is the global aggregation constant: $K_n = K_2 \cdot K_3 \cdots$. The monomers, dimers, and aggregates have typical UV–Vis spectra and can therefore be easily detected and studied, also in dilute aqueous dispersions. Figure 2.8 gives the structure of typical dyes used in exchange reactions with smectites. Table 2.3 gives the characteristic band maxima for monomers (M), dimers (D), H-aggregates (H), and J-aggregates (J). The distinction between H- and J-dimers and aggregates is in the arrangements of the monomers with respect to each other as shown in Fig. 2.9. Upon interaction of the two monomers, the energy level of the excited state splits into two levels. For the H-dimer, the transition from the ground state to the highest excited state is allowed, causing a blue shift of the absorption band of the H-dimer with respect to that of the monomer. For the J–dimer, the transition to the lowest excited state level is allowed and the absorption band of the J-dimer is red shifted with respect to that of the monomer.

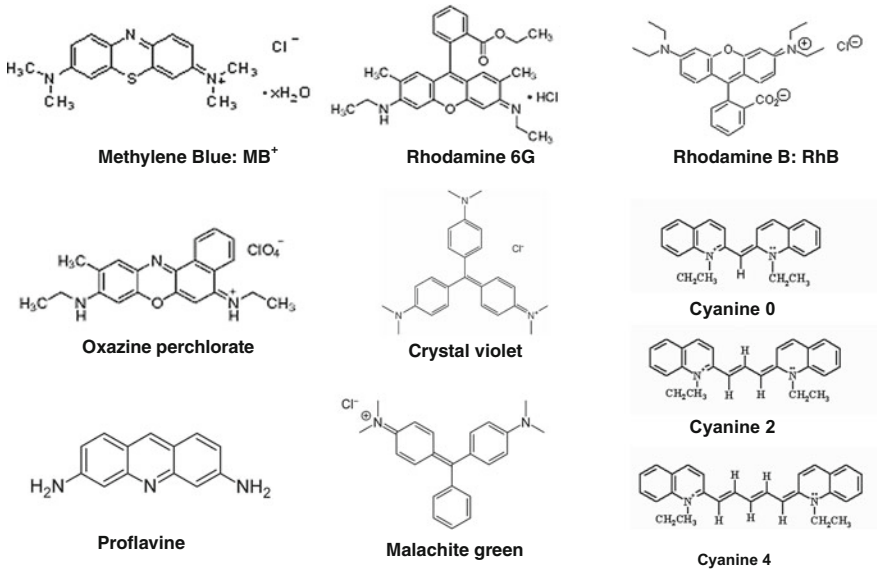

Fig. 2.8 Structure of dye molecules

Table 2.3 Typical band maxima of dyes in dilute aqueous dispersions

Dye[a]	Monomer/nm	Dimer/nm	H-aggregates/nm	J-aggregates/nm
MB	665	605	570	725
Rh6G	528	503		545
Ox4	628	575	475	
CV	590	550		
Cyanin0	520	480		570
Cyanin1	610		500	
Cyanin2	710		560	

[a]*MB* methylene blue; *Rh6G* rhodamine 6G; *CV* crystal violet; *Ox4* oxazine; Cyanin

This aggregation behavior in aqueous solution can be considered as a kind of molecular organization. What happens then in the presence of clay mineral layers in aqueous dispersion and in films?

The organization of cationic organic dyes in the interlayer space of clay mineral films depends mainly on (1) the size and shape of the dye molecules; (2) the layer charge of the clay mineral; and (3) the type of solvent. In dilute aqueous dispersions, the dye molecules are instantaneously adsorbed. The monomer spectrum of the solution is transformed into a spectrum dominated by the band of H-aggregates, as illustrated in Fig. 2.10 for MB. In the next few minutes, a redistribution of the dye molecules over the surface occurs, as seen by the decrease of the 570 nm band of the H-aggregate and the increase of the monomer band and dimer bands. Then the dispersion slowly goes to a metastable equilibrium situation. Cenens et al. [16, 17]

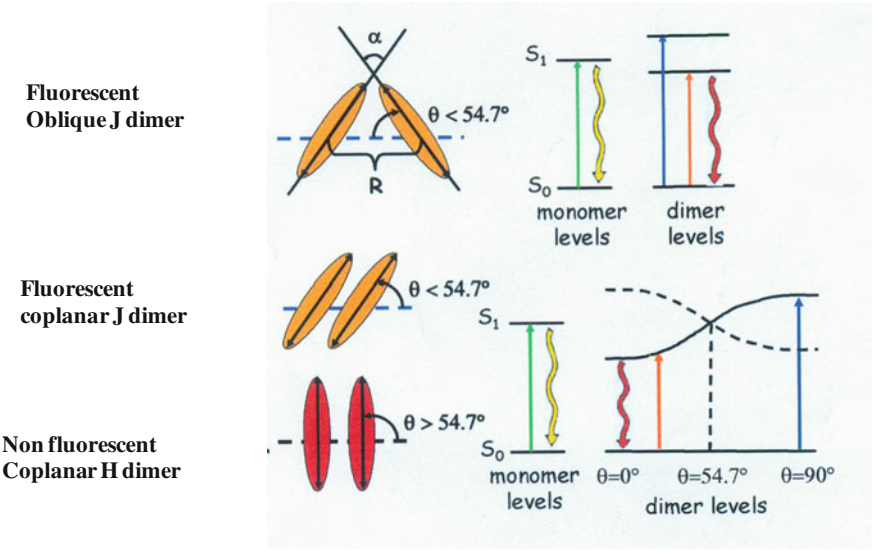

Fig. 2.9 Organization of monomers to obtain H and J dimmers and the corresponding electronic transitions: *vertical arrows up* are allowed absorptions; *curved arrows down* are radiationless transitions

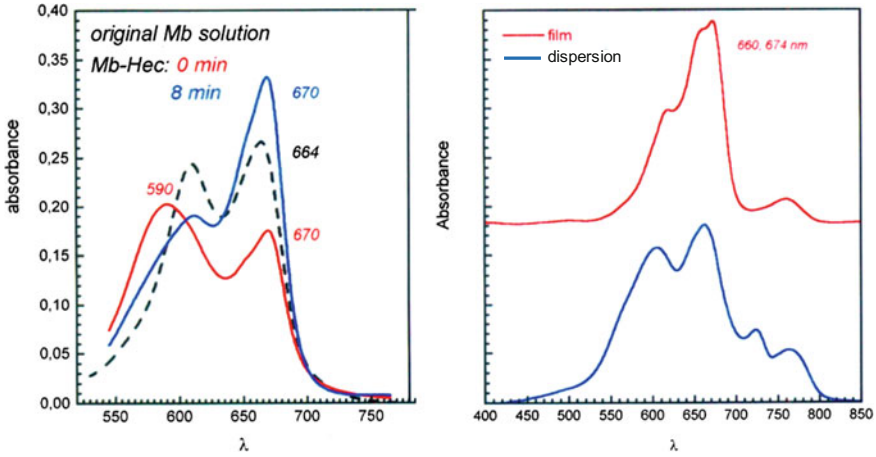

Fig. 2.10 *Left* Spectra of methylene blue (MB) in an aqueous dispersion of hectorite: solution spectrum (*black*), instantaneously after mixing the MB solution with the hectorite dispersion (*red*), and 8 min later (*blue*). *Right* Spectrum of a hectorite-MB dispersion (*blue*) and the corresponding film (*red*). Spectra are taken from [16] and [17]

have tried to calculate the dimerization and trimerization constants of MB and PF in these aqueous dispersions at quasi-equilibrium, assuming that (1) the MB molecules are confined at the surface layer in a layer of 1 nm thickness; and (2) the total surface

area is available for the MB molecules. The data are compared with those in solution in Table 2.4.

The surface areas are assumed to be 775 m^2/g for hectorite and 133 m^2/g for barasym. The latter is a mica-type montmorillonite and only the external surface is available. These data indicate that the dimerization constants at the clay mineral surface are significantly smaller than in aqueous solution. In the latter case dye–dye and dye–water interactions are operating. In the case of dilute aqueous dispersions two forces are added: dye–surface and water–surface interactions. Dye molecules and water molecules compete for interaction with the surface. If water wins, the dye molecules remain surrounded by water molecules and aggregation is favored. If the dye–surface interaction is dominant, dye molecules displace the water molecules at the surface and monomers are favored. The small K_2 (dispersion) values are indicative for the dominance of dye–surface interactions over the water–surface interactions. This competition is moderated by the layer charge density and the position of the layer charge (in the octahedral sheet or in the tetrahedral sheets). Finally, is the total theoretical surface area available for the dye molecules? Cenens et al. [16, 17] have argued on the basis of the decrease of the fluorescence intensity of proflavine with loading that this is only the case for Na^+ and Ca^{2+} exchanged hectorite and Laponite. In the case of K^+ and Cs^+, the available or effective surface area decreased from 775 m^2/g (Na^+-hectorite) to respectively 485 and 580 m^2/g. This means that K^+- and Cs^+-exchanged smectites are only partially swollen in dilute aqueous dispersion.

In films the amount of water is limited. The dye molecules interact predominantly with the clay mineral surfaces. Monomers, dimers, and aggregates have nevertheless been detected. Their relative amounts depend on the loading and the charge density of the clay mineral. At low loadings, the dye molecules maximize

Table 2.4 Dimerization and trimerization constants of MB and PF in water and in dilute aqueous dispersions

Dye	Clay mineral	K_2 (water)	K_2 (dispersion)	K_3 (dispersion)
MB	Hectorite	2000–5900	126–153	
	Barasym[a]			772
PF	Hectorite	395–2700	266–294	

[a]Barasym is a synthetic mica-type montmorillonite; *PF* proflavine

Table 2.5 Estimated sizes of typical dyes

Dye	Width/nm	Height/nm	Length/nm	Width × length/nm^2	Height × length/nm^2
MB	0.47	0.79	1.64	0.87	1.30
CV	0.61	1.50	1.65	1.01	2.48
Cyanin0	0.53	0.97	1.69	0.90	1.64
Cyanin1	0.51	0.96	1.93	0.98	1.85
Cyanin2	0.51	0.95	2.23	1.14	2.19

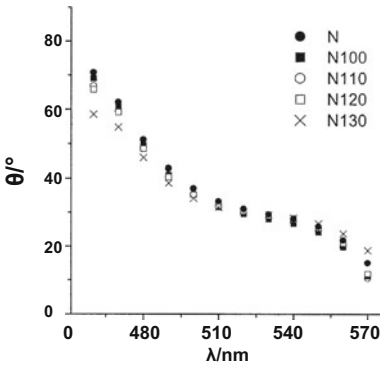

Fig. 2.11 Relationship between the orientation angle θ and the wavelength of absorbed light, calculated for rhodamine6G in reduced charge montmorillonites (from [20] with permission of the Royal Society of Chemistry)

their interaction with the surface with their main molecular axis parallel to the surface. As the loading increases dye molecules form dimers and aggregates with their molecular axes inclined or perpendicular to the surface. Table 2.5 summarizes estimated sizes and occupied surface areas of some typical dyes. They range from 0.87 to 2.48 nm^2 depending on the molecular structure and on how the molecules are situated on the surface. These numbers have to be compared with the average surface area per charge e of the clay minerals: 1e/0.48 nm^2 for mica and 0.82–2.16 nm^2 for smectites with a CEC of 1.5–0.5 mmol/g. It is clear that for a fully exchanged clay mineral, the dye molecules cannot lie flat on the surface. They have to be tilted and they are so close together that intermolecular interaction lead to dimers and aggregates.

This is exactly what is observed. The tilt angles of crystal violet and malachite green were determined to be 55°–59° and 57°–61° respectively on a mica surface [18]. Iwasaki et al. [19] found that the monomers of CV, MB and cyanine dyes were with their main molecular plane parallel with the surface at low loadings, while at higher loadings the J- and H-aggregates were oriented vertically. Bujdak et al. [20] established a relation between the tilt angle and the absorption band maximum of Rh6G in montmorillonite and charge reduced montmorillonite films. This relation is shown in Fig. 2.11. At low loadings the band maximum is at high wavelengths, characteristic of the monomers. The corresponding tilt angle is around 30°. As the loading increases, the band maximum shifts to shorter wavelengths indicative of the presence of H-dimers and H-aggregates. The tilt angles increases to 60°–70°, indicative of an almost perpendicular orientation of the main plane of the molecule with respect to the siloxane surface.

In order to produce functional films, the functionalities of the molecules in the interlayer space (e.g., dipole moment, magnetic moment/susceptibility) must be organized in such a way that an overall functionality (e.g., dipole moment, magnetic dipole moment/susceptibility) is produced in the films. This will not only depend on the organization of the molecules in the interlayer space, but also on the organization of the clay mineral layers, as illustrated in Fig. 2.3. For instance, if one wants to maximize the fluorescence intensity of the films, aggregations of the dye

molecules must be avoided. Dye molecules easily aggregate in water. It might then be advantageous to change to less polar organic solvents such as methanol or ethanol, which are known to suppress aggregation.

2.4.3 Cationic Inorganic Dyes

Inorganic dyes are transition metal ion complexes with intense absorption bands in the visible region of the electromagnetic spectrum. Examples are the bipyridine (bipy) and phenanthroline (phen) complexes. The tris complexes such as $Ru(bipy)_3^{2+}$ and $Ru(phen)_3^{2+}$ are optically active and racemic solutions and enantiomeric solutions can be prepared. Upon exchange in the interlayer space of smectites, the organization of the complexes becomes immediately evident. Exchange with a racemic solution of $Ru(bipy)_3^{2+}$ leads to a monolayer in the interlayer space and the amount adsorbed equals the CEC. In the case of exchange of enantiomeric complexes the amount adsorbed is twice the CEC [21]. For the phenanthroline complexes the opposite occurs: the amount adsorbed from a racemic solution is twice the CEC; that from an enantiomeric solution equals the CEC. This behavior is explained with the hypothesis that the phen complexes in a racemic solution are adsorbed as racemic pairs. Table 2.6 gives a list of complexes which show these effects and complexes which do not [22, 23]. All these complexes are chelates. The chelates with no charge or a positive charge of 1 and 2 (left column of Table 2.6) adsorb as racemic pairs and the amount adsorbed is twice the CEC. A closely packed array of chelates is formed on the surface (Fig. 2.12). When enantiomers of $[Ru(bipy)_3]^{2+}$ are exchanged, empty sites remain on the surface. These sites are used to adsorb selectively the optical antipodes: if Λ-chelates are adsorbed, the clay mineral will selectively adsorb Δ-forms from racemic solutions

Table 2.6 Classification of complexes according to their adsorption behavior on smectites (from Ref. [22] with permission of ACS)

Racemic adsorption (2 × CEC)	Enantiomeric adsorption (2 × CEC)	No stereochemical effect
$[Ni(phen)_3]^{2+}$	$[Ru(bipy)_3]^{2+}$	$[Co(phen)_3]^{3+}$
$[Fe(phen)_3]^{2+}$		$[Co(en)_3]^{2+}$ (en = ethylenediamine)
$[Ru(phen)_3]^{2+}$		*cis*-$[Co(en)_2(Cl_2]^{+}$
$[Fe(phen)_2(CN)_2]$		$[Co(phen)(glyc)_2]^{+}$ (glyc = glycinato)
$[Fe(bipy)_2(CN)_2]$		$[Co(en)(glyc)_2]^{+}$
$[Co(pan)_2]^{2+}$ (pan = pyridylazoresorcinol)		$[Co((en)_2(phegly)]^{2+}$ (phegly = phenylglycinato)
$[Co(pan)_2]^{+}$		$[Co(c\text{-}hexan)_3]^{3+}$ (c-hexan = cyclohexanediamine)

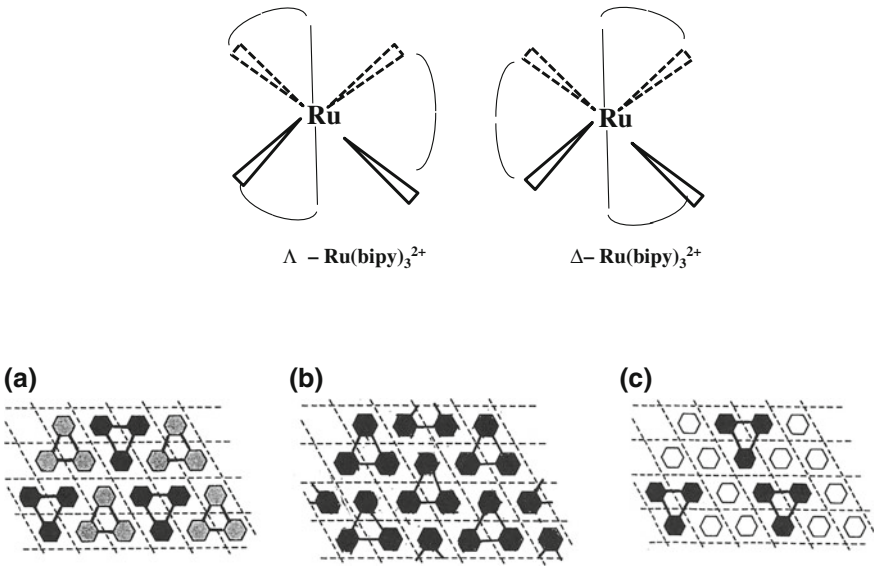

Fig. 2.12 *Upper part* Schematic drawing of lambda (Λ) and delta (Δ) forms of Ru(bipy)$_3^{2+}$. *Lower part* Schematic views of clay layer surfaces occupied with (a) rac – Ru(phen)$_3^{2+}$, (b) Λ- or Δ-Ru(bipy)$_3^{2+}$, and (c) Λ- or Δ-rac – Ru(phen)$_3^{2+}$ (from [23])

and vice versa for adsorbed Δ-chelates. This phenomenon is called chirality recognition [22, 23]. The chelates that do not show this stereochemical behavior have either a too high charge (+3) or the size and the shape of the complexes do not fit the hexagonal hole structure of the siloxane surface on which they are adsorbed.

The importance of this organization is immediately clear when LB films of Ru complexes and smectites are prepared [10]. LB films prepared with saponite and the amphiphilic [Ru(phen)$_2$(dcCl2bpy)] (dcCl2bpy=4,4′-carboxyl-2,2′-bipyridyl didocylester) do not have a second harmonic generation (SHG) signal. However, if the films are made hydrophobic by co-deposition of octadecylammonium cations, an SHG signal is generated, which is more intense with the Λ complex than with the racemic mixture. This is an indirect proof of molecular organization, which is influenced by the surrounding environment in the interlayer space (water, octadecylammonium, surface), a phenomenon that needs a more detailed investigation.

2.5 Organization of Clay Mineral Layers

The organization of particles in films is strongly size- and shape-dependent. A two-dimensional opal structure consisting of hexagonally close-packed, uniform silica spheres is obtained with the LB technique. Multilayers can also be constructed, which act as structures with photonic band gaps [24, 25]. In LB films, the

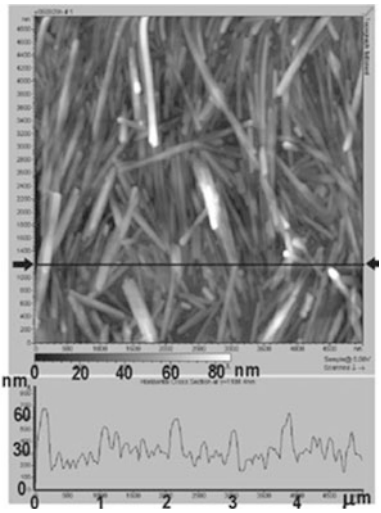

Fig. 2.13 AFM image of a Langmuir–Blodgett film of sepiolite fibers (from [26])

fibers of sepiolite are aligned perpendicularly to the direction of compression, although they overlap to some extent as shown in Fig. 2.13 [26].

For smectites the situation is more complicated for three reasons: (1) a broad range of sizes and shapes is present in the samples; (2) the swelling to complete delamination is an ideal that is difficult, if not impossible, to obtain; (3) impurity particles might be present, either attached to the clay mineral layers or separately. Representative AFM images are shown in Fig. 2.1. One observes that all the clay mineral layers are deposited with their ab plane parallel to the surface of the substrate. This is confirmed with polarized ATR-FTIR spectroscopy of the Si–O and O–H stretching vibrations [27]. The in-plane and out-of-plane Si–O stretching vibrations are at 996 and 1063 cm^{-1}, respectively. The former has a polarization-independent intensity; the out-of-plane vibration is polarization dependent. The structural O–H groups are vibrating almost perpendicularly to the plane of the layers in trioctahedral smectites and parallel with the plane of the layers in dioctahedral smectites.

In all pictures in Fig. 2.1, one sees dark spot and white spots. They are due to the empty spaces between the clay mineral layers and particles or aggregates of clay mineral layers. One observes the differences in sizes and shapes of the different clay minerals. Saponite consists of plate-like and lath-like layers. The layers are more or less randomly oriented and overlap of clay mineral layers also occurs. They have various sizes and shapes and are randomly oriented with some tendency of alignment of the lath-like layers. This is not the case of hectorite which consists solely of lath-like layers. They are overlapping and randomly oriented. Montmorillonite from Wyoming consists of plate-like layers with strongly corrugated edges. Finally, Laponite forms a more or less closely packed array of spherical particles. A comparison of the AFM pictures of sepiolite and hectorite is instructive. The fibers of sepiolite are aligned, while the lath-like layers of hectorite are randomly oriented. It is intriguing to find out the reasons for this difference in behavior. Is it only due to the shape of the minerals?

In cast films, spin-coated films, and LbL films, there is also ordering of clay mineral layers. The evidence comes from spectroscopic analysis of molecules in the interlayer space. For instance, the low spin square planar $[Co(en)_2]^{2+}$ complex in the interlayer space of cast films is characterized by an axially symmetric EPR spectrum. The molecular plane formed by the 2 en ligands and Co^{2+} is parallel with the surface of the clay mineral [28]. The data confirm that the clay mineral layers are deposited with their main surface parallel to the surface of the substrate. However, due to random orientation in the plane and to overlap the films have a rough surface. The surface roughness can reach 10% of the thickness or more, depending on the synthesis conditions [5].

References

1. Breu J, Seidl W, Stoll A, Lange KG, Probst TU (2001) Charge homogeneity in synthetic fluorohectorite. Chem Mater 13:4213–4220
2. Stöter M, Kunz DA, Schmidt M, Hirsemann D, Kalo H, Putz B, Senker J, Breu J (2013) Nanoplatelets of sodium hectorite showing aspect ratios up to 20000 and superior purity. Langmuir 29:1280–1285
3. Lotsch BV, Ozin GA (2008) ACS Nano 2:2065–2074
4. Lotsch BV, Ozin GA (2008) Adv Mater 20:4079–4084
5. Van Duffel B, Schoonheydt RA, Grim CPM, De Schryver FC (1999) Langmuir 15:7520–7529
6. Kotov NA, Meldrum FC, Fendler JH (1994) Langmuir 10:3797–3804
7. Inukai K, Hotta Y, Tomura S, Takahasi M, Yamagishi A (2000) Langmuir 16:7679–7684
8. Tamura K, Setsuda H, Taniguchi M, Yamagishi A (1999) Langmuir 15:6915–6920
9. Umemura Y, Yamagishi A, Schoonheydt RA, Persoons A, De Schryver FC (2001) Langmuir 17:449–455
10. Umemura Y, Yamagishi A, Schoonheydt R, Persoons A, De Schryver F (2002) J Am Chem Soc 124:992–997
11. Umemura Y (2002) J Phys Chem 106:11168–11171
12. Toma LM, Gengler RYN, Cangussu D, Pardo E, Lloret F, Rudolf P (2011) J Phys Chem Lett 2:2004–2008
13. Umemura Y, Shinohara E (2005) Langmuir 21:4520–4525
14. Hussain SA, Chakraborty S, Bhattacharjee D, Schoonheydt RA (2013) Thin Solid Films 536:261–268
15. Lagaly G, Ogawa M, Dékany I (2006) Clay mineral organic interactions. In: Bergaya F, Theng BKG, Lagaly G (eds) Handbook of Clay Science. Elsevier, Amsterdam, pp 309–377
16. Cenens J, Schoonheydt RA, De Schryver FC (1990) Probing the surface of clays in aqurous suspension by fluorescence spectroscopy of proflavine. In: Coyne LM, McKeever SWS, Blake DF (eds) Spectroscopic characterization of minerals and their surfaces, ACS symposium series 415, Chap. 19, pp 378–395
17. Cenens J, Schoonheydt RA (1990) Quantitative absorption spectroscopy of cationic dyes on clays. In: Farmer VC, Tardy Y (eds) Proceedings of the 9th international clay conference, sciences Géologiques Mémoires, vol 85, pp 15–23
18. Fisher D, Caseri WR, Hanher G (1998) J Colloid Interface Sci 198:337–346
19. Iwasaki M, Kita M, Ito K, Kohno A, Fukunishi K (2000) Clays Clay Miner 48:392–399
20. Bujdak J, Iyi N, Kaneko Y, Czimerova A, Sasai R (2003) Phys Chem Chem Phys 5:4680–4685
21. Villemure G (1990) Clays Clay Miner 38:622–630

22. Yamagishi A (1987) J Coord Chem 16:131–211
23. Yamagishi A (1993) Chirality recognition by a clay surface modified with an optically active metal chelate. In: Tamaru K (ed) Dynamic processes on solid surfaces, Chap. 12. Plenum Press, New York, pp 307–347
24. Van Duffel B, Ras RHA, De Schryver FC, Schoonheydt RA (2001) J Mater Chem 11:3333–3336
25. Szekeres M, Kamalin O, Schoonheydt RA, Wostyn K, Persoons A, Dekany I (2002) J Mater Chem 12:3268–3274
26. Umemura Y, Shinohara E, Schoonheydt RA (2009) Phys Chem Chem Phys 11:9804–9810
27. Ras RHA, Johnston CT, Franses EI, Ramaekers R, Maes G, Foubert P, De Schryver FC, Schoonheydt RA (2003) Langmuir 19:4295–4302
28. Schoonheydt RA, Pelgrims J (1983) J Chem Soc. Faraday Trans II 79:1169–1180

Chapter 3
Synthetic Nanosheets from Ion-Exchangeable Layered Solids

Teruyuki Nakato

3.1 Introduction

Exfoliated inorganic nanosheets of ion-exchangeable layered solids were obtained for the first time from the smectite group of clay minerals, which are natural cation-exchangeable layered crystals consisting of negatively charged aluminosilicate layers with interlayer exchangeable cations [1, 2]. These clay minerals spontaneously undergo infinite swelling in water by taking the solvent into their interlayer spaces when the interlayer cations are Na^+ or Li^+, which can be hydrated to a large extent. The infinite swelling leads to exfoliation of individual layers to yield clay nanosheets. Such interlayer swelling is possible for various other ion-exchangeable layered solids if efficient interactions exist between the interlayer cations and solvent molecules. To date, exfoliation by the interlayer swelling has been realized for numerous synthetic ion-exchangeable layered solids.

Because the ion-exchangeable layered solids include both of cation- and anion-exchangeable materials, we now have a rich library of negatively and positively charged inorganic nanosheets [3–5]. Negatively charged nanosheets are usually obtained by exfoliation of layered oxometallates and metal phosphates, while positively charged ones are prepared from layered hydroxides. The nanosheets possess a wide variety of physicochemical properties. Nanosheets of the oxides, metal phosphates, and hydroxides composed of main-group elements are rather electronically inert and optically transparent. Oxometallates and hydroxides of transition metal and rare-earth elements are often photochemically and electronically active, showing various electric, optic, and magnetic functions.

This chapter describes fundamental aspects of the inorganic nanosheets obtained from ion-exchangeable layered solids other than the smectite group of clay minerals

T. Nakato (✉)
Department of Applied Chemistry, Kyushu Institute of Technology,
1-1 Sensui-cho, Tobata-ku, 804-8550 Kitakyushu, Fukuoka, Japan
e-mail: nakato@che.kyutech.ac.jp

T. Nakato et al. (eds.), *Inorganic Nanosheets and Nanosheet-Based Materials*,
Nanostructure Science and Technology, DOI 10.1007/978-4-431-56496-6_3

that are reviewed in the preceding chapter. It includes details of exfoliation such as the role of exfoliating reagents and delamination mechanisms, the state of the exfoliated nanosheets in the solvents, preparation and structures of nanosheet assemblies, and brief comments on the structure and functions of some typical nanosheet species.

3.2 Cation-Exchangeable Layered Solids and Their Exfoliation

3.2.1 Cation-Exchangeable Layered Solids

Most of the cation-exchangeable layered solids that can be exfoliated into the nanosheets are layered oxometallates and metal phosphates. Table 3.1 lists such materials except for the clay minerals. Structures of these layered solids consist of negatively charged metal oxide or phosphonate layers and interlayer exchangeable cations. For many transition metal-based oxometallates such as titanates, niobates, manganates, and ruthenates, the oxide layers are usually constructed of metal-oxygen (MO_6) octahedral connected by corner- and edge-sharing, while layered silicates are built up from corner-sharing SiO_4 tetrahedra. The metal phosphates layers consist of MO_6 octahedra and PO_4 tetrahedra. These layers have negative charges stoichiometrically determined by their composition. In most cases,

Table 3.1 Representative synthetic ion-exchangeable layered solids that can be exfoliated into nanosheets

Exchangeable ion	Category	Representative compounds	References
Cation	Titanate	$H_xTi_{2-x/4}\square_{x/4}O_4$, $H_{0.8}Ti_{1.2}Fe_{0.8}O_4$, $H_2Ti_3O_7$, $H_2Ti_4O_9$	[6–9]
	Niobate	$K_4Nb_6O_{17}$, HNb_3O_8, $HTiNbO_5$, HTi_2NbO_7, $HNbWO_6$,	[10–14]
	Tantalate	$HTaO_3$, $HTaWO_6$	[13, 15]
	Perovskite-type niobate, tantalate	$HCa_2Nb_3O_{10}$, $HLaNb_2O_7$, $H_2SrTa_2O_7$	[16–18]
	Manganate	$K_xMnO_2{\cdot}nH_2O$	[19]
	Cobaltate	$HCoO_2$	[20]
	Ruthenate	$K_{0.2}RuO_{2.1}$, $Na_{0.22}RuO_2$	[21, 22]
	Tungstate	$H_2W_2O_7$, $Cs_{6+x}W_{11}O_{36}$	[23, 24]
	Silicate	Octosilicate ($Na_8H_8Si_{32}O_{72}{\cdot}32H_2O$)	[25]
	Metal phosphate	α-$Zr(HPO_4)_2$, $H_3Sb_3P_2O_{14}$	[26, 27]
Anion	Layered double hydroxide	$[Mg_{1/3}Al_{2/3}(OH)_2](NO_3)_{1/3}]$ $[Co_{1/3}Al_{2/3}(OH)_2](CO_3)_{1/6}$	[28, 29]
	Hydroxide salt	$Cu_2(OH)_3(CH_3COO){\cdot}H_2O$ $La(OH)_2NO_3$	[30, 31]

the layer charge density is too high to allow spontaneous exfoliation through the interlayer solvation. This situation is overcome by the use of exfoliating reagents as described below.

3.2.2 *Exfoliation*

Cation-exchangeable layered solids are usually exfoliated into nanosheets through exchange of the interlayer cations for appropriate cations that are often called exfoliating reagents. The exfoliating reagents are usually organic cations with appropriate bulkiness and high affinity for the solvent. The exfoliating reagents are first intercalated to the layered crystals through ion exchange, and then drag the solvent molecules into the interlayer spaces (Fig. 3.1). Typically, organic cations represented by tetrabutylammonium ions (TBA^+) are used for the exfoliation in water while long-chain organic species are employed for exfoliation in organic solvents. The organoammonium exfoliating reagents are often intercalated to the layered solids with the aid of acid-base reactions when they cannot be directly incorporated [32]. This method involves acid treatment of the starting layered solids, by the treatment of which the interlayer cations are exchanged for H^+ ions, and subsequent reaction with organic amine molecules that react with the H^+ ions by the acid–base mechanism to form interlayer organoammonium ions that induce exfoliation.

The exfoliation through the ion-exchange route facilitates formation of the single nanosheets. This is guaranteed by the presence of interlayer exchangeable cations located in all the interlayer spaces with the same crystallographic microenvironment because of the stoichiometric distribution of the layer charges; a known exception is hexaniobate ($Nb_6O_{17}^{4-}$) nanosheets as described in Sect. 3.4.2 [33]. The incorporated exfoliating reagents attract solvent molecules equally into all of the interlayer spaces to infinitely swell the interlayer spaces. The driving force for the swelling is solvation of the exfoliating reagents by dipole interactions with water and other polar solvent molecules. As a result of infinite swelling, individual layers of the mother crystals are exfoliated into the nanosheets. Because the obtained nanosheets bear negative charges, exfoliating reagents such as TBA^+ ions are attached to the nanosheets to compensate the layer charge.

In contrast to exfoliation in aqueous systems, that in nonpolar organic solvents has rarely been examined. Such exfoliation can be realized by the use of

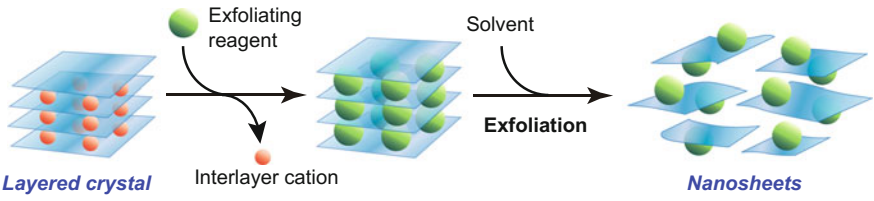

Fig. 3.1 Schematic model of the exfoliation of cation-exchangeable layered solids

organophilic exfoliating reagents such as long-chain organic molecules through hydrophobic interactions with the nonpolar solvents. However, this process is more difficult than exfoliation in water because the inorganic layers themselves are highly polar, and tend to expel the nonpolar solvents because of their electric charges. Although this problem can be overcome by covalent bonding of organic molecules, this technique has only been applied to selected materials as described later.

3.3 Exfoliation Mechanism in Aqueous Systems

According to the systematic studies conducted by Sasaki and coworkers on lepidocrocite-type layered titanate [6, 34–39], $H_xTi_{2-x/4}\square_{x/4}O_4$ ($x \sim 0.7$, $\square$: vacancy) [40–42], osmotic swelling plays a key role in the exfoliation mechanism of cation-exchangeable layered solids in water (Fig. 3.2). This section describes the exfoliation mechanism and important factors affecting the nanosheet generation of the titanate in water as an example of the exfoliation of cation-exchangeable layered solids.

3.3.1 Osmotic Swelling

The exfoliation of cation-exchangeable layered solids begins by gigantic or infinite swelling of the interlayer spaces. Such swelling is generally called osmotic swelling. This concept was proposed in the 1930s and discussed until the 1970s to

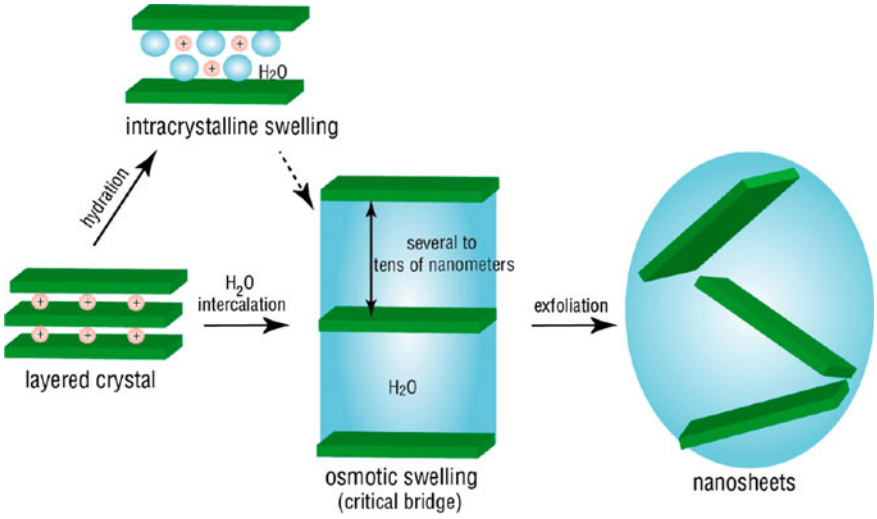

Fig. 3.2 Schematic illustration of the swelling and exfoliation process of lepidocrocite-type titanate. Reprinted with permission from [38]. Copyright 2014 American Chemical Society

explain very high degree of swelling observed for the smectite group of clay minerals in water [1, 2, 43]. For the case of the layered titanate $H_xTi_{2-x/4}\square_{x/4}O_4$, each crystallite effectively draws a huge amount of water molecules into its interlayer spaces through dipole interactions with the interlayer cations when they are TBA^+ ions [6, 35]. As a result, the basal spacing of the titanate layers reaches more than several tens of nanometers, which is more than ten times that of the starting titanate crystal ($\sim$1 nm). However, the amount of incorporated water molecules in the swollen state is too large to be explained by molecular interactions between the interlayer TBA^+ ions and water. In fact, the process is rationalized by the osmotic pressure between the interlayer spaces and outside solvents. Because the hydrated interlayer space is recognized as a TBA^+ solution with a high concentration, a large amount of water molecules outside the interlayer spaces can penetrate into the interlayer spaces driven by the difference in osmotic pressure between inside and outside the interlayer spaces.

In addition to such a qualitative explanation, recent studies on layered titanate $H_{0.8}Ti_{1.2}Fe_{0.8}O_4$ have enabled quantitative understanding of its osmotic swelling. In these studies, swelling by several primary, tertiary, and quaternary organoammonium ions are compared [36–38]. Most of the organoammonium ions show the same amount of incorporation, and the same degree of interlayer expansion induced by the gigantic swelling (Fig. 3.3). In the fully swollen stage, the concentration of organoammonium ions in the interlayer regions, i.e., in the swollen phase gives an osmotic pressure equal to the atmospheric pressure; the outside solvents contain few organoammonium ions under such conditions. These facts indicate that the

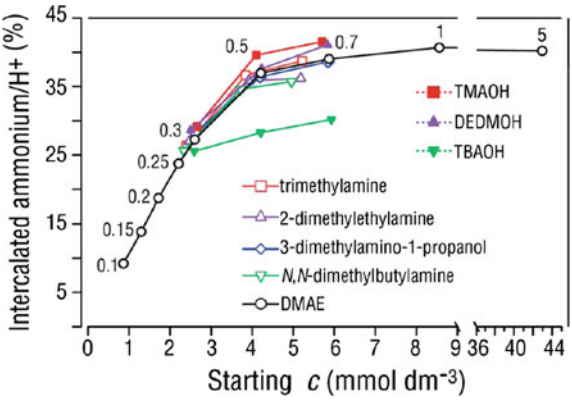

Fig. 3.3 Quantity of intercalated ammonium for tertiary amines and quaternary ammonium hydroxides as a percentage ratio of the cation-exchange capacity (CEC) of the lepidocrocite-type titanate crystals. The *open symbols* represent tertiary amines, while the *filled symbols* represent quaternary ammonium hydroxides. The *numbers* in the panel are the ratios of the starting amine or ammonium hydroxide to the CEC of the crystals. *All lines* except the one for TBAOH overlap, suggesting that these tertiary amines and quaternary ammonium hydroxides have similar affinities for the crystals. The lower intercalation of TBAOH is likely due to steric effects. Reprinted with permission from [38]. Copyright 2014 American Chemical Society

swelling of the layered titanate proceeds until the interlayer osmotic pressure is balanced by the atmospheric pressure. This is the evidence for the osmotic, i.e., colligative nature of the gigantic swelling caused by the organoammonium ions.

3.3.2 *From Swelling to Exfoliation*

Exfoliation of the cation-exchangeable layered solids is understood as shear-induced liberation of the stacked nanosheets in the gigantically swollen state. The attractive electrostatic interactions between the negatively charged layers through the interlayer cations are weakened under the swollen conditions, and overcome with mechanical shear applied by stirring the solvents. The shear stress causes the exfoliation to form the nanosheets dispersed in the solvent.

Formation of the monolayer (single) nanosheets has been clarified in the exfoliation of lepidocrocite-type titanate $H_xTi_{2-x/4}\square_{x/4}O_4$ [6, 34, 35]. X-ray diffraction (XRD) showed that the basal spacing of the titanate increased while maintaining high stacking regularity upon the intercalation of TBA^+ ions and their hydration as indicated by the shift of the basal reflection accompanied by higher order peaks to lower diffraction angles with maintaining their sharpness. However, when the sample reached the osmotic swelling, the basal reflection disappeared and broad peaks appeared at higher angles. The broad peaks were assigned to the exfoliated monolayer nanosheets according to the X-ray scattering because they were fitted by the square of the structural factor estimated by assuming the single nanosheets. Similar patterns have been obtained following exfoliation of other ion-exchangeable layered solids such as a perovskite-type niobate [44], manganate [45], and layered double hydroxide (LDH) [29]. Their scattering profiles depended on the exfoliated compounds and were fitted by the square of the structural factors of the corresponding nanosheet species (Fig. 3.4).

3.3.3 *Effects of the Exfoliating Reagent and Temperature*

Regarding the relationship between the interlayer swelling and exfoliation, the osmotic swelling is essentially independent of the exfoliation although the former is a prerequisite for the latter. This relationship has been clarified by studying the swelling of lepidocrocite-type titanate $H_{0.8}Ti_{1.2}Fe_{0.8}O_4$ with different primary, tertiary, and quaternary organoammonium ions [36, 38]. The organoammonium ions that can exfoliate the titanate are limited to several species such as TBA^+, ethylammonium, and propylammonium (PA^+). In contrast, although 2-(dimethylamino) ethanol ($DMAE^+$) gigantically swelled this titanate, it hardly induced the exfoliation even when the swollen titanate powders were mechanically shaken in water (Fig. 3.5). In addition, quaternary TBA^+ and tetramethylammonium (TMA^+) ions

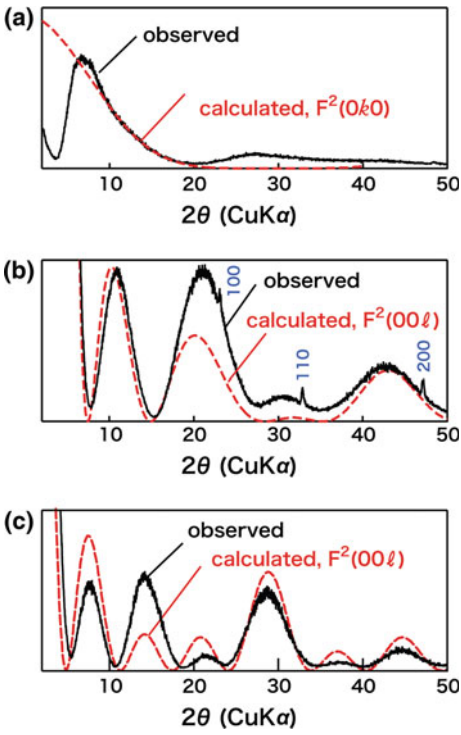

Fig. 3.4 Typical experimental profile of the diffraction envelope (*solid line*) and square of calculated structure factor (*broken line*) for nanosheets. **a** Repidocrocite-type titanate $Ti_{0.91}O_2^{0.36-}$; **b** Perovskite-type niobate $Ca_2Nb_3O_{10}^-$; and **c** Tungstate $Cs_4W_{11}O_{36}^{2-}$. The square of calculated structure factor fits well with the experimental profile. Reprinted with permission from [4]. Copyright 2010 John Wiley and Sons

both exfoliated this titanate, but the former species induced swelling to give unilamellar nanosheets faster than the latter.

These observations indicate that appropriately bulky and moderately polar organoammonium ions work as efficient exfoliating reagents. Cations that are small such as methylammonium and alkali metal cations strongly attaches to the anionic inorganic layers in close proximity in the interlayer spaces, which prohibits hydration of the cations. Highly polar cations such as $DMAE^+$, with positive charges that are localized at the end or edge of the molecules, are thought to strongly interact with water to form hydrogen-bonding networks between the layers to withstand the shear force inducing the exfoliation. A recent study has indicated that organic cations other than the organoammonium species act as the exfoliating reagents of lepidocrocite-type titanate $H_{0.8}Ti_{1.2}Fe_{0.8}O_4$ if the organic species fulfils the above requirement. In fact, tetrabutylphosphonium ions can exfoliate the titanate; they work better than TBA^+ ions because of their bulkiness [39].

Temperature can be another critical parameter affecting the exfoliation. Titanate nanosheets directly synthesized by hydrolysis–polycondensation of a titanium alkoxide in the presence of tetraalkylammonium ions [46] showed reversible exfoliation–stacking behavior under thermal stimuli [47]. The titanate nanosheets prepared by this method were similar to those obtained by exfoliation of tetratitanate $H_2Ti_4O_9$, and dispersed stably in water at room temperature to give a

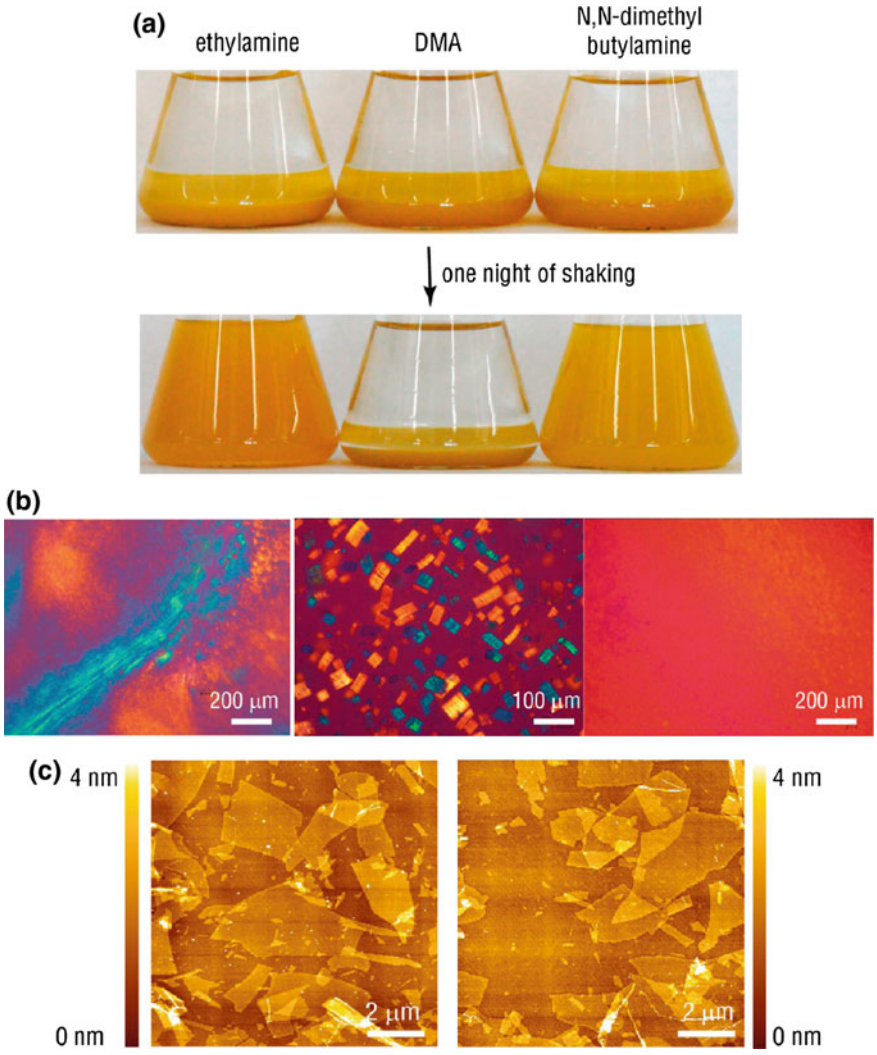

Fig. 3.5 **a** Optical photographs of the crystals swollen with ethylamine, DMA, and *N*,*N*-dimethylbutylamine before and after overnight mechanical shaking. **b** Optical microscopy images of solutions after overnight shaking. *Left* ethylamine, *middle* DMA, and *right* *N*,*N*-dimethylbutylamine. **c** AFM images of delaminated nanosheets in ethylamine and *N*,*N*-dimethylbutylamine. Reprinted with permission from [38]. Copyright 2014 American Chemical Society

transparent colloid. However, these nanosheets were stacked at high temperatures to make the colloid turbid, and were then re-exfoliated by lowering the temperature again. This temperature-induced stacking–exfoliation was reversible for many times, and the transition temperature depended on the tetraalkylammonium species coexisting in the system (Fig. 3.6). This behavior has been ascribed to the

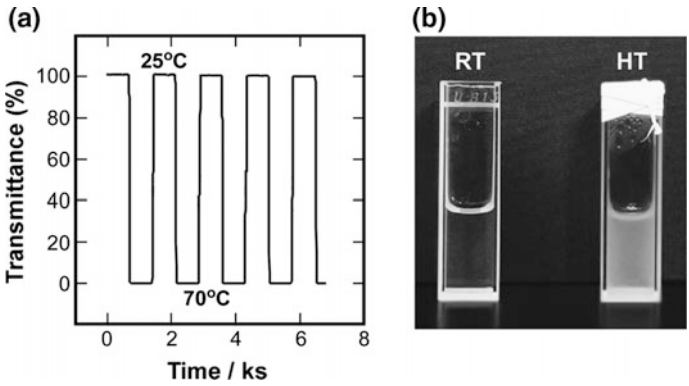

Fig. 3.6 **a** Transient transmittance at 550 nm of TBA^+–TiO_x during temperature switching between 25 and 70 °C. **b** Photographs of TBA^+–TiO_x colloidal solution at room (*RT*) and high temperature (*HT* around 60 °C). Reprinted with permission from [47]. Copyright 2014 Royal Society of Chemistry

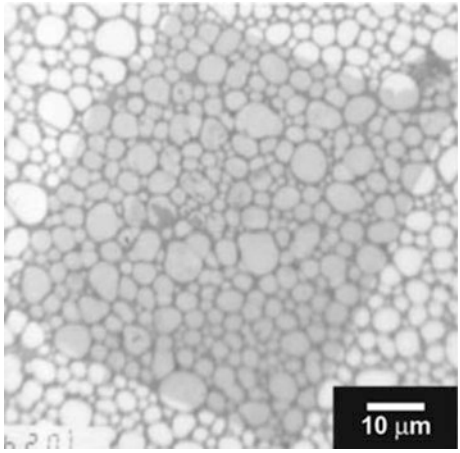

Fig. 3.7 TEM image of a large niobate nanosheet prepared by exfoliation of single crystalline $K_4Nb_6O_{17}$. Reprinted with permission from [33]. Copyright 2002 Royal Society of Chemistry

temperature dependence of the thickness of the electrical double layers at the titanate nanosheets.

3.3.4 Nanosheet Size

The lateral size of the exfoliated nanosheets reflects the size of the mother crystals of the layered solids. Nanosheets with a lateral dimension of micrometers have been obtained from the exfoliation of single crystalline layered titanate $H_xTi_{2-x/4}\square_{x/4}O_4$ [48] and niobate $K_4Nb_6O_{17}$ [33] with a millimeter to centimeter-scale of crystallite size (Fig. 3.7). The size decrease in the lateral direction compared with that of the

starting crystallites is caused by breakage of the nanosheets by the mechanical shear applied during the swelling and exfoliation processes. Since this is unavoidable and uncontrollable in the current experimental techniques for exfoliation, the nanosheets produced have large size distributions in the lateral direction although their thickness is monodisperse because the swelling of the ion-exchangeable layered solids occurs equally in all of the interlayer spaces as described above. The size distribution of nanosheets can be narrowed by gradient centrifugation [49]. The average lateral size of the nanosheets can be reduced by ultrasonic irradiation of the colloidal nanosheets after the exfoliation [50].

3.4 Exfoliation of Typical Cation-Exchangeable Layered Solids

This section briefly describes the structure, exfoliating behavior, and use of the exfoliated nanosheets obtained from typical cation-exchangeable layered solids.

3.4.1 Titanates

Layered titanates are the materials whose exfoliation has been studied the most of various ion-exchangeable layered solids [51], as described Sect. 3.3. These materials consist of negatively charged titanium oxide layers constructed of corner- and edge-shared TiO_6 octahedra and interlayer exchangeable cations [52, 53]. While lepidocrocite-type titanate $H_xTi_{2-x/4}\square_{x/4}O_4$ characterized by the edge-shared connection of TiO_6 octahedra in a flat manner is the most well-known compound [41], other titanates such as trititanate $H_2Ti_3O_7$ and tetratitanate $H_2Ti_4O_9$, both of which have zigzag-shape titanate layers with the corner- and edge-shared TiO_6 octahedra, are also available (Fig. 3.8) [54–58]. For the lepidocrocite-type titanate, Ti atoms in

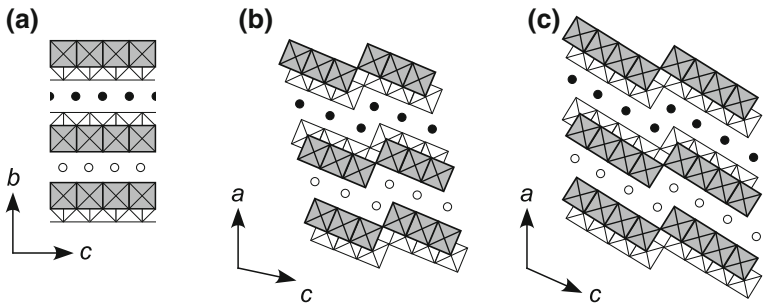

Fig. 3.8 Schematic representation of the crystal structures of **a** lepidocrocite-type titanate $H_xTi_{2-x/4}\square_{x/4}O_4$, **b** $H_2Ti_3O_7$, and **c** tetratitanate $H_2Ti_4O_9$

the layers can be partly substituted with other metallic species such as Mg, Mn, Fe, and Co, as exemplified by $H_{0.8}Ti_{1.2}Fe_{0.8}O_4$ [7, 36, 59–63].

Layered titanates are usually obtained with alkali cations as the interlayer exchangeable cations; e.g., $Cs_xTi_{2-x/4}\square_{x/4}O_4$, $Na_2Ti_3O_7$, and $K_2Ti_4O_9$ [40, 64, 65]. The alkali cations are readily exchanged for H^+ ions by acid treatments, and then the obtained titanic acids react with organoammonium ions as the exfoliating reagent by the acid-base mechanism. While TBA^+ is employed in most cases [6, 9, 34, 35, 66, 67], short-chain organoammonium monocations have been used for trititanate $H_2Ti_3O_7$ and tetratitanate $H_2Ti_4O_9$ [8, 68].

The exfoliation of the layered titanates in organic solvents has been investigated. Tetratitanate $H_2Ti_4O_9$ has been exfoliated in nonpolar solvents such as benzene, chloroform, octanol, and ethylacetate after grafting long-chain organosilyl moieties onto the titanate layers [69, 70]. A recent study has reported that lepidocrocite-type titanate $H_xTi_{2-x/4}\square_{x/4}O_4$ can be exfoliated in toluene after intercalation of tetradecylammonium and octadecylammonium ions (Fig. 3.9) [71].

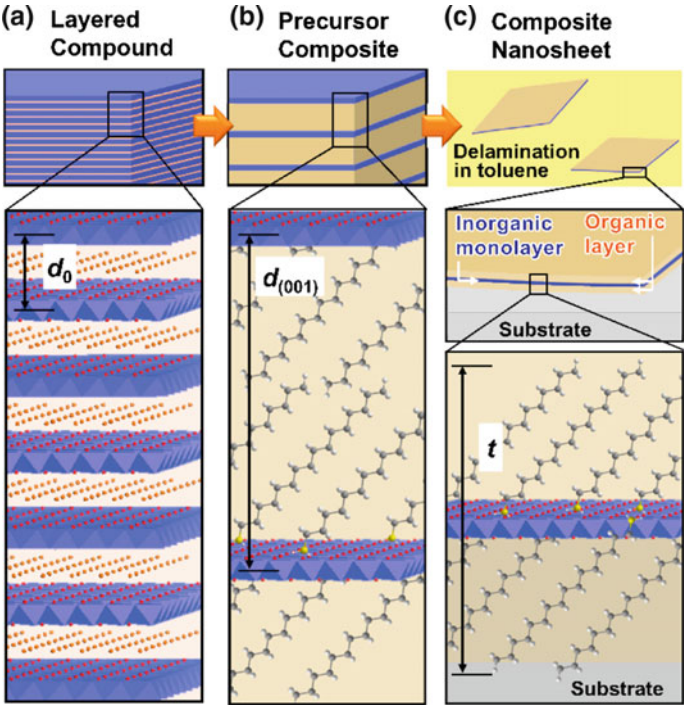

Fig. 3.9 Schematic illustration of the approach for preparing the lepidocrocite-type titanate nanosheets in an organic solvent. **a** The pristine titanate with the interlayer space of d_0; **b** The precursor composite with the intercalation of the long-chain alkylammonium ions in the interlayer space; and **c** The delamination into toluene through the hydrophobic interaction and the formation of the composite nanosheets on a silicon substrate. The $d_{(001)}$ and t indicate the interlayer distance of the precursor composite and the thickness of the composite nanosheets, respectively. Reprinted with permission from [71]. Copyright 2009 American Chemical Society

Applications of the titanate nanosheets by utilizing their wide band-gap semiconducting [72–76] and dielectric properties [4, 77, 78] have been examined. Titanate nanosheets have been investigated as photocatalysts for a long time as described in Chaps. 15–17 [79–84]. Nitrogen- and iodine-doping of lepidocrocite-type titanate nanosheets can narrow their band-gap to result in visible-light photocatalytic activity [85, 86]. In other researches, the titanate nanosheets are employed as dielectric building blocks in electronic devices prepared by layer-by-layer (LbL) assembly of various nanosheets [77, 87]. Lepidocrocite-type titanate nanosheets partially substituted by Mn, Fe, and Co exhibit redox, magnetooptic, and ferromagnetic properties that reflect the nature of dopants [59–62, 88].

3.4.2 Niobates and Tantalates

Layered niobates and tantalates, exemplified by HNb_3O_8, $K_4Nb_6O_{17}$, and $HTaO_3$, possess structures and properties similar to those of the layered titanates [15, 32, 89–93]. Figure 3.10 shows schematic structures of some layered niobates. These materials are constructed from connected NbO_6 or TaO_6 octahedra that form electrically negative layers with interlayer cations. Binary oxometallates including a transition metal in addition to Nb or Ta are also known: e.g., $HTiNbO_5$, $HNbWO_6$, and $HTaWO_6$ [94–98]. Lepidocrocite-type titanoniobate $H_{0.7}Ti_{1.825-x}Nb_xO_4$ (x = 0–0.33) has also been prepared [99]. Most of these layered materials can be exfoliated by the reaction of H^+-exchanged layered crystals with TBA^+ ions [11, 14, 15, 100, 101]. Other reported exfoliating reagents in water are triethanolammonium cations and $NH_2(CH_2)_{10}COOH$ molecules [102, 103]. Fluoroniobate K_2NbO_3F [104] has been reported to be exfoliated in water by an ultrasonic treatment without exfoliating reagents. However, this could be different from ordinary exfoliation because the exfoliated crystals are recovered as $KNbO_3$ with a 3D cubic structure [105, 106].

Among the layered niobates and titanates, hexaniobate $K_4Nb_6O_{17}$ shows special exfoliating behavior. This material is characterized by two types of alternating interlayer spaces called interlayers I and II. The interlayer K^+ ions can be directly exchanged for various cations without acid treatment and those in interlayer I show

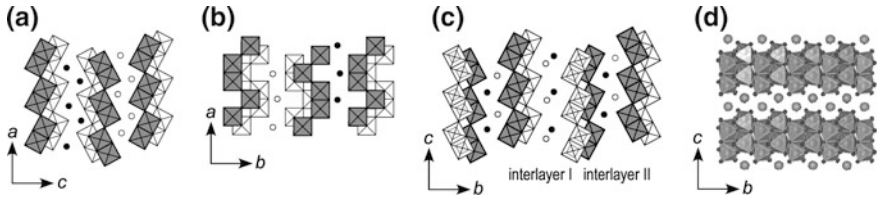

Fig. 3.10 Schematic representation of the crystal structures of **a** $HTiNbO_5$, **b** HNb_3O_8, **c** $K_4Nb_6O_{17}$, and **d** $LiMWO_6$ (M=Nb, Ta). **d** Reprinted with permission from [107]. Copyright 2009 American Chemical Society

higher reactivity than those in interlayer II [91, 108, 109]. Exfoliation induced by treating $K_4Nb_6O_{17}$ with PA^+ ions yielded bilayer nanosheets through swelling of interlayer I, because PA^+ ions displace the K^+ ions only in interlayer I [33, 110, 111]. Exfoliation was also achieved by the two-stage process of acid treatment and subsequent TBA^+ or butylammonium exchange, which also generates the bilayer nanosheets [10, 100, 112, 113].

Exfoliation of the layered niobates in organic solvents has been achieved for $K_4Nb_6O_{17}$ by making the interlayer spaces hydrophobic by grafting long-chain organic moieties onto the niobate layers. Grafting is attained after expanding the interlayer spaces with dodecylammonium ions (DA^+). Because the exchange of K^+ for DA^+ occurred in both interlayers I and II [109], grafting took place in both interlayer spaces to give monolayer nanosheets. Grafting of octadecyltrimethylsilyl groups enabled exfoliation in tetrachloromethane [114]. To graft phenylphosphonate moieties in $K_4Nb_6O_{17}$, interlayer expansion was carried out with dioctadecyldimethylammounium ions in addition to DA^+; the former only expanded interlayer I, while the latter expanded both interlayer spaces. This enabled two types of grafting of phenylphosphonate groups, and provided both of the bilayer and monolayer nanosheets upon exfoliation in acetonitrile (Fig. 3.11) [115].

Niobate and tantalate nanosheets have been used as semiconducting photocatalysts and dielectric materials similar to the titanate nanosheets [10, 78, 87, 102, 116–125]. Photoelectrochemical cells have also been constructed containing these nanosheets [126–128]. In addition, because the acid strength of H^+ ions on the niobate and tantalate nanosheets is greater than those on the titanate nanosheets [32], they have been applied as strong solid acid catalysts [13, 107, 129, 130].

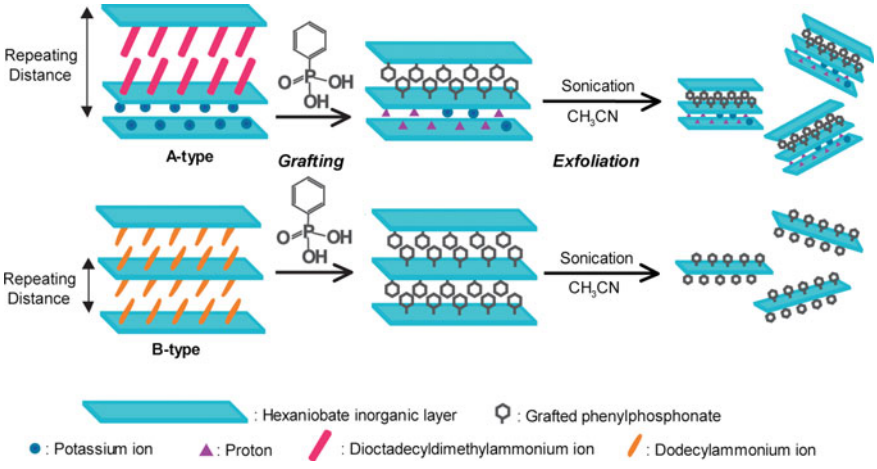

Fig. 3.11 Preparation of monolayer- and bilayer-nanosheets by exfoliation of layered hexaniobate $K_4Nb_6O_{17}$ modified with phenylphosphonic acid. Reprinted with permission from [115]. Copyright 2014 American Chemical Society

3.4.3 Perovskite-Type Titanates, Niobates, and Tantalates

Perovskite-type titanates, niobates, and tantalates are members of cation-exchangeable layered oxometallates characterized by perovskite-type oxide layers [131, 132]. Each perovskite-type layer is a slice of a cubic crystal of ABO_3 perovskite cut in parallel to its (100) direction with containing n B-site sheets (sheets of connected BO_6 octahedra), which sandwiches to interlayer cations such as alkali metal ions to build up the layered structure (Fig. 3.12). The Dion–Jacobson (DJ) phase $M[A_{n-1}B_nO_{3n+1}]$ [133, 134] and Ruddlesden–Popper (RP) phase $M_2[A_{n-1}B_nO_{3n+1}]$ (M=Na, K, etc.; A=Ca, Sr, lanthanide, etc.; B=Ti, Nb, Ta) [135–137] are known. The number of B-site sheets, n, reflects the thickness of a perovskite-type layer; the layer thickness with $n \geq 3$ is much larger than that of the conventional layered titanates, niobates, and tantalates described in the above sections. The interlayer cations are usually exchanged for H^+ ions by acid treatment prior to the exfoliation because the interlayer alkali ions M^+ are strongly held by the perovskite-type layers [138]. Considering the DJ and RP phases, the former incorporates organoammonium ions more easily than the latter because the latter has a higher layer charge density and interlayer cations in more confined environments [139].

Exfoliation of perovskite-type niobate $HCa_2Nb_3O_{10}$ (DJ phase, $n = 3$) has been investigated ahead of other layered titanates, niobates, and tantalates using a commercial monoamine surfactant as the exfoliating reagent [16]. To date, exfoliation of $HCa_2Nb_3O_{10}$ has been frequently carried out mainly with TBA^+ ions [140–143]. Formation of the monolayer nanosheets has been established by the XRD study [44]. Niobates and tantalates with thicker layers, $HCa_2Na_{n-3}Nb_nO_{3n+1}$ (DJ phase, $n = 4$–6), those partially substituted by lantanide elements such as $HLn_{1-x}La_xNb_2O_7$ (Ln = Sm^{3+}, Eu^{3+}, Gd^{3+}, etc.; DJ phase; $n = 2$), and those doped with fluorine and nitrogen such as $HRbSrNb_2O_6F$ (DJ phase, $n = 2$) can also be

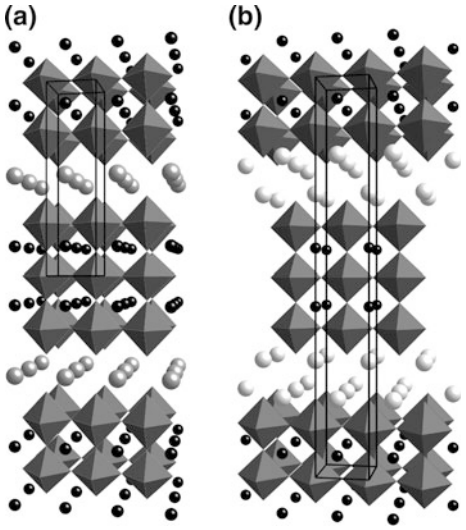

Fig. 3.12 Schematic representations of the crystal structures of perovskite-type layered **a** niobate $RbCa_2Nb_3O_{10}$ (DJ phase, $n = 3$) and **b** titanate $K_2La_2Ti_3O_{10}$ (RP phase, $n = 3$)

exfoliated [144–151]. For the RP phase, $H_2[A_{n-1}B_nO_{3n+1}]$ (A = Na, Ca, Sr, La; B = La, Ti; n = 2 or 3), $H_2SrTa_2O_7$ (n = 2), $H_{1.67}Bi_{0.21}Sr_{0.85}Ta_2O_7$ (n = 2), and $H_2Sr_{1.5}Ta_3O_{10}$ (n = 3) form nanosheets with the aid of organoammonium cations [18, 152–154]. $Li_2Bi_4Ti_3O_{12}$ (RP phase, n = 3) has been exfoliated in water without an exfoliating reagent to yield $[Bi_4Ti_3O_{12}]^-$ nanosheets accompanied by reduction of water [155]. Exfoliation in organic solvents has been achieved for $HLaNb_2O_7$ by grafting a siloxane-terminated polymers and alkoxysilane through controlled hydrolysis–condensation reactions [17].

Applications of the perovskite-type oxometallates are similar to those of the other layered titanates, niobates, and tantalates described above. Photocatalysts, photoelectrodes, and photoconductive films of the perovskite-type nanosheets have been prepared [44, 128, 156–166]. The dielectric properties of such nanosheets have also been utilized [167–169]. Rare-earth substituted nanosheets have been examined as photoluminescent materials [144–147, 150, 153].

3.4.4 Other Transition-Element Oxometallates

3.4.4.1 Manganates

Layered manganate with the birnessite-type structure $A_xMnO_2{\cdot}nH_2O$ (A=Na, K), also known as δ-MnO_2, has been exfoliated to yield manganese oxide nanosheets. The layered structure consists of anionic manganese oxide layers of edge-shared MnO_6 octahedra and interlayer cations (Fig. 3.13) [170–172]. Sodium manganate synthesized by oxidation of Mn^{2+} species in an alkaline solution [19, 173] and potassium manganate prepared by oxidation of Mn_2O_3 through calcination [45, 174] or by reduction of permanganate ions with KOH are used as the starting materials of the nanosheets [175]. After exchange of the interlayer alkali ions for H^+ ions, the layered manganate is exfoliated with the aid of TBA^+ or TMA^+ ions. Complete exfoliation to monolayers was established by the XRD analysis. In addition, the manganate nanosheets have been directly synthesized by oxidation of Mn^{2+} ions in the presence of TBA^+ ions [176]. Because of the mixed-valent and

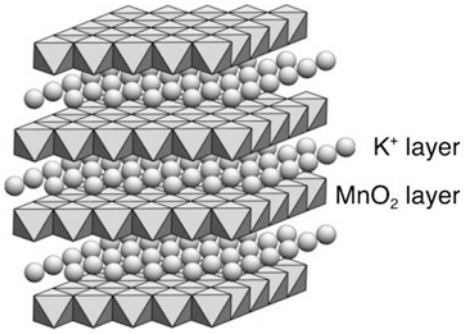

Fig. 3.13 Schematic representation of the crystal structure of layered manganate $K_{0.45}MnO_2$. Reprinted with permission from [174]. Copyright 2006 American Chemical Society

redox-active nature of the manganese oxides, the manganate nanosheets are applicable to electrochemical devices such as supercapacitors and lithium-ion batteries [175, 177, 178].

3.4.4.2 Cobaltates

Since layered lithium cobaltate $LiCoO_2$ is known as an electrode material of lithium-ion batteries [179–181], exfoliation of layered cobaltates has been investigated. $LiCoO_2$ has an α-$NaFeO_2$-type structure, which is related to the rock salt structure and consists of $[CoO_2]^-$ layers and interlayer Li^+ ions [182] (Fig. 3.14). $LiCoO_2$ has been exfoliated by the acid treatment and successive reaction with TMA^+ ions [20]. Multicomponent cobaltate $Li[Mn_{1/3}Co_{1/3}Ni_{1/3}]O_2$ and nonstoichiometric cobaltate Na_xCoO_2 have also been exfoliated in a similar manner [183]. The exfoliated cobaltate nanosheets are promising for use in lithium-ion batteries, although detailed results have not appeared yet. In addition, the p-type wide band-gap semiconducting nature of the cobaltate [184] is attractive because many other semiconducting oxometallates, such as titanates and niobates, are n-type. Nanosheets prepared from Na_xCoO_2 exhibited thermoelectric properties after reconstruction of the layered structure with Ca^{2+} ions [185].

3.4.4.3 Ruthenates

Inspired by the excellent properties of RuO_2 as an electrochemical capacitor [186], exfoliation of layered ruthenates has been investigated. The first ruthenate exfoliated was $K_{0.2}RuO_{2.1}$ whose structure has not been determined [21]. Exfoliation was

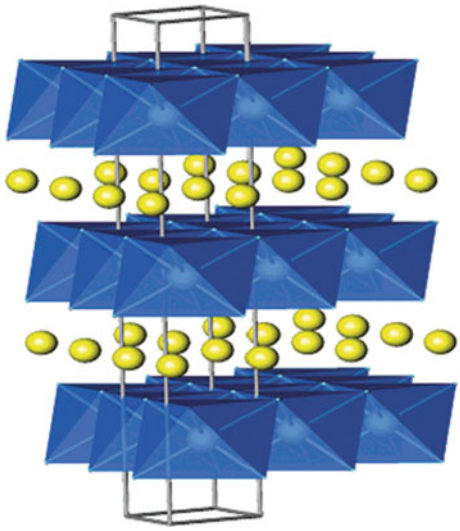

Fig. 3.14 Schematic representation of the crystal structure of layered manganate $LiCoO_2$. Reprinted with permission from [181]. Copyright 2004 American Chemical Society

realized by acid and subsequent TBA^+ treatment. $NaRuO_2$ with an α-$NaFeO_2$-related structure was also exfoliated by the same method after oxidative deintercalation of Na^+ ions to $Na_{0.22}RuO_2$ [22]. The ruthenate nanosheets exhibited superior performance as an electrochemical capacitor compared with that of bulk RuO_2 crystals. A metal–insulator–metal structure applicable to an ultrathin capacitor has been obtained by combining the $Ru_{0.95}O_2^{0.2-}$ and dielectric $Ca_2Nb_3O_{10}^-$ nanosheets [168].

3.4.4.4 Tungstates

Exfoliation of layered tungstates has been reported for $H_2W_2O_7$, which is obtained from $Bi_2W_2O_7$ possessing an Aurivillius-type perovskite structure with vacant A-sites by abstraction of the $Bi_2O_3^+$ unit through an acid treatment [23]. The protonated tungstate was exfoliated through reaction with TBA^+ ions. Exfoliation of layered tungstate $Cs_{6+x}W_{11}O_{36}$ was also achieved by acid and subsequent TBA^+ treatment. In this case, mesh-like tungstate nanosheets with interconnected pyrochlore-type channels were obtained (Fig. 3.15), and the nanosheets show photochromic behavior like that of WO_3 [24].

3.4.5 Silicates

Layered silicates are oxides consisting of anionic silicate layers constructed of corner-shared SiO_4 tetrahedra and interlayer exchangeable cations [187–189]. The structure of layered silicates can be recognized by the numbers of the sheets of

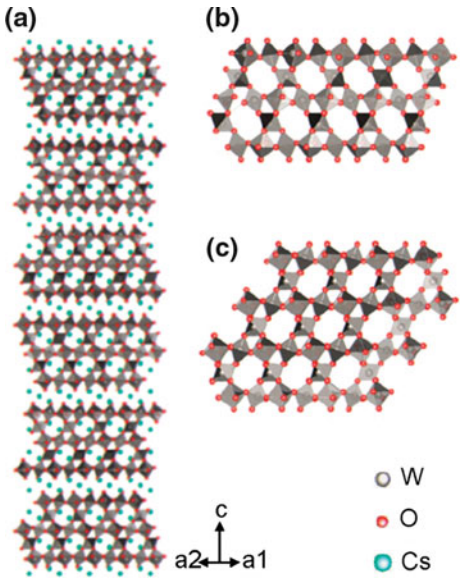

Fig. 3.15 Crystal structure of $Cs_{6+x}W_{11}O_{36}$ viewed along the [110] direction, **a** Pyrochlore-type channels appeared in **b** the section view and in **c** the plane view (a 35° tilt from the horizontal alignment); Cs ions are omitted to highlight the channel structure. Reprinted with permission from [24]. Copyright 2008 American Chemical Society

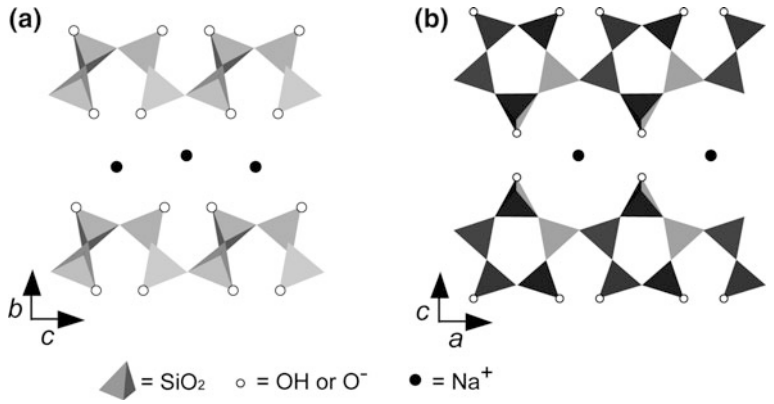

Fig. 3.16 Schematic representation of the crystal structures of **a** kanemite (single-sheet silicate) and **b** octosilicate (double-sheet silicate)

connected SiO_4 tetraheda stacked in each oxide layer. While kanemite $NaHSi_2O_5{\cdot}3H_2O$ and apophyllite $KCa_4[Si_4O_{10}]_2(F, OH){\cdot}38H_2O$ are single-sheet silicates [190, 191], octosilicate $Na_8H_8Si_{32}O_{72}{\cdot}32H_2O$ is a double-sheet silicate [192] (Fig. 3.16). Magadiite has thick silicate layers (more than three sheets), although its crystal structure has not been determined [193]. From a physicochemical point of view, the layered silicates are chemically stable and optically transparent similar to the clay minerals but they do not show specific electronic and photochemical properties. Such properties are different from those of the transition-metal oxometallates described above.

Although the cation-exchangeable layered silicates intercalate many guest molecules through various mechanisms including cation exchange, acid-base reaction, polar adsorption, and grafting, they do not show high exfoliating reactivity. There is no reliable report of the TBA^+-induced exfoliation of a silicate in water. Exfoliation of octosilicate in water has been realized by multistep modification of the silicate layers; the Si–OH groups on the layer surfaces were grafted with organosilyl moieties possessing mercapto terminal groups, and then the terminals were oxidized to hydrophilic $–SO_3H$ groups [25]. Grafting of a silane coupling reagent with imidazolium functional groups has also enabled exfoliation of octosilicate in water (Fig. 3.17) [194]. As for exfoliation in an organic solvent, silylation of apophyllite has been reported to give transparent gels of the silicate nanosheets in CCl_4 [195].

3.4.6 Metal Phosphates

Metal phosphates are water-insoluble acidic salts obtained form multivalent metal ions with amphoteric nature, such as Zr^{4+}, Ti^{4+}, Al^{3+}, and Sb^{5+}, and phosphoric

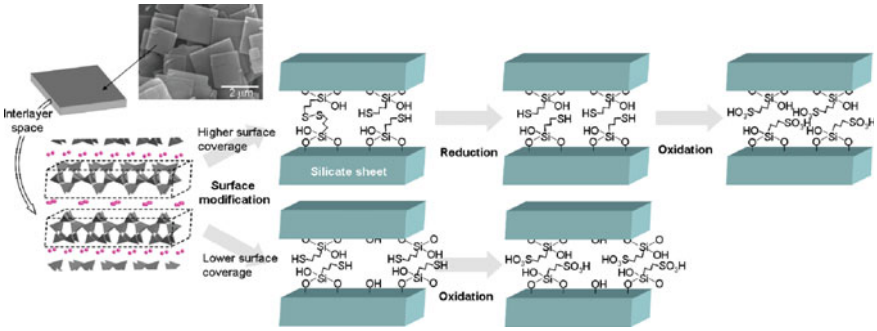

Fig. 3.17 Surface modification of octosilicate with the sulfonic acid group for exfoliation in water. Reprinted with permission from [25]. Copyright 2009 American Chemical Society

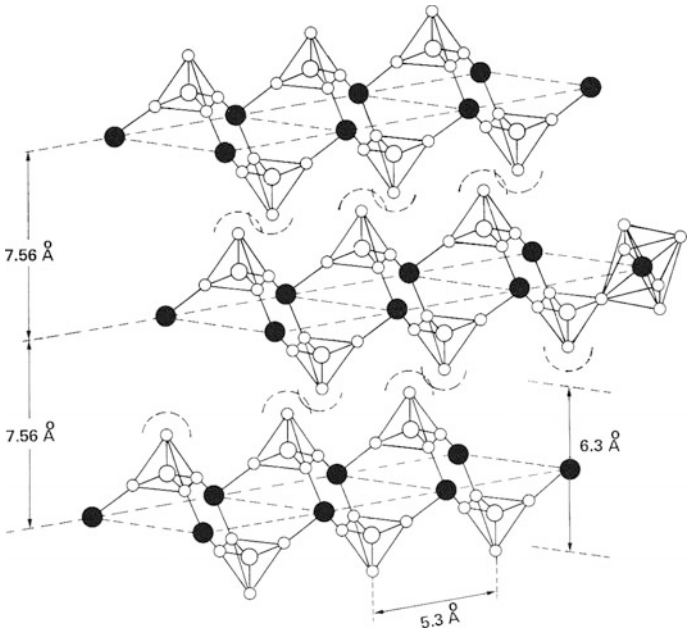

Fig. 3.18 Schematic representation of the crystal structure of α-ZrP. Reprinted from [199]. Copyright 1982 Elsevier Inc

acid. Among various cation-exchangeable amorphous metal phosphates, α-zirconium phosphate (α-$Zr(HPO_4)_2$, α-ZrP) was first found to exist as a layered solid [196]. Various cation-exchangeable layered metal phosphates have since been synthesized. Their structures are characterized by the connection of the MO_6 octahedra and PO_4 tetrahedra to form negatively charged layers (Fig. 3.18). Interlayer exchangeable cations, e.g., H^+ ions for α-ZrP, are held by the $P–O^-$ moieties on the layer surfaces. Layered metal phosphates exhibit high intercalating reactivity through various mechanisms similar to that of layered silicates [197, 198].

In 1985, α-ZrP was found to form a stable colloid in water after reaction with PA^+, which is recognized as the first example of the exfoliation of a layered metal phosphate [26]. Later, formation of α-ZrP nanosheets was confirmed by exfoliation using TBA^+ or a commercial surfactant [100, 200]. γ-ZrP, a polymorph of α-ZrP, can also be exfoliated in water using dimethylamine as the exfoliating reagent [201]. Meanwhile, α-ZrP nanosheets in an aqueous colloidal state after exfoliation with PA^+ underwent sol–gel transition of the colloid upon displacing the solvent (water) for an organic one such as *N*,*N*-dimethylformamide, *N*-methylformamide, tetrahydrofuran, alcohols, or chloroform [202].

Exfoliation of metal phosphates has been extended to materials other than ZrP. Among these materials, layered antimony phosphate $H_3Sb_3P_2O_{14}$ [203] is important because it is exfoliated in water without the aid of an exfoliating reagent. Exfoliation is induced by dialyzing $H_3Sb_3P_2O_{14}$ obtained by acid treatment of $K_3Sb_3P_2O_{14}$ in water [27]. Complete exfoliation to monolayer nanosheets is supported by the liquid crystallinity of the resulting nanosheet colloid (see Chap. 8). Layered aluminophosphate $(C_2H_5NH_3)_3Al_3P_4O_{16}$ was also directly delaminated in a water–ethanol mixture [204]. Ultrasound irradiation assisted exfoliation of iron phenylphosphate $Fe(OH)(C_6H_5PO_4H)_{1.6}(HPO_4)_{0.4}$ in water and olivine-type iron phosphate NH_4FePO_4 in formamide [205]. In contrast, exfoliation of α-titanium phosphate and α-tin phosphate was realized using TBA^+ in acetonitrile [206].

3.4.7 Other Cation-Exchangeable and Related Materials

There are a few layered oxides that can be exfoliated through appropriate interlayer modifications. Although layered oxovanadium phosphate $VOPO_4{\cdot}2H_2O$ is not ion-exchangeable, it can intercalate various polar organic molecules including alcohols and amines [207]. Exfoliation occurs in polar organic solvents after intercalation of aromatic 4-butylaniline or acrylamide [208, 209]. Layered cuprate $Bi_2Sr_2Ca_{m-1}Cu_mO_y$, known as a high-temperature superconducting oxide having a perovskite-related structure, can also be exfoliated [210, 211]. After the starting cuprate was intercalated with HgX_2 (X=Br, I), and then with alkylpyridinium iodide, the material was exfoliated in acetone. Exfoliation of layered molybdate $Na_{0.9}Mo_2O_4$ in water was realized by conventional acid and TBA^+ treatment [212].

Layered solids that do not intrinsically have exchangeable cations can be converted to cation-exchangeable materials through reductive intercalation of interlayer cations. The reduced materials have nonstoichiometric interlayer charges with a low density compared with that of the stoichiometric compounds, and the interlayer spaces can often be infinitely swollen spontaneously like clay minerals. For example, $Fe^{III}OCl$ can be reduced by Fe^0 to $Fe^{II}_{x/2}[Fe^{II}_xFe^{III}_{1-x}]OCl$. The intercalated Fe^{2+} ions are exchangeable, and the interlayer space is swelled infinitely in water [213]. Many transition-metal dichalcogenides can be intercalated with alkali cations such Li^+ and Na^+ through partial reduction of the chalcogenide layers [214].

Solvation of the cations in polar solvents yields colloidal dispersions of the chalcogenide nanosheets [215].

3.5 Exfoliation of Anion-Exchangeable Layered Solids

The library of anion-exchangeable layered solids is still not as rich as that of cation-exchangeable ones. Anion-exchangeable layered solids are classified into LDHs and layered hydroxide salts, and the former is more common than the latter. Exfoliation of these anion-exchangeable layered solids yields positively charged nanosheets, which are important as the counterparts of the negatively charged nanosheets obtained from the cation-exchangeable materials.

3.5.1 Layered Double Hydroxides (LDHs)

LDHs are binary metal hydroxides with a general formula of $[M^{2+}_{1-x}M^{3+}_{x}(OH)_2][X^{m-}]_{x/m}{\cdot}nH_2O$, where M^{2+} and M^{3+} are metal ions and X^{m-} is an interlayer exchangeable anions. Usually, M^{2+} is Ca^{2+}, Mg^{2+}, Fe^{2+}, Ni^{2+}, or Zn^{2+}, M^{3+} is Al^{3+}, Cr^{3+}, Mn^{2+}, Fe^{3+}, or Gd^{3+}, and X^{m-} is $CO_3{}^{2-}$, $SO_4{}^{2-}$, Cl^-, or $NO_3{}^-$. Combination of Li^+ and Al^{3+} is also possible. Organic anions such as carboxylate and sulfonate can also be the X^{m-} species. LDHs are easily synthesized by liquid phase reactions under ambient conditions: typically, controlled precipitation of M^{2+} and M^{3+} species in an alkaline solution. Investigations of LDHs began before the 1940s and their structure and anion exchange behavior were clarified until the 1980s [216–220]. Today, chemical science of LDHs has been grown into a large research field in materials chemistry, and many review articles and books on LDHs have been published [4, 221–225]. Exfoliation of LDHs has also been summarized in detail in a recent review [226], which complements the present section.

The most ubiquitous LDH is $[Mg_{1-x}Al_x(OH)_2](CO_3)_{x/2}$ (Mg–Al–CO_3 LDH), known as hydrotalcite. The layered structure of Mg–Al LDHs is derived from that of brucite $Mg(OH)_2$, which has hexagonal layers consisting of connecting MgO(OH) octahedra. Although the hydroxide layers of brucite are attracted by van der Waals interactions, partial isomorphous substitution of Mg^{2+} for Al^{3+} in Mg–Al LDHs generates positive charges in the layers to allow electrostatic stacking with the interlayer anions for charge compensation. Such electrostatic layering is also observed for other LDHs; nevertheless, they are classified into hexagonal and rhombohedral polymorphs (Fig. 3.19) [216, 222]. The interlayer anions of LDHs are exchanged for many other inorganic and organic anions. However, $CO_3{}^{2-}$ is highly selective compared with other anions, particularly inorganic ones. Thus, selection of the initial interlayer anion is important to accomplish the desired anion exchange.

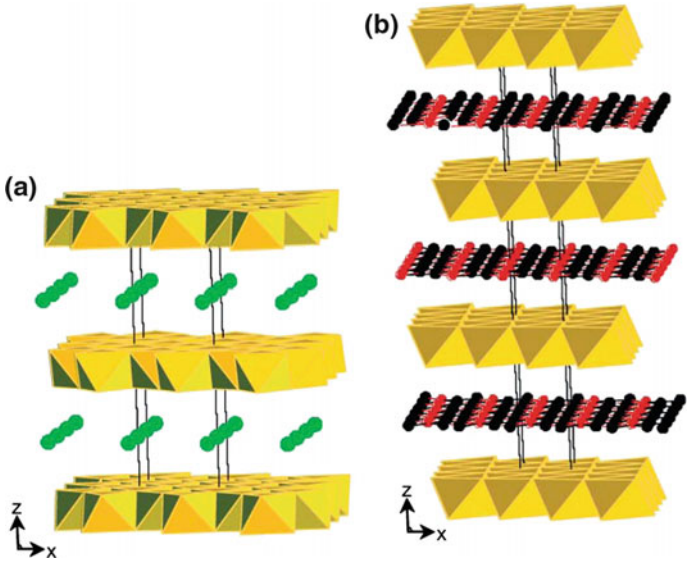

Fig. 3.19 Schematic representation of the crystal structure of an LDH showing the polymorphic stacking patterns: **a** hexagonal, **b** rhomohedral. Reprinted with permission from [222]. Copyright 2002 Royal Society of Chemistry

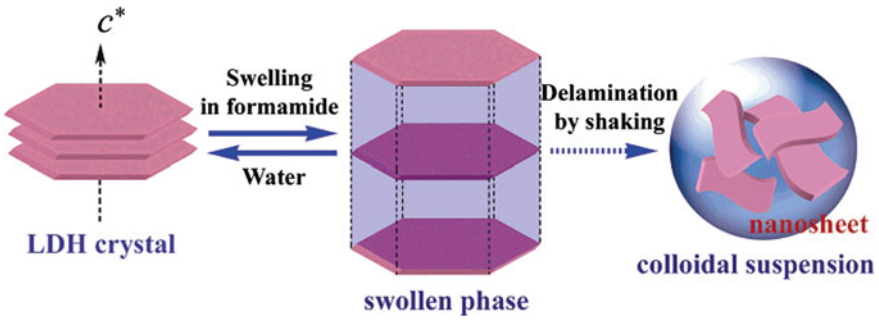

Fig. 3.20 Schematic model of the possible exfoliation mechanism for LDHs in formamide. Reprinted with permission from [29]. Copyright 2006 American Chemical Society

Although exfoliation of LDHs has been achieved by various methods since its discovery in 2000 [227], treating LDHs with interlayer NO_3^- anions in formamide is the most common method today [228]. In the first study of this method, Mg–Al–NO_3^- LDH prepared by a hydrothermal reaction of $Mg(NO_3)_2$ and $Al(NO_3)_2$ in the presence of hexamethyleneteramine was mechanically shaken in formamide [28]. Exfoliation into unilamellar LDH nanosheets through osmotic swelling has been confirmed by the XRD measurements, as mentioned in Sect. 3.3.2. Figure 3.20 schematically illustrates the exfoliation process in formamide. The use

of hexamethylenetetramine as the alkaline reagent and the high reaction temperature under hydrothermal or refluxing conditions yielded large LDH crystallites and thus large exfoliated nanosheets with a lateral dimension of micrometers. The formamide method has been rapidly expanded to a wide range of LDHs such as Co–Al–NO_3^- LDH prepared from other routes like conventional coprecipitation [29, 229, 230]. Other interlayer anions such as CO_3^{2-}, ClO_4^-, and amino acids also tolerate exfoliation in formamide; in fact, amino acids were identified as appropriate anions for formamide prior to NO_3^-.

LDHs incorporating long-chain organic species, e.g., dodecylsulfate anions, as an exfoliating reagent are exfoliated in organic solvents. The interlayer organic anions are introduced by anion exchange from inorganic anions or direct synthesis before exfoliation. Various organic solvents, from polar butanol and acrylate to nonpolar toluene and tetrachloromethane, are available for exfoliation [227, 231–233]. Exfoliation of dodecylsulfate-intercalated LDHs in toluene causes gelation of the solvents (Fig. 3.21) [234, 235]. Borate anions can also be utilized as the exfoliating reagent of LDHs for exfoliation in nonpolar hydrocarbons [236].

Exfoliation of LDHs in water can be achieved by introducing carboxylate anions such as lactate, acetate, and formate into their interlayer spaces [237–240]. Hydrogels were obtained upon exfoliation of Mg–Al–acetate LDH in water. For the case of Mg–Al–methoxide LDH, addition of water causes hydrolysis of the methoxide species in the interlayer spaces, and the hydrolysis induces exfoliation in water [241]. LDHs with interlayer perchlorate anions have been exfoliated in an aqueous solution of amino acids [242].

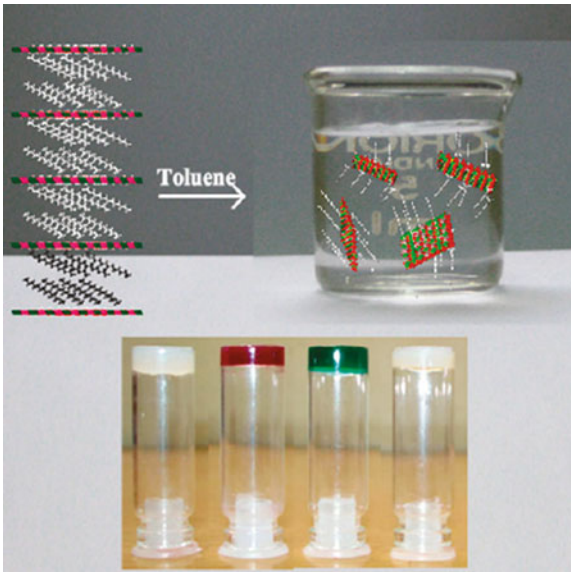

Fig. 3.21 Schematic representation of the exfoliation of organically modified LDHs in toluene and photographs of the gelled nanosheet colloids. Reprinted with permission from [234]. Copyright 2006 American Chemical Society

Like the nanosheets of cation-exchangeable layered solids such as clay minerals and oxometallates, exfoliated LDH nanosheets have been examined for various applications. Specific functions have been designed by the combination of divalent and trivalent metal cations in the LDHs and the positively charged nature of the nanosheets. Although Mg–Al LDHs are chemically inert, those containing transition metals show a variety of physicochemical properties. Redox-active LDHs are obtained with Ni^{2+}, Co^{2+}, and Mn^{2+}, and they have been prepared and examined in supercapacitors and lithium-ion batteries [243, 244]. LDHs with Cr^{3+} and Fe^{3+} have optical absorption in the visible region, and thus exhibit photocatalytic activities [245, 246]. In addition, the positively charged nature of LDH nanosheets allows them to be used as supports of anionic functional molecules that are luminescent, thermochromic, piezochromic, or photosensitizing molecules [247–250]. The positively charged nanosheets can also be used as macro-countercations of the negatively charged oxometallate nanosheets to yield heterocoagulated and superstructured nanosheet assemblies [251, 252]. Used as supports or carriers of bioactive molecules such as proteins, genes, and drugs [253–255] based on the biocompatibility of Mg–Al and Zn–Al LDHs [256, 257] is another growing field.

3.5.2 *Layered Hydroxide Salts*

There are metal hydroxide salts (or metal basic salts) that possess anion-exchangeable layered structures. A typical example is copper hydroxyacetate (basic copper acetate) $Cu_2(OH)_3(CH_3COO)\cdot H_2O$, also known as botallackite [258, 259]. In this compound, acetate groups coordinated to Cu^{2+} in the hydroxide layers are projected into the interlayer spaces, and are partly exchanged for other anions. This layered hydroxide salt can be exfoliated in formamide under solvothermal conditions to yield CuO nanosheets [30]. Analogs of this compound with long-chain carboxylates $M^{II}(OH)_3(C_nH_{2n+1}COO)$ (M^{II} = Cu, Ni, Co; n = 17, 19, 21) are swollen and stably dispersed in toluene, suggesting exfoliation occurs [260]. This system is characterized by colloidal liquid crystallinity. Layered zinc hydroxybenzoate $Zn(OH)_{1.66}(C_6H_5COO)_{0.34}$, which is structurally different from the botallackite analogs, has been exfoliated in C_3–C_5 alcohols [261].

Another class of layered hydroxide salts subjected to exfoliation is lanthanide hydroxides $Ln_2(OH)_3[A^{m-}]_{1/m}$ (Ln = lanthanide; A^{m-} = interlayer anion such as Cl^- and NO^{3-}). Although basic salts of lanthanides have been known for a long time [262, 263], they have recently been rediscovered as anion-exchangeable layered solids [264–266]. Their luminescent and magnetic properties originating from the lanthanide ions have activated this research [264, 266]. Nanosheets of these compounds are also attracting interests in this trend. Exfoliation of layered lanthanide hydroxides has been accomplished by intercalating dodecylsulfate ions through anion exchange and subsequent agitation in formamide (Fig. 3.22) [31, 267].

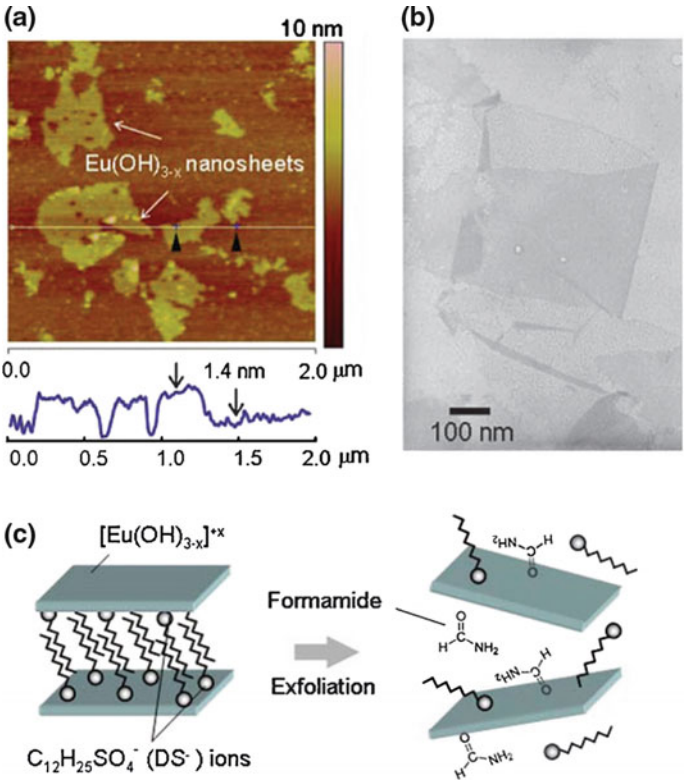

Fig. 3.22 **a** AFM image, **b** TEM image, and **c** model of the preparation process for $Eu(OH)_{3-x}$ nanosheets. Reprinted with permission from [31]. Copyright 2002 Royal Society of Chemistry

3.6 Assembly of the Nanosheets

The exfoliated nanosheets obtained from ion-exchangeable layered solids can be used in practical applications by assembling them appropriately. Employing each nanosheet as a building block, we can construct various nanostructured materials. Nanosheets with different physicochemical properties can be integrated with themselves or other species, including molecules, polymers, and nanoparticles to yield desired materials by fusion of their structures and functions. In such nanosheet assemblies, the electric charges and 2D morphology of the nanosheets play vital roles. Various nanostructures have been organized through electrostatic interactions between the nanosheets, and their 2D shape readily leads to anisotropic nanostructures. The colloidal and interfacial properties of the nanosheets are also important because the nanosheets are usually manipulated in solvents. This section briefly summarizes research on nanosheet assemblies, which are classified into three types based on their preparation techniques.

3.6.1 Aggregation to Bulk Solids

3.6.1.1 Porous Solids

Evaporation of the solvent from colloidal nanosheets usually causes reformation of the layered structure through restacking of the nanosheets. However, porous structures with high surface areas can be obtained if the restacking is appropriately interrupted. To ensure pore generation, templates or pillaring reagents are often used in the aggregation processes. As a direct method without templates, disordered porous aggregates of clay nanosheets with "house-of-cards" structure have been produced [1]. This structure has been obtained by aggregation of small clay nanosheets through face-to-edge electrostatic interactions between them.

For oxometallate and metal phosphate nanosheets, aggregates with high surface areas have been prepared from the nanosheets of, for example, lepidocrocite-type titanate $H_xTi_{2-x/4}\square_{x/4}O_4$, perovskite-type niobate $HCa_2Nb_3O_{10}$, and α-ZrP without the aid of templates [268–270]. Flocculation of titanate nanosheets with Keggin-type $[Al_{13}O_4(OH)_{24}(H_2O)_{12}]^{7+}$ (Al_{13}^{7+}) cations yielded pillared porous structures with a high surface area (>200 $m^2\ g^{-1}$) [271, 272]. Aggregation with metal or oxide nanoparticles is also an effective approach to generate porous structures (Fig. 3.23) [10, 273]. However, hybridization with inorganic nanoparticles has attracted more attention from a functional viewpoint. Based on their cocatalyst or visible-light antenna functions, hybridization with titanate and niobate nanosheets has led to advanced photocatalysts [157, 274, 275].

Deposition of the nanosheets onto polystyrene (PSt) particles yielded core-shell and macroporous aggregates [276]. Removal of the PSt particles by calcination produced macroporous structures. However, the final structure depended the relative size of the nanosheets and PSt particles. While using nanosheets larger than the PSt particles yielded disordered pores with crumpled nanosheets, employing smaller nanosheets than the PSt particles formed ordered pores reflecting the colloidal crystallinity of the PSt particles. A recent study revealed that surfactant micelles can also act as macropore templates in nanosheet aggregates (Fig. 3.24) [277].

Heterocoagulation of negatively charged nanosheets such as titanate with cationic species is also a useful method to aggregate nanosheets into specific structures. Although disordered aggregates are generally obtained upon mixing negatively and positively charged colloidal nanosheets [278], aggregates with layered structures have been obtained for mixtures of lepidocrocite-type titanate or perovskite-type niobate with LDH nanosheets (Fig. 3.25) [251]. The titanate or niobate nanosheets and LDH nanosheets are stacked by sandwiching with each other. The basal spacing determined by XRD analyses corresponded to the sum of the monolayer thicknesses of titanate or niobate and LDH nanosheets, confirming the alternating stacking of nanosheets. Meanwhile, heterocoagulation of lepidocrocite-type titanate nanosheets with biomolecules can improve the functions of the biomolecules. One example is the stabilization of enzyme molecules by the

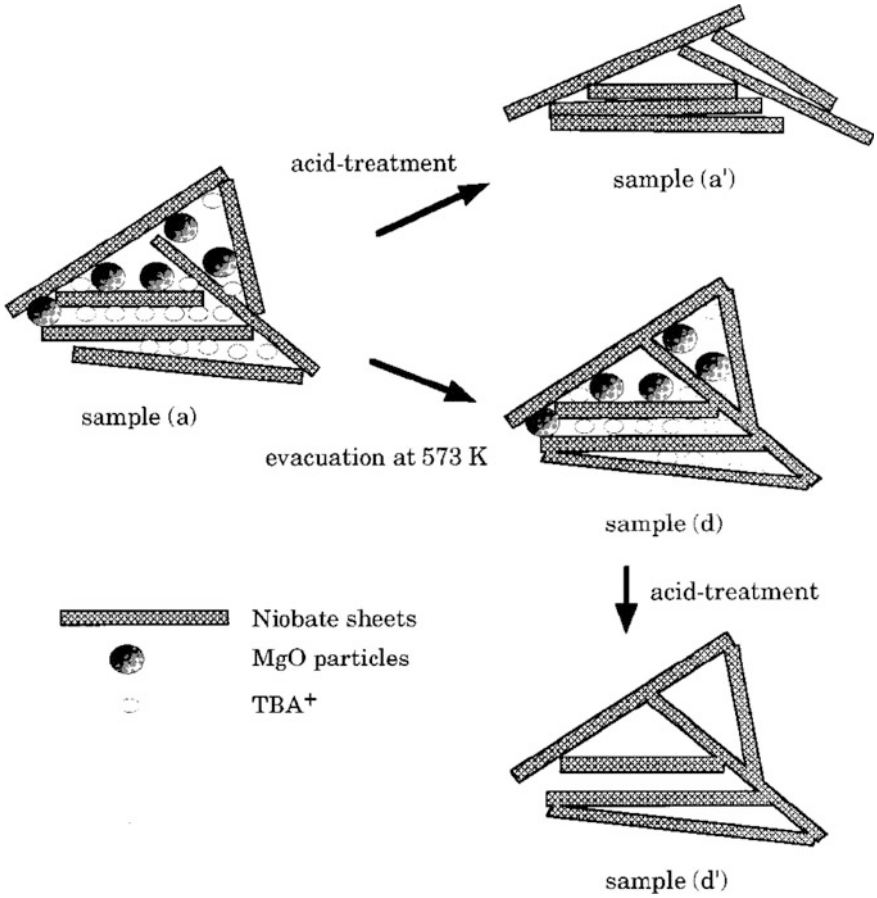

Fig. 3.23 Schematic illustration of the formation of porous structures by aggregation of niobate nanosheets in the presence of oxide nanoparticles. Reprinted with permission from [10]. Copyright 1997 American Chemical Society

titanate nanosheets against UV light exposure [279]. Another example is that antibody molecules immobilized on the nanosheets underwent antigen recognition [280].

3.6.1.2 Cast Films

Deposition of nanosheets onto flat substrates generally produces films because of their 2D morphology. Such nanosheet films are usually prepared by drop- or spin-casting on a substrate [281–284]. Electrophoretic deposition of titanate, cobaltate, and LDH nanosheets has also been reported [9, 20, 285]. Nanosheet films

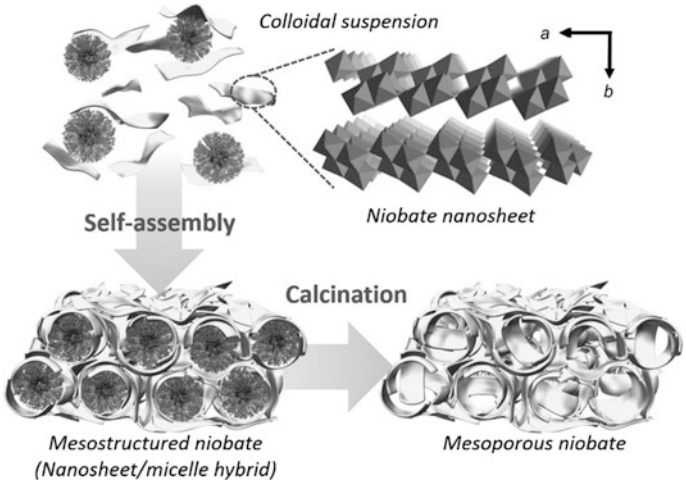

Fig. 3.24 Synthesis of crystalline mesoporous materials from coassembly of niobate nanosheets and polymeric micelles based on colloidal chemistry. Reprinted with permission from [277]. Copyright 2015 John Wiley & Sons, Inc

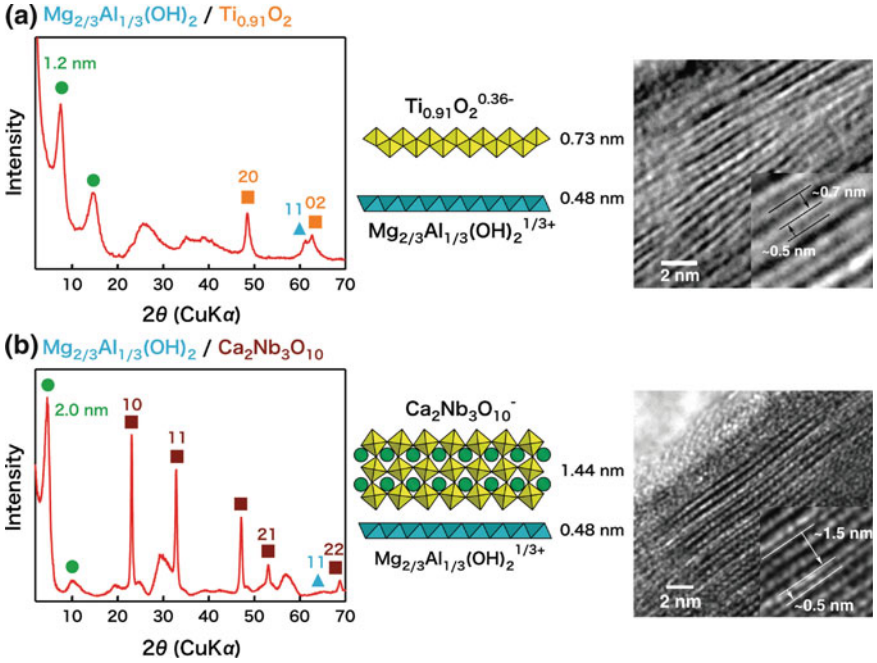

Fig. 3.25 XRD and TEM characterizations of the LDH/titanate or niobate nanosheet aggregates with alternately stacked layered structures. **a** $[Mg_{2/3}Al_{1/3}(OH)_2]^{1/3+}/Ti_{0.91}O_2{}^{0.36-}$ and B) $[Mg_{2/3}Al_{1/3}(OH)_2]^{1/3+}/Ca_2Nb_3O_{10}{}^{-}$. Reprinted with permission from [4]. Copyright 2010 John Wiley & Sons, Inc

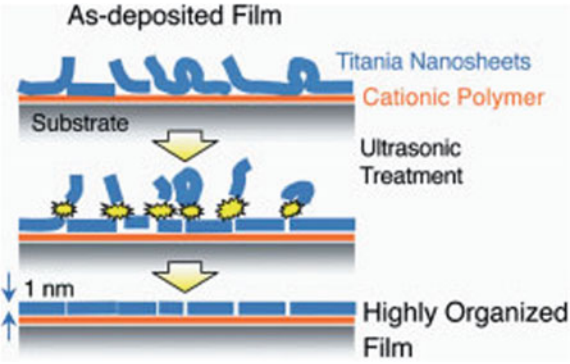

Fig. 3.26 Schematic illustration of the preparation of "perfect" cast film of lepidocrocite-type titanate nanosheets. Reprinted with permission from [286] (illustration of graphical abstract). Copyright 2004 John Wiley & Sons, Inc

have been used as electrodes and ion-exchangeable films. In these cast films, the deposited nanosheets are usually restacked to form layered structures that are disordered compared with the structures before exfoliation and often possess pores among the restacked nanosheets. Interstices and overlaps between the nanosheets are also usually unavoidable. These features facilitate molecular diffusion in the films, which is desirable for the electrochemical and ion-exchange processes. However, an almost "perfect" cast film with neat sheet tiling has been fabricated with lepidocrocite-type titanate nanosheets [286]. In this process, large nanosheets prepared from single crystals were deposited onto a substrate, which was modified in advance with cationic polymers in order to ensure the attachment of the negative nanosheets in a flat manner without interstices. Overlapping patches were then removed by ultrasonication (Fig. 3.26).

Nanosheet cast films are often prepared with ionic functional molecules, which can be incorporated in and/or adsorbed on the restacked nanosheets. The ionic molecules are immobilized through electrostatic interactions with the electrically charged nanosheets. Titanate nanosheets of $H_2Ti_3O_7$ exfoliated by PA^+ can regulate the orientation of cyanine dye molecules in their cast films [8]. When cast films of niobate nanosheets of $K_4Nb_6O_{17}$ exfoliated by triethanolammonium ions were soaked in an aqueous methylviologen (MV^{2+}) solution, photoinduced electron transfer occurred from the niobate nanosheets to the adsorbed MV^{2+} ions. The photochemical behavior was somewhat different from that observed for a conventional intercalation compound of the niobate and MV^{2+}, reflecting the difference in microenvironment of the MV^{2+} ions [102]. MV^{2+} has also been incorporated into an electrophoretically deposited titanate nanosheet film, and the film exhibited photoinduced electron transfer [287, 288]. Confinement of rare-earth cations in titanate and hydroxide nanosheet films through electrostatic self-assembly can provide specific microenvironments to realize photoluminescence of the rare-earth ions [289].

Hierarchically organized heterostructures consisting of titanate nanosheet cast films with immobilized MV^{2+} and mesoporous silica powders including porphyrin have been produced (Fig. 3.27) [290–292]. Upon visible-light excitation of the

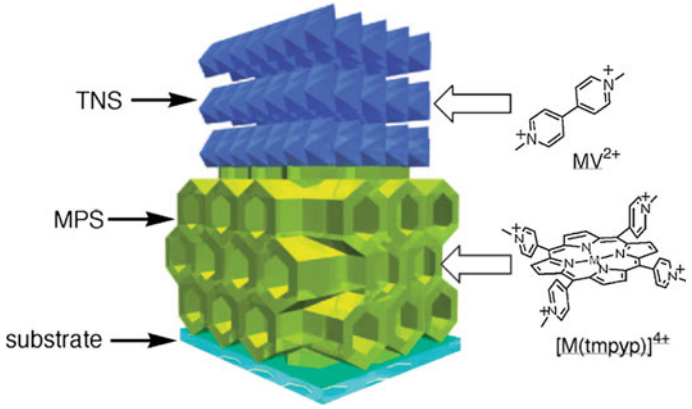

Fig. 3.27 Schematic structure of the [porphyrin–mesoporous silica (MPS)]/[MV^{2+}–titanate nanosheet (TNS)] hybrid films. Reprinted from [290]. Copyright 2006 The Chemical Society of Japan

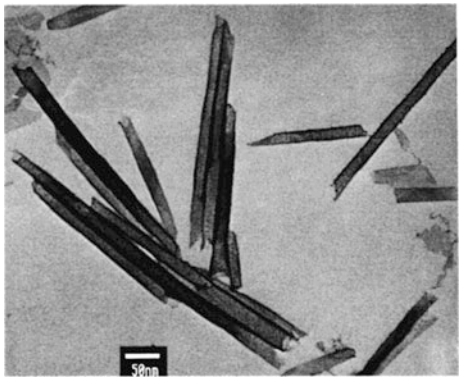

Fig. 3.28 TEM image of the niobate nanoscrolls of obtained from hexaniobate nanosheets. Reprinted with permission from [112]. Copyright 2000 American Chemical Society

porphyrin molecules, photoinduced electron transfer occurred from the porphyrin to MV^{2+} across the interface of the titanate nanosheets and mesoporous silica. A long-lived photoproduct was obtained by appropriate modification of the higher order structure.

3.6.1.3 Transformation to Nanoscrolls

Morphological transformation of nanosheets to nanoscrolls has been reported for nanosheets exfoliated from several cation-exchangeable layered solids. This transformation occurs by scrolling of the nanosheets into tubules. This phenomenon was discovered for niobate nanosheets obtained from $K_4Nb_6O_{17}$ (Fig. 3.28), and ascribed to their asymmetric surface structure given by the bilayer structure as

mentioned in Sect. 3.4.2 [112]. However, the scrolling has also been found for nanosheets exfoliated from other precursors such as lepidocrocite-type titanate, perovskite-type titanate and niobate, and manganate, which all form monolayer nanosheets [152, 293, 294].

The niobate nanoscrolls prepared from $K_4Nb_6O_{17}$ have been used as a 1D analog of the nanosheets. Their photo- and thermocatalytic properties have been examined in detail [10, 295–297]. In addition, incorporation of an azobenzene derivative (Azo) into niobate nanoscrolls has been investigated [298, 299]. In this system, cationic Azo molecules were intercalated into the scrolled nanosheets by cation exchange. The incorporated Azo molecules underwent photoisomerization, and their *trans–cis* transformation at the molecular level was magnified as sliding of the scrolled nanosheets, resulting in shape change at the micrometer-level.

It should be noted that all of the nanoscrolls mentioned above were identified only after the removal of solvents; clear evidence for scrolling of the nanosheets in the colloidal state has not been reported yet. This suggests that the nanosheets are scrolled as they dry, which is supported by the liquid crystallinity of the colloidal nanosheets. The liquid crystalline behavior of the niobate and titanate nanosheets is explained by individual nanosheets being well dispersed and retaining their 2D shape in the colloids [50, 300, 301]. Therefore, scrolling would occur during drying of the nanosheets. Removal of the solvent from the colloids concentrates coexisting electrolytes to facilitate aggregation of the nanosheets. This leads to wrinkling of the nanosheets and then the formation of nanoscrolls; thus, scrolling can be recognized as self-aggregation of nanosheets.

3.6.2 Layer-by-Layer Assemblies

LbL assembly is a technique used for fabricating multilayer thin films by repeated deposition of a monolayer onto a substrate. Although this method requires more elaborate operations than conventional film preparation techniques such as simple casting and spin-coating, LbL assembly is advantageous to precisely assemble thin films with defined nanostructures. Because the nanosheets exfoliated from ion-exchangeable layered solids bear electric charges, electrostatic sequential deposition, which is only called LbL assembly in a narrow sense, has been used more frequently for preparing thin films than the Langmuir–Blodgett (LB) method.

3.6.2.1 Electrostatic LbL Assemblies

This type of assemblies is obtained by alternating deposition of cationic and anionic monolayers onto a substrate [302, 303]. The first example of an electrostatic LbL assembly using exfoliated nanosheets was reported in 1984 for clay, α-ZrP, and niobate (from $K_4Nb_6O_{17}$) nanosheets [100, 304]. Film fabrication was initiated by grafting cationic groups onto a glass substrate. The substrate was soaked in an

aqueous colloidal suspension of nanosheets to deposit them on the substrate. Then, the substrate was withdrawn from the colloid, rinsed adequately, and transferred to an aqueous solution of polycations, such as poly(allylammonium), poly(diallyldimethylammonium), and polyethyeneimine, which caused the polymer countercations to adsorb on the nanosheets [305]. Multilayer films were fabricated by repeating the alternate deposition of nanosheets and polycations. Figure 3.29 illustrates the deposition process. Electrostatic LbL assembly has been rapidly extended to other electrically charged nanosheets such as titanates, manganates, and LDHs [28, 305, 306]. For the LbL assembly of LDH nanosheets, poly(styrene 4-sulfonate) has been used as a typical polymer counteranion. Inorganic clusters (e.g., $Al_{13}{}^{7+}$), biomacromolecules (e.g., cytochrome c), and nanoparticles can also be employed as the countercations [100, 307]. Alternating deposition of more than two kinds of the nanosheets such as cationic and anionic ones has yielded superstructured nanosheet multilayer films [251, 308, 309].

By appropriately combining nanosheets and counterions, the resulting nanosheet assemblies can show various functions. As an example, photoenergy conversion systems have been organized by assembling nanosheets and photofunctional molecules such as a sensitizers, electron/energy donors, and acceptors (Fig. 3.30) [12, 310]. Interlayer electron/energy transfer separated by the nanosheets has been identified. Use of the photocatalytically active semiconductor nanosheets, exemplified by titanates, enables their contribution to the photoprocesses [12, 311]. Photoinduced electron transfer between the electron-donating and -accepting nanosheets has been observed in a superstructured nanosheet film [308]. Meanwhile, LbL assembly of dielectric titanate and niobate nanosheets produces multilayer films with unusual electronic and magnetic properties, such as high-κ dielectric property [59–61, 87].

The LbL method is not limited to deposition on flat substrates. LbL fabrication of α-ZrP multilayer films on SiO_2 particles with polymer countercations was reported in 1995 [310]. In this system, by attaching photofunctional moieties such as photoseisitizing ruthenium-bipyridine and electron accepting viologen units to the polymer side chains, and by stacking the polymer layers to sandwich the α-ZrP nanosheets, photoinduced electron transfer occured in the multilayer films reflecting the stacking sequence of the polymer layers and nanosheets. The formation of nanosheet multilayers on PSt particles by LbL assembly gave materials with a core-shell structure [312–314]. These core-shell particles were converted to hollow capsules after removal of the PSt cores by calcination.

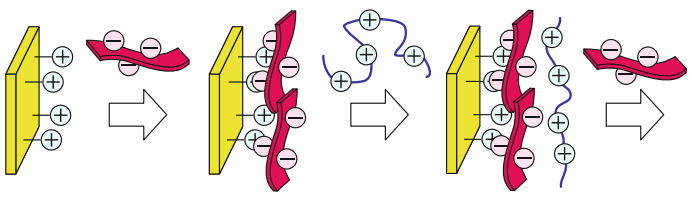

Fig. 3.29 Schematic illustration of the preparation of multilayer films through electrostatic LbL deposition of anionic nanosheets and cationic polymers

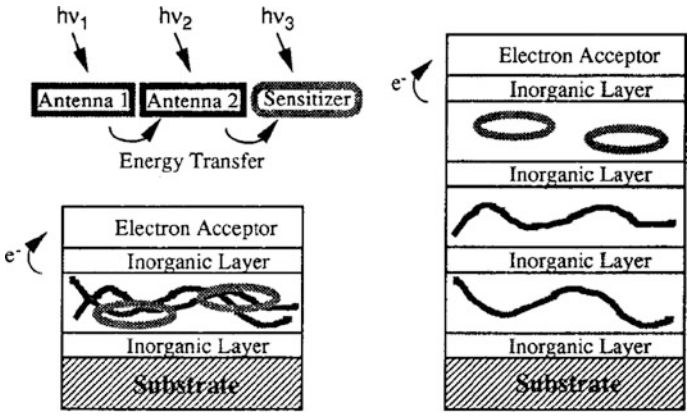

Fig. 3.30 Possible architectures for photoinduced intra- (*left*) and interlayer (*right*) energy transfer followed by interlayer electron transfer. Reprinted with permission from [12]. Copyright 119 American Chemical Society

3.6.2.2 Langmuir–Blodgett Films

The LB technique has also been used for fabricating inorganic nanosheet films although it is more complicated and time-consuming than electrostatic LbL deposition [315]. The LB method is advantageous to obtain high quality films with neat tiling. In fact, high-quality nanosheet multilayer films with few interstices and overlaps have been obtained with this technique [77]. LB films have been fabricated from the nanosheets of exfoliated layered titanates and niobates as well as clay minerals [77, 316–318]. Since these nanosheets are hydrophilic because of their layer charges, they are electrostatically attached by long-chain organic cations prior to LB casting (Fig. 3.31). By this treatment, they become located at the air–water interface and can be transferred onto a substrate at an appropriate surface pressure. Film deposition without the amphiphilic additives has also been achieved [77, 318].

Nanosheet LB films prepared from perovskite-type niobate $HSr_2Nb_3O_{10}$ displayed photoconductivity [80]. When a LB film deposited with long-chain alkylammonium ions was irradiated with UV light, the alkylammonium ions were decomposed by the photocatalytic activity of the niobate nanosheets, and then the film showed conductivity under the irradiation [156, 319]. Although LB films of nanosheets exfoliated from perovskite-type niobate ($HCa_2Nb_3O_{10}$) were paraelectric, they became ferroelectric when the perovskite nanosheets were appropriately superstructured with other niobate and titanate nanosheets [320].

3.6.2.3 Nanosheet Monolayer Films as Substrates for Crystal Growth

Nanosheet monolayer films deposited by the LB technique have been used as seed layers on which 3D crystals are grown with specific orientations. Thin films of

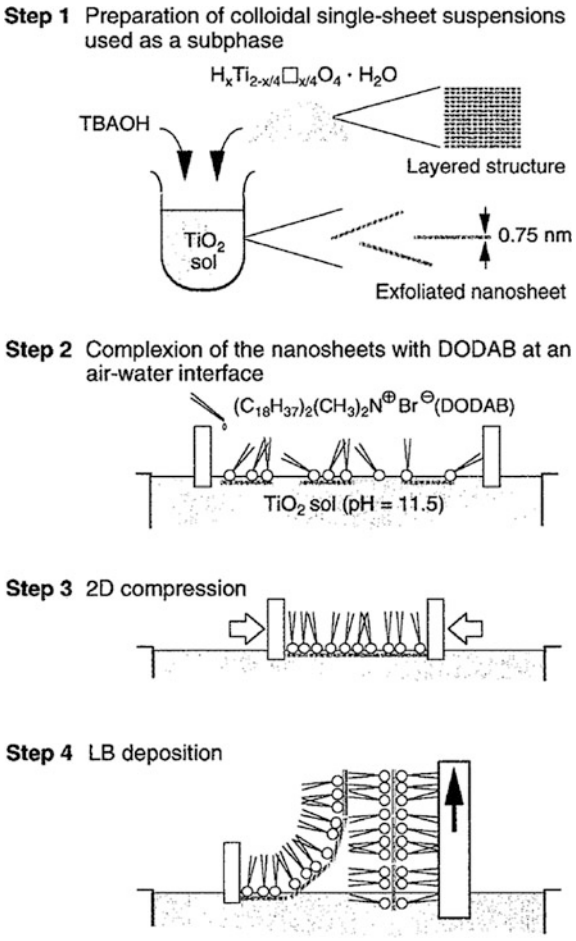

Fig. 3.31 Schematic illustration of the preparation process of the dioctadecyldimethylammonium bromide (DODAB)/titanate nanosheet alternating film using the LB technique. Reprinted with permission from [316]. Copyright 2001 American Chemical Society

cubic perovskites $SrTiO_3$ and $BaTiO_3$ have been epitaxially grown in the [100] direction on the LB monolayer perovskite-type niobate nanosheets exfoliated from $HCa_2Nb_3O_{10}$. Epitaxial growth was realized because of the crystallographic compatibility of the nanosheet surface and the (100) plane of the cubic perovskites (Fig. 3.32) [321–323]. LB monolayers of manganate and tungstate ($Cs_4W_{11}O_{36}$) nanosheets have been used for the growth of ZnO thin films in the [001] direction [321, 324].

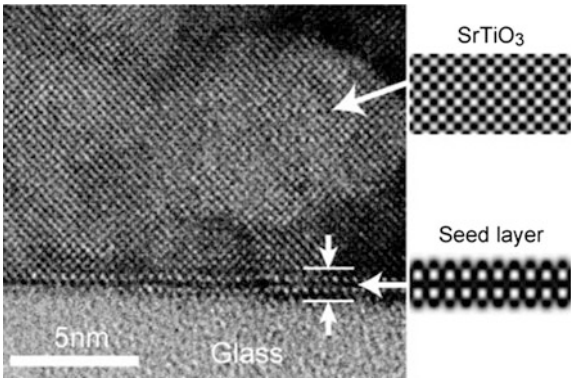

Fig. 3.32 Cross-sectional HRTEM image of an $SrTiO_3$ thin film on a nanosheet seed layer taken from the $SrTiO_3$ [100] direction. Reprinted with permission from [321]. Copyright 2004 John Wiley & Sons, Inc

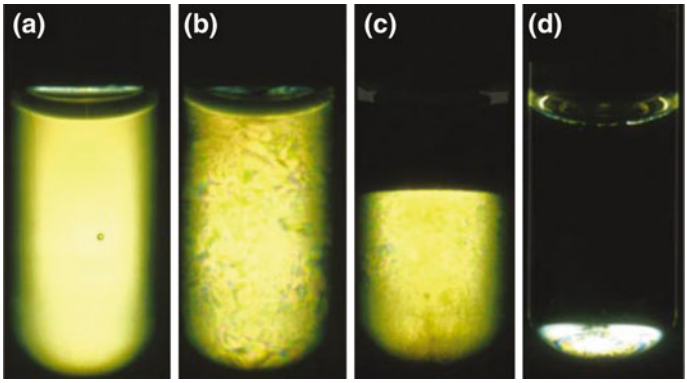

Fig. 3.33 Naked-eye observation of liquid crystalline nanosheet colloids of $H_3Sb_3P_2O_{14}$. Test-tubes filled with aqueous suspensions of the nanosheets, observed between crossed polarizers (**a**–**e**) (the isotropic phase in **c** and **d** appears dark). Reprinted with permission from [27]. Copyright 2001 Nature Publishing Group

3.6.3 Assemblies of the Nanosheets in the Colloidal State

Organization of nanosheets in the colloidal state yields characteristic assembled structures that are different from the bulk and LbL assemblies. A typical example is the liquid crystalline phase transition of the colloids (Fig. 3.33) [27, 325–328]. The liquid crystalline phases provide orientationally ordered structures of nanosheets in solvents, as described in Chap. 8. The fluid nature of the liquid crystalline phases enables macroscopic alignment of the colloidal nanosheets under external fields [325, 329, 330]. Another example is the sol–gel transition of colloidal nanosheets. While the exfoliated nanosheets are obtained as colloidal gels in some cases, a reversible sol–gel transition upon external pH stimuli has been reported for a colloid of niobate ($K_4Nb_6O_{17}$) nanosheets [331].

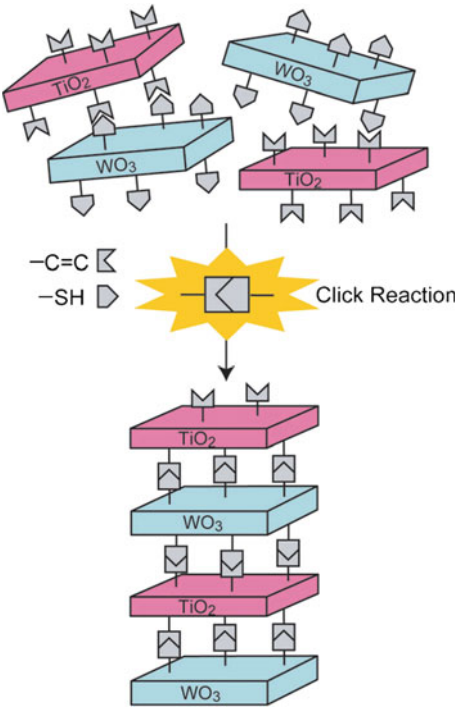

Fig. 3.34 Alternating layers of metal oxide obtained by a click reaction. Reprinted with permission from [332]. Copyright 2004 John Wiley & Sons, Inc

Controlled aggregation of the colloidal nanosheets can provide specifically organized nanosheets in the powder form. Alternate stacking of niobate/titanate (exfoliated from $K_4Nb_6O_{17}$ or $H_xTi_{2-x/4}\square_{x/4}O_4$, respectively) and tungstate (prepared from $H_2W_2O_7$) nanosheets has been attained through a thiol–ene click reaction (Fig. 3.34) [332, 333]. When niobate or titanate nanosheets with attached alkene moieties were mixed with tungstate nanosheets anchored by thiol groups, the click reaction proceeded between the niobate/titanate and tungstate nanosheets to bind them, resulting in the selective formation of a heterostructured product that was settled out from the colloid. Because the product consisted of two semiconducting oxides with different band positions, it realized efficient photoinduced electron transfer.

Emulsification of oil–water systems is also a promising way to assemble the colloidal nanosheets. Moderately hydrophobized solid particles are known to stabilize emulsions like organic surfactants. Such emulsions, called Pickering emulsions, have recently attracted attention because of their high stability and unusual properties induced by the particle emulsifiers [334, 335]. The emulsification induces particle aggregation at the oil–water interface. Ion-exchangeable layered crystals have also been examined as solid emulsifiers because their hydrophobicity can be modified by intercalation of organic molecules into the interlayer spaces or grafting them to the nanosheet surfaces. Although non-exfoliated layered crystals have been used in most cases [336–339], emulsification by α-ZrP and graphene

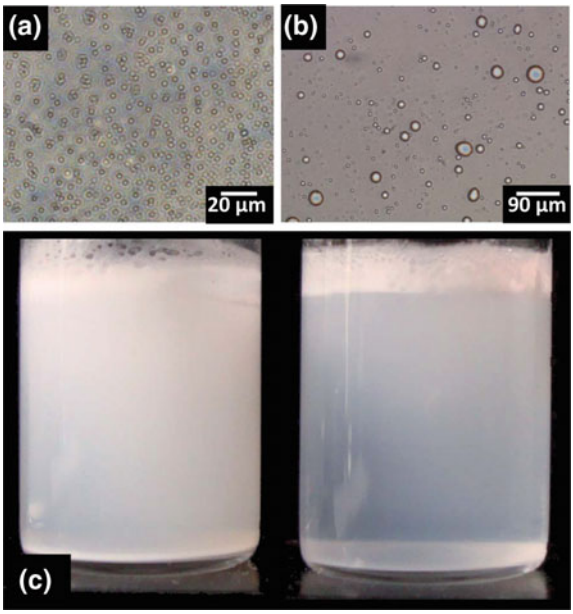

Fig. 3.35 Toluene-in-water emulsions stabilized by α-ZrP-ODI and nonmodified α-ZrP nano-sheets. **a** Micrograph of uniform toluene-in-water droplets stabilized by α-ZrP-ODI nano-sheets. **b** Micrograph of polydispersed toluene-in-water emulsion droplets stabilized by non-modified α-ZrP nano-sheets. **c** Toluene-in-water emulsions stabilized by non-modified α-ZrP (*right*) and stabilized by α-ZrP-ODI nano-sheets (*left*). Reprinted with permission from [341]. Copyright 2012 Royal Society of Chemistry

oxide nanosheets has recently been reported (Fig. 3.35) [340, 341]. This suggests the applicability of other exfoliated nanosheets as solid emulsifiers.

3.7 Summary and Outlook

Ion-exchangeable layered solids can be exfoliated by osmotic swelling with solvents; in most cases after displacing the interlayer ions for suitable ones called exfoliating reagents, which have an affinity for the employed solvent. There are a number of ion-exchangeable layered solids such as oxometallates, metal phosphates, and hydroxides, with a broad range of compositions. Thus, the inorganic nanosheets obtained through exfoliation possess diverse physicochemical functions based on their electric, magnetic, optic, photochemical, catalytic, and redox properties. The nanosheets can be assembled to form a variety of hierarchical structures; they are not limited to stacked films but can form porous solids, transformed structures such as nanoscrolls, and structured colloids. Many inorganic ion-exchangeable layered solids are still waiting for the development of exfoliation technology, and a much richer library of advanced materials based on exfoliated nanosheets should be established in the near future. In addition, combination of nanosheets with other building blocks with different structural motifs, such as porous powders, 0D and 1D particles, and biological macromolecules, will expand both the structural and functional variety of nanosheet-based materials.

References

1. van Olphen H (1991) Clay colloid chemistry (reprinted edition). Krieger, Malabar
2. Smalley M (2006) Clay swelling and colloid stability. Taylor & Francis, Boca Raton
3. Sasaki T (2007) J Ceram Soc Jpn 115:9
4. Ma R, Sasaki T (2010) Adv Mater 22:5082
5. Gunjakar JL, Kim IY, Lee JM, Jo YK, Hwang S-J (2014) J Phys Chem C 118:3847
6. Sasaki T, Watanabe M, Hashizume H, Yamada H, Nakazawa H (1996) Chem Commun 229
7. Harada M, Sasaki T, Ebina Y, Watanabe M (2002) J Photochem Photobiol, A 148:273
8. Miyamoto N, Kuroda K, Ogawa M (2004) J Mater Chem 14:165
9. Sugimoto W, Terabayashi O, Murakami Y, Takasu Y (2002) J Mater Chem 12:3814
10. Abe R, Shinohara K, Tanaka A, Hara M, Kondo JN, Domen K (1997) Chem Mater 9:2179
11. Nakato T, Miyamoto N, Harada A (2004) Chem Commun 78
12. Kaschak DM, Lean JT, Waraksa CC, Saupe GB, Usami H, Mallouk TE (1999) J Am Chem Soc 121:3435
13. Takagaki A, Yoshida T, Lu D, Kondo JN, Hara M, Domen K, Hayashi S (2004) J Phys Chem B 108:11549
14. Prasad G, Takei T, Arimoto K, Yonesaki Y, Kumada N, Kinomura N (2006) Solid State Ionics 177:197
15. Fukuda K, Nakai I, Ebina Y, Ma RZ, Sasaki T (2007) Inorg Chem 46:4787
16. Treacy MMJ, Rice SB, Jacobson AJ, Lewandowski JT (1990) Chem Mater 2:279
17. Tahara S, Takeda Y, Sugahara Y (2005) Chem Mater 17:6198
18. Schottenfeld JA, Kobayashi Y, Wang J, Macdonald DD, Mallouk TE (2008) Chem Mater 20:213
19. Liu Z-h, Ooi K, Kanoh H, Tang W-p, Tomida T (2000) Langmuir 16:4154
20. Kim TW, Oh E-J, Jee A-Y, Lim ST, Park DH, Lee M, Hyun S-H, Choy J-H, Hwang S-J (2009) Chem Eur J 15:10752
21. Sugimoto W, Iwata H, Yasunaga Y, Murakami Y, Takasu Y (2003) Angew Chem Int Ed 42:4092
22. Fukuda K, Saida T, Sato J, Yonezawa M, Takasu Y, Sugimoto W (2010) Inorg Chem 49:4391
23. Schaak RE, Mallouk TE (2002) Chem Commun 706
24. Fukuda K, Akatsuka K, Ebina Y, Ma R, Takada K, Nakai I, Sasaki T (2008) ACS Nano 2:1689
25. Ide Y, Ozaki G, Ogawa M (2009) Langmuir 25:5276
26. Alberti G, Casciola M, Costantino U (1985) J Colloid Interface Sci 107:256
27. Gabriel J-CP, Camerel F, Lemaire BJ, Desvaux H, Davidson P, Batail P (2001) Nature 413:504
28. Li L, Ma R, Ebina Y, Iyi N, Sasaki T (2005) Chem Mater 17:4386
29. Liu Z, Ma R, Osada M, Iyi N, Ebina Y, Takada K, Sasaki T (2006) J Am Chem Soc 128:4872
30. Demel J, Zhigunov A, Jirka I, Klementova M, Lang K (2015) J Colloid Interface Sci 452:174
31. Ida S, Sonoda Y, Ikeue K, Matsumoto Y (2010) Chem Commun 46:877
32. Raveau B (1984) Rev Chim Miner 21:391
33. Miyamoto N, Yamamoto H, Kaito R, Kuroda K (2002) Chem Commun 2378
34. Sasaki T, Watanabe M, Hashizume H, Yamada H, Nakazawa H (1996) J Am Chem Soc 118:8329
35. Sasaki T, Watanabe M (1998) J Am Chem Soc 120:4682
36. Geng F, Ma R, Nakamura A, Akatsuka K, Ebina Y, Yamauchi Y, Miyamoto N, Tateyama Y, Sasaki T (2013) Nat Commun 4:1632
37. Maluangnont T, Matsuba K, Geng F, Ma R, Yamauchi Y, Sasaki T (2013) Chem Mater 25:3137

38. Geng F, Ma R, Ebina Y, Yamauchi Y, Miyamoto N, Sasaki T (2014) J Am Chem Soc 136:5491
39. Geng F, Ma R, Yamauchi Y, Sasaki T (2014) Chem Commun 50:9977
40. Hervieu M, Raveau B (1981) Rev Chim Miner 18:642
41. Sasaki T, Watanabe M, Michiue Y, Komatsu Y, Izumi F, Takenouchi S (1995) Chem Mater 7:1001
42. Sasaki T, Izumi F, Watanabe M (1996) Chem Mater 8:777
43. Barbier G (1934) Compt Rend 199:226
44. Ebina Y, Sasaki T, Watanabe M (2002) Solid State Ionics 151:177
45. Omomo Y, Sasaki T, Wang L, Watanabe M (2003) J Am Chem Soc 125:3568
46. Ohya T, Nakayama A, Takahasbi B, Ohya Y, Takahashi Y (2002) Chem Mater 14:3082
47. Kamada K, Soh N (2014) RSC Adv 4:8682
48. Tanaka T, Ebina Y, Takada K, Kurashima K, Sasaki T (2003) Chem Mater 15:3564
49. O'Neill A, Khan U, Coleman JN (2012) Chem Mater 24:2414
50. Miyamoto N, Nakato T (2004) J Phys Chem B 108:6152
51. Wang L, Sasaki T (2014) Chem Rev 114:9455
52. Le Granvalet-Mancini M, Brohan L, Marie A-M, Tournoux M (1994) Eur J Solid State Inorg Chem 31:767
53. Ide Y, Sadakane M, Sano T, Ogawa M (2014) J Nanosci Nanotechnol 14:2135
54. Fujiki Y, Komatsu Y, Ohta N (1980) Chem Lett 1023
55. Izawa H, Kikkawa S, Koizumi M (1982) J Phys Chem 86:5023
56. Clément P, Marchand R (1983) C R Acad Sci Paris II(296):1161
57. Izawa H, Kikkawa S, Koizumi M (1983) Polyhedron 2:741
58. Sasaki T, Watanabe M, Komatsu Y, Fujiki Y (1985) Inorg Chem 24:2265
59. Osada M, Ebina Y, Takada K, Sasaki T (2006) Adv Mater 18:295
60. Osada M, Ebina Y, Fukuda K, Ono K, Takada K, Yamaura K, Takayama-Muromachi E, Sasaki T (2006) Phys Rev B 73:153301
61. Osada M, Itose M, Ebina Y, Ono K, Ueda S, Kobayashi K, Sasaki T (2008) Appl Phys Lett 92:253110
62. Dong XP, Osada M, Ueda H, Ebina Y, Kotani Y, Ono K, Ueda S, Kobayashi K, Takada K, Sasaki T (2009) Chem Mater 21:4366
63. Gao T, Fjellvåg H, Norby P (2009) J Mater Chem 19:787
64. Berry KL, Aftandilian VD, Gilbert WW, Meibohm EPH, Young HS (1960) J Inorg Nucl Chem 14:231
65. Andersson S (1961) Acta Crystallogr 14:1245
66. Besselink R, Stawski TM, Castricum HL, Blank DHA, ten Elshof JE (2010) J Phys Chem C 114:21281
67. Wang Y, Sun C, Yan X, Xiu F, Wang L, Smith SC, Wang KL, Lu GQ, Zou J (2011) J Am Chem Soc 133:695
68. Sugimoto W, Ohuchi K, Murakami Y, Takasu Y (2005) Bull Chem Soc Jpn 78:633
69. Ide Y, Ogawa M (2005) Chem Lett 34:360
70. Ide Y, Ogawa M (2006) J Colloid Interface Sci 296:141
71. Honda M, Oaki Y, Imai H (2014) Chem Mater 26:3579
72. Shibata M, Kudo A, Tanaka A, Domen K, Maruya K, Onishi T (1987) Chem Lett 1017
73. Miyata H, Sugahara Y, Kuroda K, Kato C (1988) J Chem Soc, Faraday Trans 1(84):2677
74. Nakato T, Kuroda K (1995) Eur J Solid State Inorg Chem 32:809
75. Domen K, Kondo JN, Hara M, Takata T (2000) Bull Chem Soc Jpn 73:1307
76. Osterloh FE (2008) Chem Mater 20:35
77. Akatsuka K, Haga M, Ebina Y, Osada M, Fukuda K, Sasaki T (2009) ACS Nano 3:1097
78. Osada M, Sasaki T (2012) Adv Mater 24:210
79. Choy J-H, Lee H-C, Jung H, Kim H, Boo H (2002) Chem Mater 14:2486
80. Umemura Y, Shinohara E, Koura A, Nishioka T, Sasaki T (2006) Langmuir 22:3870
81. Shibata T, Sakai N, Fukuda K, Ebina Y, Sasaki T (2007) Phys Chem Chem Phys 9:2413
82. Matsumoto Y, Ida S, Inoue T (2008) J Phys Chem C 112:11614

83. Allen MR, Thibert A, Sabio EM, Browning ND, Larsen DS, Osterloh FE (2010) Chem Mater 22:1220
84. Jo YK, Kim IY, Gunjakar JL, Lee JM, Lee NS, Lee SH, Hwang SJ (2014) Chem Eur J 20:10011
85. Liu G, Wang LZ, Sun CH, Chen ZG, Yan XX, Cheng L, Cheng HM, Lu GQ (2009) Chem Commun 1383
86. Liu G, Sun C, Wang L, Smith SC, Lu GQ, Cheng H-M (2011) J Mater Chem 21:14672
87. Osada M, Takanashi G, Li B-W, Akatsuka K, Ebina Y, Ono K, Funakubo H, Takada K, Sasaki T (2011) Adv Funct Mater 21:3482
88. Osada M, Sasaki T, Ono K, Kotani Y, Ueda S, Kobayashi K (2011) ACS Nano 5:6871
89. Bizeto MA, Shiguihara AL, Constantino VRL (2009) J Mater Chem 19:2512
90. Lagaly G, Beneke K (1976) J Inorg Nucl Chem 38:1513
91. Gasperin M, Le Bihan MT (1982) J Solid State Chem 43:346
92. Gasperin M (1982) Acta Cryst. B 38:2024
93. Nedjar R, Borel MM, Raveau B (1985) Mater Res Bull 20:1291
94. Wadsley AD (1964) Acta Cryst 17:623
95. Blasse G, de Pauw ADM (1970) J Inorg Nucl Chem 32:3960
96. Rebbah H, Borel MM, Raveau B (1980) Mater Res Bull 15:317
97. Rebbah H, Hervieu M, Raveau B (1981) Mater Res Bull 16:149
98. Bhat V, Gopalakrishnan J (1988) Solid State Ionics 26:25
99. Song H, Sjåstad AO, Fjellvåg H, Okamoto H, Vistad ØB, Arstad B, Norby P (2011) J Solid State Chem 184:3135
100. Keller SW, Kim H-N, Mallouk TE (1994) J Am Chem Soc 116:8817
101. Du GH, Yu Y, Chen Q, Wang RH, Zhou W, Peng LM (2003) Chem Phys Lett 377:445
102. Nakato T, Edakubo H, Shimomura T (2009) Micropor Mesopor Mater 123:280
103. Park I, Han YS, Choy JH (2009) J Nanosci Nanotechnol 9:7190
104. Galasso F, Darby W (1962) J Phys Chem 66:1318
105. Toda K, Tokuoka S, Uematsu K, Sato M (2002) Key Eng Mater 214–215:67
106. Toda K, Ohtake N, Kawakami M, Tokuoka S, Uematsu K, Sato M (2002) Jpn J Appl Phys 41:7021
107. Tagusagawa C, Takagaki A, Hayash S, Domen K (2009) J Phys Chem C 113:7831
108. Kinomura N, Kumada N, Muto F (1985) J Chem Soc, Dalton Trans 2349
109. Nakato T, Sakamoto D, Kuroda K, Kato C (1992) Bull Chem Soc Jpn 65:322
110. Nakato T, Miyamoto N (2002) J Mater Chem 12:1245
111. Miyamoto N, Nakato T (2003) Langmuir 19:8057
112. Saupe GB, Waraksa CC, Kim H-N, Han YJ, Kaschak DM, Skinner DM, Mallouk TE (2000) Chem Mater 12:1556
113. Bizeto MA, Constantino VRL (2004) Mater Res Bull 39:1811
114. Nakato T, Hashimoto S (2007) Chem Lett 36:1240
115. Kimura N, Kato Y, Suzuki R, Shimada A, Tahara S, Nakato T, Matsukawa K, Mutin PH, Sugahara Y (2014) Langmuir 30:1169
116. Miyamoto N, Yamada Y, Koizumi S, Nakato T (2007) Angew Chem Int Ed 46:4123
117. Usami H, Nakamura T, Makino T, Fujimatsu H, Ogasawara S (1998) J Chem Soc, Faraday Trans 94:83
118. Sarahan MC, Carroll EC, Allen M, Larsen DS, Browning ND, Osterloh FE (2008) J Solid State Chem 181:1678
119. Huang J, Ma R, Ebina Y, Fukuda K, Takada K, Sasaki T (2010) Chem Mater 22:2582
120. Shibata T, Takanashi G, Nakamura T, Fukuda K, Ebina Y, Sasaki T (2011) Energy Environ Sci 4:535
121. Liang S, Wen L, Lin S, Bi J, Feng P, Fu X, Wu L (2014) Angew Chem Int Ed Engl 53:2951
122. Nakato T, Fujita T, Mouri E (2015) Phys Chem Chem Phys 17:5547
123. Yin G, Nishikawa M, Nosaka Y, Srinivasan N, Atarashi D, Sakai E, Miyauchi M (2015) ACS Nano 9:2111

124. Liu Y, Xiong J, Luo S, Liang R, Qin N, Liang S, Wu L (2015) Chem Commun (Camb) 51:15125
125. Xiong J, Wen L, Jiang F, Liu Y, Liang S, Wu L (2015) J Mater Chem A 3:20627
126. Koinuma M, Seki H, Matsumoto Y (2002) J Electroanal Chem 531:81
127. Akatsuka K, Takanashi G, Ebina Y, Sakai N, Haga M, Sasaki T (2008) J Phys Chem Solids 69:1288
128. Akatsuka K, Takanashi G, Ebina Y, Haga M-a, Sasaki T (2012) J Phys Chem C 116:12426
129. Takagaki A, Sugisawa M, Lu D, Kondo JN, Hara M, Domen K, Hayashi S (2003) J Am Chem Soc 125:5479
130. Takagaki A, Lu D, Kondo JN, Hara M, Hayashi S, Domen K (2005) Chem Mater 17:2487
131. Schaak RE, Mallouk TE (2002) Chem Mater 14:1455
132. Ranmohotti KG, Josepha E, Choi J, Zhang J, Wiley JB (2011) Adv Mater 23:442
133. Dion M, Ganne M, Tournoux M (1981) Mater Res Bull 16:1429
134. Jacobson AJ, Johnson JW, Lewandowski JT (1985) Inorg Chem 24:3727
135. Ruddlesden SN, Popper P (1957) Acta Crystallogr 10:538
136. Ruddlesden SN, Popper P (1958) Acta Crystallogr 11:54
137. Gopalakrishnan J, Bhat V (1987) Inorg Chem 26:4299
138. Gopalakrishnan J, Bhat V, Raveau B (1987) Mater Res Bull 22:413
139. Tahara S, Ichikawa T, Kajiwara G, Sugahara Y (2007) Chem Mater 19:2352
140. Schaak RE, Mallouk TE (2000) Chem Mater 12:2513
141. Han Y-S, Park I, Choy J-H (2001) J Mater Chem 11:1277
142. Xu FF, Ebina Y, Bando Y, Sasaki T (2003) J Phys Chem B 107:9638
143. Gao H, Shori S, Chen X, zur Loye HC, Ploehn HJ (2013) J Colloid Interface Sci 392:226
144. Ozawa TC, Fukuda K, Akatsuka K, Ebina Y, Sasaki T (2007) Chem Mater 19:6575
145. Ida S, Ogata C, Eguchi M, Youngblood WJ, Mallouk TE, Matsumoto Y (2008) J Am Chem Soc 130:7052
146. Ozawa TC, Fukuda K, Akatsuka K, Ebina Y, Sasaki T, Kurashima K, Kosuda K (2008) J Phys Chem C 112:17115
147. Ozawa TC, Fukuda K, Akatsuka K, Ebina Y, Kurashima K, Sasaki T (2009) J Phys Chem C 113:8735
148. Ebina Y, Akatsuka K, Fukuda K, Sasaki T (2012) Chem Mater 24:4201
149. Ozawa TC, Fukuda K, Ebina Y, Sasaki T (2013) Inorg Chem 52:415
150. Ozawa TC, Onoda M, Iyi N, Ebina Y, Sasaki T (2014) J Phys Chem C 118:1729
151. Ida S, Okamoto Y, Matsuka M, Hagiwara H, Ishihara T (2012) J Am Chem Soc 134:15773
152. Schaak RE, Mallouk TE (2000) Chem Mater 12:3427
153. Ida S, Ogata C, Unal U, Izawa K, Inoue T, Altuntasoglu O, Matsumoto Y (2007) J Am Chem Soc 129:8956
154. Inaba K, Suzuki S, Noguchi Y, Miyayama M, Toda K, Sato M (2008) Eur J Inorg Chem 2008:5471
155. Kim J-Y, Chung I, Choy J-H, Park G-S (2001) Chem Mater 13:2759
156. Saruwatari K, Sato H, Kameda J, Yamagishi A, Domen K (2005) Chem Commun 1999
157. Ebina Y, Sakai N, Sasaki T (2005) J Phys Chem B 109:17212
158. Izawa K, Yamada T, Unal U, Ida S, Altuntasoglu O, Koinuma M, Matsumoto Y (2006) J Phys Chem B 110:4645
159. Okamoto K, Sato H, Saruwatari K, Tamura K, Kameda J, Kogure T, Umemura Y, Yamagishi A (2007) J Phys Chem C 111:12827
160. Sato H, Okamoto K, Tamura K, Yamada H, Saruwatari K, Kogure T, Yamagishi A (2008) Appl Phys Exp 1:0355001
161. Sabio EM, Chi M, Browning ND, Osterloh FE (2010) Langmuir 26:7254
162. Compton OC, Carroll EC, Kim JY, Larsen DS, Osterloh FE (2007) J Phys Chem C 111:14589
163. Compton OC, Osterloh FE (2009) J Phys Chem C 113:479
164. Sabio EM, Chamousis RL, Browning ND, Osterloh FE (2012) J Phys Chem C 116:3161
165. Maeda K, Eguchi M, Oshima T (2014) Angew Chem Int Ed 53:13164

166. Oshima T, Lu D, Ishitani O, Maeda K (2015) Angew Chem Int Ed Engl 54:2698
167. Li BW, Osada M, Ebina Y, Akatsuka K, Fukuda K, Sasaki T (2014) ACS Nano 8:5449
168. Wang CX, Osada M, Ebina Y, Li BW, Akatsuka K, Fukuda K, Sugimoto W, Ma RZ, Sasaki T (2014) ACS Nano 8:2658
169. Osada M, Akatsuka K, Ebina Y, Funakubo H, Ono K, Takada K, Sasaki T (2010) ACS Nano 4:5225
170. Feng Q, Kanoh H, Ooi K (1999) J Mater Chem 9:319
171. Giovanoli R, Staehli E, Feitknecht W (1970) Helv Chim Acta 53:209
172. Golden DC, Dixon JB, Chen CC (1986) Clays Clay Miner 34:511
173. Liu ZH, Yang XJ, Makita Y, Ooi K (2002) Chem Mater 14:4800
174. Fukuda K, Nakai I, Ebina Y, Tanaka M, Mori T, Sasaki T (2006) J Phys Chem B 110:17070
175. Borgohain R, Selegue JP, Cheng YT (2014) J Mater Chem A 2:20367
176. Kai K, Yoshida Y, Kageyama H, Saito G, Ishigaki T, Furukawa Y, Kawamata J (2008) J Am Chem Soc 130:15938
177. Kang J-H, Paek S-M, Hwang S-J, Choy J-H (2010) J Mater Chem 20:2033
178. Song MS, Lee KM, Lee YR, Kim IY, Kim TW, Gunjakar JL, Hwang SJ (2010) J Phys Chem C 114:22134
179. Mizushima K, Jones PC, Wiseman PJ, Goodenough JB (1980) Mater Res Bull 15:783
180. Alcántara R, Lavela P, Tirado JL, Zhecheva E, Stoyanova R (1999) J Solid State Electrochem 3:121
181. Whittingham MS (2004) Chem Rev 104:4271
182. Johnston WD, Heikes RR, Sestrich D (1958) J Phys Chem Solids 7:1
183. Kim J-Y, Kim J-I, Choi S-M, Soo Lim Y, Seo W-S, Hwang HJ (2012) J Appl Phys 112:113705
184. Carewska M, Scaccia S, Croce F, Arumugam S, Wang Y, Greenbaum S (1997) Solid State Ionics 93:227
185. Aksit M, Toledo DP, Robinson RD (2012) J Mater Chem 22:5936
186. Conway BE (1999) Electrochemical supercapacitors: scientific fundamentals and technological applications. Plenum Press, New York
187. Schwieger W, Lagaly G (2004) In: Auerbach SM, Carrado KA, Dutta PK (eds) Handbook of layered materials. Marcel Dekker, New York
188. Takahashi N, Kuroda K (2011) J Mater Chem 21:14336
189. Selvam T, Inayat A, Schwieger W (2014) Dalton Trans 43:10365
190. Colville AA, Anderson CP, Black PM (1971) Am Mineral 56:1220
191. Vortmann S, Rius J, Marler B, Gies H (1999) Eur J Mineral 11:125
192. Vortmann S, Rius J, Siegmann S (1997) J Phys Chem B 101:1292
193. Brandt A, Schwieger W, Bergk K-H (1987) Rev Chim Miner 24:564
194. Takahashi N, Hata H, Kuroda K (2011) Chem Mater 23:266
195. Boucher MA, Katsoulis DE, Kenney ME (2006) Chem Mater 18:360
196. Clearfield A, Smith DG (1969) Inorg Chem 8:431
197. Alberti G, Costantino U (1982) In: Whittingham MS, Jacobson AJ (eds) Intercalation chemistry. Academic Press, New York
198. Kumar CV, Bhambhani A, Hnatiuk N (2004) In: Auerbach SM, Carrado KA, Dutta PK (eds) Handbook of layered materials. Marcel Dekker, New York
199. Whittingham MS, Jacobson AJ (eds) (1982) Intercalation chemistry. Academic Press, New York
200. Wong M, Ishige R, Hoshino T, Hawkins S, Li P, Takahara A, Sue H-J (2014) Chem Mater 26:1528
201. Alberti G, Cavalaglio S, Dionigi C, Marmottini F (2000) Langmuir 16:7663
202. Casciola M, Alberti G, Donnadio A, Pica M, Marmottini F, Bottino A, Piaggio P (2005) J Mater Chem 15:4262
203. Piffard Y, Verbaere A, Lachgar A, Deniard-Courant S, Tournoux M (1987) Rev Chim Miner 23:766
204. Huang Q, Wang W, Yue Y, Hua W, Gao Z (2003) J Colloid Interface Sci 257:268

205. Tanaka H, Okumiya T, S-k Ueda, Taketani Y, Murakami M (2009) Mater. Res Bull 44:328
206. Takei T, Yonesaki Y, Kumada N, Kinomura N (2008) Langmuir 24:8554
207. Kalousová J, Votinský J, Beneš L, Melánová K, Zima V (1998) Collect Czech Chem Commun 63:1
208. Nakato T, Furumi Y, Okuhara T (1998) Chem Lett 611
209. Yamamoto N, Okuhara T, Nakato T (2001) J Mater Chem 11:1858
210. Choy JH, Kwon SJ, Hwang SJ, Kim YI, Lee W (1999) J Mater Chem 9:129
211. Jang ES, Chang JJ, Jeon SH, Khim ZG, Choy JH (2005) Adv Mater 17:1742
212. Kim DS, Ozawa TC, Fukuda K, Ohshima S, Nakai I, Sasaki T (2011) Chem Mater 23:2700
213. Weiss A, Sick E (1978) Z Naturforsch 33b:1087
214. Lévy FA (ed) (1979) Intercalated layered materials. D. Reidel, Dordrecht
215. Lerf A, Schöllhorn R (1977) Inorg Chem 16:2950
216. Frondel C (1941) Am Mineral 26:295
217. Feitknecht W (1942) Helv Chim Acta 25:555
218. Miyata S (1983) Clays Clay Miner 31:305
219. Taylor RM (1984) Clay Miner 19:591
220. Reichle WT (1986) ChemTech 16:58
221. Duan X, Evans DG (2005) Layered double hydroxides. Springer, Berlin, New York
222. Khan AI, O'Hare D (2002) J Mater Chem 12:3191
223. Leroux F, Taviot-Gueho C (2005) J Mater Chem 15:3628
224. Williams GR, O'Hare D (2006) J Mater Chem 16:3065
225. Debecker DP, Gaigneaux EM, Busca G (2009) Chem Eur J 15:3920
226. Wang Q, O'Hare D (2012) Chem Rev 112:4124
227. Adachi-Pagano M, Forano C, Besse JP (2000) Chem Commun 91
228. Ma R, Liu Z, Li L, Iyi N, Sasaki T (2006) J Mater Chem 16:3809
229. Wu Q, Olafsen A, Vistad ØB, Roots J, Norby P (2005) J Mater Chem 15:4695
230. Ma R, Liu Z, Takada K, Iyi N, Bando Y, Sasaki T (2007) J Am Chem Soc 129:5257
231. O'Leary S, O'Hare D, Seeley G (2002) Chem Commun 1506
232. Singh M, Ogden MI, Parkinson GM, Buckley CE, Connolly J (2004) J Mater Chem 14:871
233. Jobbagy M, Regazzoni AE (2004) J Colloid Interface Sci 275:345
234. Naik VV, Ramesh TN, Vasudevan S (2011) J Phys Chem Lett 2:1193
235. Naik VV, Vasudevan S (2011) Langmuir 27:13276
236. Wang Q, O'Hare D (2013) Chem Commun 49:6301
237. Hibino T, Kobayashi M (2005) J Mater Chem 15:653
238. Jaubertie C, Holgado MJ, San Roman MS, Rives V (2006) Chem Mater 18:3114
239. Hou W, Kang L, Sun R, Liu Z-H (2008) Colloids Surf A 312:92
240. Manohara GV, Kunz DA, Kamath PV, Milius W, Breu J (2010) Langmuir 26:15586
241. Gardner E, Huntoon KM, Pinnavaia TJ (2001) Adv Mater 13:1263
242. Iyi N, Ishihara S, Kaneko Y, Yamada H (2013) Langmuir 29:2562
243. Wang Y, Yang W, Chen C, Evans DG (2008) J Power Sources 184:682
244. Latorre-Sanchez M, Atienzar P, Abellán G, Puche M, Fornés V, Ribera A, García H (2012) Carbon 50:518
245. Lee JM, Gunjakar JL, Ham Y, Kim IY, Domen K, Hwang SJ (2014) Chem Eur J 20:17004
246. Liang YN, Li Y, Ang C, Shen Y, Chi D, Hu X (2014) ACS Appl Mater Interfaces 6:12406
247. Lee JH, Chang J, Cha JH, Jung DY, Kim SS, Kim JM (2010) Chem Eur J 16:8296
248. Yan D, Qin S, Chen L, Lu J, Ma J, Wei M, Evans DG, Duan X (2010) Chem Commun 46:8654
249. Yan D, Lu J, Ma J, Wei M, Evans DG, Duan X (2011) Angew Chem Int Ed 50:720
250. Yan D, Lu J, Ma J, Qin S, Wei M, Evans DG, Duan X (2011) Angew Chem Int Ed 50:7037
251. Li L, Ma RZ, Ebina Y, Fukuda K, Takada K, Sasaki T (2007) J Am Chem Soc 129:8000
252. Deák Á, Janovák L, Tallósy SP, Bitó T, Sebők D, Buzás N, Pálinko I, Dékány I (2015) Langmuir 31:2019
253. Xu ZP, Niebert M, Porazik K, Walker TL, Cooper HM, Middelberg AP, Gray PP, Bartlett PF, Lu GQ (2008) J Control Release 130:86

254. An Z, Lu S, He J, Wang Y (2009) Langmuir 25:10704
255. Park DH, Kim JE, Oh JM, Shul YG, Choy JH (2010) J Am Chem Soc 132:16735
256. Playle AC, Gunning SR, Llewellyn AF (1974) Pharm Acta Helv 49:298
257. Costantino U, Ambrogi V, Nocchetti M, Perioli L (2008) Micropor. Mesopor. Mater. 107:149
258. Hawthorne FC (1985) Mineral Mag 49:87
259. Yamanaka S, Sako T, Seki K, Hattori M (1992) Solid State Ionics 53–56:527
260. Backov R, Morga AN, Lane S, Perez-Cordero EE, Williams K, Meisel MW, Sanchez C, Talham DR (2002) Mol Cryst Liq Cryst 376:127
261. Miao JY, Xue M, Itoh H, Feng Q (2006) J Mater Chem 16:474
262. Haschke JM (1974) Inorg Chem 13:1812
263. Louer D, Louer M (1987) J Solid State Chem 68:292
264. Geng FX, Xin H, Matsushita Y, Ma RZ, Tanaka M, Izumi F, Iyi N, Sasaki T (2008) Chem Eur J 14:9255
265. McIntyre LJ, Jackson LK, Fogg AM (2008) Chem Mater 20:335
266. Lee K-H, Byeon S-H (2009) Eur J Inorg Chem 2009:929
267. Hu L, Ma R, Ozawa TC, Sasaki T (2010) Chem Asian J 5:248
268. Sasaki T, Nakano S, Yamauchi S, Watanabe M (1997) Chem Mater 9:602
269. Ebina Y, Sasaki T, Harada M, Watanabe M (2002) Chem Mater 14:4390
270. Zhou Y, Huang R, Ding F, Brittain AD, Liu J, Zhang M, Xiao M, Meng Y, Sun L (2014) ACS Appl Mater Interfaces 6:7417
271. Kooli F, Sasaki T, Watanabe M (1999) Micropor Mesopor Mater 28:495
272. Wang LZ, Ebina Y, Takada K, Kurashima K, Sasaki T (2004) Adv Mater 16:1412
273. Kim TW, Hur SG, Hwang S-J, Choy J-H (2006) Chem Commun 220
274. Kim TW, Hur SG, Hwang SJ, Park H, Choi W, Choy JH (2007) Adv Funct Mater 17:307
275. Hata H, Kobayashi Y, Bojan V, Youngblood WJ, Mallouk TE (2008) Nano Lett 8:794
276. Miyamoto N, Kuroda K (2007) J Colloid Interface Sci 313:369
277. Bastakoti BP, Li Y, Imura M, Miyamoto N, Nakato T, Sasaki T, Yamauchi Y (2015) Angew Chem Int Ed Engl 54:4222
278. Hu Q, Xu Z, Qiao S, Haghseresht F, Wilson M, Lu GQ (2007) J Colloid Interface Sci 308:191
279. Kamada K, Tsukahara S, Soh N (2011) J Phys Chem C 115:13232
280. Tsukahara S, Soh N, Kamada K (2012) J Phys Chem C 116:19285
281. Sumida T, Takahara Y, Abe R, Hara M, Kondo JN, Domen K, Kakihana M, Yoshimura M (2001) Phys Chem Chem Phys 3:640
282. Wang L, Takada K, Kajiyama A, Onoda M, Michiue Y, Zhang L, Watanabe M, Sasaki T (2003) Chem Mater 15:4508
283. Okamoto K, Sasaki T, Fujita T, Iyi N (2006) J Mater Chem 16:1608
284. Suzuki S, Miyayama M (2006) J Phys Chem B 110:4731
285. Matsuda A, Sakamoto H, Mohd Nor MA, Kawamura G, Muto H (2013) J Phys Chem B 117:1724
286. Tanaka T, Fukuda K, Ebina Y, Takada K, Sasaki T (2004) Adv Mater 16:872
287. Yui T, Mori Y, Tsuchino T, Itoh T, Hattori T, Fukushima Y, Takagi K (2005) Chem Mater 17:206
288. Matsumoto Y, Unal U, Kimura Y, Ohashi S, Izawa K (2005) J Phys Chem B 109:12748
289. Lee KH, Lee BI, You JH, Byeon SH (2010) Chem Commun 46:1461
290. Yui T, Tsuchino T, Akatsuka K, Yamauchi A, Kobayashi Y, Hattori T, M-a Haga, Takagi K (2006) Bull Chem Soc Jpn 79:386
291. Yui T, Tsuchino T, Itoh T, Ogawa M, Fukushima Y, Takagi K (2005) Langmuir 21:2644
292. Yui T, Kobayashi Y, Yamada Y, Yano K, Fukushima Y, Torimoto T, Takagi K (2011) ACS Appl Mater Interfaces 3:931
293. Ma RZ, Bando Y, Sasaki T (2004) J Phys Chem B 108:2115
294. Kobayashi Y, Hata H, Salama M, Mallouk TE (2007) Nano Lett 7:2142

295. Bizeto MA, Alves WA, Barbosa CAS, Ferreira AMDC, Constantino VRL (2006) Inorg Chem 45:6214
296. Ma R, Kobayashi Y, Youngblood WJ, Mallouk TE (2008) J Mater Chem 18:5982
297. Maeda K, Eguchi M, Youngblood WJ, Mallouk TE (2008) Chem Mater 20:6770
298. Tong Z, Takagi S, Shimada T, Tachibana H, Inoue H (2006) J Am Chem Soc 128:684
299. Nabetani Y, Takamura H, Hayasaka Y, Shimada T, Takagi S, Tachibana H, Masui D, Tong Z, Inoue H (2011) J Am Chem Soc 133:17130
300. Nakato T, Yamashita Y, Kuroda K (2006) Thin Solid Films 495:24
301. Miyamoto N, Yamamoto S, Shimasaki K, Harada K, Yamauchi Y (2011) Chem Asian J 6:2936
302. Iler RK (1966) J Colloid Interface Sci 21:569
303. Decher G (1997) Science 277:1232
304. Kleinfeld ER, Ferguson GS (1994) Science 265:370
305. Sasaki T, Ebina Y, Watanabe M, Decher G (2000) Chem Commun 2163
306. Wang L, Omomo Y, Sakai N, Fukuda K, Nakai I, Ebina Y, Takada K, Watanabe M, Sasaki T (2003) Chem Mater 15:2873
307. Zhao J, Kong X, Shi W, Shao M, Han J, Wei M, Evans DG, Duan X (2011) J Mater Chem 21:13926
308. Sakai N, Fukuda K, Omomo Y, Ebina Y, Takada K, Sasaki T (2008) J Phys Chem C 112:5197
309. Liu M, Wang T, Ma H, Fu Y, Hu K, Guan C (2014) Sci Rep 4:7147
310. Keller SW, Johnson SA, Brigham ES, Yonemoto EH, Mallouk TE (1995) J Am Chem Soc 117:12879
311. Akatsuka K, Ebina Y, Muramatsu M, Sato T, Hester H, Kumaresan D, Schmehl RH, Sasaki T, Haga MA (2007) Langmuir 23:6730
312. Wang L, Sasaki T, Ebina Y, Kurashima K, Watanabe M (2002) Chem Mater 14:4827
313. Wang L, Ebina Y, Takada K, Sasaki T (2004) Chem Commun (Camb) 1074
314. Li L, Ma R, Iyi N, Ebina Y, Takada K, Sasaki T (2006) Chem Commun (Camb): 3125
315. Blodgett KB (1935) J Am Chem Soc 57:1007
316. Yamaki T, Asai K (2001) Langmuir 17:2564
317. Umemura Y, Yamagishi A, Schoonheydt R, Persoons A (2002) J Am Chem Soc 124:992
318. Muramatsu M, Akatsuka K, Ebina Y, Wang KZ, Sasaki T, Ishida T, Miyake K, Haga M (2005) Langmuir 21:6590
319. Saruwatari K, Sato H, Idei T, Kameda J, Yamagishi A, Takagaki A, Domen K (2005) J Phys Chem B 109:12410
320. Li BW, Osada M, Ozawa TC, Ebina Y, Akatsuka K, Ma RZ, Funakubo H, Sasaki T (2010) ACS Nano 4:6673
321. Shibata T, Fukuda K, Ebina Y, Kogure T, Sasaki T (2008) Adv Mater 20:231
322. Tetsuka H, Takashima H, Ikegami K, Nanjo H, Ebina T, Mizukami F (2009) Chem Mater 21:21
323. Jung C, Ohnishi T, Osada M, Takada K, Sasaki T (2013) ACS Appl Mater Interfaces 5:4592
324. Shibata T, Ohnishi T, Sakaguchi I, Osada M, Takada K, Kogure T, Sasaki T (2009) J Phys Chem C 113:19096
325. Miyamoto N, Nakato T (2002) Adv Mater 14:1267
326. Gabriel J-CP, Davidson P (2003) Top Curr Chem 226:119
327. Nakato T, Miyamoto N (2009) Materials 2:1734
328. Miyamoto N, Nakato T (2012) Isr J Chem 52:881
329. Paineau E, Antonova K, Baravian C, Bihannic I, Davidson P, Dozov I, Impéror-Clerc M, Levitz P, Madsen A, Meneau F, Michot LJ (2009) J Phys Chem B 113:15858
330. Nakato T, Nono Y, Mouri E, Nakata M (2014) Phys Chem Chem Phys 16:955
331. Nakato T, Miyamoto N, Harada A, Ushiki H (2003) Langmuir 19:3157
332. Mochizuki D, Kumagai K, Maitani MM, Wada Y (2012) Angew Chem Int Ed 51:5452
333. Mochizuki D, Kumagai K, Maitani MM, Suzuki E, Wada Y (2014) J Phys Chem C 118:22968

334. Pickering SU (1907) J Chem Soc Trans 91:2001
335. Aveyard R, Binks BP, Clint JH (2003) Adv Colloid Interface Sci 100–102:503
336. Abend S, Bonnke N, Gutschner U, Lagaly G (1998) Colloid Polym Sci 276:730
337. Ashby NP, Binks BP (2000) Phys Chem Chem Phys 2:5640
338. Yang F, Liu S, Xu J, Lan Q, Wei F, Sun D (2006) J Colloid Interface Sci 302:159
339. Nakato T, Ueda H, Hashimoto S, Terao R, Kameyama M, Mouri E (2012) ACS Appl Mater Interfaces 4:4338
340. Imperiali L, Liao KH, Clasen C, Fransaer J, Macosko CW, Vermant J (2012) Langmuir 28:7990
341. Mejia AF, Diaz A, Pullela S, Chang Y-W, Simonetty M, Carpenter C, Batteas JD, Mannan MS, Clearfield A, Cheng Z (2012) Soft Matter 8:10245

Chapter 4
Graphene: Synthesis and Functionalization

Tomo-o Terasawa and Koichiro Saiki

4.1 Introduction

4.1.1 Bulk Form of Graphene and Related Layered Materials

Graphene is an atom-thick sheet which constitutes graphite. Graphite, a natural mineral, has long been known by mankind since ancient times and used in various ways, as refractory substances in a furnace, crucibles, lubricants, pencils, neutron moderator in nuclear reactors, and so on (Fig. 4.1). In basic research the electronic state of graphite was first investigated by Wallace in 1947 and its peculiar feature was ascribed to a geometrical form of the lattice having two carbon atoms per unit cell [1]. Afterward in 1970s graphite intercalated compounds (GICs) attracted attention in the field of materials science [2]. GICs are complex materials in which metals, organic substances, etc. are inserted between the layers of graphite. Some of GICs show superconductivity, and the technological application to batteries, catalysts, etc. was also explored. In 1990s the electronic state of graphite edge was focused among solid-state physicists. Fujita et al. predicted the appearance of a flat energy band at the zigzag edge of graphite and electron–electron interaction would cause a magnetic order in the localized state [3].

Several kinds of natural layered materials other than graphite have been also known. One of the most popular ones is mica, used as an insulator for electricity and heat for a long time. Molybdenite, MoS_2, is also a natural mineral and has been used as a lubricant at high temperatures or in a vacuum (Fig. 4.1). In basic research metal

Tomo-o Terasawa
Nagoya University, Furocho, Chikusa, Nagoya, Aichi 464-8603, Japan

K. Saiki (✉)
The University of Tokyo, 5-1-5 Kashiwanoha, Kashiwa, Chiba 277-8561, Japan
e-mail: saiki@k.u-tokyo.ac.jp

T. Nakato et al. (eds.), *Inorganic Nanosheets and Nanosheet-Based Materials*,
Nanostructure Science and Technology, DOI 10.1007/978-4-431-56496-6_4

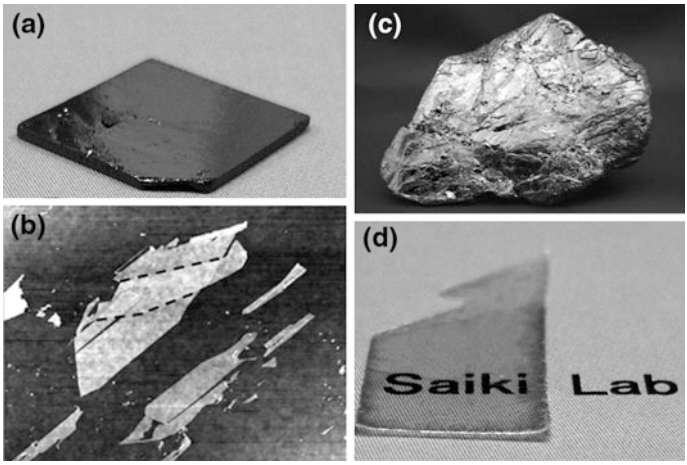

Fig. 4.1 Layered materials. **a** Graphite (Highly oriented pyrolytic), **b** Graphene adhered on SiO_2, with the bilayer region between *dashed lines*, **c** Molybdenite (MoS_2) (courtesy of Keiji Ueno), and **d** Mica (muscovite)

dichalcogenides (MX_2) became a target of solid-state physics in 1970s after the study of GICs. Transition metal dichalcogenides (TMDC) shows a wide range of electric conductivity from an insulator to a superconductor depending on the number of *d* electrons of the transition metal [4]. Low dimensionality was focused in those researches in which charge density waves were found in metallic TMDCs [5]. People tried to thin down the TMDC specimens for optical measurement, but had not ever challenged the thinnest monolayer [6]. Since mid-1980s epitaxial growth of TMDC, named van der Waals epitaxy, was investigated by Koma et al. The thin films of TMDC and their heterostructures were grown by molecular beam epitaxy [7].

4.1.2 Graphene Isolation and the Following Researches

In 2004 Andre Geim and Konstantin Novoselov isolated a monolayer sheet graphene by exfoliating graphite with an adhesive tape [8]. They put the exfoliated flake on a Si substrate with an oxide layer of 300 nm, the thickness of which was appropriate for them to recognize by optical microscopy [9] (Fig. 4.1). They measured the electrical properties which revealed the peculiar features of the characteristic of Dirac fermion: extremely large carrier mobility at room temperature, anomalous quantum Hall effect, optical absorption relating to the fine-structure constant, etc. [8, 10, 11]. Until their discovery no one had ever thought of isolation of an atom-thick sheet and evaluated the properties because such a thin layer had been considered to roll up or disappear [12]. Since then the graphene research has expanded explosively worldwide. Their groundbreaking works were awarded the 2010 Nobel Prize in Physics.

Application of the excellent properties of graphene to electronic devices has been examined just after the graphene isolation. For that purpose a scalable production method is indispensable. The mechanical exfoliation requires a skill of an expert and is less productive. Alternate synthesis methods such as chemical exfoliation, decomposition of SiC, chemical vapor deposition (CVD), etc. have been investigated up to now [13–15]. These fabrication methods will be described in Sect. 4.3. Most of these methods are also applicable to other layered materials.

Studies on the functionalization of graphene have also started from the initial stage. Addition of functional groups to the graphene lattice and the incorporation of heteroatoms into the graphene plane could tune the electronic states of graphene and yield novel properties [16, 17]. Fabrication of the graphene shape is another research topic. Graphene nanoribbon (GNR) is considered to represent additive properties. The GNR with a controlled edge structure is predicted to have a finite energy gap, although graphene itself is a semimetal with zero energy gap [18]. The method to prepare the GNR with a well-defined edge structure, however, is yet to be done. The effect of edge structures, zigzag or armchair (see the caption of Fig. 4.2), on the macroscopic properties is one of the fascinating characteristics of graphene, which should be clarified in the future.

4.2 Basic Properties

4.2.1 Structure and Mechanical Properties

Graphene is a one-atom-thick sheet in which carbon atoms form a honeycomb lattice as shown in Fig. 4.2. The s, p_x, and p_y states of carbon atoms are combined to form sp^2-hybrids directed toward the neighbor atoms in the plane. The sp^2-hybrids form the σ-bond between neighboring carbon atoms with the interatomic

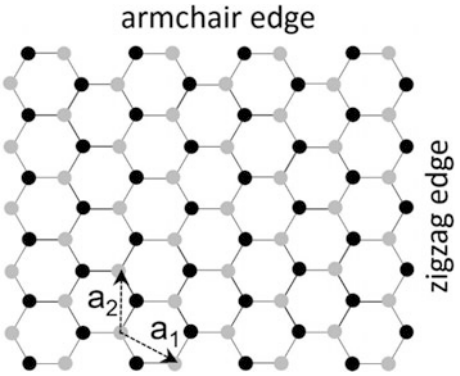

Fig. 4.2 Honeycomb lattice of graphene consisting of two sublattice A (*gray circles*) and B (*black circles*). a_1 and a_2 are the basis vectors of the unit cell. The distance between the neighboring carbon atoms is 0.142 nm. *Top* and *bottom* sides correspond to the armchair edge, while the *left* and *right* sides to the zigzag edge

distance of 0.142 nm. The remaining p_z orbital (π orbital) extends normal to the plane, and the π orbitals neighboring in the plane form the π band. The in-plane covalent σ-bonds provide the strong planar stiffness of graphene. The short interatomic distance makes a graphene membrane impermeable to standard gases including helium in spite of one atom thickness [19]. The specific surface area amounts theoretically to 2630 m^2/g due to its two dimensionality.

The feature of graphene lattice is the existence of two inequivalent carbon atoms in the unit cell. Each of them forms the two sublattices, designated A and B. The atom in the sublattice A(B) is surrounded by three atoms in the sublattice B(A). In bilayer graphene or graphite, the atom in the sublattice A is located on the atom in the overlying or underlying layer, while the atom in the sublattice B is located on the center of the hexagon of the overlying or underlying layer. This type of stacking is called Bernal stacking. In the monolayer graphene all the carbon atoms are equivalent in electron density. In the Bernal stacking, however, the carbon atoms in the sublattice A are distinguished from those in the sublattice B owing to the difference in interlayer interaction. We observed a honeycomb lattice in the scanning tunneling microscope (STM) image of graphene as shown in Fig. 4.3 (left). In the case of graphite, however, only half of the carbon atoms are observed as shown in Fig. 4.3 (right). A triangular lattice was observed because the tunneling current was different between the two sublattices.

The strong chemical bond in the graphene layer leads to the tensile strength of 130 GPa [20], which is much larger than those of steel (1–5 GPa), copper (0.2 GPa), etc. The Young modulus is approximately 1 TPa, which is large among various materials [19, 20]. The spring constant for the bend perpendicular to the plane is as large as 40 N/m for the length of 1 nm, while 4×10^{-5} N/m for the length of 1 μm. The nanometer-scale graphene is quite rigid, while the micrometer-scale graphene becomes flexible enough to adhere to the undulating substrate.

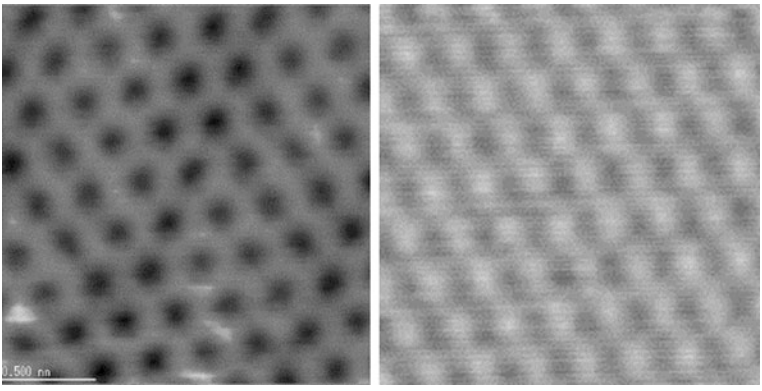

Fig. 4.3 Scanning tunneling microscope images of monolayer graphene (*left*) and graphite (*right*)

4.2.2 Electronic State and Electrical Properties

Graphene has a peculiar electronic state, originating from the existence of two inequivalent carbon atoms in the unit cell. The electronic state of graphene is described by Dirac Hamiltonian and the band dispersion is shown in Fig. 4.4 [21–23]. Solid lines correspond to three σ bands lying 3 eV above and below the Fermi level. Dotted lines are π bands crossing each other at the K and K′ points of the Brillouin zone. The characteristic feature of the graphene electronic structure is that the π bands have a linear relation with respect to the wavevector $\boldsymbol{k}$ around the K and K′ points at which the Fermi level is located. The linear relation between energy and momentum is obtained if we assume zero mass in the equation of special theory of relativity. Since the wavevector is proportional to the momentum, the linear dispersion in graphene makes the carrier called massless Dirac fermion [22]. The energy of graphene π band is depicted as a function of k_x and k_y in Fig. 4.5. The linear relation forms cones at K and K′ points, which are called Dirac cones. The electrons or holes are accumulated at the bottom of the cones by charge transfer. The minimum in the energy band is called a valley. Graphene has K and K′ valleys: a valley degree of freedom [24]. Wherever the Fermi level is located, the energy gap is absent in the electronic states of graphene. The gapless feature is disadvantageous for the application to transistors even though the carrier mobility is extraordinarily high in graphene.

Electron–electron scattering is small in graphene because graphene is intrinsically a semimetal, and the carrier density is small. Electron–phonon scattering is also small because excitation of phonon is suppressed due to the large Debye frequency. In addition to these features direct backscattering of electrons is forbidden owing to the lattice symmetry. This enhances the electron mobility up to 200,000 $cm^2\ V^{-1}\ s^{-1}$ [21, 22]. The large carrier mobility enabled the measurement of quantum phenomena such as quantum Hall effect [10, 25, 26]. The peculiarity of

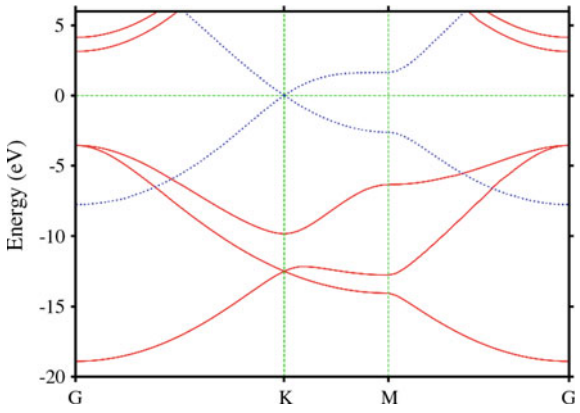

Fig. 4.4 Band structure of a single graphene layer. *Solid lines* are σ bands and *dotted lines* are π bands. Reprinted with permission from ref. [23]. Copyright 2008 by American Physical Society

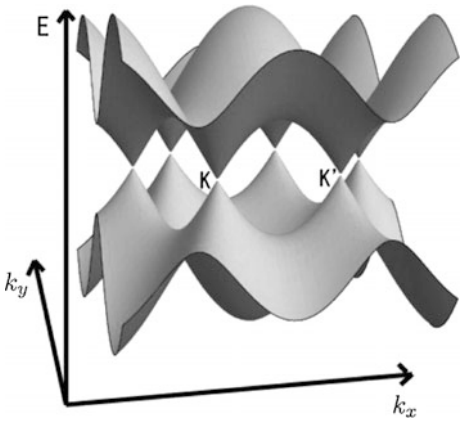

Fig. 4.5 Electron energy of graphene as a function of k_x and k_y. Conduction band and valence band touch each other at K and K′ points (Courtesy of Hideo Aoki)

Dirac fermion is prominent in the magnetic property of graphene. The cyclotron frequency is proportional to the square root of magnetic field, in contrast with a linear relation in conventional two-dimensional electron systems. Anomalous quantum Hall effect is characteristic of graphene electrons. Taking account of the degeneracy of the valley (K, K′) (Fig. 4.5) and spin degrees of freedom, Hall conductivity of graphene is calculated as $4\frac{e^2}{h}\left(n+\frac{1}{2}\right)$, where e and h are an elementary charge and Planck's constant, respectively. This half-integer quantum Hall effect was found experimentally, which confirmed the appearance of massless Dirac fermion in graphene [10, 25]. Quantum Hall effect was observed only in very clean materials such as Si at very low temperatures [27]. In graphene, however, such quantum effect is observed even at room temperature [26].

A small spin–orbit interaction arising from the low atomic number of carbon is considered favorable for application to spintronics, in which information can be transported or stored using the spin states of electrons [28]. The injection, transport, and detection of spin-polarized electrons are important issues in spintronics, the research of which are now in progress. The valley degree of freedom is also considered to transfer the information, the use of which would lead to so-called valleytronics [29, 30].

A few layer graphenes have a different electronic structure from that of graphene, depending on the stacking nature [21]. The bilayer graphene with Bernal stacking does not have a linear dispersion at K points, but has a conventional quadratic dependence. This loses the peculiar characteristics of Dirac fermion (suppression of backscattering, Dirac cones, etc.). The mobility is, however, still high due to the long range order in covalent bonds, small electron–electron, and electron–phonon scattering. One of the fascinating features of bilayer graphene is the energy gap opening when electric field is applied between the two layers [31]. The finite energy gap is important for device application.

4.3 Fabrication and Functionalization

To use graphene for various applications, the method for fabricating large quantity of graphene of high quality should be established. The size, density of defects, number of layers, stacking nature of multilayer graphene, etc. are key issues. The mechanical exfoliation of graphite has been always the best way to prepare a high-quality monolayer graphene [8] despite its poor productivity. For mass production, chemical exfoliation of graphite [13], decomposition of SiC [14], and chemical vapor deposition (CVD) [15] were then developed afterward. Figure 4.6 shows the relation between the quality of obtained graphene and the productivity of these methods. The quality and productivity have not been satisfied simultaneously. In this section, we review the fabrication methods of graphene from the perspective of high-quality and large quantity production. We introduce how the monolayer graphene is obtained and discuss the advantages and disadvantages of each method.

4.3.1 Mechanical Exfoliation

The mechanical exfoliation of graphite was first developed to prepare a monolayer graphene by Novoselov, Geim and co-authors [8]. In contrast to the in-plane

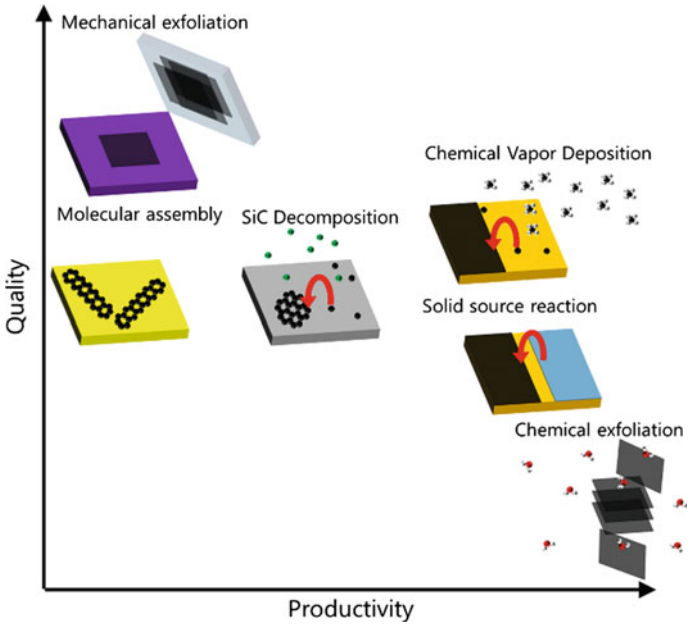

Fig. 4.6 Schematic illustrations of the fabrication methods of graphene. The *horizontal* and *vertical axes* stand for the productivity and the quality of grown graphene for each method

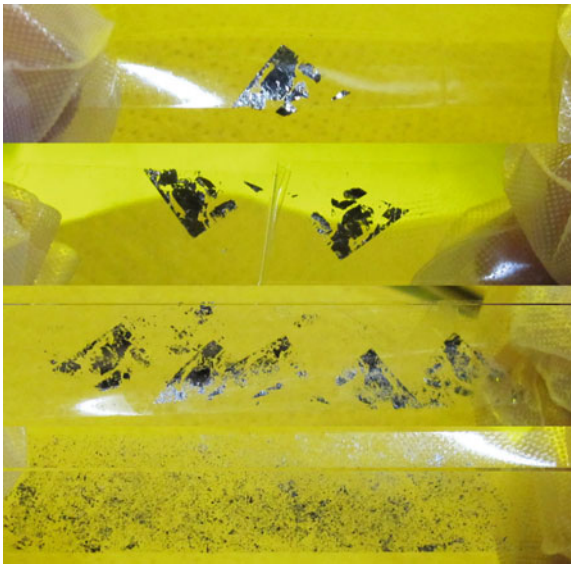

Fig. 4.7 Photographs of the mechanical exfoliation process of graphene. From the *top* to the *bottom*: Graphite flake on an adhesive tape, cleaved to two, four, and several times

carbon–carbon bonds, the van der Waals interaction between graphene layers is weak. Thus, graphene layers in graphite are easily exfoliated from each other, as described below. First, the graphite flake was set onto one adhesive tape and another tape onto the top side of the flake as shown in Fig. 4.7. Then the graphite flakes are repeatedly cleaved by the adhesive tape. Finally, the tape is rubbed onto an SiO_2/Si substrate (or other arbitrary substrates). The number of graphene layers in each flake varies and is determined using optical contrast, Raman spectroscopy, and atomic force microscopy. Particularly, Raman spectroscopy plays important roles to characterize the structure and properties of graphene [32–34]. The D, G, and 2D bands of graphene appearing at approximately 1350, 1580, and 2700 cm^{-1} are influenced by the number of layers and defects, carrier concentration, strain, and so on. Such the characterization showed that the mechanical exfoliation method has achieved the best quality of graphene for the investigation of basic physics such as quantum Hall effect [10, 25, 26] and valleytronics [29, 30].

4.3.2 Chemical Exfoliation

The exfoliation of graphite in a solution, so-called chemical exfoliation, is a scalable method to produce a large amount of graphene dispersion. Although graphene is intrinsically hydrophobic and less soluble in water, the introduction of oxygen containing functional groups such as hydroxy, carboxy, epoxide, and carbonyl changes the graphene surface to a hydrophilic one. The strongly oxidized graphite

[35] could be dispersed in water, and the monolayer graphene oxide (GO) was obtained after the careful sonication and centrifugation in water or other solvents. Please see Chap. 12 to know the detail of the chemical exfoliation method using GO to prepare graphene dispersion.

The properly chosen organic solvent, ionic liquid, and/or surfactants can improve the solubility of graphene in chemical exfoliation methods [36–38]. Particularly, Hernandez et al. [37] suggested that the surface tension of the solvent from 25 to 60 mJ/m^2 is suitable to form a monolayer graphene dispersion. Among the organic solvents, N-methylpyrrolidone (NMP) is considered to be the appropriate solvent that fulfills the surface tension condition [37].

The chemical exfoliation of graphite, as well as the mechanical exfoliation, belongs to a top-down fabrication method of graphene. The size of graphene sheets is limited by that of the starting material, graphite. In addition, harsh processes such as oxidation, reduction, and sonication create defects in the graphene lattice. Hence, this method is appropriate to the mass production of the middle quality of graphene for the use as the transparent conducting films and catalysts, for example [38].

4.3.3 Decomposition of SiC

Silicon carbide is a compound of silicon and carbon. The hexagonal {0001} planes, composed of (0001) Si face or (000-1) C face, alternately pile up along the [0001] direction. Berger et al. [14] reported the thermal decomposition of SiC{0001} substrates produces a high-quality monolayer graphene. During the heating of SiC at temperatures as high as 1500 °C, Si atoms preferentially sublime to vacuum, and the remaining C atoms create a graphene lattice [39]. A monolayer graphene grows on the Si face in a layer-by-layer manner in Bernal stacking. At the interface between the graphene and the Si face of SiC, C atoms bound strongly to the SiC substrate form the "buffer layer" as shown in Fig. 4.8 [39], the phonons of which could scatter the carrier [40]. On the C face, a turbostratic multilayer graphene grows from the middle of the terrace [41]. Emtsev et al. [42] reported the higher quality monolayer graphene was grown under Ar atmosphere due to the suppression of the Si sublimation.

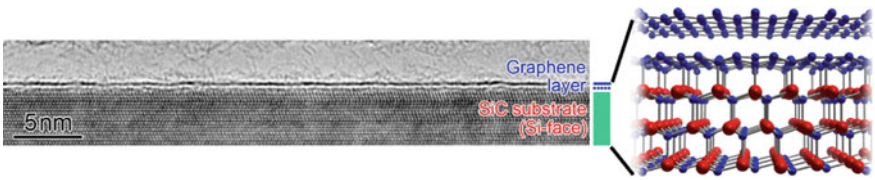

Fig. 4.8 HRTEM image of single-layer graphene on the SiC (0001) surface, together with the structural model [39]. Articles Copyrighted by JPS © [2015] The Physical Society of Japan (J Phys Soc Jpn 84:121,014)

Various properties of a monolayer graphene such as a high carrier mobility and peculiar quantum Hall effect were observed in the high-quality graphene grown on SiC substrates [14, 43]. When we consider the device application, it should be borne in mind that the graphene is strongly n-doped by the difference of the work function between graphene and SiC. The way to compensate this doping by the non-covalent functionalization will be mentioned in the Sect. 4.4.2. The high cost of the SiC substrate and the high-temperature treatment during the growth process are the disadvantages of this method.

4.3.4 Chemical Vapor Deposition

In chemical vapor deposition, gaseous source molecules are decomposed to produce the target materials on a substrate. For graphene, hydrocarbon molecules such as CH_4, C_2H_4, C_2H_5OH, C_6H_6, and so on are supplied to a heated substrate [15]. These source gases are often diluted by a carrier gas of Ar and H_2 to suppress the sublimation and oxidation of the substrate at high growth temperatures of approximately 1000 °C. The substrates that catalyze the synthesis of graphene are mainly transition metals; therefore, the grown graphene should be transferred onto an insulating substrate for the electronic device fabrication [44]. The size of graphene grown by chemical vapor deposition (CVD) can be as large as that of the substrate, which is one of the most important advantages of CVD method. However, the carrier mobility of CVD graphene has been smaller than that of the mechanically exfoliated graphene due to the electron scattering at the grain boundaries and defects [45, 46]. High growth temperatures and the transfer from the catalytic substrate onto an insulating substrate are considered as another problem to use CVD for the industrial production. Here, we review the characteristics of the CVD growth of graphene, which is the most promising method that forms a high-quality monolayer graphene at a moderate cost.

4.3.4.1 Precipitation

Transition metals with a high carbon solubility can form the solid solution with C at high temperatures as illustrated in Fig. 4.9. Cooling of the substrate decreases the C solubility, and the segregated C atoms form the graphene on the substrate surface. This kind of graphene growth occurs on the substrates like Ni, Ru, etc. [47, 48]. In this growth process, the cooling rate is an essential parameter. The fast cooling quenches the precipitation of C atoms and decreases the number of layers of growing graphene. However, the insufficient diffusion and the shortage of C atoms might create the defects in the graphene lattice and cause inhomogeneity of the number of layers. The slow cooling process forms the graphene lattice with less defects and a uniform thickness while this process may result in multilayer graphene [47, 49].

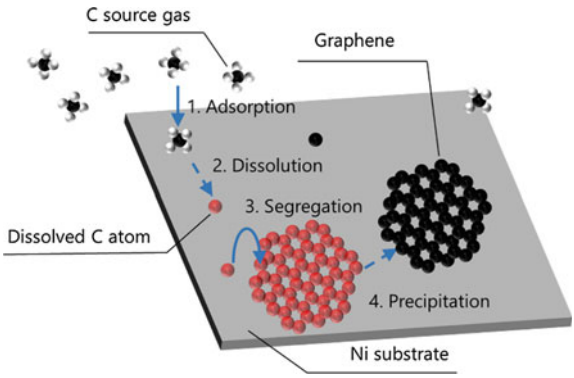

Fig. 4.9 Schematic illustration of the growth model of graphene by precipitation mechanism. *Black* and *red* balls stand for the C atoms dissolved in and adsorbed on a Ni substrate (*gray*)

4.3.4.2 Surface Reaction

On the substrate with a lower carbon solubility, adsorbed hydrocarbon molecules are dissociated to carbon fragments rather than dissolved into the inside of the metal substrate as illustrated in Fig. 4.10. Part of these carbon fragments on the substrates such as Cu, Pt, Ir, and Ge become the precursor of graphene growth [15, 50–53]. As the catalytic metal substrates dissociate hydrocarbons, the growth of second-layer graphene on the first-layer graphene is suppressed as compared with the first layer adjacent to the substrate [54]. This self-limiting growth has encouraged the researchers to produce a high-quality monolayer graphene particularly on Cu substrates. Since numerous growth parameters affect the CVD process of graphene, their optimization requires intensive studies [55–57]. The in situ observation during the graphene growth would accelerate such optimization, although it is difficult in the surface reaction CVD. Continuously supplied source gas molecules would hamper the use of conventional electron microscope except the environmental scanning electron microscopy [58, 59]. Radiation-mode optical microscopy achieved the real-time observation that pursued the growth of graphene on Cu from CH_4 by CVD [60, 61]. Other kinds of in situ observations also provide information on the growth mechanism [62, 63]. Recently, the oxygen concentration in the CVD atmosphere was found to play an important role that determines the nucleation density [60, 64]. In addition, the increased oxygen partial pressure changes the rate-limiting process from the attachment of growth precursors to the diffusion of growth precursors, leading to the change in shape of growing graphene from compact to dendritic as shown in Fig. 4.11 [60, 64]. The optimized growth conditions result in the large-area and high-quality monolayer graphene available for the industrial and scientific applications.

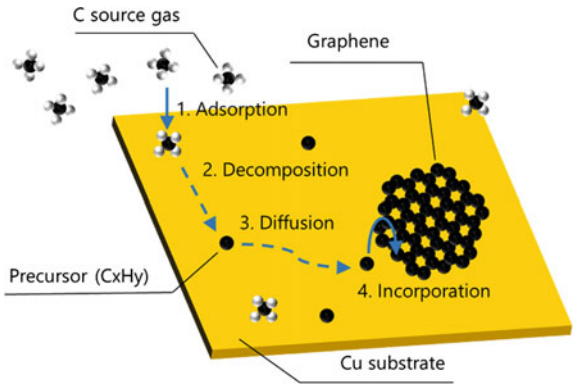

Fig. 4.10 Schematic illustration of the growth model of graphene by surface reaction mechanism. *Black* balls stand for the precursors decomposed from the source molecule, diffusing on a Cu substrate (*yellow*)

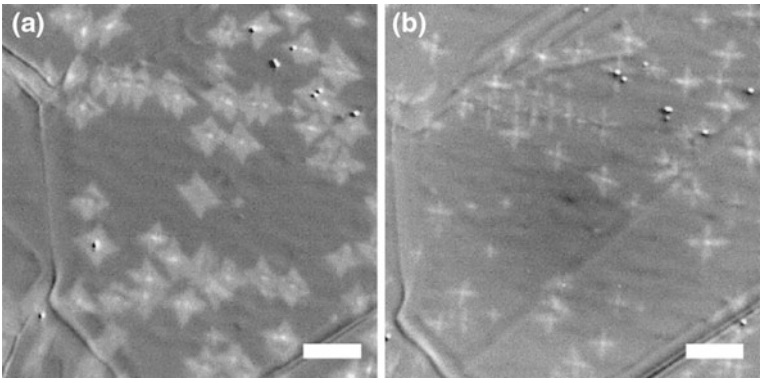

Fig. 4.11 Snapshots taken by radiation-mode optical microscopy during graphene growth. The partial pressure of oxygen of **a** 0.09 and **b** 0.12 Pa. *Bright patches* indicate the graphene grain on the dark background of Cu. The scale bar is 50 μm. Reproduced with permission from ref [60]. Copyright 2015, The Japan Society of Applied Physics

4.3.4.3 Other Methods Related to CVD

The CVD graphene grown on metal substrates requires the transfer onto a SiO_2/Si or other insulating substrate for electrical measurement and device application. Thus, the direct growth of graphene on an insulating substrate (e.g., sapphire and strontium titanium oxide) has been investigated [65, 66]. At very high temperature of 1500 °C, the catalytic activity of the substrate dissociates the source hydrocarbon

gases and creates a honeycomb lattice of graphene. Such high growth temperature is, however, not compatible with the industrial process.

Use of plasma in the CVD process was examined to create the growth precursors of graphene even at lower temperatures, which is called plasma-enhanced CVD (PECVD) [67–71]. The higher growth rate is appropriate for scalable production [70, 71]. Although graphene grows at lower temperatures even on the insulating substrate, the energetic ions coming from the plasma might cause defects in the graphene lattice. The self-limiting process of a monolayer graphene growth does not work because the growth precursors are generated in gas phase not on the substrate. These problems should be taken into account for the mass production of graphene by PECVD.

The gases such as CH_4 and H_2 used for the CVD growth of graphene are inflammable, which might impose high cost in the construction of production apparatus. The solid carbon source can avoid this problem. The amorphous carbon deposited on Ni dissolves inside at high temperatures and segregates to form graphene during the cooling process [72]. GO was used as another carbon source, which could control the position and the number of layers of precipitated graphene [73]. Cu and Pt substrates also catalyzed the formation of graphene from polymethyl methacrylate [74–76]. If the quality is increased and the number of layers is controlled, the growth from solid carbon sources will be promising for the large-area fabrication of graphene.

4.4 Functionalization

The chemical functionalization is one of the methods to tune graphene's fascinating properties such as electronic states, chemical stability, and optical properties. The functionalization of graphene with the hydrophilic and lipophilic groups makes graphene soluble in various solvents, for example [77]. Here we introduce typical four methods for functionalizing graphene. The first method, the covalent bond functionalization, is reliable and strong, although the peculiar electronic structure of graphene is likely to be lost [78]. The second method, non-covalent functionalization using van der Waals interaction, tunes the electronic properties of graphene indirectly [17]. The third method, the doping of the heteroatoms such as boron, nitrogen, and so on into graphene, is a familiar method in the field of semiconductor research [16]. Finally, the fabrication of one-dimensional (1D) GNR or zero-dimensional (0D) graphene quantum dots (GQD) from two-dimensional (2D) graphene exhibits the specific electronic and optical properties due to the confinement effect of electrons.

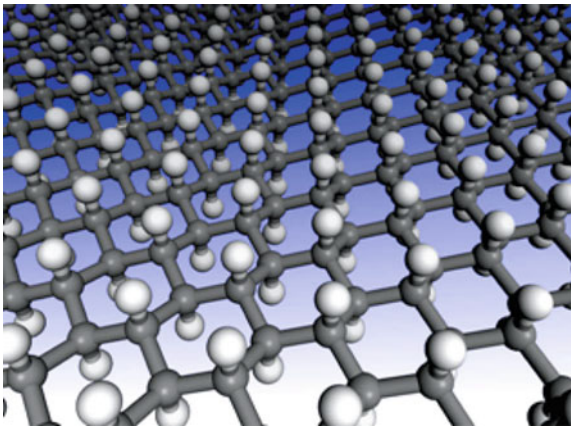

Fig. 4.12 Structure of graphane. The carbon atoms are shown in *gray* and the hydrogen atoms in *white*. The figure shows the hexagonal network with carbon in the sp^3 hybridization. Reprinted with permission from ref. [79]. Copyright 2007 by American Physical Society

4.4.1 Covalent Functionalization

The chemical, electronic, and physical properties of graphene are tuned by forming a covalent bond between the functional group and C atoms in the graphene lattice. The formation of covalent bonds consumes π electrons and opens the energy gap in graphene [78]. As the simplest functional group, the addition of H atoms transforms the graphene lattice to the buckled sp^3 honeycomb lattice as shown in Fig. 4.12 [79]. This sp^3-hybridized graphitic sheets, "graphane", is an insulator, which has an energy gap of 3.5 eV [79]. The hydrogen atoms desorb from graphane by annealing at 400 °C [78].

Fluorination is also a simple functionalization method of graphene. Robinson et al. [80] and Cheng et al. [81] reported the energy gap of 3.5 eV in fluorinated graphene. Similar to the hydrogenated graphene, the desorption of the fluorine during annealing was also reported [81]. Withers et al. [82] exfoliated the fluorinated graphite mechanically for producing a monolayer fluorinated graphene. The stability of graphene halides was in order of F, Cl, B, and I, although the chlorinated graphene is thermally unstable even at 0 °C [83].

The functionalization using organic chemistry is essential for tuning the properties of graphene. There are two types of methods that add the functional groups to the intrinsically inert sp^2 network of graphene: to enhance the reactivity of graphene or to enhance the chemical reaction. Use of GO, already functionalized graphene with oxygen containing functional groups, is a former example as explained in Chap. 12. The free radical addition reaction is a latter example. Diazonium acid and benzoyl peroxide are reported to add the nitrobenzene and benzene to the graphene lattice [84, 85] as shown in Fig. 4.13. In those reports, the functionalized graphene exhibits the decreased electrical conductivity and the energy gap opening. Many sp^2 bonds in graphene play as a reaction agent of Diels–Alder reaction with dienophiles such as perfluorophenylazide [86].

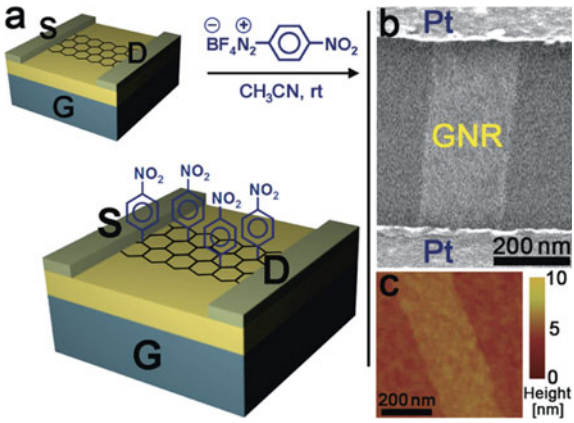

Fig. 4.13 **a** Schematic of the chemical functionalization of GNR devices with 4-nitrophenyl groups. Electronic devices consisted of monolayer GNRs contacted with Pt source (S) and drain (D) electrodes. The devices were fabricated on a 200-nm-thick thermal SiO_2 over heavily doped p-type Si that was used as a back gate (G). **b** Top-view SEM image of a typical electronic device based on a single-layer GNR. **c** AFM image of a fragment of a typical monolayer GNR reduced by annealing at 900 °C in Ar/H_2 on the Si/SiO_2 substrate. This GNR has an average thickness ~0.7 nm. Reprinted with permission from ref. [84]. Copyright 2010 American Chemical Society

4.4.2 *Non-covalent Functionalization*

The functionalization using van der Waals interaction has attracted attention since the sp^2 network is kept even after the adsorption of the functional molecules. The large sp^2 network of graphene arouses the π–π interaction with the molecule containing sp^2 bonds, such as pyrene, porphyrin, and coronene derivatives. The pyrene structure with electron donating and withdrawing groups changes the electronic properties and solubility of graphene as shown in Fig. 4.14 [17, 77, 87]. The functionalization of the porphyrin derivatives enhances the catalytic activity of the oxygen reduction reaction and the sensing efficiency of the glucose concentration in vivo [88]. The electron-withdrawing groups in a coronene derivative reduced the electron density of graphene [89]. Polymers such as polyaniline are added to graphene to make a composite to improve the mechanical strength and the capacitance [90]. The functionalization with the ionic liquid polymer is reported to change graphene from hydrophobic to hydrophilic [91].

The intercalation of molecules and atoms into graphite is known as one of the methods to tune the electronic properties of graphite [2]. Multilayer graphene also forms the intercalated compounds. For example, the electrode of Li^+ ion battery, considered as an application of graphene, utilizes the intercalation of Li^+ ion [92]. The interface between graphene and the substrate also confines the materials to create new properties. The intercalation of materials between the CVD grown graphene and its catalytic substrates such as Ir and Ru is known as a new functionalization method [93, 94]. The intercalation of hydrogen and nitrogen between

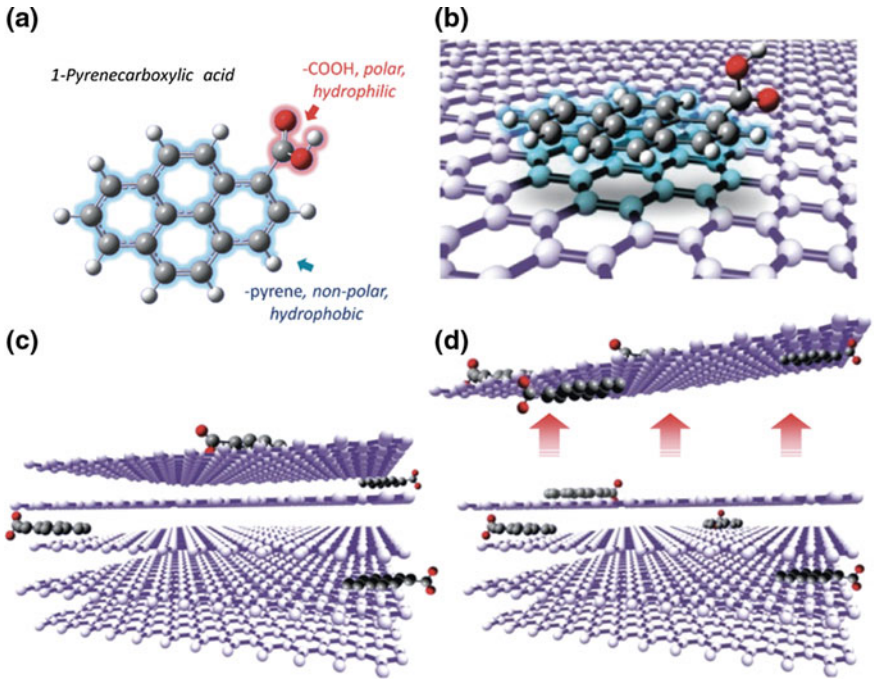

Fig. 4.14 **a** Molecular structure of 1-pyrenecarboxylic acid with its polar (hydrophilic) and nonpolar (hydrophobic) parts indicated. **b** A 1-pyrenecarboxylic acid (PCA) molecule can form a stable π-stacking bond with graphitic surfaces. **c** In a polar medium (H_2O) and with agitation, the nonpolar pyrene part prefers to attach itself on top of the graphitic surface via the π-stacking mechanism, or penetrates within the layers of graphite to reduce hydrophobic interactions with water. **d** Continuing this process releases single or few layers of graphene. Reprinted with permission from ref. [87]. Copyright 2010 American Chemical Society

the epitaxial graphene and the SiC substrate results in the quasi-freestanding graphene on the SiC substrate due to the termination of Si dangling bonds [95, 96].

4.4.3 Heteroatom Doping

Heteroatom doping is a well-known method to tune the electronic properties of materials. To keep the lattice structure of graphene, boron and nitrogen are promising as a dopant [97]. The B-doping results in the hole doping as reported in the literatures [98]. In addition to the substitutional doping, the edges and defects are the active sites as illustrated in Fig. 4.15. The doping site is crucial for the tuning of the electronic properties because the charge transfer between the dopant

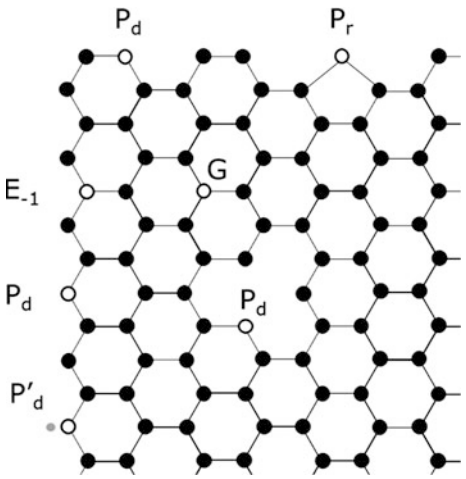

Fig. 4.15 Doping sites of nitrogen atoms in graphene lattice: G; graphitic, P_d; pyridinic, P_r; pyrrolic, P'_d; pyridinium, E_{-1}; edge−1, sites. *Black*, *white*, and *gray balls* stand for C, N, and H atoms, respectively

and carbon atoms depends on the site. The work function of N-doped graphene was tuned by controlling the doping site and its amount [99, 100]. The electronic states modified by doping give rise to the catalytic activity of doped graphene while the non-doped graphene is chemically inert. Particularly, the nitrogen-doped graphene enhances the oxygen reduction reaction (ORR), which could be applied for fuel cells [101]. Similar to N-doping, B-doping also enhances the adsorption ability of gaseous molecules and the catalytic activity of ORR [102]. The co-doping of B and N atoms in graphene is also researched [98, 103, 104] to enhance the catalytic activity of ORR and to create BN domains in the graphene lattice which forms the two-dimensional electric circuit. The doped atoms in graphene lattice and the defects created during the doping process, on the other hand, scatter electrons, reducing the mean free path and mobility of carriers compared with pristine graphene [97].

The methods that fabricate doped graphene are categorized into two types: the top-down method to substitute C atoms with heteroatoms and the bottom-up method to add heteroatoms during the formation of graphene lattice. Joule heating of graphene in an ammonia atmosphere [16], bombardment of N^+ ion [105], and treatment with N containing plasma [99] were reported as the examples of the top-down method. Annealing of graphite and graphene in a boron containing atmosphere leads to B-doped graphene [106, 107]. The addition of ammonia in CVD [108] and that of nitrogen in PECVD [68] achieved the bottom-up synthesis of N-doped graphene. The CVD growth by CH_4 and B_2H_6 [109, 110] and the molecular assembly of B containing molecules [111] are available to produce B-doped graphene.

4.4.4 Graphene Nanoribbon and Graphene Quantum Dot

The reduction of dimensionality from 2D graphene to 1D graphene nanoribbons (GNRs) or to 0D graphene quantum dots (GQDs) causes the confinement of electrons, which modifies the electronic and optical properties depending on the size, edge structures, and functional groups. For example, the width of GNR with armchair edges strongly changes the energy gap [18]. Here we briefly review the fabrication and characterization of GNR and GQD.

Two types of production methods of GNR are explored: a top-down method from 2D graphene sheets and a bottom-up method from precursor molecules. The simplest fabrication method of GNR is the lithography of graphene [112]. However, the control of the width and edge structure is a difficult problem due to the limiting of the resolution of electron beam lithography. The oxidative unzipping of carbon nanotube forms GNR, the width of which depends on the diameter of CNT [113]. The assembly of carefully designed aromatic molecules on catalytic metal substrates is a representative of the bottom-up fabrication of GNR [114], in which cyclodehydrogenation of aromatic rings on Au, Cu, and so on at 500 °C forms GNR. The width, edge structure, and heteroatom doping are controlled by properly designed molecules as illustrated in Fig. 4.16 [115]. The terrace and step structure of the substrate is used for the bottom-up fabrication of GNR. The GNRs selectively grew on the steps of the Ni and Cu substrates as a CVD graphene [116, 117] and grew on those of SiC substrates as an epitaxial graphene [118]. The high on/off ratio of the field-effect transistor made of GNR proved the energy gap opening [18, 112]. The method that controls the edge structure should be developed to tune the electronic properties.

GQD can also be prepared by a top-down method or a bottom-up method. As the former example, the chemical reaction of GO in liquid phase is often used to prepare GQD since GO is easily broken into small fragments. The modification of graphene and CNT are often used to produce the GQD solution [119, 120]. In addition to such top-down fabrication, the simple precursor molecules form GQD as the bottom-up fabrication [121]. The size and edge structures are also important in GQD to tune the band gap energy for electronic and optical applications, similar to the case of GNR [119]. In addition, the type and amount of the oxygen containing functional groups, defects, and the type and pH of solvents strongly affect the band gap energy, optical absorbance, photoluminescence characteristics, and quantum yield as shown in Fig. 4.17 [122, 123]. Use of such optical characteristics results in PL devices, electrochemical sensors, and photocatalysts. The low toxicity of GQD leads to the bio-imaging and drag delivery systems [124].

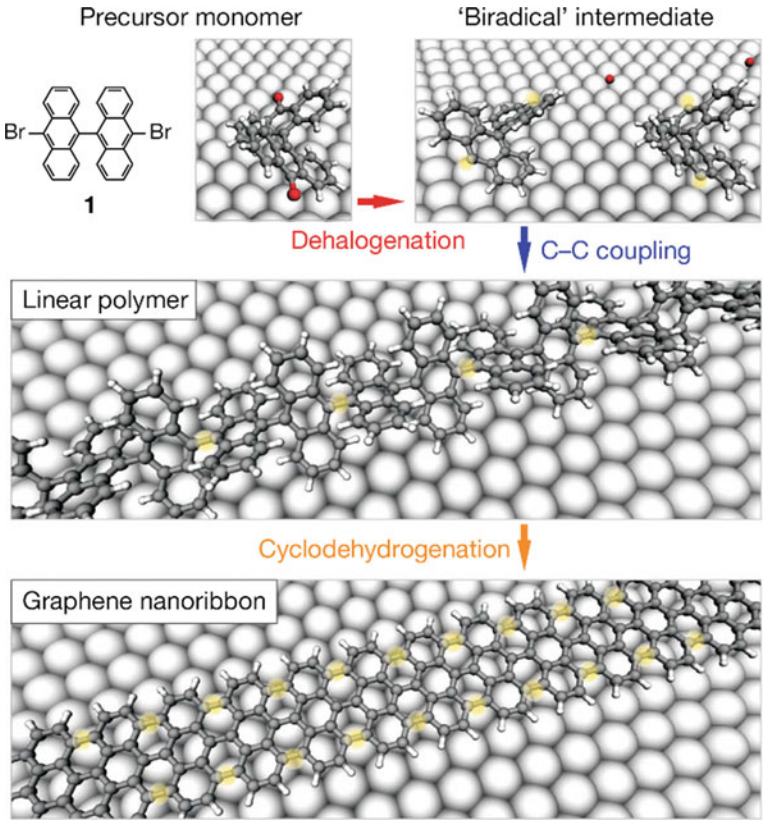

Fig. 4.16 Bottom-up fabrication of atomically precise GNRs. Basic steps for surface-supported GNR synthesis, illustrated with a ball-and-stick model of the example of 10,10′-dibromo-9,9′-bianthryl monomers (1). *Gray* Carbon; *white* Hydrogen; *red* Halogens; underlying surface atoms shown by *large spheres*. *Top* Dehalogenation during adsorption of the di-halogen functionalized precursor monomers. *Middle* Formation of linear polymers by covalent interlinking of the dehalogenated intermediates. *Bottom* Formation of fully aromatic GNRs by cyclodehydrogenation. Reprinted by permission from Macmillan Publishers Ltd: ref. [115], Copyright 2010

4.5 Related Materials

Following the isolation of graphene, the ways of fabricating other atomically thin materials have been developed [125, 126] expecting the variety of specific characteristics: electric conductivity, chemical stability, and interaction with photons. The mechanical exfoliation [126], liquid phase exfoliation [127], and CVD [128] are applied to these materials. In addition to the atomically thin materials, the heterostructures of them gives rise to new properties and applications [125].

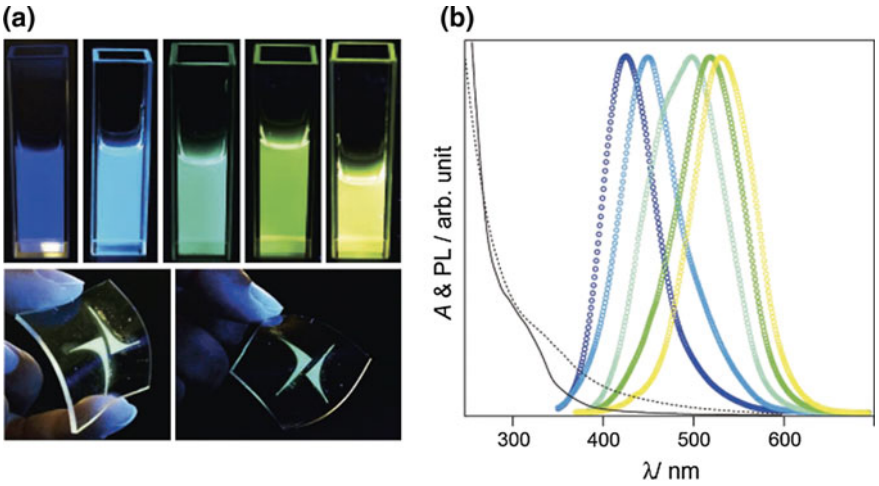

Fig. 4.17 **a** Emission images of amino-functionalized GQDs (af-GQDs) dispersed in water (*upper*) and af-GQD@polymer hybrids (*bottom*) under irradiation from a 365 nm UV lamp. The af-GQDs in the upper images were prepared under the following conditions: 150, 120, 70, 90, and 90 °C in ×2 conc. ammonia solution, respectively from the left. The bottom images show flexible polydimethylsiloxane (PDMS) elastomer with a luminescent piece of af-GQDs@PDMS hybrid patterned in the logo of our institute. **b** Photoluminescence and selected UV/VIS absorption spectra of af-GQDs. In the absorption spectra, *solid* and *broken lines* denote the spectra of af-GQDs prepared at 120 and 90 °C, respectively. Reproduced from ref. [123] by permission of John Wiley & Sons Ltd

Here we introduce the fabrication methods and characteristics of the atomically thin materials related to graphene, accompanied with those of the heterostructure.

4.5.1 Silicene, Germanene, Stannene, Phosphorene

The counterpart of graphene consisting of Si, P, Ge, and Sn is called silicene, phosphorene, germanene, and stannene, respectively. Due to their graphene-like honeycomb structures, the electrons near the Fermi level would behave as a Dirac fermion. The first-principles calculations for these materials suggest that the low-buckled structure is more stable than the planer honeycomb structure, as shown in Fig. 4.18 [129], which results in the chemical instability and reactivity with the species in the atmosphere. The bulk-layered materials composed of these elements are not stable except the bulk-black phosphorus so that the mechanical exfoliation cannot be applicable.

Among these materials, silicene grown on an Ag single crystal was first observed by STM, which was prepared by molecular beam epitaxy [129, 130]. The angle-resolved photoemission spectroscopy suggested the existence of the Dirac fermion with a linear band dispersion. The unstable silicene grown on Ag was

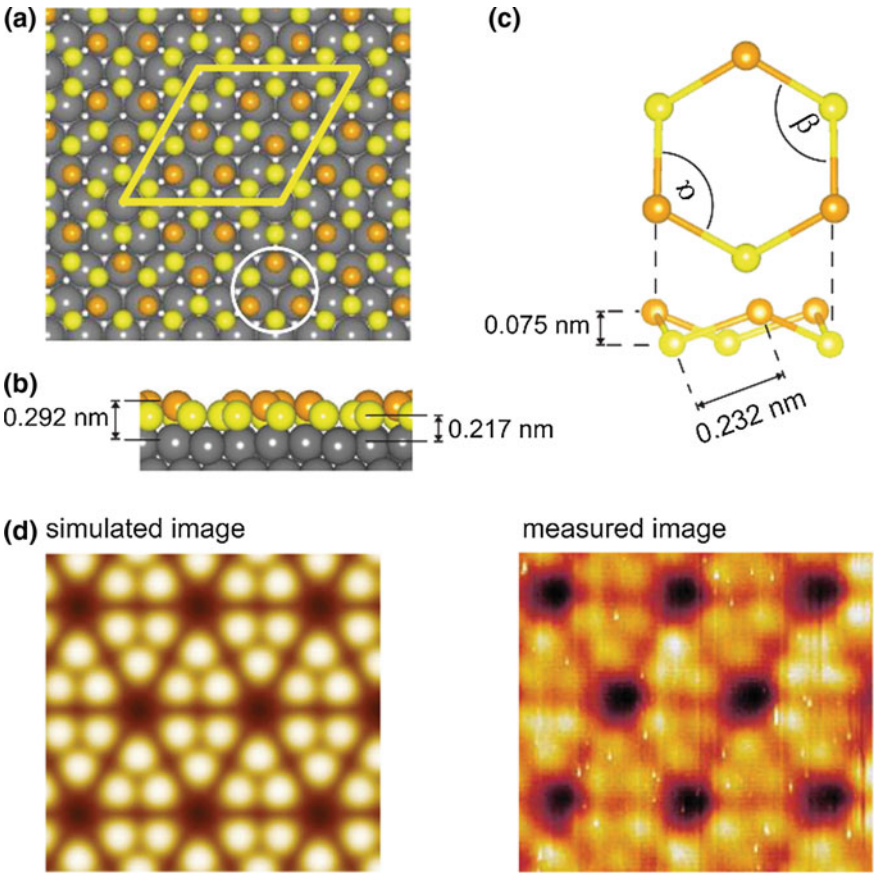

Fig. 4.18 DFT results for the silicene on Ag(111). **a** Top view of the fully relaxed atomic geometries of the model for silicene on the Ag(111) surface. **b** Side view of (**a**). **c** Enlarged image of the hexagonal silicene ring indicated by the *white circle* in (**a**). **d** Simulated STM image (*left*) for the structure shown in (**a**). The simulated image exhibits the same structural features as those observed in the experimental STM image (*right*), i.e., a hexagonal arrangement of the triangular structure around dark centers. Reprinted with permission from ref. [129]. Copyright 2012 by American Physical Society

capped by alumina layers, which could work as the field-effect transistor [131]. Silicene was also grown on the ZrB_2 substrates [132]. The weak interaction between Si and ZrB_2 provided the linear band dispersion in the angle-resolved photoemission spectra.

Phosphorene is a monolayer sheet of the black phosphorous, an allotrope of phosphorous stable under high pressures and temperatures, with the buckled honeycomb lattice, and its isolation was reported in 2014 first [133]. Mechanical exfoliation of the black phosphorous results in the fabrication of phosphorene, while phosphorene is chemically unstable against oxidation within several tens of

minutes in the ambient conditions. The mobility, energy gap, and on/off ratio in FET are 1000 cm^2/Vs, 1 eV, and 10^5, respectively [133, 134].

The isolation of germanene and stannene was also reported. The exfoliation of Ca intercalated Ge, $CaGe_2$, and the removal of Ca from it led to the synthesis of germanene, though they were unstable and accompanied with impurities [135]. Germanene with a buckled honeycomb structure on Au and Al was observed by STM [136, 137]. The growth of stannene on a Bi_2Te_3(111) substrate was reported, and the electronic structure of stannene was in agreement with results of the first-principles calculations [138]. Further modification of the fabrication and encapsulation will lead to the fundamental studies and industrial applications of these materials.

4.5.2 *Hexagonal Boron Nitride and Transition Metal Dichalcogenide*

Chemical compounds with a layered honeycomb lattice, such as hexagonal boron nitride (h-BN) and TMDC, can be thinned down to a monolayer. Here we introduce the properties and fabrication methods of h-BN and TMDC monolayers. The lattice structure of h-BN is almost similar to that of graphene, but the two atoms in the unit cell are substituted with a pair of B and N atoms. h-BN is chemically stable like graphene, while the valence electrons are strongly localized around the electrophilic N atoms resulting in an insulating behavior. The energy gap, the tunneling barrier, and the breakdown field of h-BN amount to 5.9 eV [128, 139], 3.07 eV, and 7.95 MV/cm [140], respectively. h-BN can be used as an insulating substrate for the electronic devices of atomically thin materials. The fabrication of atomically thin h-BN was reported by the mechanical exfoliation from the bulk materials [126], and by chemical exfoliations [127]. The CVD growth of h-BN was done on Pt and Ru using $B_3N_3H_6$ as a source gas [141, 142]. NH_3BH_3 was used to synthesize h-BN on Ni and Cu [128, 143].

The group 4, 5, 6, 7, and 10 transition metals and chalcogen elements of S, Se, and Te form the compound with a chemical formula of MX_2 where M and X stand for metal and chalcogen, respectively [144]. As shown in Fig. 4.19 [145], the hexacoordinated transition metal in the center of the unit cell forms the two types of coordination: trigonal prismatic (point group of D_{3h}) and octahedral (that of O_h). The number of *d* electrons depending on the transition metal determines the electrical properties of TMDCs among semiconductor, semimetal, and metal [145]. Although TMDCs itself have a long history of research, [4] the intriguing properties inherent in one to a few layers TMDCs have not been known to date. For example, the bulk MoS_2 has an indirect energy gap of 1.3 eV, while the monolayer one has a direct gap of 1.8 eV at Brillouin zone center [146]. The transition from the indirect energy gap to the direct one affects the optical property such as photoluminescence. The monolayer TMDCs lost the reverse symmetry, making the

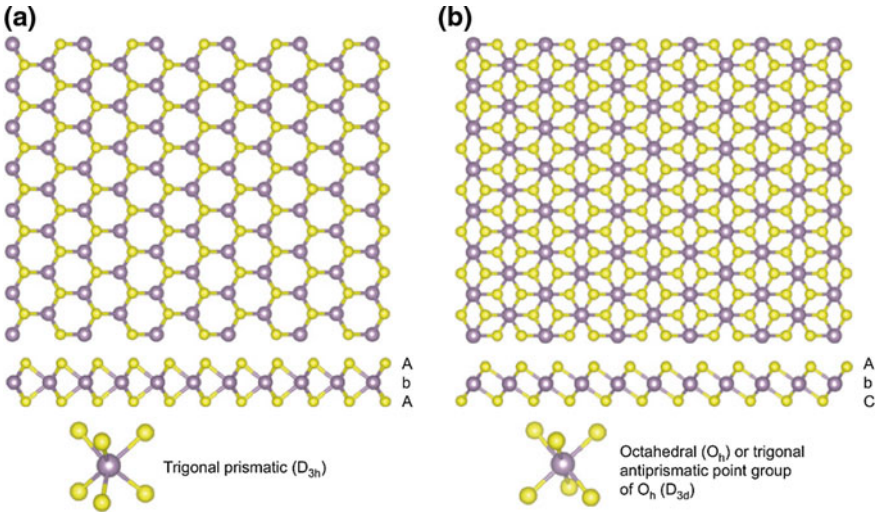

Fig. 4.19 Structure of monolayered TMDCs. c-Axis and [11–20] section view of single-layer TMD with trigonal prismatic (*left*) and octahedral (*right*) coordinations. Atom color code: *purple*, metal; *yellow*, chalcogen. The labels AbA and AbC represent the stacking sequence where the upper and lower case letters represent chalcogen and metal elements, respectively. Reproduced by permission from Macmillan Publishers Ltd: ref. [145]. Copyright 2013

degree of freedom of the valley accessible by circular polarized light [147]. Such fascinating electronic and optical characteristics encourage the studies of the monolayer TMDCs [148]. The recent progress in the studies of atomically thin TMDCs is described in Chap. 5.

4.5.3 Heterostructures

In addition to the fabrication of the atomically thin materials, the combination of them would create new physical properties [125]. Such heterostructures composed of these materials are categorized into two types: lateral and vertical, as shown in Fig. 4.20 [149]. In the lateral-type heterostructure, the one-atom-thick film contains the regions of different properties which are covalently bound with each other at the boundaries. For example, the connection of graphene and h-BN provides the monolayer electrical circuit [150]. The heterostructure composed of TMDCs with a different carrier type results in the atomically thin *p*–*n* junction, photoluminescence device, and CMOS inverters [149, 151]. The bottom-up CVD growth builds up such structures.

The vertical heterostructure of atomically thin materials would provide novel properties because the nature of the interface and the stacking orientation dominate its properties [125]. For example, the SiO_2/h-BN/graphene structure achieved a mobility of 100,000 cm^2/Vs at room temperature, while the SiO_2/graphene needed

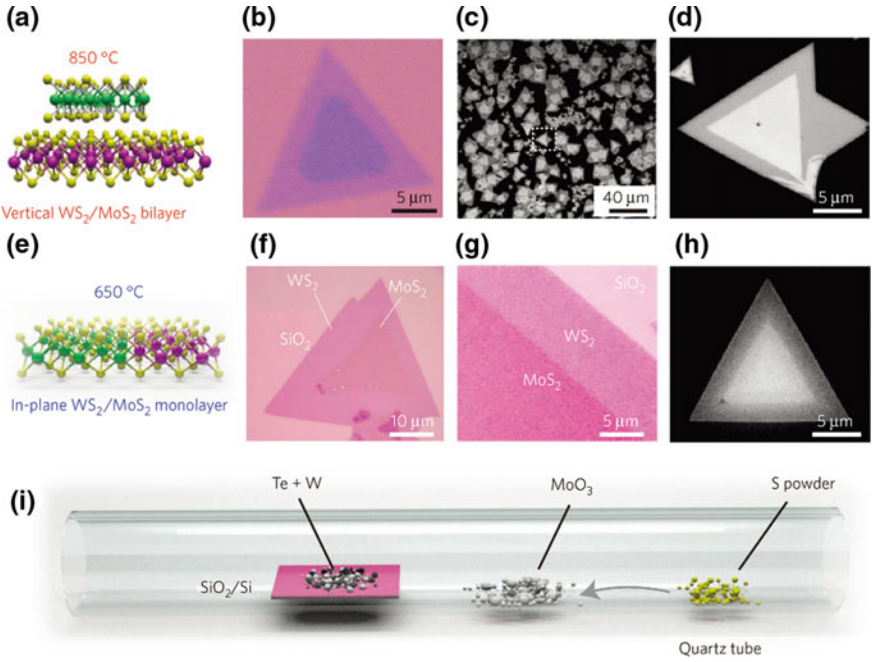

Fig. 4.20 Schematic of the synthesis and the overall morphologies of the vertically stacked and in-plane WS_2/MoS_2 heterostructures. **a–d**, Schematic, optical, and SEM images of the vertically stacked WS_2/MoS_2 heterostructures synthesized at 850 °C. **e–h**, Schematic, optical, and SEM images of the WS_2/MoS_2 in-plane heterojunctions grown at 650 °C. **g** is an optical image of the interface between WS_2 and MoS_2 with enhanced color contrast, showing the abrupt change of contrast at the interface. SEM images are presented in reverse contrast. The *green*, *purple,* and *yellow spheres* in **a, e** represent W, Mo, and S atoms, respectively. **i** Schematic of the synthesis process for both heterostructures. Reprinted by permission from Macmillan Publishers Ltd: ref. [149]. Copyright 2014

to be cooled to low temperatures to represent such mobility. The absence of dangling bonds and the high frequency of optical phonons in h-BN contributes to the enhancement of mobility [152]. Furthermore, the encapsulated graphene as SiO_2/h-BN/graphene/h-BN shows a mobility up to 500,000 cm^2/Vs [152, 153]. Another example of the h-BN/graphene structure is the appearance of new phenomenon by controlling the stacking orientation between them. The stacking of h-BN and graphene with a certain angle can lose the reverse symmetry of the lattice. In this structure, the K and K′ points which are degenerated in the pristine graphene become accessible by the circular polarized light, resulting in the observation of the valley degree of freedom [154].

The two types of the fabrication methods are known for the vertical heterostructure: the mechanical stacking of materials and the fabrication of one layer on another layer. The former way requires the highly trained person, the special fixture, and the clean room [125]. However, any combination of the stable

atomic layers can be stacked within an orientation accuracy of less than 1° [125]. Due to these advantages, the top-down stacking has been studied to find new physical phenomena [152, 153]. In the bottom-up synthesis using CVD growth the large-area hetero-structured samples are expected [149, 155]. The combination of materials and their orientation relation is, however, limited because the condition for the epitaxial growth is strict [156]. The universal way to grow the vertical heterostructure of atomic layers is required to utilize new physics in the realistic devices.

References

1. Wallace P (1947) The band theory of graphite. Phys Rev 71:622
2. Dresselhaus MS, Dresselhaus G (2002) Intercalation compounds of graphite. Adv Phys 51:1
3. Nakada K, Fujita M, Dresselhaus G, Dresselhaus MS (1996) Edge state in graphene ribbons: nanometer size effect and edge shape dependence. Phys Rev B 54:17954
4. Wilson JA, Yoffe AD (1969) The transition metal dichalcogenides discussion and interpretation of the observed optical, electrical and structural properties. Adv Phys 18:193
5. Wilson JA, Di Salvo FJ, Mahajan S (1974) Charge-density waves in metallic, layered, transition-metal dichalcogenides. Phys Rev Lett 32:882
6. Saiki K, Yoshimi M, Tanaka S (1978) Modulation spectroscopy on the group IV and VI transition-metal dichalcogenides. Phys Status Solidi 88:607
7. Koma A, Sunouchi K, Miyajima T (1985) Summary Abstract: fabrication of ultrathin heterostructures with van der Waals epitaxy. J Vac Sci Technol B 3:724
8. Novoselov KS, Geim AK, Morozov SV, Jiang D, Zhang Y, Dubonos SV, Grigorieva IV, Firsov AA (2004) Electric field effect in atomically Thin Carbon Films. Science 306:666
9. Blake P, Hill EW, Castro Neto AH, Novoselov KS, Jiang D, Yang R, Booth TJ, Geim AK (2007) Making graphene visible. Appl Phys Lett 91:063124
10. Novoselov KS, Geim AK, Morozov SV, Jiang D, Katsnelson MI, Grigorieva IV, Dubonos SV, Firsov AA (2005) Two-dimensional gas of massless Dirac fermions in graphene. Nature 438:197
11. Nair RR, Blake P, Grigorenko AN, Novoselov KS, Booth TJ, Stauber T, Peres NMR, Geim AK (2008) Fine structure constant defines visual transparency of graphene. Science 320:1308
12. Mermin ND (1968) Crystalline order in two dimensions. Phys Rev 176:250
13. Stankovich S, Piner RD, Chen X, Wu N, Nguyen ST, Ruoff RS (2006) Stable aqueous dispersions of graphitic nanoplatelets *via* the reduction of exfoliated graphite oxide in the presence of poly(sodium 4-styrenesulfonate). J Mater Chem 16:155
14. Berger C, Song Z, Li T, Li X, Ogbazghi AY, Feng R, Dai Z, Marchenkov AN, Conrad EH, First PN, de Heer WA (2004) Ultrathin Epitaxial Graphite: 2D electron gas properties and a route toward graphene-based nanoelectronics. J Phys Chem B 108:19912
15. Li X, Cai W, An J, Kim S, Nah J, Yang D, Piner R, Velamakanni A, Jung I, Tutuc E, Banerjee SK, Colombo L, Ruoff RS (2009) Large-area synthesis of high-quality and uniform graphene films on copper foils. science 324:1312
16. Wang X, Li X, Zhang L, Yoon Y, Weber PK, Wang H, Guo J, Dai H (2009) N-Doping of graphene through electrothermal reactions with ammonia. Science 324:768
17. Cheng H, Shiue R-J, Tsai C-C, Wang W-H, Chen Y-T (2011) High-quality graphene $p-n$ junctions *via* resist-free fabrication and solution-based noncovalent functionalization. ACS Nano 5:2051

18. Han MY, Özyilmaz B, Zhang Y, Kim P (2007) Energy band-gap engineering of graphene nanoribbons. Phys Rev Lett 98:206805
19. Bunch JS, Verbridge SS, Alden JS, Van Der Zande AM, Parpia JM, Craighead HG, McEuen PL (2008) Impermeable atomic membranes from graphene sheets. Nano Lett 8:2458
20. Lee C, Wei X, Kysar JWJJW, Hone J (2008) Measurement of the elastic properties and intrinsic strength of monolayer graphene. Science 321:385
21. Castro Neto AH, Guinea F, Peres NMR, Novoselov KS, Geim AK (2009) The electronic properties of graphene. Rev Mod Phys 81:109
22. Geim AK, Novoselov KS (2007) The rise of graphene. Nat Mater 6:183
23. Boukhvalov DW, Katsnelson MI, Lichtenstein AI (2008) Hydrogen on graphene: electronic structure, total energy, structural distortions and magnetism from first-principles calculations. Phys Rev B 77:035427
24. Zhang Y, Jiang Z, Small JP, Purewal MS, Tan Y-W, Fazlollahi M, Chudow JD, Jaszczak JA, Stormer HL, Kim P (2006) Landau-level splitting in graphene in high magnetic fields. Phys Rev Lett 96:136806
25. Zhang Y, Tan Y-W, Stormer HL, Kim P (2005) Experimental observation of the quantum Hall effect and Berry's phase in graphene. Nature 438:201
26. Novoselov KS, Jiang Z, Zhang Y, Morozov SV, Stormer HL, Zeitler U, Maan JC, Boebinger GS, Kim P, Geim AK (2007) Room-temperature quantum hall effect in graphene. Science 315:1379
27. Klitzing KV, Dorda G, Pepper M (1980) New method for high-accuracy determination of the fine-structure constant based on quantized hall resistance. Phys Rev Lett 45:494
28. Tombros N, Jozsa C, Popinciuc M, Jonkman HT, van Wees BJ (2007) Electronic spin transport and spin precession in single graphene layers at room temperature. Nature 448:571
29. Xiao D, Yao W, Niu Q (2007) Valley-contrasting physics in graphene: magnetic moment and topological transport. Phys Rev Lett 99:236809
30. Gorbachev RV, Song JCW, Yu GL, Kretinin AV, Withers F, Cao Y, Mishchenko A, Grigorieva IV, Novoselov KS, Levitov LS, Geim AK (2014) Detecting topological currents in graphene superlattices. Science 346:448
31. Castro EV, Novoselov KS, Morozov SV, Peres NMR, dos Santos JMBL, Nilsson J, Guinea F, Geim AK, Neto AHC (2007) Biased bilayer graphene: semiconductor with a gap tunable by the electric field effect. Phys Rev Lett 99:216802
32. Ferrari AC (2007) Raman spectroscopy of graphene and graphite: disorder, electron–phonon coupling, doping and nonadiabatic effects. Solid State Commun 143:47
33. Malard LM, Pimenta MA, Dresselhaus G, Dresselhaus MS (2009) Raman spectroscopy in graphene. Phys Rep 473:51
34. Ferrari AC, Basko DM (2013) Raman spectroscopy as a versatile tool for studying the properties of graphene. Nat Nanotechnol 8:235
35. Hummer WS, Offeman RE (1958) Preparation of graphitic oxide. J Am Chem Soc 80:1339
36. Matsumoto M, Saito Y, Park C, Fukushima T, Aida T (2015) Ultrahigh-throughput exfoliation of graphite into pristine 'single-layer' graphene using microwaves and molecularly engineered ionic liquids. Nat Chem 7:730
37. Hernandez Y, Nicolosi V, Lotya M, Blighe FM, Sun Z, De S, McGovern IT, Holland B, Byrne M, Gun'Ko YK, Boland JJ, Niraj P, Duesberg G, Krishnamurthy S, Goodhue R, Hutchison J, Scardaci V, Ferrari AC, Coleman JN (2008) High-yield production of graphene by liquid-phase exfoliation of graphite. Nat Nanotechnol 3:563 (2008)
38. Paton KR, Varrla E, Backes C, Smith RJ, Khan U, O'Neill A, Boland C, Lotya M, Istrate OM, King P, Higgins T, Barwich S, May P, Puczkarski P, Ahmed I, Moebius M, Pettersson H, Long E, Coelho J, O'Brien SE, McGuire EK, Sanchez BM, Duesberg GS, McEvoy N, Pennycook TJ, Downing C, Crossley A, Nicolosi V, Coleman JN (2014) Scalable production of large quantities of defect-free few-layer graphene by shear exfoliation in liquids. Nat Mater 13:624

39. Kusunoki M, Norimatsu W, Bao J, Morita K, Starke U (2015) Growth and features of epitaxial graphene on SiC. J Phys Soc Jpn 84:121014
40. Tanabe S, Sekine Y, Kageshima H, Nagase M, Hibino H (2011) Carrier transport mechanism in graphene on SiC(0001). Phys Rev B 84:115458
41. Hass J, Varchon F, Millán-Otoya JE, Sprinkle M, Sharma N, de Heer WA, Berger C, First PN, Magaud L, Conrad EH (2008) Why multilayer graphene on 4*H*−SiC ($000\bar{1}$) behaves like a single sheet of graphene. Phys Rev Lett 100:125504
42. Emtsev KV, Bostwick A, Horn K, Jobst J, Kellogg GL, Ley L, McChesney JL, Ohta T, Reshanov SA, Röhrl J, Rotenberg E, Schmid AK, Waldmann D, Weber HB, Seyller T (2009) Towards wafer-size graphene layers by atmospheric pressure graphitization of silicon carbide. Nat Mater 8:203
43. Wu YQ, Ye PD, Capano MA, Xuan Y, Sui Y, Qi M, Cooper JA, Shen T, Pandey D, Prakash G, Reifenberger R (2008) Top-gated graphene field-effect-transistors formed by decomposition of SiC. Appl Phys Lett 92:092102
44. Kim KS, Zhao Y, Jang H, Lee SY, Kim JM, Kim KS, Ahn J-H, Kim P, Choi J-Y, Hong BH (2009) Large-scale pattern growth of graphene films for stretchable transparent electrodes. Nature 457:706
45. Yu Q, Jauregui LA, Wu W, Colby R, Tian J, Su Z, Cao H, Liu Z, Pandey D, Wei D, Chung TF, Peng P, Guisinger NP, Stach EA, Bao J, Pei SS, Chen YP (2011) Control and characterization of individual grains and grain boundaries in graphene grown by chemical vapour deposition. Nat Mater 10:443
46. Orofeo CM, Hibino H, Kawahara K, Ogawa Y, Tsuji M, Ikeda K, Mizuno S, Ago H (2012) Influence of Cu metal on the domain structure and carrier mobility in single-layer graphene. Carbon 50:2189
47. Shelton JC, Patil HR, Blakely JM (1974) Equilibrium segregation of carbon to a nickel (111) surface: a surface phase transition. Surf Sci 43:493
48. Sutter PW, Flege J-I, Sutter EA (2008) Epitaxial graphene on ruthenium. Nat Mater 7:406
49. Yu Q, Lian J, Siriponglert S, Li H, Chen YP, Pei S-S (2008) Graphene segregated on Ni surfaces and transferred to insulators. Appl Phys Lett 93:113103
50. Coraux J, N'Diaye AT, Busse C, Michely T (2008) Structural coherency of graphene on Ir (111). Nano Lett 8:565
51. Land TA, Michely T, Behm RJ, Hemminger JC, Comsa G (1992) STM investigation of single layer graphite structures produced on Pt(111) by hydrocarbon decomposition. Surf Sci 264:261
52. Oznuluer T, Pince E, Polat EO, Balci O, Salihoglu O, Kocabas C (2011) Synthesis of graphene on gold. Appl Phys Lett 98:183101
53. Lee J-H, Lee EK, Joo W-J, Jang Y, Kim B-S, Lim JY, Choi S-H, Ahn SJ, Ahn JR, Park M-H, Yang C-W, Choi BL, Hwang S-W, Whang D (2014) Wafer-scale growth of single-crystal monolayer graphene on reusable hydrogen-terminated germanium. Science 344:286
54. Li X, Cai W, Colombo L, Ruoff RS (2009) Evolution of graphene growth on Ni and Cu by carbon isotope labeling. Nano Lett 9:4268
55. Vlassiouk I, Smirnov S, Regmi M, Surwade SP, Srivastava N, Feenstra R, Eres G, Parish C, Lavrik N, Datskos P, Dai S, Fulvio P (2013) Graphene nucleation density on copper: fundamental role of background pressure. J Phys Chem C 117:18919
56. Vlassiouk I, Regmi M, Fulvio P, Dai S, Datskos P, Eres G, Smirnov S (2011) Role of hydrogen in chemical vapor deposition growth of large single-crystal graphene. ACS Nano 5:6069
57. Celebi K, Cole MT, Choi JW, Wyczisk F, Legagneux P, Rupesinghe N, Robertson J, Teo KBK, Park HG (2013) Evolutionary kinetics of graphene formation on copper. Nano Lett 13:967
58. Wang Z-J, Weinberg G, Zhang Q, Lunkenbein T, Klein-Hoffmann A, Kurnatowska M, Plodinec M, Li Q, Chi L, Schloegl R, Willinger M (2015) Direct observation of graphene

growth and associated copper substrate dynamics by *in Situ* scanning electron microscopy. ACS Nano 9:1506
59. Kidambi PR, Bayer BC, Blume R, Wang Z-J, Baehtz C, Weatherup RS, Willinger M-G, Schloegl R, Hofmann S (2013) Observing graphene grow: catalyst–graphene interactions during scalable graphene growth on polycrystalline copper. Nano Lett 13:4769
60. Terasawa T, Saiki K (2015) Effect of vapor-phase oxygen on chemical vapor deposition growth of graphene. Appl Phys Express 8:035101
61. Terasawa T, Saiki K (2015) Radiation-mode optical microscopy on the growth of graphene. Nat Commun 6:6834
62. Niu T, Zhou M, Zhang J, Feng Y, Chen W (2013) Growth intermediates for CVD graphene on Cu(111): carbon clusters and defective graphene. J Am Chem Soc 135:8409
63. Puretzky AA, Geohegan DB, Pannala S, Rouleau CM, Regmi M, Thonnard N, Eres G (2013) Real-time optical diagnostics of graphene growth induced by pulsed chemical vapor deposition. Nanoscale 5:6507
64. Hao Y, Bharathi MS, Wang L, Liu Y, Chen H, Nie S, Wang X, Chou H, Tan C, Fallahazad B, Ramanarayan H, Magnuson CW, Tutuc E, Yakobson BI, McCarty KF, Zhang Y, Kim P, Hone J, Colombo L, Ruoff RS (2013) The role of surface oxygen in the growth of large single-crystal graphene on copper. Science 342:720
65. Hwang J, Kim M, Campbell D, Alsalman HA, Kwak JY, Shivaraman S, Woll AR, Singh AK, Hennig RG, Gorantla S, Rümmeli MH, Spencer MG (2013) van der Waals epitaxial growth of graphene on sapphire by chemical vapor deposition without a metal catalyst. ACS Nano 7:385
66. Sun J, Gao T, Song X, Zhao Y, Lin Y, Wang H, Ma D, Chen Y, Xiang W, Wang J, Zhang Y, Liu Z (2014) Direct growth of high-quality graphene on high-κ dielectric $SrTiO_3$ substrates. J Am Chem Soc 136:6574
67. Terasawa T, Saiki K (2012) Growth of graphene on Cu by plasma enhanced chemical vapor deposition. Carbon 50:869
68. Terasawa T, Saiki K (2012) Synthesis of nitrogen-doped graphene by plasma-enhanced chemical vapor deposition. Jpn J Appl Phys 51:055101
69. Wei D, Lu Y, Han C, Niu T, Chen W, Wee ATS (2013) Critical crystal growth of graphene on dielectric substrates at low temperature for electronic devices. Angew Chem Int Ed Engl 52:14121
70. Kim J, Ishihara M, Koga Y, Tsugawa K, Hasegawa M, Iijima S (2011) Low-temperature synthesis of large-area graphene-based transparent conductive films using surface wave plasma chemical vapor deposition. Appl Phys Lett 98:091502
71. Yamada T, Ishihara M, Kim J, Hasegawa M, Iijima S (2012) A roll-to-roll microwave plasma chemical vapor deposition process for the production of 294 mm width graphene films at low temperature. Carbon 50:2615
72. Weatherup RS, Baehtz C, Dlubak B, Bayer BC, Kidambi PR, Blume R, Schloegl R, Hofmann S (2013) Introducing carbon diffusion barriers for uniform, high-quality graphene growth from solid sources. Nano Lett 13:4624
73. Tanaka H, Obata S, Saiki K (2013) Reduction of graphene oxide at the interface between a Ni layer and a SiO_2 substrate. Carbon 59:472
74. Sun Z, Yan Z, Yao J, Beitler E, Zhu Y, Tour JM (2010) Growth of graphene from solid carbon sources. Nature 468:549
75. Ruan G, Sun Z, Peng Z, Tour JM (2011) Growth of graphene from food, insects, and waste. ACS Nano 5:7601
76. Obata S, Tanaka H, Saiki K (2011) Reduction of a single layer graphene oxide film on Pt (111). Appl Phys Express 4:025102
77. Su Q, Pang S, Alijani V, Li C, Feng X, Müllen K (2009) Composites of graphene with large aromatic molecules. Adv Mater 21:3191
78. Elias DC, Nair RR, Mohiuddin TMG, Morozov SV, Blake P, Halsall MP, Ferrari AC, Boukhvalov DW, Katsnelson MI, Geim AK, Novoselov KS (2009) Control of graphene's properties by reversible hydrogenation: evidence for graphane. Science 323:610

79. Sofo JO, Chaudhari AS, Barber GD (2007) Graphane: A two-dimensional hydrocarbon. Phys Rev B 75:153401
80. Robinson JT, Burgess JS, Junkermeier CE, Badescu SC, Reinecke TL, Perkins FK, Zalalutdniov MK, Baldwin JW, Culbertson JC, Sheehan PE, Snow ES (2010) Properties of fluorinated graphene films. Nano Lett 10:3001
81. Cheng S-H, Zou K, Okino F, Gutierrez HR, Gupta A, Shen N, Eklund PC, Sofo JO, Zhu J (2010) Reversible fluorination of graphene: evidence of a two-dimensional wide bandgap semiconductor. Phys Rev B 81:205435
82. Withers F, Dubois M, Savchenko AK (2010) Electron properties of fluorinated single-layer graphene transistors. Phys Rev B 82:073403
83. Hamwi A (1996) Fluorine reactivity with graphite and fullerenes. fluoride derivatives and some practical electrochemical applications. J Phys Chem Solids 57:677
84. Sinitskii A, Dimiev A, Corley DA, Fursina AA, Kosynkin DV, Tour JM (2010) Kinetics of diazonium functionalization of chemically converted graphene nanoribbons. ACS Nano 4:1949
85. Liu H, Ryu S, Chen Z, Steigerwald ML, Nuckolls C, Brus LE (2009) Photochemical reactivity of graphene. J Am Chem Soc 131:17099
86. Liu L-H, Lerner MM, Yan M (2010) Derivitization of pristine graphene with well-defined chemical functionalities. Nano Lett 10:3754
87. An X, Simmons T, Shah R, Wolfe C, Lewis KM, Washington M, Nayak SK, Talapatra S, Kar S (2010) Stable aqueous dispersions of noncovalently functionalized graphene from graphite and their multifunctional high-performance applications. Nano Lett 10:4295
88. Zhang S, Tang S, Lei J, Dong H, Ju H (2011) Functionalization of graphene nanoribbons with porphyrin for electrocatalysis and amperometric biosensing. J Electroanal Chem 656:285
89. Ghosh A, Rao KV, George SJ, Rao CNR (2010) Noncovalent functionalization, exfoliation, and solubilization of graphene in water by employing a fluorescent coronene carboxylate. Chem. Eur. J. 16:2700
90. Wang D-W, Li F, Zhao J, Ren W, Chen Z-G, Tan J, Wu Z-S, Gentle I, Lu GQ, Cheng H-M (2009) Fabrication of graphene/polyaniline composite paper *via* in situ anodic electropolymerization for high-performance flexible electrode. ACS Nano 3:1745
91. Kim T, Lee H, Kim J, Suh KS (2010) Synthesis of phase transferable graphene sheets using ionic liquid polymers. ACS Nano 4:1612
92. Yoo E, Kim J, Hosono E, Zhou H, Kudo T, Honma I (2008) Large reversible Li storage of graphene nanosheet families for use in rechargeable lithium ion batteries. Nano Lett 8:2277
93. Sutter P, Sadowski JT, Sutter EA (2010) Chemistry under cover: tuning metal−graphene interaction by reactive intercalation. J Am Chem Soc 132:8175
94. Schumacher S, Huttmann F, Petrović M, Witt C, Förster DF, Vo-Van C, Coraux J, Martínez-Galera AJ, Sessi V, Vergara I, Rückamp R, Grüninger M, Schleheck N, Meyer zu Heringdorf F, Ohresser P, Kralj M, Wehling TO, Michely T (2014) Europium underneath graphene on Ir(111): intercalation mechanism, magnetism, and band structure. Phys Rev B 90:235437
95. Masuda Y, Norimatsu W, Kusunoki M (2015) Formation of a nitride interface in epitaxial graphene on SiC (0001). Phys Rev B 91:075421
96. Riedl C, Coletti C, Iwasaki T, Zakharov AA, Starke U (2009) Quasi-free-standing epitaxial graphene on SiC obtained by hydrogen intercalation. Phys Rev Lett 103:246804
97. Bult JB, Crisp R, Perkins CL, Blackburn JL (2013) Role of opants in long-range charge carrier transport for p-type and n-type graphene transparent conducting thin films. ACS Nano 7:7251
98. Panchakarla LS, Subrahmanyam KS, Saha SK, Govindaraj A, Krishnamurthy HR, Waghmare UV, Rao CNR (2009) Synthesis, structure, and properties of boron- and nitrogen-doped graphene. Adv Mater 21:4726
99. Akada K, Terasawa T, Imamura G, Obata S, Saiki K (2014) Control of work function of graphene by plasma assisted nitrogen doping. Appl Phys Lett 104:131602

100. Schiros T, Nordlund D, Pálová L, Prezzi D, Zhao L, Kim KS, Wurstbauer U, Gutiérrez C, Delongchamp D, Jaye C, Fischer D, Ogasawara H, Pettersson LGM, Reichman DR, Kim P, Hybertsen MS, Pasupathy AN (2012) Connecting dopant bond type with electronic structure in N-doped graphene. Nano Lett 12:4025
101. Zhang L, Xia Z (2011) Mechanisms of oxygen reduction reaction on nitrogen-doped graphene for fuel cells. J Phys Chem C 115:11170
102. Sheng Z-H, Gao H-L, Bao W-J, Wang F-B, Xia X-H (2012) Synthesis of boron doped graphene for oxygen reduction reaction in fuel cells. J Mater Chem 22:390
103. Wu T, Shen H, Sun L, Cheng B, Liu B, Shen J (2012) Nitrogen and boron doped monolayer graphene by chemical vapor deposition using polystyrene, urea and boric acid. New J Chem 36:1385
104. Imamura G, Chang CW, Nabae Y, Kakimoto M, Miyata S, Saiki K (2012) Electronic structure and graphenization of hexaphenylborazine. J Phys Chem C 116:16305
105. Guo B, Liu Q, Chen E, Zhu H, Fang L, Gong JR (2010) Controllable N-doping of graphene. Nano Lett 10:4975
106. Kim YA, Fujisawa K, Muramatsu H, Hayashi T, Endo M, Fujimori T, Kaneko K, Terrones M, Behrends J, Eckmann A, Casiraghi C, Novoselov KS, Saito R, Dresselhaus MS (2012) Raman spectroscopy of boron-doped single-layer graphene. ACS Nano 6:6293
107. Pan L, Que Y, Chen H, Wang D, Li J, Shen C, Xiao W, Du S, Gao H, Pantelides ST (2015) Room-temperature, low-barrier boron doping of graphene. Nano Lett 15:6464
108. Reddy ALM, Srivastava A, Gowda SR, Gullapalli H, Dubey M, Ajayan PM (2010) Synthesis of nitrogen-doped graphene films For lithium battery application. ACS Nano 4:6337
109. Gebhardt J, Koch RJ, Zhao W, Höfert O, Gotterbarm K, Mammadov S, Papp C, Görling A, Steinrück H-P, Seyller T (2013) Growth and electronic structure of boron-doped graphene. Phys Rev B 87:155437
110. Cattelan M, Agnoli S, Favaro M, Garoli D, Romanato F, Meneghetti M, Barinov A, Dudin P, Granozzi G (2013) Microscopic view on a chemical vapor deposition route to boron-doped graphene nanostructures. Chem Mater 25:1490
111. Kawai S, Saito S, Osumi S, Yamaguchi S, Foster AS, Spijker P, Meyer E (2015) Atomically controlled substitutional boron-doping of graphene nanoribbons. Nat Commun 6:8098
112. Wang X, Dai H (2010) Etching and narrowing of graphene from the edges. Nat Chem 2:661
113. Jiao L, Zhang L, Wang X, Diankov G, Dai H (2009) Narrow graphene nanoribbons from carbon nanotubes. Nature 458:877
114. Li X, Wang X, Zhang L, Lee S, Dai H (2008) Chemically derived, Ultrasmooth graphene nanoribbon semiconductors. Science 319:1229
115. Cai J, Ruffieux P, Jaafar R, Bieri M, Braun T, Blankenburg S, Muoth M, Seitsonen AP, Saleh M, Feng X, Müllen K, Fasel R (2010) Atomically precise bottom-up fabrication of graphene nanoribbons. Nature 466:470
116. Hayashi K, Sato S, Ikeda M, Kaneta C, Yokoyama N (2012) Selective graphene formation on copper twin crystals. J Am Chem Soc 134:12492
117. Ago H, Tanaka I, Ogawa Y, Yunus RM, Tsuji M, Hibino H (2013) Lattice-oriented catalytic growth of graphene nanoribbons on heteroepitaxial nickel films. ACS Nano 7:10825
118. Sprinkle M, Ruan M, Hu Y, Hankinson J, Rubio-Roy M, Zhang B, Wu X, Berger C, de Heer WA (2010) Scalable templated growth of graphene nanoribbons on SiC. Nat Nanotechnol 5:727
119. Pan D, Zhang J, Li Z, Wu M (2010) Hydrothermal route for cutting graphene sheets into blue-luminescent graphene quantum dots. Adv Mater 22:734
120. Zhou X, Zhang Y, Wang C, Wu X, Yang Y, Zheng B, Wu H, Guo S, Zhang J (2012) Photo-fenton reaction of graphene oxide: a new strategy to prepare graphene quantum dots for DNA cleavage. ACS Nano 6:6592
121. Yan X, Cui X, Li L-S (2010) Synthesis of large, stable colloidal graphene quantum dots with tunable size. J Am Chem Soc 132:5944

122. Güttinger J, Molitor F, Stampfer C, Schnez S, Jacobsen A, Dröscher S, Ihn T, Ensslin K (2012) Transport through graphene quantum dots. Rep Prog Phys 75:126502
123. Tetsuka H, Asahi R, Nagoya A, Okamoto K, Tajima I, Ohta R, Okamoto A (2012) Optically tunable amino-functionalized graphene quantum dots. Adv Mater 24:5333
124. Zhu S, Zhang J, Qiao C, Tang S, Li Y, Yuan W, Li B, Tian L, Liu F, Hu R, Gao H, Wei H, Zhang H, Sun H, Yang B (2011) Strongly green-photoluminescent graphenequantum dots for bioimaging applications. Chem Commun 47:6858
125. Geim AK, Grigorieva IV (2013) Van der Waals heterostructures. Nature 499:419
126. Novoselov KS, Jiang D, Schedin F, Booth TJ, Khotkevich VV, Morozov SV, Geim AK (2005) Two-dimensional atomic crystals. Proc Natl Acad Sci U S A 102:10451
127. Kim J, Kwon S, Cho D-H, Kang B, Kwon H, Kim Y, Park SO, Jung GY, Shin E, Kim W-G, Lee H, Ryu GH, Choi M, Kim TH, Oh J, Park S, Kwak SK, Yoon SW, Byun D, Lee Z, Lee C (2015) Direct exfoliation and dispersion of two-dimensional materials in pure water via temperature control. Nat Commun 6:8294
128. Kim KK, Hsu A, Jia X, Kim SM, Shi Y, Hofmann M, Nezich D, Rodriguez-Nieva JF, Dresselhaus M, Palacios T, Kong J (2012) Synthesis of monolayer hexagonal boron nitride on Cu foil using chemical vapor deposition. Nano Lett 12:161
129. Vogt P, De Padova P, Quaresima C, Avila J, Frantzeskakis E, Asensio MC, Resta A, Ealet B, Le Lay G (2012) Silicene: compelling experimental evidence for graphene like two-dimensional silicon. Phys Rev Lett 108:155501
130. De Padova P, Quaresima C, Ottaviani C, Sheverdyaeva PM, Moras P, Carbone C, Topwal D, Olivieri B, Kara A, Oughaddou H, Aufray B, Le Lay G (2010) Evidence of graphene-like electronic signature in silicene nanoribbons. Appl Phys Lett 96:261905
131. Tao L, Cinquanta E, Chiappe D, Grazianetti C, Fanciulli M, Dubey M, Molle A, Akinwande D (2015) Silicene field-effect transistors operating at room temperature. Nat Nanotechnol 10:227
132. Fleurence A, Friedlein R, Ozaki T, Kawai H, Wang Y, Yamada-Takamura Y (2012) Experimental evidence for epitaxial silicene on diboride thin films. Phys Rev Lett 108:245501
133. Koenig SP, Doganov RA, Schmidt H, Castro AH Neto, Özyilmaz B (2014) Electric field effect in ultrathin black phosphorus. Appl Phys Lett 104:103106
134. Liu H, Neal AT, Zhu Z, Luo Z, Xu X, Tománek D, Ye PD (2014) Phosphorene: an unexplored 2D semiconductor with a high hole mobility. ACS Nano 8:4033
135. Bianco E, Butler S, Jiang S, Restrepo OD, Windl W, Goldberger JE (2013) Stability and exfoliation of germanane: a germanium graphane analogue. ACS Nano 7:4414
136. Derivaz M, Dentel D, Stephan R, Hanf M-C, Mehdaoui A, Sonnet P, Pirri C (2015) Continuous germanene layer on Al(111). Nano Lett 15:2510
137. Dávila ME, Xian L, Cahangirov S, Rubio A, Le Lay G (2014) Germanene: a novel two-dimensional germanium allotrope akin to graphene and silicene. New J Phys 16:095002
138. Zhu F-F, Chen W-J, Xu Y, Gao C-L, Guan D-D, Liu C-H, Qian D, Zhang S-C, Jia J-F (2015) Epitaxial growth of two-dimensional stanene. Nat Mater 14:1020
139. Kubota Y, Watanabe K, Tsuda O, Taniguchi T (2007) Deep ultraviolet light-emitting hexagonal boron nitride synthesized at atmospheric pressure. Science 317:932
140. Lee G-H, Yu Y-J, Lee C, Dean C, Shepard KL, Kim P, Hone J (2011) Electron tunneling through atomically flat and ultrathin hexagonal boron nitride. Appl Phys Lett 99:243114
141. Zhang Y, Weng X, Li H, Li H, Wei M, Xiao J, Liu Z, Chen M, Fu Q, Bao X (2015) Hexagonal boron nitride cover on Pt(111): a new route to tune molecule–metal interaction and metal-catalyzed reactions. Nano Lett 15:3616
142. Sutter P, Lahiri J, Zahl P, Wang B, Sutter E (2013) Scalable Synthesis of uniform few-layer hexagonal boron nitride dielectric films. Nano Lett 13:276
143. Song L, Ci L, Lu H, Sorokin PB, Jin C, Ni J, Kvashnin AG, Kvashnin DG, Lou J, Yakobson BI, Ajayan PM (2010) Large scale growth and characterization of atomic hexagonal boron nitride layers. Nano Lett 10:3209

144. Xu M, Liang T, Shi M, Chen H (2013) Graphene-like two-dimensional materials. Chem Rev 113:3766
145. Chhowalla M, Shin HS, Eda G, Li L-J, Loh KP, Zhang H (2013) The chemistry of two-dimensional layered transition metal dichalcogenide nanosheets. Nat Chem 5:263
146. Mak KF, Lee C, Hone J, Shan J, Heinz TF (2010) Atomically thin MoS_2: a new direct-gap semiconductor. Phys Rev Lett 105:136805
147. Zeng H, Dai J, Yao W, Xiao D, Cui X (2012) Valley polarization in MoS_2 monolayers by optical pumping. Nat Nanotechnol 7:490
148. Yin Z, Li H, Li H, Jiang L, Shi Y, Sun Y, Lu G, Zhang Q, Chen X, Zhang H (2012) Single-layer MoS_2 phototransistors. ACS Nano 6:74
149. Gong Y, Lin J, Wang X, Shi G, Lei S, Lin Z, Zou X, Ye G, Vajtai R, Yakobson BI, Terrones H, Terrones M, Tay BK, Lou J, Pantelides ST, Liu Z, Zhou W, Ajayan PM (2014) Vertical and in-plane heterostructures from WS_2/MoS_2 monolayers. Nat Mater 13:1135
150. Levendorf MP, Kim C-J, Brown L, Huang PY, Havener RW, Muller DA, Park J (2012) Graphene and boron nitride lateral heterostructures for atomically thin circuitry. Nature 488:627
151. Huang C, Wu S, Sanchez AM, Peters JJP, Beanland R, Ross JS, Rivera P, Yao W, Cobden DH, Xu X (2014) Lateral heterojunctions within monolayer $MoSe_2$–WSe_2 semiconductors. Nat Mater 13:1096
152. Dean CR, Young AF, Meric I, Lee C, Wang L, Sorgenfrei S, Watanabe K, Taniguchi T, Kim P, Shepard KL, Hone J (2010) Boron nitride substrates for high-quality graphene electronics. Nat Nanotechnol 5:722
153. Wang L, Meric I, Huang P, Gao Q, Gao Y (2013) One-dimensional electrical contact to a two-dimensional material. Science 342:614
154. Ju L, Shi Z, Nair N, Lv Y, Jin C, Velasco J, Ojeda-Aristizabal C, Bechtel HA, Martin MC, Zettl A, Analytis J, Wang F (2015) Topological valley transport at bilayer graphene domain walls. Nature 520:650
155. Gao T, Song X, Du H, Nie Y, Chen Y, Ji Q, Sun J, Yang Y, Zhang Y, Liu Z (2015) Temperature-triggered chemical switching growth of in-plane and vertically stacked graphene-boron nitride heterostructures. Nat Commun 6:6835
156. Koma A (1992) Van der Waals epitaxy—a new epitaxial growth method for a highly lattice-mismatched system. Thin Solid Films 216:72

Chapter 5
Chalcogenide Nanosheets: Optical Signatures of Many-Body Effects and Electronic Band Structure

Ivan Verzhbitskiy and Goki Eda

Abbreviations

1D	One-dimensional
2D	Two-dimensional
2P-PLE	Two-photon photoluminescence excitation
ADF	Annular dark field
ALD	Atomic layer deposition
ARPES	Angle-resolved photoemission spectroscopy
BLG	Bilayer graphene
CBM	Conduction band minimum
CDW	Charge density wave
CL	Cathodoluminescence
CVD	Chemical vapor deposition
CVT	Chemical vapor transport
DFT	Density functional theory
DoS	Density of state
dR	Differential reflectance
HOPG	Highly oriented pyrolytic graphite
jDoS	Joint density of states
MBE	Molecular beam epitaxy

I. Verzhbitskiy · G. Eda (✉)
Department of Physics, National University of Singapore,
2 Science Drive 3, Singapore 117551, Singapore
e-mail: g.eda@nus.edu.sg

G. Eda
Department of Chemistry, National University of Singapore,
3 Science Drive 3, Singapore 117543, Singapore

G. Eda
Centre for Advanced 2D Materials, National University of Singapore,
6 Science Drive 2, Singapore 117546, Singapore

T. Nakato et al. (eds.), *Inorganic Nanosheets and Nanosheet-Based Materials*,
Nanostructure Science and Technology, DOI 10.1007/978-4-431-56496-6_5

MX_2	Metal atoms (M) and chalcogen atoms (X)
IR	Infra-red
UV	Ultra-violet
PL	Photoluminescence
PLE	Photoluminescence excitation spectroscopy
SHG	Second harmonic generation spectroscopy
STEM	Scanning transmission electron microscopy
STM	Scanning tunneling microscopy
STS	Scanning tunneling spectroscopy
TA	Transient absorption
TMD	Transition metal dichalcogenide
VBM	Valence band maximum
XPS	X-ray photoelectron spectroscopy

5.1 Introduction

Layer compounds of metal chalcogenides (sulfides, selenides, and tellurides) form a large family of materials with a wide range of properties. Many transition metal and post-transition metal chalcogenides such as MoS_2 and GaS have been studied extensively since the early 60s due to their quasi-two-dimensional (quasi-2D) character and excitonic absorption properties [1–4]. Similar to graphite, many of these compounds intercalate guest molecules and ions [5], and superconductivity of such intercalation compounds has also been a subject of intense research [6, 7]. More recently, experimental observation of symmetry-protected topological surface states in bismuth selenides and tellurides have generated tremendous interest in the condensed matter physics community [8].

Metal chalcogenide layer compounds can be categorized into several groups accordingly to their chemistry. Layered transition metal dichalcogenides (TMDs) form a well-defined family consisting of about forty distinct compounds [9]. MoS_2 is an archetypal group 6 TMD well known for its naturally occurring molybdenite and its lubricating properties [10–12]. Transition metal trichalcogenides such as TiS_3 can be characterized by their unique quasi-one-dimensional (quasi-1D) structure [13]. Group 13 metal monochalcogenides such as GaS and InSe form a class of semiconducting hexagonal materials whose monolayers consist of four atomic layers [14]. Group 14 monochalcogenides are semiconductors but are found in distorted NaCl structure. Sn-based dichalcogenides are also semiconductors having the same crystal structure as some TMDs such as TiS_2 [15]. In_2Se_3 and Bi_2Se_3 share a similar crystal structure consisting of quintuple layers. Many of these compounds exhibit band gap in the visible to near-IR frequencies. Figure 5.1 shows the crystal structure (Fig. 5.1a) of different classes of layered chalcogenides and their bandgap values (Fig. 5.1b).

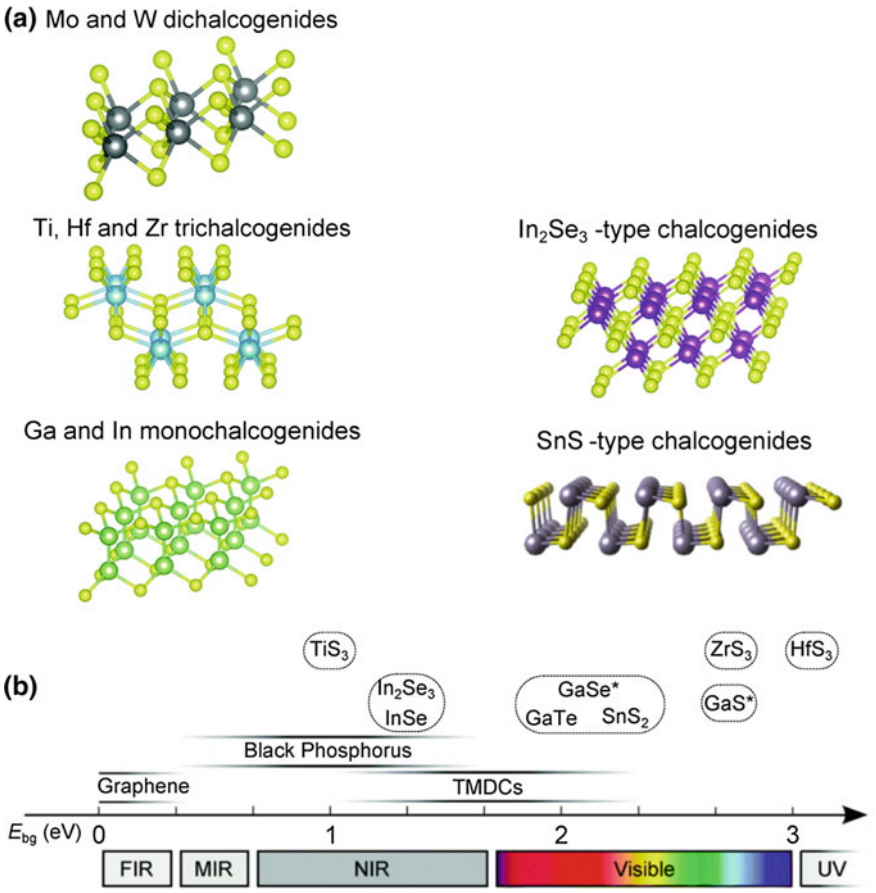

Fig. 5.1 **a** Overview of the crystal structures of layered TMDs nanosheets. The *yellow* atoms correspond to chalcogen species. **b** Bandgap of different layered semiconductors with respect to electromagnetic spectrum. The exact bandgap value would depend on the number of layers, strain level and chemical doping. Reprinted with permission from Refs. [16, 17] with slight modification (copyright 2015, Royal Society of Chemistry, American Physics Society)

While studies on chalcogenide nanosheets appear in early literatures [18], the seminal work on graphene by Geim and coworkers in 2004 [19] renewed interest in the field and led to a number of milestone studies. In particular, nanosheets of semiconducting group 6 TMDs have been extensively studied in recent years due to their emerging rich physics and potential in technological applications [20, 21]. This Chapter will introduce some basic aspects of group 6 TMDs and other semiconducting chalcogenide nanosheets with a focus on their electronic structure, excitonic properties, and spectroscopic signatures. For more general overviews, readers may be referred to recent review articles on this class of materials [22, 23].

5.2 Transition Metal Dichalcogenides

The family of TMDs shares a chemical formula of MX_2 (M: transition metal, X: chalcogen) and assumes a van der Waals layer structure in which the individual monolayer consists of a covalently bonded X–M–X sandwich. The basic properties of TMDs have been studied for over half a century (see [1] for a comprehensive review of early studies). The recent surge of interest in 2D TMDs was partly triggered by the reports on direct band gap photoluminescence (PL) from monolayer MoS_2 by two independent research teams [24, 25]. Studies further revealed a number of emerging properties inherent to mono- and few-layer sheets of MoS_2 and its isoelectronic compounds. These include optically accessible valley polarization [26, 27], large nonlinear susceptibility [28–30], piezo-electricity [31, 32], large exciton binding energy [33–35], and electrically tunable many-body states [36]. Semiconducting TMD nanosheets are effectively quantum wells but with accessible surfaces and mechanical flexibility. These unique characteristics make TMD nanosheets attractive as fundamental building blocks for novel optoelectronics and photonics applications [20–23, 37].

5.2.1 Crystal Structure

Layered TMDs occur in various polymorphs (metal coordination geometry) and polytypes (stacking order). Group 6 TMDs are stable in trigonal prismatic coordination with a 2H (2-layer unit cell, hexagonal) or a 3R (3-layer unit cell, rhombohedral) crystal structure [38]. TMDs from other transition metal groups such as TiS_2 are stable in octahedral coordination with a 1T (1-layer unit cell, trigonal) structure. For monolayer MX_2, there is no distinction between 2H and 3R polytypes. Monolayer MX_2 in trigonal prismatic coordination is non-centrosymmetric in contrast to its 2H bulk counterpart, which is centrosymmetric. This difference in crystal symmetry is responsible for some of the unique characteristics of monolayer TMDs. Some TMDs such as WTe_2 and β-$MoTe_2$ exhibit distorted 1T (1T′) crystal lattice structure [39, 40]. Polymorphism and *d*-electron count of transition metal largely determine whether TMD is metallic or semiconducting. For example, MoS_2 (formally a d^2 compound) in trigonal prismatic coordination is semiconducting whereas its octahedral polymorph is metallic (Fig. 5.2). Based on a simple ligand field model, the semiconducting nature of trigonal prismatic MoS_2 is due to the splitting between the completely filled d_{z^2} and empty d_{xy} and $d_{x^2-y^2}$ orbitals (Fig. 5.2a). In contrast, octahedral MoS_2 is metallic because of partially filled t_{2g} band (d_{xy}, d_{xz}, d_{yz}) as depicted in Fig. 5.2b. The M–X bonding states (σ) appear deep in the valence band due to its strong covalent character. The precise position of the M-X antibonding states (σ*) has been debated [1, 41] but for clarity it is shown to be above the nonbonding states in Fig. 5.2a, b.

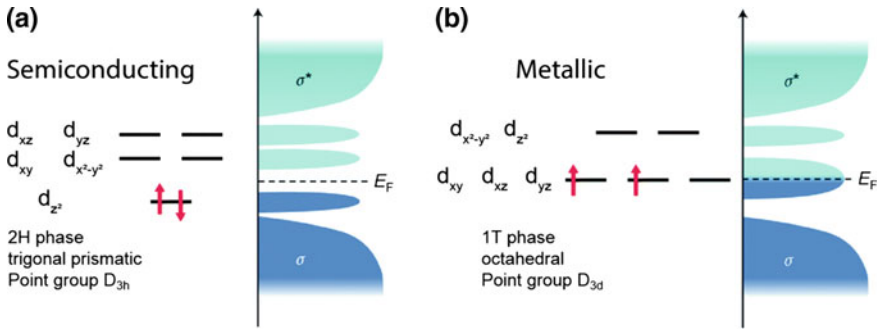

Fig. 5.2 Filling of the nonbonding *d*-orbitals for a typical d^2 TMD along with the band structure and the representative position of the Fermi level for **a** 2H phase and **b** 1T phase. Reprinted with permission from Ref. [20] with slight modification (Copyright 2013, Nature Publishing Group)

5.2.2 *Preparation*

Mono- and few-layer MX_2 can be readily obtained by micromechanical exfoliation of bulk crystals onto a substrate [42]. The starting bulk crystals can be obtained either from natural sources or synthesized by techniques such as chemical vapor transport (CVT) [43]. The size of mechanically exfoliated nanosheets is typically limited to tens of micrometers. Nanosheets can also be obtained via chemical vapor deposition (CVD), molecular beam epitaxy (MBE) [44], solution-based exfoliation techniques [45, 46], etching of bulk crystals (chemical [47, 48], plasma [49] and photothermal [50]), chemical synthesis [51], and atomic layer deposition (ALD) [52]. CVD-growth of monolayer MoS_2 [53–68], $MoSe_2$ [69, 70], WS_2 [71] and WSe_2 [72, 73] on various substrates has been demonstrated by many groups. Growth of semiconducting alloys such as MoS_xSe_{2-x} [74] and doped MX_2 [75] has also been reported. The exciton resonance features and charge transport properties of some CVD-grown monolayer samples reveal their high electronic quality equivalent to or superior to that of mechanically exfoliated counterparts.

Recent studies have shown that sulfur vacancies and antisite substitutions (S replaced by Mo) are the most commonly occurring point defects in MoS_2 [76, 77]. For bulk MoS_2, n-type doping has been attributed to donor states arising from sulfur vacancies [78]. It is believed that vacancy defects also play a role [79] in the observed strong n-type doping of monolayer MoS_2 [66, 80–82]. The reported sulfur vacancy densities vary from 3.5×10^{10} cm^{-2} in bulk MoS_2 samples [78] as measured by scanning tunneling microscopy (STM) to significantly higher values of the order of 10^{13} cm^{-2} for monolayer MoS_2 [83, 84] as measured by scanning transmission electron microscopy (STEM).

5.2.3 Energy Band Structure

Layered TMDs display a wide spectrum of electronic properties depending on the number of electrons in their nonbonding *d*-orbitals and the coordination geometry of the metal atom (see [2, 3, 85] for discussion of the crystal structure, band structure, and optical properties). As discussed above, basic electronic properties of TMDs can be predicted from filling of crystal-field-split d-orbitals. However, many interesting properties of TMD nanosheets arise from the unique dispersion of the electronic states that extend over the 2D plane. A more precise description of their electronic structure requires rigorous density functional theory (DFT) calculations. Figure 5.3a shows the electronic energy band structure of monolayer and bilayer 2H-WS_2 from DFT calculations. The key features are the two valence band hills and the two conduction band valleys. The valence band hills are at the center (Γ) and corners (K) of the Brillouin zone. On the other hand, the conduction band valleys are at the K point and the Λ point (sometimes called the Q point), which is midway between the K-Γ line. The valence band at the K point is split due to spin-orbit coupling. The conduction band also exhibits spin-orbit splitting at the K point but with a much smaller strength. In contrast to bulk WS_2, which is an indirect gap semiconductor, monolayer WS_2 is a direct gap semiconductor with the conduction band minimum (CBM) and the valence band maximum (VBM) coinciding at the K point. Bilayer WS_2 is an indirect gap semiconductor with CBM at the Λ point and the VBM at the Γ point, similar to bulk WS_2. Other group 6 TMDs such as MoS_2, $MoSe_2$, and WSe_2 exhibit similar evolution of band structure when thinned down to a single monolayer [24, 25, 86–90]. However, the indirect-to-direct crossing point is still a subject of debate for some materials such as WSe_2 [91] and $MoTe_2$ [92].

The origin of band structure evolution cannot be simply explained by quantum confinement effect. Figure 5.3a shows that the number of layers most strongly influences the conduction band valley at the Λ point (Λ_c) and the valence band hill at the Γ point (Γ_v). DFT calculations reveal that the wavefunction associated with these points consists of an admixture of the metal *d*-orbitals and the chalcogen p_z-orbitals (Fig. 5.3b). In contrast, the wavefunctions at the K_c and K_v regions exhibit predominantly *d*-character. In other words, the wavefunctions at the Λ_c and Γ_v points spatially extend to the outer surface of the X–M–X sandwich layer whereas K_c and K_v states are confined in the middle of the layer (Fig. 5.3b). Thus, the indirect band gap between the Λ_c and Γ_v points increases more rapidly with reducing number of layers compared to the direct gap at the K point, leading to a crossover in the monolayer limit.

According to a simple particle-in-a-well model, change in the band gap E_g of a 2D semiconductor should scale as $\Delta E_g = \pi^2 h^2 / 8\mu L_z^2$ where h is the Planck's constant, μ is the reduced mass of the exciton, and L_z is the thickness of the crystals [95]. This simple relation does not apply to the optical gap of TMD crystals in the few-layer thickness regime for various reasons. First, thickness reduction does not only influence carrier confinement but also average interlayer interaction,

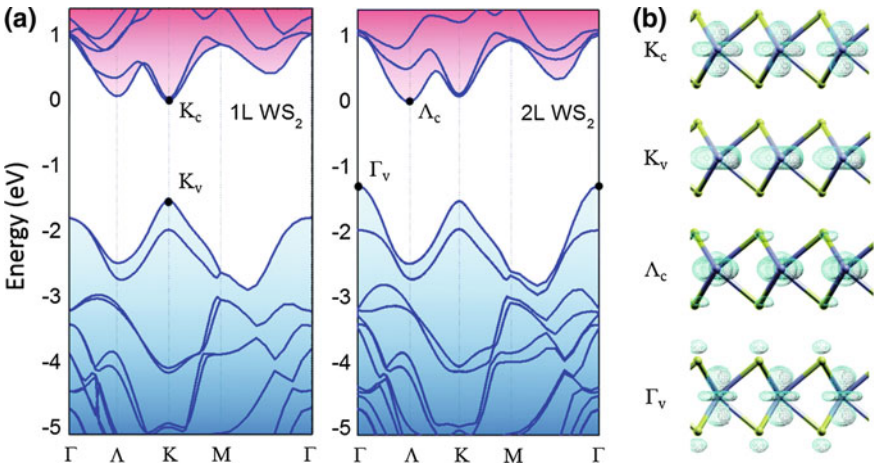

Fig. 5.3 **a** Calculated electronic band structure of mono- (*left*) and bilayer (*right*) WS_2. The *dots* indicate the valence band maximum (VBM) and the conduction band minimum (CBM). **b** Representative isosurface plot for states associated with different points of the band structure. **a** reprinted with permission from Ref. [93] with slight modification (copyright 2015, Royal Society of Chemistry), **b** reprinted with permission from Ref. [94] with slight modification (copyright 2015, American Chemical society)

thus resulting in modification of the band structure and effective mass of carriers as discussed above. Second, exciton binding energy increases rapidly with thickness reduction due to reduced screening [96]. As a result, the optical gap scales only weakly with the number of layers. Third, extrinsic effects such as unintentional doping by surface adsorbates [97] and substrate [98] obscure the band gap absorption and emission in mono- to few-layer materials.

Another important consequence of thinning group 6 TMDs down to monolayer limit is the loss of inversion symmetry and corresponding changes in the electronic structure. Since K and K′ valleys are connected by time reversal symmetry, the spin-orbit splitting is opposite in these two valleys such that they are degenerate in energy but nondegenerate in spin states. Thus, spin and valley quantum degrees of freedom are inherently coupled in monolayers. This makes the valley degrees of freedom optically accessible by circularly polarized light [99].

The hexagonal symmetry of monolayer group 6 TMDs is the same as that of monolayer graphene. The main difference is that the A and B sublattices in TMDs are occupied by metal and chalcogen atoms, respectively. The effective two-band Hamiltonian is that of a massive Dirac fermion model

$$\widehat{H} = at\left(\tau_z k_x \widehat{\sigma}_x + k_y \widehat{\sigma}_y\right) + \frac{\Delta}{2}\widehat{\sigma}_z \tag{5.1}$$

where $\tau_z = \pm 1$ is the valley index, a is the lattice constant, t is the effective nearest neighbor hopping integral, Δ is the band gap, σ is the Pauli matrices for the two

basis functions representing metal *d*-orbitals with $m = 0$ and $m = 2\tau_z$. A more complete Hamiltonian has an additional term on spin-orbit coupling, which splits the valence band top [100].

5.2.4 *Optical Signatures of Band Structure*

Linear absorption and emission spectroscopies have proven to be simple yet powerful tools to probing a number of key features of TMD nanosheets such as their electronic band structure [101], many-body interaction [102, 103], valley polarization [27], excited-state coherence [104], doping [105], defects [79], and strain [106, 107]. In 2010, Splendiani et al. [24] and Mak et al. [25] independently reported that PL from monolayer MoS_2 is distinctly stronger than that from bilayer and thicker multiplayer samples, which is contrary to the expectation that the optical response scales with the volume of the material. The authors attributed the bright PL from monolayer MoS_2 is due to its direct band gap. The emission quantum yield of indirect gap multilayer MoS_2 is substantially lower because the radiative recombination of indirect excitons is a phonon-assisted second order process and is significantly slower than non-radiative decay processes. Following these initial studies, similar observations on enhanced PL were reported for monolayer WS_2 (Fig. 5.4a), WSe_2, $MoSe_2$, and $MoTe_2$ [86, 87, 90, 92]. Figure 5.4 shows PL spectra and fluorescence image of mechanically exfoliated mono- and few-layer WS_2 sheets, demonstrating the distinctly bright PL from the monolayer region of the sample.

Absorption spectrum of group 6 TMDs exhibits characteristic excitonic resonance peaks in the near-IR to ultraviolet frequencies [1, 25]. Unlike typical

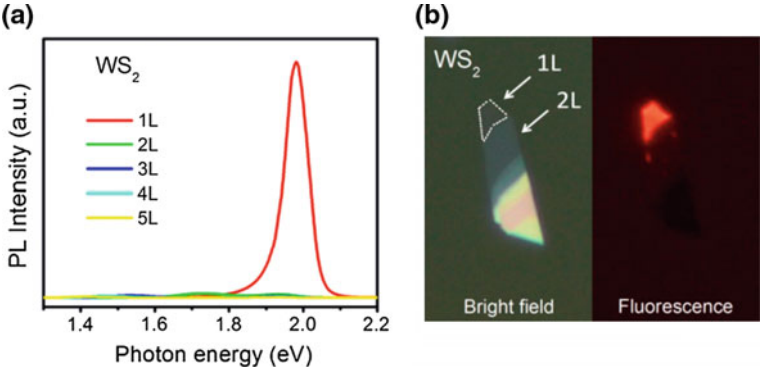

Fig. 5.4 **a** PL spectra of 1L–5L WS_2. **b** Bright field optical and fluorescence images of mechanically exfoliated WS_2. The monolayer region shows bright fluorescence compared to other multilayer regions. Adapted with permission from Ref. [86] with slight modification (Copyright 2015, American Chemical society)

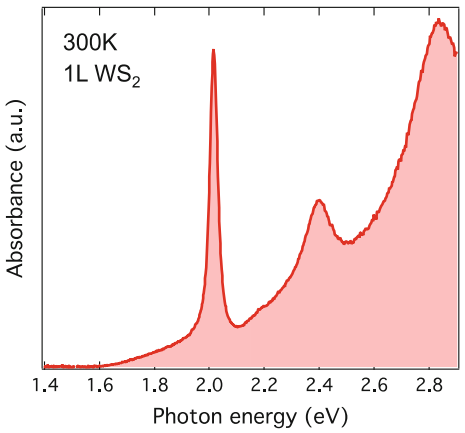

Fig. 5.5 Room temperature differential reflectance spectrum of monolayer WS_2. Note the sharp peak due to A exciton at $\sim$2 eV. Next prominent feature is due to B exciton $\sim$2.4 eV, while broad peak at $\sim$2.8 eV is due to C exciton absorption

conventional quantum wells for which free carrier absorption features dominate at room temperature, excitonic features are dominant in TMDs and obscure the onset of free carrier absorption [34, 108]. Figure 5.5 shows the room temperature absorption spectrum of monolayer WS_2 obtained by a differential reflectance measurement. A sharp ground exciton resonance feature (labeled as A) is clearly visible at $\sim$2 eV. The origin of such absorption features for bulk crystals has been discussed in early studies by Beal et al. [109] and Bromley et al. [3]. The A and B resonances are associated with excitonic transitions involving electrons in the spin-orbit-split valance band valley and the nearly degenerate conduction band valley at the K and K′ points. Thus, the energy separation of the A and B resonances roughly represent the spin-orbit interaction strength. The C absorption peak, which appears at higher energies of $\sim$2.8 eV has been attributed to band nesting, which leads to a singularity in the joint Density of States (jDoS) for 2D systems [110]. Additional peaks referred to as A′ and B′ are observed in selenides and tellurides. High quality crystals of monolayer TMDs typically absorb more than 10% of incident photons at their band gap ground exciton resonance and more strongly at the C peak resonance [111]. This unusually large absorption [112, 113] is in contrast with that of graphene, whose absorption is 2.3% in the optical frequencies [114].

Bilayer and thicker multilayer TMDs exhibit both direct and indirect exciton emission peaks. Figure 5.6a shows confinement-induced shift of PL emission peaks in 1–5 layer (L) WS_2. The shift of emission and absorption peaks are summarized in Fig. 5.6b. Indirect emission in multilayer WS_2 involves electrons and holes in the Λ and Γ valley, respectively. Thus, indirect emission peak shift indicates changes in the valley energies that are sensitive to interlayer interaction as discussed above. The direct A and B exciton energy is only weakly dependent on the number of layers while the indirect emission peak energy increases rapidly with reduction in the number of layers. It is worth noting that the hot exciton emission from B excitons is also observable at higher energies (2.3–2.4 eV).

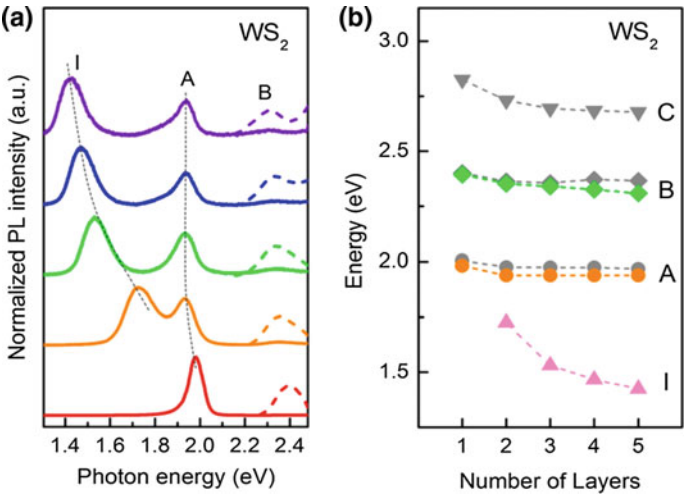

Fig. 5.6 **a** Normalized PL spectra of 1L–5L WS_2. **b** PL (*colored symbols*) and absorption (*grey symbols*) peak energies of WS_2 as a function of the number of layers. The letter *I* refers to indirect exciton peak. Reprinted with permission from Ref. [86] (Copyright 2013, American Chemical Society)

Confinement-induced shift of indirect and direct emission is a general trend reported for MoS_2, $MoSe_2$, WS_2, WSe_2, and $MoTe_2$. However, subtle details of the band structure evolution are unique to each material and are still a subject of debate. For instance, since the conduction band valleys at the K and Λ point are nearly degenerate in energy in few-layer materials, experimental determination of the CBM has been a nontrivial task. DFT results show little consensus on the conduction band structure of few-layer MX_2. For bilayer MoS_2 some calculations [96, 115] show that the CBM is located at the K point while others [24, 87, 116, 117] show that it is at the **Λ** point. On the other hand, the DFT calculations consistently show the VBM to be at the Γ point in few-layer MX_2. The calculated valence band structure shows good agreement with the experimental observations by angle-resolved photoemission spectroscopy (ARPES) [89, 118]. Direct investigation of the dispersion of unfilled conduction band states, however, is generally a challenging task. Several groups used ARPES to investigate the conduction band structure of MX_2 by introducing heavy electron doping from potassium [88]. While this approach is effective in identifying CBM, it is yet unclear how heavy doping and surface electric fields influence the band structure. Studies [119] suggest that the band renormalization effect is nonnegligible. For instance, a change in doping density by 10^{13} cm^{-2} is reported to result in a bandgap shift on the order of ~100 meV for monolayer WS_2 [120]. Large electric fields can also substantially modify the band structure according to theoretical predictions [121].

Our research team employed a less invasive approach to determining the conduction band structure in bilayer and thicker multilayer MX_2 samples [101].

In this approach, we used temperature as the knob to continuously change the band structure of the sample and studied the corresponding changes in the direct and indirect PL emission energies. Indirect emission in bilayer MX_2 involves holes in the Γ_c valley and electrons in either K_c or Λ_c valleys (Fig. 5.3). DFT calculations predict that thermal expansion of the lattice leads to opposite temperature dependence for $K_c-\Gamma_v$ gap and $\Lambda_c-\Gamma_v$ gap. We found the temperature coefficient of the indirect emission energy of bilayer WSe_2 to be negative. This suggests that the indirect optical transition involves the CBM at the K_c valley. On the other hand, the temperature coefficient for bilayer MoS_2 and WS_2 was positive, suggesting that the Λ_c valley is the CBM for these materials. Interestingly, $3 \sim 8$L WSe_2 samples showed two indirect emission peaks with opposite temperature dependence. These observations further highlight that the conduction band valleys in WSe_2 are nearly degenerate.

Ditellurides of molybdenum and tungsten exhibit multiple crystal phases that are not commonly seen in other group 6 TMDs [39, 40]. There are limited reports on the behaviors of monolayer $MoTe_2$ and WTe_2. Bulk 2H-$MoTe_2$ is an indirect gap semiconductor with a band gap of $\sim$1.0 eV. Ruppert et al. [122] reported that thinning 2H-$MoTe_2$ down to monolayer limit yields a direct gap material with an enhanced PL yield similar to the case of other group 6 TMDs. The authors concluded that multilayer samples are indirect gap semiconductors based on reduced PL emission intensities. Lezama et al. [92] further investigated low temperature absorption and emission properties of mono- and few-layer $MoTe_2$ samples and found that the PL quantum yield remains largely unchanged up to 3L sample and drops substantially for thicker materials (Fig. 5.7). These authors concluded that 2H-$MoTe_2$ remains a direct gap up to 3L, unlike MoS_2 and WS_2 that exhibit direct to indirect crossover only at the monolayer limit. Both studies agree that direct and indirect transition energies are close in energy such that indirect emission peak is not readily observable for 2H-$MoTe_2$.

It is well known that semiconducting 2H-MoS_2 and 2H-WS_2 undergo phase transformation to metallic 1T structure upon alkali metal intercalation [123, 124]. 1T phase is metastable for these materials after deintercalation and the stable 2H phase is mostly restored upon mild annealing or aging. We studied the electronic structure evolution of 1T and distorted 1T (1T′) phase of MoS_2 during progressive restoration of the stable 2H phase [125]. The samples were prepared by lithium intercalation followed by liquid phase exfoliation in water following the pioneering work by Joensen et al. [126]. X-ray photoelectron spectroscopy (XPS) analyses [127] and STEM revealed that the 2H and 1T phases coexist in the as-exfoliated materials at variable fractions. Figure 5.8a shows the optical absorption spectrum of as-produced and progressively annealed chemically exfoliated MoS_2 samples. The as-produced sample in which the metallic phase response is dominant exhibits no clear characteristic peaks of pristine 2H-MoS_2 except for the exciton-like features in the near-UV range (200–300 nm). The Drude-like broad absorption background that extends to the near-IR region below the optical gap of 2H-MoS_2 reveals the predominantly metallic character of the material. Characteristic exciton absorption and emission features of 2H-MoS_2 emerge with annealing, indicating gradual

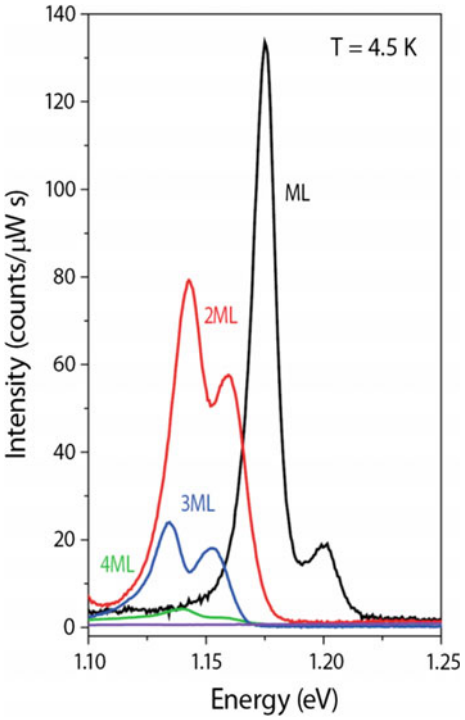

Fig. 5.7 Photoluminescence spectra of few-layer $MoTe_2$ measured at 4.5 K plotted in linear scale. Note the relative difference in intensity for 1-3L and 4L samples. Adapted from Ref. [92] (Copyright 2015, American Chemical Society)

restoration of the 2H phase. Similar to mechanically exfoliated samples, restacked nanosheets of chemically exfoliated MoS_2 exhibit thickness-dependent PL energy and intensity (Fig. 5.8b), revealing the presence of interlayer coupling despite stacking disorder.

5.2.5 *Optical Signatures of Excitons*

Layered TMDs are known as an ideal platform to study many-body effects that give rise to myriads of unique phenomena such as superconductivity [36] and charge density wave (CDW) [128]. Strong excitonic character of monolayer MX_2 is also a manifestation of enhanced many-body effects in these systems. Exciton binding energy is a measure of how strongly electrons and holes interact with each other through Coulomb forces. Its magnitude corresponds to the difference between the electronic and optical gap as schematically shown in Fig. 5.9. According to a simple hydrogen model, exciton binding energy is four times greater for 2D systems compared to bulk systems. In practice, reduced dielectric screening also enhances Coulomb interaction (Fig. 5.10). Large electron and hole effective masses in TMDs also contribute to the large exciton binding energy. The large binding

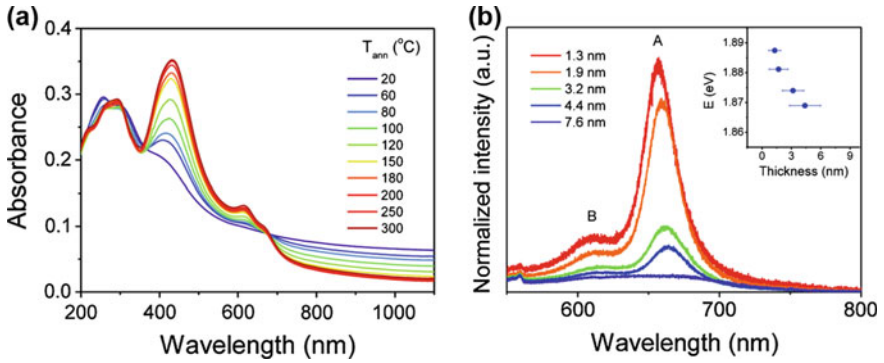

Fig. 5.8 **a** Absorption of MoS_2 thin films annealed at various temperatures. Note the restoration of A and B features (~600–700 nm) at high-temperature annealed samples. **b** PL spectra of annealed MoS_2 films as a function of film thickness. *Inset* shows peak energies extracted from PL spectra in the main panel. Note the absence of clear A exciton peak in 7.6 nm film. Reprinted with permission from Ref. [125] (Copyright 2011, American Chemical Society)

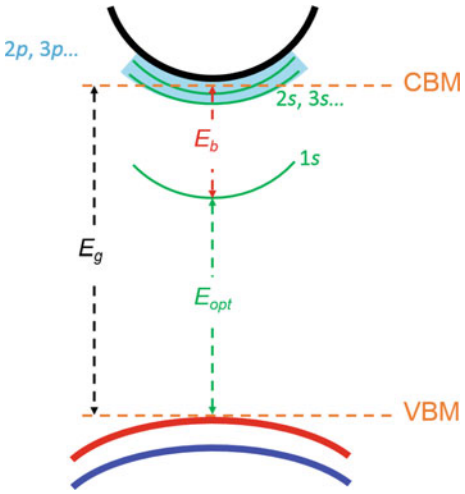

Fig. 5.9 Typical exciton excitation spectrum of monolayer group 6 TMDs. *Green lines* (1*s*, 2*s*, 3*s*, etc.) denote one-photon active states; *wide blue line* are the two-photon active states (2*p*, 3*p*, etc.). E_g, E_{opt} and E_b stands for quasiparticle gap, optical gap and binding energy, respectively

energy classifies excitons in monolayer TMDs to Frenkel-type, however, their comparatively large Bohr radius of 0.7 ~ 1 nm [108, 129] that extend over several unit cells makes them behave as Wannier-Mott excitons. Such dual-character excitons are also a fingerprint of single-wall carbon nanotubes [130].

In conventional quantum wells, the electronic gap can be identified from the onset of free carrier absorption, which has a distinct step-like function reflecting the density of states (DoS) of a 2D electronic system. As it can be seen from Fig. 5.5 excitonic absorption dominates in group 6 TMDs [108, 131] and the onset of interband transition is not immediately evident. Thus, the determination of electronic gap or conversely the exciton binding energy needs to resort to other

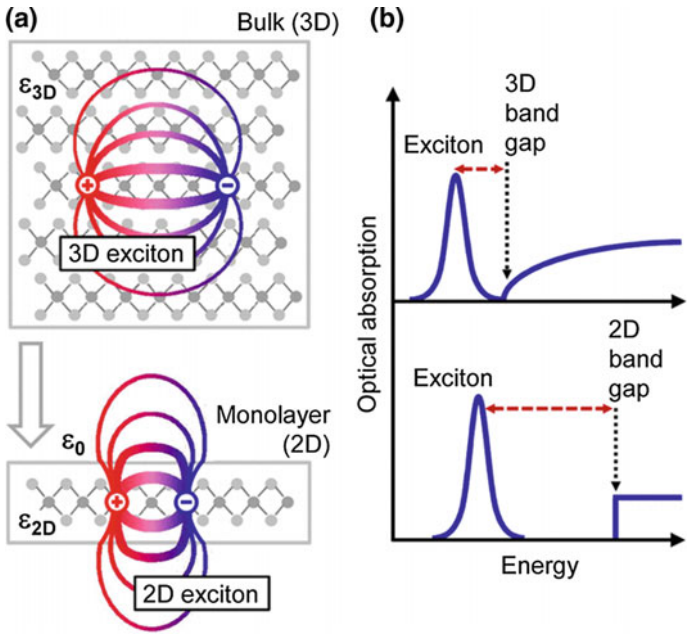

Fig. 5.10 **a** Real-space representation of bound excitons for the 3D bulk and a quasi-2D monolayer. The changes in the dielectric environment are indicated schematically by different dielectric constants ϵ_{3D} and ϵ_{2D} and by the vacuum permittivity ϵ_0. **b** Changes in the electronic and excitonic properties upon reduction of dimensionality, schematically represented by optical absorption. The transition from 3D to 2D is expected to lead to an increase of both the band gap and the exciton binding energy (indicated by the *dashed red line*). Adapted from Ref. [34] (Copyright 2014, American Physical Society)

measurement techniques. These include scanning tunneling spectroscopy (STS), ARPES, two-photon photoluminescence excitation (2P-PLE) spectroscopy, and photocurrent spectroscopy. A number of papers reporting fundamental electronic gap and exciton binding energy of various TMDs appeared in the past few years. These values are summarized in Table 5.1. While the reported values vary, exciton binding energies are typically found to be of the order of few hundreds of meV, which is one order of magnitude larger than that of conventional quasi-2D GaAs-type quantum wells [132, 133] and bulk TMDs [134].

Ugeda et al. [119] investigated the electronic gap of MBE-grown monolayer $MoSe_2$ on an epitaxial bilayer graphene (BLG) and graphite (HOPG) surface by STS. The electronic gap was measured to be 2.18 ± 0.04 eV for $MoSe_2$/BLG system. The measured optical band gap of 1.63 eV for this sample implied exciton binding energy of 0.55 eV. Further, the authors found the electronic gap of $MoSe_2$/HOPG sample to be smaller by 11% and attributed this to the different dielectric screening properties of BLG and HOPG substrates. Interestingly, the optical gap was nearly identical for the two samples, indicating that the exciton binding energy

Table 5.1 Electronic gap and exciton binding energies of quasiparticles in group 6 TMD monolayers

Material	References	E_X^0 (eV)	$E_X^{\pm}$ (eV)	E_X^2 (eV)	$E_{g,elec}$ (eV)	Substrate[a]	T (K)	Sample source[b]	Method
MoS_2	[102]		0.018				10		PL, abs
	[129]		0.032				5		abs
	[135]	0.57			2.5	susp.	77	CVD	Photocurrent
	[33]	0.22–0.42			2.15–2.35	HOPG	77	CVD	STS, PL
	[145]			0.07			74	CVD	TA[c]
	[146]			0.04, 0.06		Al_2O_3	10		TA
WS_2	[147]		0.02–0.04				4		PL
	[137]	0.71	0.034		2.73		10		PL, 2P-PLE
	[35]	0.7					10		2P-PLE
	[34]	0.32			2.41		5		dR
	[148]		0.043	0.065			4		PL
	[149]		0.01–0.015	0.045			4		PL
$MoSe_2$	[119]	0.55			2.18	BLG	77	MBE	STS, PL
	[119]	0.27			1.94	HOPG	77	MBE	STS, PL
	[150]				2.1	HOPG	4	MBE	STS, PL
	[105]		0.03				55		PL
	[91]	0.5			2.15	HOPG	79	MBE	STS
WSe_2	[104]		0.024–0.04				30		PL
	[151]	0.37			2.02		300		2P-PLE
	[152]	0.6[d]					4		SHG[f], 2P-PLE
	[103]			0.052			50		PL
	[91]	0.5			2.12[e]	HOPG	79	CVD	STS
$MoTe_2$	[92]		0.025				4.5		PL
	[153]	0.58	0.024, 0.027		1.8	gel film[g]	300		PLE

[a]SiO_x/Si substrate is used if not mentioned otherwise

[b]Flakes were exfoliated from bulk crystal if not mentioned otherwise

[c]Transient absorption (TA)

[d]The quasiparticle bandgap was calculated (GW-BSE) to be 2.73 eV [152]

[e]Quasiparticle gap in monolayer WSe_2 was found to be indirect (from Q to K). However, similarly accessed direct gap (from K to K, ~2.20 eV) was found to nearly degenerate with indirect [91]

[f]Second harmonic generation (SHG) spectroscopy

[g]Elastic (PDMS-like) GEL film by Gel-Pack was used as the substrate

was reduced by as much as 51% for the $MoSe_2$/HOPG sample. It is worth noting that the electronic gap of similarly prepared but heavily potassium-doped monolayer $MoSe_2$ on BLG was measured to be 1.58 eV by ARPES by Zhang et al. [88]. These reports indicate that band renormalization effect is significant in these materials.

Zhang et al. [33] conducted similar STS investigation on CVD-grown monolayer MoS_2 on a HOPG surface. These authors found the electronic gap and exciton binding energy to be 2.15 ± 0.06 and 0.22 eV, respectively, at 77 K. Klots et al. [135] utilized photocurrent spectroscopy to measure the electronic gap of mechanically exfoliated and suspended monolayer MoS_2. The authors attributed the step-like increase in photocurrent at ~2.5 eV to the onset of interband transition, and reported a significantly larger exciton binding energy of 0.57 eV. The discrepancies may be related to different dielectric screening effects in suspended and supported samples.

Chernikov et al. [34] proposed a simpler approach based purely on linear optical spectroscopy to estimate the exciton binding energy of monolayer WS_2 on a SiO_2/Si substrate. This requires examination of low temperature reflectance contrast (differential reflectance, dR) spectrum of a high quality sample. As shown in Fig. 5.11, derivative of reflectance contrast reveals higher lying exciton transition features that can be identified as 2*s*, 3*s*, 4*s*, and 5*s* states of the A exciton. Assuming 2D hydrogenic Rydberg series for the 3*s*, 4*s*, and 5*s* states, the authors extract an electronic gap to be 2.41 ± 0.04 eV, which yields an exciton binding energy of 320 meV. The same group [136] confirmed the assignment of higher lying exciton transitions using photoluminescence excitation spectroscopy (PLE). Interestingly,

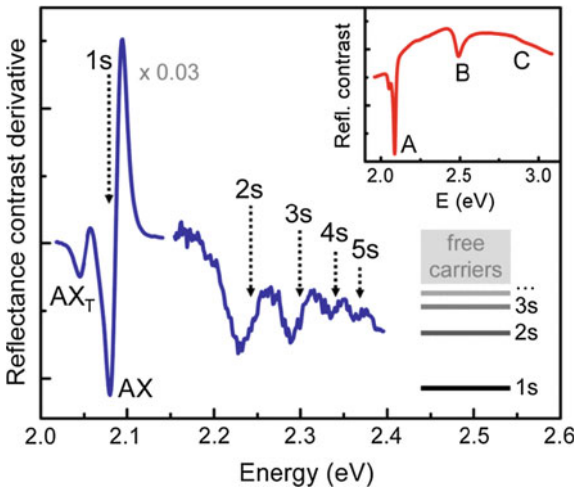

Fig. 5.11 The first derivative of the reflectance contrast spectrum of the WS_2 monolayer. The notion 1*s*, (2*s*, 3*s*,…, 5*s*) stands for exciton ground state and the higher excited states. Neutral 1*s* transition (AX) accompanied by the trion peak (AX_T) at the low-energy shoulder, this part of the spectrum is scaled for clarity. The *Inset* shows the as-measured reflectance contrast for comparison, allowing for the identification of the A, B, and C transitions. Adapted from Ref. [34] (Copyright 2014, American Physical Society)

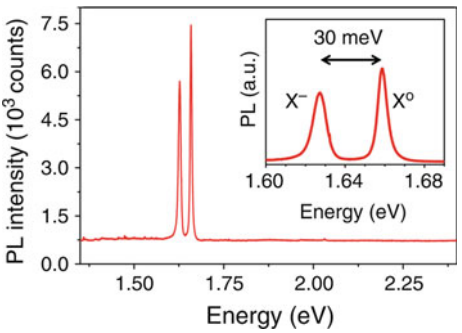

Fig. 5.12 PL spectrum of monolayer $MoSe_2$ at 20 K shows neutral exciton (X^o) and the lower energy charged exciton (trion, X^-). *Inset* shows PL of the exciton and trion peaks. Trion energy was estimated to be ~30 meV. Adapted from Ref. [105] (Copyright 2013, Nature publishing group)

this binding energy is nearly half of what was measured in the same material in nonlinear optical excitation. While *s* exciton states (1*s*, 2*s*, 3*s*,…) are accessible via one-photon excitation, *p* states (2*p*, 3*p*,…) can only be probed through two-photon spectroscopy. Ye et al. [35] and Zhu et al. [137] employed 2P-PLE spectroscopy to probe 2*p* and 3*p* states of A excitons in monolayer WS_2. These dipole-forbidden states were found at energies close to the 2*s* and 3*s* states measured by one-photon excitation.

Exciton complexes such as trions and biexcitons are also indications of strong many-body Coulomb interactions. A trion or a charged exciton is a quasi-particle consisting of either two electrons and one hole (negative trion) or two holes and one electron (positive trion) [138]. These particles have been observed in monolayer TMDs with excess charges (Fig. 5.12). Mak et al. [102] and Ross et al. [105] reported observation of trions in electrically gated monolayer MoS_2 and $MoSe_2$, respectively. The trion binding energies were found to be 20 and 30 meV in these studies. These values are one order of magnitude larger compared to trion binding energies in conventional quantum wells [139, 140]. For isotropic 2D semiconductors with equal electron and hole masses, the exciton binding energy is expected to be approximately 10 times larger than the trion binding energy [141, 142]. The reported exciton and trion binding energies for TMDs are roughly consistent with this rule of thumb.

A biexciton is a four-particle complex comprised of two free excitons. Biexciton emission typically occurs at a lower energy of a neutral exciton emission line and its emission intensity increases superlinearly with excitation power. Biexcitons in monolayer WSe_2 have been observed at high-power pulsed laser excitation at low temperatures [103]. Theory and experiments indicate that biexciton binding energy of 52 meV and Bohr radius of ~4 nm. Ratio of biexciton and free exciton binding energies, known as the Haynes factor, was found to be comparable with that of GaAs quantum wells [143]. Thermally activated dissociation suppresses biexciton emission peak at room temperature [103, 144].

5.2.6 *Many-Body Effects in Bilayers and van der Waals Heterostructures*

Two quantum wells separated by a thin insulating barrier layer are considered to be coupled when carriers with opposite charge in the two layers interact by Coulomb forces and form a bound state. Coupled quantum wells of InGaAs have been studied both experimentally and theoretically for Bose–Einstein condensation [154, 155] and giant Stark effects [156, 157] of such spatially indirect excitons. A bilayer TMD sheet is effectively a coupled quantum well in that electrons and holes can form a bound state across the van der Waals gap. In a typical intrinsic bilayer system, however, intralayer exciton states are anticipated to dominate. The findings by Schuller et al. [158] indicate that in-plane dipoles, i.e., intralayer excitons, are solely responsible for emission from bilayer MoS_2. Jones et al. [159] reported that in an electrostatically gated bilayer WSe_2, the trion emission peak splits into a doublet in the presence of large vertical electric fields. The authors attributed this splitting to electric-field-induced Zeeman-type splitting of energy bands associated with upper and lower layers. The doublet could then be explained by inter- and intralayer trion species. These interlayer trions consist of an intralayer exciton bound to an electron in the other layer.

Several groups have also reported observation of interlayer excitons in van der Waals heterostructures [160–162]. These interlayer excitons are effectively charge-transfer species that are commonly seen in donor-acceptor molecular complexes [163]. Monolayer group 6 TMDs typically form a type-II junction when placed in contact with each other [164, 165]. Photoemission studies indeed indicate that band alignment of a monolayer MoS_2/WSe_2 heterostack is type-II as predicted by DFT calculations [166, 167]. In such heterojunctions, excitation of intralayer excitons leads to spontaneous interlayer charge transfer and formation of interlayer excitons. Several research groups reported observation of a low-energy PL peak that does not belong to intralayer emission species and attributed it to interlayer excitons (Fig. 5.13). Rivera et al. [161] found that this low-energy emission peak redshifts with external electric field and concluded that their observation is consistent with the out-of-plane exciton dipole. Studies suggest that the brightness of interlayer excitons strongly depends on the orientation of the two layers [162]. This is consistent with the fact that misorientation of the layers renders the interlayer species indirect not only in space but also in momentum [168].

5.3 Other Layered Chalcogenides

Semiconducting nanosheets derived from other families of layered chalcogenides exhibit properties that are unique to their crystal symmetry and bonding. We briefly review chalcogenide nanosheets that have recently attracted interest for their

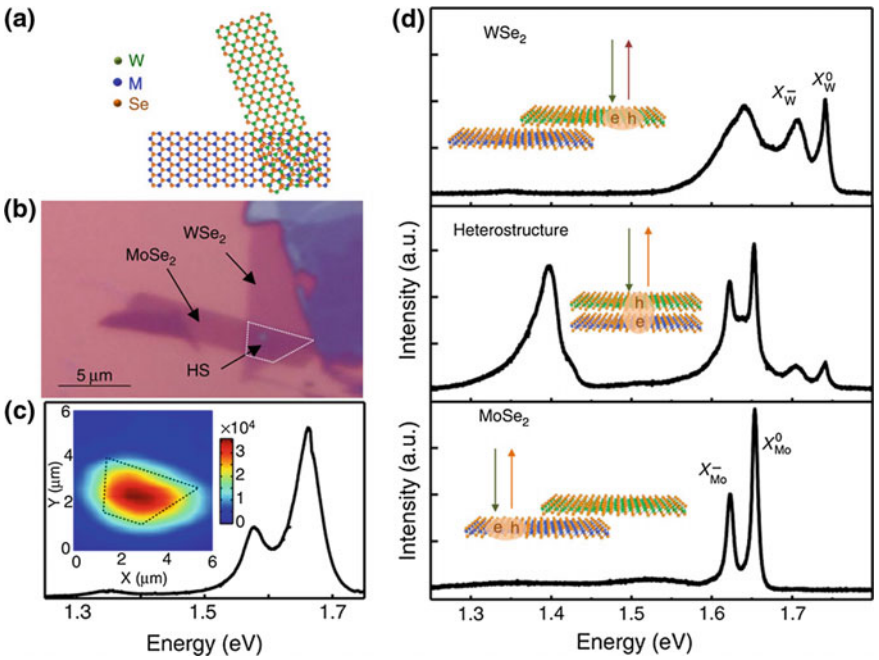

Fig. 5.13 **a** Depiction of a $MoSe_2$–WSe_2 heterostructure (HS). **b** Microscope image of a $MoSe_2$–WSe_2 HS with a *white dashed line* outlining the overlapping region. **c** Room-temperature PL of the HS. *Inset* shows spatial map of integrated PL intensity from the low-energy peak (1.273–1.400 eV), which can only be observed in HS area. **d** Photoluminescence of individual monolayers and the HS at 20 K (plotted on the same scale). Notations X_W^0 (X_W^-) and X_M^0 (X_M^-) stand for neutral (charged) exciton peak emissions due to WSe_2 and $MoSe_2$, respectively. Reprinted with permission from Ref. [161] (Copyright 2014, Nature Publishing group)

potential in nanoelectronics [169, 170], optoelectronics [171–174], solar cells [175], photonics [176], and many other fields.

5.3.1 Sn-Based Monochalcogenides

Tin monochalcogenides (SnS and SnSe) represent an interesting class of layered materials with structural in-plane anisotropy. Along with their dichalcogenide compounds SnS_2 and $SnSe_2$, they are known for their attractive thermoelectric properties. Recently reported ZT of 2.6 for SnSe at 923 K [177] its potential uses in thermoelectric devices. Bulk SnS and SnSe have orthorhombic crystal structure of distorted NaCl type. The α phase of SnS, also known as herzenbergite, is a naturally occurring mineral. Its bandgap of $\sim$1.3 eV and large absorption coefficient makes it attractive as the absorbing layer for solar cells [172, 175].

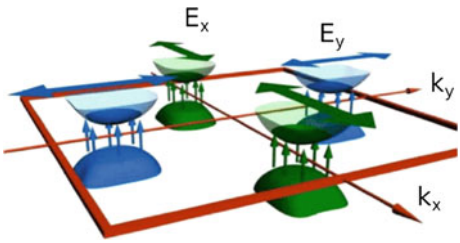

Fig. 5.14 Valley selection in monolayer SnS for an external oscillating electric field. Depending on the polarization of the field, different valleys are excited. Reprinted with permission from Ref. [171] (Copyright 2016, American Physical Society)

DFT calculations predict the bandgap of SnS to increase with decreasing thick from 1.3 eV for bulk to 1.96 eV for monolayer, similar to the case of MoS_2. The gap, however, is predicted to remain indirect for SnS for all thicknesses. In contrast, indirect-to-direct gap crossover is predicted for SnSe. Monolayer SnSe is expected to be a direct gap semiconductor with a band gap of $\sim$1.4 eV [17].

Lack of inversion symmetry in monolayer SnS and SnSe and strong spin-orbit coupling imply presence of energy degenerate but spin dependent valleys like in monolayer MoS_2. It is worth noting that according to DFT calculations, spin-orbit splitting of both valence and conductance bands reduces the electronic gap as much as 95 meV for SnS and 85 meV for SnSe [17]. Theory also predicts that the four spin- and momentum-dependent valleys in the rectangular Brillouin zone can be accessed by linearly polarized light [171] (Fig. 5.14). This is different from group 6 TMD monolayers, where a circular polarized light is needed to achieve valley polarization [99]. While experimental investigation of monolayer SnS and SnSe is limited, these attributes of SnS and SnSe make them attractive for valleytronics and spintronics.

5.3.2 Ga-Based Monochalocogenides

Monolayer GaX (X=S, Se, Te), which is made up of a X–Ga–Ga–X sandwich, has recently attracted attention for its potential as high performance photodetectors [174, 178–180]. GaTe is an exceptional member of GaX family that possesses a direct gap of $\sim$1.7 eV [181] in its bulk form. This is attributed to the unique crystal structure of monoclinic GaTe, where the Ga–Ga bonds are slightly tilted with respect to the c-axis, unlike in GaS and GaSe, whose Ga–Ga bonds are perpendicular to the layer plane [180]. Interestingly, monolayer GaTe is predicted to be an indirect gap semiconductor with a hexagonal structure [14, 182].

A recent experimental report showed that GaS and GaSe exhibit no clear signature of indirect-to-direct gap crossover as their thickness is reduced to monolayer [183]. However, the authors suggest that the difference between the direct and indirect gap in mono- and few-layer GaSe is small enough for electrons to thermally distribute over conduction band valley minima when electrons are injected into the system [183, 184]. Cathodoluminescence (CL) spectroscopy of GaSe nanosheets

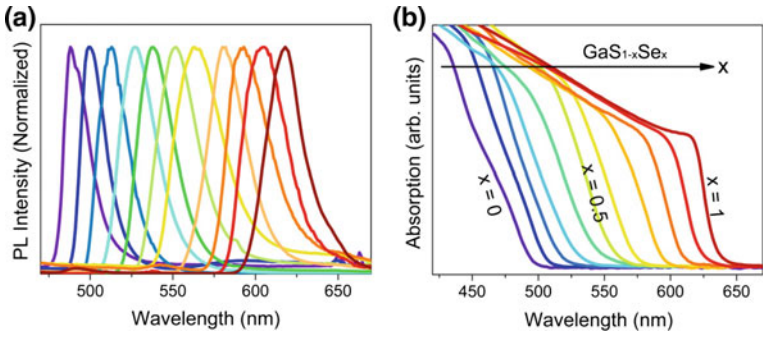

Fig. 5.15 Band gap tuning of $GaS_{1-x}Se_x$ multilayers. **a** UV-visible diffuse reflectance spectrum (in absorption) and **b** PL spectrum (at 8 K) of the $GaS_{1-x}Se_x$ nanosheets with various values of x. Reprinted with permission from Ref. [183] (Copyright 2015, American Chemical Society)

showed pronounced enhancement of the band gap emission with increasing number of layers, suggesting that the energy difference between the direct and indirect gaps are reduced for thicker flakes. Interestingly, CL spectra of GaS showed an opposite trend with emission from monolayer most strongly enhanced. Theoretical analysis [183] suggested that oxygen chemisorption induces indirect-to-direct gap transition in monolayer GaS. According to CL measurements, electronic gap of GaS (GaSe) increases from 2.5 eV (2.0 eV) to about 3.4 eV (3.3 eV) when the thickness is reduced from bulk to monolayer.

$GaS_{1-x}Se_x$ alloys are interesting for their highly tunable band gap due to the distinctly separated band gaps of GaS and GaSe. A broad tuning of PL from near-UV to red range has been demonstrated for alloys with varying sulfur and selenium compositions as shown in Fig. 5.15. The accessible range of band gaps is distinctly larger than that for group 6 TMD alloys [185–187].

5.3.3 Re-Based Dichalcogenides

ReX_2 (X=S, Se) exhibits 1T crystal structure common to TMDs but with a periodic lattice distortion and Re–Re bonding network (Fig. 5.16a, b). Owing to this structural deformation, interlayer coupling in stacked layers is weak and correspondingly, the thickness dependence of band gap is marginal. DFT predicts that ReS_2 remains a direct bandgap semiconductor independent of crystal thickness and estimates band gap of $\sim$1.35 eV for bulk and $\sim$1.43 eV for monolayer [188]. However, $ReSe_2$ is an indirect gap semiconductor with an experimentally measured optical gap of $\sim$1.26 eV and $\sim$1.32 eV for bulk and monolayer at 80 K, respectively [189]. PL intensity of RX_2 scales directly with thickness of the flakes, unlike for group 6 TMDs (Fig. 5.16c, d). A recent experimental study reported that the direct gap of bulk ReS_2 lies just 0.07 eV above the indirect gap [190].

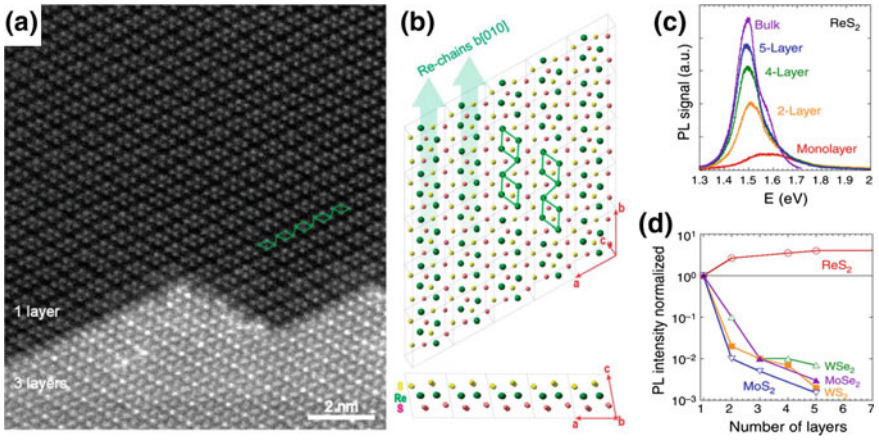

Fig. 5.16 Low magnification annular dark field (ADF) STEM image of ReS_2. The *upper part* is single-layer with the *diamond-shape-chain* phase structure, while the *lower part* is three-layer stacking. **b** Schematic illustrations of the ReS_2 atomic structure in the basal plane and cross section (Re, *green*; top S, *yellow*; bottom S, *pink*). Four Re atoms form a diamond cluster (*green line*). The *diamond-shape clusters* form a chain-like structure along the b[010] direction. **c** PL spectrum of ReS_2 flakes with different number of layers. **d** Integrated PL intensity as a function of the number of layers (normalized to that of monolayer) in ReS_2, MoS_2, $MoSe_2$, WS_2, and WSe_2. Unlike for group 6 TMDs, PL intensity of ReS_2 scales proportionally with thickness of the flake. (**a**) and (**b**) reprinted with permission from Ref. [169] (Copyright 2015, American Chemical Society), (**c**) and (**d**) reprinted with permission from Ref. [188] (Copyright 2014, American Chemical Society)

The zig-zag Re–Re bonded chains break the in-plane hexagonal symmetry and give rise to the anisotropy of optical, electrical and mechanical properties [169, 191, 192].

5.3.4 Trichalcogenides

Transition metal trichalcogenides such as TiS_3 and NbS_3 are another family of materials with strong in-plane anisotropy [170, 193]. TiS_3 has a monoclinic structure with individual layers consisting of an array of 1D chains of triangular TiS_3 units. Bulk TiS_3 is a direct gap semiconductor with an optical gap of $\sim$1 eV and a strong anisotropy in electrical conductivity [194]. Niobium trisulfide, NbS_3, is a model CDW metal that was found to exhibit characteristic 1D transport properties in thin exfoliated samples [195, 196].

Recently Island et al. [173] exfoliated 2D nanosheets of TiS_3 down to monolayer and field-effect transistors and photodetectors have been demonstrated [13, 197]. Experiments have shown that TiS_3 nanosheets exhibit pronounced in-plane anisotropy in electron transport (carrier mobility anisotropy of 2.3 and 7.6 at room temperature and 25 K, respectively) and strong linear optical dichroism,

i.e., change of absorption with rotation of polarization axis [198]. Strong quasi-1D behavior combined with large photoresponsivity [197] and predicted high carrier mobility in monolayers (10,000 $cm^2\ V^{-1}\ s^{-1}$) [170] make this material attractive for both fundamental and applied research.

5.4 Summary

The rapid development of chalcogenide nanosheet research in recent years has seen a number of key discoveries that highlight the unique potential of this class of materials in a range of novel applications. TMDs are diverse in basic material properties and rich in physics due to enhanced many-body effects and unique crystal symmetry. This chapter focused on the fundamental understanding of the electronic structure and spectroscopic signatures of excitonic effects in group 6 TMDs. There are, however, a large number of other TMDs and chalcogenides that remain unexplored in terms of their fundamental electronic properties and many-body-induced phenomena. While these 2D systems exhibit familiar features of conventional III-V quantum wells, dramatically enhanced many-body interactions, optically accessible valley quantum indices, and other emerging physical properties make them attractive for technological exploitations. Van der Waals heterostructures are not limited by lattice matching conditions, and allow preparation and study of any combination of chalcogenide nanosheets and other 2D materials. The prospects for realizing heterostructures with tailored physical properties and desired functionalities offer an exciting vista in many aspects of physical sciences and materials research.

References

1. Wilson AD, Yoffe JA (1969) The transition metal dichalcogenides discussion and interpretation of the observed optical, electrical and structural properties. Adv Phys 18:193–335
2. Murray RB, Bromley RA, Yoffe AD (1972) The band structures of some transition metal dichalcogenides. II. Group IVA; octahedral coordination. J Phys C Sol Stat Phys 5:746
3. Bromley RA, Murray RB, Yoffe AD (1972) The band structures of some transition metal dichalcogenides. III. Group VIA: trigonal prism materials. J Phys C Sol Stat Phys 5:759
4. Liang WY (1973) Optical anisotropy in layer compounds. J Phys C Solid Stat Phys 6:551–565
5. Lévy F (1979) Physics and chemistry of materials with layered structures: intercalated layered materials. Reidel, Dordrecht
6. Somoano RB, Hadek V, Rembaum A (1973) Alkali metal intercalates of molybdenum disulfide. J Chem Phys 58:697
7. Woollam JA, Somoano RB (1976) Superconducting critical fields of alkali and alkaline-earth intercalates of MoS_2. Phys Rev B 13:3843
8. Hasan MZ, Kane CL (2010) Topological insulators. Rev Mod Phys 82:3045

9. Butler SZ et al (2013) Progress, challenges, and opportunities in two-dimensional materials beyond graphene. ACS Nano 7:2898–2926
10. Kasowski RV (1973) Band structure of MoS_2 and NbS_2. Phys Rev Lett 30:1175
11. Lebègue S, Eriksson O (2009) Electronic structure of two-dimensional crystals from ab initio theory. Phys Rev B 79:115409
12. Hu KH et al (2009) Tribological properties of molybdenum disulfide nanosheets by monolayer restacking process as additive in liquid paraffin. Tribol Int 42:33–39
13. Lipatov A et al (2015) Few-layered titanium trisulfide (TiS_3) field-effect transistors. Nanoscale 7:12291–12296
14. Zolyomi V, Drummond ND, Fal'ko VI (2003) Band structure and optical transitions in atomic layers of hexagonal gallium chalcogenides. Phys Rev B 87:195403
15. Malone BD, Kaxiras E (2013) Quasiparticle band structures and interface physics of SnS and GeS. Phys Rev B 87:245312
16. Buscema M et al (2015) Photocurrent generation with two-dimensional van der Waals semiconductors. Chem Soc Rev 44:3691–3718
17. Gomes LC, Carvalho A (2015) Phosphorene analogues: isoelectronic two-dimensional group-IV monochalcogenides with orthorhombic structure. Phys Rev B 92:085406
18. Consadori F, Frindt RF (1970) Crystal size effects on the exciton absorption spectrum of WSe_2. Phys Rev B 2:4893–4896
19. Novoselov KS et al (2005) Electric field effect in atomically thin carbon films. Science 306:666
20. Chhowalla M et al (2013) The chemistry of two-dimensional layered transition metal dichalcogenide nanosheets. Nat Chem 5:263–275
21. Wang QH et al (2012) Electronics and optoelectronics of two-dimensional transition metal dichalcogenides. Nat Nanotechnol 7:699–712
22. Bhimanapati GR et al (2015) Recent advances in two-dimensional materials beyond graphene. ACS Nano 9:11509–11539
23. Gupta A, Sakthivel T, Seal S (2015) Recent development in 2D materials beyond graphene. Prog Mat Sci 73:44–126
24. Splendiani A et al (2010) Emerging photoluminescence in monolayer MoS_2. Nano Lett 10:1271–1275
25. Mak KF et al (2010) Atomically thin MoS_2: a new direct-gap semiconductor. Phys Rev Lett 105:136805
26. Zeng H et al (2012) Valley polarization in MoS_2 monolayers by optical pumping. Nat Nanotechnol 7:490–493
27. Mak KF et al (ed) (2012) Control of valley polarization in monolayer MoS_2 by optical helicity. Nat Nanotechnol 7:494–498
28. Malard AM et al (2013) Observation of intense second harmonic generation from MoS_2 atomic crystals. Phys Rev B 87:201401
29. Li Y et al (2013) Probing symmetry properties of few-layer MoS_2 and h-BN by optical second-harmonic generation. Nano Lett 13:3329–3333
30. Kumar N et al (2013) Second harmonic microscopy of monolayer MoS_2. Phys Rev B 87:161403
31. Wu W et al (2014) Piezoelectricity of single-atomic-layer MoS_2 for energy conversion and piezotronics. Nature 514:470–474
32. Zhu H et al (2015) Observation of piezoelectricity in free-standing monolayer MoS_2. Nat Nanotechnol 10:151–155
33. Zhang C et al (2014) Direct imaging of band profile in single layer MoS_2 on graphite: quasiparticle energy gap, metallic edge states and edge band bending. Nano Lett 14:2443–2447
34. Chernikov A et al (2014) Exciton binding energy and nonhydrogenic rydberg series in monolayer WS_2. Phys Rev Lett 113:076802
35. Ye Z et al (2014) Probing excitonic dark states in single-layer tungsten disulphide. Nature 513:214–218

36. Ye JT et al (2012) Superconducting dome in a gate-tuned band insulator. Science 30:1193–1196
37. Geim AK, Grigorieva IV (2013) Van der Waals heterostructures. Nature 499:419–425
38. Lee JU et al (2016) Raman signatures of polytypism in molybdenum disulfide. ACS Nano 10:1948–1953
39. Brown BE (1966) The crystal structures of WTe_2 and high-temperature $MoTe_2$. Acta Cryst 20:268–274
40. Vellinga MB, Jonge R, Haas C (1970) Semiconductor to metal transition in $MoTe_2$. J Solid Stat Chem 2:299–302
41. Coehoorn R, Haas C, de Groot RA (1987) Electronic structure of $MoSe_2$, MoS_2, and WSe_2. II. The nature of the optical band gaps. Phys Rev B 35:6203–6206
42. Novoselov KS et al (2005) Two-dimensional atomic crystals. PNAS 102:10451
43. Schafer H (1964) Chemical transport reactions. Academic Press, New York
44. Koma A, Sunouchi K, Miyajima T (1984) Fabrication and characterization of heterostructures with subnanometer thickness. Microelectron Eng 2:129–136
45. Zheng J et al (2014) High yield exfoliation of two-dimensional chalcogenides using sodium naphthalenide. Nature Commun 5:2995
46. Nicolosi V et al (2013) Liquid exfoliation of layered materials. Science 340:6139
47. Amara KK et al (2014) Wet chemical thinning of molybdenum disulfide down to its monolayer. APL Mater 2:092509
48. Huang Y et al (2013) An innovative way of etching MoS_2: characterization and mechanistic investigation. Nano Res 6:200
49. Liu Y et al (2013) Layer-by-layer thinning of MoS_2 by plasma. ACS Nano 7:4202
50. Castellanos-Gomez A et al (2012) Laser-thinning of MoS_2: on demand generation of a single-layer semiconductor. Nano Lett 12:3187
51. Altavilla C, Sarno M, Ciambelli P (2011) A novel wet chemistry approach for the synthesis of hybrid 2D free-floating single or multilayer nanosheets of MS_2@oleylamine (M=Mo, W). Chem Mater 23:3879
52. Tan LK et al (2014) Atomic layer deposition of a MoS_2 film. Nanoscale 6:10584
53. Zhan Y et al (2012) Large-area vapor-phase growth and characterization of MoS_2 atomic layers on a SiO_2 substrate. Small 8:966
54. Liu K-K et al (2012) Growth of large-area and highly crystalline MoS_2 thin layers on insulating substrates. Nano Lett 12:1538
55. Lee Y-H et al (2012) Synthesis of large-area MoS_2 atomic layers with chemical vapor deposition. Adv Mater 24:2320
56. Amani M et al (2013) Electrical performance of monolayer MoS_2 field-effect transistors prepared by chemical vapor deposition. Appl Phys Lett 102:193107
57. van der Zande AM et al (2013) Grains and grain boundaries in highly crystalline monolayer molybdenum disulphide. Nat Mater 12:554
58. Wang H et al (2012) Integrated circuits based on bilayer MoS_2 transistors. Nano Lett 12:4674
59. Najmaei S et al (2013) Vapour phase growth and grain boundary structure of molybdenum disulphide atomic layers. Nat Mater 12:754
60. Yu Y et al (2013) Controlled scalable synthesis of uniform, high-quality monolayer and few-layer MoS_2 films. Sci Rep 3:1866
61. Gong C et al (2013) Metal contacts on physical vapor deposited monolayer MoS_2. ACS Nano 7:11350
62. Liu Y et al (2014) Mesoscale imperfections in MoS_2 atomic layers grown by a vapor transport technique. Nano Lett 14:4682
63. Liu H et al (2013) Statistical study of deep submicron dual-gated field-effect transistors on monolayer chemical vapor deposition molybdenum disulfide films. Nano Lett 13:2640
64. Liu B et al (2014) High-performance chemical sensing using schottky-contacted chemical vapor deposition grown monolayer MoS_2 transistors. ACS Nano 8:5304

65. Najmaei S et al (2014) Electrical transport properties of polycrystalline monolayer molybdenum disulfide. ACS Nano 8:7930
66. Schmidt H et al (2014) Transport properties of monolayer MoS_2 grown by chemical vapor deposition. Nano Lett 14:1909
67. Dumcenco D et al (2015) Large-area epitaxial monolayer MoS_2. ACS Nano 9:4611–4620
68. Zhu W et al (2014) Electronic transport and device prospects of monolayer molybdenum disulphide grown by chemical vapour deposition. Nat Commun 5:3087
69. Wang X et al (2014) Chemical vapor deposition growth of crystalline monolayer $MoSe_2$. ACS Nano 8:5125
70. Shaw JC et al (2014) Chemical vapor deposition growth of monolayer $MoSe_2$ and nanosheets. Nano Res 7:1
71. Zhang Y et al (2013) Controlled growth of high-quality monolayer WS_2 layers on sapphire and imaging its grain boundary. ACS Nano 7:8963
72. Sirlina T et al (2000) Study on preparation, growth mechanism, and optoelectronic properties of highly oriented WSe_2 thin films. J Mater Res 15:2636
73. Huang J-K et al (2014) Large-area synthesis of highly crystalline WSe_2 monolayers and device applications. ACS Nano 8:923
74. Gong Y et al (2014) Band gap engineering and layer-by-layer mapping of selenium-doped molybdenum disulfide. Nano Lett 14:442
75. Lin Y-C et al (2014) Properties of individual dopant atoms in single-layer MoS_2: atomic structure, migration, and enhanced reactivity. Adv Mater 26:2857
76. Hong J et al (2015) Exploring atomic defects in molybdenum disulphide monolayers. Nat Commun 6:6293
77. Zhou W et al (2013) Intrinsic structural defects in monolayer molybdenum disulfide. Nano Lett 13:2615
78. Lu C-P et al (2014) Bandgap, mid-gap states, and gating effects in MoS_2. Nano Lett 14:4628
79. Tongay S et al (2013) Defects activated photoluminescence in two-dimensional semiconductors: interplay between bound, charged, and free excitons. Sci Rep 3:2657
80. Radisavljevic B et al (2011) Single-layer MoS_2 transistors. Nat Nanotechnol 6:147
81. Kim S et al (2012) High-mobility and low-power thin-film transistors based on multilayer MoS_2 crystals. Nat Commun 3:1011
82. Baugher BWH et al (2013) Intrinsic electronic transport properties of high-quality monolayer and bilayer MoS_2. Nano Lett 13:4212
83. Wang Z et al (2013) Hopping transport through defect-induced localized states in molybdenum disulphide. Nat Commun 4:2642
84. Yu Z et al (2014) Towards intrinsic charge transport in monolayer molybdenum disulfide by defect and interface engineering. Nat Commun 5:5290
85. Liu G-B et al (2015) Electronic structures and theoretical modelling of two-dimensional group-VIB transition metal dichalcogenides. Chem Soc Rev 44:2643–2663
86. Zhao W et al (2013) Evolution of electronic structure in atomically thin sheets of WS_2 and WSe_2. ACS Nano 7:791–797
87. Tongay S et al (2012) Thermally driven crossover from indirect toward direct bandgap in 2D semiconductors: $MoSe_2$ versus MoS_2. Nano Lett 12:5576–5580
88. Zhang Y et al (2014) Direct observation of the transition from indirect to direct bandgap in atomically thin epitaxial $MoSe_2$. Nat Nanotechnol 9:111–115
89. Jin W et al (2013) Direct measurement of the thickness-dependent electronic band structure of MoS_2 using angle-resolved photoemission spectroscopy. Phys Rev Lett 111:106801
90. Zeng H et al (2013) Optical signature of symmetry variations and spin-valley coupling in atomically thin tungsten dichalcogenides. Sci Rep 3:1608
91. Zhang C et al (2015) Probing critical point energies of transition metal dichalcogenides: surprising indirect gap of single layer WSe_2. Nano Lett 15:6494–6500
92. Lezama IG et al (2015) Indirect-to-direct band gap crossover in few-layer $MoTe_2$. Nano Lett 15:2336–2342

93. Schmidt H, Giustiniano F, Eda G (2015) Electronic transport properties of transition metal dichalcogenide field-effect devices: surface and interface effects. Chem Soc Rev 44:7715–7736
94. Zhao W, Mendes Ribeiro R, Eda G (2015) Electronic structure and optical signatures of semiconducting transition metal dichalcogenide nanosheets. Acc Chem Res 48:91–99
95. Yoffe AD (2002) Low-dimensional systems: quantum size effects and electronic properties of semiconductor microcrystallites (zero-dimensional systems) and some quasi-two-dimensional systems. Adv Phys 51:799–890
96. Cheiwchanchamnangij T, Lambrecht WRL (2012) Quasiparticle band structure calculation of monolayer, bilayer, and bulk MoS_2. Phys Rev B 85:205302
97. Tongay S et al (2013) Broad-range modulation of light emission in two-dimensional semiconductors by molecular physisorption gating. Nano Lett 13:2831–2836
98. Komsa HP, Krasheninnikov AV (2012) Effects of confinement and environment on the electronic structure and exciton binding energy of MoS_2 from first principles. Phys Rev B 86:241201
99. Yu H et al (2015) Valley excitons in two-dimensional semiconductors. Natl Sci Rev 2:57–70
100. Xu X et al (2014) Spin and pseudospins in layered transition metal dichalcogenides. Nat Phys 10:343–350
101. Zhao W et al (2013) Origin of indirect optical transitions in few-layer MoS_2, WS_2, and WSe_2. Nano Lett 13:5627–5634
102. Mak KF et al (2013) Tightly bound trions in monolayer MoS_2. Nat Mater 12:207–211
103. You Y et al (2015) Observation of biexcitons in monolayer WSe_2. Nat Phys 11:477–481
104. Jones AM et al (2013) Optical generation of excitonic valley coherence in monolayer WSe_2. Nat Nanotechnol 8:634–638
105. Ross JS et al (2013) Electrical control of neutral and charged excitons in a monolayer semiconductor. Nat Commun 4:1474
106. Castellanos-Gomez A et al (2013) Local strain engineering in atomically thin MoS_2. Nano Lett 13:5361
107. Conley HJ et al (2013) Bandgap engineering of strained monolayer and bilayer MoS_2. Nano Lett 13:3626
108. Qiu DY, da Jornada FH, Louie SG (2013) Optical spectrum of MoS_2: many-body effects and diversity of exciton states. Phys Rev Lett 111:216805
109. Beal AR, Hughes HP (1979) Kramers-Kronig analysis of the reflectivity spectra of 2H-MoS_2, 2H-$MoSe_2$ and 2H-$MoTe_2$. J Phys C Solid Stat Phys 12:881
110. Carvalho A, Ribeiro RM, Castro Neto AH (2013) Band nesting and the optical response of two-dimensional semiconducting transition metal dichalcogenides. Phys Rev B 88:115205
111. Kumar R, Verzhbitskiy I, Eda G (2015) Strong optical absorption and photocarrier relaxation in two-dimensional semiconductors. IEEE J Quant Elec 51:0600206
112. Britnell L et al (2013) Strong light-matter interactions in heterostructures of atomically thin films. Science 340:1311–1314
113. Feng J et al (2012) Strain-engineered artificial atom as a broad-spectrum solar energy funnel. Nat Photon 6:865–871
114. Nair RR et al (2008) Fine structure constant defines visual transparency of graphene. Science 320:1308
115. Yun WS et al (2012) Thickness and strain effects on electronic structures of transition metal dichalcogenides: 2H-MX_2 semiconductors (M=Mo, W; X=S, Se, Te). Phys Rev B 85:033305
116. Kuc A, Zibouche N, Heine T (2011) Influence of quantum confinement on the electronic structure of the transition metal sulfide TS_2. Phys Rev B 83:245213
117. Ramasubramaniam A, Naveh D, Towe E (2011) Tunable band gaps in bilayer transition-metal dichalcogenides. Phys Rev B 84:205325
118. Klein A et al (2001) Electronic band structure of single-crystal and single-layer WS_2: influence of interlayer van der Waals interactions. Phys Rev B 64:205416

119. Ugeda MM et al (2014) Giant bandgap renormalization and excitonic effects in a monolayer transition metal dichalcogenide semiconductor. Nat Mater 13:1091–1095
120. Chernikov A et al (2015) Electrical tuning of exciton binding energies in monolayer WS_2. Phys Rev Lett 115:126802
121. Yuan H et al (2013) Zeeman-type spin splitting controlled by an electric field. Nat Phys 9:563–569
122. Ruppert C, Aslan OB, Heinz TF (2014) Optical properties and band gap of single- and few-layer $MoTe_2$ crystals. Nano Lett 14:6231–6236
123. Py MA, Haering RR (1983) Structural destabilization induced by lithium intercalation in MoS_2 and related compounds. Can J Phys 61:76–84
124. Voiry D, Mohite A, Chhowalla M (2015) Phase engineering of transition metal dichalcogenides. Chem Soc Rev 44:2702–2712
125. Eda G et al (2011) Photoluminescence from chemically exfoliated MoS_2. Nano Lett 11:5111–5116
126. Joensen P, Frindt RF, Morrison SR (1986) Single-layer MoS_2. Mater Res Bull 21:457–461
127. Papageorgopoulos CA, Jaegermann W (1995) Li intercalation across and along the van der Waals surfaces of MoS_2 (0001). Surf Sci 338:83–93
128. Li LJ et al (2016) Controlling many-body states by the electric-field effect in a two-dimensional material. Nature 529:185–189
129. Zhang C et al (2014) Absorption of light by excitons and trions in monolayers of metal dichalcogenide MoS_2: experiments and theory. Phys Rev B 89:205436
130. Nguyen DT et al (2011) Elastic exciton-exciton scattering in photoexcited carbon nanotubes. Phys Rev Lett 107:127401
131. Qiu DY, da Jornada FH, Louie SG (2015) Erratum: optical spectrum of MoS_2: many-body effects and diversity of exciton states. Phys Rev Lett 115:119901
132. Miller RC et al (1981) Observation of the excited level of excitons in GaAs quantum wells. Phys Rev B 24:1134
133. Greene RL, Bajaj KK, Phelps DE (1984) Energy levels of Wannier excitons in GaAs−$Ga_{1-x}Al_xAs$ quantum-well structures. Phys Rev B 29:1807
134. Beal AR, Knights JC, Liang WY (1972) Transmission spectra of some transition metal dichalcogenides. II. Group VIA: trigonal prismatic coordination. Phys C Sol Stat Phys 5:3540–3551
135. Klots AR et al (2014) Probing excitonic states in suspended two-dimensional semiconductors by photocurrent spectroscopy. Sci Rep 4:6608
136. Hill HM et al (2015) Observation of excitonic rydberg states in monolayer MoS_2 and WS_2 by photoluminescence excitation spectroscopy. Nano Lett 13:2992–2997
137. Zhu B, Chen X, Cui X (2015) Exciton binding energy of monolayer WS_2. Sci Rep 5:9218
138. Berkelbach TC, Hybertsen MS, Reichman DR (2013) Theory of neutral and charged excitons in monolayer transition metal dichalcogenides. Phys Rev B 88:045318
139. Kheng K et al (1993) Observation of negatively charged excitons X^- in semiconductor quantum wells. Phys Rev Lett 71:1752
140. Finkelstein G, Shtrikman H, Bar-Joseph I (1995) Optical spectroscopy of a two-dimensional electron gas near the metal-insulator transition. Phys Rev Lett 74:976
141. Sergeev RA, Suris RA (2001) Ground-state energy of X^- and X^+ trions in a two-dimensional quantum well at an arbitrary mass ratio. Phys Sol Stat 43:746–751
142. Thilagam A (1997) Two-dimensional charged-exciton complexes. Phys Rev B 55:7804–7808
143. Klingshirn CF (2007) Semiconductor Optics. Springer, Berlin
144. He Z et al (2016) Biexciton formation in bilayer tungsten disulfide. ACS Nano 10:2176–2183
145. Mai C et al (2014) Many-body effects in valleytronics: direct measurement of valley lifetimes in single-layer MoS_2. Nano Lett 14:202–206
146. Sie EJ et al (2015) Intervalley biexcitons and many-body effects in monolayer MoS_2. Phys Rev B 92:125417

147. Mitioglu AA et al (2013) Optical manipulation of the exciton charge state in single-layer tungsten disulfide. Phys Rev B 88:245403
148. Plechinger G et al (2015) Identification of excitons, trions and biexcitons in single-layer WS_2. Phys Stat Sol RRL 9:457–467
149. Shang J et al (2015) Observation of excitonic fine structure in a 2D transition-metal dichalcogenide semiconductor. ACS Nano 9:647–655
150. Liu H et al (2014) Dense network of one-dimensional midgap metallic modes in monolayer $MoSe_2$ and their spatial undulations. Phys Rev Lett 113:066105
151. He K et al (2014) Tightly bound excitons in monolayer WSe_2. Phys Rev Lett 113:026803
152. Wang G et al (2015) Giant enhancement of the optical second-harmonic emission of WSe_2 monolayers by laser excitation at exciton resonances. Phys Rev Lett 114:097403
153. Yang J et al (2015) Robust excitons and trions in monolayer $MoTe_2$. ACS Nano 9:6603–6609
154. Zhu X et al (1995) Exciton condensate in semiconductor quantum well structures. Phys Rev Lett 74:1633
155. Butov LV et al (2002) Towards Bose-Einstein condensation of excitons in potential traps. Nature 417:47–52
156. Fox AM et al (1992) Suppression of the observation of Stark ladders in optical measurements on superlattices by excitonic effects. Phys Rev B 46:15365
157. Kato Y et al (1994) Observation of the Stark effect in coupled quantum wells by electroluminescence and circularly polarized photoluminescence excitation spectroscopy. J Appl Phys 75:7476
158. Schuller JA et al (2013) Orientation of luminescent excitons in layered nanomaterials. Nat Nanotechnol 8:271–276
159. Jones AM et al (2014) Spin–layer locking effects in optical orientation of exciton spin in bilayer WSe_2. Nat Phys 10:130–134
160. Fang H et al (2014) Strong interlayer coupling in van der Waals heterostructures built from single-layer chalcogenides. PNAS 111:6198–6202
161. Rivera P et al (2015) Observation of long-lived interlayer excitons in monolayer $MoSe_2$–WSe_2 heterostructures. Nat Commun 6:6242
162. Rivera P et al (2016) Valley-polarized exciton dynamics in a 2D semiconductor heterostructure. Science 351:688–691
163. Li G, Zhu R, Yang Y (2012) Polymer solar cells. Nat Photonics 6:153–161
164. Kośmider K, Fernández-Rossier J (2013) Electronic properties of the MoS_2–WS_2 heterojunction. Phys Rev B 87:075451
165. Özçelik VO et al (2016) Band alignment of 2D semiconductors for designing heterostructures with momentum space matching. Phys Rev B 94:035125
166. Kang J et al (2013) Band offsets and heterostructures of two-dimensional semiconductors. Appl Phys Lett 102:012111
167. Terrones H, Lopez-Urias F, Terrones M (2013) Novel hetero-layered materials with tunable direct band gaps by sandwiching different metal disulfides and diselenides. Sci Rep 3:1549
168. Yu H et al (2015) Anomalous light cones and valley optical selection rules of interlayer excitons in twisted heterobilayers. Phys Rev Lett 115:187002
169. Lin Y-C et al (2015) Single-layer ReS_2: two-dimensional semiconductor with tunable in-plane anisotropy. ACS Nano 9:11249–11257
170. Dai J, Zeng XC (2015) Titanium trisulfide monolayer: theoretical prediction of a new direct-gap semiconductor with high and anisotropic carrier mobility. Angew Chem Int Ed 54:7572–7576
171. Rodin AS et al (2016) Valley physics in tin (II) sulfide. Phys Rev B 93:045431
172. Tritsaris GA, Malone BD, Kaxiras E (2013) Optoelectronic properties of single-layer, double-layer, and bulk tin sulfide: a theoretical study. J Appl Phys 113:233507
173. Island JO et al (2015) TiS_3 transistors with tailored morphology and electrical properties. Adv Mater 27:2595–2601
174. Hu P et al (2012) Synthesis of few-layer GaSe nanosheets for high performance photodetectors. ACS Nano 6:5988–5994

175. Ramakrishna Reddy KT, Koteswara Reddy N, Miles RW (2006) Photovoltaic properties of SnS based solar cells. Sol Energy Mater Sol Cells 90:3041–3046
176. Schwarz S et al (2014) Two-dimensional metal−chalcogenide films in tunable optical microcavities. Nano Lett 14:7003–7008
177. Zhao L-D et al (2014) Ultralow thermal conductivity and high thermoelectric figure of merit in SnSe crystals. Nature 508:373–377
178. Li X et al (2014) Controlled vapor phase growth of single crystalline, two-dimensional GaSe crystals with high photoresponse. Sci Rep 4:5497
179. Hu P et al (2013) Highly responsive ultrathin GaS nanosheet photodetectors on rigid and flexible substrates. Nano Lett 13:1649–1654
180. Liu F et al (2014) High-sensitivity photodetectors based on multilayer GaTe flakes. ACS Nano 8:752–760
181. Sanchez-Royo JF et al (2002) Angle-resolved photoemission study and first-principles calculation of the electronic structure of GaTe. Phys Rev B 65:115201
182. Zhang HL, Hennig RG (2003) Single-layer group-III monochalcogenide photocatalysts for water splitting. Chem Mater 25:3232–3238
183. Jung CS et al (2015) Red-to-ultraviolet emission tuning of two-dimensional gallium sulfide/selenide. ACS Nano 9:9585–9593
184. Ma Y et al (2013) Tunable electronic and dielectric behavior of GaS and GaSe monolayers. Phys Chem Chem Phys 15:7098–7105
185. Li H et al (2014) Growth of alloy $MoS_{2x}Se_{2(1-x)}$ nanosheets with fully tunable chemical compositions and optical properties. J Am Chem Soc 136:3756–3759
186. Dumcenco DO et al (2013) Visualization and quantification of transition metal atomic mixing in $Mo_{1-x}W_xS_2$ single layers. Nat Commun 4:1351
187. Zhang M et al (2014) Two-dimensional molybdenum tungsten diselenide alloys: photoluminescence, raman scattering, and electrical transport. ACS Nano 8:7130–7137
188. Tongay S et al (2014) Monolayer behaviour in bulk ReS_2 due to electronic and vibrational decoupling. Nat Commun 5:3252
189. Zhao H et al (2015) Interlayer interactions in anisotropic atomically thin rhenium diselenide. Nano Res 8:3651–3661
190. Aslan OB et al (2016) Linearly polarized excitons in single- and few-layer ReS_2 crystals. ACS Photon 3:96–101
191. Chenet DA et al (2015) In-plane anisotropy in mono- and few-layer ReS_2 probed by Raman spectroscopy and scanning transmission electron microscopy. Nano Lett 15:5667–5672
192. Zhong H-X et al (2015) Quasiparticle band gaps, excitonic effects, and anisotropic optical properties of the monolayer distorted 1T diamond-chain structures ReS_2 and $ReSe_2$. Phys Rev B 92:115438
193. Jin Y, Li X, Yang J (2015) Single layer of MX_3 (M=Ti, Zr; X=S, Se, Te): a new platform for nano-electronics and optics. Phys Chem Chem Phys 17:18665–18669
194. Gorlova I et al (2012) Nonlinear conductivity of quasi-one-dimensional layered compound TiS_3. Physica B 407:1707
195. Zaitsev-Zotov SV, Pokrovskii V Ya, Monceau P (2001) Transition to 1D conduction with decreasing thickness of the crystals of TaS_3 and $NbSe_3$ quasi-1D conductors. J Exp Theor Phys Lett 73:25–27
196. Slot E et al (2004) One-dimensional conduction in charge-density-wave nanowires. Phys Rev Lett 93:176602
197. Island JO et al (2014) Ultrahigh photoresponse of few-layer TiS_3 nanoribbon transistors. Adv Opt Mat 2:641–645
198. Island JO et al (2016) Titanium trisulfide (TiS_3): a 2D semiconductor with quasi-1D optical and electronic properties. Sci Rep 6:22214

Chapter 6
Inorganic–Organic Interactions

Tomohiko Okada and Makoto Ogawa

6.1 Introduction

Intercalation of guest species into layered materials is a way of constructing two-dimensionally ordered inorganic–organic molecular or supramolecular or hybrid assembly with unique microstructures controlled by host–guest and guest–guest interactions [1–9]. One of the most unique characteristics of intercalation chemistry is the expansion of the interlayer space upon intercalation of guest species. The expanded interlayer space by the intercalation can be used to immobilize guest species further, since the space was geometrically and chemically modified to accommodate wider variety of guest species. This '*expandable*' 2-dimensional nano-space is useful as a nano-vessel or nano-reaction environment for immobilizing various kinds of molecular functional species.

The properties of intercalation compounds are largely affected by the population (or density or distance between adjacent species) of functional units and some useful functions are emerged only when appropriate population (nanostructure) is achieved. The interactions between host and guest have been investigated based on the structural consideration of resulting intercalation compounds (or interlayer microstructures). The characterization includes X-ray and electron diffraction and composition, chemical bonding between host and guest using vibrational spectroscopy, electronic states of the confined guests by electronic spectroscopy, strength of interactions using thermal analyses (desorption and decomposition), and more directly using advanced microscopies.

T. Okada
Department of Chemistry and Material Engineering, Faculty of Engineering, Shinshu University, Nagano, Japan

M. Ogawa (✉)
School of Energy Science and Engineering, Vidyasirimedhi Institute of Science and Technology (VISTEC), Rayong, Thailand
e-mail: makoto.ogawa@vistec.ac.th

T. Nakato et al. (eds.), *Inorganic Nanosheets and Nanosheet-Based Materials*, Nanostructure Science and Technology, DOI 10.1007/978-4-431-56496-6_6

In the present chapter, we will discuss the possible interactions between host and guest in intercalation compounds.

6.2 Electrostatic Interactions

One of the characteristics of the cation exchange in layered materials is possible guest–guest interactions in the interlayer space, which is due to the density of the cation exchange site and two-dimensional structural regularity. Smectite adsorbs various organic cations by the electrostatic interactions with the permanent negative charge generated by the isomorphous substitution in the silicate layer. The interactions between smectite and organic cations also involve van der Waals interactions between adjacent organic cations and the solvation energy of the cations [8, 9]. Maes et al. [10] pointed out that the charge delocalization of alkylammonium ions affects the affinity toward smectite from the viewpoint of Gibbs free energy. The highly charge-delocalized cations are strongly adsorbed on smectite, and the thermodynamic selectivity order is primary < secondary < tertiary < quaternary alkylammonium ions, because the substitution of H by CH_3 groups in NH_4^+ delocalizes the charge into the CH_3 groups. As to the adsorption of quaternary dialkylammonium ions on a Ca^{2+}-exchanged Camp Berteau montmorillonite, standard Gibbs energy gradually increases when the carbon number in the alkyl chain is higher than 4, indicating stronger adsorption for longer chain alkylammonium. On the contrary, diethylammonium and dibutylammonium ions have same level of affinity toward montmorillonite (Table 6.1). Mizutani et al. [11] reported that solvation energy of organic cations (hydrophobic interactions) determines the cation exchange selectivity for organodiammonium cations. From aqueous solution, larger amount of $CH_2(p\text{-}C_6H_4CH_2N^+(CH_3)_3)_2$ was adsorbed than that of $(CH_2N^+(CH_3)_3)_2$ on a synthetic saponite (Sumecton SA), whereas smaller amount of $CH_2(p\text{-}C_6H_4CH_2N^+(CH_3)_3)_2$ was adsorbed from DMSO or acetonitrile in the competitive adsorption experiments.

Affinity between smectite and alkylammonium relates to the molecular size except for methylammonium and tetra(alkyl)ammonium ions. The longer alkyl chain resulted in larger contribution of van der Waals interactions to the alkylammonium adsorption [12]. The intercalated alkylammonium ions arrange as mono-, bi-, *pseudo*-tri-molecular layers with their alkyl chains parallel to the silicate layers, in addition to the paraffin-type arrangements as schematically shown in Fig. 6.1 [7, 13]. The structures varied depending on the size of the intercalated ions (Fig. 6.1) and the layer charge density (Fig. 6.2). Cation exchange capacity (CEC) directly correlates to the layer charge density. For the determination of the CEC, several techniques have been used: ammonium acetate [14], triethanolamine buffered barium chloride [15–17], calcium chloride [18], methylene blue [19, 20], silver thiourea [21], Cu(II) ethylenediamine [22], and so on. It should be noted that some organic and organometallic cations may be adsorbed over the CEC by van der Waals interactions (intersalation) [23].

Table 6.1 Standard Gibbs energies, enthalpies (kJ/mol), and entropies (e.u./mol) at 298 K and 0.01 total normality for the exchange of Ca Camp Berteau by α,ω-bistrimethylammoniumalkanes (BTM-*n*) cations of different chain length

BTM-*n*	ΔG^{o}_{298}	ΔH^{o}	ΔS^{o}	d_{001} (nm)[a]	
				Dry	Wet
2	–17.26	–14.84	7.44	1.38	1.44
4	–17.26	–14.42	9.53	1.39	1.45
5	–	–13.71	–	1.37	–
6	–19.48	–18.14	4.47		1.42
8	–	–19.65	–	1.38	–
10	–22.20	–20.48	5.77	1.38	1.43

Reprinted from Ref. [10] with permission; copyright 1979, Elsevier
[a]The interlayer distances (d_{001}) for the vacuum-dry and the wet states are given

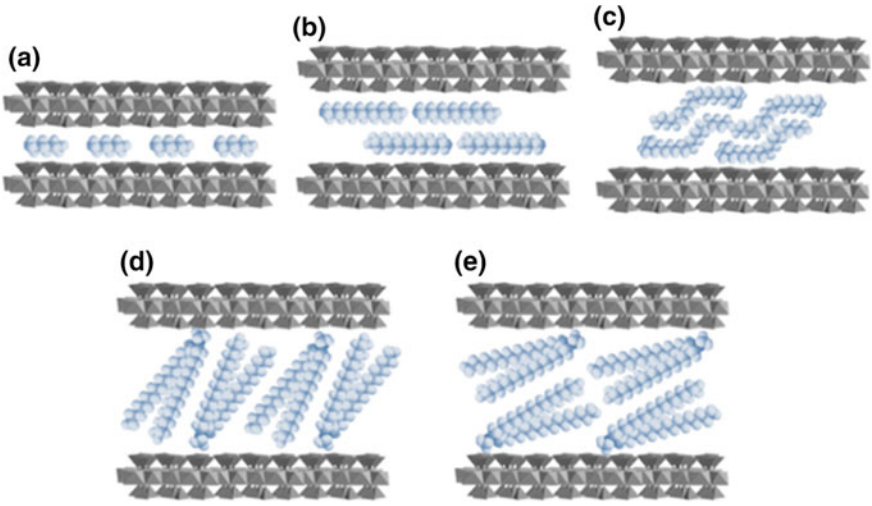

Fig. 6.1 Schematic drawing for the arrangements of the intercalated alkylammonium ions in the interlayer spaces of smectites. **a** monolayer, **b** bilayer, and **c** *pseudo*-trimolecular layer. **d** and **e**, paraffin-type arrangements with mono (**d**) and bilayers (**e**)

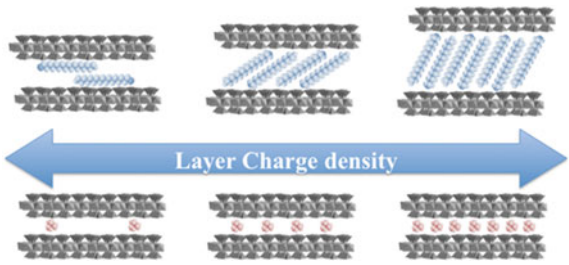

Fig. 6.2 Schematic drawing for the variation in arrangements of the intercalated alkylammonium ions in layered solids depending on the layer charge density

Quantitative exchange of the interlayer cation by alkylammonium ions has been proposed as a method for the determination of their layer charge density [24]. The basal spacing, which corresponds to the inclination of the alkyl chains, should increase with the layer charge of clays (Fig. 6.2). CECs of hectorite (isomorphous substitution of Mg^{2+}-Li^{+} in the octahedral sheet)- and saponite (tetrahedral Si^{4+}-Al^{3+} substitution)-like layered silicates varied by changing the Mg^{2+}/Li^{+} and Si^{4+}/Al^{3+} ratios in the starting mixtures [25], which affected the spatial distribution of cationic guest distribution [26]. Ion exchange of the hectorite-like silicates with dioctadecyldimethylammonium (abbreviated as $2C_{18}2C_2N^{+}$) resulted in paraffin-type arrangements of the intercalated $2C_{18}2C_2N^{+}$ (Fig. 6.1d, e), which was ascribed to the low layer charge density.

Long-chain quaternary alkylammonium ions have been used extensively for the surface modification of bentonite and purified bentonites. After the ion exchange with surfactants, interactions of guest (solvent) with the intercalated surfactant became a dominant driving force for the guest inclusion to expand the interlayer space, giving a term of "organophilic clay" [27, 28]. Molecular modeling and calculation of the surfactant assembly in the interlayer space of bentonites have been reported to predict the packing density, tilt angle, and thermal behavior (melting on heating: Fig. 6.3) [29, 30]. Rheology controlling agents [28, 31] and plastics fillers [32] are well-known examples of applications of organophilic clays. For these applications, the choice of surfactant is one of the most important parameters to determine the affinity with guest species. Accordingly, various surfactant intercalated clay minerals have been investigated and some of them are commercially available [33, 34]. In addition to the selection of surfactant, the choice of bentonite (and the purification) and the amount of the surfactant are

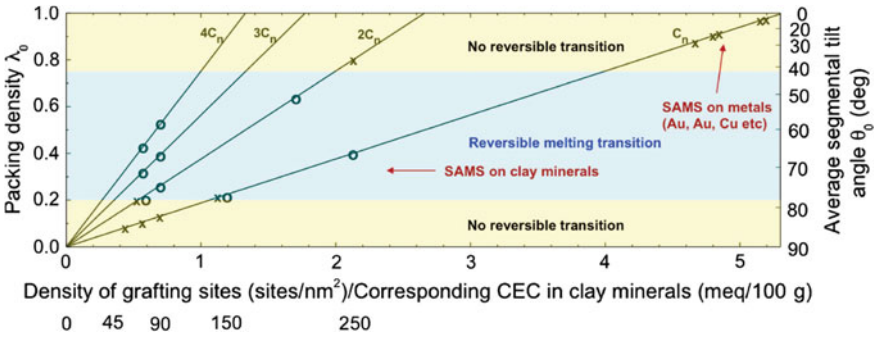

Fig. 6.3 Diagram of packing density, tilt angle, and thermal behavior for a given combination of surfactant and surface. The *four straight lines* indicate the packing density of monoalkylammonium, dialkylammonium, trialkylammonium and tetraalkylammonium surfactants on a clay mineral surface of known cation density (grafting density) or CEC respectively. The occurrence (O) or absence (X) of reversible melting transitions on heating is indicated for data points from laboratory measurements. The prediction also holds for other oxide and metal surfaces, assuming a homogenous distribution of surfactant molecules and a minimum chain length more than C10. Reprinted from Ref. [30b]. Copyright 2008 American Chemical Society

known to affect the properties of the organophilic clays. Purification and classification are possible for bentonite to lead optimized materials performance in the application of organophilic bentonites [35].

The organophilic smectites have been investigated as supports of guest species (both cationic and nonionic), and the states of the guest species are affected by the nanostructures of the organophilic smectites [7, 13, 36–46]. Pyrene is a useful photoluminescence molecule to provide the information on the interlayer nanostructure by the formation of excited state dimer (excimer) even at low concentration. The ratio of excimer to monomer fluorescence intensity is often utilized as a measure of pyrene mobility and proximity. The vibronic fine structure of the pyrene monomer is sensitive to its surrounding polarity. Therefore, the molecule is an ideal probe to investigate the controlled distribution of guest species in the interlayer space of organophilic clays. Intercalation of pyrene into long-chain quaternary alkylammonium-smectites occurred by solid–solid reactions [39], where both species were ground together with a mortar and a pestle at room temperature. Hydrophobic interactions between pyrene and organoammonium ions are thought to be the driving force for the intercalation. Upon solid-state reaction of octadecyltrimethylammonium ($C_{18}3C_1N^+$)-montmorillonite (Kunipia F) and pyrene, a d_{001} diffraction peak at ca. 3.7 nm appeared, and the intensity due to unreacted $C_{18}3C_1N^+$-montmorillonite decreased. On the contrary, the basal spacing of dioctadecyldimethylammonium ($2C_{18}2C_1N^+$)-montmorillonite increased gradually as a function of the added pyrene amount. Pyrene molecules are solubilized at high concentrations, which are not available in solutions due to the solubility limit, in alkylammonium-montmorillonites while retaining the layered structure. In the fluorescence spectra of the pyrene intercalated compounds, monomer fluorescence with vibrational structure was observed together with broad excimer fluorescence. Higher monomer/excimer intensity ratio for the $2C_{18}2C_1N^+$-montmorillonite system than that for the $C_{18}3C_1N^+$-system suggests that the adsorbed pyrene molecules are more isolated in the interlayer space of the $2C_{18}2C_1N^+$-montmorillonite. Similar tendency was observed when other smectite clays were used [13].

It was proposed that these spectral differences are due to different arrangements of the interlayer alkylammonium ions (Fig. 6.1). The intercalated alkylammonium ions arrange as a monolayer (Fig. 6.1a) and a bilayer (Fig. 6.1b) with their alkyl chains parallel to the silicate layers as well as a paraffin-type layers depending on the size of the intercalated ions and the surface layer charge density. The alkylammonium ions in $C_{18}3C_1N^+$-montmorillonite, $C_{18}3C_1N^+$-fluorotetrasilicic mica and $2C_{18}2C_1N^+$-saponite (Sumecton SA) arranged as a *pseudo*-trimolecular layer (Fig. 6.1c), while paraffin-type arrangement in $2C_{18}2C_1N^+$-montmorillonite (Fig. 6.1d, e). Arene molecules in alkylammonium-smectites with a paraffin-type arrangement tend to solubilize molecularly. In other words, one can create various reaction environments by layer charge density and molecular size.

Azobenzene is a photochromic dye, which shows reversible *trans*-to-*cis* photoisomerization by UV irradiation and subsequent visible light irradiation or thermal treatment [47]. Nonionic [40, 48–50] and cationic azobenzenes [51–57] photo-isomerized reversibly in the interlayer spaces of organophilic modified and

non-modified layered silicates, respectively. There are some examples on XRD-detectable nano-structural changes triggered by the photoisomerization. The change in the basal spacings upon the photoirradiation has been observed for organophilic smectite-nonionic azobenzene systems [49, 50]. However, the location of the intercalated azobenzene is difficult to be determined in those systems, since the dyes were solubilized in the hydrophobic interlayer spaces surrounded by alkylchains of the interlayer alkylammonium ions. When a cationic azo dye, *p*-[2-(2-hydroxyethyldimethylammonio)ethoxy]azobenzene, was used, photo-responsible XRD-detectable interlayer structural changes have been observed [56, 58–60]. When excess phenol was added to the intercalation compound, greater changes in the basal spacings were induced upon the photoirradiations [58–60]. The last phenomenon can be useful for possible photoresponsive adsorbents.

The phase transition of dialkyldimethylammonium ($2C_n2C_1N^+$; where *n* denotes the carbon number in the alkyl chain)-silicates has been investigated via temperature dependences of pyrene fluorescence and azobenzene photochromism [36, 49]. $2C_{18}2C_1N^+$- and $2C_{12}2C_1N^+$-bentonite films containing pyrene or 1,3-di(1-pyrenyl) propane have been prepared by casting their suspensions in chloroform on transparent electrodes, and luminescence has been examined at a temperature range from 0 to 75 °C [36]. The relative intensity of the excimer peak increased gradually with increasing temperature, suggesting a lower viscosity at temperatures above the phase transition. The enhanced excimer peak of 1,3-di(1-pyrenyl)propane reflects the increase in the mobility of the alkyl chains. These results are consistent with the increased diffusion rates of solutes in $2C_n2C_1N^+$-clay films above the phase transition temperature [61]. Such phase transition has been known to affect the permeability of luminescent probe molecule as well as catalytic reactivity.

An important aspect of $2C_n2C_1N^+$-clay films is the change in the states of guest species after soaking in water. The probes are initially solubilized in a polar region close to the head groups of the surfactant. This region is thought to be relatively rigid, and this might explain the large microviscosities suggested by the probe. Upon soaking in water, the probe microenvironment slowly becomes less polar and much less viscous, indicating the probe molecule diffused into the part surrounded by alkyl chains.

The introduction of retinal, which is the chromophore of rhodopsin, into a $2C_{18}2C_1N^+$ modified clay was investigated in order to mimic the properties of rhodopsin [62]. The spectroscopic and photochemical properties of retinal in vitro are of interest in studying the primary chemical process of vision and in developing novel photoresponsive materials. The modified clay interlayer offers environments for retinal similar to rhodopsin in two respects; color regulation and efficient isomerization at a cryogenic temperature. Protein environments have the ability to tune the color of retinal Schiff bases; however, the color regulation in artificial systems has not been satisfactory. In rhodopsins, a retinal molecule forms a Schiff base linkage with a lysine residue and the retinal Schiff base is protonated. The *trans–cis* isomerization of a protonated retinal Schiff base occurs even at 77 K as revealed by visible and infrared spectroscopy. The efficient isomerization of retinal at 77 K was worth mentioning as a successful mimic of the primary photochemical reaction in

rhodopsin. We have reported the formation of a protonated retinal Shiff base in montmorillonite without surfactant modification, while it is difficult to explain the variation of the spectral shift depending on the clay type [63].

Cation exchange reactions of smectites with the organic cations that contain aromatic rings have been investigated as basic research concerning (1) removal of contaminants from a viewpoint of environmental purification, (2) enantio-selective adsorption from a viewpoint of "Origin of Life" matter, and (3) organization of cationic dyes for photo- and electrofunctional applications using clay-dye and/or dye–dye interactions.

Because of the increased concern for the presence of pesticides and other organic pollutants in groundwater, smectites have been used [64, 65]. Paraquat (1,1′-dimethyl-4,4′-bipyridinium, methylviologen, MV^{2+}) and diquat (1,1′-ethylene-2,2′-bipyridinium) are most widely studied as a model system of the immobilization of herbicides (cationic pesticides) on smectites [8]. The adsorption isotherms of both herbicides on montmorillonite from aqueous solutions belonged to H-type (high affinity) [66]. The immobilization of paraquat in smectites inhibits the growth of young plants [67]. The localized positive charge on the diquat and paraquat is a possible reason for the strong interactions with the negative charge on the silicate layer, which exists as discrete entities rather than smeared out over the surface [68]. Fluorescence study of methylviologen in a colloidal clay system [69, 70] indicated that there are two adsorption sites for MV^{2+}; one is the external surface in which MV^{2+} retained some internal flexibility and the other is the interlayer surface where the MV^{2+} rigidity bounded.

Yamagishi has shown that optical isomers of Ru and Fe polypyridine and phen (phen=1,10-phenanthroline) chelate complex ions have different adsorption behavior toward smectites [71–74]. When a racemic mixture of $[Fe(phen)_3]^{2+}$ is adsorbed by a clay, the ions are adsorbed as a racemic pair rather than in a random distribution of optical isomers [71]. Enantiomeric $[Fe(phen)_3]^{2+}$ was adsorbed beyond the CEC when the chelate was added in excess over the CEC. The racemic mixture adsorbed in two successive steps: the initial adsorption within CEC and subsequent adsorption beyond CEC. When a tris(phen)metal chelate is placed on a silicate layer with its threefold symmetry axis perpendicular to the surface, the three bottoms of the coordinated phen ligands make a regular triangle with the side length of about 0.65 nm. Because this distance is close to that between the centers of neighboring SiO_4 hexagonal holes (0.55 nm) on a silicate layer, the three hydrogen atoms of the phen ligands buried into the surface. A bound chelate adsorbed up to such a density interacts stereochemically with its neighbors, where a molecule (>0.5 nm) with two positive charges is required to prevent interacting sterically with its neighbors. Motivated by the phenomena on the strict stereochemical restriction, the discussion on the enantio-selective adsorption and reaction using the smectite surfaces has been further conducted [75].

The silicate layers have been known to exhibit redox ability. The interactions of smectites with some aromatic amines gave rise to the formation of colored complexes through electron transfer between silicate layers. The sole feature of benzidine blue reaction is that the reaction involves the transfer of an electron from

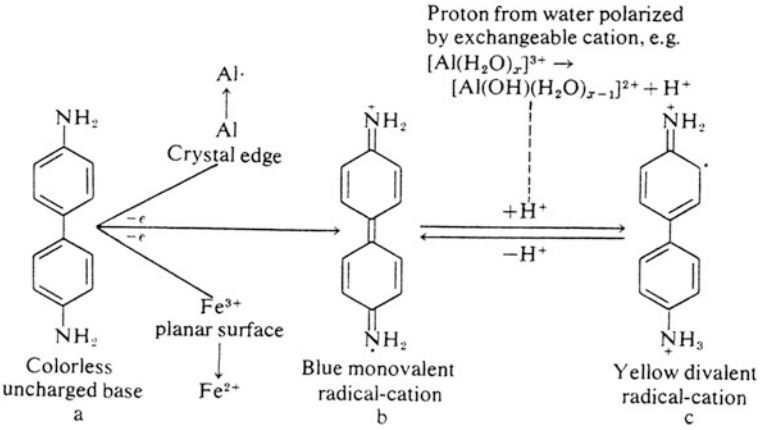

Fig. 6.4 Transformation of benzidine into its colored radical cation forms by clays. Reprinted from Ref. [76] with permission; copyright 1971, The Clay Minerals Society

benzidine to clay to give the blue monovalent radical cation (semiquinone) (Fig. 6.4) [76]. They indicated that conjugation of the unpaired $2p_z$ electron from nitrogen with the π-electron system of the aromatic ring and resonance involving both rings account for the stability and blue color. The divalent radical cation formed under acidic condition (pH < 2) by accepting a proton on the lone pair of electrons of the nitrogen atom. Possible electron acceptor sites are crystal edges of smectites and Fe^{3+} in octahedral sheet. Pretreatment with polyphosphate, which is specifically adsorbed at crystal edges, caused a marked reduction in the color intensity of benzidine-montmorillonite and -hectorite [77]. Iron in octahedral sheet of montmorillonite is also involved in the reaction as shown by ESR measurement [78]. Because of the electron accepting ability of viologens, the electron-transfer reactions between interlayer viologens and some electron donors have been studied. The photoreduction of viologens in smectites by incorporating an electron donor, poly(vinylpyrrolidone) (abbreviated as PVP), was reported [79]. We reported photo-induced reduction of methylviologen dications (MV^{2+}) in smectites, showing the electron-donating ability (Fig. 6.5) [80].

Layered alkali silicates such as octosilicate (SiO_2/Na_2O = 8), magadiite (SiO_2/Na_2O = 14–16), and kenyaite (SiO_2/Na_2O = 20–22) are known to possess cation exchange ability due to the silanol groups existing in the interlayer spaces [81–84]. Because protons of the silanol groups in the interlayer surface are exchanged with alkali ions, the cation exchange capacity is strongly pH dependent [81]; protons compete with other cations at pH < 7 to lead the transformation of into the silicic acid [85]. Because large amounts of the base are required to adjust the pH for the cation exchange with organic cations (pH > 10), competition with alkali ions (e.g., Na^+ and K^+) reduces the amount of exchanged organic cations. Therefore, the reaction is not so easy if compared with that on smectite, and the studies have been limited except for the cation exchanges with alkylammonium ions. It was shown

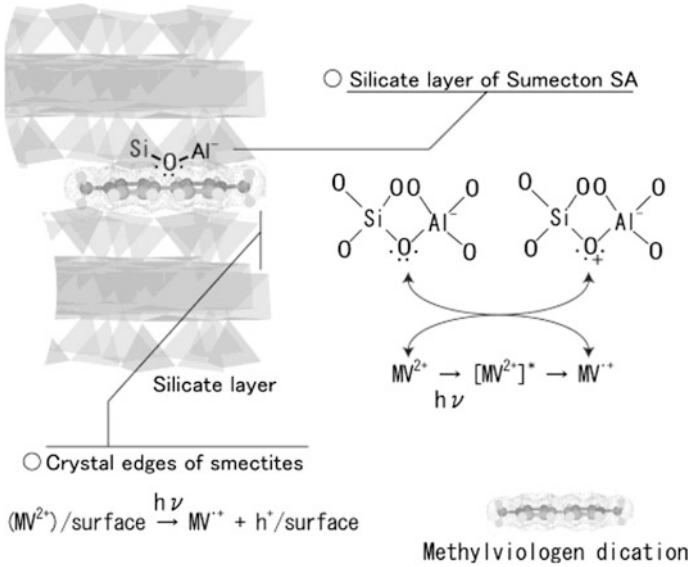

Fig. 6.5 Proposed electron-donating sites in MV^{2+}-smectite (Sumecton SA) system. Reprinted from Ref. [80] with permission; copyright 2003, American Chemical Society

that a crown ether (15-crown-5) interacted with interlayer Na^+ of magadiite to induce $[Ru(bpy)_3]^{2+}$ intercalation, while $[Ru(bpy)_3]^{2+}$ was not exchanged directly with the interlayer Na ions [86]. The intercalation of alkylammonium ions with complex structures into layered silicates has been investigated in order to design hydrophobic nanospace from the viewpoints of the gallery height and the chemical nature. When the cation exchange is quantitative, the gallery height depends on the molecular weight of guest cation (for organoammonium ions) [87].

Cation exchange reactions of layered titanate [88] and layered niobate [89] with long-chain alkylammonium ions have been known as a way to modify the surface property from hydrophobic to hydrophobic. The exchange from $H_2Ti_3O_7$ and $H_2Ti_4O_9{\cdot}H_2O$, which were prepared by HCl treatment of $Na_2Ti_3O_7$ and $K_2Ti_4O_9$, respectively [88], with *n*-alkylammonium ions leads intercalation compounds. However, the alkylammonium intercalation compounds did not form directly from $Na_2Ti_3O_7$ and $K_2Ti_4O_9$. The *n*-propylammonium-intercalated tetratitanic acid has been used as intermediates for constructing photofunctional layered titanate intercalation compounds. Ion exchange reactions of MV^{2+} [90], methylene blue [91], and 5,10,15,20-tetrakis(1-methyl-4-pyridinio)porphyrin [92] with propylammonium was reported in the interlayer space of tetratitanic acid. It was shown that a crown ether (18-crown-6) interacted with interlayer K^+ of a potassium titanate ($K_2Ti_4O_7$) induce $[Ru(bpy)_3]^{2+}$ intercalation, $[Ru(bpy)_3]^{2+}$ was not exchanged directly with the interlayer K ions in the absence of 18-crown-6 [93].

Cation exchange reactions with alkylammonium proceed for layered hexaniobate ($K_4Nb_6O_{17}$) systems similar to the layered alkali silicates (silicic acids) and

titanates (titanic acids) [89], and a unique intercalation behavior for some organic cations has been observed [94–97]. The layered structures are composed of alternating two interlayers with different reactivities; interlayers I (hydrated) and II (not hydrated), which were determined from electron density projections along the *b* axis [98]. It has been thought that selective exchange of K^+ ions in the interlayer II with monovalent cations occurs whereas both mono- and divalent cations can exchange with K^+ in interlayer I, from the observed changes in the basal spacings.

In the MV^{2+}-$K_4Nb_6O_{17}$, intercalation compounds with two different nanostructures were obtained depending on the reaction conditions. In both of the intercalation compounds, MV^{2+} are located only in the interlayer I (Fig. 6.6a) [94]. HNb_3O_8 also gave two different intercalation compounds; one was prepared by the direct reaction with MV^{2+} and the other was obtained using propylammonium-exchanged HNb_3O_8 as an intermediate. In the latter compound, propylammonium and MV^{2+} are located in the same layer (Fig. 6.6b). The MV^{2+} cations accepted electrons from host layers upon photoirradiation. The co-intercalated propylammonium and remained K^+ affected the decay of reduced MV^{2+} cations (the radical form) as exemplified by varying with the photoinactive propylammonium and K^+ amounts in both niobate systems. Intercalation of $[Ru(bpy)_3]^{2+}$ into layered titanate and niobates ($K_4Nb_6O_{17}$, $HTiNbO_5$, $H_2Ti_4O_9$) has been investigated by Nakato et al. [95]. The co-intercalated alkylammonium suppressed the self-quenching of the adsorbed $[Ru(bpy)_3]^{2+}$ to some extent. In aqueous $K_4Nb_6O_{17}$/clay dual-component colloidal system, montmorillonite (Kunipia F) preferentially adsorbed a cationic cyanine dye, showing that the affinity with cationic dye differs depending on the layered solids [97].

Positively charged layer can interact anion through electrostatic interactions. Different from cation exchangeable layered solids, anion exchangeable layered solids are limited. Layered double hydroxides (LDHs) are known anion exchangers [99–105]. LDHs are a class of layered materials consisting of positively charged brucite like layer, where some M^{2+} cations are substituted with M^{3+} cations to give

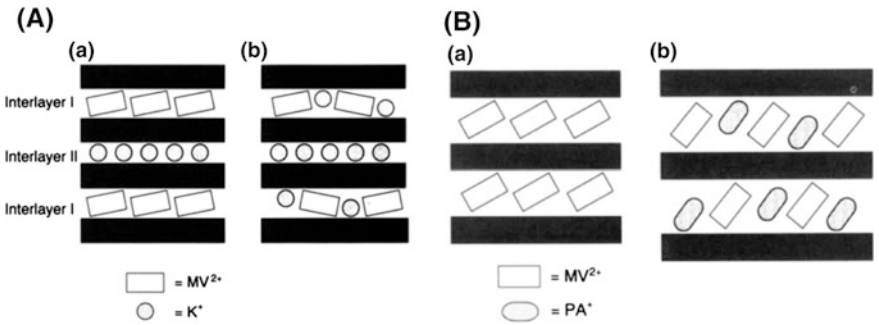

Fig. 6.6 Schematic drawing of the interlayer structure of **A** (*a*) MV^{2+}-$K_2Nb_6O_{17}$, (*b*) MV^{2+}/K-$K_2Nb_6O_{17}$, **B** (*a*) MV^{2+}-HNb_3O_8 and MV^{2+}/propylammonium-HNb_3O_8. Reprinted from Ref. [94]. Copyright 1992 American Chemical Society

positive charge, and the charge compensating interlayer exchangeable anions. Organic anions such as carboxylates, dicarboxylates, benzenecarboxylates, alkylsulfates, alkanesulfonates have been intercalated into LDHs [106, 107]. Since the layer charge density is high, the distance between adjacent anion exchange site is close to induce the interactions between adjacent anions. Thanks to the proximity and controlled orientation, stereo-selective dimerization of cinnamate has been reported so far [108, 109]. In addition to the antiparallel packing of the guest, the intermolecular distances of two double bonds of adjacent carboxylates were found to affect the stereoselectivity of the photochemical cycloaddition (Fig. 6.7). By UV irradiation, cinnamate yielded head-to-head dimers exclusively (Fig. 6.8a), while stilbenecaroboxylates gave a significant amount of head-to-tail dimer in addition to a head-to-head dimer (Fig. 6.8b). This difference was explained by molecular packing of the anions in the interlayer space of LDH. Similar to the dilution effects of organoammonium ions on the photochemistry of stilbazolium ions in smectite, the addition of sodium *p*-phenethylbenzoate, a photochemically inactive coadsorbate, affected the product distribution in the photolysis of *p*-(2-phenylethenyl) benzoate intercalated in hydrotalcite [109].

LDHs also produce hydrophobic environments by intercalating long-chain alkyl carboxylates and sulfates [101, 106, 110]. The alkanesulfonates ($C_nH_{2n+1}SO_3^-$, n = 5–9) were intercalated competitively into Mg/Al–Cl-typed LDH (Mg/Al = 2), where the anion exchange was employed under reflux and nitrogen atmosphere [111]. The intercalated alkanesulfonates were packed as paraffin-type arrangement irrespective of the alkyl-chain length (Fig. 6.9) [106, 111]. When two sulfonate anions with the difference by only one methylene group were added, their simultaneous intercalation results in a single uniform LDH phase, in which the interlayer space varies linearly with the ratio between the two anions [111].

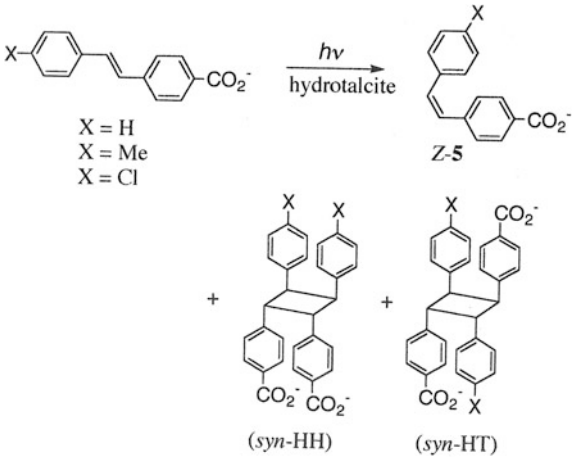

Fig. 6.7 Photochemical reaction paths of stilbenecarboxylates

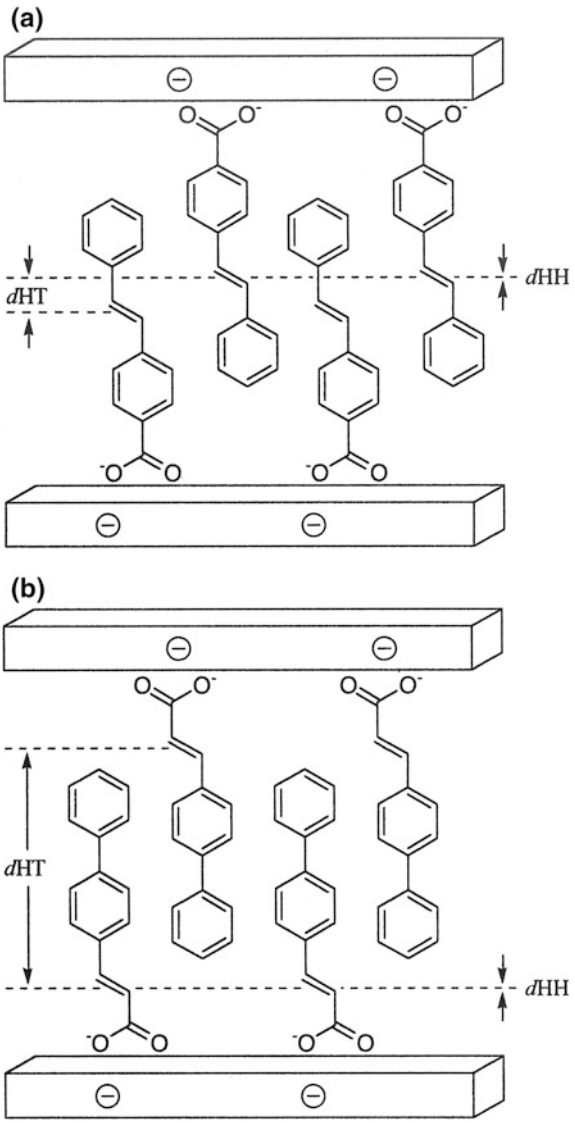

Fig. 6.8 Simplified drawing of antiparallel packing of **a** *p*-phenyl-cinnamate and **b** stilbene carboxylate ions in LDH

6.3 Other Driving Forces for the Intercalation

Layered solids adsorb polar organic molecules, and among them, smectites are well-known adsorbents for various polar molecules. Polar molecules such as alcohols, ketones, and amide are adsorbed by ion–dipole interactions with the interlayer cations and/or hydrogen bonding with the surface oxygen atom of the silicate layers. The intercalation of polar molecules usually occurs through

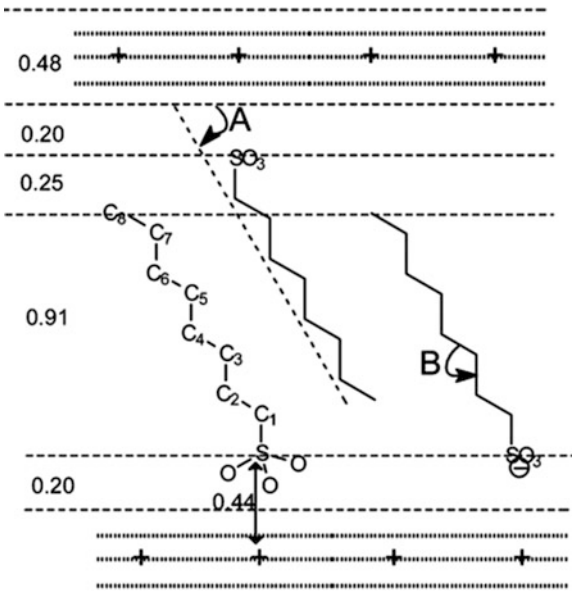

Fig. 6.9 Proposed packing mode of the alkanesulfonates (C = 8) anions in the interlayer space of Mg/Al-LDH (Mg/Al = 2); unit is nm. Reprinted from Ref. [111]. Copyright 2007 American Chemical Society

solid–liquid or solid–gas reactions [1, 7, 8, 112, 113], while solid–solid reactions are also possible [114, 115].

In a smectite–polar molecule interactions in the solid-state, novel selectivity, which is not observed in the intercalation from solution [115], was observed. Maleic acid was intercalated into montmorillonite by solid–solid reactions, while its geometrical isomer, fumaric acid was not intercalated. From ethanolic solutions, both maleic and fumaric acids were intercalated. Such selectivity observed only in the solid–solid reaction was explained by the difference in the crystal structure of the molecules in addition to the ability of maleic acid to form a chelate like structure with the interlayer cations. In the solid-state reactions, chelation of 2,2′-bipyridine to Co(II) occurred in montmorillonite stoichiometrically, forming tris(2,2′-bipyridine)cobalt(II) complexes [116]. Fluorescent complexes formed as a result of coordination of 8-hydroxyquinoline to Li(I), Zn(II), and Mn(II)-montmorillonites through solid–solid reactions [117]. Two kinds of ligands (8-hydroxyquinoline and 4,4′-bipyridine) were co-intercalated into Zn(II)-montmorillonite, giving coordination polymers of mixed-ligand Zn complexes [118].

Benzene and phenols were intercalated through charge-transfer interactions with Cu(II)—[119, 120] and MV^{2+}—[121, 122] intercalated smectites, and they usually form colored electron donor–acceptor complexes.

Covalent bonding is also definitive interactions for the intercalation, and that is useful for the introduction of organic functionality into the interlayer space. Reactions between layered silicates and silane coupling agents become possible after the pioneering work by Ruiz-Hitzky and Rojo [123] and studies on this topic have been summarized in recent reviews [124, 125]. Several examples on facilitating uptakes of

metal cations [126–128] and organic molecules [129–135] have been reported through the surface coverage. Introduction of trimethylsilyl groups into a layered silicate (kanemite) led to effective benzene adsorption by weakening the interaction between the interlayer hydrogen bonds of the surface hydroxyl groups [129]. Distance between adjacent organic groups has been controlled by covalent attachment of octylsilyl groups to a layered silicate, magadiite [130–133]. Alkylalcohols were intercalated into the organic derivatives modified with controlled amounts of octylsilyl groups, while alkanes were not intercalated [130]. Larger amounts of alklyalcohols were intercalated into the derivatives with lower surface coverage of octylsilyl group. These results have been explained as the cooperative effect of the geometry and the chemical nature of the surface covered with octyl groups and silanol groups. By using covalently attachments, the cooperative effect was observed when two functional units (octadecyl and phenyl groups) were arranged in an interlayer space of a layered lithium potassium titanate ($K_{0.8}Ti_{1.73}Li_{0.27}O_4$) [134] and a layered alkali silicate (octosilicate) [135] to give the selective binding of 4-nonylphenol from the mixtures of *n*-nonane, phenol, and 4-nonylphenol in water (Fig. 6.10).

For immobilizing and shape-controlling metal nanoparticles, thiol-bearing organoammonium and silane coupling reagent have been utilized for immobilization of gold nanoparticles into the interlayer space of a layered alkali silicate and titanate [136–138]. Disk-shaped nanoparticles formed owing to densely attached 3-(mercaptopropyl)trimethoxysilyl groups in the titanate, and the hybrid showed efficient and selective photocatalytic oxidation of benzene to phenol in water under visible light irradiation ($\lambda > 420$ nm) when the reaction was performed conducted in the presence of additional phenol [138].

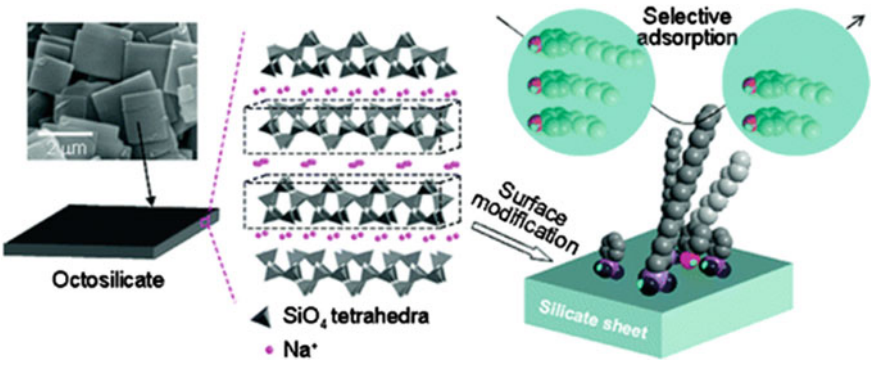

Fig. 6.10 Schematic representation of interlayer modification of octosilicate with octadecyl and phenyl groups using covalently attaching. Reprinted from Ref. [135]. Copyright 2011 American Chemical Society

6.4 Guest–Guest Interactions

Guest–guest interactions may affect distribution of guest species (distance between adjacent guest, and spatial density of guests) in the interlayer space of layered solids. The covalent attachment of functional units by silylation to the silicates and the titanates, as descried above, has been a useful method for the spatially controlled distribution [139]. However, in organic cations-smectite systems, segregation phenomena are often observed, as schematically shown in Fig. 6.11, and the segregation makes it difficult to be homogeneity of the guest distribution. When a cationic surfactant was intercalated into a synthetic Na^+-fluorohectorite (produced by Corning Inc.), the distribution of surfactant and Na^+ was different depending on the size of head group of the surfactant [140]. Trimethyl(octadecyl)ammonium and Na^+ co-existed in the same interlayer when the added amount of trimethyl(octadecyl)ammonium was 50% of the CEC. On the contrary, tributhyl(hexadecyl) phosphonium cation, which requires surface area for the head group larger than trimethyl group, was segregated from exchangeable Na ions.

Ghosh and Bard reported that smectite interlayer segregates tris(2,2′-bipyridine) ruthenium(II) (abbreviated as $[Ru(bpy)_3]^{2+}$) from exchangeable Na ions, resulting in high local concentration of the complex ions in the interlayer space even when the added concentration of $[Ru(bpy)_3]^{2+}$ is only 1–2% of the cation exchange capacity (CEC) of Wyoming bentonite. Although $[Ru(bpy)_3]^{2+}$ is a good electron donor, MV^{2+} does not quench the excited state of $[Ru(bpy)_3]^{2+}$ in the interlayer due to the segregation phenomena, where MV^{2+} cations located in different region from the $[Ru(bpy)_3]^{2+}$ [141]. In addition to the guest–guest interactions, charge heterogeneity may also involve the segregation and random interstratification. A fluorohectorite with homogeneous charge distribution has been obtained from

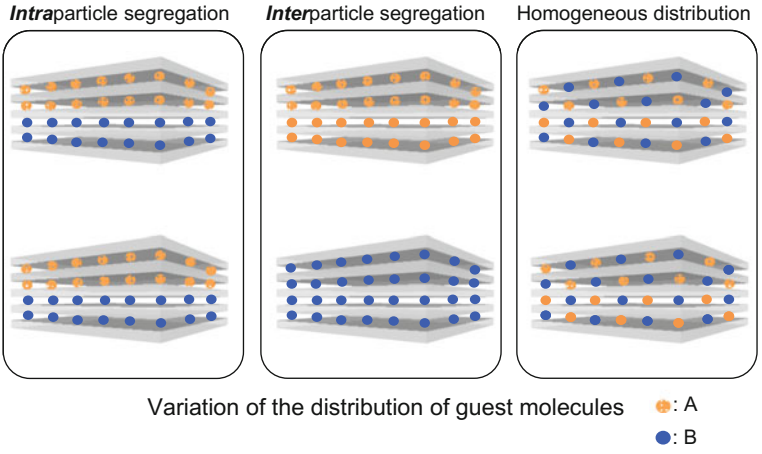

Fig. 6.11 Schematic drawing of segregated or homogeneously distributed two kinds of cations in smectite

melt syntheses [142], and the homogeneity of the cationic species has been reported [143].

Co-intercalation of a water-soluble polymer including PVP plays a role in controlling the state and the spatial distribution of cationic dyes on smectites [79, 144–148]. The $[Ru(bpy)_3]^{2+}$-TSM-PVP intercalation compound (TSM: fluorte-trasilisic mica) have been prepared with varied amounts of $[Ru(bpy)_3]^{2+}$ by cation exchange [144, 146]. When $[Ru(bpy)_3]^{2+}$ was intercalated in TSM without PVP, the diffraction peaks split into two, indicating segregation. On the other hand, $[Ru(bpy)_3]^{2+}$ was isolated effectively by PVP to suppress self-quenching even at high concentration loading. It was suggested that co-intercalated PVP was forced to surround $[Ru(bpy)_3]^{2+}$ in close contact in the sterically limited interlayer spaces.

Electron-transfer quenching of $[Ru(bpy)_3]^{2+}$ by MV^{2+} in aqueous suspension of clays (Sumecton SA, Laponite XLG, and ME-100) in the presence of PVP was also investigated (Fig. 6.12) [146]. It has been known that MV^{2+} strongly interacts with clay surfaces [65, 149, 150] and does not quench the excited state of $[Ru(bpy)_3]^{2+}$ on clay due to segregation. On the contrary, the co-adsorption of PVP on clay resulted in the co-adsorption of $[Ru(bpy)_3]^{2+}$ and MV^{2+} without segregation as shown by the efficient electron-transfer quenching of the photo-excited $[Ru(bpy)_3]^{2+}$ by MV^{2+}, indicating the homogeneous distribution of the adsorbed dyes.

The controlled expansion of the interlayer space (design the size of two-dimensional nanospace) was achieved by changing PVP amount on synthetic saponite (Sumecton SA) [148]. PVP was intercalated into Rhodamine 6G-Sumecton SA (0.1–1% of the CEC: 0.71 meq./g) to investigate how the interlayer expansion affects the photo-induced event in the interlayer space. The interlayer expansion of Rhodamine 6G-clay increased linearly when PVP/clay

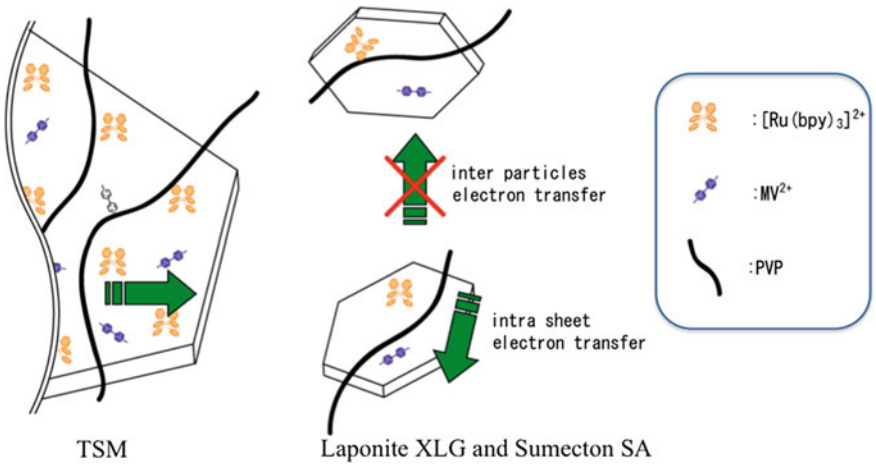

Fig. 6.12 Schematic drawing of the spatial arrangement of $[Ru(bpy)_3]^{2+}$, MV^{2+}, and PVP on clays in aqueous suspension. Reprinted from Ref. [146]. Copyright 2004 American Chemical Society

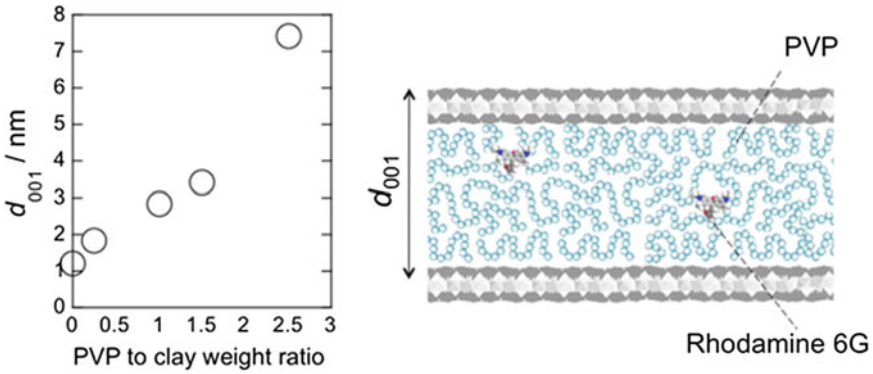

Fig. 6.13 The relationship between the weight ratio of PVP to Sumecton SA (SA) and the basal spacing (d_{001}) in a Rhodamine 6G(R6G)-PVP-SA system

weight ratio was lower than 3 (Fig. 6.13, left). The luminescence self-quenching efficiency varied depending upon the expansion of the interlayer space due to the varied distance between the adjacent Rhodamine 6G (the distance correlated to the possibility of self-quenching).

If compared with the modification with organoammonium ions, the polymer intercalation has advantages; the interlayer expansion can be controlled by the amount of polymer; for the organoammonium case, the amount cannot be used to control the expansion due to the segregation. In order to control the interlayer expansion, clays with different layer charge density [24–26, 151–155] or alkylammonium ions with different molecular structures should be used. These may bring other factors such as different levels of impurity and variation of the particle size to affect the photoprocesses of the adsorbed species. The interactions of polymers with varied molecular weight, branched structure, and modification is worth investigating to vary structure and property.

The spatial distribution of organic species in the interlayer spaces is an important parameter as seen by the efficient photo-induced energy transfer, which was achieved by the controlled distance between adjacent photoactive species on the clay surface [156, 157]. Takagi and co-workers empirically suggested from steady state and time-resolved fluorescence spectroscopy that segregation behavior sensitively depends on the structure of the dye [150]. It became possible to construct efficient electron-transfer systems on the smectite clay surface [157] as shown by the fluorescence quenching behavior due to electron-transfer reaction between excited singlet cationic porphyrins and a viologen (1′,1-bis(2,4-dinitrophenyl)-4′,4-bipyridinium) on a smectite (Sumecton SA) surface. Selection of organic cations prevented dye from aggregation ("size-matching rule") [158–160] that made photochemical behavior systematically controlled. They have proposed variation in segregated dye distribution depending on the cationic porphyrin used (Fig. 6.14).

As indicated by the above section, multi-point interactions between adsorbate and adsorbent should contribute to the selective adsorption (binding) of target

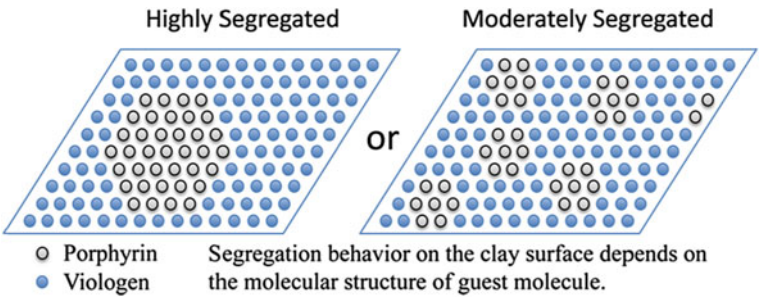

Fig. 6.14 Distribution images of the clay-porphyrin-viologen system. (*left*) highly segregated type for tetrakis(1-methylpyridinium-4-yl) porphyrin and (*right*) moderately segregated type for zinc tetrakis(trimethylanilinium-4-yl) porphyrin. Reprinted from Ref. [150]. Copyright 2014 American Chemical Society

molecules as is usually seen in natural and artificial molecular recognition systems [130, 134, 135]. Interlayer expansion (swelling) occurred when larger amount of organic molecules was intercalated into an organically modified layered silicate [130, 132]. Fukushima and Inagaki [161] pointed out the swelling by polymerization to 6-polyamide in the interlayer space of montmorillonite as a result of a balance between the interlayer cohesive force (attractive force including van der Waals or electrostatic interaction) and the force required to swell. The latter force would be attractive one between interlayer cations and ε-caprolactam, depending on the strength of the electric field around the interlayer cations. Strong guest–guest interactions including acid–base, electrostatic interactions, and covalent bonding should make a contribution to cause the interlayer expansion triggered by the post-intercalation of organic molecules. Sulfonic acid group attached to octosilicate [162] has been shown to act as adsorption sites of *n*-dodecylamine and quaternary alkylammonium ions via acid–base and electrostatic interactions, respectively, to expand the interlayer space (Fig. 6.15) [163]. Covalent attachments of polymerizable groups are meaningful to combine nanosheet to polymer in polymer-clay nanocomposite (poly(methylmethacrylate) [164] and epoxy resin [165]). Metal–thiol interactions are also strong attractive force; thiol groups in the interlayer space have participated the formation and the immobilization of metal nanoparticles with the morphology defined by the two-dimensional nanospace [136]. Thus, sequential extension of host–guest system design by guest A, guest B, guest C, interactions, novel interlayer architectures is expected.

Though the pore is not expandable, the designable pore size of mesoporous materials has been utilized as host of various kinds of molecular species [2, 166–168]. Owing to their nanospace in the range of several nm and large pore volume, bulky organic species have been confined by using specific interactions. In order to utilize one-dimensional nanospace (channel) with possible interconnection for a wider variety of host–guest architectures, the interactions between mesopore surface (siloxane and silanol) and guest play dominant roles. Accordingly, the sequential

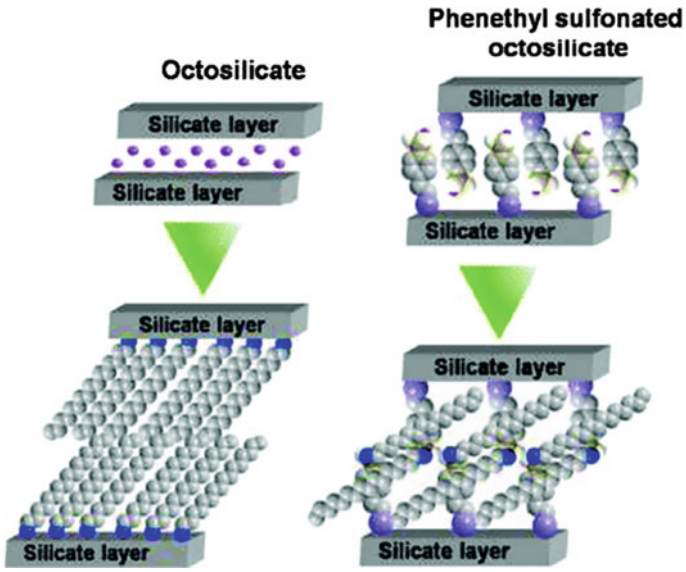

Fig. 6.15 Schematic drawing of *n*-dodecylamine intercalation into the interlayer space of (*left*) pristine octosilicate and (*right*) phenethyl sulfonated octosilicate. Reprinted from Ref. [163]. Copyright 2012 American Chemical Society

reactions to extend host–guest systems have been reported; for example, $[Ru(bpy)_3]^{2+}$ was dispersed molecularly via electrostatic interactions with sulfonic groups covalently attached on the pore of mesoporous silicas [169, 170]. Not only the electrostatic interactions, such interactions as hydrogen bonding and hydrophobic interactions are also included in the host–guest interactions and the structures are determined through cooperative effects. The comparison of the expandable two-dimensional nanospace of layered solids discussed in the present chapter and the fixed (but designable) nanospace of mesoporous silica as the hosts [167, 168] is worth discussing. Multi-points and hetero host–guest interactions in a material need complicated multi-step syntheses and careful characterization, while it is a direction to make host–guest systems more sophisticated and artistic.

6.5 Summary and Future Perspectives

Interactions between inorganic layered materials with organic guest species have been discussed with the emphasis on the structural consideration of the resulting intercalation compounds (organic guest intercalated into the two-dimensional interlayer nanospace). The interactions between exfoliated nanosheets (or for exfoliation) and polymers are another important phenomena to be discussed in Chap. 7 by Professor Yoshiaki Fukushima, who is the pioneer of the clay

nanoplatelets reinforcements into polymers. Besides the main driving forces for the intercalation (electrostatic interactions between oppositely charged inorganic and organic species, redox reactions, ion–dipole interactions and coordination between organic molecules with the interlayer cations, hydrogen bonding), the interactions between the guest species can concern the intercalation reaction and to determine the nanostructures and the properties of the resulting intercalation compounds. Thanks to the careful and systematic design of the layer charge density and distribution, the intercalation chemistry became more sophisticated at nanometer-level architecture. The molecular design of the guest molecules and the extended variation of host–guest systems made the materials more versatile and useful. In addition to the chemical approaches for the host–guest systems, the developments of new characterization tools and skills, and the progress in the purification and processing for practical applications, have continuously been done in both scientific fields and industry. For the huge variety of present and potential applications, the inorganic–organic interactions in various host–guest systems [166] should be examined further and the designed interface will play important role for the materials design for future [167, 168].

References

1. Bergaya F, Theng BKG, Lagaly G (eds) (2006) Handbook of clay science. Elsevier Science, Amsterdam
2. Ruiz-Hitzky E, Aranda P, Darder M, Ogawa M (2011) Hybrid and biohybrid silicate based materials: molecular vs. blockassembling bottom–up processes. Chem Soc Rev 40:801
3. Alberti G, Bein T (eds) (1996) Comprehensive supramolecular chemistry. vol 7. Pergamon, Oxford
4. Auerbach SM, Carrado KA, Dutta PK (eds) (2004) Handbook of layered materials. Marcel Dekker
5. Thomas JK (1988) Acc Chem Res 21:275
6. Ogawa M, Kuroda K (1995) Chem Rev 95:399
7. Ogawa M, Kuroda K (1997) Bull Chem Soc Jpn 70:2593
8. Theng BKG (1974) The chemistry of clay-organic reactions. Adam Hilger, London
9. van Olphen H (1977) An introduction to clay colloid chemistry, 2nd edn. Wiley-Interscience, New York
10. Maes A, van Leemput L, Cremers A, Uytterhoeven J (1980) J Colloid Interface Sci 77:14
11. Mizutani T, Takano T, Ogoshi H (1995) Langmuir 11:880
12. Theng BKG, Greenland DJ, Quirk JP (1967) Clay Miner 7:1
13. Ogawa M, Wada T, Kuroda K (1995) Langmuir 11:4598
14. Lewis DR (1949) Analytical data on reference clay materials. In sect. 3, base-exchange data. american petroleum institute project 49 clay mineral standards, preliminary report no. 7, Columbia University, New York, p 91
15. Mehlich A (1948) Soil Sci 66:429
16. Bascomb CL (1964) J Sci Food Agric 15:821
17. Dohrmann R (2006) Appl Clay Sci 34:31
18. Ogawa M, Nagafusa Y, Kuroda K, Kato C (1992) Appl Clay Sci 7:291
19. Hang PT, Brindley GW (1970) Clays Clay Miner 10:203
20. ASTM C 837-09 (2014) Standard test methods of methylene blue index of clay. Am Soc Test Mater

21. Dohrmann R (2006) Appl Clay Sci 34:38
22. Bergaya F, Vayer M (1997) Appl Clay Sci 12:275
23. (a) Grim RE, Allaway WH, Cuthbert FL (1947) J Am Ceram Soc 30:137 (b) Traynor MF, Mortland MM, Pinnavaia TJ (1978) Clays Clay Miner 26:318
24. Mermut AR (1994) CMS workshop lectures vol. 6, Layer charge characteristics of 2:1 silicate clay minerals. Clay Minerals Society, Aurora, USA
25. Ogawa M, Matsutomo T, Okada T (2008) J Ceram Soc Jpn 116:1309
26. Egawa T, Watanabe H, Fujimura T, Ishida Y, Yamato M, Masui D, Shimada T, Tachibana H, Yoshida H, Inoue H, Takagi S (2011) Langmuir 27:10722
27. Jordan JW (1950) J Phys Colloid Chem 54:294
28. Lagaly G (1981) Clay Miner 16:1
29. Cygan RT, Greathouse JA, Heinz H, Kalinichev AG (2009) J Mater Chem 19:2470
30. (a) Heinz H (2012) Clay Miner 47:205 (b) Heinz H, Vaia RA, Farmer BL (2008) Langmuir 24:3727
31. Jones TR (1983) Clay Miner 18:399
32. Pinnavaia TJ, Beall GW (eds) (2001) Polymer-clay nanocomposites. John Wiley & Sons Ltd., New York
33. Cloisite (http://www.byk.com/en/additives/additives-by-name/cloisite.php)
34. HOJUN Organophilic bentonite (http://www.hojun.co.jp/eng/e29_f_chemicals_no.html)
35. Hayakawa T, Minase M, Fujita K, Ogawa M (2016) Clays Clay Miner 64:275
36. Ahmadi M, Rusling J (1995) Langmuir 11:94
37. Seki T, Ichimura K (1990) Macromolecules 23:31
38. Ogawa M, Shirai H, Kuroda K, Kato C (1992) Clays Clay Miner 40:485
39. Ogawa M, Aono T, Kuroda K, Kato C (1993) Langmuir 9:1529
40. Ogawa M, Kimura H, Kuroda K, Kato C (1996) Clay Sci 10:57
41. Kakegawa N, Ogawa M (2002) Appl Clay Sci 22:137
42. Rusling JF (1991) Acc Chem Res 24:75
43. Sasai R, Sugiyama D, Takahashi S, Tong Z, Shichi T, Itoh H, Takagi K (2003) Photochem Photobiol A 155:223
44. Nagase T, Takahasi Y, Suzuki TM, Ebina T, Wakui Y, Onodera Y (2002) Chem Lett 776
45. Kinashi K, Kida H, Misaki M, Koshiba Y, Ishida K, Ueda Y, Ishihara M (2009) Thin Solid Films 518:651
46. Fujii K, Kuroda T, Sakoda K, Iyi N (2011) J Photochem Photobiol A 225:125
47. H. Rau (1990) Studies in organic chemistry: photochromism, molecules and systems. vol 40. In: Dürr H, Bouas-Laurent H (eds) Elsevier, Amsterdam, pp 165–192
48. Ogawa M, Hama M, Kuroda K (1999) Clay Miner 34:213
49. Ogawa M, Fujii K, Kuroda K, Kato C (1992) Mater Res Soc Symp Proc 233:89
50. Fujita T, Iyi N, Klapyta Z (1998) Mater Res Bull 33:1693
51. Ogawa M (1996) Chem Mater 8:1347
52. Ogawa M, Yamamoto M, Kuroda K (2001) Clay Miner 36:263
53. Iyi N, Fujita T, Yelamaggad CV, Arbeloa FL (2001) Appl Clay Sci 19:47
54. Ogawa M, Ishikawa A (1998) J Mater Chem 8:463
55. Ogawa M, Goto R, Kakegawa N (2000) Clay Sci 11:231
56. Ogawa M, Ishii T, Miyamoto N, Kuroda K (2001) Adv Mater 13:1107
57. Ogawa M, Ishii T, Miyamoto N, Kuroda K (2003) Appl Clay Sci 22:179
58. Okada T, Watanabe Y, Ogawa M (2004) Chem Commun 320
59. Okada T, Watanabe Y, Ogawa M (2005) J Mater Chem 15:987
60. Okada T, Sakai H, Ogawa M (2008) Appl Clay Sci 40:187
61. Okahata Y, Shimizu A (1989) Langmuir 5:954
62. Kandori H, Ishioka T, Sasaki M (2002) Chem Phys Lett 354:251
63. Furutani Y, Ido K, Sasaki M, Ogawa M, Kandori H (2007) Angew Chem Int Ed 46:8010
64. Nir S, Polubesova T, Serban C, Rytwo G, Undaheytia T (2002) Adsorption of organic cations on clays: experimental results and modeling. In: Yariv S, Cross H (eds) Organo-clay complexes and interactions, pp 193–222. Marcel Dekker, New York

65. Rytwo G, Nir S, Margulies L (1996) J Colloid Interface Sci 181:551
66. Weber JB, Perry PW, Upchurch RP (1965) Soil Sci Soc Proc 29:678
67. Weber JB, Scott DC (1966) Science 152:1400
68. Weed SB, Weber JB (1968) Am Miner 53:478
69. Villemure G, Detellier C, Szabo AG (1986) J Am Chem Soc 108:4658
70. Villemure G, Detellier C, Szabo AG (1991) Langmuir 7:1215
71. Yamagishi A, Soma M (1981) J Am Chem Soc 103:4640
72. Yamagishi A (1985) J Am Chem Soc 107:732
73. Yamagishi A (1983) J Chromatogr A 262:41
74. Yamagishi A (1985) J Chromatogr A 319:299
75. Yamagishi A, Sato H (2012) Clays Clay Miner 60:411
76. Theng BKG (1971) Clays Clay Miner 19:383
77. Michaels AS (1958) Ind Eng Chem 50:951
78. Solomon DH, Loft BC, Swift JD (1968) Clay Miner 7:389
79. Miyata H, Sugahara Y, Kuroda K, Kato C (1987) J Chem Soc Faraday Trans 1(83):1851
80. Kakegawa N, Kondo T, Ogawa M (2003) Langmuir 19:3578
81. Lagaly G (1979) Adv Colloid Interface Sci 11:105
82. Lagaly G, Beneke K, Weiss A (1975) Am Mineral 60:650
83. Beneke K, Lagaly G (1977) Am Miner 62:763
84. Schwieger W, Lagaly G (2004) Alkali silicates and crystalline silicic acids. In: Auerbach SM, Carrado KA, Dutta PK (eds) Handbook of layered materials, Marcel Dekker, New York, pp 541–629
85. Lagaly G, Beneke K, Weiss A (1975) Am Miner 60:642
86. Ogawa M, Takizawa Y (1999) J Phys Chem B 103:5005
87. Ogawa M, Iwata D (2010) Cryst Growth Des 10:2068
88. Izawa H, Kikkawa S, Koizumi M (1983) Polyhedron 2:741
89. Lagaly G, Beneke K (1976) J Inorg Nucl Chem 38:1513
90. Miyata H, Sugahara Y, Kuroda K, Kato C (1988) J Chem Soc Faraday Trans 1:2677
91. Nakato T, Iwata Y, Kuroda K, Kato C (1992) J. Inclusion Phenom Mol Recog 13:249
92. Nakato T, Iwata Y, Kuroda K, Kaneko M, Kato C (1993) J Chem Soc Dalton Trans 1405
93. Ogawa M, Takizawa Y (1999) Chem Mater 11:30
94. Nakato T, Kuroda K, Kato C (1992) Chem Mater 4:128
95. (a) Nakato T, Sakamoto D, Kuroda K, Kato C (1992) Bull Chem Soc Jpn 65:322 (b) Nakato T, Kusunoki K, Yoshizawa K, Kuroda K, Kaneko M (1995) J Phys Chem 99:17896
96. Tong Z, Shichi T, Kasuga Y, Takagi K (2002) Chem Lett 1206
97. Miyamoto N, Nakato T (2003) Langmuir 19:8057
98. Kinomura N, Kumada N, Muto F (1985) J Chem Soc Dalton Trans 2349
99. Reichle WT (1986) Solid States Ionics 22:135
100. Miyata S (1983) Clays Clay Miner 31:305
101. Yamaoka T, Abe M, Tsuji M (1989) Mater Res Bull 24:1183
102. Iyi N, Sasaki T (2008) J Colloid Interface Sci 322:237
103. Ogawa M, Inomata K (2011) Clay Sci 15:131
104. Li F, Duan X (2006) In: Duan X, Evans DG (eds) Applications of layered double hydroxides. Layered double hydroxides. Springer, Heidelberg
105. Rives V, Ulibarri MA (1999) Coord Chem Rev 181:61
106. Meyn M, Beneke K, Lagaly G (1990) Inorg Chem 29:5201
107. Newman SP, Jones W (1998) New J Chem 22:105
108. Takagi K, Shichi T, Usami H, Sawaki Y (1993) J Am Chem Soc 115:4339
109. Shichi T, Takagi K, Sawaki Y (1996) Chem Commun 2027
110. Morioka S, Tagaya H, Karasu M, Kadokawa J, Chiba K (1995) J Solid State Chem 117:337
111. Xu ZP, Braterman PS (2007) J Phys Chem C 111:4021
112. Okada T, Ide Y Ogawa M (2012) Chem Asian J 7:1980
113. Okada T, Seki Y, Ogawa M (2014) J Nanosci Nanotech 14:2121

114. Ogawa M, Kuroda K, Kato C (1989) Chem Lett 18:1659
115. Ogawa M, Hirata K, Kuroda K, Kato C (1992) Chem Lett 21:365
116. Ogawa M, Hashizume T, Kuroda K, Kato C (1991) Inorg Chem 30:584
117. Khaorapapong N, Ogawa M (2007) Appl Clay Sci 35:31
118. Pimchan P, Khaorapapong N, Sohmiya M, Ogawa M (2014) Appl Clay Sci 95:310
119. Doner HE, Mortland MM (1969) Science 166:1406
120. Pinnavaia TJ, Mortland MM (1971) J Phys Chem 75:3957
121. Okada T, Ogawa M (2002) Chem Lett 812
122. Okada T, Ogawa M (2003) Chem Commun 1378
123. Ruiz-Hitzky E, Rojo JM (1980) Nature 287:28
124. Takahashi N, Kuroda K (2011) J Mater Chem 21:14336
125. Ide Y, Sadakane M, Sano T, Ogawa M (2014) J Nanosci Nanotech 14:2135
126. Ruiz VSO, Petrucelli GC, Airoldi C (2006) J Mater Chem 16:2338
127. Macedo TR, Airoldi C (2009) Dalton Trans 7402
128. Macedo TR, Airoldi C (2009) New J Chem 33:2081
129. Toriya S, Kobayashi S, Takei T, Fuji M, Watanabe T, Chikazawa M (2003) Colloid Polym Sci 281:1121
130. Ogawa M, Okutomo S, Kuroda K (1998) J Am Chem Soc 120:7361
131. Okutomo S, Kuroda K, Ogawa N (1999) Appl Clay Sci 15:253
132. Fujita I, Kuroda K, Ogawa M (2003) Chem Mater 15:3134
133. Fujita I, Kuroda K, Ogawa M (2005) Chem Mater 17:3717
134. Ide Y, Ogawa M (2007) Angew Chem Int Ed 46:8449
135. Ide Y, Iwasaki S, Ogawa M (2011) Langmuir 27:2522
136. Ide Y, Fukuoka A, Ogawa M (2007) Chem Mater 19:964
137. Ide Y, Nakasato Y, Ogawa M (2008) Bull Chem Soc Jpn 81:757
138. Ide Y, Matsuoka M, Ogawa M (2010) J Am Chem Soc 132:16762
139. Ogawa M, Saito K, Sohmiya M (2014) Dalton Trans 43:10341
140. Ozkan D, Kerman K, Meric B, Kara P, Demirkan H, Polverejan M, Pinnavaia TJ, Ozsoz M (2002) Chem Mater 14:1755
141. Ghosh PK, Bard AJ (1984) J Phys Chem 88:5519
142. Breu J, Seidl W, Stoll AJ, Lange KG, Probst TU (2001) Chem Mater 13:4213
143. (a) Stöcker M, Seidl W, Seyfarth L, Senker J, Breu J (2008) Chem Commun 629 (b) Stöcker M, Seyfarth L, Hirsemann D, Senker J, Breu J (2010) Appl Clay Sci 48:146 (c) Mariychuk R, Baumgartner A, Wagner FE, Lerf A, Dubbe A, Moos R, Breu J (2007) Chem Mater 19:5377 (d) Baumgartner A, Sattler K, Thun J, Breu J (2008) Angew Chem Int Ed 47:1640
144. Ogawa M, Inagaki M, Kodama N, Kuroda K, Kato C (1993) J Phys Chem 97:3819
145. Ogawa M, Tsujimura M, Kuroda K (2000) Langmuir 16:4202
146. Kakegawa N, Ogawa M (2004) Langmuir 20:7004
147. Martin JE, Patil AJ, Butler MF, Mann S (2011) Adv Funct Mater 21:674
148. Sohmiya M, Omata S, Ogawa M (2012) Polym Chem 3:1069
149. Raupach M, Emerson WW, Slade PG (1979) J Colloid Interface Sci 69:398
150. Konno S, Fujimura T, Otani Y, Shimada T, Inoue H, Takagi S (2014) J Phys Chem C 118:20504
151. Okada T, Matsutomo T, Ogawa M (2010) J Phys Chem C 114:539
152. Hofmann U, Klemen RZ (1950) Anorg Allg Chem 262:95
153. Jaynes WF, Traina SJ, Bigham JM, Johnston CT (1992) Clays Clay Miner 40:397
154. Jaynes WF, Boyd SA (1991) Clays Clay Miner 39:428
155. Herling MM, Kalo H, Seibt S, Schobert R, Breu J (2012) Langmuir 28:14713
156. Margulies L, Rozen H, Cohen E (1985) Nature 315:658
157. Ishida Y, Shimada T, Masui D, Tachibana H, Inoue H, Takagi S (2011) J Am Chem Soc 133:14280
158. Takagi S, Shimada T, Eguchi M, Yui T, Yoshida H, Tryk DA, Inoue H (2002) Langmuir 18:2265

159. Takagi S, Eguchi M, Tryk DA, Inoue H (2006) J Photochem Photobiol C Photochem Rev 7:104
160. Takagi S, Shimada T, Ishida Y, Fujimura T, Masui D, Tachibana H, Eguchi M, Inoue H (2013) Langmuir 29:2108
161. Fukushima Y, Inagaki S (1987) J Incl Phenomena 5:473
162. Ide Y, Ozaki G, Ogawa M (2009) Langmuir 25:5276
163. Nakamura T, Ogawa M (2012) Langmuir 28:7505
164. Isoda K, Kuroda K, Ogawa M (2000) Chem Mater 12:1702
165. Fuse Y, Ide Y, Ogawa M (2010) Polym Chem 1:849
166. Ogawa M (2002) J Photochem Photobiol C 3:129
167. Sohmiya M, Saito K, Ogawa M (2015) Sci Tech Adv Mater 16:054201
168. Ogawa M, Saito K, Sohmiya M (2015) Eur J Inorg Chem 1126
169. Ogawa M, Kuroda K, Nakamura T (2002) Chem Lett 632
170. Sohmiya M, Sugahara Y, Ogawa M (2007) J Phys Chem B 111:8836

Chapter 7
Hybridization with Polymers

Yoshiaki Fukushima and Kenji Tamura

7.1 Introduction

As natural layered silicates, clay minerals are widely available and cheap; they have been mixed with organic polymers as bulking fillers in the industry. On the other hands, intercalated compounds of layered clay minerals, such as smectite, with organic molecules have been studied in the academic field. The intercalated compounds are expected to have hybridized characters and properties, which are somewhat alike to those of the parent compounds; but different from those of them also.

The organic polymers are widely used because of their easy formability, light weight, and ductility. Fillers have been mixed with polymers to reduce costs and modify the polymer properties, such as increasing the Young modulus, hardness, and heat resistance. However, ceramic fillers in particular adversely affect the formability and increase the specific weight and brittleness. To overcome the trade-off effects, fine and uniform dispersing and surface modification techniques have been developed. The composites of polymers with fine dispersed organic-modified clay minerals are called hybrid materials or nanocomposite materials. We have an excellent example of a hybrid material in metal alloys, in which ductility and high young modulus is realized together. When we compared structures and mechanical properties of the polymer base "hybrid" materials with the metal alloy, we could not call them "hybrid" but they are still mixtures.

Y. Fukushima (✉)
Comprehensive Research Organization for Science and Society (CROSS),
162-1, Shirakata, Tokai, Naka, Ibaraki 319-1106, Japan
e-mail: y_fukushima@cross.or.jp

K. Tamura
National Institute for Materials Science (NIMS), 1-1 Namiki,
Tsukuba, Ibaraki 305-0044, Japan

T. Nakato et al. (eds.), *Inorganic Nanosheets and Nanosheet-Based Materials*,
Nanostructure Science and Technology, DOI 10.1007/978-4-431-56496-6_7

Exfoliation and surface modification have been the key technologies to develop hybrid materials.

Another way to approach hybrid composites is expected in the extension of the intercalation reactions. "Clay" materials, that is, a typical hybrid material of silicate layers with water, are distinguishing and useful rheological characters. Although it seems simple to imagine silicate layers dispersing in organic polymer matrix, to make hybrids by intercalation is not so easy. Polymerization in the interlayer region or solvent assist penetration of organic polymers into the interlayer spacing has been tried. The tendency to infinite swelling in Na^+-montmorilonite with water could not observed in smectites with organic polymers, due to the strong face-to-face cohesion force between the silicate layers and inadequate driving force to penetrate into the gallery spaces. Surface modification is also one of the key factors to approach the hybridization of silicate layers with polymers. Swelling of layered silicates with various molecules, the motive force for the intercalation reaction and the modification of silicate layers for approaching hybridization will be overviewed below.

7.2 Typical Examples of Hybrid Materials; A Goal of Hybridization with Polymers

7.2.1 Clay; A Hybrid of Silicate Layers with Water

We apply the word "clay" to a sticky and deformable agglomerate. The clays are an important raw material for ceramics. They should have an excellent deforming and forming properties which are controlled by water content, addition of organic additives, kneading, aging, and other traditional pretreatments. Raw materials for ceramics are composed of sticky minerals and nonsticky minerals. Typical sticky minerals are layered silicates for example sericite, kaolinite, or smectite. As they are essential minerals for the plastic deformation properties, they are called "clay minerals." Mixtures of the clay minerals with water are too sticky, and they are not suitable for usual ceramic formation processes. Fine particles of nonsticky minerals, such as quartz, cristobalite or feldspar, are also necessary for plastic formation of ceramics.

Water molecules adsorbed on the surface of silicate layers are polarized due to the negative charge of the silicate or interlayer cations and the polar interaction between the water molecules chain forms an adsorbed water phases as shown in Fig. 7.1a. The interaction with the negative charges of silicate layers and interlayer cations is a driving force to make an intercalated compound of layered silicates with water molecules following an infinite swelling by water [1, 2]. The layered silicates hybridize with water molecules to form the clay (Fig. 7.1b) with characteristic plastic deformation properties. Although an infinite swelling tendency by water was confirmed [1, 2], the card house structure shown in Fig. 7.1b has not been observed.

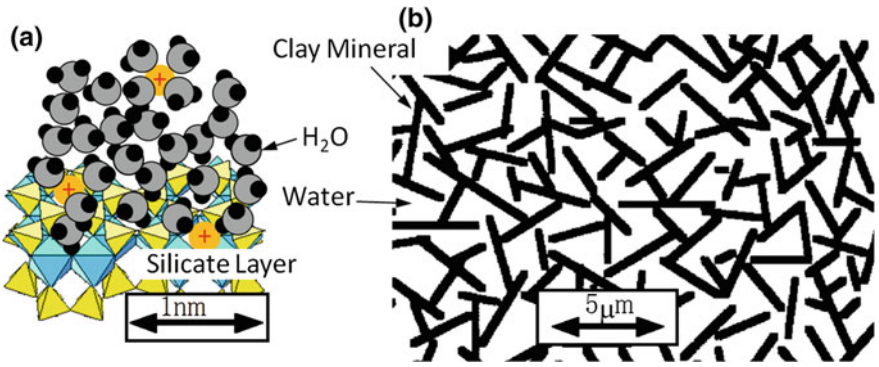

Fig. 7.1 Models of adsorbed water molecule chains on the surface of silicates (**a**), and layered silicates dispersion in plastic clay (**b**)

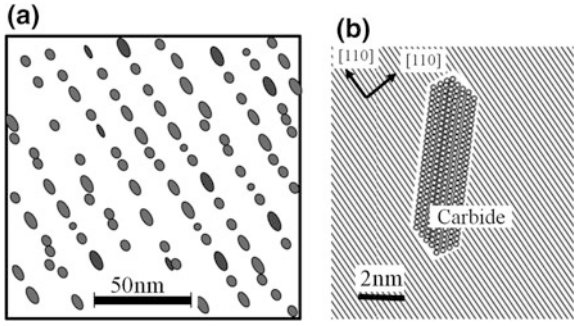

Fig. 7.2 Sketches of **a** Dispersion of nano-precipitates and **b** Carbide disks in FCC lattice in high performance steel

If we could replace the water phase in Fig. 7.1b with a polymer, we would get silicate layers hybridized with organic polymer.

7.2.2 Alloys; Good Examples of Ideal Hybrids

Iron and steel have a long history in our life and through controlled hybridization we have developed ferrite (BCC), austenite (FCC), and metastable phases, carbon, and various carbide precipitates. The continuing challenge in steel for satisfying requests of consumers has been produced high performance steels. A recent severe request for automobile applications brought about a high performance steel; NANO-HEIGHTEN®, in which carbide disks with 2–3 nm size are aligned in a ferrite matrix as shown in Fig. 7.2a [3]. The additive elements and C are dissolved in FCC-austenite at high temperature, followed by precipitation of nano-carbide along the interfaces between FCC-austenite and BCC-ferrite phases during a hot rolling and cooling process. The precipitates are disk shape with FCC structure and

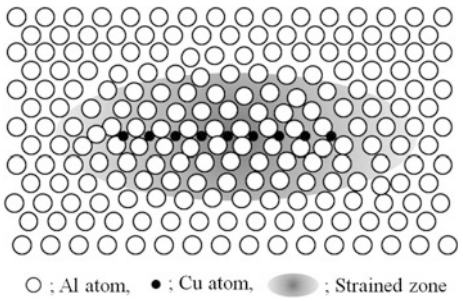

Fig. 7.3 Model for G.P. zone in Al-Cu Alloy

the atomic arrangement on the disk faces fit together with the BCC ferrite matrix as shown in Fig. 7.2b [3]. The high performances of these steels are attributed to the stable nanometer-size carbide dispersion and the well matching of atomic arrangement at the precipitate/matrix interfaces. The hot rolling and cooling process is a key technology for controlling the precipitation and dispersion of nanometer-size carbides [3]. A heat treatment process is also key for aluminum alloys such as Al–Cu–Mg alloy.

An age hardening process at low temperature of supersaturated solid solution of Al with Cu following quenching from high temperatures (at about 500 °C) produced a high performance material [4]. Based on this discovery, the Durener Metallwerke Inc. commercializes this aluminum alloy as "duralmin." A high temperature aging higher than 200 °C precipitates a stable $CuAl_2$ (θ) phase with cubic structure which does not fit the matrix phase at interfaces. The hybrid with stable θ-phase precipitation does not have good performance but shows brittle behavior. During aging at temperatures lower than 150 °C, Cu clusters are formed in a supersaturated solid solution. These clusters are precursors of an intermediate phase (θ′) in the form of plates with CaF_2 structure. Guinier [5] and Preston [6] confirmed the precursor was one atom layer of Cu with a distortion of the Al arrangement around them as shown in Fig. 7.3 [7]. The high performance of the Aluminum alloys is attributed to the nanometer-size thin precursor G.P.-zone. This alloy, "duralmine," has been used in the aerospace industry [8]. A dispersion of nanometer precipitates and the interface structure between the precipitates and the matrix are again the key factors for the good performance of the hybridizations.

7.3 Intercalation Reaction of Sheet Silicates with Organic Compounds

The process of precipitation in solutions, which has been successful in the development of the metal alloys, has not been applied for the hybridization of clay minerals with polymers. Silicate layer stacking clay minerals are dispersed in water, and the smectite group (montmorillonite, nontronite, beidelite, saponite, hectorite)

clay minerals are swollen by water. Single silicate layers constituted by two tetrahedral sheets and one octahedral sheet can be dispersed [1, 2]. Linear uncharged or cationic polymers dissolved in the aqueous matrix adsorbed on silicate layers and flocculate dispersed silicate layers [9]. The flocculation involves interparticle or interlayer bonding including an intercalation reaction. Polymers were added to soil in agriculture to form hybrids with clay minerals and water in soil as conditioners to increase the mechanical strength of soil aggregates [9]. Long linear chains of polymers have adsorbed parts on silicate layer surfaces and also have hydrated parts with water molecules. Adsorption enthalpies of normal chain aliphatic compounds on silica-gel at room temperature [10] (36.8 kJ/mole for n-C_5H_{12}, 43.7 kJ/mole for C_6H_{12} and 59.4 kJ/mole for n-C_8H_{18}) suggested that the attractive force of the single methylene (–CH_2–) with the silicate surface is about 7 kJ/mole. Although the attractive forces between the silicate surface and single segments of polymers are weak, the total energy would be large because of the multi-point attachment. The polymer additives for soil reinforcement are a good example of the hybridization of silicates with organic polymers, but they are not nano-hybrids. Water molecules are essential for the excellent properties of soil hybrids, which could not be applied to most engineering uses.

The smectite clay minerals form intercalated compounds with organic compounds, in which the organic molecules penetrate interlayer spaces and these spaces are increased to form intercalated nano-hybrid compounds. Interlayer water molecules exchange for polar organic monomers such as acrylamide, vinyl acetate or amino acid, which can be polymerized to form intercalated hybrids of clay minerals with organic polymers. The attractive force of polar parts should be comparable with water molecules, that is about 15 kJ/mole, but additional hydrophilic interaction estimated at about 50 kJ/mole is enough for penetration of the guest organic molecules into interlayer spacing or driving off adsorbed water molecules to form intercalated compounds. The attractive driving force for the intercalations makes hybrid compounds in which the guest gallery aligned single or double molecular layers. Polymerization of interlayer monomers makes intercalation type hybrids of organic polymers with silicate layers. Usually, gallery spaces; Δd, are 0.2–0.8 nm, which corresponds to single and double molecular layer thicknesses as shown in Fig. 7.4a and b [11]. Except the amino acids and poly amino acids which formed triple molecular layer compounds shown in Fig. 7.4c [11], penetration was limited to double layers because of inadequate driving force to further increase space.

Polymerization enthalpies were expected to have enough force for increasing interlayer spaces to make compounds with wider gallery spaces. However, even when the monomer contents in clay mineral/monomer mixtures were increased, excess monomers polymerized outer spaces to form mixtures of polymer and intercalated compounds with double or triple polymer layers in interlayer spaces. Although the intercalated compounds with polymers were expected to have a high affinity with similar polymers, the limited swelling compounds were not suitable as fillers due to tight aggregations of intercalated compound particles.

Nonpolar monomers, such as styrene, could not penetrate into the interlayer spaces. When exchangeable interlayer cations in the smectites were exchanged for

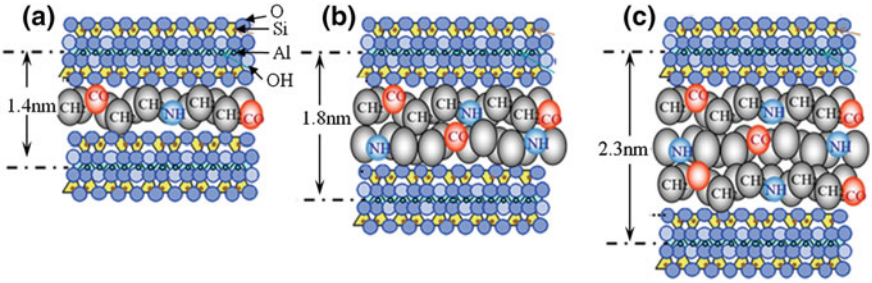

Fig. 7.4 Models for polyamide/montmorillonite intercalated compounds: **a** mono-amino acid layer, **b** double-amino acid layer, and **c** triple-amino acid layer

tri-methyl alkyl ammonium [$(CH_3)_3$-N-$(NH_2)_{n-1}CH_3$ n = 12–18], the monomer molecules could go into the interlayer spaces by hydrophobic interaction with the methyl group in the organic cation. The cation exchanged clay minerals for organic surfactants are called organo-clays and research is continuing to apply these organo-clays as fillers for polymers. The interlayer space; Δd, of the intercalated compound of the organo-montmorillonite with polystyrene was 3.7 nm [12]. An attractive force between the silicate layers with Δd = 3.7 nm was estimated about 1/1000 of that with Δd = 0.2 nm and about 1/10 of that of Δd = 0.8 nm. The weak attractive force between the silicate layers suggested easy exfoliation by shear stress during mixing and exclusion process with polymer melts. Unfortunately poly-ethylene was not suitable for the matrix with silicate layers, but a good electric insulator character was expected for the hybrid [12].

7.4 Nylon-Clay Mineral Hybrids (NCH) by Toyota R&D Lab

In early stages of the development of inorganic filler with organic polymer in Toyota R&D Labs in the early 1980s, the combination of smectite and polyamide (Nylon) was decided. Nylon, which has been widely used as an engineering plastic, is a most suitable matrix because of the plentiful polar segments to interact with the surfaces of inorganic additives. An infinite swelling of Na-montmorillonite with water has been confirmed and a similar swelling was expected for smectites and organo-smectites with suitable guest molecules.

Amino acid-6 [$NH_2(CH_2)_5COOH$] formed an intercalated compound with montmorillonite cation exchanged with $NH_3^+(CH_2)_5COOH$ and polymerized to 6-polyamide by heating at 250 °C. Although the interlayer spacing was increased by increasing the amino acid content to form single, double, and triple polymer layers as shown in Fig. 7.4, the interlayer distance was not increased more than

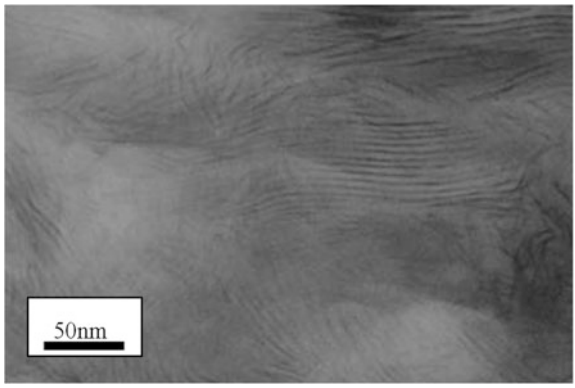

Fig. 7.5 TEM images of 81.8 wt% 6-polyamide/ montmorillonite compound

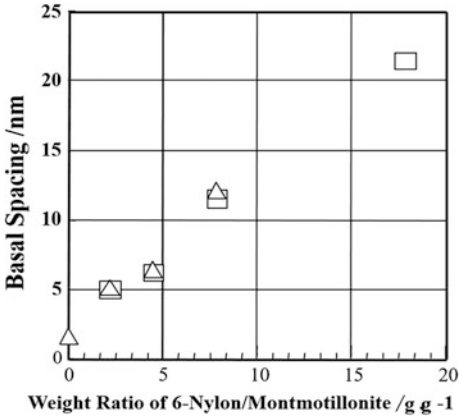

Fig. 7.6 Interlayer distance of 6-polyamide/ montmorillonite compounds. *Open triangle*; by X-ray diffraction, *Open square*; by TEM

2.3 nm [11]. An attractive force between the amino acid molecules and the dehydration polymerization enthalpy were not enough for infinite swelling.

A ring molecule ε-caprolactam (NH–CO–$(NH_2)_5$) is also a monomer of 6-polyamide. The ε-caprolactam formed an intercalated compound with the cation exchanged montmorillonite for $NH_3^+(CH_2)_{11}COOH$ whose interlayer space; Δd, was 3.9 nm [13], at 100 °C, about 32 °C higher than the melting point of ε-caprolactam. A following heating at 250 °C made ring-opening type polymerization to form 6-polyamide. The interlayer space; Δd, of X-ray diffraction peaks at d = 5.2, 6.9, and 10 nm, which correspond Δd = 4.2, 5.9, and 9 nm respectively, were observed for the compounds with 68.5, 81.8 and 88.7 wt% of 6-polyamide [14]. A TEM image of 81.8 wt% 6-polyamide/montmorillonite shown in Fig. 7.5 also confirm the black line of silicate layers were dispersed in the polyamide matrix [14]. The interlayer distance shown in Fig. 7.6 was increased with increasing the polymer contents and the results of X-ray diffraction and TEM observations were in

good agreement. These results suggested the tendency of infinite swelling like water/Na-montmorillonite was also observed for 6-polyamide/montmorillonite compounds. The driving force for the swelling was not the interaction between the silicate layer surface and guest molecules. The –COOH part in the interlayer cation initiated open ring polymerization, followed by the polymerization in the interlayer regions. The polymerization enthalpy of the ε-caprolactam; about 14 kJ/mol, is sufficient to promote the swelling. Pre-swelling of the cation exchanged clay with liquid ε-caprolactam at above the melting point, 68 °C, encouraged the subsequent swelling. The tendency to indefinite swelling after polymerization was also observed for montmorillonite with other exchangeable cations, $NH_3^+(CH_2)_5COOH$, Al^{3+}, H^+, and Cu^{2+}, which had the polymerization initiation effect, but they were not swollen by liquid ε-caprolactam at 100 °C [13]. The increase of interlayer spaces before the polymerization was not an essential condition, but the initiation site in the interlayer region was essential for infinite swelling.

The compounds in which the silicate layers had separated more than 5 nm could disperse in a 6-polyamide matrix during subsequent mixing, excluding and forming processes. They have excellent mechanical properties, heat resistivity, high transparency, and gas barrier effects [15, 16]. They were commercialized and named NCH.

7.5 Exfoliation Process for Clay-Polymer Nanocomposites (CPNs)

Following the development of NCH, dispersing the silicate layers in engineering plastics has been investigated, these materials are the clay-polymer nanocomposites (CPNs). As polyolefin is one of the most widely used engineering plastics, the challenge to get well dispersed CPNs has been concentrated on nonpolar polypropylene nanocomposites with polar clay minerals. Modifications of clay minerals to increase an affinity with nonpolar polymers and to decrease the attractive force of face-to-face stacking of silicate layers and the following exfoliation processes are common methods for developing engineering plastics.

Distearyldimethylammonium $[(CH_3)_2N^+((CH_2)_{17}CH_3)_2]$ cations covers the polar surfaces of silicate layers. Polypropylene oligomer modified with maleic anhydride has polar groups to mediate the intercalation process with the cation exchanged montmorillonite [17]. Expanding the interlayer gallery by intercalation facilitated exfoliation of the modified silicate layers. These exfoliated layers are dispersed in a melted polypropylene matrix during the melt mixing and excluding processes. The obtained clay-polypropylene hybrid wherein many fractions of silicate single layers were exfoliated exhibited good mechanical properties [17].

7.6 Polymer Processing and Optimization of Properties for CPNs

CPNs have been prepared by various molding processing methods in the past. Almost all of the processes are conventional, such as injection molding, extrusion, blow molding or film formation, and so on. On the other hand, much effort in the field of CPN has been focused toward increasing the mechanical strength, barrier property, and flame retardency of the composites using clay nanosheets. The next topic is the development of nanocomposites that have practical levels of flame retardency, rigidity, and moldability while using the morphology control technique by changing the melt-compounding procedures.

In terms of environmental conservation, the use of nonhalogen compounds for flame-retardant plastics is already receiving a lot of attention. When CPNs burn, the dispersed nanoparticles in the polymers form a char layer on the surface. In the plastic electronic field, UL94 recognition (a plastics flammability standard developed by Underwriters Laboratories in the USA) is required, and in many cases the standard required for parts is UL94 V0. In conventional nonhalogen techniques for attaining the UL 94 V0 standard, it was needed to blend more flame retardant even though they achieved V0 flame retardancy. Consequently, we tried to prepare 66-polyamide (PA66) nanocomposites containing small amounts of melamine-modified clay (MelClay) and melamine cyanurate (MC) by changing the compounding procedures [18].

The compounding procedure includes a single- and a multi-stage kneading process which enables control of the dispersion of MelClay (Fig. 7.7). In the single-stage kneading, the raw materials, PA66 and MelClay, are integrally placed

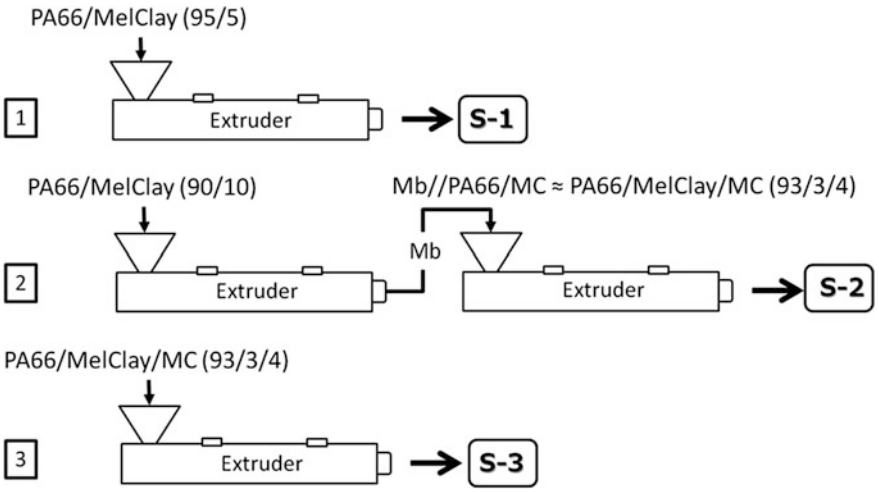

Fig. 7.7 Schematic illustration of the melt-compounding procedures using extruder

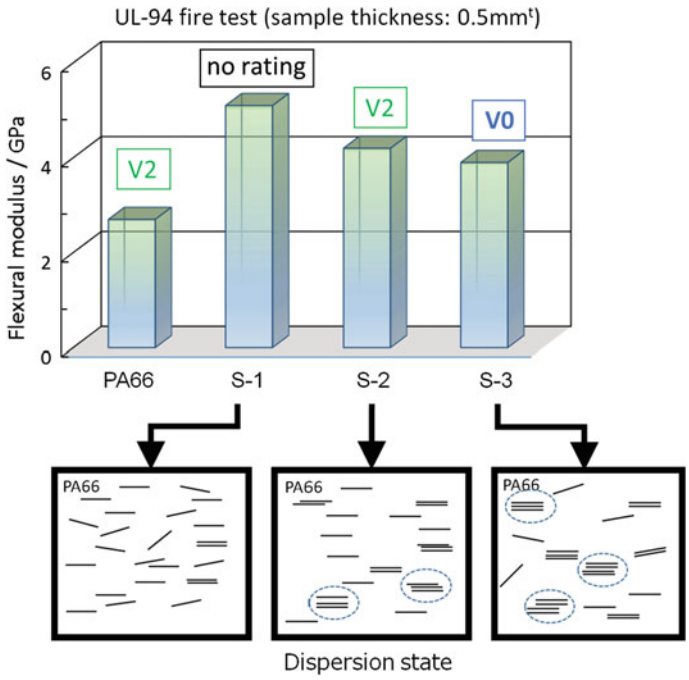

Fig. 7.8 Correlation between the dispersion state of the clay mineral layers and flame retardancy. S-3 has good flame-retardant properties and high mechanical performance

in the kneader (sample: S-1). The multi-stage kneading method comprises, as a first step, the production of a 10 wt%-MelClay master batch (Mb) by mixing and kneading of the PA66 pellet with MelClay, and, as a second step, production of the final compound by mixing and kneading the Mb and MC with PA66 as a diluents (sample: S-2). Samples of MelClay with different dispersion states were obtained by changing the melt-compounding procedures for PA66, MelClay, and MC (sample: S-3). In the experiment, we also found a correlation between the dispersion state of the MelClay layers and flame retardancy in this system.

Ultimately, the S-3 nanocomposite manufactured by one-stage kneading together of PA66, MelClay, and MC was given a UL94 rating of V0 (Fig. 7.8). The flame retardancy in dripping particles during combustion was found to be due to the uneven dispersion of MelClay in the PA66 matrix. The nanocomposites also have high mechanical performance. Additionally, the material shows good workability due to its low viscosity, resulting from the addition of significantly less flame retardant, and can be used to manufacture thin-wall products.

Finally, let us move on to another topic. Electrospinning is a technology that uses electric fields to produce nonwoven fabrics comprising small fibers with diameters that average from a few tens of nanometers to microns (Fig. 7.9). Electrospun nonwoven fabrics can be used in a variety of applications, such as

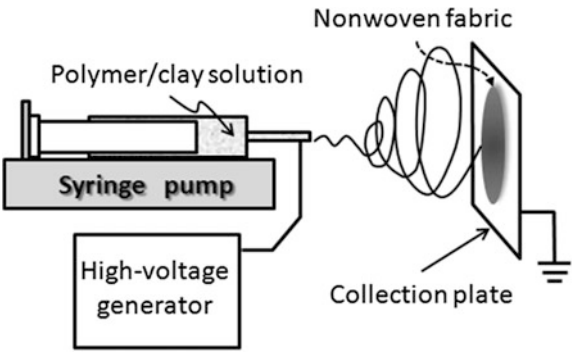

Fig. 7.9 Illustration of electro-spinning apparatus. A fibrous material is formed from the released raw material by electrostatic drawing phenomenon and collected by a collection plate

filtration, tissue engineering, fuel cell membranes, catalytic systems, and sensors. New functional nonwoven fabrics might be obtained by applying this technique to CPNs. For example, to create electrospun nanofiber membranes for direct contact membrane distillation (DCMD) applications, membrane pore wetting consisting of poly(vinylidene fluoride) (PVDF) blended with clay nanofiller has been investigated [19]. The effect of clay on the contact angle of the PVDF–clay nanocomposite membrane was clearly identified to be increasing as the clay concentration increases. Additionally, the melting point of the nanocomposite increased with the increasing concentration of clay particles since the clay particle influenced the crystallization process of the nanocomposite membrane.

In the CPN electro-spinning technique, a solvent capable of dissolving the polymer and swelling the clay have to be selected. Therefore, even if an enthalpy gain is insufficient in the system, an entropy-driven intercalation might be expected to occur due to favorable interactions between the polymers and the surface of the clay layers. One key factor might be the need for high-energy mixing that often was accomplished with sonication. The development of polymer processes in which components are mixed will become more and more important in the future.

7.7 Progress in the Development of New Hybrids

Some clays form smooth gels when mixed with sufficient water. By utilizing this nature, research on hydrogels containing clay nanosheets have been reported. In earlier studies, Haraguchi et al. synthesized nanocomposite gel (NC gel) through in situ free-radical polymerization of N-isopropylacrylamide (NIPA) in the presence of inorganic clay in aqueous solution [20]. The NC gel possesses very large deformability, amazing toughness, and high optical transparency [21], because the material could be prepared using a covalent cross-linkage between the clay surface and the polymer. This NC gel has upset the existing common knowledge that polymer gels are brittle and weak, and carved out new growth investigation areas.

In contrast, a clay-dendrimer hydrogel which is formed only by noncovalent forces was also reported [22]. The components are water and clay (2–3% by mass), which when mixed with a very small proportion (−0.4% by mass) of organic components quickly form a transparent hydrogel. This material can be molded into shape-persistent, free-standing objects owing to its exceptionally great mechanical strength, and rapidly and completely self-heals when damaged. These new NC hydrogel systems could extend the field of high performance materials beyond traditional applications to encompass new unexpected functionalities.

Incidentally, clay minerals include not only layer structures, but also forms of spherical or round tubular pedestals. Each of them has their unique physicochemical properties including adsorption characteristics and colloidal nature [23, 24]. Here, we also refer to the hybrids with tubular clay. Imogolite, consisting of hollow tubes with an external diameter of approximately 2–3 nm (Fig. 7.10a), is a naturally occurring hydrous aluminosilicate found in soils of volcanic origin with a SiO_2/Al_2O_3 ratio of about 1.0 [25]. It has high aspect ratio and surface area with length runs from several hundred nanometers to micrometers (Fig. 7.10b). However, there are some problems in imogolite nanotechnology that remain to be overcome. These include the uniform dispersion of imogolite inside a polymer matrix, tunability of imogolite dimensions (diameter and length), and interfacial adhesion between nanotube and polymer matrix. However, if these problems are resolved, it is anticipated to have numerous applications as a nanofiller similar to a carbon nanotube.

The affinity at interfaces between the inorganic nano-materials and organic matrix has to be appropriately adjusted when forming the hybrid materials. Sometimes, the incompatibility with the hydrophobic polymer has prompted the need to surface modify the imogolite. Several methods have been investigated to convert the surface property of imogolite by grafting with organic modifiers such as organosilanes, and organophosphonic acids [26, 27]. If water-soluble polymers or hydrophilic polymers were used, what effects are imparted for the improving properties of CPN? Sohn et al. have reported that a nanocomposite hydrogel composed of acrylic acid-modified imogolite by grafting techniques has excellent mechanical properties [28]. It shows great tensile strength up to about 1800% extension, and it recovers its original shape immediately after the release of stress.

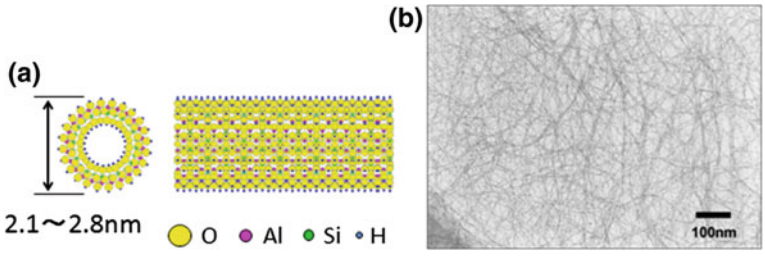

Fig. 7.10 Imogolite images: **a** the molecular structure models of imogolite, and **b** TEM image of synthetic imogolite

Many problems still remain unresolved before it can be put to practical use, however, the unique developments of these new hybrid systems are expected to significantly expand in the future.

7.8 Conclusions

Now, a wide variety of silicate layer hybrids with polymers are available. An approach to intercalation reactions using swelling followed by hybridization was confirmed. Although the subsequent mixing processes with melted polymers offer useful materials, it is not clear if the process is exfoliation or delamination, and if the obtained materials are hybrids or mixtures. The goal of developing hybrid clay materials should be to consider clay characteristics and the assimilation/adaption of metal alloy technology.

References

1. Norrish K (1954) Discuss Faraday Soc 18:120–134
2. Fukushima Y (1984) Clay Clay Miner 32:320–326
3. Sato K, Murakami T (2014) Nanotech Jpn Bull 7(2):1–11
4. Wilm A (1911) Metallurgie 8:225–227
5. Guinier A (1938) Nature 142:569–570
6. Preston GD (1938) Nature 142:570
7. Gerold V (1954) Z Metallk 45:599–607
8. Koyama K (2010) Furukawa-Sky Rev 6:7–22
9. Theng BKG (1970) Clay Clay Miner 18:357–362
10. The Chemical Society of Japan (1984) Kagaku Binran PPII-327. Maruzen, Tokyo
11. Fukushima Y (1994) J Jpn Soc Powder Powder Metal 41:1189–1192
12. Friedlander FZ, Frink CR (1964) J Polym Sci B Polym Lett 2:475–479
13. Fukushima Y, Inagaki S (1987) J Inclu Phen 5:473–482
14. Fukushima Y, Okada A, Kawasumi M, Kurauchi T, Kamigaito O (1988) Clay Miner 23: 27–34
15. Kojima Y, Usuki A, Kawasumi M, Okada A, Kurauchi T, Kamigaito O (1993) J Mater Res 8:1185–1189
16. Kojima Y, Fukumori K, Usuki A, Okada A, Kurauchi T (1993) J Mater Sci Lett 12:889–890
17. Hasegawa N, Kawasumi M, Kato M, Usuki A, Okada A (1998) J Appl Polym Sci 67:87–92
18. Tamura K, Ohyama S, Umeyama K, Kitazawa T, Yamagishi A (2016) Appl Clay Sci 126:107–112
19. Prince JA, Singh G, Rana D, Matsuura T, Anbharasi V, Shanmugasundaram TS (2012) J Membr Sci 397–398:80–86
20. Haraguchi K, Takehisa T (2002) Adv Mater 14:1120–1124
21. Haraguchi K, Li H-J, Matsuda K, Takehisa T, Elliott E (2005) Macromolecules 38:3482–3490
22. Wang Q, Mynar JL, Yoshida M, Lee E, Lee M, Okuro K, Kinbara K, Aida T (2010) Nature 463:339–343
23. Cradwick PDG, Farmer VC, Russell JD, Masson CR, Wada K, Yoshinaga N (1972) Nature Phys Sci 240:187–189

24. Ohashi F, Tomura S, Akaku K, Hayashi S, Wada S-I (2004) J Mater Sci 39:1799–1801
25. Tamura K, Kawamura K (2002) J Phys Chem B 106:271–278
26. Johnson LM, Pinnavaia TJ (1991) Langmuir 7:2636–2641
27. Yamamoto K, Otsuka H, Wada S-I, Takahara A (2001) Chem Lett 30:1162–1163
28. Lee H, Ryu J, Kim D, Joo Y, Lee SU, Sohn D (2013) J Colloid Interf Sci 406:165–171

Chapter 8
Colloidal Nanosheets

Nobuyoshi Miyamoto, Yutaka Ohsedo and Teruyuki Nakato

8.1 Introduction

Nanosheet materials are obtained as colloidal dispersions through the exfoliation of a layered solid in a solvent. In many cases, colloidal dispersions of nanosheets are considered homogeneous and structureless dispersions that are just a passing point for the fabrication of many types of important solid-state nanomaterials, as introduced in other chapters of this book.

However, we emphasize that the nanosheet colloids themselves have controllable meso-scale structures and intriguing properties and functions. From the viewpoint of fundamental colloid sciences, nanosheet colloids are regarded as a very unusual colloidal system compared to other ordinary colloids because of the huge anisotropy of the particles. From the viewpoint of practical applications, nanosheet colloids serve as functional soft materials due to their interesting rheological properties, liquid crystallinity, and response to external stimuli. In addition, we can expect the development of smart soft materials by coupling the properties of nanosheet colloids with various functions inherent to the inorganic nanosheets, such as their electric, catalytic, magnetic, and optical properties. To obtain functional solid-state nanomaterials using nanosheets as nanomodules, it is also important to understand and control the structure and properties of the nanosheets in the state of colloidal dispersion because most of these solid materials are fabricated using colloidal dispersions of nanosheets as a precursor.

N. Miyamoto (✉) · Y. Ohsedo
Department of Life, Environment, and Materials Science, Fukuoka Institute of Technology, 3-30-1 Wajiro-higashi, Higashi-ku, Fukuoka 811-0295, Japan
e-mail: miyamoto@fit.ac.jp

T. Nakato
Department of Applied Chemistry, Kyushu Institute of Technology, 1-1 Sensui-cho, Tobata-ku, Kitakyushu-shi, Fukuoka 804-8550, Japan

T. Nakato et al. (eds.), *Inorganic Nanosheets and Nanosheet-Based Materials*, Nanostructure Science and Technology, DOI 10.1007/978-4-431-56496-6_8

This chapter addresses colloidal nanosheets dispersed in a solvent. Starting with the fundamental aspects of the nanosheet colloids based on classical models, we then focus on the two important aspects of the nanosheet colloids: liquid crystal phase formation and rheological properties. Theories related to the colloid properties are also described. The studies on applications of the nanosheet colloids for soft materials and nanofabrication are also introduced.

8.2 Classical Theory of Colloids Applicable for Nanosheets

Let us first start with a general description of the classical models of colloids: the Stern model and DLVO theory [1]. In these models, the surface charge is important because it determines the stability and structure formation of a colloidal dispersion. Generally, colloid particles are charged in water, regardless of their chemical composition. Even if the particle has an electrostatically neutral chemical composition, the particle is normally charged due to dissociation or protonation of the surface functional groups. In the case of a particle of an oxide MO_x, where M is Si, Al, Fe, etc., the charge depends on pH because the hydroxy groups on the particle dissociate into $M–O^-$ and H^+ at higher pH, while it is protonated to form positively charged $M-OH_2^+$ at lower pH. The charge becomes zero at intermediate pH, which is called the point of zero charge. The amount of charge on the surface is quantified by the charge density σ_0 [C m^{-2}] or surface potential ψ_0 [V]. However, these values are difficult to directly measure experimentally. Hence, the zeta potential ζ [V], which is the potential at the *slipping surface* of the particle, is generally used. The zeta potential is slightly lower than the surface potential.

The charge of the particles should be compensated by the same amount of opposite charge of the counter ions. The Stern model is the standard model to depict the spatial distribution of the counter ions around the particle. According to this model, the particle is surrounded by an electric double layer composed of a Stern layer and a Gouy–Chapman layer (or diffuse layer). The Stern layer is the first layer in which the ions are strongly bound onto the particle surface due to the affinity of the ions to the surface. In the Gouy–Chapman layer, the ions are weakly bound to the particle and form an *ionic cloud*. The concentration of counter ions, or potential, decreases as the distance x from the surface increases. Under some assumptions and approximations, the potential at distance x is expressed as

$$\psi = \psi_0 \exp(-\kappa x). \tag{8.1}$$

Here, κ^{-1} is called as Debye screening length, which is usually regarded as a measure of the thickness of the diffuse layer and is expressed as

$$\kappa^{-1} = \sqrt{\frac{\varepsilon_r \varepsilon_0 kT}{2000 N_A e^2 I}}, \tag{8.2}$$

where ε_r is the specific dielectric constant of the solvent, ε_0 is the dielectric constant of vacuum, T is temperature, k is Boltzmann's constant, N_A is the Avogadro's constant, e is the charge of an electron, and I is the ionic strength. An important point is that the thickness of the diffuse layer decreases with increasing ionic strength I.

The simplest theory on the interactions between colloid particles is the DLVO (Derjaguin–Landau–Verwey–Overbeek) theory [1]. In this theory, the potential energy V_T for a pair of colloid particles is expressed as the sum of van der Waals attraction V_A and the repulsion V_R due to overlap of the diffuse layers as

$$V_T = V_A + V_R. \tag{8.3}$$

The potential due to attraction between two parallel thin plates with thickness L, which are separated by distance h, is expressed as

$$\begin{aligned} V_A &= -\frac{A}{12\pi}\left\{\frac{1}{h^2} + \frac{1}{(h+2L)^2} - \frac{2}{(h+L)^2}\right\}, \\ &\sim \frac{A}{2\pi}\frac{L^2}{h^4} (\text{if } L \ll h) \end{aligned} \tag{8.4}$$

where A is the Hamaker constant, which indicates the strength of the van der Waals interaction. The repulsion term is expressed as

$$V_R = \frac{64nkT}{\kappa}\left[\tanh\left(\frac{e\psi_0}{4kT}\right)\right] \exp(-\kappa h). \tag{8.5}$$

Based on DLVO theory, we can discuss the stability of the dispersed state and the structure formation of a colloid. When the ionic strength is lower and the surface charge is higher, the repulsion V_R is dominant, giving a maximum on the V_T–h curve. In this case, the colloid dispersion is stable and the average distance between the particles is determined simply based on the particle concentration. When the ionic strength is higher and the surface charge is lower, the attraction force V_A dominates the system so that V_T is always negative and only the deep minimum appears on the curve. In this case, the colloid particles aggregate. With intermediate ionic strength and surface charge, a shallow, secondary minimum sometimes appears on the V_T–h curve as a result of the balancing of V_R and V_A. In this case, the particles may be loosely trapped at the position of the secondary minimum. These behaviors are qualitatively in accordance with many experiments, as shown in Chap. 3, while quantitative formulation is difficult with this simple theory.

To apply these theories to nanosheet colloids, Eqs. (8.1)–(8.5) can be valid, but the charge of the nanosheets should be considered. Most known nanosheets, such as

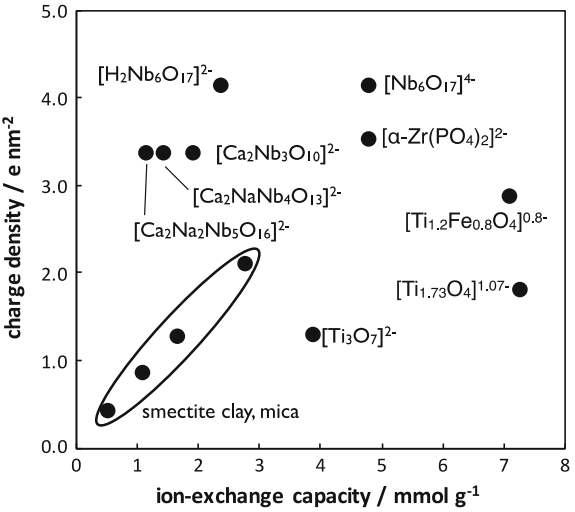

Fig. 8.1 Comparison of the charge densities of nanosheets

clay minerals, metal oxides, metal phosphates, and graphene oxides, are negatively charged, while the rare example is layered double hydroxides that have permanent positive charges. The ideal charge density for each layered material can be calculated based on the chemical composition and crystal structure. Comparison by the unit of [e nm^{-2}], charge per unit surface area, is useful for many purposes, while, in the case of clay minerals, the unit of [meq g^{-1}] is often used. Figure 8.1 compares the ideal layer charge of several nanosheet materials. The charge density ranges from 0.5 to 4.0 [e nm^{-1}], and the ion exchange capacity ranges from 0.5 to 8 [meq g^{-1}]. For a nanosheet surface with this range of layer charge, a surface potential as high as several hundreds of mV is expected. However, a zeta potential value of several tens of mV is often obtained experimentally [2] due to a low dissociation constant of the surface group and adsorption of counter ions in the Stern layer, which is largely affected by the type of counter cations. In contrast to most other materials, smectite-type clay minerals have permanent negative charges inside the layer, while the edge charge depends on the pH due to the presence of hydroxy group. The edges are normally negatively charged at higher pH, at which we usually address clay colloids. We note there are many publications in which the discussions are based on the misunderstanding that the edge is always positively charged.

8.3 Liquid Crystal Phases of Nanosheet Colloids

Because of the huge anisotropy of nanosheets, the nanosheet colloids form liquid crystal (LC) phases. In a dilute colloidal dispersion, nanosheets are moving around in translational and rotational manners, that is, Brownian motion. However, if the

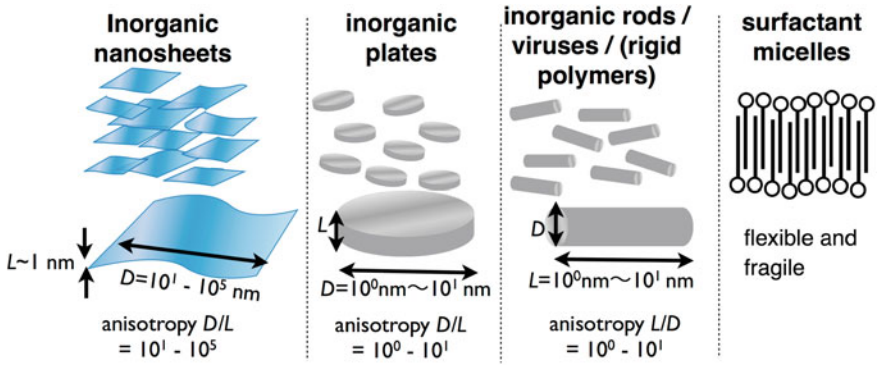

Fig. 8.2 Comparison of lyotropic liquid crystals based on nanosheets, plates, rods, and surfactants

concentration of the nanosheets increases, the free rotational motion is restricted and the nanosheets cooperatively orient themselves along a certain direction to form an LC phase. We have named this type of liquid crystals as *nanosheet liquid crystals* and have been studying these materials as a new type inorganic LCs. Nanosheet LCs are classified as a lyotropic LCs, as distinguished from thermotropic LCs. A lyotropic LC is generally composed of a solvent and anisotropic dispersoids, and the LC phase formation depends on the concentration of the dispersoid. Many types of lyotropic LCs have been reported, as shown in Fig. 8.2: surfactant micelles, rigid polymers [3–5] (e.g., poly(paraphenylene terephthalamide) and DNA), rod-shaped particles (viruses [6], metals [7], oxides [8–10], and semiconductors [11]), nanoplates (gibbsite ($Al(OH)_3$) [12, 13], $Ni(OH)_2$ [14], and layered double hydroxides [15]), and nanosheets. Among them, nanosheets are regarded as ultimately anisotropic two-dimensional particles.

Although many nanosheet materials have been reported so far, only a few of them are reported as nanosheet liquid crystals for several reasons. One reason is that, in some cases, only a lower degree of exfoliation and lower yield of exfoliated single-layered nanosheets can be attained. In other cases, the colloids themselves are unstable so that they precipitate and aggregate within short time, preventing their use as a colloidal material. It is also a problem that, as often observed in layered clay mineral systems, the colloidal dispersions becomes viscose or gelated at low concentration, and the characterization as a fluid liquid crystal cannot be performed. Considering various applications, it is desirable that the system has a wider concentration range for the liquid crystal phase with high fluidity. Therefore, it is important to optimize various parameters, such as particle size, distribution of the particle size, and salt concentration, to improve the properties of the colloid to be suitable for nanosheet liquid crystal materials. Although we have a few numbers of the examples satisfying these conditions, Figs. 8.3 and 8.4 summarize the schematic structures of the reported nanosheet LCs and the phase diagram, respectively. In the following subsections, the individual research works of each material will be presented.

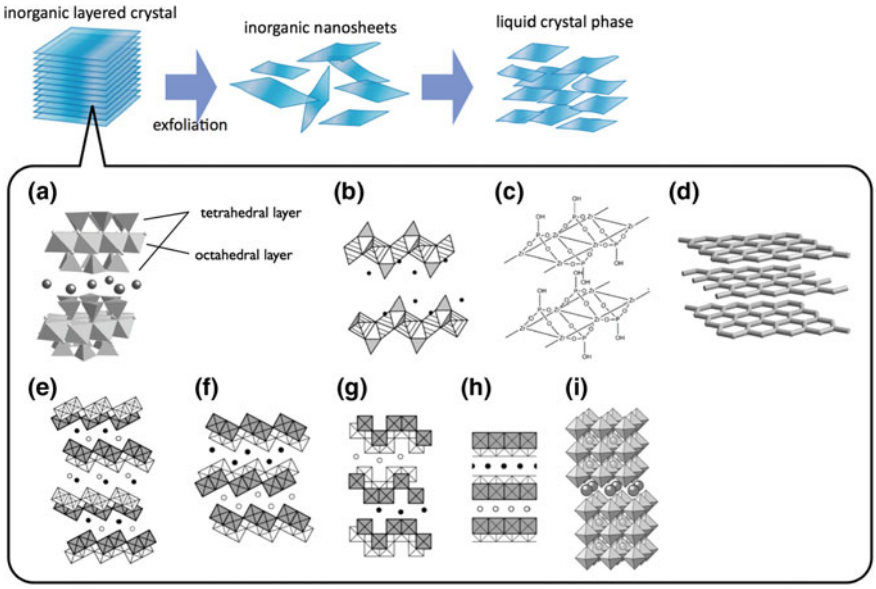

Fig. 8.3 Schematic model of intercalation, exfoliation, and liquid crystal phase formation, and the structures of the layered materials that form liquid crystal phases: **a** clay mineral, **b** $K_3Sb_3P_2O_{14}$, **c** α-ZrP, **d** graphite, and transition metal oxides of **e** $K_4Nb_6O_{17}$, **f** $KTiNbO_5$, **g** KNb_3O_8, **h** $Cs_{1.07}Ti_{1.73}O_4$ and **i** $KCaNb_3O_{10}$

8.3.1 Layered Phosphates

In a 2001 article in *Nature* [16], Gabriel et al. reported phosphoric antimony nanosheets obtained from layered $K_2Sb_3P_2O_{14}$ as a nanosheet LC with a swollen lamellar structure. $K_2Sb_3P_2O_{14}$ is composed of SbO_6 octahedrons and PO_4 tetrahedrons combined with a shared apex (Fig. 8.3b). The layer has a thickness of 1.1 nm, and the negative charges are compensated by interlayer K^+. The homogeneous, clear, and transparent nanosheet colloid was obtained by exchanging the interlayer K^+ with H^+, followed by washing and dialysis. In contrast to most other systems, this material does not require the addition of a stabilizer or exfoliating agent. Figure 8.5 shows the phase diagram of this system. In the range of the nanosheet concentration of 0.75–1.78 vol.%, this colloid possesses fluidity and birefringence. At more than 1.78 vol.%, it becomes a gel with birefringence. Below 0.75 vol.%, it enters a biphasic state, that is, the coexistence of birefringent and isotropic phases. After storing the biphasic sample, the dense birefringent phase and the dilute isotropic phase are macroscopically separated into the lower and upper parts of the sample, respectively, with a clear interface. Because the isotropic phase shows flow-induced birefringence, this upper phase is confirmed to be a colloid with dispersed nanosheets but not a simple solvent. Although not mentioned in the literature, at lower concentration, the system should transition to a purely isotropic phase.

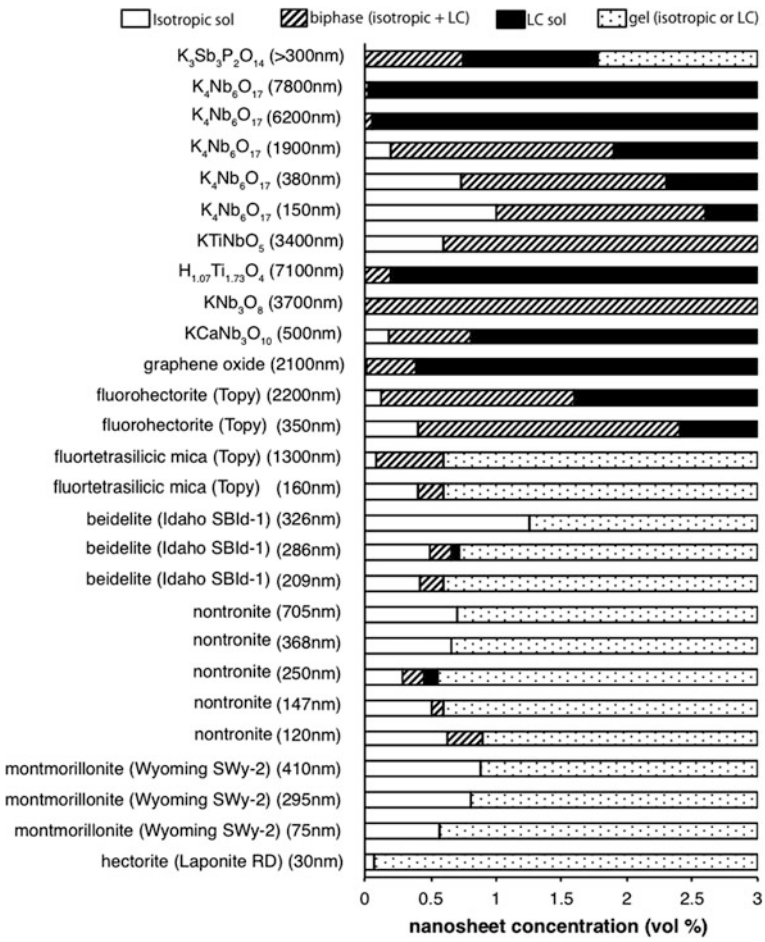

Fig. 8.4 The summary of the phase diagram of the aqueous nanosheet dispersions of $K_3Sb_3P_2O_{14}$ [16], $K_4Nb_6O_{17}$ [17], $KTiNbO_5$ [18], $H_{1.07}Ti_{1.73}O_4$ [19], KNb_3O_8 [18], $KCaNb_3O_{10}$ [20], graphene oxide [21], fluorohectorite [22], fluortetrasilicic mica [22], beidlite [23], nontronite [24], montmorillonite [25], and hectorite [26] at relatively low salt concentrations, collected from the references. The *parenthetic values* are average lateral length of the nanosheets

Thus, with increasing concentration, the system transitions from the isotropic phase to the complete liquid crystal phase, passing through the coexistence of the two phases. This is the general behavior of anisotropic colloids as theoretically predicted by Onsger [27], the theory of which is explained in detail in Sect. 4.1.

In this system, a swollen lamellar structure with the basal spacing of up to 225 nm was identified by small-angle X-ray scattering (SAXS). As shown in Fig. 8.6a, multiple narrow diffraction peaks appeared, indicating high structural order. Because of the large basal spacing, structural colors from blue to red were observed under white illumination. Of the several reported nanosheet colloid

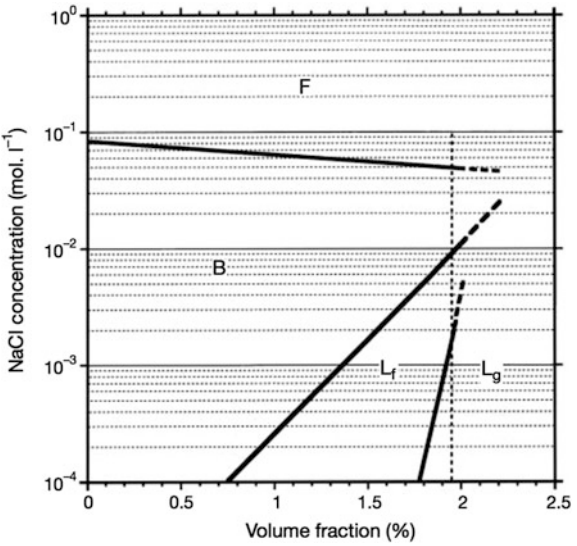

Fig. 8.5 Phase diagram of $H_3Sb_3P_2O_{14}$ suspensions versus volume fraction and salt concentration. Upon decreasing the volume fraction, the suspensions first form a lamellar gel phase (L_g), then a lamellar fluid phase (L_f) and finally enter a biphasic regime (B). The system flocculates (F) at high salt molarity. Reprinted with permission from Ref. [16]. Copyright 2001 Nature Publishing Group

systems, there are only a few examples with the very large basal spacing, high structural order, and structural colors observed in this system. As shown in Fig. 8.6b, the basal spacing d increases with decreasing nanosheet concentration; it reaches the maximum of 225 nm. If the lamellar structure with layer thickness L undergoes ideal one-dimensional swelling, the basal spacing d follows the following formula,

$$d = L/\varphi^{-1}. \tag{8.6}$$

In the range of $\varphi^{-1} < 100$, the plot in Fig. 8.6b follows this formula. Extrapolation of the straight line gives the value $L = 1.05$ nm, and this value approximately coincides with the crystallographically estimated thickness of the nanosheet. By adding the salt to the colloid, phenomena such as flocculation, gelation, and decrease of basal spacing (Fig. 8.6c) occurred. However, these phenomena occurred only when a salt concentration was more than 10^{-2} M. Thus, adding a small amount of salt does not greatly influence the state of the system.

As another phosphate nanosheet system, Cheng et al. investigated nanosheet colloids derived from layered zirconium phosphate α-ZrP [28]. In this report, powders of layered crystals of α-ZrP were synthesized by a hydrothermal method so that the average particle size and size distribution were precisely controlled by varying the reaction time and the concentration of the starting solution. Through exfoliation of these crystals, a series of the samples with different lateral size and size distribution were obtained. The phase transition concentrations ϕ_I (for the isotropic phase to biphase) and ϕ_N (for the biphase to liquid crystal phase) for these samples are shown in Fig. 8.7. Both ϕ_I and ϕ_N decrease with increasing average particle size. Although Miyamoto et al. had already reported the influence of particle size at the time [17], the importance of Cheng's study is that they clarified

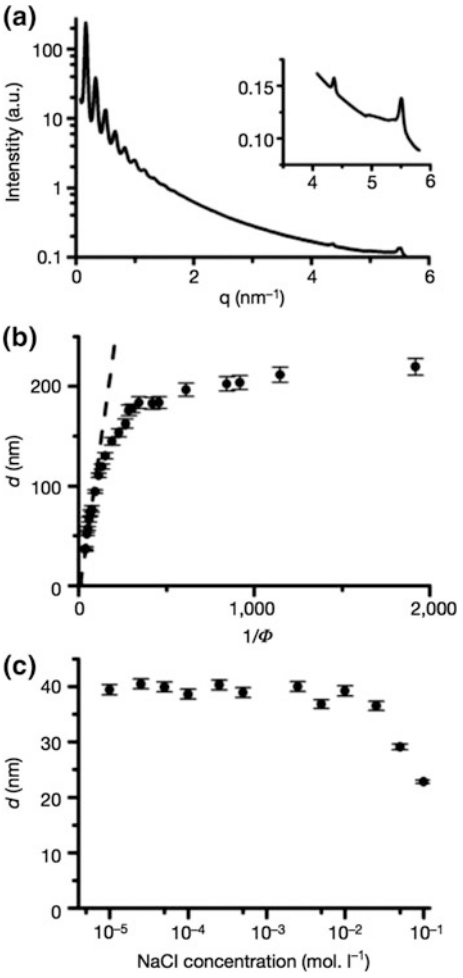

Fig. 8.6 Small-angle X-ray scattering (SAXS) study of the liquid crystalline anitimophosphate nanosheet colloid. **a** The SAXS pattern of the sample of 2.0 vol. %. **b** Variation of the basal spacing d with the inverse of the concentration. **c** Variation of the basal spacing d with the NaCl concentration added to the system of φ = 1.9 vol. %. Reprinted with permission from Ref. [16]. Copyright 2001 Nature Publishing Group

the effect of the particle size distribution. As the particle size distribution increased, ϕ_N exceedingly increased, while ϕ_I did not change, resulting in widening of the concentration range for the biphase and the coexistence of the isotropic and LC phases. This result is in harmony with the theoretical prediction by the modified Onsager's theory. Moreover, Cheng et al. reported the α-ZrP system, of which the nanosheet surface is chemically modified with thermosensitive poly(*N*-isopropylacrylamide). This system showed reversible liquid crystal-isotropic phase transition induced by temperature change.

Recently, by adsorbing the amphiphilic polyoxyalkyleneamine onto the surface of α-ZrP nanosheets, Wong et al. [29] prepared nanosheets dispersed in nonaqueous solvent, butyronitrile, stabilized by the steric effect of the adsorbed polymer layer. Nanosheet LCs dispersed in organic solvent are applicable for the fabrication of

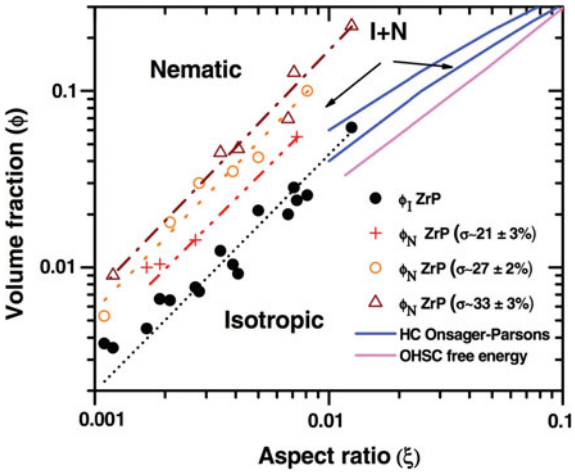

Fig. 8.7 Comparison of the experimental o_I and o_N with those evaluated by the Monte Carlo simulation based on the free energy calculation with oblate hard spherocylinders (OHSC) model, and the Onsager-Parsons theory based on hard cylinder (HC) models. The power law scaling of 2 for o are (*filled circle*) $\phi_I = 23.1 \pm 8.12^{1.36\pm0.10}$, (*open triangle*) $\phi_N = 115.5 \pm 78.62^{1.41\pm0.20}$, (*open circle*) $\phi_N = 68.6 \pm 48.32^{1.36\pm0.10}$ and (*plus*) $\phi_N = 36.9 \pm 6.92^{1.32\pm0.04}$. The *lines* are guides for the eye. Reprinted with permission from Ref. [28]. Copyright 2012 American Physical Society

various inorganic/organic composites, although such a system has not been reported previously. Furthermore, in this system, similarly to the study of $K_3Sb_3P_2O_{14}$ reported by Gabriel [16], a lamellar structure with very large basal spacing of up to ca. 240 nm was confirmed, and structural colors attributable to this structure were observed (Fig. 8.8).

8.3.2 Layered Transition Metal Oxides

In 2002, Miyamoto and Nakato reported a liquid crystal nanosheet colloid prepared from the layered niobate, $K_4Nb_6O_{17}$ [30, 31]. They also confirmed the liquid crystallinity in the related oxide materials, such as $KTiNbO_5$ [18], KNb_3O_8 [18], and $H_{1.07}Ti_{1.73}O_4$ [19]. In 2004, they clarified the effect of the lateral size of the nanosheets on the formation of the LC phase for the first time. In that study, nanosheets with controlled large lateral size were obtained by exfoliation of a $K_4Nb_6O_{17}$ crystal of cm scale, synthesized by the flux method [32]. The obtained colloid was ultrasonicated to crush the nanosheets to a smaller average size, as controlled by the duration of the ultrasonication. A series of samples with average particle size ranging from 0.15 to 7.8 μm were obtained. The dependence of ϕ_I and ϕ_N on the average lateral size of the nanosheets is summarized in Table 8.1.

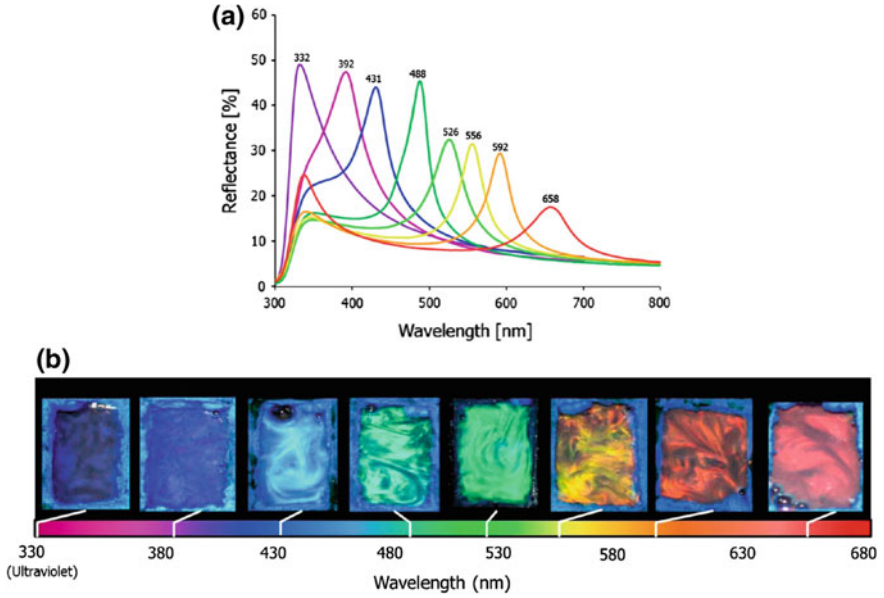

Fig. 8.8 Photonic crystals of nanoplatelets in organic solution. **a** Reflection spectra of 625 nm α-ZrP nanoplatelets in butyronitrile at various concentrations. Reflectance peak shifts from red to ultraviolet as concentration of nanoplatelets increases. **b** Photographic images of butyronitrile solutions containing α-ZrP nanoplatelets demonstrating colors shifting from *violet* to *red* as concentration decreases from *left* to *right*. Reprinted with permission from Ref. [29]. Copyright 2014 American Chemical Society

Table 8.1 Mean lateral sizes and critical concentrations of the phase transitions

Ultrasonication/min	D_m/μm	$\sigma_{(log)}$	ϕ_I^a(vol/vol)	ϕ_{LC}^b(vol/vol)
0	7.8	9.2	$<5 \times 10^{-2}$	$\sim 3 \times 10^{-3}$
10	6.2	7.7	$<5 \times 10^{-2}$	$\sim 5 \times 10^{-3}$
50	1.9	6.8	1.9×10^{-3}	1.9×10^{-2}
90	0.38	9.5	7.3×10^{-3}	2.3×10^{-2}
180	0.15	11	1.0×10^{-2}	2.6×10^{-2}
0 (from powder)	3.6	9.8		

Reprinted with permission from Ref. [17]. Copyright 2004 American Chemical Society
[a]The concentration where the colloid transits from isotropic to biphasic
[b]The concentration where the colloid transits from biphasic to liquid crystalline

The simple trend is found that ϕ_I increases as the average particle size increases. This trend roughly coincides with the prediction of Onsager theory. This niobate system is advantageous because the fluidic liquid crystal phase is obtained in a very large concentration range. Owing to the fluidity, macroscopic orientation by an

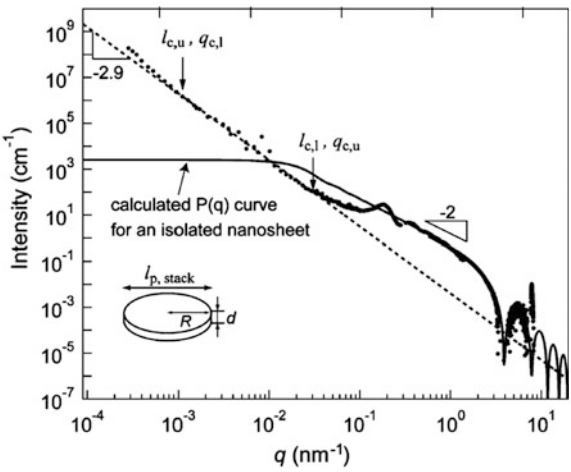

Fig. 8.9 Analysis of the scattering profile of an aqueous dispersion of niobate nanosheets. Reprinted with permission from Ref. [34]. Copyright 2007 International Union of Crystallography

external field is easy. The liquid crystal phase of the niobate nanosheets with an adsorbed organic dye was macroscopically aligned by gravitational field, providing a hierarchical organization of the dye structure.

Yamaguchi et al. conducted detailed structural analyses for the $K_4Nb_6O_{17}$ nanosheet LC system [33, 34]. Figure 8.9 shows the combined small-angle neutron/X-ray scattering patterns for the nanosheets with an average particle size of 3200 nm. The scattering profile roughly coincides with the theoretical form factor P (q) of a thin disc with radius R and thickness L. P(q) is represented as follows:

$$P(q) = \left(\frac{2}{q^2R^2}\right)\left[1 - \frac{J_1(2qR)}{qR}\right]\frac{\sin^2(qL/2)}{(qL/2)^2} \tag{8.7}$$

Here, q is the scattering vector and J_1 is the first-order Bessel function. This form factor is reduced as: $P(q) \sim q^{-2}$ in the range of $L^{-1} < q < R^{-1}$, $P(q) \sim 1$ in the range of $q < R^{-1}$, and $P(q) \sim q^{-4}$ in the range of $q > L^{-1}$. The solid line in Fig. 8.9 is the theoretical curve of $P(q)$ calculated with sufficiently large R and with $L = 1.6$ nm. Because the theoretical curve coincides well with the experimental results at $q > 10^0$, it is confirmed that there are mostly completely exfoliated nanosheets with the thickness of 1.6 nm in this colloid, rather than incompletely exfoliated layered crystals. In the range of $10^{-1} < q < 100$, several peaks appeared at the positions corresponding to $q/2\pi = 1/d$, $2/d$, $3/d$ and so on. The peaks are ascribed to the regulated structure with the basal spacing d. This suggests that there exists not only the orientational order explained by Onsager theory but also positional order in the nanosheet colloid forming the LC phase. In the ultra-small-angle region ($q < 10^{-2}$ nm^{-1}), the scattering of $q^{-2.9}$ is observed. This shattering is in excess compared to the q^{-2} expected for a two-dimensional object and may be ascribable to a fractal structure, which is composed of sparse and dense domains due to the inhomogeneous distribution of the nanosheets in the solvent. Several

studies have suggested the existence of fractal structures in nanosheet colloids [35–40]. The sparse and dense structure is formed because the system is not dominated by repulsive force; attractive interaction among the nanosheets also exists.

On the other hand, Miyamoto et al. [20] reported the LC phase of the nanosheet colloid obtained from $KCa_2Nb_3O_{10}$ (Fig. 8.3i). $KCa_2Nb_3O_{10}$ is a type of Dion–Jacobson layered perovskite with the general formula $M[A_{n-1}B_nO_{3n+1}]$ (M = K, Na, H, etc.; A = Ca, Ba, K, Sr, etc.; B = Nb, Ti, etc.) [41]. Layered perovskites are suitable for systematic basic research because a series of compounds with various chemical compositions and structures can be synthesized. In addition, the layered perovskites have intriguing functions, such as photocatalytic activity [42], catalytic activity as solid acids [43], and luminescent properties [44], so they are expected to be applicable to advanced soft materials.

8.3.3 Layered Clay Minerals

Layered clay minerals have been studied historically for the longest time of all layered materials and are very important materials for many types of industrial applications because of their low cost, abundance in earth soils, and low toxicity. The liquid crystallinity of a clay mineral was first reported by Langmuir in 1938 [45]. Langmuir found that the colloidal sol of bentonite clay produced in California had a birefringent texture, and he identified this as a liquid crystal phase. However, this observation was not reproduced and the liquid crystallinity of the clay mineral colloid was not reported for a long time afterward. One of the reasons is that most clay mineral colloids lose the fluidity at relatively low concentrations (at several wt %) and become physical gels. In many cases, the transition to a physical gel occurs below the concentration of the liquid crystal phase transition so that it is impossible to observe the emergence of the liquid crystal phase clearly. Even if birefringence is observed in the gel, it is difficult to confirm the permanent birefringence due to the liquid crystal phase, which should be distinguished by flow birefringence with very slow relaxation. In the late 1990, several research groups reported birefringent clay colloidal gels. In 1996, Gabriel et al. [46] carefully observed the gels of montmorillonite or hectorite and obtained birefringent gels at specific clay and salt concentrations. Mourchid et al. reported that hectorite formed a nematic liquid crystal phase at above 3 wt% [26]. Fossum et al. reported that the colloid of synthetic fluorohectorite was separated into three phases, the precipitate, birefringent gel, and isotropic, after allowing the colloid to stand for a period of time [47]. On the other hand, Michot et al. [25] reported that the montmorillonite colloid becomes a sol, gel, aggregate, or the partially birefringent gel depending on the particle size and salt concentration. However, the fluidity is lost in the nanosheet colloids in these reports, and it is difficult to confirm that these observations correspond to a true liquid crystal phase.

A clay mineral colloid with permanent birefringence and fluidity was reported by Michot et al. [24, 48, 49] in 2006 for the first time. The exfoliated nontronite

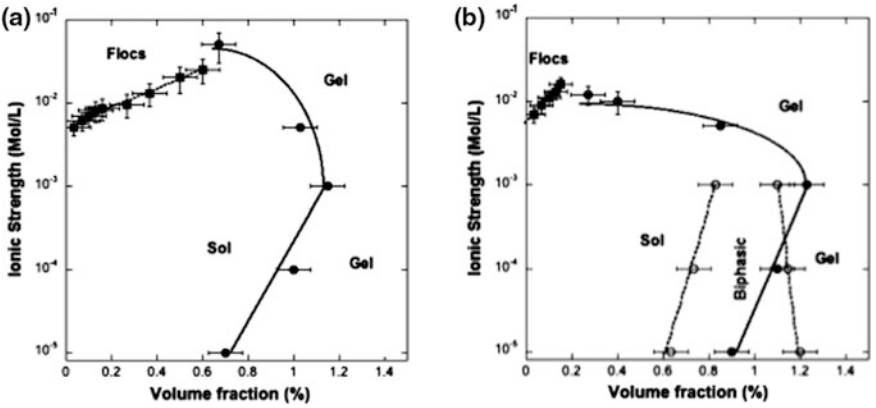

Fig. 8.10 Phase diagram of nontronite with an average lateral size of **a** 2200 nm and **b** 250 nm. Reprinted with permission from Ref. [24]. Copyright 2008 American Chemical Society

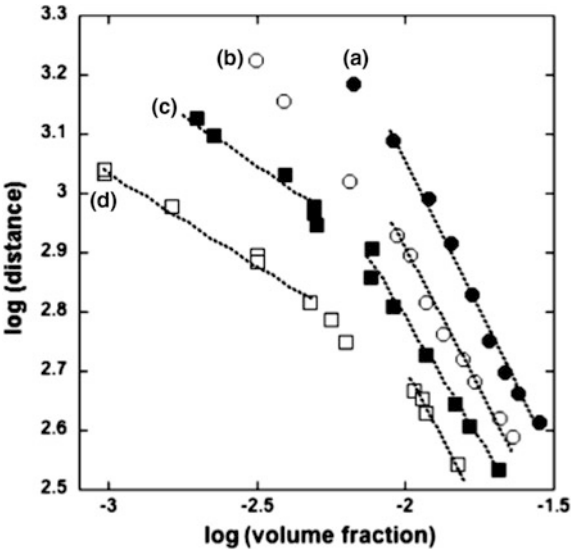

Fig. 8.11 Evolution of the average interparticular distances as functions of the concentration and average lateral size of the nanosheets at ionic strength of 10^{-5} M. The average size are *a* 2200, *b* 986, *c* 346 and *d* 250 nm, respectively. Reprinted with permission from Ref. [24]. Copyright 2008 American Chemical Society

nanosheet had a strip-like shape with a long side to short side ratio of 2.9–5.5, and the length of the long side was 2200 nm. Figure 8.10 shows the phase diagram with the particle size and ionic strength as the parameters. In the sample with small particle size (250 or 345 nm) and salt concentration less than 10^{-3} M, the phase transition from the isotropic phase to the liquid crystal phase occurred at a nanosheet concentration of 0.6–0.7 wt%. In contrast, in the sample with large average particle size, only the sol-gel transition was observed. In the relationship between the average particle-particle distance d determined by SAXS and the nanosheet concentration (Fig. 8.11), the system followed the law of one-dimensional swelling of

Eq. (8.6) in the region of high nanosheet concentration. On the other hand, d was proportional to $\phi^{1/3}$ in the range of the lower nanosheet concentration, which corresponds to isotropic swelling. Whereas the ionic strength did not greatly influence the liquid crystal phase transition, very high ionic strength caused flocculation or gelation.

Michot et al. also reported the liquid crystal formation of the natural beidellite clay system [23, 50]. Using several clay mineral systems, they conducted an investigation of the rheological, osmotic pressure, and SAXS measurements. Based on these observations, they concluded that the electrostatic repulsive force between nanosheets dominates the rheological properties and liquid crystallinity, while the hydrodynamic capture effect may also be related [50–52].

On the other hand, Miyamoto et al. [22] reported that the synthetic fluorohectorite and fluorotetrasilicic mica with controlled particle size prepared by purification and sonication processes formed liquid crystal phases with very high fluidity. Figure 8.12 shows photos of these colloids under crossed polarizers. The sample with large particle size has a texture with interference colors ascribable to the liquid crystal phase at 1.0 wt%, while typical phase separation behavior occurs (Fig. 8.12d–g). In contrast, the sample with small particle size at 1.0 wt% is isotropic and only shows flow birefringence (Fig. 8.12b, i), and the permanent liquid crystal phase (Fig. 8.8c, j) is observed only at the higher concentration (2.0 wt%).

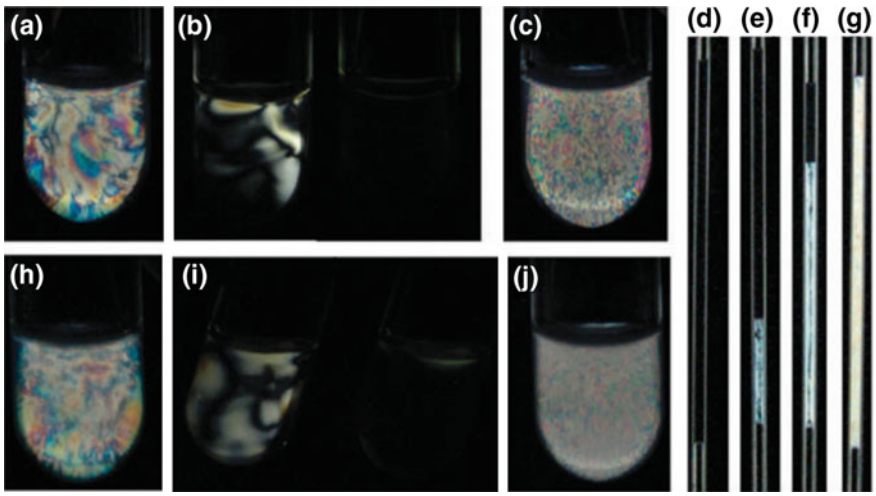

Fig. 8.12 Observation of the **a**–**g** FHT and **h**–**j** FTSM colloids in glass tubes (10 mm or 1 mm in diameter) with crossed polarizers: the mean lateral size D = (**a**)(**d**)–(**g**) 2.2, (**b**)(**c**) 0.35, (**h**) 1.3, and (**i**)(**j**) 0.16 nm and the colloid concentration c = (**a**)(b)(**h**)(b) 1.0, (**c**)(**j**)2.0, (**d**) 0.28, (**e**) 0.81, (**f**) 2.0, (**g**) 4.0 wt%. The *left-hand* images of (**b**) and (**i**) are transient states observed just after shaking the tubes; they relax to a dark isotropic state (*right-hand images*) in a second. The photos (**a**)–(**c**) and (**h**)–(**j**) were taken just after preparation, while (**d**)–(**g**) were taken after macroscopic phase separation of the samples to upper isotropic and lower LC phases by standing the sample for 5 h. Reprinted with permission from Ref. [22]. Copyright 2010 The Royal Society of Chemistry

Compared to other clay mineral systems, these systems are very fluid up to very high concentrations, which is suitable for various basic research and applications. In these systems, gelation did not occur even at 7.0 wt%. Fossum et al. also investigated synthetic fluorohectorite systems; they used a sample with impurities. The viscosity was high, and it was difficult to study the phase behavior [47, 53]. In addition to these fluorinated clays, Miyamoto et al. found that the natural montmorillonite produced in Tsukinuno and purified by a similar method showed liquid crystallinity.

8.3.4 Graphene and Grapheme Oxide

Graphene has received much attention due to its excellent electronic and mechanical properties, and it was selected as the subject for the Nobel Prize in 2010. However, it is difficult to obtain a large amount of completely exfoliated graphene, and the graphene reported in many papers is not a nanosheet but a " stacked graphene". There are few reports on the liquid crystal phase of graphene; Dan et al. [54] obtained exfoliated graphene with high yield by dispersing in chlorosulfonic acid and observed the schlieren texture, which is characteristic of nematic liquid crystals.

In contrast to graphenes, it is easy to obtain single-layer graphene *oxide* nanosheets dispersed in a solvent, and many investigations have been carried out. However, graphene oxides have hydroxyl and/or carboxyl groups irregularly placed on their surface, and they have no defined chemical structure. The electronic properties characteristic of graphene are not retained in the graphene oxides, but the lost electronic properties can be recovered to some extent by post-reduction treatments. The liquid crystal phase of a graphene oxide was reported in 2001, followed by many additional reports. Kim et al. [55] obtained a single graphene oxide nanosheet with the thickness of 0.8 nm and the average particle size ranging from 0.75 to 1.65 μm. They observed an optical texture characteristic of a nematic phase by polarized optical microscopy, and the structure was confirmed for the freeze-dried sample by SEM (Fig. 8.13). In the system with the particle size of 0.75 μm, the phase transition concentration was 0.78 wt%. Aboutalebi et al. [56] prepared graphene oxide with the much larger average particle size of 33 μm, and the system had the ϕ_I of 0.1 wt%. Xu et al. [21] investigated the graphene oxide with the average particle size of 2.1 μm. This system had the ϕ_I of 0.025 wt% and the ϕ_{LC} of 0.5 wt%. When increasing the salt concentration by adding NaCl, ϕ_I and ϕ_{LC} tended to increase, while the colloid aggregated at higher salt concentrations. In the SAXS results, a peak attributed to the loose lamellar structure with basal spacing of 63 nm was observed at 2.5 wt%. The basal spacing was similar to that estimated from the one-dimensional swelling law. Because the graphene oxide nanosheet has strong luminescent properties, the characterization of the structure was carried out by direct observation by confocal laser scanning microscopy (Fig. 8.14).

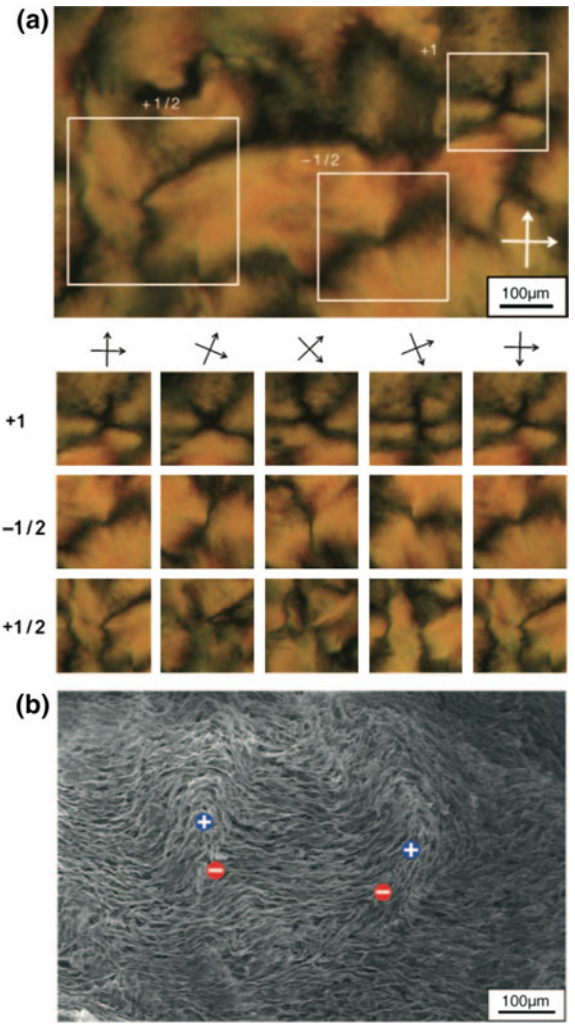

Fig. 8.13 Disclination morphologies of graphene oxide liquid crystals. **a** Typical nematic schlieren texture of a 0.3 wt% dispersion with ±1/2 disclinations and **a** +1 disclination. Successive rotations of crossed polarizers accompanied the rotation of brushes at various rotating rates and directions. **b** SEM image of a graphene oxide liquid crystal in a freeze-dried sample (0.5 wt%). *Blue* and *red* symbols indicate +1/2 and −1/2 disclinations, respectively. Reprinted with permission from Ref. [55]. Copyright 2002 WILEY–VCH

Xu et al. [57] also reported that graphene oxide nanosheets form LC phases with lamellar structures or the twist-grain boundary phases of chiral liquid crystals with long-range chiral frustration. The thickness of the nanosheet was 0.8 nm, and the average particle size was 0.81 μm. By observation of the schlieren texture, the phase transition from the isotropic phase to the nematic phase at 0.23 vol.% was determined. At greater than 0.39 vol.%, the clear and oriented strip-shaped structure similar to the fingerprint-like structure of the cholesteric phase was observed. The chiral spatial arrangement of the graphene oxide nanosheet was verified by the strong signal of circular dichroism in the wide wavelength range from 380 to 800 nm. The graphene oxide nanosheet with liquid crystallinity was injected into an

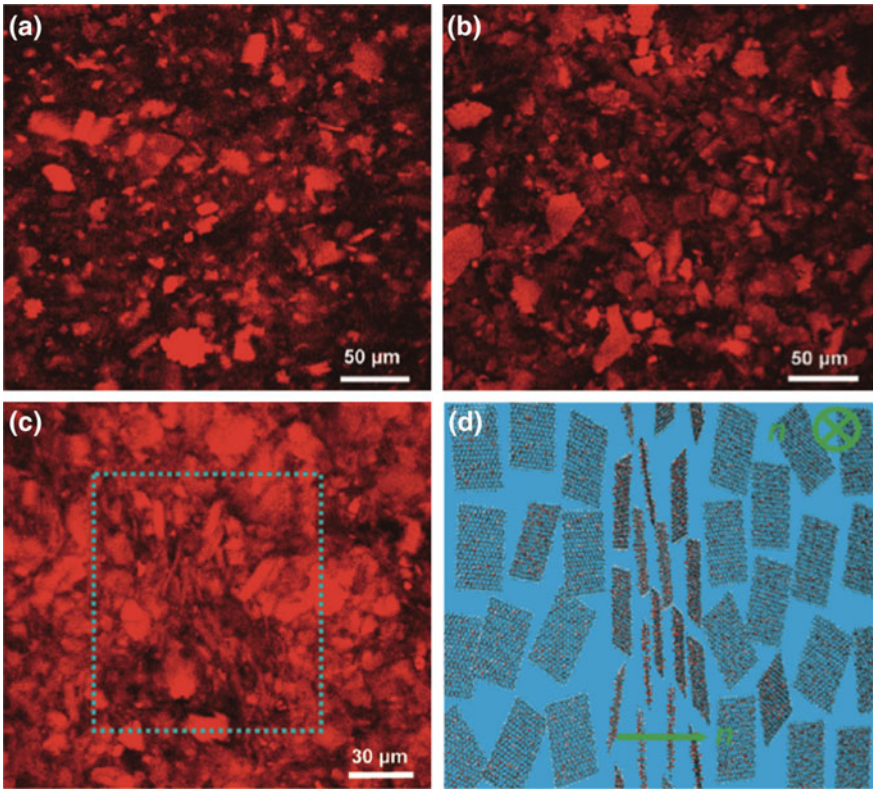

Fig. 8.14 Real-time confocal laser microscopy inspections of GO aqueous dispersions. ϕ is 2.5×10^{-4} (**a**), 5.0×10^{-3} (**b**), and 1×10^{-2} (**c**). A model **d** depicts the rotation of orientation vectors (n) in (**c**); the arrow directs the vector (n) on the paper, and the *cross* indicates a direction into the paper. Reprinted with permission from Ref. [21]. Copyright 2011 American Chemical Society

NaOH/methanol solution from a syringe, leading to coagulation of the nanosheets as a fiber, which showed high mechanical strength and electrical conductivity.

8.3.5 Other Related Materials

V_2O_5 nanoribbons are obtained by a sol-gel method from a homogeneous solution, not by exfoliation of a layered crystal. The shape is a thin ribbon with a uniform thickness rather than a nanosheet. However, they may be considered a type of nanosheet. The study of the liquid crystal phase of V_2O_5 colloid was first reported by Zocher in the 1920s [58]. In the 1990s, French research groups [59–64] conducted many investigations on the formation of the nematic phase and the response

to electric and magnetic fields [62]. Application to anisotropic media for NMR measurement was also reported [63].

Layered double hydroxides are an important class of layered materials because of their anion exchange capability, in contrast to most of other layered materials with cation exchange capability. Because they are synthesized by a hydrothermal reaction from an aqueous solution of starting chemicals, the particle size and chemical composition are controllable. Although many reports on the exfoliation of layered double hydroxide (LDH) have been published [65–68], it is difficult to obtain fully exfoliated nanosheets with the thickness of 0.6 nm while retaining the large lateral size in high yield. For that reason, there is no report on the liquid crystallinity of exfoliated nanosheets of LDH. However, the liquid crystallinity was reported by several groups for aqueous colloids of unexfoliated Mg/Al-type LDH particles. In 2003, Liu et al. reported that the colloid of LDH microparticles (Mg/Al ratio = 2, average particle size 60 nm, thickness unknown) had a liquid crystal phase at greater than 27 wt% [15]. Wan et al. [69] investigated the LDH with Mg/Al ratio = 1, average particle size of 130 nm, and thickness of 5.5 nm. This system showed the liquid crystal/isotropic biphase at 10–25 wt%. At 13 wt%, a lamellar structure with basal spacing of 40 nm was identified by SAXS. In the system with Mg/Al ratio = 2, average particle size of 102 nm, and thickness of 7.4 nm, Zhang et al. [70] observed a liquid crystal/isotropic biphase at concentrations ranging from 16 to 30 wt%. It was also reported that the concentration range shifted to the higher side with increasing salt concentration. Mourad et al. [71] synthesized various LDH microparticles with Mg/Al ratio = 2 with controlled average particle size ranging from 46 to 146 nm. Although the liquid crystal phase was not observed in these systems, the liquid crystal phase appeared when polyisobutylene was added. Zhu et al. [72] and Luan et al. [73, 74] reported that, by adding polymers to LDH microparticles, phase separation to more than three phases was observed. Thus, the formation of the liquid crystal phase of LDH microparticle system requires a higher concentration than other true nanosheet systems (below several %) because they have a low anisotropic ratio of particles due to the low degree of exfoliation.

8.4 Theories for the Liquid Crystal Phase Formation of Nanosheet Colloids

8.4.1 Onsager Theory

A theory for the formation of the liquid crystal phase of anisotropic particles, such as rods and sheets, was presented in 1949 by Onsager [27]. In this theory, the formation of a nematic phase, that is, a liquid crystal phase with orientational order and no positional order, is explained by the excluded volume effect on particles. According to this theory, it is expected that the colloid changes from an isotropic

phase to the nematic liquid crystal phase through isotropic-liquid crystal coexistence phase with increasing concentration. This behavior almost corresponds to the observations in experiments. Onsager's theory uses a simple model that assumes only hard core repulsions between cylinder particles with diameter D and height L. Because a particle with $L \gg D$ is regarded as a rod and a particle with $L \ll D$ is regarded as a disc, this theory is applicable for both cases.

When an anisotropic particle is rotating freely by Brownian motion, the particle occupies a very large excluded volume b compared with its solid volume v_p ($=\pi D^2 L/4$). The ratio of volumes is calculated as follows:

$$\frac{b}{v_p} = \frac{1}{v_p}\frac{1}{4}\pi D\left(L^2 + \frac{1}{2}(\pi+3)DL + \frac{1}{4}\pi D^2\right). \tag{8.8}$$

In the limit of L ≪ D, namely, in the infinitely thin plate particle limit, Eq. 8.8 reduces to:

$$\frac{b}{v_p} = \frac{\pi}{4}\frac{D}{L}. \tag{8.9}$$

In the case of the anisotropy ratio D/L = 100, b/v_p is 79. On the other hand, supposing that the particle is not rotating but is perfectly oriented, $b/v_p = 4$. Because of the large difference of b/v_p, large free volume for translational motion is gained if rotation is inhibited. In other words, translational entropy is gained if rotational entropy is lost. Therefore, in the situation that the particles have a large anisotropic ratio, the translational entropy gained by prohibited rotation of the particle, that is, orientation of the particle, should be larger than the rotational entropy lost. Thus, the nanosheets tend to be oriented and form a nematic liquid crystal phase.

Based on this simple theory, Onsager carried out numerical calculations of the transition concentration from the isotropic phase to the isotropic-liquid crystal coexistence phase, ϕ_I, and the transition concentration from the isotropic-liquid crystal coexistence phase-liquid crystal, ϕ_{LC}, and the results are as follows;

$$\phi_I = 3.3\left(\frac{v_p}{b}\right) = 3.3\left(\frac{4L}{\pi D}\right) \tag{8.10}$$

$$\phi_{LC} = 4.5\left(\frac{v_p}{b}\right) = 4.5\left(\frac{4L}{\pi D}\right) \tag{8.11}$$

As is obvious from these results, the concentration needed for the formation of the liquid crystal phase decreases as the anisotropic ratio D/L increases. Figure 8.15 summarizes the relationship between ϕ_I and D/L for the nanosheet and nanoplate systems reported so far. The trends found in the experimental results are mostly in accordance with the theoretically calculated results.

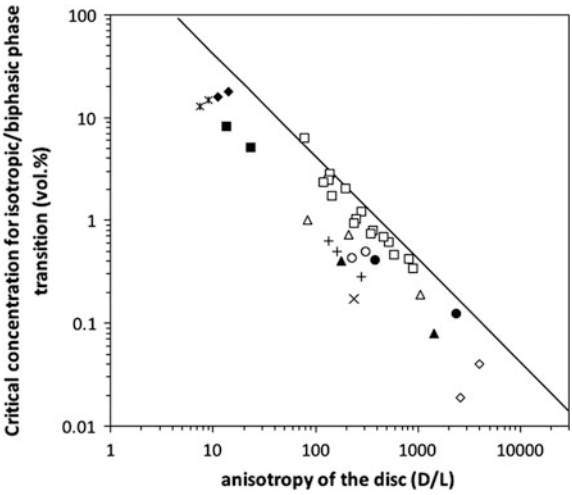

Fig. 8.15 Anisotropy-dependence of the critical concentration for the phase transition from isotropic to isotropic/liquid crystal biphase observed in disc-like colloidal dispersion systems: (*solid line*) Onsager's theory, (*open square*) α-ZrP [28], (*open triangle*) $K_4Nb_6O_{17}$ [17], (*cross*) $KCaNb_3O_{10}$ [20], (*open diamond*) graphe oxide [21, 75], (*filled circle*) fluorohectorite [22], (*filled triangle*) fluortetrasilicic mica [22], (*open circle*) beidelite [23], (*plus*) nontronite [24], (*filled square*) layered double hydroxide [69, 70], (*asterisks*) $Ni(OH)_2$ [14, 76], (*filled diamond*) Gibbsite [12, 13]

Onsager's theory has been modified in various ways through theoretical and simulation approaches. The original Onsager's theory is inaccurate in the case of extremely high concentration because it takes into consideration only two-particle interactions, but multiparticle interactions cannot be ignored at high concentrations. If the multiparticle interactions are taken into consideration, the concentrations of the phase transitions should decrease compared to the original theoretical value [77]. In many cases, nanosheet systems show a large polydispersity of particle size, and this has a great effect. Monte Carlo simulation was carried out on disc-shaped particle systems with polydispersity in particle size. It was shown that the gap between ϕ_I and ϕ_{LC} increases with increasing polydispersity [77]. This theoretical prediction was confirmed experimentally [28]. The flexible shape of nanosheets can also influence the liquid crystal properties. In the experimental and theoretical studies of solution systems of rigid polymers regarded as flexible and long rods, it was revealed that ϕ_I and ϕ_{LC} are larger for polymers with larger flexibility [5]. On the other hand, the emergence of the liquid crystal phase with one-dimensional or two-dimensional positional order, namely, a smectic phase or a columnar phase, was predicted by both theoretical and simulation studies [14]. Experimentally, Lekkerkerker et al. reported the emergence of the columnar phase in ideal experimental systems, such as rod-shaped boehmite particles and plate-shaped gibbsite particles [12]. However, in the nanosheet systems, columnar phases have not been reported due to their very large D/L ratio and large polydispersity.

8.4.2 Other Theories

Provided that the interaction between nanosheets is completely repulsive, considering only the simple Onsager theory is sufficient for understanding the nanosheet liquid crystal systems. However, in many cases, it is not enough. Whereas Onsager's theory and its modified theory explain the emergence of nematic, smectic, and columnar phases, the theories do not explain the liquid crystal phases with swollen lamellar structure and high structural order, which have been observed in many nanosheet liquid crystal systems.

If the repulsive force between nanosheets is strong enough, we can easily guess that nanosheets in the nematic phase form a lamellar structure with the basal spacing predicted by the one-dimensional swelling law of Eq. (8.6). However, in many cases, a smaller basal spacing is observed compared to that predicted by the one-dimensional swelling law. These phenomena can be related to the fractal-like inhomogeneous structure composed of sparse and dense parts of nanosheets in nanosheet colloidal systems. The existence of the fractal structure in nanosheet colloidal systems was noted by many researchers. If the inhomogeneous structure exists, what is the origin of this structure? It is reasonable that relatively strong attractive forces, other than the weak van der Waals attractive force considered in DLVO theory, affect the formation of the fractal structure.

Depletion interaction is thought to be one of the origins of these attractive forces. This interaction is the entropic attractive force induced by the addition of smaller colloid particles to the original colloid. As the distance between two large colloid particles decreases, it becomes difficult for the small particles to be present in the narrow space between the two large colloid particles. As a result, the pressure from the small particles to the large particles works more strongly in the direction that is advantageous to drive the two large particles closer, that is, the attractive force is substantial. Because nanosheet systems have high polydispersity, it is possible that the attractive depletion force from the coexisting smaller nanosheets is working between the larger nanosheets.

The Ise-Sogami theory is also remarkable [78]. According to this theory, attractive forces are acting between the particles with the same type of charge (positive–positive or negative–negative) due to the attractive interaction between a colloidal particle and its counter ion cloud surrounding the particle. Although this theory is different from DLVO theory, which is known as the classical standard, and caused many controversies, this theory can explain the structural formation of spherical colloidal particles and the swelling behavior of layered clay minerals quantitatively. Smally et al. conducted a detailed study on the ideal system in which the single-crystal layered clay mineral vermiculite swelled in aqueous *n*-butylammonium solution. From the calculation based on DLVO theory, the basal spacing calculated from a secondary minimum did not coincide with the experimental results or a minimum did not appear. In contrast, a deep secondary minimum appeared in the potential curve in the calculation based on Ise-Sogami theory. The position of the secondary minimum $d_{\min}$ is represented by the following simple

equation after some approximations, and the calculated values coincided well with the experimental results.

$$d_{\min} = 4\kappa^{-1} \tag{8.12}$$

A similar explanation is also possible in the largely swelling layered ferrotitanate [79, 80] and layered perovskite [81], both reported by Sasaki et al.

The repulsive force originating from the waviness of nanosheets may also be considered. The waviness of layers in a lamellar phase induces an entropic repulsive force known as the Helfrich interaction [82]. In general, the inorganic crystals constructed by covalent bonds have a much higher modulus of elasticity than the well-studied molecular layers composed of surfactant. However, as suggested by the bent-shaped nanosheets formed by drying on a TEM grid [17] and the wrinkles in the nanosheets formed by the elongation and compression of cast nanosheets on a PDMS substrate [83], a nanosheet is not a completely rigid plate but has flexibility to some extent in a solvent. It is thought that the modulus of elasticity of nanosheets is influenced by the chemical composition, thickness of the layers of nanosheets, coexistence of solvent molecules, and counter ions, so that the extent of waviness of a nanosheet also changes depending on these factors. Considering Helfrich interaction, the basal spacing d is expected to show the difference from the one-dimensional ideal swelling behavior as:

$$d = \frac{L}{f}\frac{A_s}{A_p} \tag{8.13}$$

Here, A_s is the substantial area of the nanosheet and A_p is the area of a crumpled nanosheet projected from the top. If the nanosheet is crumpled, A_p is smaller than A_s, so the basal spacing is larger than the rigid plane.

8.5 Orientational Control Under External Fields

The colloidal nanosheets can be easily manipulated by external fields. Because of their nature of soft matter, they can change their orientation with weak external forces. This property allows us to construct various hierarchical structures up to macroscopic scale from the nanosheets. We can obtain the desired soft colloidal structures by the controlled application of external fields. Electric and magnetic fields, shear flows, and interaction at interfaces have been examined as external fields. The orientation under an external field is induced by the intrinsic shape anisotropy of the nanosheets. Since the shape anisotropy is accompanied by anisotropy of the dielectric constants and magnetic susceptibilities, the nanosheet orientation can be altered by the external forces even in isotropically dispersed states. However, the nanosheet colloids in the LC state often show specific structures because of the collective nature of LCs.

8.5.1 *Orientation Under Electric Fields*

The orientation of the nanosheets under electric fields is principally governed by their dielectric anisotropy derived from their 2D shape. Electric field-induced orientaional control is applicable for most colloidal nanosheets. The electric alignment of nanosheets was discovered in the 1930s as a birefringence change with the application of continuous AC or pulsed DC electric fields [84–86]. This phenomenon is termed electric birefringence. Because most of the nanosheets bear permanent electric charges, AC electric fields are usually utilized for the continuous application of electric voltages; continuous DC electric fields do not retain the nanosheets in a colloidal state but electrophoretically deposit them on electrodes [87].

8.5.1.1 Electric Birefringence

Electric birefringence is an electrooptic effect that occurs when anisotropic colloidal particles are electrically aligned. Because of their 2D shape, colloidal nanosheets induce large optical retardation to the light propagating along the in-plane direction (Fig. 8.16a). If the nanosheets are lamellarly oriented with a random arrangement with respect to their in-plane direction, the index ellipsoid of the nanosheet colloid can be drawn as optically uniaxial, as in Fig. 8.16b. Birefringence of the colloid consisting of the oriented nanosheets is observed, when the light is not parallel to the n_o axis; that is, the colloid acts as a medium with a uniform refractive index when the incidence of the light is perpendicular to the nanosheet surface [88].

Historically, electric birefringence had been investigated for clay colloids under continuous AC electric fields (70–500 V cm^{-1}, 50–10^6 Hz [84–86]) to determine

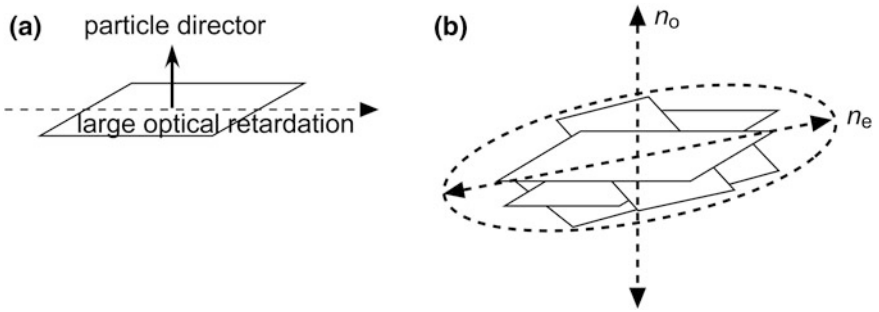

Fig. 8.16 Geometry of the crystallographic and optic parameters related the colloidal LCs of inorganic nanosheets: **a** directions of large optical retardation and particle director for each nanosheet, and **b** proposed orientational ordering of the nanosheets in the LC state and directions of large retardation (n_e) and isotropic (n_o) expected for this ordering. Adapted with permission from [88]. Copyright 2011 American Chemical Society

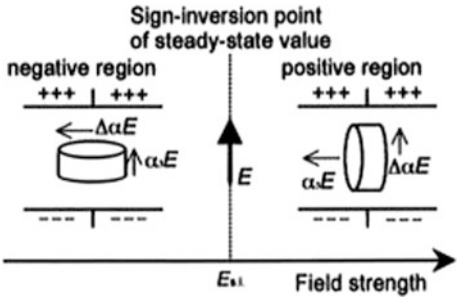

Fig. 8.17 Schematic presentation of particle orientation against field strength for Na-montmorillonite particles. Below the sign inversion field $E_{s.i.}$, the plane of the particle is oriented perpendicular to the direction of electric field (*left*). Above $E_{s.i.}$, the plane of the particle is oriented parallel to the direction of electric field (*right*). Reprinted with permission from [94]. Copyright 1996 American Chemical Society

the orientation of colloidal anisotropic particles under external fields. Later, pulsed DC electric fields were utilized to extract detailed orientation mechanism by analyzing the temporal response of the nanosheets [89–95]. Because electrically charged nanosheets dispersed in water are accompanied by a huge amount of solvated countercations, the electrooptic response of the nanosheet colloids can be ascribed not only to the alignment of nanosheets but also to the electrically induced reorganization of the countercations around the clay nanosheets. Both of the movements occur upon the application of electric voltages with different time constants, and the opposite signs of the electric charges of the nanosheets and countercations lead to positive/negative inversion of the birefringence (Fig. 8.17) [94]. Because of the different diffusion rate of the nanosheet particles and the surrounding ionic species, their responses to an applied pulsed electric field have a time lag that causes time-dependent sign inversion of the birefringence. Based on such electrooptic behavior, the kinetics of the electric alignment of clay nanosheets has been discussed.

Because the colloidal clay nanosheets can adsorb cationic dyes, the electric alignment of clay nanosheets can be used to align the adsorbed dye molecules. This dye orientation is observed as electric dichroism of the optical absorption due to the supported dye molecules. This phenomenon can be applied for color modification of the colloids and to investigate the binding state of the dyes to the clay nanosheets [96–101].

8.5.1.2 Electrorheological Behavior

The electric response of colloidal particles leads to reversible alterations of the rheological properties of the system upon the application and removal of an electric voltage. This phenomenon is termed the electrorheological (ER) effect [102]. Colloidal systems showing great ER effects have attracted interest as novel smart

fluids applicable for valves, clutches, dampers, and actuators. Layered materials, in particular clay minerals and recently graphene oxide (GO), have been examined as ER materials [103–107].

For ER applications, clay particles are usually not exfoliated but are hydrophobized and dispersed in silicone oil because the ER fluids are typically obtained as colloids of dielectric particles in insulating solvents. Interlayer modification by long-chain organic molecules or polymers is used for this purpose [103–105]. Modification of the external surfaces is also effective, as demonstrated by nanocomposites with inorganic dielectric oxide particles [108] or polymer nanospheres [109]. For GO particles, external surface modifications are mainly employed because they are exfoliated into stacked nanosheets [107, 110–112]. Under the application of an electric field (DC or AC), the modified clay or GO particles are polarized and aggregated into chain-like structures in parallel with the field. When the electric field is applied perpendicular to the flow direction, the chain-like aggregates suppress the flow of the colloid, which is a typical ER response.

However, dried clay particles with hydrophilic inorganic interlayer cations can also be dispersed in silicone oil to show ER effects [106, 113]. As shown in Fig. 8.18, chain-like structures are obtained for clay particles with inorganic interlayer cations. The difference in the structures compared to the interlayer cations indicates a critical role of the interlayer species in the ER properties of the clay minerals. Dried GO particles dispersed in silicone oil also exhibit ER behavior without hydrophobic additives [114].

The ER behavior of the exfoliated clay nanosheets has been examined in water. Aqueous clay colloids show reversible viscosity increase when applying DC or

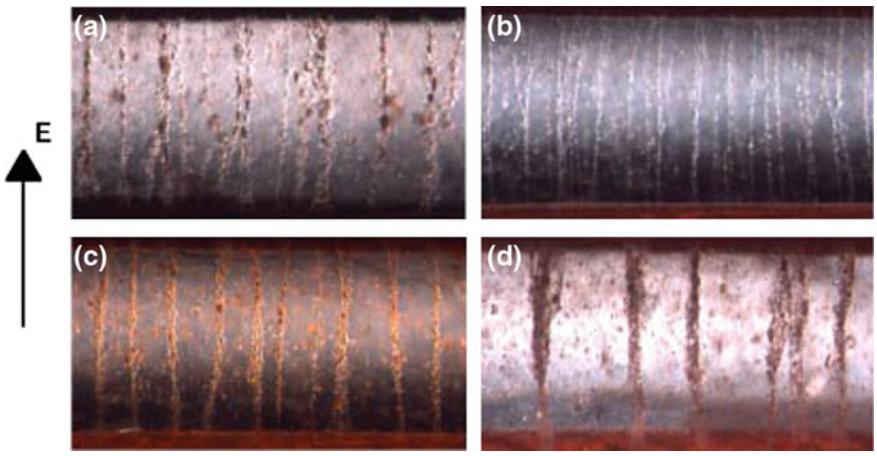

Fig. 8.18 Optical microscope images of electrorheological chain formation in oil suspensions of smectite clays. **a** Na-fluorohectorite. **b** Ni-fluorohectorite. **c** Fe-fluorohectorite. **d** Natural quick clay. Reprinted from [106]. Copyright 2006 EDP Sciences

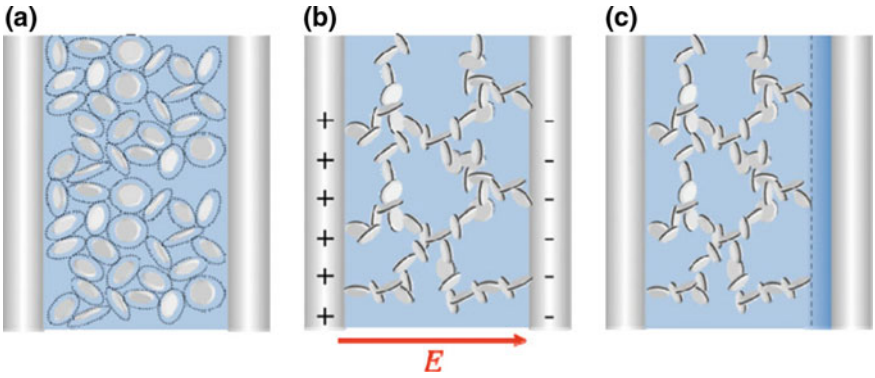

Fig. 8.19 Schematic illustration of dispersion states of hectorite particles in deionized water under steady shear. **a** without the electric field, **b** under the DC electric field, and **c** after removing the electric field. The *broken line* shows a boundary surface of colloidal-rich region and water one. Reprinted with permission from [115]. Copyright 2013 Springer

low-frequency ($\sim 10^{-3}$ Hz) AC voltages [115–117]. Their ER response is characterized by low threshold voltages of less than 100 V cm^{-1}. AC voltages with a frequency greater than 10^{-2} Hz are ineffective. The viscosity increase has been ascribed to the formation of "house-of-cards"-type networks between the clay nanosheets whose structure is not fully relaxed, as indicated by incomplete recovery of the viscosity after the removal of the electric field (Fig. 8.19).

8.5.1.3 Electric Alignment of the Nanosheets in the LC State

Application of electric fields to aqueous nanosheet LCs gives macroscopically ordered nanosheet structures, which can be ascribed to the synergy of the electric and liquid crystalline alignment of the nanosheets. High-frequency AC voltages are generally utilized to align the electrically charged liquid crystalline nanosheets in aqueous systems. The first example of the electric alignment of the nanosheet LCs was reported for the colloids of beidellite clay [23]. When a colloidal LC sample in a 0.2-mm thick and 2-mm wide flat capillary is subjected to an AC voltage of 4000 V cm^{-1} and 500 kHz between electrodes placed in parallel with 1 mm distance in the longitudinal direction of the capillary, the clay nanosheets are aligned in parallel to the electric field to give macroscopic homogeneous ordering of the nanosheets over the area of 2 mm $\times$ 1 mm (Fig. 8.20). AC voltage applications to isotropic and biphasic (coexistence of isotropic and nematic phases) colloids of the same clay mineral (beidellite) also align the nanosheets, and their ordering degree is unexpectedly high compared with those induced theoretically [118]. This behavior is explained by the strong coupling of the electrically charged clay nanosheets and the applied electric field.

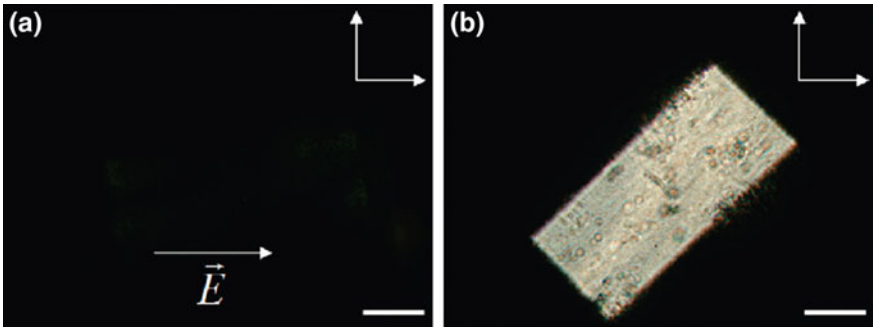

Fig. 8.20 Polarized optical microscope images of fluid nematic samples of beidellite suspensions (ionic strength = 10^{-5} mol L^{-1} and ϕ = 0.61%) in a 1 mm cylindrical glass capillary aligned in a 4×10^4 V m^{-1}, 500 kHz electric field at **a** 0°, extinction; and **b** 45°, maximum of transmission. The crossed polarizer and analyzer are indicated by the *white arrows*, and the *scale bar* indicates 500 μm. Reprinted with permission from [23]. Copyright 2009 American Chemical Society

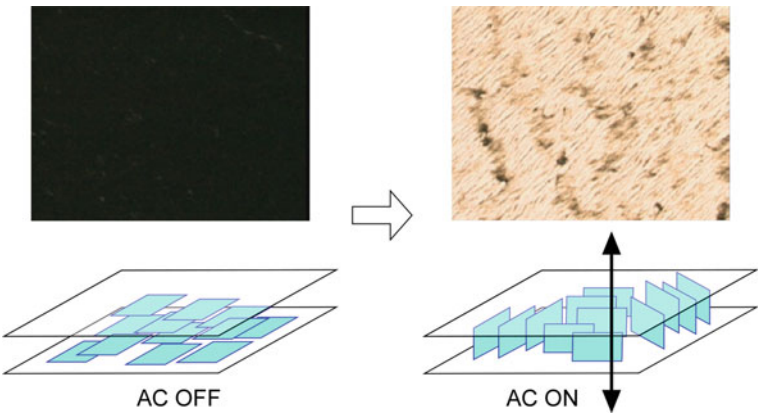

Fig. 8.21 Optical microscope images and schematic representation of the colloidal hexaniobate nanosheets (10 g L^{-1}) in LC state (*left*) before and (*right*) after the electric alignment under the AC electric field of 15×10^2 V cm^{-1} and 50 kHz in a 100 μm thick cell. Adapted with permission from [88]. Copyright 2011 American Chemical Society

The electric alignment of the colloidal LCs of the hexaniobate $K_4Nb_6O_{17}$ nanosheets was examined with AC electric fields of 500–2000 V cm^{-1} and 50 kHz [88]. The electric field is applied to the LC sample placed in a 0.1-mm thick sandwich-type cell in the direction perpendicular to the cell surface. The nanosheets in the LC colloids are aligned parallel to the electric field, i.e., perpendicular to the cell surface, showing a strong electrooptic response (Fig. 8.21). However, in contrast to the beidellite clay system, the electrooptic response of isotropically dispersed nanosheets is much weaker ($\sim$1/1000) than that of the LC samples. This result indicates a contribution of the collective nature of the LC state to the

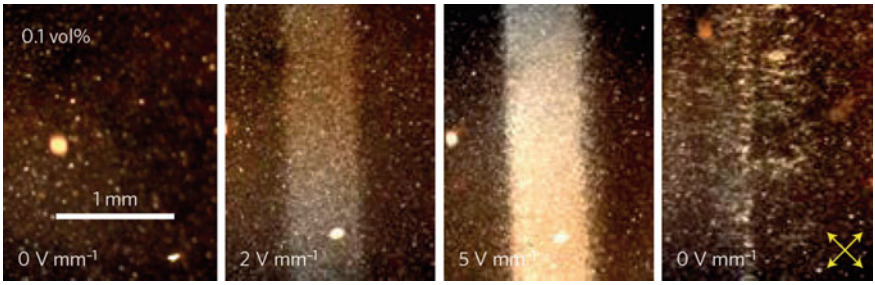

Fig. 8.22 Electric-field-induced birefringence of colloidal GO nanosheets. Field-induced birefringence was generated by applying electric fields (10 kHz) to a cell with thickness of 300 μm thick and distance between the electrodes of 500 μm filled with an aqueous 0.1 vol.% GO dispersion. When the field was switched off, the field-induced birefringence almost disappeared, with only slight nematic aggregation remaining. Reprinted with permission from [75]. Copyright 2014 Nature Publishing Group

nanosheet alignment under the external fields. The electrooptic behavior of the nanosheet LCs is characterized by a slow response and low threshold voltage; the nanosheet alignment shifts in a time range of seconds with a less than 1 V cm^{-1} electric field. This is ascribed to the mesogen size of the nanosheet LCs, which is much larger than that of conventional molecular LCs. Retention of the electrically induced alignment, being a type of a memory effect, is observed for the LCs with high nanosheet concentrations. A macroscopic monodomain structure is obtained by repeated AC voltage applications, which reorient the nanosheets through backflow in the sample cell.

Graphene oxide (GO) nanosheet LCs also show electric alignment under AC electric fields of 10–200 V cm^{-1} and 10 kHz [75] (Fig. 8.22). A 0.3-mm thick thin-layer cell is used with electrodes placed in parallel to the cell surface with a 0.5 mm distance. Similar to the niobate system, the GO nanosheet LCs show slow electric response and sensitivity to low electric fields. The electrooptic response also depends on the concentration of coexisting ionic species [119]. The electric response of the colloidal LCs were lost with 10^{-3} mol L^{-1} of NaCl or HCl, while NaOH did not have large effect. This behavior is explained by the modification of the electric charges on the GO nanosheet surfaces in the presence of coexisting electrolytes, depending on their concentration and species; the surface charge alters the polarization of the nanosheets to change their electrooptic response.

8.5.2 Orientation Under Magnetic Fields

Similar to the electric fields, magnetic fields align colloidal nanosheets. Magnetic alignment is easily attained when the nanosheets contain magnetic elements. Nanosheet colloids of nontronite clay, which contains Fe(III) species in the

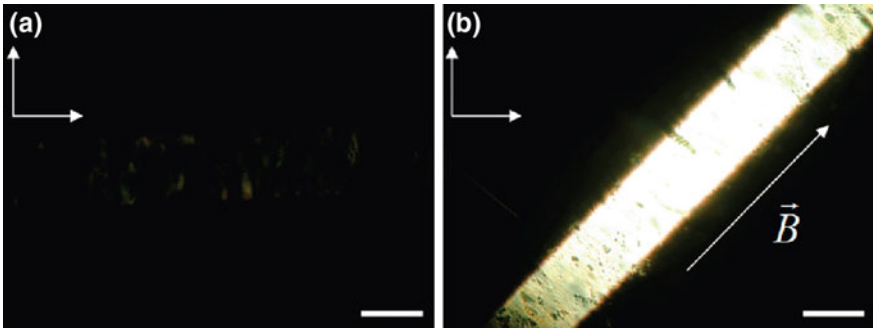

Fig. 8.23 Polarized optical microscope images of a fluid nematic phase of a beidellite suspension at an ionic strength of 10^{-4} mol L^{-1} and ϕ = 0.62% held in a 1 mm cylindrical glass capillary and submitted to an 8 T magnetic field for 15 h. Photographs were taken at **a** 0°, extinction, and **b** 45°, maximum of transmission. The crossed polarizer and analyzer are indicated by the *white arrows*, whereas the *scale bar* represents 1 mm. Reprinted with permission from [23]. Copyright 2009 American Chemical Society

aluminosilicate layers, show magnetic alignment [49, 120]. The nontronite nanosheets in the isotropic and LC states are both aligned under a magnetic field of >1 T, and their free and collective orientations are distinguished by ^{2}H-NMR analysis. When the nanosheets are diamagnetic, more intense magnetic fields are required. Examples are nanosheet LCs of layered metal phosphate $H_3Sb_3P_2O_{14}$ and beidellite clay (Fig. 8.23), which are aligned under magnetic fields of 19 and 8 T, respectively [16, 23]. Platy particles of non-exfoliated hexaniobate $K_4Nb_6O_{17}$, as well as nanoscrolls obtained from its exfoliated nanosheets, are magnetically aligned at 12 T [121]. Because GO and reduced GO (rGO) have rather high magnetic susceptibilities among the diamagnetic materials due to their π-conjugated systems, their nanosheets can be aligned slowly under relatively weak magnetic fields of $\sim$0.25 T [55, 122]. However, nanosheet LCs of synthetic fluorohectorite clay characterized by large nanosheet size and the absence of magnetic elements have been reported to show magnetic alignment at 2 T [123], which could be ascribed to the collective nature of the large-size nanosheets in the LC state.

Another technique for the magnetic alignment of the diamagnetic nanosheets is loading magnetic nanoparticles, such as Fe_3O_4, on the nanosheets. Partly restacked few-layer nanosheets of perovskite-type niobate $HCa_2Nb_3O_{10}$ are oriented under magnetic fields greater than 10^{-3} T [124, 125] when Fe_3O_4 nanoparticles are attached via covalent linkers. The 2D distribution of the magnetic nanoparticles on the nanosheets leads to biaxial superparamagnetic susceptibility of the colloidal particles, which are aligned parallel to the magnetic fields. GO and reduced GO nanosheets also become easily aligned magnetically with this method [55, 126].

8.5.3 Orientation by Shear Forces

The alignment of the colloidal nanosheets is also achieved under shear. The application of shear forces to the colloids induces nanosheet orientation along the shear direction. A typical example is observed during settlement of the colloidal nanosheets. Nanosheet alignment along gravity at a macroscopic ($\sim$ cm) scale has been reported for the colloidal LC of hexaniobate $K_4Nb_6O_{17}$ nanosheets placed in a test tube (1 cm in diameter) [30] (Fig. 8.24). This behavior is explained by the flow of the colloids induced by the settlement of the dispersed nanosheets with gravity.

The flow-induced orientation is observed more clearly by applying mechanical shear to the nanosheet colloids. When a test tube containing a hexaniobate nanosheet colloid is rotated, the colloid shows birefringence along the shear flow, indicating the shear-induced orientation of the nanosheets [17, 30]. The flow birefringence is observed for both isotropic and LC nanosheet colloids. The shear-induced alignment is temporal and gradually disappears after removal of the rotation. This phenomenon has also been observed for nanosheet LCs of montmorillonite clay [25] and GO [127]. The relaxation of the shear-induced alignment becomes slower at higher nanosheet concentrations.

The shear-induced alignment of the nanosheets has been applied for the preparation of practical materials. The preparation of self-supporting films is a known example. Casting the colloidal nanosheets on a flat substrate causes unidirectional deposition of the nanosheets, and self-supporting "paper" is obtained after

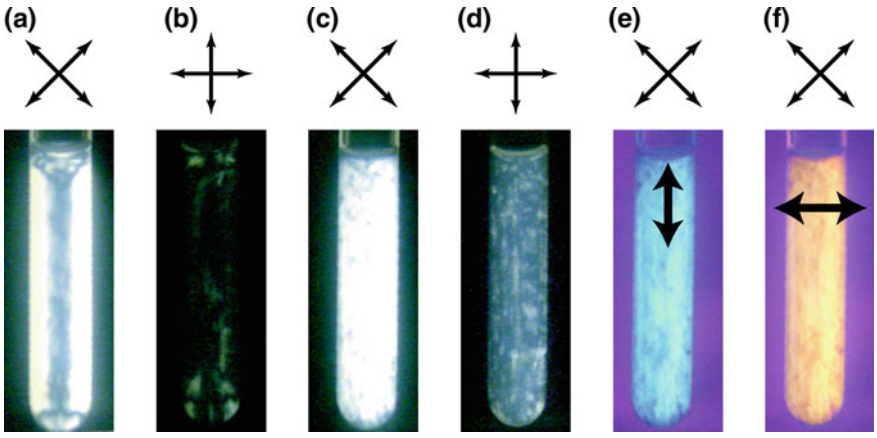

Fig. 8.24 Photographs of the hexaniobate nanosheet colloid containing 9.6×10^{-5} mol L^{-1} of $[Nb_6O_{17}]^{4-}$ in a test tube (1 cm in diameter) observed between crossed polarizers whose directions are indicated by double arrows. The images were taken after several seconds of rotation for **a** and **b** and after letting the sample stand for 60 min for **c**–**f**. A 1st-order retardation plate (optical retardation = 530 nm) was used in observations (**e**) and (**f**), setting the "slow-vibrational direction" as indicated by the *bold arrows*. Reprinted with permission from [30]. Copyright 2002 WILEY–VCH

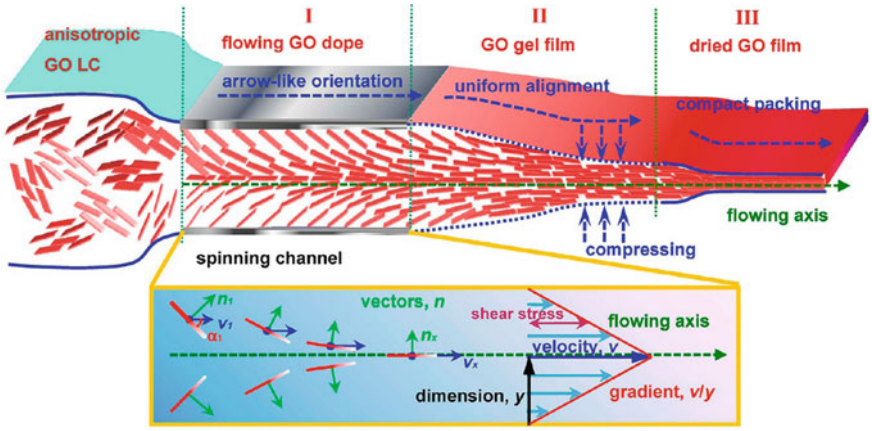

Fig. 8.25 Schematic diagram depicting the structural evolution of GO paper with three typical stages: *I*, arrow-like orientation; *II*, uniform alignment; *III*, compact packing. Here, *n*, *v*, and α denote the orientation vector of GO, the velocity of the flowing layer, and the angle between the GO sheets and the flowing direction, respectively. Reprinted from [128]. Copyright 2014 American Chemical Society

removing the substrate. While "clay papers" are utilized as colorless transparent supports of functional dyes [129, 130], films of semiconducting oxide nanosheets work as "photocatalytic paper" [131]. "Graphene papers" prepared from GO or rGO nanosheets have been investigated as membranes for adsorption and separation (Fig. 8.25) [128, 132, 133]. On the other hand, fiber-spinning of mixtures of colloidal GO or rGO nanosheets with organic polymers yields inorganic–polymer composite fibers [134–136]. The strong shear forces applied during the spinning process align the nanosheets in the fibers to give strong mechanical strength and physicochemical properties such as electrical conductivity due to graphene.

8.5.4 *Hierarchical Macroscopic Structures of Nanosheet LCs Under Dual External Fields*

The 2D shape and large particle (mesogen) size of the nanosheet LCs enable the organization of various hierarchical nanosheet-based structures at the macroscopic scale. In contrast to 1D particles (rods) that are unidirectionally aligned with a single external force, 2D particles have two orthogonal axes for regulation of their alignment so that unidirectional alignment is only attained under dual external fields. The large particle (mesogen) size of the nanosheets at the μm level is advantageous for constructing macroscopic structures hierarchically, in comparison with conventional molecular LCs.

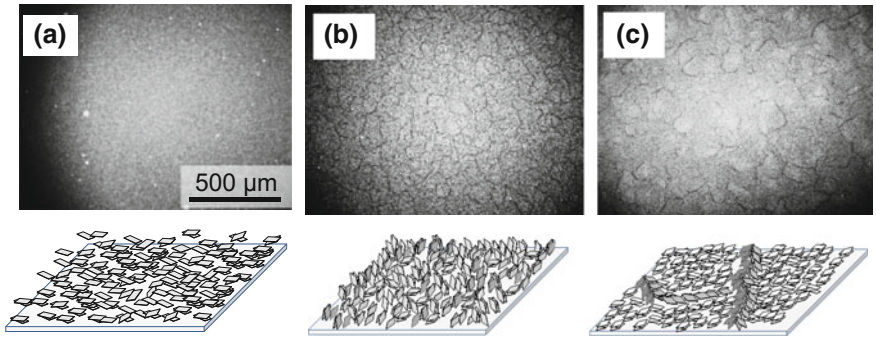

Fig. 8.26 Gray-scaled FOM images and schematic representation of the nanosheet arrangement of the niobate nanosheet LC (5 g L^{-1}) in a 100-μm thick cell before **a** and after incubation for **b** 60 and **c** 120 min. Adapted with permission from [137]. Copyright 2014 The Royal Society of Chemistry

Based on this consideration, we have organized the hierarchical macroscopic structures in the colloidal LCs of hexaniobate $K_4Nb_6O_{17}$ nanosheets [137]. An important key for the hierarchical organization is the growth of LC domains, called tactoids, as the secondary building blocks followed by controlled application of external fields. The growth of the tactoids is achieved by keeping the nanosheet LCs stand at room temperature, a process called incubation, for several tens of minutes (Fig. 8.26). The tactoid growth is analogous to Ostwald ripening in crystal growth.

The tactoids are then assembled into macroscopic higher order structures with characteristic lengths of sub-mm to mm under simultaneous application of an AC electric field and gravity, whose directions determine the final structural motif. Although a net-like structure forms when applying the electric and gravitational forces in the same direction, a stripe structure, where the nanosheets are unidirectionally aligned, is obtained when the electric field is applied in the direction perpendicular to gravity (Fig. 8.27). The use of well-grown tactoids is a key to macroscopic structural control. Among these macroscopic structures of the photocatalytically active niobate nanosheet LCs, the stripe structure is applicable to control the photocatalytic reactions. The nanosheet stripes exhibit photocatalysis, which reflects the alignment of the nanosheets with respect to the polarized direction of the impinging light.

8.5.5 Orientation at the Interfaces

Although the inorganic nanosheets are well dispersed in aqueous and organic liquid phases when they are sufficiently hydrophilic or organophilic, respectively, the particles can be accumulated at heterogeneous interfaces if they have appropriate affinity to all the related phases. Typically, a small amount of long-chain

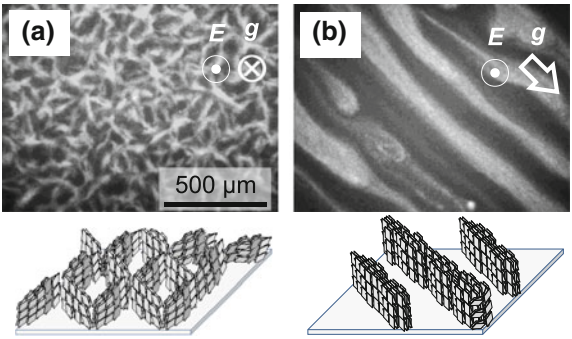

Fig. 8.27 Gray-scaled FOM images and schematic representation of the nanosheet arrangement of the niobate nanosheet LC (5 g L^{-1}) in a 100-μm thick cell under an AC electric field of 5 V cm^{-1} and 50 kHz after incubation for 120 min. The electric field was applied in the direction **a** parallel and **b** perpendicular to gravity for 8 and 60 min, respectively. The directions of the electric field (*E*) and gravity (*g*) are indicated by *circles* and an *arrow*. Adapted with permission from [137]. Copyright 2014 The Royal Society of Chemistry

organoammonium salt dissolved in an organic solvent is carefully spread on the surface of an aqueous nanosheet colloid to yield a nanosheet monolayer at the air–water interface [138, 139]. Another method of preparing an interfacial monolayer reported for synthetic saponite clay is intercalation of the organoammonium species and subsequent dispersion in an organic solvent, which is then spread on water [140]. Interfacial monolayer films have been fabricated into nanosheet multilayer films through the Langmuir–Blodgett technique.

Solid particles can stabilize interfaces when they are trapped there [141, 142]. This property is applicable to stabilizing liquid and gas droplets that are colloidally dispersed in continuous phases. Such colloidal systems of particle-stabilized droplets in continuous phases are termed Pickering emulsions (liquid in liquid) and foams (gas in liquids), and liquid marbles (liquid in air) [143, 144]. These colloidal systems provide broad practical applications in various fields, such as the petroleum, food, cosmetic, and pharmaceutical industries and are recognized as a type of multicomponent soft matter where particles are aggregated in a specific manner at structured interfaces. Inorganic particles can add unusual properties to such materials if the particles possess advanced optic, photochemical, catalytic, electric, and magnetic properties.

Particles with various morphologies have been examined as such "particle surfactants" [146]; 2D particles can effectively stabilize the interfaces if they are adsorbed in parallel to the interfaces (Fig. 8.28) [145, 147, 148]. In this regard, the exfoliation of layered crystals into nanosheets is not an essential requirement. In fact, non-exfoliated particles of layered crystals with platy morphologies have been employed for Pickering emulsions [145, 148–155] and foams [156–159], where moderately hydrophobic surfaces are required for droplet stabilization. The affinity to the droplet and continuous phases is adjusted by mixing with additives or intercalation of appropriate species into the interlayer spaces. Very recently,

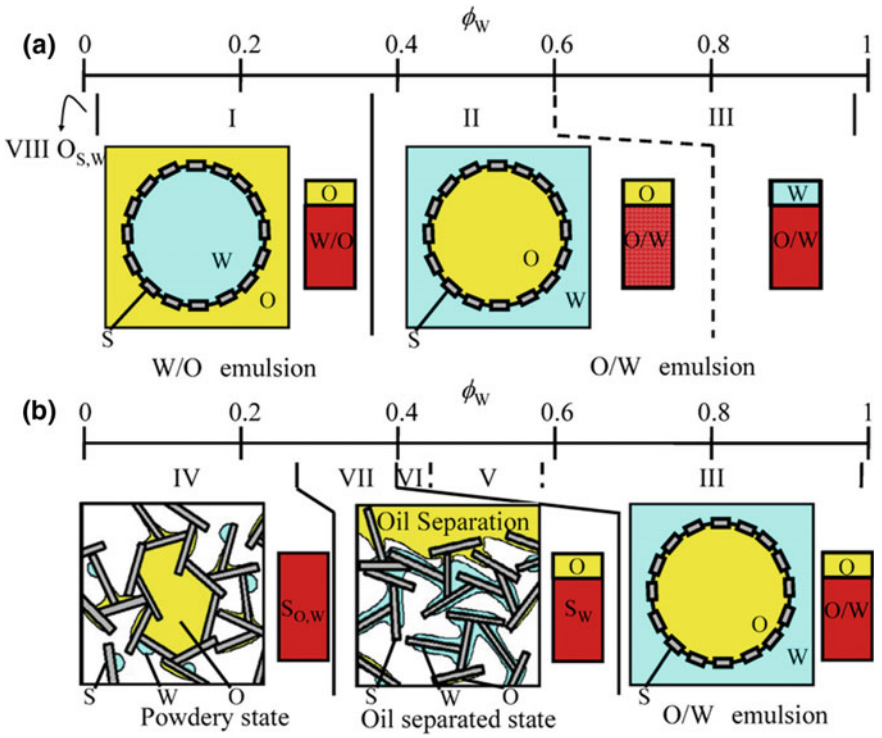

Fig. 8.28 Schematic illustrations of the mixed states of the ternary system consisting of platy clay particles, silicone oil, and water when **a** $0 < \alpha < 0.4$ and **b** $0.4 \leq \alpha < 1$. Reprinted with permission from [145]. Copyright 2009 Elsevier

few-layer GO nanosheets were used to prepare both emulsions and foams after suitable modification of their surfaces (Fig. 8.29) [160–163]. α-ZrP nanosheets also stabilize Pickering emulsions and foams [147, 164].

8.5.6 Immobilization of Aligned Nanosheet Structures

Immobilization of the nanosheet colloid structure regulated by LC phase formation or external field is important for many applications. Inorganic nanosheets, especially clay minerals, have been immobilized in polymer matrix and utilized as nanofillers for plastic polymer materials to improve the thermal stability, gas-barrier properties, and mechanical properties. Recently, nanosheets were also utilized as the fillers for polymer gels, which are network-type polymers swollen by a solvent. The gel materials are applicable for biomaterials and soft actuators. In 2002, Haraguchi et al. [165] reported that the mechanical properties of polymer gels are

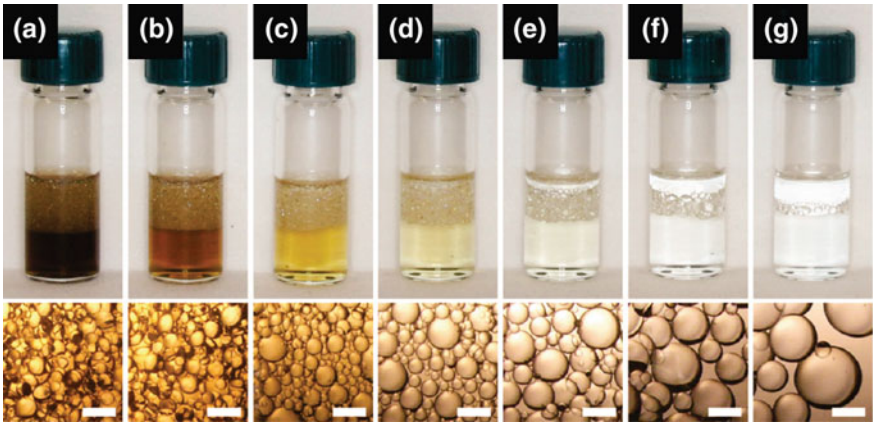

Fig. 8.29 GO at the liquid–liquid interface. GO sheets can stabilize oil droplets in water by adsorbing at the oil–water interface, forming Pickering emulsions. Toluene droplets formed upon shaking a tolune/GO water mixture, where the concentration of GO was varied from **a** 0.95 mg/mL to **b** 0.47, **c** 0.19, **d** 0.095, **e** 0.047, **f** 0.019, and **g** 0.0095 mg/mL, respectively. The *bottom row* shows microscopy images of the toluene droplets. All *scale bars* are equal to 1 mm. Reprinted with permission from [162]. Copyright 2010 American Chemical Society

largely improved by using synthetic hectorite nanosheets as the multiple physically crosslinking sites for polymer chains. Many studies with similar concepts have been reported [166–170]. The synthesis of composite gels was also carried out by photopolymerization, which allows easier control of the shape of the gels [167, 171–173].

Whereas isotropic nanosheet colloids were used in the above examples, composite materials with liquid crystalline nanosheets are expected to show better mechanical and anisotropic properties. Miyamoto et al. [174] reported the composite gel with anisotropic properties, which was synthesized using liquid crystalline clay nanosheets. An aqueous mixture of liquid crystalline fluorohectorite nanosheets, a monomer, a chemical crosslinker, and a radical initiator was flowed into glass capillary, allowing the nanosheets to be macroscopically ordered along the glass wall of the cell used for the synthesis. After polymerization and crosslinking in the capillary, the composite gel was obtained, which contained the nanosheets aligned in a tree-ring-like structure. In this report, the structural analysis during the synthetic process was carried out by SAXS (Fig. 8.30). Before the reaction started, the lamellar structure with the basal spacing of 35 nm was confirmed. The basal spacing decreased as the reaction proceeded, and it was 10 nm at the end of the reaction. After the reaction, the gel was placed in pure water and swelled macroscopically until the equilibrium swelling state. Corresponding to the macroscopic swelling, the basal spacing increased to more than 100 nm. Throughout these processes, the SAXS profile was kept anisotropic. These results confirmed that the polymerization proceeded, maintaining a well-dispersed, liquid crystal state of the nanosheets. Induced by the anisotropic structure, the gel showed

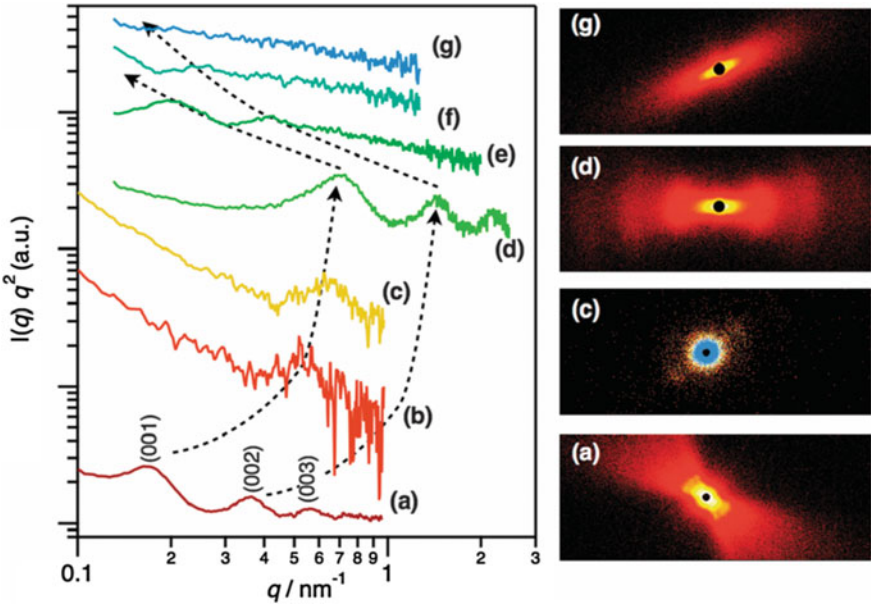

Fig. 8.30 SAXS profiles of the F5-B0-gel system: *a* FHT–NIPA–water mixture (before polymerization), the mixture during polymerization, *b* 1 and *c* 10 min after reaction initiation), *d* as-prepared gel, and the gel swollen for *e* 15, *f* 30, and *g* 60 min in water. Reprinted with permission from Ref. [174]. Copyright 2014 The Royal Society of Chemistry

anisotropic refractive index, modulus of elasticity, mass transport, and thermally induced phase transition behavior.

However, the tree-ring-like ordered structure in this system is not suitable for detailed evaluation of the anisotropic properties and for applications. Miyamoto et al. synthesized a sheet-shaped gel with a centimeter-scale ordered monodomain structure by applying alternating electric field during the synthesis. The orientation was controlled in both the out-of-plane and in-plane directions (Fig. 8.31) [173]. The gel sheet was easily printable with a tetravalent cationic dye at a resolution of tens of micrometers (Fig. 8.32a). When the gel was irradiated with light, only the colored part of the gel was heated, and the gel transformed into an asymmetric shape (Fig. 8.32b) through the thermally induced volume phase transition of PNIPA. This behavior is suitable for soft actuator applications.

Following the above reports, Mejia et al. [175] and Aida et al. [176, 177] reported anisotropic composite gels synthesized in a similar manner. Mejia et al. reported a composite of α-ZrP nanosheets and poly(acrylamide-co-*N*-isopropylacrylamide). They found that the equilibrium swelling ratio and the size of the oriented domain are controllable by tuning the synthetic conditions. Aida et al. used titanate and niobate nanosheets and magnetic field to obtain macroscopically aligned gels. Very large anisotropies in the optical, rheological, and deformation behavior were demonstrated.

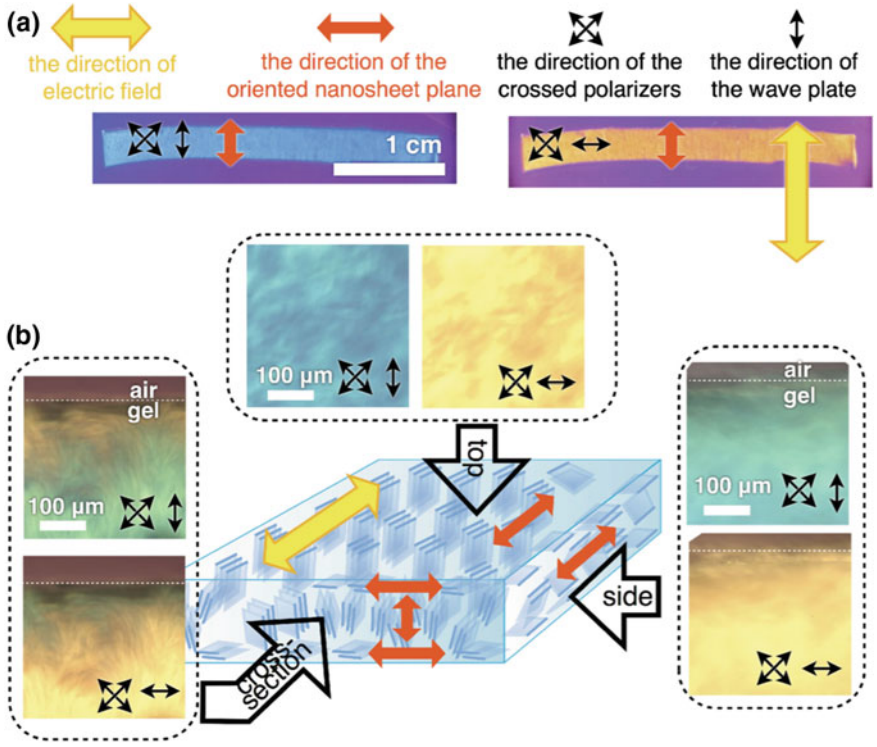

Fig. 8.31 **a** Photographs and **b** microscopic images and schematic structures of the FHT/PNIPA gels containing 1wt% of FHT synthesized with in-plane electric field. The images are observed with crossed polarizers and a wave plate. Reprinted with permission from Ref. [173]. Copyright 2014 WILEY–VCH

8.6 Multicomponent Nanosheet Colloids

8.6.1 Phase Separation in Multicomponent Colloids

The addition of other particles to the nanosheet colloids to yield multicomponent colloids is an important strategy for extracting specific functions from nanosheet-based colloidal systems by utilizing physicochemical interactions between the colloidal particles. In general, multicomponent colloids containing more than two morphologically different particle species, such as plate–rod, plate–sphere, and rod–sphere [72, 74, 178–188], show phase separation, which is demixing of the morphologically different colloidal particles based on entropically driven depletion effects. The phase separation results in rich phase behavior, which is typically observed as the coexistence of plural LC phases [189]. The phase separation of multicomponent colloids involving nanosheets or plate-like particles has been studied theoretically rather than experimentally. Computational studies

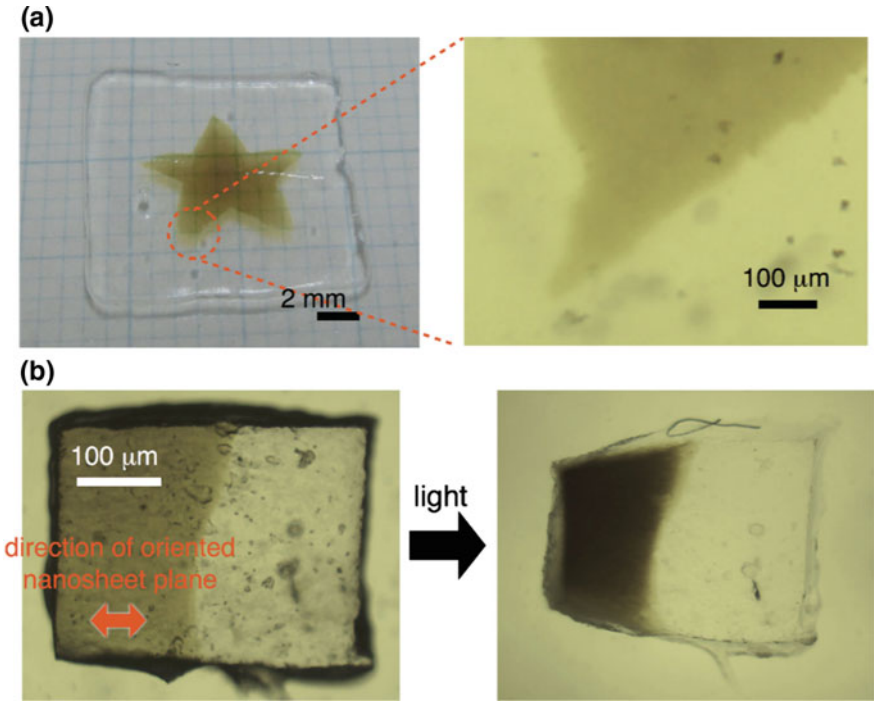

Fig. 8.32 Patterned coloration of the FHT/PNIPA gels with TMPyP dye and its partial photoresponsive deformation: **a** photograph (*left*) and microscopic image (*right*) of the gel printed with the dye pattern; **b** photoinduced partial deformation of the gel partially adsorbed with dye, as observed by optical microscopy. The *red arrow* indicates the direction of the oriented nanosheet planes. Reprinted with permission from Ref. [173]. Copyright 2014 WILEY–VCH

have clarified the multiphase coexistence in plate–rod and plate–sphere systems [190–196]. Additionally, there are theoretical studies of a plate–plate system [197–200], which is a model of the binary nanosheet LCs, indicating three-phase coexistence of one isotropic and two LC phases.

These theoretical predictions have been proved by experimental results, although the real systems are rather complicated because of the presence of particle size distributions and interparticle chemical interactions. For example, an experimental binary system of gibbsite ($Al(OH)_3$) plates and boehmite (AlOOH) rods shows five-phase coexistence (isotropic, rod-dominant nematic, plate-dominant nematic, unidentified nematic, and columnar phases), in accordance with theoretical considerations (Fig. 8.33) [179, 201]. The plate–polymer systems of gibbsite with poly (dimethylsiloxane) [202] and LDH with poly(ethylene glycol) [72] exhibit the coexistence of four to five phases (one isotropic and three to four LC). An LDH–polymer (poly(vinyl pyrrolidone) binary system shows six-phase existence (one liquid, two isotropic, two LC, and one sediment) [74].

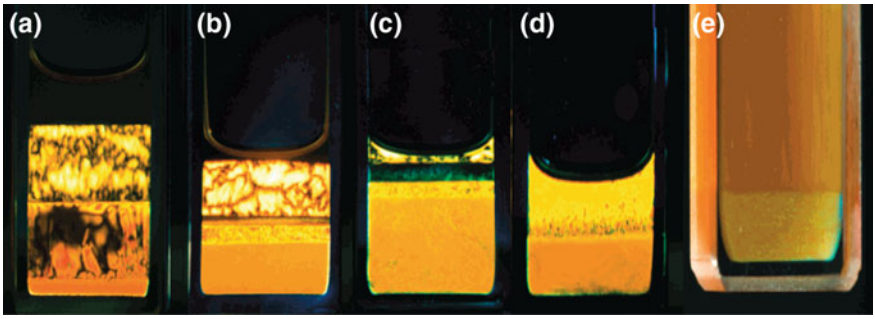

Fig. 8.33 Phase-separated rod-plate mixtures as observed between crossed polarizers. Depicted are **a** four-phase $I + N^{+} + N^{-} + C$ coexistence (denoted in order from *top* to *bottom*) in a sample with the composition (ϕ_{rod}, ϕ_{plate}) = (0.06, 0.26), **b** five-phase $I + N^{+} + X + N^{-} + C$ coexistence at (0.10, 0.22), **c** four-phase $N^{+} + X + N^{-} + C$ coexistence at (0.07, 0.29), and **d** two-phase $N^{-} + C$ coexistence at (0.03,0.35). Image **e** depicts a sample at (0.02, 0.35) exhibiting $N^{-} + C$ coexistence, photographed without crossed polarizers but illuminated by white light to demonstrate the Bragg reflections in the lower (C) phase. Reprinted with permission from [201]. Copyright 2000 American Chemical Society

With respect to multicomponent colloids involving exfoliated nanosheets, binary systems of the nanosheets and silica spheres have been examined, and their phase behavior is somewhat different from that of conventional plate–sphere systems. The beidellite clay–silica system shows only isotropic–nematic biphasic coexistence, similarly to the single beidellite system; however, introduction of silica particles accelerates the phase separation process [204]. In addition, the silica spheres suppress the sol-gel transition of the clay colloid to stabilize the nematic sol state. Binary colloids of α-ZrP nanosheets and silica particles show multiphase coexistence characterized by isotropic–isotropic demixing; isotropic–isotropic biphasic and isotropic–isotropic–nematic triphasic coexistence is observed (Fig. 8.34) [203]. Isotropic–isotropic phase separation is also observed for a binary system composed of synthetic hectorite clay (Laponite) nanosheets and Fe_2O_3 spherical nanoparticles [205]. A plate–rod system of montmorillonite clay nanosheets and sepiolite clay rods shows three-phase coexistence (one isotropic and two nematic) [206].

8.6.2 Phase Separation of Binary Nanosheet Colloids

In contrast to the plate–sphere and plate–rod systems, plate–plate binary colloids have not been thoroughly explored experimentally. Binary nanosheet colloids prepared from chemically different layered crystals are important members. In addition to the nanosheet systems, an example is a single-component colloid of gibbsite plates with a bimodal distribution of the particle thickness, which exhibits triphasic coexistence of an isotropic, nematic, and columnar phase, and the result is rationalized by computer simulation [200].

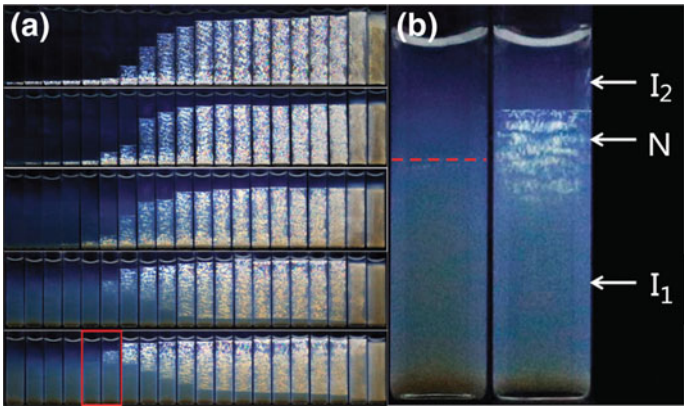

Fig. 8.34 **a** Images of plate–sphere mixtures of α-ZrP nanosheets and silica spheres observed between crossed polarizers 30 days after preparation. From *top* to *bottom*, volume fraction of added silica spheres in percentage is 0, 0.050, 0.230, 0.450, and 0.680, the error bar of which is ±0.003. From left to right, volume fraction of ZrP in percentage is 0.36, 0.42, 0.48, 0.54, 0.6, 0.66, 0.72, 0.78, 0.84, 0.9, 1, 1.1, 1.2, 1.3, 1.4, 1.5, 1.7, 2, and 3, 4; the error bar is ±0.01. **b** Detail of the two samples boxed in (**a**), showing I–I demixing and tri-phase coexistence. Reprinted with permission from [203]. Copyright 2015 The Royal Society of Chemistry

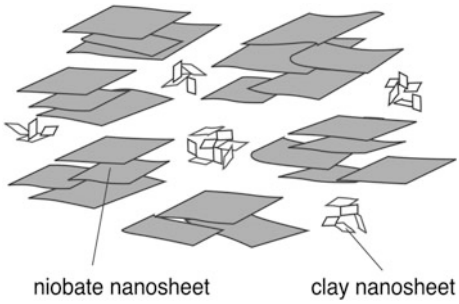

Fig. 8.35 Schematic representation of the microscopic phase separation in the niobate–clay binary nanosheet colloids

We have developed binary nanosheet colloids of niobate $K_4Nb_6O_{17}$ and smectite-type clay (natural montmorillonite or synthetic hectorite (Laponite)) nanosheets [207–209]. Although the binary nanosheet colloids are apparently homogeneous at the macroscopic (>sub-mm) scale and show liquid crystallinity, phase separation at the microscopic scale is evidenced by the SAXS analysis, which indicates compression of the LC phase due to the niobate nanosheets with the introduction of clay nanosheets. The niobate and clay nanosheets are separated and assembled into the microdomains of niobate and clay, respectively, as schematically shown in Fig. 8.35. Spectroscopic observations using a cationic organic dye as a probe also support demixing of the clay and niobate nanosheets at the microscopic

level. Based on the result that the cationic dye molecules are selectively adsorbed on the clay nanosheets and the dye does not show spectral dichroism, the clay particles are isotropically dispersed in the binary colloids to be phase-separated from the LC niobate nanosheets.

However, the binary colloids of titanate nanosheets from lepidocrocite-type layered oxide $H_{1.07}Ti_{1.78}O_4$, used instead of the niobate nanosheets combined with the clay nanosheets, result in different phase separation behavior [210], although the niobate and titanate nanosheets have similar geometric shapes and chemical properties. The titanate–clay binary LCs show macroscopic phase separation with three-phase coexistence of one isotropic and two LC phases (Fig. 8.36). The difference between the titanate and niobate nanosheets is due to the different countercations that are introduced as exfoliating reagents for the mother layered crystals: propylammonium for the niobate and TBA^+ for the titanate. Chemical interactions between the titanate and clay nanosheets, mediated by their countercations, destabilize the colloid. Although most of the nanosheets bear permanent surface charges accompanied by counterions, this fact is usually ignored in the simulations so that combination of the nanosheets with different counterions will modify the phase separation behavior.

Binary aqueous nanosheet colloids composed of synthetic hectorite (Laponite) and natural montmorillonite, which are both clay minerals with similar physicochemical properties and different particle sizes, show isotropic–isotropic biphasic coexistence in a mixed gel state [211]. The phase separation occurs at a microscopic scale, similarly to the niobate–clay system, due to kinetic arrest by the gel state (Fig. 8.37). DLS measurements suggest that the montmorillonite nanosheets form a matrix for the hectorite nanosheets by interacting with each other [212].

There are some other nanosheet–nanosheet binary systems with colloidal properties and applications. Reduced graphene (rGO) nanosheets are colloidally stabilized in the presence of montmorillonite clay nanosheets due to hydrogen-bonding interactions between the rGO and clay nanosheets [213]. The stabilized colloidal nanosheets are applicable for preparing highly oriented hybrid films. The addition of montmorillonite clay nanosheets to a colloidal LC of GO nanosheets enables preparation of graphene–clay hybrid fibers through wet spinning in the presence an appropriate organic polymer [214]. The hybrid fiber shows superior electric conductivity and thermal stability in air compared with neat graphene fibers due to the suppression of graphene oxidation by the clay nanosheets. Nanosheet–polymer hybrids with two nanosheet species have recently been explored for various applications, such as self-healable hydrogels, artificial nacres, and electrodes [215–217]. A binary system of rGO and manganate nanosheets was found to be stable at limited nanosheet concentrations and aggregated under other conditions [218], as observed for the titanate–clay system. Aggregation is a common phenomenon of binary colloids of nanosheets with opposite electric charges, such as the clay–LDH and GO–LDH systems [219–223].

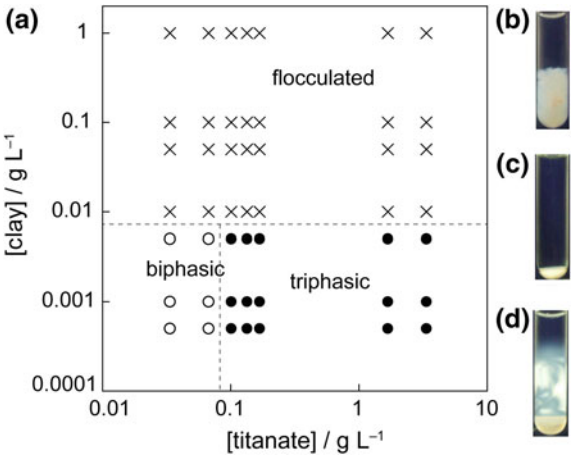

Fig. 8.36 **a** Phase diagram of the titanate–clay binary nanosheet colloids and typical appearances of the **b** flocculated, **c** isotropic–LC biphasic, and **d** isotropic–LC–LC triphasic samples between crossed polarizers. *Symbols* embedded in the diagram indicate the experimentally examined composition. Reprinted with permission from [210]. Copyright 2014 The Royal Society of Chemistry

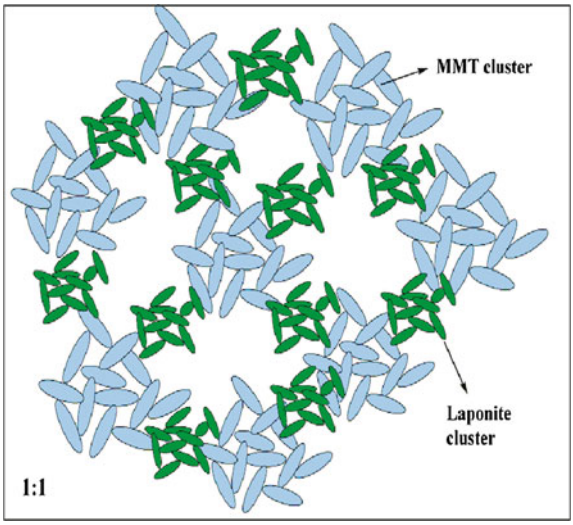

Fig. 8.37 Model of the assembled network structure of the plate–plate binary colloid composed of hectorite (Laponite) and montmorillonite (MMT) nanosheets at a mixing ratio of 1:1. Reprinted with permission from [211]. Copyright 2011 The American Chemical Society

8.6.3 Photochemical Applications of Niobate–Clay Binary Nanosheet Colloids

Niobate–clay binary nanosheet colloids that are phase separated at a microscopic scale can be applied for photofunctional systems. In such systems, photocatalytically active semiconducting niobate and physicochemically inert clay nanosheets are spatially separated but contact easily because the nanosheets are diffusive in the colloidal system and demixed only at a microscopic scale. Selective adsorption of cationic organic molecules onto the clay nanosheets leads to the existence of two

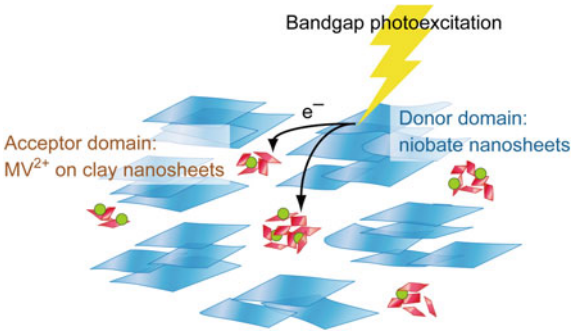

Fig. 8.38 Schematic representation of the photoinduced electron transfer in the MV^{2+}/niobate–clay colloids. Reprinted with permission from [209]. Copyright 2009 American Chemical Society

spatially separated functional moieties that are photocatalytically active niobate nanosheets and organic dye molecules on the clay nanosheets.

If an electron-accepting organic species (methyl viologen; MV^{2+}) is introduced to the niobate–clay colloids, photoinduced charge separation between the semiconducting niobate and the acceptor selectively adsorbed on the clay occurs (Fig. 8.38) [208, 209]. The photochemical behavior is characterized by controllability of both the yield and stability of the photoproduct ($MV^{+\bullet}$) by the clay content. Figure 8.39 shows the amount of photoproduct in the colloids with various clay contents and their time-dependent decay after termination of the irradiation. The yield (maximum conversion) and lifetime of the product vary in the range of 8–70% and 10 min to 40 h, respectively, depending on the clay content, indicating that efficient and stable photoinduced charge separation is achieved under the optimum conditions.

On the other hand, the niobate–clay binary colloids exhibit photoinduced electron accumulation in the niobate nanosheets in the absence of an acceptor [224]. This process is also affected by the coexisting clay component, although the clay nanosheets do not directly contribute to the electron accumulation in the semiconducting nanosheets. In contrast, the photochemical reaction is insensitive to the addition of molecular species that can work as electron donors; they somewhat destabilize the stable electron accumulation achieved by the addition of clay nanosheets. The results indicate that the photochemical reactions in the nanosheet colloid systems are not simply controlled by interactions between the semiconductor nanosheets and the additives at the molecular level but are governed by indirect interactions between the colloidal components.

Moreover, photocatalytic decomposition of a cationic dye has been studied in this binary colloid, where the dye is selectively adsorbed on the clay nanosheets to be spatially separated from the photocatalytic nanosheets [225]. Upon UV irradiation, the dye is photocatalytically decomposed in the colloids containing the niobate nanosheets, but self-photolysis of the dye is observed in the colloids lacking the photocatalytic nanosheets. In the binary colloid, the degradation is retarded

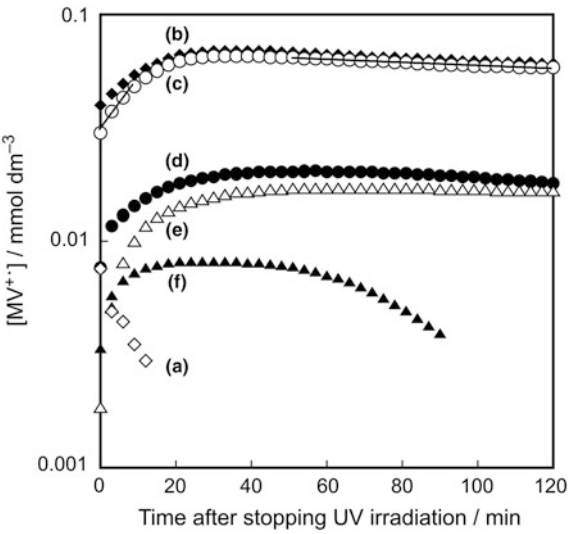

Fig. 8.39 Time courses of the concentration of $MV^{+\bullet}$ species observed after termination of UV irradiation in the MV/niobate–clay colloids with composition of [clay] = 1 (*a open diamonds*), 5 (*b filled diamonds*), 10 (*c open circles*), 20 (*d filled circles*), 25 (*e open triangles*), and 30 (*f filled triangles*) g L^{-1}, [niobate] = 1 g L^{-1} and $[MV^{2+}]$ = 0.1 mmol L^{-1}. The lines overlapping with plot (*a*) indicate first-order kinetics obtained by fitting the plot. Reprinted with permission from [209]. Copyright 2009 American Chemical Society

compared with the single-component niobate colloid. A greater clay content better stabilized the dye against decomposition. In contrast, irradiation of the colloids with visible light caused self-photolysis of the dye, even in the presence of niobate nanosheets, indicating the absence of electron transfer from the photoexcited dye to the photocatalytic nanosheets.

8.7 Rheological Properties

A colloid dispersion of smectite-type clays, such as hectorite and montmorillonite, in water loses its fluidity above a concentration of several wt%. The rheological behavior of clay colloids changes depending on the shear and the time elapsed after colloid preparation. These behaviors are referred to as thixotropy. This interesting rheological behavior is important in view of the practical applications of colloid dispersion. In particular, clay minerals have been used in a wide variety of application fields, such as paints and cosmetics, as rheology modifiers. Hence, many research works have been carried out in view of the technical aspects to understand the phenomena of rheological behavior. However, the fundamental studies are not sufficient, and research to obtain rational models to explain the rheological behavior of colloid dispersions and the control of their properties based on the obtained model is underway. In this section, the rheology of nanosheet colloids is reviewed, particularly focusing on clay mineral systems.

8.7.1 Theory and Models

According to the classical theory, anisotropic colloidal particles have a much higher viscosity than spherical colloidal particles. In a flow field, solid colloidal particles cause perturbation to the fluidic flow and flow resistance, namely, a viscosity increase, compared with an isotropic solution. In a colloid dispersion, the following viscosity equation is formulated in a dilute particle concentration:

$$\eta_r = 1 + k\phi, \tag{8.14}$$

where η_r is the relative viscosity, ϕ is the volume fraction of particles (equal to the concentration), and k is a parameter. Whereas k is 2.5 for spherical colloidal particles (Einstein equation for viscosity), on anisotropic colloidal particles, there are several cases governed by both the orientations of the particles by flow and disorder of the orientation by the rotational Brownian motion, and these relationships make k larger than 2.5.

Additionally, the particle size of nanosheets influences the viscosity. The relationship between the intrinsic viscosity of polymer solution $[h]$ and molecular weight M is known as the Mark–Houwink–Sakurada equation, as follows:

$$[h] = k\,M^a,$$

where k and a are constants. Applying this empirical formula, it can be shown that a clay nanosheet colloid (two-dimensional inorganic polymer solution) with a larger particle size (molecular weight) has a higher viscosity.

However, the complex rheological behavior on clay colloids cannot be explained by the above-mentioned simple theories because, as described in Sect. 8.4, various attractive forces (electrostatic attraction, van der Waals force, hydrogen bonding, and depletion force), repulsive forces (electrostatic repulsion and steric repulsion), and other interactions (entropy-induced orientation and phase separation) are intertwined. The rational elucidation of the rheological behavior of clay colloids using these forces is not easy, and it has become a controversial issue. At the moment, there are two probable elucidations for the aggregation and resulting gelation of clay colloids: one is the "card-house" model, which assumes the attractive force between particles as the dominant factor, and the other is the "colloidal glass" model, which assumes the repulsive force as the dominant factor.

The "card-house" model is a classical model for the gelation of clay colloids proposed by van Olphen [226]. In this model, the gel formation of a clay colloid is explained by the formation of a macroscopic network structure, like a "house built of playing cards" (Fig. 8.40a), which is composed of T-shaped connections of the plane (mainly negatively charged) and edge (mainly positively charged) of the clay sheet through electrostatic attraction. In a Monte Carlo simulation study, a card-house structure appeared in a particle dispersion system with a negatively charged plane and a positively charged edge [227]. Whereas this model was widely regarded as a standard model, there are some questions about this extreme

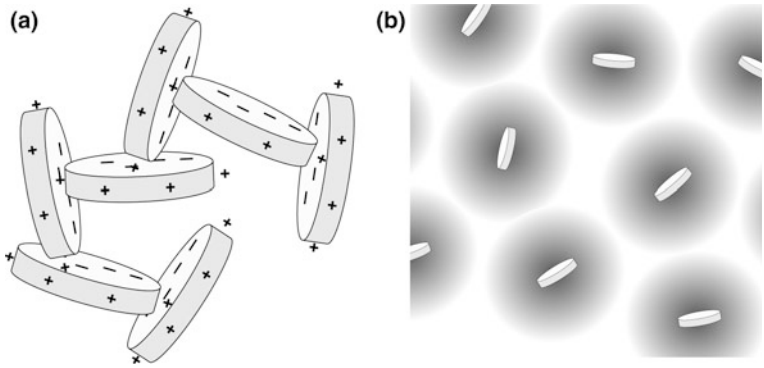

Fig. 8.40 Schematic illustration of the **a** house-of-cards structure and **b** colloidal glass of a clay nanosheet colloid

house-of-cards structure, and few experimental demonstrations of this structure formation have been reported. In a recent precise simulation [228], the card-house structure appeared only in the extremely restricted conditions. When the ionic strength is less than 5 mM, the interaction of the system is governed by only repulsive forces. When the ionic strength is greater than 5 mM, the overlapped state of the fringes of the clays becomes stable (such as the state of "layered coins"). When the ionic strength is greater than 100 mM, the van der Waals force becomes dominant, and the clay aggregates. In the first place, the AlOH and SiOH groups on the edge of the clay are charged only in the lower pH conditions in which $AlOH^{2+}$ and $SiOH^{2+}$ are generated by protonation. In the general conditions for clay colloids (pH = 12–13), AlOH and SiOH dissociate into negatively charged AlO^{-} and SiO^{-}, respectively. These dissociations are obvious from the zeta potential measurements [229].On the other hand, much of the experimental evidence suggests that the macroscopic network structure is formed in clay colloids through the attractive interaction between nanosheets. [35, 37, 39, 40, 230–233]. It is probable that the formation of a network structure similar to "layered coins" originates from the attractive forces between nanosheets, such as the hydrogen bonding and van der Waals forces through the AlOH and SiOH groups on the edge of the clay, as well as the attractive electrostatic interaction mediated by the countercations.

The other model, the colloidal glass model (or Wigner glass model) explains the gelation of nanosheet colloids as the restricted motion of negatively charged nanosheets or their clusters caused by electrostatic repulsion among them [26, 39, 234–239], as illustrated in Fig. 8.40b. Mourchid [26, 39, 235] determined the phase diagrams of the sol-gel transition semiquantitatively by rheological measurements and tried to explain the colloidal glass model based on osmotic pressure measurements. They found that the osmotic pressure decreased with increasing ionic strength and remained positive regardless of the concentration of the colloid and the ionic strength (Fig. 8.41). These results can be explained by the shielding of the electrostatic repulsion between particles due to the increased ionic strength and

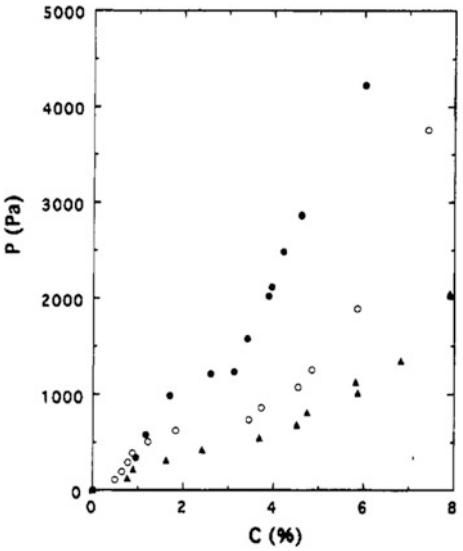

Fig. 8.41 Equations of state of the Laponite suspensions as a function of the ionic strength *I*: (*filled circle*) $I = 10^{-4}$ M, (*open circle*) $I = 5 \times 10^{-3}$ M, and (*filled triangle*) $I = 5 \times 10^{-2}$ M. Reprinted with permission from Ref. [39]. Copyright 1995 American Chemical Society

indicate that repulsive interaction was dominant in the system. The model is also supported by the phenomenon that the viscosity of the clay colloidal sol was decreased by adding a small quantity of salt [240–242] and the phenomenon that the onset concentration of the sol-gel transition increased with increasing ionic strength [243]. Michot et al. recently investigated the nontronite and montmorillonite systems and reported that the change of rheology by the colloid concentration, particle size, and ionic strength could be explained by the repulsive force only model [24, 25, 48]. However, as shown in the next section, the existence of a network structure in the gel was suggested by the structural analyses based on the results of the small-angle scattering [35, 37, 39, 40, 230–233]. These results contradict the colloid glass model.

8.7.2 Colloid Structure and Rheology

To clarify the gelation mechanism of nanosheet colloids, discussion of the colloid structure is very important. Whereas the formation of the anisotropic structure of the clay colloid in the liquid crystal state was described in the former section, detailed structural analyses by small-angle scattering methods (light, X-ray, and neutrons) have been carried out also for isotropic and gel phase clay colloids, and the relationship between the structure and its rheological behavior was discussed [35, 37–40, 244].

In small-angle scattering measurement of a dilute Laponite colloid, such as ca. 1%, the scattering curve almost coincided with the theoretical scattering curve for disc-like particles with 25 nm diameter and 1 nm thickness [36, 245–248]. In the region of the smaller scattering vector *q,* namely, the region that reflects the larger

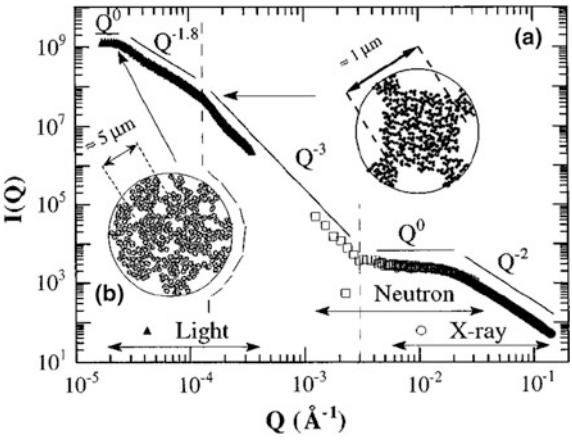

Fig. 8.42 Small-angle X-ray and neutron scattering and static light scattering from an aqueous Laponite suspension at rest, at volume fraction 1.6%, ionic strength of 1×10^{3} M, pH 9.5, and stored for 200 days. *a* Dense micrometer-sized aggregates and *b* mass fractal made of alternating aggregates and voids. Reprinted with permission from the reference [38]. Copyright 2002 American Physical Society

structure, excess scattering is sometimes observed, suggesting that the distribution of colloidal particles is not uniform. For example, Fig. 8.42 shows the results of the small-angle scattering of a Laponite colloid reported by Pignon et al. [37, 38]. The power laws of q^{-3} and $q^{-1.8}$ are observed. In general, a scattering curve with a power law of q^{-D} is ascribed to a mass fractal structure with fractal dimension D. Similar scattering results were reported by several other groups. These results were, regardless of the true structure, ascribed to an inhomogeneous structure with fractal dimension of 2–3, and some estimated structures, such as that shown in Fig. 8.43, were demonstrated.

Furthermore, Pignon et al. revealed that the power law of the SAXS pattern of the Laponite colloid changes from q^{-1} to $q^{-1.8}$ when increasing the concentration and ionic strength and as the gelation proceeds. The change of the fractal dimension (corresponding to the network structure) corresponded to a change of the yield stress so that it was concluded that the formation of a macroscopic inhomogeneous structure with up to micrometer scale dominated the rheological properties. However, the results of the small-angle scattering, ascribable to the fractal structure, were also observed in the niobate nanosheet system, showing an extremely lower viscosity compared to clay minerals [34]. Therefore, careful consideration is required to discuss the direct relationship between the structure and the high viscosity of the nanosheet colloid.

The structural changes of the colloid induced by shear [245] or with time [230, 249–256] were studied in detail, and important results to discuss the thixotropic behavior and gelation mechanism of the nanosheet colloids were obtained. Bonn and Tanaka obtained the phase diagram shown in Fig. 8.44 based on the time-course results of dynamic and static light scattering on a Laponite colloid system [239, 250, 254–256]. They claim that "clay colloids with no fluidity" can be classified as two different states, "gel" or "glass," depending on the conditions. They define "gel" as a network structure formed by dominant attractive forces, such as van der Waals force, in the region where the electrostatic repulsion force is

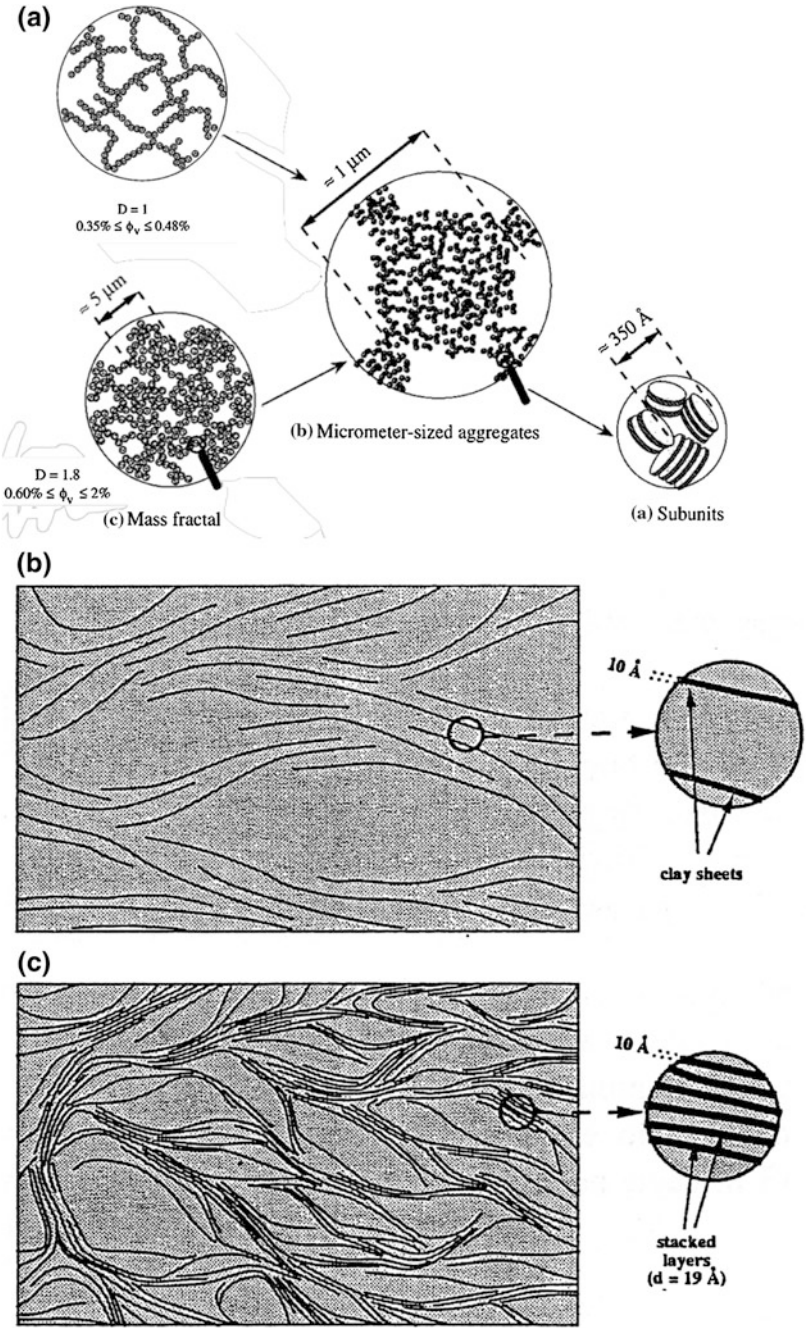

Fig. 8.43 Schematic illustrations of the fractal structure of the clay colloids presented by **a** Pignon [38] and **b**, **c** Morvan [40]. Reprinted with permission from the publishers. Copyright 1997 American Physical Society. Copyright 1994 Elsevier

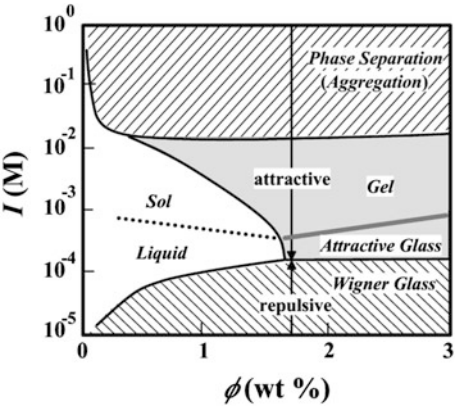

Fig. 8.44 Phase diagram of Laponite suspensions. Coexistence of phase separation and gelation is characteristic of a system that forms "physical" gel. Strictly speaking, this should be called a state diagram since a system is not in an equilibrium state. Reprinted with permission from Ref. [250]. Copyright 2002 American Physical Society

shielded at relatively high ionic strength. In this region, the growth of inhomogeneous clusters or network structures was observed with time. "Wigner glass" (repulsive colloid glass) is a typical colloidal glass that emerges when the electrostatic repulsive force is dominant in a lower salt concentration and when the sum of effective volume of colloid particles, including the Debye length, exceeds the volume of the system. In this type, the structure showed homogeneity and did not change with time. The motility of the particles was typical to colloidal glasses and was maintained with vibration in a small region, even after aging. The other phase, "attractive colloidal glass" appears in the intermediate region between the "gel" and the "Wigner glass." This phase is composed of nanosheet clusters, not individual nanosheets, as the unit particle, so that an inhomogeneous structure grows with time and the particles show no motility after aging.

8.7.3 *Control of the Rheological Properties of the Nanosheet Colloids*

In this final chapter, the reports on controlling the rheological properties of nanosheet colloids are presented. Largely et al. investigated the viscosity change of montmorillonite colloid after adding various types of salts and acids [240–242]. Figure 8.45 shows the viscosity change of montmorillonite colloids with the addition of various salts. Whereas the addition of a small quantity of salt decreased the viscosity due to shielding of the electrostatic repulsion between nanosheet colloids, a large quantity of salt caused an abrupt increase in the viscosity due to attractive interaction between nanosheets and the formation of an aggregated structure, named as an attractive gel. The viscosity depended on the species of salt. When a small amount of phosphate or pyrophosphate was added to the clay colloid,

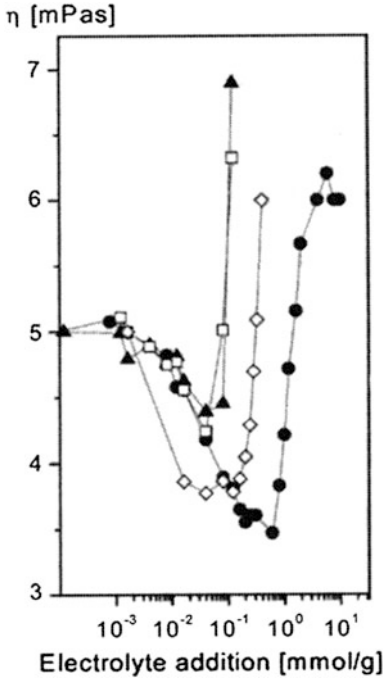

Fig. 8.45 Viscosity η at a shear rate of 120 s^{-1} for the 2% sodium montmorillonite dispersion in the presence of *filled circle* NaCl, *open diamond* $NaNO_3$, *filled triangle* HCl, and *open square* HNO_3. Reprinted with permission from Ref. [241]. Copyright 2001 Elsevier

the viscosity decreased greatly [241, 242]. The addition of polyelectrolytes, such as sodium polyacrylate [257], and nonionic polymers, such as poly(ethylene oxide), was also examined. In these cases, the viscosity decreased with the addition of a lower molecular weight polymer, whereas it increased with addition of a higher molecular weight polymer.

We found a pH-induced gelation of an exfoliated nanosheet colloid of layered niobate $K_4Nb_6O_{17}$ [258, 259]. When HCl or H_2SO_4 was added to the colloid (~ 10 gL^{-1}) and the pH was adjusted to 1.5, a physical gel was formed. Figure 8.46 shows the appearance of the colloid in the gel state. The change of pH changed the surface charge of the niobate nanosheet and influenced the electrostatic interaction between nanosheets. This process coincides with the gelation process of the clay colloid.

The lateral size of the nanosheet is also considered an important factor to control the viscosity. In the hexaniobate nanosheet system with controlled lateral size, colloids of the nanosheets with larger lateral size had higher viscosity [17]. However, in clay mineral systems, the opposite trend was reported for montmorillonite [25] and nontronite [24, 48]. Laponite, a synthetic hectorite with very small particle size of 25 nm [236], shows an extraordinarily high viscosity at low concentration. Thus we can not find any general trend for the relationship between the lateral size and the viscosity. Further systematic investigations are needed to understand the effect of nanosheet size on the viscosity.

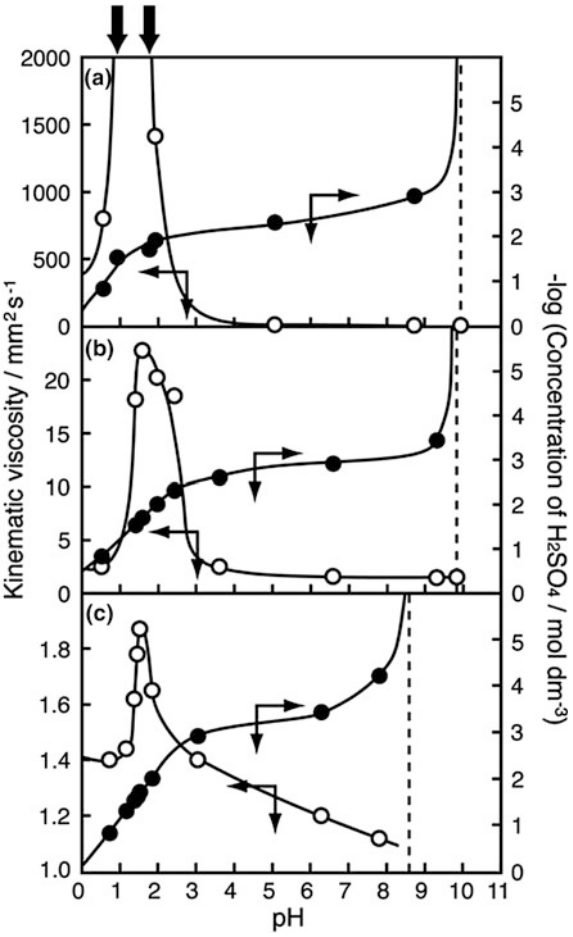

Fig. 8.46 Variations in kinematic viscosity of the niobate nanosheet colloids with pH (*open circles*), and titration curves of the colloids (relationship between pH and concentration of H_2SO_4 added) (*filled circles*). The colloids contain **a** 7.3, **b** 2.4, and **c** 0.8 g dm^{-3} of $[Nb_6O_{17}]^{4-}$, respectively. For the colloid containing 7.3 g dm^{-3} of $[Nb_6O_{17}]^{4-}$, viscosity was too high to be measured at pHs indicated by the *arrows* on the top. The dashed lines show pHs where $[[SO_4{}^{2-}] \sim 0$. Reprinted with permission from the reference [258]. Copyright 2002 The Royal Society of Chemistry

8.8 Summary and Outlook

The fundamentals and applications of colloidal nanosheets were reviewed. Liquid crystal phases of nanosheet colloids and control of them by external field are emerging as important topics because the intriguing hierarchical structure of the nanosheet can be assembled. Although we still have fundamental issues such as control of stability and rheological property and understanding of the structure formation mechanisms, some of novel colloidal materials and composite materials were successfully reported already. Further development of the researches on colloidal nanosheets will lead to many applications such as optical and electronic devices, medical materials, composite materials with good mechanical and barrier properties, structural colors materials for sensors and cosmetics, and composite gels for soft actuators.

Acknowledgements A part of this work was supported by Research Center for Materials and Energy Devices of Fukuoka Institute of Technology (FIT-ME) (Strategic Research Foundation Grant-Aided Project for Private University from MEXT) as well as by Canon Foundation, KAKENHI (#24104005 and #15K05657), and Network Joint Research Center for Materials and Devices (#201507 and #20166009).

References

1. Verwey EJW, Overbeek JTG (1948) Theory of the stability of lyophobic colloids. Elsevier, Amsterdam
2. Smalley M (2006) Clay swelling and colloid stability. CRC Press, New York
3. Livolant F, Levelut AM, Doucet J, Benoit JP (1989) Nature 339:724
4. Strzelecka TE, Davidson MW, Rill RL (1988) Nature 331:457
5. Sato T, Teramoto A (1996) Adv Polymer Sci 126:85
6. Bawden FC, Pirie NW, Bernal JD, Fankuchen I (1936) Nature 138:1051
7. Jana NR, Gearheart LA, Obare SO, Johnson CJ, Edler KJ, Mann S, Murphy CJ (2002) J Mater Chem 12:2909
8. Kajiwara K, Donkai N, Hiragi Y, Inagaki H (1986) Makromol Chem 187:2883
9. van Bruggen MPB, van der Kooij FM, Lekkerkerker HNW (1996) J Phys: Condens Matter 8:9451
10. Lemaire BJ, Panine P, Gabriel JCP, Davidson P (2002) Europhys Lett 69:55
11. Li L, Walda J, Manna L, Alivisatos AP (2002) Nano Lett 2:557
12. van der Kooij FM, Kassapidou K, Lekkerkerker HNW (2000) Nature 406:868
13. van der Kooij FM, Lekkerkerker HNW (1998) J Phys Chem B 102:7829
14. Brown ABD, Ferrero C, Narayanan T, Rennie AR (1999) Eur Phys J B 11:481
15. Liu S, Zhang J, Wang N, Liu W, Zhang C, Sun D (2003) Chem Mater 15:3240
16. Gabriel J-CP, Camerel F, Lemaire BJ, Desvaux H, Davidson P, Batail P (2001) Nature 413:504
17. Miyamoto N, Nakato T (2004) J Phys Chem B 108:6152
18. Nakato T, Miyamoto N, Harada A (2004) Chem Commun 78
19. Nakato T, Yamashita Y, Kuroda K (2006) Thin Solid Filims 495:24
20. Miyamoto N, Yamamoto S, Shimasaki K, Harada K, Yamauchi Y (2011) Chem Asian J 6:2936
21. Xu Z, Gao C (2011) ACS Nano 5:2908
22. Miyamoto N, Iijima H, Ohkubo H, Yamauchi Y (2010) Chem Commun 46:4166
23. Paineau E, Antonova K, Baravian C, Bihannic I, Davidson P, Dozov I, Impéror-Clerc M, Levitz P, Madsen A, Meneau F, Michot LJ (2009) J Phys Chem B 113:15858
24. Michot LJ, Bihannic I, Maddi S, Baravian C, Levitz P, Davidson| P (2008) Langmuir 24:3127
25. Michot LJ, Bihannic I, Porsch K, Maddi S, Baravian C, Mougel J, Levitz P (2004) Langmuir 20:10829
26. Mourchid A, Lécolier E, van Damme H, Levitz P (1998) Langmuir 14:4718
27. Onsager L (1949) Ann NY Acad Sci 51:627
28. Mejia AF, Chang Y-W, Ng R, Shuai M, Mannan MS, Cheng Z (2012) Phys Rev E 85:061708
29. Wong M, Ishige R, Hoshino T, Hawkins S, Li P, Takahara A, Sue H-J (2014) Chem Mater 26:1528
30. Miyamoto N, Nakato T (2002) Adv Mater 14:1267
31. Miyamoto N, Kuroda K, Ogawa M (2004) J Phys Chem B 108:4268
32. Miyamoto N, Yamamoto H, Kaito R, Kuroda K (2002) Chem Commun 2378

33. Yamaguchi D, Miyamoto N, Fujita T, Nakato T, Koizumi S, Ohta N, Yagi N, Hashimoto T (2012) Phys Rev E 85:011403
34. Yamaguchi D, Miyamoto N, Koizumi S, Nakato T, Hashimoto T (2007) J Appl Cryst 40: s101
35. Bhatia S, Barker J, Mourchid A (2003) Langmuir 19:532
36. Kroon M, Vos WL, Wegdam GH (1998) Phys Rev E 57:1962
37. Pignon F, Magnin A, Piau J-M (1997) Phys Rev Lett 4689:4689
38. Pignon F, Magnin A, Piau J-M, Cabane B, Lindner P, Diat O (1997) Phys Rev E 56:3281
39. Mourchid A, Delville A, Lambard J, Lécolier E, Levitz P (1995) Langmuir 11:1942
40. Morvan M, Espinat D, Lambard J, Zemb T (1994) Colloids Surf A 82:193
41. Treacy MMJ, Rice SB, Jacobson AJ, Lewandowski JT (1990) Chem Mater 2:279
42. Ebina Y, Sasaki T, Harada M, Watanabe M (2002) Chem Mater 14:4390
43. Takagaki A, Sugisawa M, Lu D, Kondo JN, Hara M, Domen K, Hayashi S (2003) J Am Chem Soc 125:5479
44. Kudo A, Sakata T (1995) J Phys Chem 99:15963
45. Langmuir I (1938) J Chem Phys 6:873
46. Gabriel J-CP, Sanchez C, Davidson P (1996) J Phys Chem 100:11139
47. DiMasi E, Fossum JO, Gog T, Venkataraman C (2001) Phys Rev E 64:061704
48. Michot LJ, Baravian C, Bihannic I, Maddi S, Moyne C, Duval JFL, Levitz P, Davidson P (2009) Langmuir 25:127
49. Michot LJ, Bihannic I, Maddi S, Funari SS, Baravian C, Levitz P, Davidson P (2006) Proc Nat Acad Sci 103:16101
50. Paineau E, Michot LJ, Bihannic I, Baravian C (2011) Langmuir 27:7806
51. Paineau E, Bihannic I, Baravian C, Philippe A-M, Davidson P, Levitz P, Funari Ses, Rochas C, Michot LJ (2011) Langmuir 27:5562
52. Baravian C, Michot LJ, Paineau E, Bihannic I, Davidson P, ´ror-Clerc MI, Belamie E, Levitz P (2010) Europhys Lett 60:36005
53. Hemmen H, Ringdal NI, Azevedo END, Engelsberg M, Hansen EL, Meheust Y, Fossum JO, Knudsen KD (2009) Langmuir 25:12507
54. Dan B, Behabtu N, Martinez A, Evans JS, Kosynkin DV, Tour JM, Pasquali M, Smalyukh II (2011) Soft Matter 7:11154
55. Kim JE, Han TH, Lee SH, Kim JY, Ahn CW, Yun JM, Kim SO (2011) Angew Chem Int Ed 50:3043
56. Aboutalebi SH, Gudarzi MM, Zheng QB, Kim J-K (2011) Adv Funct Mater 21:2978
57. Xu Z, Gao C (2011) Nat Commun 2:571
58. Zocher VH (1925) Anorg Allg Chem 147:91
59. Davidson P, Garreau A, Livage J (1994) Liq Cryst 16:905
60. Davidson P, Bourgaux C, Schoutteten L, Sergot P, Williams C, Livage J (1995) J Phys II France 5:1577
61. Pelletier O, Bourgaux C, Diat O, Davidson P, Livage J (1999) Eur Phys J B 12:541
62. Lamarque-Forget S, Pelletier O, Dozov I, Davidson P, Martinot-Lagarde P, Livage J (2000) Adv Mater 12:1267
63. Desvaux H, Gabriel J-CP, Berthault P, Camerel F (2001) Angew Chem Int Ed 40:373
64. Commeinhes X, Davidson P, Bourgaux C, Livage J (1997) Adv Mater 9:900
65. Adachi-Pagano M, Forano C, Besse J-P (2000) Chem Commun 91
66. Hibino T, Jones WJ (2001) J Mater Chem 11:1321
67. Iyi N, Ebina Y, Sasaki T (2008) Langmuir 24:5591
68. Iyi N, Ebina Y, Sasaki T (2011) J Mater Chem 21:8085
69. Wang N, Liu S, Zhang J, Wu Z, Chenb J, Sun D (2005) Soft Matter 1:428
70. Zhang J, Luan L, Zhu W, Liu S, Sun D (2007) Langmuir 23:5331
71. Mourad MCD, Devid EJ, Schooneveld MMv, Vonk C, Lekkerkerker HNW (2008) J Phys Chem B 112:10142
72. Zhu W, Sun D, Liu S, Wang N, Zhang J, Luan L (2007) Colloids Surf A 301:106
73. Luan L, Liu S, Sun D (2009) J Solid State Chem 182:1462

74. Luan L, Li W, Liu S, Sun D (2009) Langmuir 25:6349
75. Shen T-Z, Hong S-H, Song J-K (2014) Nature Mater 13:394
76. Brown ABD, Clarke SM, Rennie AR (1998) Langmuir 14:3192
77. Bates M, Frenkel D (1999) J Chem Phys 110:6553
78. Ise N, Sogami IS (2005) Structure formation in solution—ionic polymers and colloidal particles. Springer, Berlin
79. Geng F, Ma R, Nakamura A, Akatsuka K, Ebina Y, Yamauchi Y, Miyamoto N, Tateyama Y, Sasaki T (2013) Nat Commun 4:1632
80. Geng F, Ma R, Ebina Y, Yamauchi Y, Miyamoto N, Sasaki T (2014) J Am Chem Soc 136:5491
81. Song Y, Iyi N, Hoshide T, Ozawa TC, Ebina Y, Ma R, Miyamoto N, Sasaki T (2015) Chem Commun 51:17068
82. Helfrich W (1978) Naturforsch 33a:305
83. Kunz DA, Feicht P, Godrich S, Thurn H, Papastavrou G, Fery A, Breu J (2013) Adv Mater 25:1337
84. Marshall CE (1930) Trans Faraday Soc 26:173
85. Mueller H (1939) Phys Rev 55:508
86. Mueller H (1939) Phys Rev 55:792
87. Sugimoto W, Terabayashi O, Murakami Y, Takatsu Y (2002) J Mater Chem 12:3814
88. Nakato T, Nakamura K, Shimada Y, Shido Y, Houryu T, Iimura Y, Miyata H (2011) J Phys Chem C 115:8934
89. Shah MJ (1963) J Phys Chem 67:2215
90. Yamaoka K, Sasai R, Ikuta N (1994) Chem Lett 563
91. Sasai R, Yamaoka K (1995) J Phys Chem 99:17754
92. Shah MJ, Thompson DC, Hart CM (1963) J Phys Chem 67:1170
93. Yamaoka K, Tanigawa M, Sasai R (1994) J Chem Phys 101:1625
94. Sasai R, Ikuta N, Yamaoka K (1996) J Phys Chem 100:17266
95. Holzheu S, Hoffmann H (2002) J Phys Chem B 106:4412
96. O'Konski CT, Bergmann K (1962) J Chem Phys 37:1573
97. Yamagishi A, Soma M (1981) J Phys Chem 85:3090
98. Yamagishi A, Taniguchi M, Takahashi M, Asada C, Matsushita N, Sato H (1994) J Phys Chem 98:7555
99. Yamaoka K, Sasai R, Takata N (2000) Colloids Surf A 175:23
100. Yamaoka K, Sasai R (2000) J Colloid Interface Sci 225:82
101. Yamagishi A (1982) Inorg Chem 21:1778
102. Winslow WM (1949) J Appl Phys 20:1137
103. Dürrschmidt T, Hoffmann H (1999) Colloids Surf A 156:257
104. Kim JW, Kim SG, Choi HJ, Jhon MS (1999) Macromol Rapid Comm 20:450
105. Lu J, Zhao XP (2002) J Mater Chem 12:2603
106. Fossum JO, Méheust Y, Parmar KPS, Knudsen KD, Måløy KJ, Fonseca DM (2006) Europhys Lett 74:438
107. Zhang WL, Liu YD, Choi HJ (2011) J Mater Chem 21:6916
108. Xiang LQ, Zhao XP (2003) J Mater Chem 13:1529
109. Kim YJ, Liu YD, Choi HJ, Park S-J (2013) J Colloid Interface Sci 394:108
110. Zhang WL, Choi HJ (2011) Chem Commun 47:12286
111. Yin J, Wang X, Chang R, Zhao X (2012) Soft Matter 8:294
112. Yin J, Chang R, Kai Y, Zhao X (2013) Soft Matter 9:3910
113. Parmar KPS, Meheust Y, Schjelderupsen B, Fossum JO (2008) Langmuir 24:1814
114. Shin KY, Lee S, Hong S, Jang J (2014) ACS Appl Mater Interfaces 6:5531
115. Kimura H, Sugiyama T, Takahashi S, Tsuchida A (2013) Rheol Acta 52:139
116. Kimura H, Ueno M, Takahashi S, Tsuchida A, Kurosaka K (2014) Appl Clay Sci 99:160
117. Kimura H, Nakashima A, Takahashi S, Tsuchida A, Kurosaka K (2015) Appl Clay Sci 114:120

118. Dozov I, Paineau E, Davidson P, Antonova K, Baravian C, Bihannic I, Michot LJ (2011) J Phys Chem B 115:7751
119. Hong S-H, Shen T-Z, Song J-K (2014) J Phys Chem C 118:26304
120. Porion P, Faugere AM, Michot LJ, Paineau E, Delville A (2011) J Phys Chem C 115:14253
121. Eguchi M, Angelone MS, Yennawar HP, Mallouk TE (2008) J Phys Chem C 112:11280
122. Wu LL, Ohtani M, Takata M, Saeki A, Seki S, Ishida Y, Aida T (2014) ACS Nano 8:4640
123. Azevedo ENd, Engelsberg M, Fossum JO, Souza REd (2007) Langmuir 23:5100
124. Osterloh FE (2002) J Am Chem Soc 124:6248
125. Kim JY, Osterloh FE, Hiramatsu H, Dumas RK, Liu K (2005) J Phys Chem B 109:11151
126. Beydaghi H, Javanbakht M (2015) Ind Eng Chem Res 54:7028
127. Guo F, Kim F, Han TH, Shenoy VB, Huang J, Hurt RH (2011) ACS Nano 5:8019
128. Liu Z, Li Z, Xu Z, Xia Z, Hu X, Kou L, Peng L, Wei Y, Gao C (2014) Chem Mater 26:6786
129. Takagi S, Shimada T, Eguchi M, Yui T, Yoshida H, Tryk DA, Inoue H (2002) Langmuir 18:2265
130. Kawamata J, Suzuki Y, Tenma Y (2010) Phil Mag 90:2519
131. Miyamoto N, Kuroda K, Ogawa M (2004) J Mater Chem 14:165
132. Jalili R, Aboutalebi SH, Esrafilzadeh D, Konstantinov K, Moulton SE, Razal JM, Wallace GG (2013) ACS Nano 7:3981
133. Yang X, Qiu L, Cheng C, Wu Y, Ma ZF, Li D (2011) Angew Chem Int Ed 50:7325
134. Jalili R, Aboutalebi SH, Esrafilzadeh D, Shepherd RL, Chen J, Aminorroaya-Yamini S, Konstantinov K, Minett AI, Razal JM, Wallace GG (2013) Adv Funct Mater 23:5345
135. Seyedin MZ, Razal JM, Innis PC, Jalili R, Wallace GG (2015) Adv Funct Mater 25:94
136. Kim YS, Kang JH, Kim T, Jung Y, Lee K, Oh JY, Park J, Park CR (2014) Chem Mater 26:5549
137. Nakato T, Nono Y, Mouri E, Nakata M (2014) Phys Chem Chem Phys 16:955
138. Yamaki T, Asai K (2001) Langmuir 17:2564
139. Umemura Y, Yamagishi A, Schoonheydt R, Persoons A, Schryver FD (2002) J Am Chem Soc 124:992
140. Inukai K, Hotta Y, Taniguchi M, Tomura S, Yamagishi A (1994) J Chem Soc Chem Commun 959
141. Binks BP (2002) Curr Opin Colloid Inter Sci 7:21
142. Binks BP, Horozov TS (2006) Colloidal particles at liquid interfaces. Cambridge University Press, Cambridge
143. Aveyard R, Binks BP, Clint JH (2003) Adv Colloid Interface Sci 100–102:503
144. Fujii S, Murakami R (2008) KONA Powder Technol J 26:153
145. Nonomura Y, Kobayashi N (2009) J Colloid Inter Sci 330:463
146. Booth SG, Dryfe RAW (2015) J Phys Chem C 119:23295
147. Mejia AF, Diaz A, Pullela S, Chang Y-W, Simonetty M, Carpenter C, Batteas JD, Mannan MS, Clearfield A, Cheng Z (2012) Soft Matter 8:10245
148. Tsugita A, Takemoto S, Mori K, Yoneya T, Otani Y (1983) J Colloid Inter Sci 95:551
149. Ashby NP, Binks BP (2000) Phys Chem Chem Phys 2:5640
150. Abend S, Bonnke N, Gutschner U, Lagaly G (1998) Colloid Polym Sci 276:730
151. Bolhuis P, Frenkel D (1994) J Chem Phys 101:9869
152. Yang F, Liu S, Xu J, Lan Q, Wei F, Sun D (2006) J Colloid Inter Sci 302:159
153. Hirsemann D, Shylesh S, De Souza RA, Diar-Bakerly B, Biersack B, Mueller DN, Martin M, Schobert R, Breu J (2012) Angew Chem Int Ed 51:1348
154. Nakato T, Ueda H, Hashimoto S, Terao R, Kameyama M, Mouri E (2012) ACS Appl Mater Interfaces 4:4338
155. Dong J, Worthen AJ, Foster LM, Chen Y, Cornell KA, Bryant SL, Truskett TM, Bielawski CW, Johnston KP (2014) ACS Appl Mater Inter 6:11502
156. Zhang S, Sun D, Dong X, Li C, Xu J (2008) Colloids Surf A 324:1
157. Liu Q, Luan L, Sun D, Xu J (2010) J Colloid Interface Sci 343:87
158. Tran DN, Whitby CP, Fornasiero D, Ralston J (2010) J Colloid Interface Sci 348:460
159. Binks BP, Sekine T, Tyowua AT (2014) Soft Matter 10:578

160. He Y, Wu F, Sun X, Li R, Guo Y, Li C, Zhang L, Xing F, Wang W, Gao J (2013) ACS Appl Mater Interfaces 5:4843
161. McCoy TM, Pottage MJ, Tabor RF (2014) J Phys Chem C 118:4529
162. Kim J, Cote LJ, Kim F, Yuan W, Shull KR, Huang J (2010) J Am Chem Soc 132:8180
163. Gudarzi MM, Sharif F (2011) Soft Matter 7:3432
164. Guevara JS, Mejia AF, Shuai M, Chang Y-W, Mannan MS, Cheng Z (2013) Soft Matter 9:1327
165. Haraguchi K, Li H-J, SOng L, Murata K (2007) Macromolecules 40:6973
166. Ma X, Li Y, Wang W, Ji Q, Xi Y (2013) Eur Polymer J 49:389
167. Liu M, Ishida Y, Ebina Y, Sasaki T, Aida T (2013) Nat Commun 4:2029
168. Liu J, Song G, He C, Wang H (2013) Macromol Rapid Commun 34:1002–1007
169. Fan J, Shi Z, Lian M, Li H, Yin J (2013) J Mater Chem A 1:7433
170. Shen J, Yan B, Li T, Long Y, Li N, Ye M (2012) Soft Matter 8:1831
171. Haraguchi K, Takada T (2010) Macromolecules 43:4294
172. Paineau E, Dozov I, Bihannic I, Baravian C, Krapf M-EM, Philippe A-M, Rouziere SAh, Michot LJ, Davidson P (2012) ACS Appl Mater Interfaces 4:4296
173. Inadomi T, Ikeda S, Okumura Y, Kikuchi H, Miyamoto N (2014) Macromol Rapid Commun 35:1741
174. Miyamoto N, Shintate M, Ikeda S, Hoshida Y, Yamauchi Y, Motokawa R, Annaka M (2013) Chem Commun 49:1082
175. Mejia AF, Ng R, Nguyen P, Shuai M, Acosta HY, Mannan MS, Cheng Z (2013) Soft Matter 9:10257
176. Liu M, Ishida Y, Ebina Y, Sasaki T, Hikima T, Takata M, Aida T (2015) Nature 517:68
177. Kim YS, Liu M, Ishida Y, Ebina Y, Osada M, Sasaki T, Hikima T, Takata M, Aida T (2015) Nat Mater 14:1002
178. Adams M, Dogic Z, Keller SL, Fraden S (1998) Nature 393:349
179. van der Kooij FM, Lekkerkerker HNW (2000) Phys Rev Lett 84:781
180. Oversteegen SM, Wijnhoven JGEJ, Vonk C, Lekkerkerker HNW (2004) J Phys Chem B 108:18158
181. Dogic Z, Purdy K, Grelet E, Adams M, Fraden S (2004) Phys Rev E 69:051702
182. Moulton SE, Maugey M, Poulin P, Wallace GG (2007) J Am Chem Soc 129:9452
183. Yasarawan N, van Duijneveldt JS (2010) Soft Matter 6:353
184. Kleshchanok D, Petukhov AV, Holmqvist P, Byelov DV, Lekkerkerker HN (2010) Langmuir 26:13614
185. Doshi N, Cinacchi G, van Duijneveldt JS, Cosgrove T, Prescott SW, Grillo I, Phipps J, Gittins DI (2011) J Phys: Condens Matter 23:194109
186. Kleshchanok D, Meijer J-M, Petukhov AV, Portale G, Lekkerkerker HNW (2012) Soft Matter 8:191
187. Kleshchanok D, Meester V, Pompe CE, Hilhorst J, Lekkerkerker HN (2012) J Phys Chem B 116:9532
188. Zhang J, Lang PR, Meyer M, Dhont JKG (2013) Langmuir 29:4679
189. Harnau L (2008) Mol Phys 106:1975
190. Stroobants A, Lekkerkerker HNW (1984) J Phys Chem 88:3669
191. Bates MA, Frenkel D (2000) Phys Rev E 62:5225
192. Varga S, Galindo A, Jackson G (2002) J Chem Phys 117:7207
193. Camp PJ, Allen MP (1996) Phys A 229:410
194. Varga S, Galindo A, Jackson G (2002) Phys Rev E 66:011707
195. Oversteegen SM, Lekkerkerker HN (2004) J Chem Phys 120:2470
196. Harnau L, Dietrich S (2004) Phys Rev E 69:051501
197. Harnau L, Dietrich S (2002) Phys Rev E Stat Nonlin Soft Matter Phys 66:051702
198. Bier M, Harnau L, Dietrich S (2005) J Chem Phys 123 No. 114906
199. Phillips J, Schmidt M (2010) Phys Rev E 81:041401
200. Verhoeff AA, Wensink HH, Vis M, Jackson G, Lekkerkerker HNW (2009) J Phys Chem B 113:13476

201. van der Kooij FM, Lekkerkerker HNW (2000) Langmuir 16:10144
202. van der Kooij FM, Vogel M, Lekkerkerker HNW (2000) Phys Rev E 62:5397
203. Chen M, Li H, Chen Y, Mejia AF, Wang X, Cheng Z (2015) Soft Matter 11:5775
204. Landman J, Paineau E, Davidson P, Bihannic I, Michot LJ, Philippe AM, Petukhov AV, Lekkerkerker HN (2014) J Phys Chem B 118:4913
205. Cousin F, Cabuil V, Grillo I, Levitz P (2008) Langmuir 24:11422
206. Woolston P, van Duijneveldt JS (2015) Langmuir 31:9290
207. Miyamoto N, Nakato T (2003) Langmuir 19:8057
208. Miyamoto N, Yamada Y, Koizumi S, Nakato T (2007) Angew Chem Int Ed 46:4123
209. Nakato T, Yamada Y, Miyamoto N (2009) J Phys Chem B 113:1323
210. Nakato T, Yamashita Y, Mouri E, Kuroda K (2014) Soft Matter 10:3161
211. Pujala RK, Pawar N, Bohidar HB (2011) Langmuir 27:5193
212. Pujala RK, Bohidar HB (2012) Soft Matter 8:6120
213. Zhang C, Tjiu WW, Fan W, Yang Z, Huang S, Liu T (2011) J Mater Chem 21:18011
214. Fang B, Peng L, Xu Z, Gao C (2015) ACS Nano 9:5214
215. Zhang E, Wang T, Zhao L, Sun W, Liu X, Tong Z (2014) ACS Appl Mater Interfaces 6:22855
216. Wan SJ, Li YC, Peng JS, Hu H, Cheng QF, Jiang L (2015) ACS Nano 9:708
217. Ramphal IA, Hagerman ME (2015) Langmuir 31:1505
218. Lee YR, Kim IY, Kim TW, Lee JM, Hwang S-J (2012) Chem Eur J 18:2263
219. Wan-Guo H, De-Jun S, Shu-Hua H, Chun-Guang Z, Guo-Ting W (1998) Colloid Polym Sci 276:274
220. Li SP, Hou WG, Sun DJ, Guo PZ, Jia CX (2003) Langmuir 19:3172
221. Werner S, Lau VW, Hug S, Duppel V, Clausen-Schaumann H, Lotsch BV (2013) Langmuir 29:9199
222. Hu Q, Xu Z, Qiao S, Haghseresht F, Wilson M, Lu GQ (2007) J Colloid Interface Sci 308:191
223. Deák Á, Janovák L, Tallósy SP, Bitó T, Sebők D, Buzás N, Pálinko I, Dékány I (2015) Langmuir 31:2019
224. Nakato T, Yamada Y, Nakamura M, Takahashi A (2011) J Colloid Interface Sci 354:38
225. Nakato T, Inoue S, Hiraragi Y, Sugawara J, Mouri E, Aritani H (2014) J Mater Sci 49:915
226. van Olphen H (1977) An introduction to clay colloid chemistry, 2nd edn. Krieger, Malabar
227. Dijkstra M, Hansen JP, Madden PA (1995) Phys Rev Lett 75:2236
228. Jönsson B, Labbez C, Cabane B (2008) Langmuir 24:11406
229. Tombácz E, Szekeres M (2004) Appl Clay Sci 27:75
230. Mongondry P, Tassin JF, Nicolai T (2005) J Colloid Interface Sci 283:397
231. Nicolai T, Cocard S (2001) Eur Phys J E 5:221
232. Pignon F, Magnin A, Piau J-M (1996) J Rheol 40:573
233. Schmidt G, Nakatani AI, Butler PD, Han CC (2002) Macromolecules 35:4725
234. Norrish K (1954) Discuss Faraday Soc 18:120
235. Mourchid A, Delville A, Levitz P (1995) Faraday Discuss 101:275
236. Avery RG, Ramsay JDF (1986) J Colloid Interf Sci 109:448
237. Rand B, Peken E, Goodwin JW, Smith RW (1980) J Chem Soc Faraday Trans 1(76):225
238. Shalkevich A, Stradner A, Bhat SK, Muller F, Schurtenberger P (2007) Langmuir 23:3570
239. Bonn D, Kellay H, Tanaka H, Wegdam G, Meunier J (1999) Langmuir 15:7534
240. Abend S, Lagaly G (2000) Appl Clay Sci 16:201
241. Penner D, Lagaly G (2001) Appl Clay Sci 19:131
242. Permien T, Lagaly G (1994) Appl Clay Sci 9:251
243. Levitz P, Lecolier E, Mourchid A, Delville A, Lyonnard S (2000) Europhys Lett 49:672
244. Kroon M, Wegdam GH, Sprik R (1996) Phys Rev B 54:6541
245. Ramsay JDF, Lindner P (1993) J Chem Soc Faraday Trans 89:4207
246. Ramsay JDF (1986) J Colloid Interface Sci 109:441
247. Ramsay JDF, Swanton SW, Bunce J (1990) J Chem Soc Faraday Trans 86:3919
248. Balnois E, Durand-Vidal S, Levitz P (2003) Langmuir 19:6633

249. Ruzicka B, Zulian L, Ruocco G (2006) Langmuir 22:1106
250. Tanaka H, Meunier J, Bonn D (2004) Phys Rev E 69:031404
251. Ruzicka B, Zulian L, Ruocco G (2004) Phys Rev Lett 93: 258301
252. Ruzicka B, Zulian L, Angelini R, Sztucki M, Moussaïd A, Ruocco G (2008) Phys Rev E 77:020402
253. Ruzicka B, Zulian L, Ruocco G (2004) J Phys: Condens Matter 16:S4993
254. Jabbari-Farouji S, Wegdam GH, Bonn D (2007) Phys Rev Lett 99:065701
255. Jabbari-Farouji S, Wegdam GH, Bonn D (2008) Phys Rev E 78:061405
256. Tanaka H, Jabbari-Farouji S, Meunier J, Bonn D (2005) Phys Rev E 71:021402
257. Labanda J, Sabaté J, Llorens J (2007) Colloids Surf A 301:8
258. Nakato T, Miyamoto N (2002) J Mater Chem 12:1245
259. Nakato T, Miyamoto N, Harada A, Ushiki H (2003) Langmuir 19:3157

Part II
Functions and Applications of the Inorganic Nanosheets

Chapter 9
Adsorbents Derived from Layered Solids

Tomohiko Okada and Makoto Ogawa

9.1 Introduction

Concentration of noble elements and compounds from environments are topics of interests for environmental purification, pharmaceutical, and food sciences. For the concentration of a target-specific compound, adsorption is one of the most reliable and useful chemical phenomenon, therefore, the preparation of adsorbents and the studies on the adsorption phenomena to elucidate the adsorbent–adsorbate interactions have been investigated extensively. Extraction and storage, which are phenomena relevant to the adsorption, are topic of interests in materials chemistry because of the potential for the environments and future sustainable energy issues.

Layered materials, especially smectite group of clay minerals, have been used as adsorbents for a variety of species from metal ion, organic molecules, polymers, and colloidal particles. The adsorbent's design toward specific targets has also been done based on the intercalation chemistry of smectites, chemical modification, and structural transformation into three-dimensional network (pillaring). Pillaring of various layered solids has been examined for the applications as adsorbents and catalysts [1]. As to the chemical modification, organophilic clays are the most famous example and there are several commercially available organophilic clays for industrial uses. The organophilic clays are developed in 1950s [2] and the successful industrial application and more recent advanced materials applications attract materials chemists for the organic modification of various layered solids.

T. Okada
Department of Chemistry and Materials Engineering, Faculty of Engineering, Shinshu University, Nagano, Japan

M. Ogawa (✉)
School of Energy Science and Engineering, Vidyasirimedhi Institute of Science and Technology (VISTEC), Rayong, Thailand
e-mail: makoto.ogawa@vistec.ac.th

T. Nakato et al. (eds.), *Inorganic Nanosheets and Nanosheet-Based Materials*, Nanostructure Science and Technology, DOI 10.1007/978-4-431-56496-6_9

Ion-exchanger application is also another useful example, in which noble (or toxic) metal ions in environments (sea water for example) have been collected by the ion exchangers. Materials variation of layered solids from cation exchangers with varied ion-exchange capacity and selectivity to anion exchangers, chemical stability superior to organic and polymeric ion exchangers, as well as possible morphosyntheses made layered materials more attractive as adsorbents of various ionic species for practical uses. In this chapter, we summarized the potential of layered materials as present and future adsorbents for practical uses. The attention is focused on the mechanism of the adsorption on layered solids and the chemical design of adsorbents from layered solids.

9.2 Adsorption of Metal Ions

9.2.1 Cation Exchange

Smectite is a group of layered clay mineral consisting of negatively charged silicate layers and readily exchangeable interlayer cations. Isomorphous substitution of metal cations with similar size and lower valency generates a net negative charge of layers. To compensate the negative charge, metal cations (generally Na^+ and/or Ca^{2+}) occupy the interlayer space as exchangeable cations [3]. Due to this structural feature, smectite has been investigated as a cation exchanger.

Thermodynamic data for alkali metal cation exchanges on smectite at 298 K (standard free energy) were summarized by Maes and Cremers [4a] based on the previous publications [4b–e], giving the following selectivity sequence for monovalent cations.

$$Li^+ < Na^+ < K^+ < Rb^+ < Cs^+$$

The selectivity is governed by the hydration energy; cations with smaller hydration energy are preferred.

It is known that K^+ is fixed on weathered mica and vermiculite, which are 2:1 type layered silicates with the structures analogous to smectite [5]. K^+ has lower hydration energy and the diameter of K^+ (0.266 nm) is close to the size of the hexagonal hole of oxygen surface of the silicate layer. Therefore, K^+ is stably (irreversibly) trapped in the hexagonal hole followed by the interlayer dehydration. K^+ in mica is not exchangeable in general. There are some examples of the ion exchange of micas with some modification; the stable K^+ in phlogopite, ideal formula of $KMg_3Si_3AlO_{10}(OH)_2$, was replaced with exchangeable Na^+ using sodium tetraphenylboron [6]. The selective uptake of Cs^+ has been shown on the Na^+-exchanged phlogopite mica [7]. Na^+–Cs^+ exchange isotherm of the Na^+-exchanged phlogopite mica (Fig. 9.1) laid above diagonal line, showing that Cs^+ is highly preferred over Na^+. The basal spacing (1.158 nm) of the phlogopite mica after the Cs^+ uptake was slightly small compared to that (1.223 nm) of the

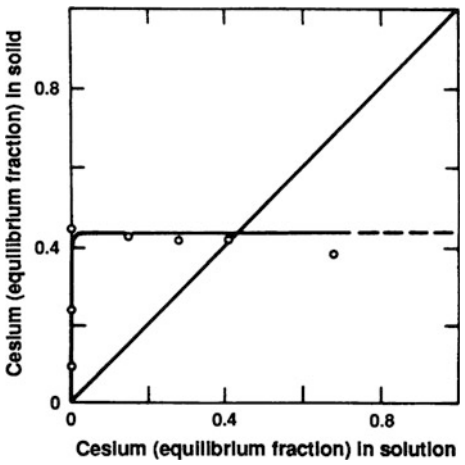

Fig. 9.1 Na/Cs exchange isotherm of K-depleted phlogopite mica, where *diagonal line* represents equal preference for both the cations. Reprinted from Ref. [7] with permission; copyright 1988, American Association for the Advancement of Science

Na^+-exchanged phlogopite mica, while larger than that (1.003 nm) of K^+-form. It was suggested that the diffusion of less hydrated Cs^+ ions is possible. Taking the possibility of remediation of nuclear waste, the selective adsorption to concentrate metal ions from quite dilute solution has been investigated using various natural and synthetic micas [8].

Concentration of rare earth elements by the adsorption is an important topic from the viewpoints of environmental (collecting rare elements) geochemical interests. Competitive adsorption of a series of rare earth elements on a montmorillonite (Ceca bentonite) was examined [9] to show the adsorbed Na^+ on the surface behaved as a barrier for the adsorption of rare earth ions at high ionic strength of 0.5 mol/L (background electrolytes are Na salts). Light rare earth elements showed this tendency due to their large ionic radius. At low ionic strength of 0.025 mol/L, the sorption coefficients were independent on the nature of the rare earths. Na-fluorotetrasilicic mica (abbreviated as Na-TSM) adsorbed Eu^{3+} effectively if compared with two smectites (Kunipia F, a natural montmorillonite and Sumecton SA, a synthetic saponite) as shown by the adsorption isotherms (Type-H for TSM, and type-L for smectites) [10]. The high affinity of Eu^{3+} to TSM is accounted for the structural in the octahedral sheet: TSM contains highly electronegative fluorine groups instead of the hydroxyls in smectites.

Layered alkali silicates such as octosilicate ($SiO_2/Na_2O = 8$), magadiite ($SiO_2/Na_2O = 14–16$) and kenyaite ($SiO_2/Na_2O = 20–22$) are known to possess cation exchange ability. Because protons of the silanol groups in the interlayer surface are exchanged with alkali ions, the cation-exchange capacity is strongly pH dependent [11]; protons compete with other cations at $pH < 7$, leading the silicates transform into the silicic acid [12]. In addition, sodium ions in the polysilicates cannot be exchanged with Fe^{3+} or Al^{3+}, because these cations exist only in acidic aqueous solutions. On the other hand, exchange of sodium ions in a sodium silicate ($SiO_2/Na_2O = 8$) with various inorganic cations (e.g., lithium, potassium, ammonium,

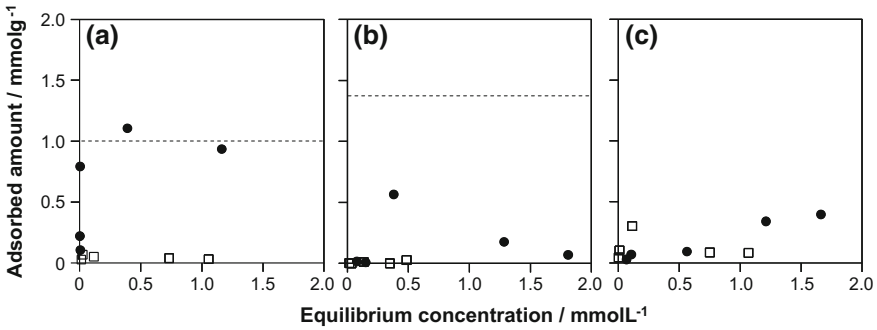

Fig. 9.2 Adsorption isotherms of (*black circle*) Zn^{2+} and (*white square*) Cd^{2+} on **a** magadiite, **b** octosilicate, and **c** ion exchange resin (IRC748, Organo Co.) from a seawater-mimicking solution containing Zn^{2+} and Cd^{2+}. *Horizontal line* denotes the ion-exchange capacity for the dication of the silicates. Reprinted from Ref. [14]. Copyright 2011 Wiley VCH

magnesium, copper) occurs [13]. Recently, concentration of Zn^{2+} on a layered alkali silicate, magadiite, from a seawater-mimicking aqueous solution was reported. Magadiite selectively and effectively adsorbed Zn^{2+} even when Cd^{2+} was present (Fig. 9.2a). The selectivity was not achieved for another sodium-type layered alkali silicate, octosilicate (Fig. 9.2b), and commercially available ion-exchange resin (Fig. 9.2c). Although the origin of the selectivity was not understood, ionic radius and hydration energy of cations are thought to be concerned for the affinity toward layer surface of magadiite [14].

Cation exchangeable-layered titanate and niobates are also available, and the selectivity ion exchange has been observed [15–18]. Komatsu and Fujiki [16] reported uptake of Cs^+ on hydrous layered titanate, $H_2Ti_4O_9{\cdot}nH_2O$, in the presence of alkali metal cations (Li^+, Na^+, H^+, or Rb^+). Even the concentration of Na^+ or Li^+ in solution increased, the uptake of Cs^+ on $H_2Ti_4O_9{\cdot}nH_2O$ did not decrease. $Rb_{0.14}H_{7.9}Nb_{22}O_{59}{\cdot}8.2H_2O$; Na^+ or K^+ cations were selectively exchanged with protons of $Rb_{0.14}H_{7.9}Nb_{22}O_{59}{\cdot}8.2H_2O$ in a concentrated LiCl aqueous solution [17]. $HCa_2Nb_3O_{10}{\cdot}1.5H_2O$; Selective uptake of NH_4^+ from the mixture of Na^+, K^+, and NH_4^+ in solution on a protonated layered perovskite, $HCa_2Nb_3O_{10}{\cdot}1.5H_2O$, has also been reported [18]. The uptake amount of NH_4^+ was 7- and 10-fold those of Na^+ and K^+, respectively, from mixed solution (NaCl, KCl, and NH_4Cl) containing 1.0 mM of each ion at pH 2.2.

The cation exchange of $K_4Nb_6O_{17}{\cdot}nH_2O$ [19] shows a unique site selectivity. By the reactions using aqueous solutions of LiCl, NaCl, $CaCl_2$, and $NiCl_2$ at 90 °C, complete exchange K^+ was attained only for Na^+, while a half of K^+ was exchanged with the divalent cations. The layered structures are composed of alternating two interlayers with different reactivities; interlayers I (hydrated) and II (not hydrated), which were determined from electron density projection along the *b* axis. It has been thought that selective exchange of K^+ ions in the interlayer II with monovalent cations occurs, whereas both mono- and divalent cations can exchange with K^+ in the interlayer I, from the observed changes in the basal spacings.

9.2.2 Anion Exchange

Layered double hydroxides (LDHs) have been investigated as anion exchangers. LDHs are a class of layered materials consisting of positively charged brucite like layer, where some M^{2+} cations are substituted with M^{3+} cations to give positive charge, and the charge compensating interlayer exchangeable anions. After the careful and extensive investigation on the anion-exchange properties of LDHs, the guest selectivity has been sequenced as the size and charge of anions [20–22]. Small and highly charged anions preferentially occupy the LDH interlayers with the order of preference

$$\begin{aligned} &NO_3^- < Br^- < Cl^- < F^- < OH^- < MoO_4^{2-} < SO_4^{2-} \\ &< CrO_4^{2-} < HAsO_4^{2-} < PO_4^{2-} < \text{Naphthol Yellow}^{2-} < CO_3^{2-} \end{aligned}$$

It is known that carbonate ion is the most stable as the interlayer anion and the replacement of the intercalated carbonate anion is difficult. Therefore, in order to incorporate various functional anions, nitrate or chloride forms of LDHs have been synthesized and employed as the intermediate for functional intercalation compounds. Experiments have been carefully done to find the experimental condition to overcome the anion-exchange sequence. In aqueous HCl solution, by the protonation of CO_3^{2-} to form HCO_3^-, Cl^- was effectively intercalated into Zn/Al-LDH instead of CO_3^{2-} [23a, b]. Iyi and Sasaki [23c] revealed that the deintercalation of CO_3^{2-} from Mg/Al-LDHs with the Mg/Al ratios of 2 and 3 by using acetate-buffer (sodium acetate and acetic acid)/NaCl mixed solutions at 25 °C. The addition of NaCl to the acetate-buffer solution was shown to be important in the decarbonation without any morphological and weight changes. Even in the presence of acetate anion, only chloride ions were incorporated into the LDHs due to their extremely low acetate selectivity. Hayashi and Nakayama have reported the anion-exchange reactions of a CO_3^{2-} form of Mg/Al-LDH with chloride, nitrate, and some organic anions in alcohols [24].

LDHs have been used as anion exchangers for environmental purifications. The removal of phosphates, arsenates, iodide, and chromate from water has been reported so forth [25, 26]. The removal of oxyanions such as phosphate from seawater has been investigated [26]. Dichromate anions ($Cr_2O_7^{2-}$) are reported to strongly interact with CO_3^{2-} form of Mg/Al-LDH, which is an important advantage for the removal of monochromate (CrO_4^{2-}) from the viewpoint of the efficient (two times) remediation of chromium contaminated water. The adsorption was possible under an acidic aqueous solution at pH 3 without dissolution of the LDHs, probably due to the large particle size of the used LDH [27]. In addition to anion exchange reactions, calcination-rehydration (reconstruction) is also useful for the uptake of anionic species [28–30]. The variation of removable anions is larger for the reconstruction method.

9.3 Adsorption of Molecules

9.3.1 Carbon Dioxides

Adsorption of CO_2 has been a topic of interests in scientific and practical aspects, most notable example is global warming issue. Adsorption of CO_2 onto layered solids also has several aspects. CO_2 was used to determine specific surface areas of smectites [31, 32]. Thomas and Bohor [31] reported a larger specific surface area of the Cs^+-exchanged from obtained from CO_2 BET plot (315 m^2/g at 195 K) than that (138 m^2/g at 77 K) from N_2 adsorption, even though the difference was negligible in kaolinite (a nonexpandable clay mineral) system. Because the adsorption temperature of CO_2 was high, CO_2 molecules are kinetically more energetic (with a larger diffusion coefficient), and thus the penetration into the interlayer space of the Cs^+-smectite occurred.

Fripiat et al. [32] reported regarding the CO_2 penetration from XRD analysis, where the basal spacing of dehydrated Na-montmorillonite (1.00 nm) increased to 1.23 nm. They also empirically predicted that the degree of hydration of the interlayer exchangeable cations (Li, Cs, K) should be a factor responsible for the greater amount of CO_2 adsorption, because the amounts of adsorbed CO_2 varied depending on the interlayer exchangeable cations. Although it was impossible to explicit about the detailed orientation of CO_2 molecules in the interlayer space, a significant fraction is shown to be oriented with respect to the clay layer as revealed by infrared dichroic spectroscopy.

More recently, the interactions of CO_2 with smectites have attracted another kind of attention as storage sites for anthropogenic CO_2, which related to the CO_2 sequestration, which is a global warming issue. Permeation ability of caprocks, which contain clay minerals such as smectites and kaolinite, for CO_2 strongly correlates with the geological CO_2 storage. Lower permeability is required for sealing CO_2 by caprock for a long period. Exchange of water molecule in clay minerals with CO_2 is negative phenomenon for sealing, therefore, it is important to understand the interactions of CO_2 with water-bearing minerals (including intercalation behavior). Experiments [33–36] and simulations [37–41] have been conducted in order to elucidate the interactions between CO_2 and smectites under supercritical conditions.

Michels et al. [34] reported the intercalation of gaseous CO_2 into a synthetic fluorohectorite at ambient conditions. The retention ability of CO_2 was strongly dependent on the nature of the interlayer cation (Li, Na, and Ni). For Li-exchanged fluorohectorite (LiFh), threshold temperature, which means deintercalation of CO_2 from the interlayer space, was about 35 °C, whereas that was about −15 °C for Na-exchanged fluorohectorite (NaFh). Because of the difference in size between the Li^+ and Na^+, Li^+ has a more concentrated charge than Na^+ and can thus polarize CO_2, forming a stronger bond. Similar discussion was reported [35] using such in situ techniques as XRD, ^{13}C NMR, and ATR-IR. In Fig. 9.3, the CO_2 adsorption isotherm on LiFh at room temperature is examined under a pressure range from 1 to 45 bar [34]. The initial part (0 to ca. 9 bar) of the adsorption isotherm represents

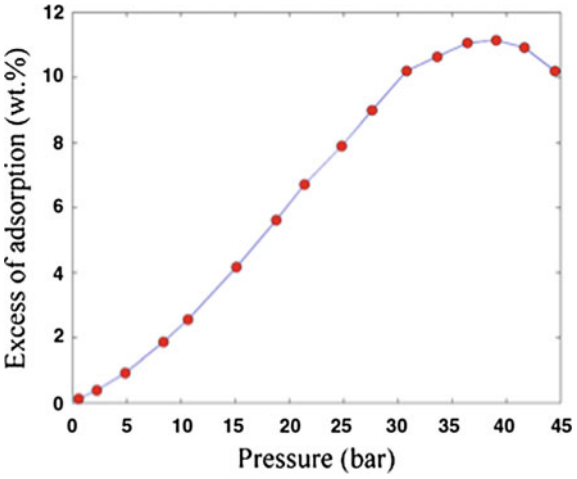

Fig. 9.3 CO_2 adsorption isotherm on Li-fluorohectorite at room temperature and pressure range 0–45 bar. Reprinted from Ref. [34]. Copyright 2015 Nature Publishing Group

diffusion of CO_2 into LiFh. The swelling of LiFh occurred under the pressure above 9 bar, as confirmed by XRD. Further increase in CO_2 pressure led the increased adsorption to be around 11 wt% at 38 bar. Above this pressure (approaching the critical pressure for CO_2), the adsorbed amount started to decrease, probably due to the formation of an adsorbed layer with higher density and shrinking the volume of CO_2 –LiFh complex to the pristine LiFh.

Recently, in situ characterization (XRD and IR) on the intercalation behavior of CO_2 using supercritical CO_2 ($scCO_2$) at 50 °C, 90 bar in the presence of water into Na-montmorillonite has been reported [36]. Molecular simulation studies on $scCO_2$ intercalation into hydrated montmorillonite have been conducted using a Monte Carlo [38] and a DFT-based MD [38–41]. As an example of molecular simulations of CO_2 intercalation into hydrated montmorillonite using Clayff force field [42], the change in the basal spacing upon increased water content and with addition of CO_2 (two molecules per unit cell) is shown in Fig. 9.4 [37]. The basal spacing increased in the monolayer hydrate (arrow in Fig. 9.4) from 10.77 ± 0.04 to 12.22 ± 0.03 Å (12% swelling) after CO_2 intercalation, and in the bi-layer hydrated system from 12.98 ± 0.09 to 14.78 ± 0.09 Å. Density profiles of atoms in the interlayer region showed separation of CO_2 molecules into two distinct layers similar to that observed for a bi-layer water network.

Calcined LDHs has been recognized as CO_2 adsorbents at high temperature [43–47]. While it has been widely understood that the pristine LDHs do not accommodate CO_2 at ambient temperature, carbonate anion-intercalated LDH (hydrotalcite) underwent a carbon cycle with the uptake of atmospheric CO_2 under ambient conditions [48]. As shown in Fig. 9.5, ^{13}C-labeled CO_2 (or CO_3^{2-}) was used to monitor the dynamics of the exchange between initially intercalated ^{13}C-labeled carbonate anions and carbonate anions derived from atmospheric CO_2 by IR spectroscopy. Exchange was promoted at a lower humidity with a half-life of exchange of ~24 h. The research group subsequently reported the interactions of CO_2 with

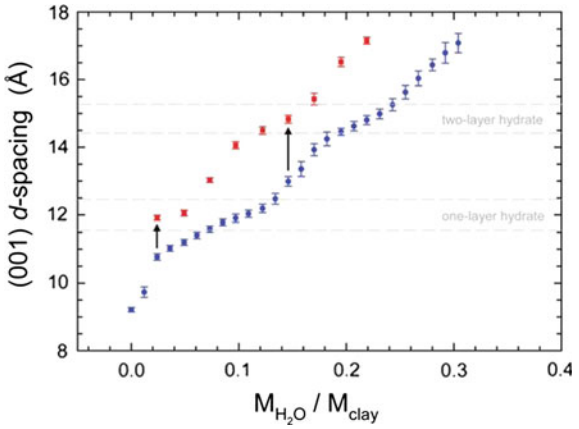

Fig. 9.4 Swelling behavior of Na-montmorillonite upon hydration (*blue circles*) and after additional intercalation of two molecules of CO_2 per unit cell (*red squares*) based on *NPT* MD simulations at 310 K and 20 MPa. *Arrows* indicate swelling occurring after CO_2 intercalation with approximately one and six water molecules per unit cell. Reprinted from Ref. [37]. Copyright 2012 American Chemical Society

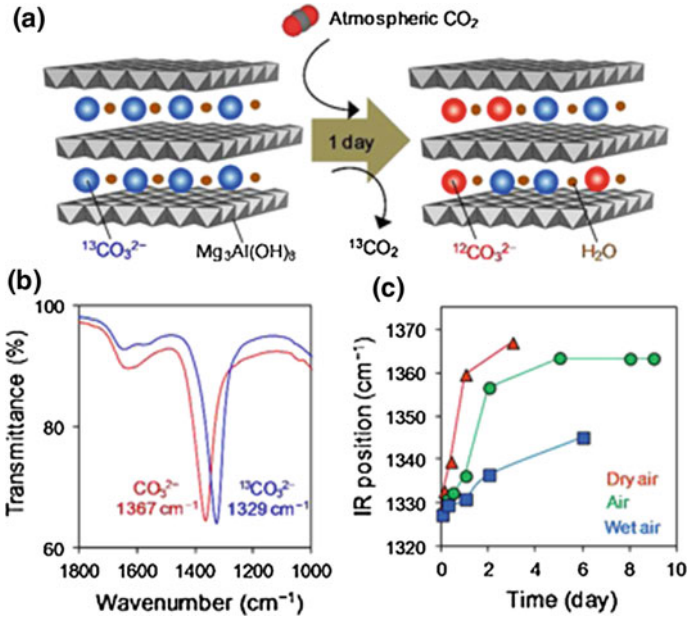

Fig. 9.5 **a** Dynamic exchange of carbonate anions of LDH with atmospheric CO_2. **b** IR spectra of $^{13}CO_3^{2-}$-LDH and CO_3^{2-}-LDH. **c** Variation of IR frequency of $^{13}CO_3^{2}$-LDH upon exposure to air at different relative humidity. Reprinted from Ref. [48]. Copyright 2013 American Chemical Society

hydrotalcites of different Mg/Al ratios (Mg/Al = 2, 3, and 4, which are named as LDH2, LDH3, and LDH4, respectively) [49]. Adsorption/desorption isotherms of CO_2 and N_2 (the competitive adsorption test) have been done to evaluate how the Mg/Al ratio affects the adsorption capacities (Fig. 9.6); the LDHs selectively

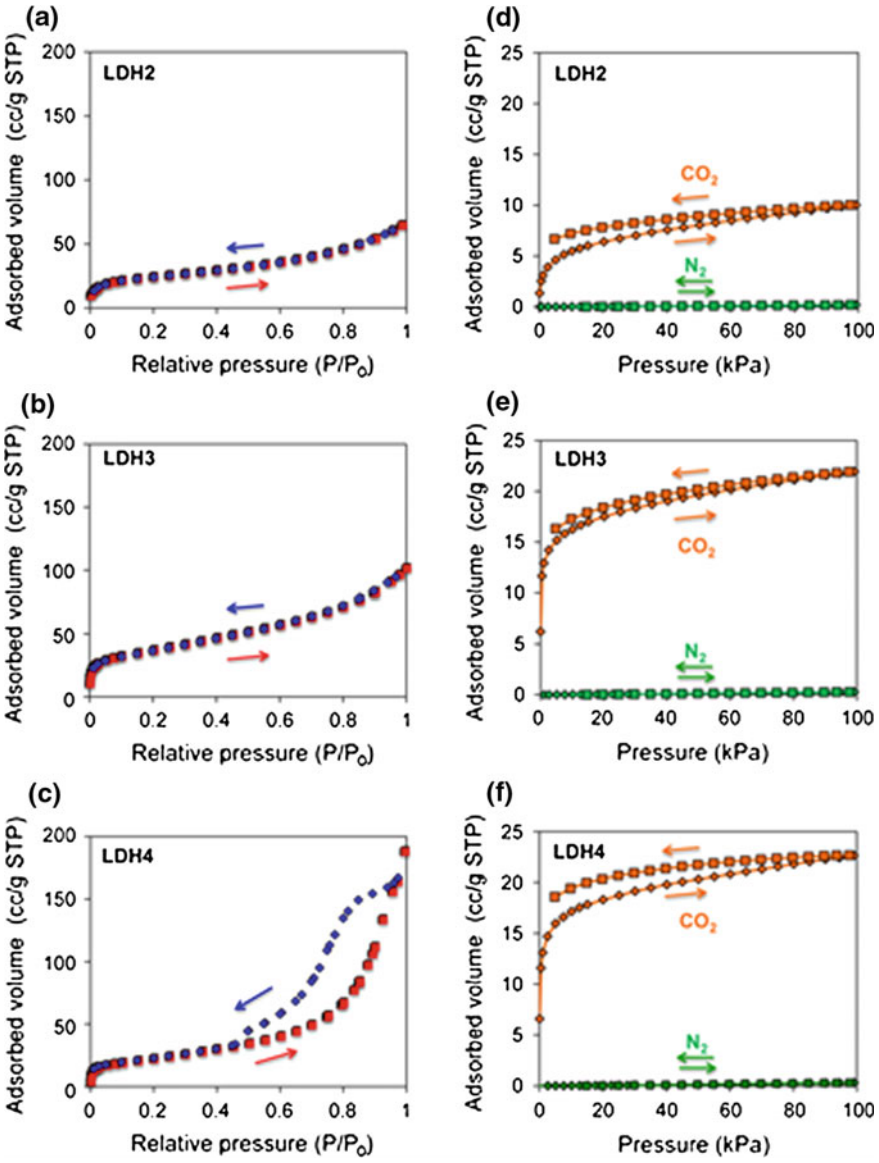

Fig. 9.6 N_2 adsorption–desorption isotherms of **a** LDH2, **b** LDH3, and **c** LDH4 measured at 77.35 K. CO_2 and N_2 adsorption–desorption isotherms of **d** LDH2, **e** LDH3, and **f** LDH4 measured at 25 °C. Reprinted from Ref. [49]. Copyright 2014 American Chemical Society

incorporated CO_2 with the capacities sequence of LDH2 < LDH3 ≈ LDH4. They ascribed the adsorption site of CO_2 to the basic Mg–OH based on the report that Mg-rich LDH promoted base catalyzed reactions [50].

9.3.2 Organic Molecules

Layered solids may adsorb polar organic molecules, and it is well known that smectites adsorb various polar molecules. Polar molecules such as alcohols, ketones, and amide are adsorbed by ion–dipole interactions with the interlayer cations and/or hydrogen bonding with the surface oxygen atom of the silicate layers. The intercalation of polar molecules usually occurs through solid–liquid or solid–gas reactions [1, 3, 51–54], while solid–solid reactions are also possible [55, 56].

In a smectite-polar molecule interactions in the solid-state, novel selectivity, which is not observed in the intercalation from solution [56], was observed. Maleic acid was intercalated into montmorillonite by solid–solid reactions, while its geometrical isomer, fumaric acid was not intercalated. From ethanolic solutions, both maleic and fumaric acids were intercalated. Such selectivity observed only in the solid–solid reaction was explained by the difference in the crystal structure of the molecules in addition to the ability of maleic acid to form a chelate like structure with the interlayer cations.

9.4 Adsorbents Design by the Modification of Layered Solids

9.4.1 Organic Modification with Ionic Species

Surface properties of layered solids have been modified to alter affinity toward target molecules. Cation exchange reactions of smectite [2, 57], layered titanate [58], layered niobate [59] with long-chain alkylammonium ions have been used to modify the surface property. The organophilic clays swell in aprotonic organic solvents for possible application as rheology controlling reagents [2, 60]. LDHs also became hydrophobic by incorporating long-chain alkyl carboxylates and sulfates [61, 62]. The adsorption characteristics of these ionic surfactants on layered solids via ion exchange reactions have been described separately in Chap. 6. Here, we will describe the adsorption of nonionic organic compounds from vapor and aqueous solution at lower concentration, as a way of the remediation of contaminated soil and water, which are important environmental problems.

The adsorption of nonionic organic compounds from water by soil depends on soil organic matter content [63]. Organic phase composed of hexadecyltrimethylammonium (HDTMA) behaved as partitioning medium that was more effective than natural soil organic matter for removing hydrocarbons (benzene and 1,2-dichlorobenzene) from water [64]. There are many fundamental studies on the adsorption behavior into hydrophobic clays with the structures varied by changing the surfactant amount and the alkyl-chain length [65].

Jaynes and Boyd [66] reported the sorption behavior of ethylbenzene in HDTMA-clays with different layer charge density from aqueous solution. Vermiculite (CEC = 80 meq/100 g clay), illite (CEC = 24 meq/100 g clay), kaolinite (CEC = 4 meq/100 g clay), and smectites (CECs = 87–130 meq/100 g clay) were used as host materials. Partition coefficients of ethylbenzene for HDTMA-clays varied depending upon the nature of smectites and HDTMA contents. Both the greater HDTMA contents and the larger basal spacings of high charged HDTMA-clays (vermiculite and smectites) led larger adsorption amounts of ethylbenzene.

Mortland et al. [67] have discussed hydrophobic interactions of nonionic organic compounds with HDTMA-montmorillonite (Wyoming bentonite). Whereas 3,4,5-trichlorophenol was adsorbed into HDTMA-montmorillonite from water, phenol was not adsorbed at all, as shown in the adsorption isotherms from water (Fig. 9.7 top). On the other hand, these two phenols were adsorbed into HDTMA-montmorillonite from hexane (Fig. 9.7 bottom). This difference has been ascribed to the relative importance of both adsorbate–solvent and adsorbate–adsorbent interactions on partitioning of adsorbates between adsorbent and solvent. In aqueous solution, phenol interacted strongly with water and was not attracted sufficiently to the hydrophobic surfaces of HDTMA-montmorillonite.

Modification of other layered solids as LDHs [68–70], layered hexaniobate [71, 72], and layered phosphate [73] provides hydrophobic intercalation compounds for uptake of chlorinated phenols from water. Competitive adsorption of three phenols (phenol, 4-chlorophenol and 2,4-dichlorophenol) from water on alkylammonium modified layered niobate was examined [72] to find preferential adsorption of 2,4-dichlorophenol among three phenols. The uptake of each solute was reduced by the presence of other solutes, and the reduction in the multi-solute systems depended on the hydrophobicity of the solutes coexisted in the solution.

In order to facilitate uptake of aromatic molecules, layered solids modified with various cationic species with aromatic nature have been reported. Cation exchange reactions of smectites with various aromatic ammonium ions have been reported [74]. The role of aromatic rings in the phenol adsorption was illustrated by Langmuir-type adsorption isotherm observed for the adsorption on tris(2,2′-bipyridine)nickel(II) modified Sumecton SA, while the adsorption of phenol on tris (ethylenediamine)nickel(II) modified Sumecton SA was less effective [75]. Charge-transfer interactions have been used for adsorption of phenols as reveal by using methylviologen (MV^{2+}) modified smectites (Kunipia F and Sumecton SA) in the absence of solvent [76] and from aqueous solution [77]. Effective adsorption of 2,4-dichlorophenol was achieved through the charge-transfer interactions with

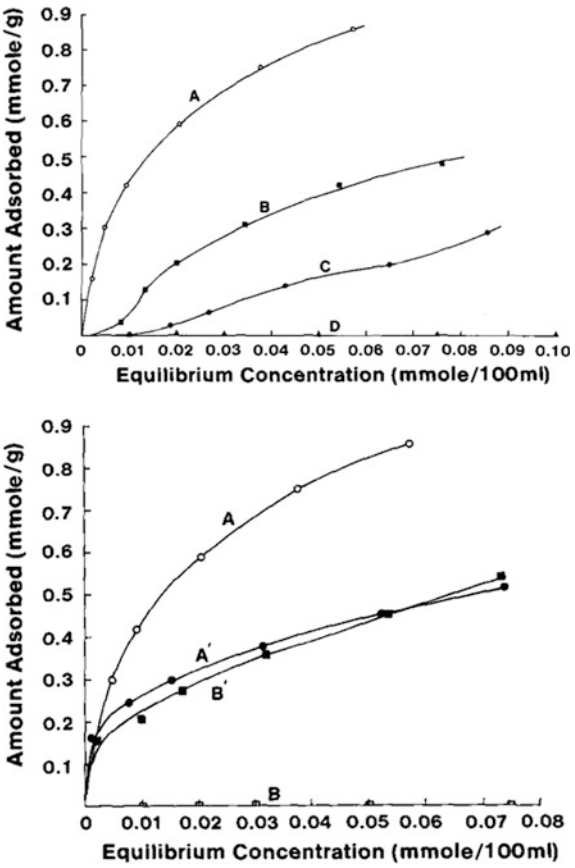

Fig. 9.7 *Top* Adsorption isotherms (293 K) of phenols on the HDTMA-montmorillonite. A = 3,4,5-trichlorophenol; B = 3,5-dichlorophenol; C = 3-chlorophenol; D = phenol. *Bottom* Adsorption isotherms for 3,4,5-trichlorophenol from water (A) and hexane (A′), and phenol from water (B) and hexane (B′) onto HDTMA-smectite. Reprinted from Ref. [67]. Copyright 1986 The Clay Minerals Society

MV^{2+} in the interlayer space of Sumecton SA. A possible reason for the effective adsorption was lower ionization potential of 2,4-dichlorophenol than phenol [77].

Adsorption selectivity of aromatic molecules from aqueous solutions has been emerged using aromatic functionality for the modification. Neostigmine, TMPA, and 3-(trifluoromethyl)phenyltrimethylammonium (Fig. 9.8) were used to find the effects of the surface modification on the adsorption capacity of 2-phenylphenol [78]. Among tested adsorbents, the neostigmanine-modified Sumecton SA was most effective to remove 2-phenylphenol. Even in the presence of sucrose, 2-phenylphenol was effectively adsorbed on neostigmine-modified smectites [79].

9.4.2 Pillared-Layered Materials

Layered solids have also been used as scaffolds to design nanospace by the intercalation of bulky organic species into the interlayer spaces as pillar. Specific surface

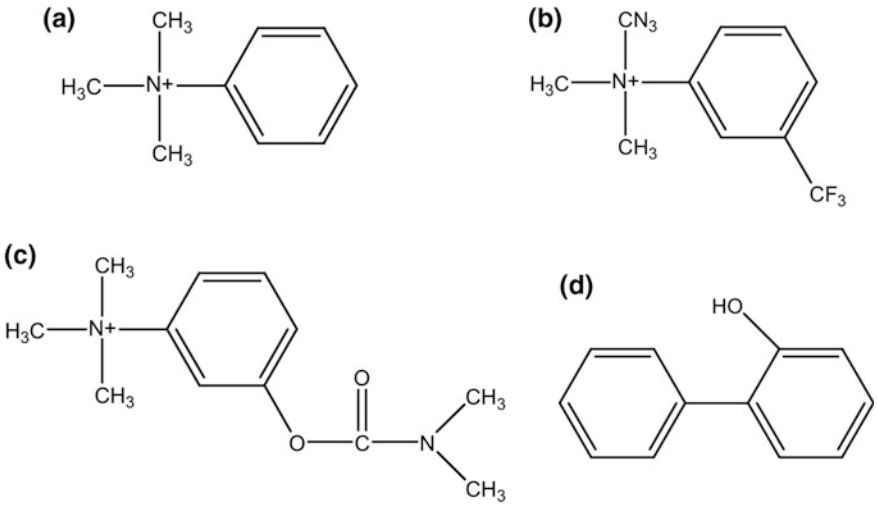

Fig. 9.8 Molecular structures of **a** trimethylphenylammonium, **b** 3-(trifluoromethyl) phenyltrimethylammonium, **c** neostigmine, and **d** 2-phenylphenol

area and micropore volume varied depending on the interlayer cations of a natural montmorillonite (SWy-1: Wyoming montmorillonite), and that increased with cationic radius in the order of TMA > Cs > K > Ca > Na, which correlates with the gallery height [80]. Intercalation of TMA ions produces significant volumes of micropore in the interlayer space, which are readily accessible to N_2. The accessibility of the micropores to other gases would depend on the molecular dimensions (molecular sieving effects). This kind of materials has been named as "pillared clays." Pillared clays have been studies for the application as hosts of photo- and electro-functional materials, catalyst supports and adsorbents [52–54, 81]. Pore size, porosity, and surface area vary depending on the molecular geometry of pillaring agents and the spatial distribution (density). Interactions of nonionic organic compounds with these pillared-layered solids are essentially different from those with the hydrophobic clays [52–54, 82, 83].

Detellier et al. reported a gas chromatographic separation of CH_4/CO_2 on montmorillonite (SWy-1 from Clay Source Repository, University of Missouri) modified with quaternarized polyammonium cations. A strong dependence of CO_2 retention times upon the free surface area was observed and the CH_4/CO_2 separation was interpreted principally by interactions with the surface and not by interactions with the polar moieties of the organic cations [84].

The larger molecular size of tetraethylammonium (TEA) than TMA led to the smaller surface area of TEA-smectite, so that the adsorbed amounts of various molecules were relatively small [82]. We have reported the adsorption behavior of *o*-xylene and *p*-xylene vapor to a series of *N,N′*-hexamethylalkyldiammonium ions $[(CH_3)_3N^+(C_nH_{2n+1})(CH_3)_3N^+$, where $n = 2$, 3, 6, 10, abbreviated as $C_n^{2+}]$-exchanged montmorillonites (Kunipia F: CEC of 119 meq/100 g clay and

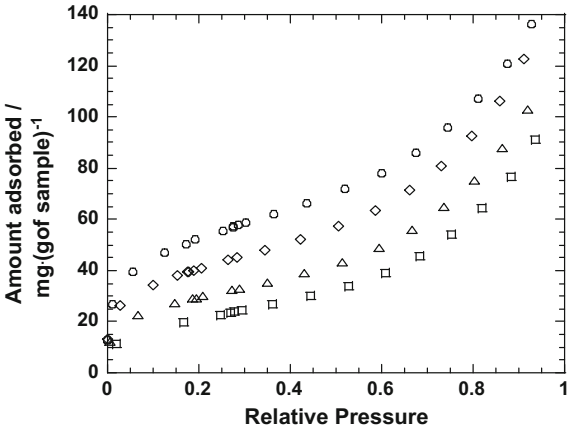

Fig. 9.9 Adsorption isotherms of *p*-xylene (298 K). (*White circle*) Adsorption isotherm for C_2^{2+}-BB11, (*white diamond*) adsorption isotherm for C_3^{2+}-BB11, (*white up pointing triangle*) adsorption isotherm for C_6^{2+}-BB11, (*white square*) adsorption isotherm for C_{10}^{2+}-BB11. Reprinted from Ref. [85]. Copyright 2009 Elsevier

BENGEL BLIGHT 11 (BB11) from Hojun, Japan: CEC of 78 meq/100 g clay) [85]. All the examined organo-montmorillonites adsorbed these gases to show their microporous nature. The adsorbed amounts of xylenes increased when the size of C_n^{2+} was smaller (Fig. 9.9), showing possible pore volume engineering.

Lee [86] reported the adsorption of benzene, toluene, and *o*-xylene on TMA-smectites with different layer charge density (SAz: Arizona montmorillonite: CEC = 120 meq/100 g clay and SAC: Wyoming montmorillonite: CEC = 90 meq/100 g clay) (Fig. 9.10). The adsorbed amount of toluene from vapor phase on the TMA-smectites varied depending upon the nature of the smectites. The closer packing of TMA in the TMA-SAz resulted in a higher degree of shape-selective adsorption (adsorbed amount decreased in the order of benzene > toluene > *o*-xylene). The adsorption capacities of aromatic molecules were significantly reduced in the presence of water (Fig. 9.10). The lower adsorption capacity of aromatic molecules accompanied the increased shape selectivity. The reduction in the capacity and the increased selectivity were pronounced for the water saturated, high-charge TMA-smectite than for the low charge TMA-smectite. Hydration of TMA ions or the siloxane surfaces apparently reduced the accessibility of the aromatic molecules to interlamellar regions. Phenol and 4-chlorophenol were adsorbed from aqueous solution on tetramethylphosphonium (TMP)-smectite (Wyoming montmorillonite, CEC = 90 meq/100 g), while a negligible adsorption of 2- and 3-chlorophenols was observed [87]. In addition, these phenols were not adsorbed on high CEC TMP-smectite (SAz, Arizona montmorillonite, CEC = 120 meq/100 g). These observations were interpreted from the difference in the size of the pore created by TMP. Phenols were not adsorbed on the TMA-smectite even when the host is lower layer charge density (CEC = 90 meq/100 g). It has been pointed out that higher degree of hydration of TMA compared with TMP resulted in the observed size exclusion.

Adsorption behavior of phenols onto Kunipia F, Sumecton SA and a synthetic fluor-tetrasilicic mica (TSM) modified with $[Ru(bpy)_3]^{2+}$ is an example to show that

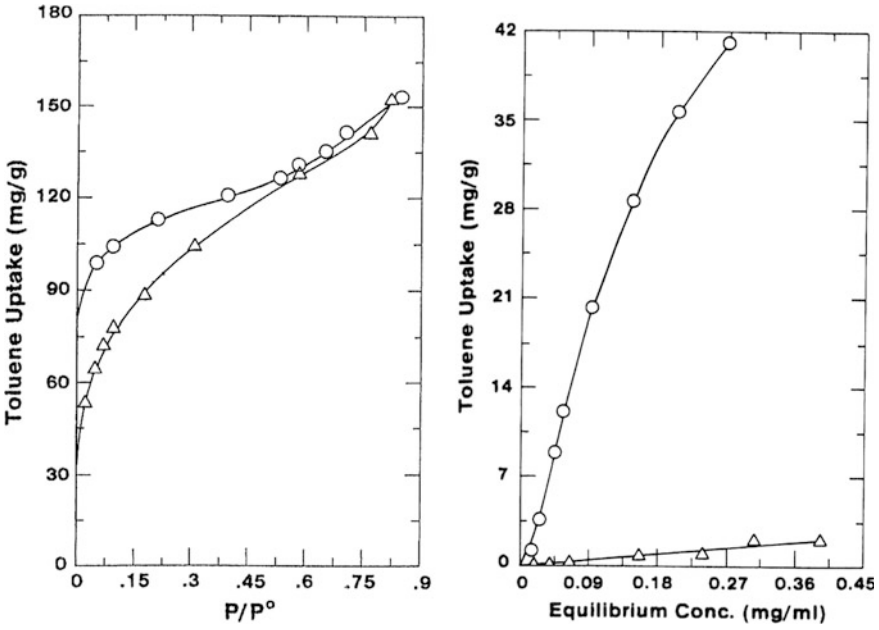

Fig. 9.10 Adsorption isotherms of toluene (*left*) from vapor phase and (*right*) from aqueous solution by high charge (*triangles*) and low charge (*circles*) TMA-smectite. Reprinted from Ref. [86]. Copyright 1990 The Clay Minerals Society

the distance between adjacent cations plays a role in the adsorbent design [88]. Intercalation of $[Ru(bpy)_3]^{2+}$ into layered clay minerals has extensively been investigated for probing the surface of clays as well as for electrochemical applications [89–92]. A few examples on the adsorptive properties of the $[Ru(bpy)_3]^{2+}$ modified clays has been published [93, 94], where $[Ru(bpy)_3]^{2+}$ acts as pillar to create micropore in the interlayers. Sumecton SA produces relatively large pore volume in the interlayer space by $[Ru(bpy)_3]^{2+}$, resulting in larger adsorption capacities of phenols (phenol and chlorophenol). The $[Ru(bpy)_3]^{2+}$-Sumecton SA can be utilized as adsorbent for relatively bulkier compared with phenols used in this study to arise molecular sieving effects for such bulkier molecules. More defined porous structure, which is a 2-dimensional long range order for racemic and enantiomerically pure $[Ru(bpy)_3]^{2+}$, has been obtained by intercalating into synthetic fluorohectorite [95].

Thus, in smectite systems, the CEC is a key factor to determine the adsorptive properties for nonionic organic molecules [96]. However, some characteristics, which depend on the origin of smectites, as position of isomorphous substitution and particle size make it difficult to discuss the effects of CEC on the physicochemical properties of smectites and their intercalation compounds. It is possible to reduce the layer charge by thermal treatment of Li-exchanged forms (Hofmann-Klemen Effect) [97, 98]. Reduction of layer charge of montmorillonites

[99] and a F-rich potassium hectorite (obtained by a high temperature melt synthesis) [100] by Hofmann–Klemen effect allows the tailoring of pore sizes of pillared clays.

Varied CEC by changing the amount of Mg^{2+}/Li^{+} in hectorite-like layered silicates [101, 102] affected the size or volume of the interlayer pore created by MV^{2+} to vary adsorption capacity of organic molecules [102]. The intercalated *N,N′*-dimethylaniline polymerized to develop purple color when the layered silicates with the CECs of 74 and 42 meq/100 g were used. On the other hand, the intercalation compound with larger MV^{2+} content (CEC: 85 meq/100 g) suppressed the polymerization of *N,N′*-dimethylaniline due to the smaller pore. The smaller MV^{2+} content, the adsorption capacity of 2,4-dichlorophenol was larger.

Breu and co-workers [103] have (re-)established synthetic strategy of structurally well-ordered pillared clays (>100 μm) with homogeneous (ultra)micropore distribution. For this purpose, they have made efforts to make homogeneous charge distribution in synthetic fluorohectorite ($Na_{0.5}(Mg_{2.5}Li_{0.5})Si_4O_{10}F_2$) [104] through very careful melt synthesis. There is no structural disorder in the synthetic fluorohectorite in contrast to naturally occurring swellable layered silicates. In order to avoid phase separation in the silicate melt, the crucible has been rotated during the synthesis. The homogeneous charge distribution has been confirmed by founding X-ray reflection due to the two-dimensional $3a \times b$ super-cell (Fig. 9.11) in Me_2DABCO^{2+}(*N,N*-dimethyl-1,1-diazabicyclo[2.2.2]octane dication) [103a] and 2H-DABCO (diprotonated 1,4-diazabicyclo[2.2.2]octane) exchanged fluorohectorites [103b]. As a result, homogeneous micropore distribution and only ultramicropore with pore width of 0.4–0.6 nm were obtained. Charge homogeneity was also achieved for iron-containing Cs-taeniolite ($Cs_{0.98}Fe^{2+}_{1.93}Li_{1.01}Si_4O_{10}F_2$) [103c]. They have provided preferred molecular structure of pillaring agents for generating homogeneous porous network by considering results of MD simulations. Figure 9.12 illustrates that the pillar (Me_2DABCO^{2+}) is oriented with its C_3 axis

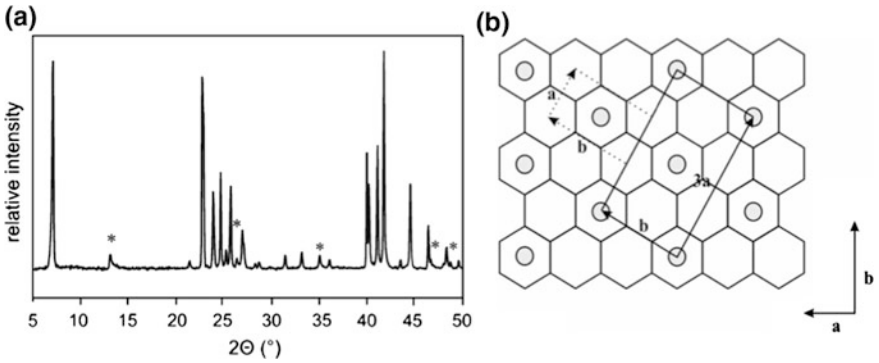

Fig. 9.11 **a** Powder XRD pattern of 2H-DABCO-hectorite. *Asterisks* (*) mark reflections due to the two-dimensional $3a \times b$ super-cell; **b** Scheme of the $a \times b$ super-cell of pillars in 2H-DABCO-hectorite. The unit cell of the parent hectorite is shown as *dotted lines*. Reprinted from Ref. [103a]. Copyright 2008 Royal Society of Chemistry

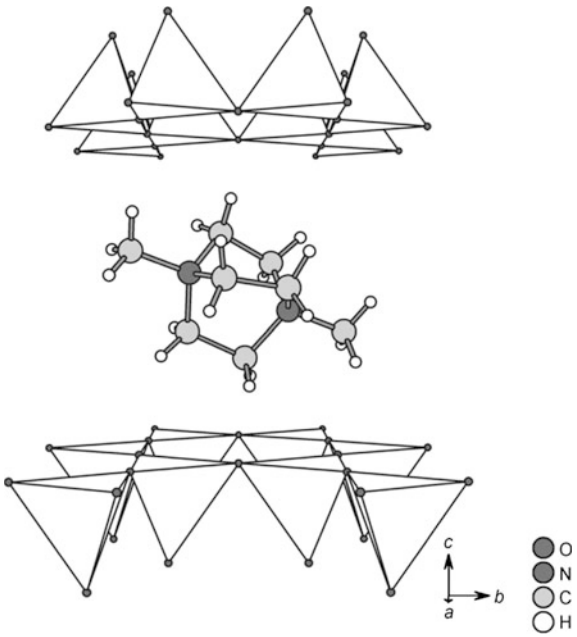

Fig. 9.12 Results of the X-ray single-crystal refinement (tetrahedral layer of the layered silicate and Me_2DABCO^{2+} in the interlayer space). Reprinted from Ref. [103d]. Copyright 2008 Wiley VCH

tilted by approximately 24° against the *ab* plane. While two of the C_2H_4 handles protrude into the silicate layers, the third one is in the hexagonal plane of the interlayer space [103d]. The sizes and volume of the micropores created by Me_2DABCO^{2+} and $[Rh(bpy)_3]^{3+}$ were shown to be increased through layer charge reduction of the synthetic fluorohectorite using Hofmann–Klemen effect from CEC = 84 to 59 meq/100 g [100].

9.4.3 Grafting

Immobilization of organic functionality into the interlayer space through covalent bonding is a way of the surface modification, and this is available for layered solids with interlayer hydroxyl groups. Reactions between layered silicates and silane coupling agents became possible after the pioneering work by Ruiz-Hitzky and Rojo [105], and studies on this topic have been summarized in a recent review [106]. Introduction of trimethylsilyl groups into a layered silicate (kanemite) led to effective benzene adsorption by weakening the interaction between the interlayer hydrogen bonds of the surface hydroxyl groups [107]. Distance between adjacent organic groups has been controlled by covalent attachment of octylsilyl groups to layered silicate, magadiite [108–111]. Alkyl alcohols were intercalated into the organic derivatives modified with controlled amounts of octylsilyl groups, while alkanes were not adsorbed [108]. Larger amounts of alcohols were intercalated into

the derivatives with lower surface coverage. These results have been explained as the cooperative effect of the geometry and the chemical nature of the surface covered with octyl groups and silanol groups.

Selective adsorption of 4-nonylphenol from the mixtures of *n*-nonane, phenol and 4-nonylphenol in water was observed by attaching both functionalities of octadecyl and phenyl groups when layered lithium potassium titanate ($K_{0.8}Ti_{1.73}Li_{0.27}O_4$) [112] and layered alkali silicate (octosilicate) [113] were modified through silylation. These phenomena were explained as the result of the cooperative effect of chemical interactions and geometrical matching of the modified titanate and silicates, where two functional units (octadecyl and phenyl groups) were arranged to give the selective binding of 4-nonylphenol.

9.4.4 Inorganic Modification

Deposition/immobilization of nanoparticles of metals and their oxides onto inorganic layered solids have been widely investigated for applications as developing molecular-sieve-like catalysts. The reduction of Cu^{2+}-exchanged montmorillonite (Kunipia F) with ethylene glycol resulted in the formation of Cu nanoparticle with the diameter less than 0.5 nm on montmorillonite [114]. We have investigated the immobilization of gold nanoparticles into the interlayer space of a layered alkali silicate and titanate utilizing a thiol-bearing organoammonium and silane coupling reagent [115, 116]. Disk-like gold nanoparticles formed in the interlayer space of a layered titanate modified with 3-(mercaptopropyl)trimethoxysilane, and the hybrid showed efficient and selective photocatalytic oxidation of aqueous benzene to phenol under visible light irradiation ($\lambda > 420$ nm) when the reaction was conducted in the presence of aqueous phenol [117]. Choy, Hwang and co-workers have reported pillaring layered titanate with NiO by the reaction between the aqueous (exfoliated) $H_{0.67}Ti_{1.83}\square_{0.17}O_4$ ($\square$ = vacancy) suspension and the precursor of NiO and the application for selective cyclohexane epoxidation [118].

Smectites pillared with metal oxides, represented by Al_2O_3- or ZrO_2-pillared clays, have been studied as useful adsorbents and catalyst supports because of their thermal stability [119–123]. An alumina pillared montmorillonite (Wyoming bentonite) fabricated by using $[AlO_4Al_{12}(OH)_{24}(H_2O)_{12}]^{7+}$ polyoxycations as the pillaring agent was proposed as a recyclable surfactant support for the adsorption of organic toxicants in water and subsequent combustion [124]. Besides smectites, layered alkali silicates [125] and layered titanates [125, 126] have also been used as scaffolds for designing such pillared materials.

Controlled hydration of layered titanates ($M_xTi_{2-x/3}Li_{x/3}O_4$; M = K, Li, Na; x = 0.61–0.76) in water affected adsorption of organic molecules and photocatalytic activity [127]. The interlayer cation and layer charge density of the titanates determined the water vapor adsorption and hydration in liquid water, and the Na-form with the lowest layer charge density ($Na_xTi_{2-x/3}Li_{x/3}O_4$; x = 0.61) showed a larger amount of water vapor uptake and the expansion of the interlayer space

(Fig. 9.13). The greater water uptake played an important role in photocatalytic selective benzene oxidation on the titanate from aqueous mixture; benzene was preferentially decomposed in the aqueous mixture with phenol and 4-butylphenol by UV irradiation (Fig. 9.14). The selectivity was thought to be due to the access into the interlayer space; size of benzene was smaller than the gallery height ($\sim$0.7 nm) of the Na-form for effective access of benzene to the interlayer surface to be decomposed. On the other hand, benzene was hardly intercalated into the

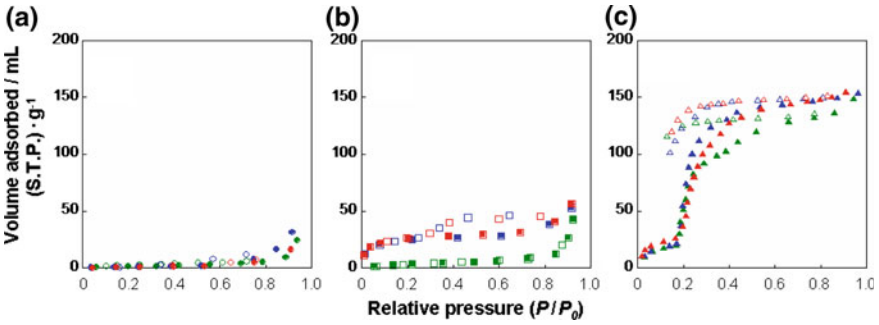

Fig. 9.13 Water adsorption (*filled symbol*)/desorption (*open symbol*) isotherms of **a** $K_xTi_{2-x/3}Li_{x/3}O_4$ [x = (*red filled/open circle*) 0.61, (*blue filled/open circle*) 0.67, (*green filled/open circle*) 0.74], **b** $Li_xTi_{2-x/3}Li_{x/3}O_4$ [x = (*red filled/open square*) 0.61, (*blue filled/open square*) 0.67, (*green filled/open square*) 0.76], and **c** $Na_xTi_{2-x/3}Li_{x/3}O_4$ [x = (*red filled/open triangle*) 0.61, (*blue filled/open triangle*) 0.67, (*green filled/open triangle*) 0.76]. Reprinted from Ref. [127]. Copyright 2010 American Chemical Society

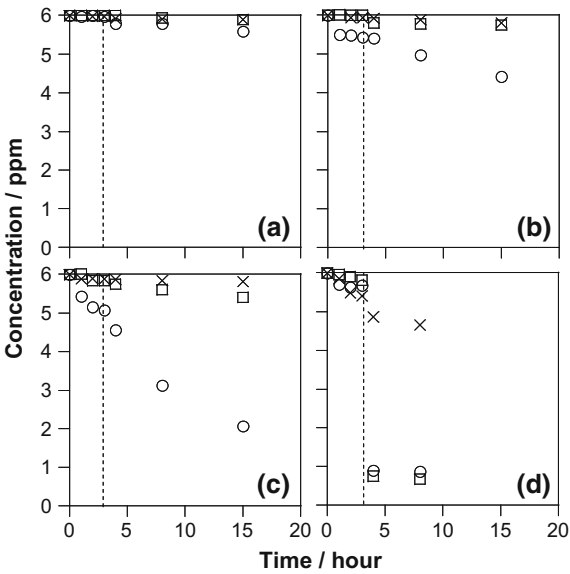

Fig. 9.14 Photocatalytic decomposition of (*white circle*) benzene, (*white square*) phenol, and (*cross sign*) 4-butylphenol in water by **a** $K_xTi_{2-x/3}Li_{x/3}O_4$ (x = 0.74), **b** $Li_xTi_{2-x/3}Li_{x/3}O_4$ (x = 0.76), **c** $Na_xTi_{2-x/3}Li_{x/3}O_4$ (x = 0.61), and **d** titanium dioxide (P25). *Vertical lines* indicate the beginning of ultraviolet light irradiation. Reprinted from Ref. [127]. Copyright 2010 American Chemical Society

K-titanate, which does not swell, and into the Li-titanate with lower swelling ability than that of the Na-form (Fig. 9.14).

9.4.5 Characterization

Understanding the interlayer hydrated structures of smectites (the orientation and the dynamics of the intercalated water) has been recognized as prime importance for assessing chemical and geological phenomena. The phenomena include barriers for underground storage of radioactive waste and rheological behavior of soil, which contributes to slipping processes in plate-boundary faults. Intercalation of water molecules is characterized by the stepwise expansion of the interlayer space with increasing water amount, which was controlled by the atmospheric humidity [128, 129]. The interlayer hydrated structures have been assessed using in situ XRD along water adsorption/desorption isotherms [130], ^{1}H and ^{2}H NMR [131], and neutron scattering [132]. A recent synchrotron-radiation X-ray diffraction study by Sasai et al. [133] showed large thermal vibration of hydrated Cl ions in the interlayer space because of higher mobility compared with the dehydrated form (Fig. 9.15). Difference in the vibration in the presence of water depending on the nature of anion should be important in anion-exchange properties of LDHs. The structure and dynamics of interlayer water molecules in smectites and LDHs can be revealed by computer simulations including Monte Carlo and molecular dynamics (MD). The structure and swelling behavior of smectites and LDHs have been more precisely understood at a molecular level [42, 134–139], although the nano-sized nature and lack of suitable large single crystals for accurate structure determinations except for a recent example on Na-fluorohectorite with quite large aspect ratio [140a]. Hydrated interlayer structure of well-ordered crystalline Na-fluorohectorite have been evaluated at 2 GPa in an excess of liquid water, resulting in successful detection of the phase transition from 2 to 3 water layers as a stepwise fashion [140b].

A transmission X-ray diffraction technique has been adopted to pursue the interlayer structural change upon the intercalation of caffeine from aqueous solution [141]; benzylammonium-exchanged smectites with the basal spacing of 1.3–1.4 nm swelled in liquid water to be 1.60 nm, and further expanded to 1.70 nm in an aqueous caffeine solution (Fig. 9.16). It has been assumed that the expansion by water molecules facilitates caffeine adsorption (intercalation) into the interlayer space.

9.4.6 Stimuli Responsive Adsorbents

Stimuli responsive properties have been investigated for the creation of smart materials. Intercalation of photo-responsive functional groups into layered solids

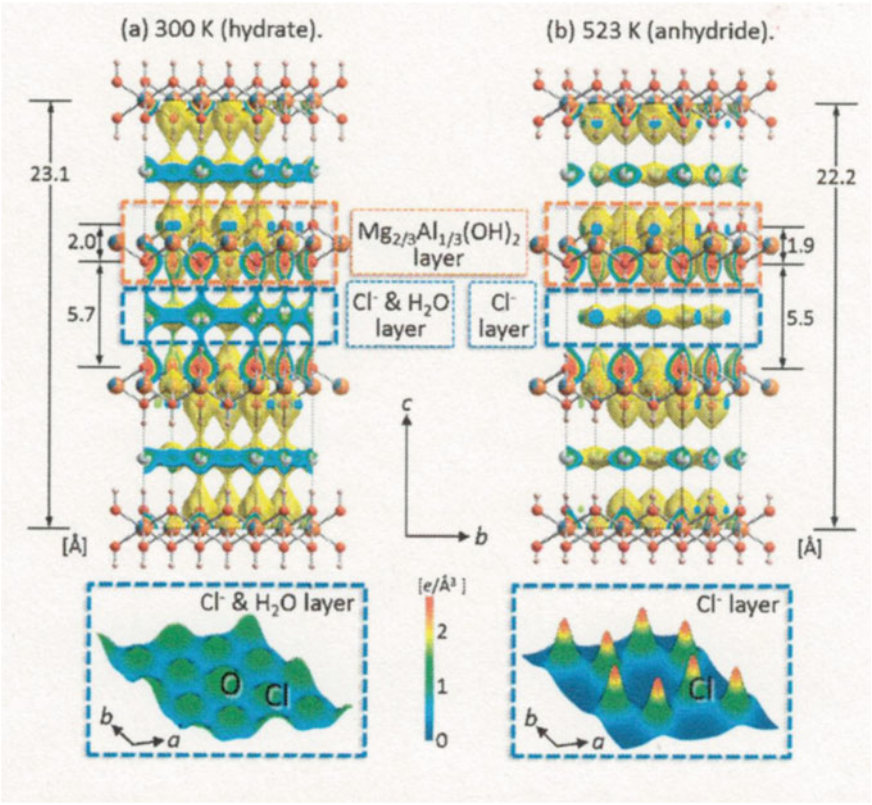

Fig. 9.15 Fine crystal structure and electron density distribution of Cl–Mg/Al-LDH (Mg/Al = 2) derived by the MEM and Rietveld method from SXRD data measured at 300 and 523 K. Isosurface level of the charge density is 0.5eÅ^{-3}. Reprinted from Ref. [133]. Copyright 2013 The Chemical Society of Japan

has been examined. In some cases, reversible change in the basal spacing has been observed in response to alteration of molecular configuration triggered by photoirradiation. Azobenzene is a photochromic dye, which shows reversible *trans*-to-*cis* photoisomerization by UV irradiation and subsequent visible light irradiation or thermal treatment (Fig. 9.17a) [142]. When a cationic azo dye, *p*-[2-(2-hydroxyethyldimethylammonio)ethoxy]azobenzene (Fig. 9.17b, abbreviated as $AZ(OH)^+$) was intercalated in magadiite with the adsorbed amount of 1.90 meq/g silicate, the basal spacing changed after UV irradiation from 2.69 to 2.75 nm and the value came back to 2.69 nm upon visible light irradiation [143]. Intercalated $AZ(OH)^+$ as *J*-aggregate in montmorillonite (CEC: 1.19 meq/g) did not exhibit the photoresponses of the basal spacing during the photoisomerization [144]. Even careful consideration of controlled orientation using amphiphilic cationic azobenzenes in layered silicates (smectites and magadiite), photoresponse of the basal

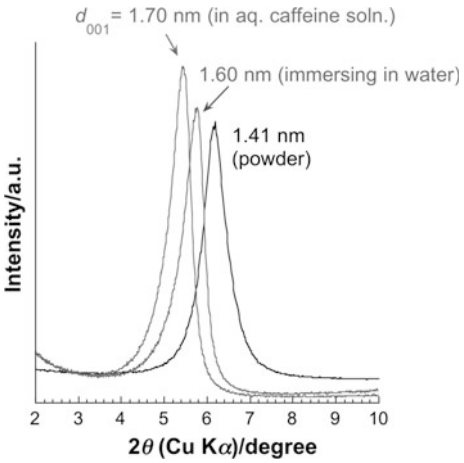

Fig. 9.16 Change in the XRD pattern of caffeine-adsorbing benzylammonium-Kunipia F. The patterns of the aqueous dispersions were measured by a transmission technique in the presence and absence of caffeine (2.1 mM). The powder diffractions were recorded using a conventional method at room temperature with relative humidity ca. 50%

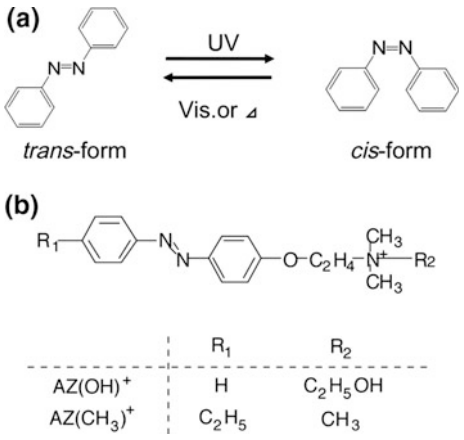

Fig. 9.17 **a** *cis–trans* Photoisomerization of azobenzene and **b** molecular structure of the cationic azobenzene derivatives used in our studies

spacing has hardly been observed [145–148]. A molecular dynamics simulation [149] indicates an importance of the flexibility of the functional groups attached to azobenzene in inducing such XRD detectable structural change. The $AZ(OH)^+$ dye does not contain flexible long alkylchains, therefore, the photoisomerization induced the change in the microstructure detectable by XRD. At the photostationary state, a densely packed aggregate of $AZ(OH)^+$ is possibly difficult to form in magadiite due to the geometric difference of the two isomers (approximate molar *trans*:*cis* ratio of 1:1), and this causes the change in the basal spacing.

Inoue and his co-workers have reported a densely packed intercalation of a polyfluorinate cationic azo dye ([2-(2,2,3,3,4,4,4-heptafluorobutylamino)ethyl]-{2-[4-(4-hexyphenylazo)-phenoxy]-ethyl}dimethylammonium: C3F-Azo) into a layered niobate [150] and a layered titanoniobate [151]. Reversible *trans*-to-*cis* photoisomerization of the intercalated azobenzene moiety accompanied the repeated

changes in the basal spacings. The direction of the interlayer distance upon each isomerization was opposite to that observed in the magadiite system as described above. Morphological change was detected by AFM when the C3F-Azo-layered niobate hybrid film was used [152]. After the irradiation of *ca.* 370 nm light, the bottom edge of the film slid out (the sliding distance of *ca.* 1500 nm), while the height of the top edge maintained. Subsequent higher wavelength light (*ca.* 460 nm) irradiation resulted in sliding back to the original position before the photoirradiation. Photoresponsive morphological changes have also been reported in a hybrid film composed of an azobenzene containing polymer and a LDH obtained by using a layer-by-layer self-assembly technique [153]. In this case, AFM observations of the resulting film exhibited changes in the surface roughness with responses to UV and visible light irradiation.

These phenomena demonstrated a type of photomechanical effect and larger volume change is expected. In order to amplify the change in the basal spacing upon the photoirradiation, we examined photoresponse of phenol intercalation in smectites modified with $AZ(OH)^+$ [154]. Phenol was intercalated into $AZ(OH)^+$-Kunipia F to expand the interlayer space from 1.8 to 2.6 nm by mechanical mixing without solvent. As shown in the XRD patterns (Fig. 9.18), the basal spacing increased to 3.2 nm by the UV light irradiation, indicating phenol intercalation. Subsequent visible light irradiation resulted in the decrease in the basal spacing to the value before the UV irradiation, suggesting phenol deintercalation. It was assumed to the intercalation and deintercalation of phenol induced by reversible *trans*-to-*cis* isomerization of the intercalated $AZ(OH)^+$. More polar nature of *cis*-$AZ(OH)^+$ compared to the *trans*-form possibly caused the intercalation of phenol. We have defined this kind of materials as photoresponsive adsorbents.

To investigate the effects of the nano-structure on the photoinduced intercalation behavior, layered silicates with different layer charge density (Kunipia F,

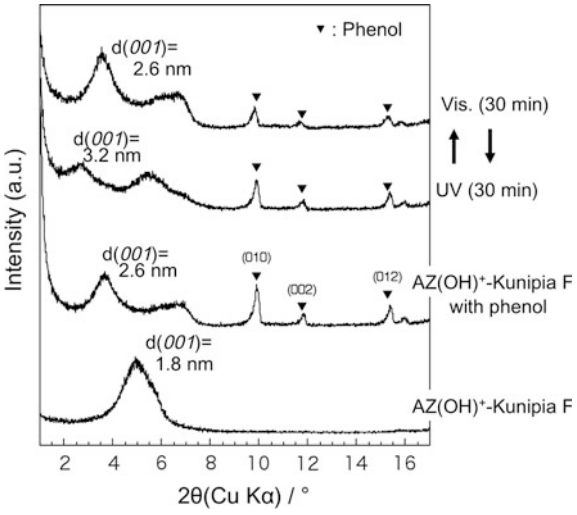

Fig. 9.18 Change in the XRD patterns of $AZ(OH)^+$-Kunipia F by the reaction with phenol and by photoirradiations. Reprinted from Ref. [154]. Copyright 2004 Royal Society of Chemistry

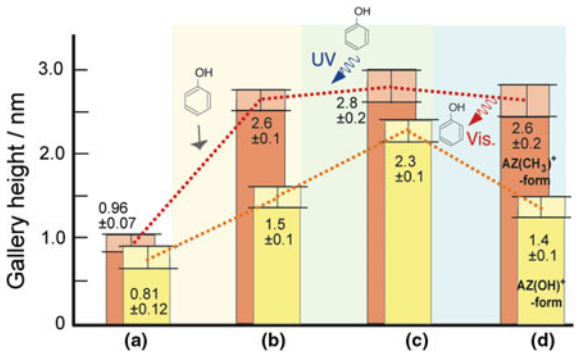

Fig. 9.19 The change in the gallery heights of $AZ(CH_3)^+$- and $AZ(OH)^+$-Kunipia F; **a** before the intercalation of phenol, **b** after phenol intercalation, **c** after UV irradiation and **d** after subsequent visible light irradiation. Reprinted from Ref. [156]. Copyright 2008 Elsevier

Sumecton SA and TSM) have been used [155]. While intercalation and photoinduced intercalation of phenol into $AZ(OH)^+$-TSM and $AZ(OH)^+$-Kunipia F were observed, those phenomena were not seen for $AZ(OH)^+$-Sumecton SA. The structure of the $AZ(OH)^+$-clays before the intercalation is different; an interdigitated monolayer of $AZ(OH)^+$ with the longer molecular axis inclined to the silicate layer in Kunipia and TSM, and a monolayer coverage of $AZ(OH)^+$ with their molecular long axis parallel to the silicate layer in Sumecton SA. The dye orientation correlates the intercalation and photoinduced intercalation of phenol.

Another cationic azo dye, $AZ(CH_3)^+$, in which hydroxyl group is absent (Fig. 9.17b), was synthesized to compare the adsorptive properties of $AZ(OH)^+$-Kunipia F [156] (Fig. 9.19). Although the gallery height of $AZ(CH_3)^+$-Kunipia F also changed by the phenol intercalation as also seen in the $AZ(OH)^+$-Kunipia F system, the amount of the intercalated phenol into $AZ(CH_3)^+$-Kunipia F was relatively large compared with that in $AZ(OH)^+$-Kunipia F. Due to the absence of the hydroxyl group, the hydrophobic nature enhanced to lead larger amount of the intercalated phenol before irradiation. On the contrary, the amount of the intercalated phenol after the UV irradiation for $AZ(CH_3)^+$-Kunipia F was relatively small. No intercalation at ground state, larger amount of intercalation by irradiation, complete deintercalation by subsequent irradiation and smooth response will be required to find practical application of these phenomena as advanced smart adsorbents.

9.5 Adsorption of Polymers

Layered solids dispersed in water often adsorb polymers including polyelectrolytes and nonionic polymers from aqueous solution. The adsorption of water-soluble polymers onto clay minerals (montmorillonite, in particular) have long been studied, because of many useful applications as flocculation aids, soil conditioners, drilling mud-extenders, and protection of salt–water drilling fluids [157]. The sol of clay minerals (suspension) in water readily flocculated by adding only small

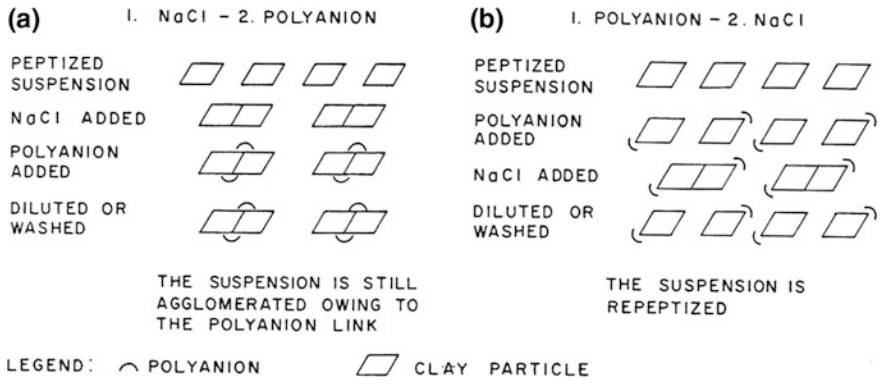

Fig. 9.20 Schematic representation of the interaction of clay particles with polyanions and salt as a function of the sequence of addition. **a** Salt added before adding polyanions. **b** Salt added after the addition of polyanions. Reprinted from Ref. [157]

amount of positively charged polyelectrolyte due to the electrostatic interactions. Crystal edges of montmorillonite are thought to be a possible adsorption sites for a negatively charged polyelectrolyte. Although the polyanions (e.g., Na-polymethacrylate) alone do not flocculate the clay sol, addition of salt to the suspension causes the flocculation [158, 159]. Small amount of polyanion is thought to be adsorbed on several clay sol particles, followed by forming a bridge between them. The salt played a role to allow the sol particles to come closer together by the reduction of the range of double-layer repulsion and thus to promote bridging of the particles. The sequence of the addition of the polyanion and the salt is important in order to prevent re-dispersion (repeptized) by washing with water (or in order to act as flocculation aids effectively); salt should be added to the sol before the polyelectrolyte addition. Otherwise, the suspension is repeptized during the washing with water, because the clay surfaces are not covered completely with the polyions due to less coagulated clay particles in the absence of salt (Fig. 9.20) [157, 158].

Adsorption of enzymes (urease and glucose oxidase) on smectites [160, 161] was also reported in order to apply smectites as a support to reproduce enzymatic function. While the adsorption of enzyme on smectites is pH dependent, the enzyme is strongly bound by alkylammonium-smectites through hydrophobic interactions. Such interactions may involve hydrophobic portion of the enzymes interacting with the hydrophobic alkyl groups on the surface of clays.

Nonionic polymers (for examples of polysaccharides and polyoxyethylenes) were also adsorbed on smectites. At higher concentrations, the polymers usually have a protective action on clay sols (behaving as protective colloids), while at lower concentrations, they sometimes flocculate a clay sol (the flocculation does not occur for low-molecular weight polymers) [157]. Adsorption of a water-soluble polymer has been used to control the state of organic cations as well as the spatial distribution on smectites [162–164]. The isolation of $[Ru(bpy)_3]^{2+}$ has been

achieved by the co-intercalation of poly(vinyl pyrrolidone) (abbreviated as PVP) [162, 163]. The controlled expansion of the interlayer space (design the size of two-dimensional nanospace) was achieved by changing PVP amount on synthetic saponite (Sumecton SA) [164].

9.6 Adsorption of Nanoparticles

Adsorption of colloidal nanoparticles including silica [165, 166], titania [167, 168], and CdS [169, 170] into montmorillonite was reported. Material's applications of these resulting solids have been investigated in fields of photo- and electrochemistry. The adsorption often leads to provide intercalation compounds (to form pillared-layered solids). TiO_2 sol (1.5 nm in diameter) pillared montmorillonite was prepared for the photocatalytic decomposition of *n*-carboxylic acids with up to 8 carbons, while the catalytic activity for capric acid was lower than that over bare TiO_2. The adsorption, in some cases, gives homogeneous gels in which the order in the layer stacking is partially or completely lost (hetero-coagulation) [166, 168].

Besides the interest in advanced materials applications, the immobilization of nanoparticles on solids is a concern involving general environmental issues [171–173]. Nanoparticles in nature (especially those in air and water) are often regarded as contaminants and reservoir of toxic compounds, and their removal is required for environmental remediation. Depending on the nature of environmental nanoparticles (clays, pollen, etc.), various methods (filtration, precipitation, chemically induced aggregation, and so forth) have been used for their removal from the environment. Electrostatic interactions between negatively charged colloidal particles (β-FeOOH and a synthetic smectite) and positively charged LDH (hydrotalcite) have been used as a driving force for the nanoparticle immobilization [174]. β-FeOOH, which dispersed stably in water, precipitated after the addition of LDH as shown in the photograph (Fig. 9.21). The relationship of the β-FeOOH amounts between remaining and removed in/from the aqueous phase was similar to the shape of the Langmuir-type adsorption isotherm, suggesting strong interactions between β-FeOOH and LDH. A synthetic saponite (Sumecton SA) also precipitated after the

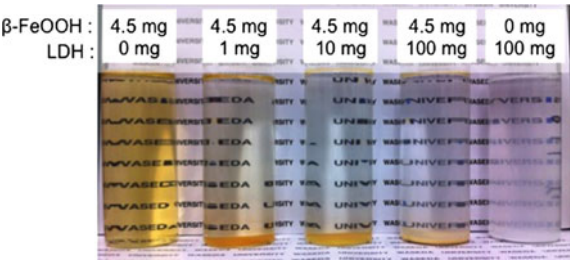

Fig. 9.21 β-FeOOH precipitation after addition of LDH. The photograph was taken after the sample stood for 7 h. Reprinted from Ref. [174]. Copyright 2013 American Chemical Society

LDH addition. The concept was adopted to cause precipitation of a positively charged colloidal particle (fine LDH particle) by micrometer-sized platy particles (octosilicate: a layered sodium silicate).

9.7 Morphosynthesis of Layered Solids for System Design

In order to regulate macroscopic shapes required for some uses and sensing and electronics, bottom-up self-assembly of layered solid nanosheets using the electrostatic interactions has been developed by depositing exfoliated nanosheets on a substrate and by molding to useful shapes using spray-drying [175] and freeze-drying techniques [176–178]. Optically transparent films [179–181] have been obtained by means of various fabrication techniques, including simple casting, Langmuir–Blodgett method [182], and layer-by-layer deposition technique [183–186].

Thanks to the optically transparent films, sensors with optical detection are possible. When the adsorption of a certain molecular species causes color change of the transparent films, it can be applied to colorimetric sensing for the environmental pollutants detection. Takagi et al. have reported solvatochromism of porphyrin-Sumecton SA complex membrane prepared by filtering the aqueous dye-clay suspension with PTFE membrane filter before transferring the residual membrane on the PTFE to a cover glass. The orientation of the porphyrin in the clay interlayer space changes by organic solvents to cause the color change [187].

Structural color (interference) is also applicable for the detection. The films coated on a high reflective index substrate (titania or Si) leads to the structural color as a result of the controlled thickness, which is a possible way to detect the adsorption without chromophores [185, 186]. By the adsorption (intercalation) of organic molecules or cations, an interference color changes, according to the optical Bragg low as the following equation:

$$\lambda_{\mathrm{B}} = 2n_{\mathrm{eff}}\Lambda$$

(where n_{eff} and Λ are the refractive index of a substrate and its period, respectively). This equation can be met by modulation of n_{eff} and by changing the clay layer dimension (Λ) through swelling by the intercalation of organic substances. Since the observed interference color (derived from λ_{B}) is a function of clay film thickness and refractive index, changes in the latter parameters directly translate into optically perceptible color change. A color change, corresponding to a red-shift of stop-band (which does not allow visible light to pass), was able to be visually observed, when exposing the film to aliphatic quaternary organoammoniums ions, cationic polyelectrolytes and a nonionic surfactant. Bulky surfactants and their higher loading gave rise to the increase in the basal spacing of Laponite, thus leading to a larger red-shift of the stop-band (Fig. 9.22). On the contrary, only a

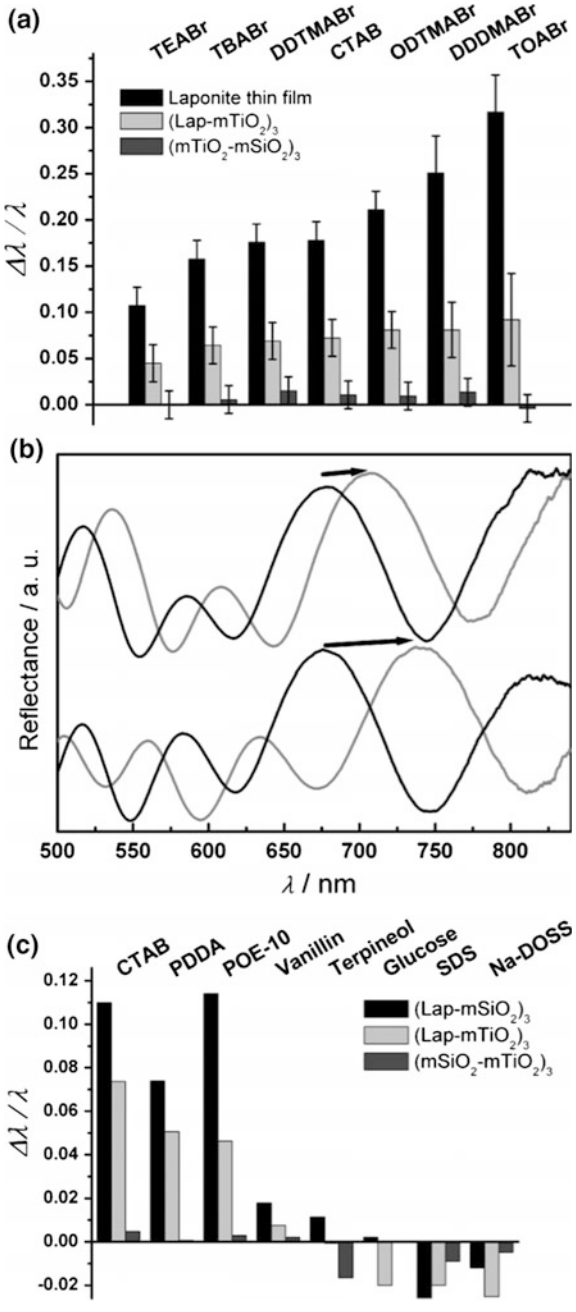
(a)
TEABr
TBABr
DDTMABr
CTAB
ODTMABr
DDDMABr
TOABr
Laponite thin film
(Lap-mTiO2)3
(mTiO2-mSiO2)3
Δλ / λ
0.35
0.30
0.25
0.20
0.15
0.10
0.05
0.00
(b)
Reflectance / a. u.
500
550
600
650
700
750
800
λ / nm
(c)
CTAB
PDDA
POE-10
Vanillin
Terpineol
Glucose
SDS
Na-DOSS
(Lap-mSiO2)3
(Lap-mTiO2)3
(mSiO2-mTiO2)3
Δλ / λ
0.12
0.10
0.08
0.06
0.04
0.02
0.00
-0.02

◂**Fig. 9.22** **a** Relative optical shifts of Laponite thin films after exposure to 0.03 M surfactant solutions in ethanol. Increasing bulkiness translates into an enhanced optical response. **b** Position of the stop-band of a TiO_2 hybridized film before (*black*) and after (*gray*) exposure of DDTMABr (*top*) and PDDA (*bottom*). **c** Relative optical shifts of three films with respect to different analytes. Legend of abbreviations: *CTAB* cetyltrimethylammonium bromide; *DDDMABr* didodecyldimethylammonium bromide; *DDTMABr* dodecyltrimethylammonium bromide; *NaDOSS* sodium dioctyl sulfosuccinate; *PDDA* poly(diallyldimethylammonium chloride); *POE-10* polyoxyethylene-10-laurylether; *SDS* sodium dodecylsulfate; *TEABr* tetraethylammonium bromide; *TBABr* tetrabutylammonium bromide; *TOABr* tetraoctylammonium bromide. Reprinted from Ref. [185]. Copyright 2008 Wiley VCH

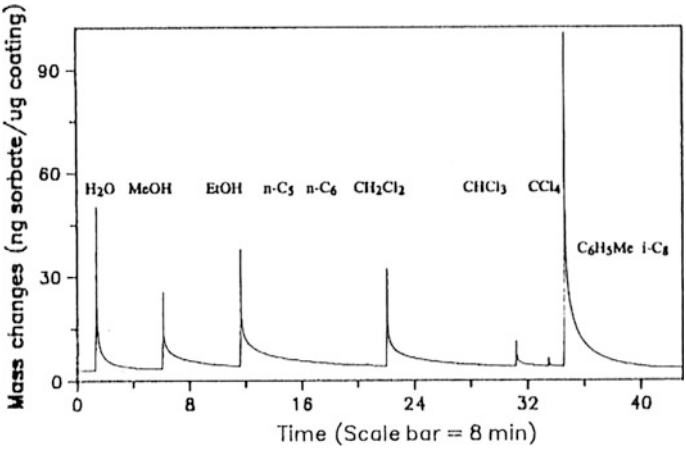

Fig. 9.23 Transient sorption of vapor pulses at 100 °C on 6.0 MHz QCMs coated with ODTMA-hectorite film (181 μg/cm^2). Reprinted from Ref. [189]. Copyright 1993 American Chemical Society

slight change in the stop-band was observed when immersing in a solution of neutral aromatic compound probably due to small amount of the intercalate.

The film of layered solids was also applied for electrochemical detection of organic contaminants. Redox reactions in response to selective adsorption of analytes on electrodes modified with layered solids (e.g., smectites and LDHs) have been widely investigated as electrochemical sensors and biosensors [188]. Piezoelectronic sensors have also been developed; Organoammonium-hectorites (i.e., ODTMA-, TMA-hectorite) were coated on the gold electrodes of the QCM by dipping the crystal in their suspensions [189]. Water, acetonitrile/water or chloroform was used as solvents depending upon the dispersion properties of the organoammonium-hectorites. The ODTMA-hectorite film on the electrode adsorbed dichloromethane and toluene. On the contrary, the adsorption of *n*-hexane and *n*-octane on the ODTMA-hectorite did not occur even when the interlayer microenvironment was hydrophobic (Fig. 9.23). They deduced that the molecular

size of sorbates as well as hydrophobic interactions affected the unique sorption behavior.

In addition to the macroscopic organization of layered materials, controlled particle morphology has been a topic of interests. Application as chromatography stationary phase was achieved by the processing of layered materials into spherical particle. Spherical particles of a synthetic hectorite (average radius 5 μm) were obtained by spray-drying and has been used as a HPLC column packing material. The ion exchange of the spherical particles of hectorite (RU-1 from Shiseido Co. Ltd) with enantiomers has been reported for chiral discrimination [175, 190–192]; an ion-exchanged adduct of a clay and enantiomeric tris(1,10-phenanthroline) ruthenium(II) ion (Δ- or Λ-$[Ru(phen)_3]^{2+}$) was used as a packing material [193–197], where a vacant space surrounded by enantio pure $[Ru(phen)_3]^{2+}$ molecules provides an adsorption site with high chiral discrimination [198].

Rectangular single crystals such as layered niobate with mm-scale [199–201], silicate (octosilicate) with μm-scale [13, 202, 203] are known examples of controlled and defined morphology. Crystal (particle) size and morphology of LDHs are also controllable [204]. Monodisperse particles of LDHs have been obtained [205–210]. To obtain high quality-homogeneous crystals, homogeneous precipitation using urea hydrolysis has been adopted because pH rises homogeneously in the solution to avoid heterogeneity of mixing (or pH change); successful preparation of LDHs with huge hexagonal platy hydrotalcite particles (25 μm) [207] and associated to a relatively narrow particle size distribution [208–210]. Nanometer-sized LDH particles with narrow particle size distribution have been obtained using an anion-exchange resin to adjust the pH for the precipitation [211]. Using a tripodal ligand of tris(hydroxymethyl)aminomethane is an example on producing smaller LDH particles (10 nm) [212].

The direct (in situ) crystallization of layered solids on bulk solid substrates has been reported as an adsorbent design [213–223], which is a way to produce mechanically improved supporting materials (avoid exfoliation). When other chemical sources are supplied from the solution, the solid substrate has been used as a source of layered materials. As a result of the reactions at the interface (heterogeneous nucleation reactions), fine crystals form only on the substrates (maintaining the shapes of the substrate). The choice of solid substrate chemicals in a solution leads to forming various fine crystals at the interfaces such as M(=Ni, Zn)/Al layered double hydroxides (LDHs)–Al_2O_3 plates (Fig. 9.24) [213, 214], M(=Mg, Zn)/Al-LDH–Al_2O_3 microfibers [215, 216], hectorite–silica microspheres [217–219], saponite–silica microspheres [220], hectorite–silica microfiber filter paper (Fig. 9.25) [221], and titanosilicate–silica microfibers (Fig. 9.26) [222].

Because the direct crystallization technique leads thin layer coating of layered solids on a substrate, the adsorption–desorption equilibrium for such core-shell particle is likely accomplished within the thin shell layer. For the application to a chiral HPLC application, elution would proceed rapidly, maintaining high degree of

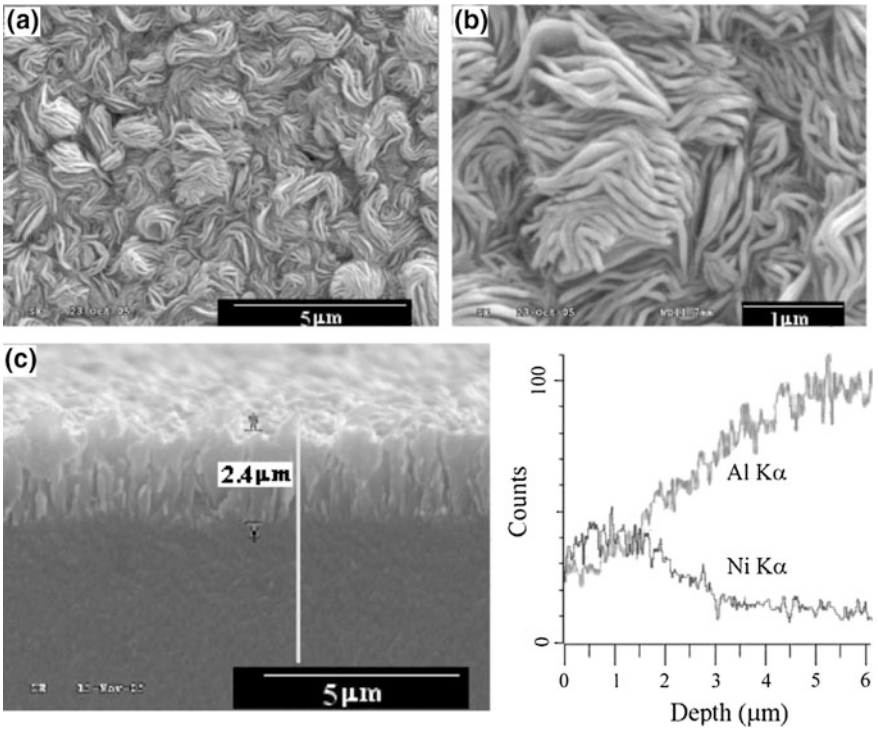

Fig. 9.24 SEM images of Ni/Al-LDH films obtained after 36 h at 120 °C on porous alumina/aluminum substrates: **a** *top view* of the Ni/Al-LDH film, **b** a high-magnification SEM image of **a**, and **c** cross-section of the Ni/Al-LDH film and the corresponding EDX line scan. Reprinted from Ref. [213]. Copyright 2006 Wiley-VCH

chiral discrimination. Motivated by this expectation, a clay column based on a hectorite-coated silica gel was prepared and its chromatographic behavior has been investigated [223]. A number of racemic mixtures including chiral neutral metal complexes and 1,1′-binaphthol were optically resolved. In case of tris(acetylacetonato)ruthenium(III), for example, the total elution volume was 100 mL when the racemic mixture was eluted with methanol on a 4 mm (i.d.) × 25 cm column in which Δ-$[Ru(phen)_3]^{2+}$ was mounted on the commercial RU-1, indicating that the clay column adsorbed molecules so strongly that a large volume of solvent was required for elution. On the other hand, the silica gel with a thin layer (ca. 0.1 μm thickness) elution volume was reduced to 10% when it was compared with RU-1.

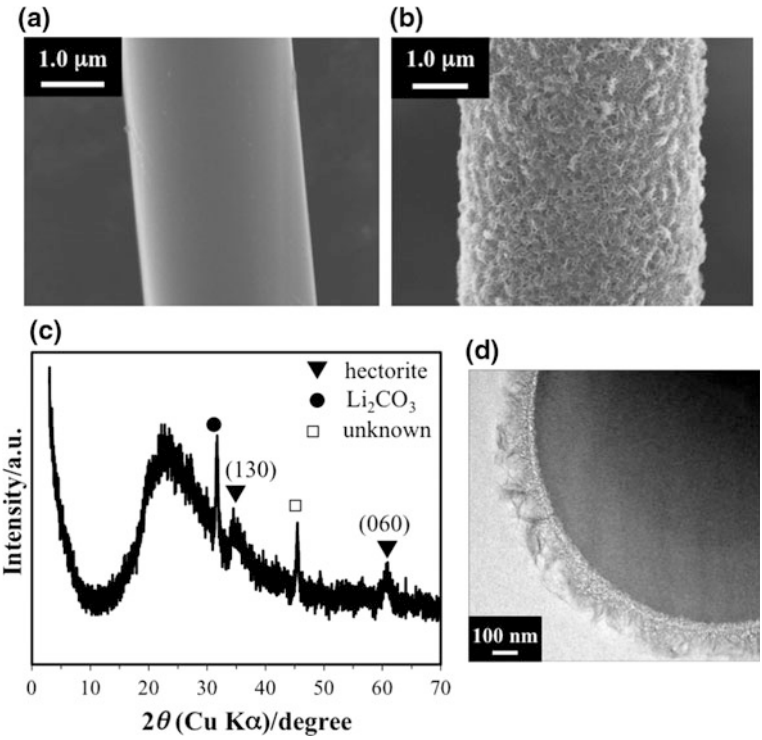

Fig. 9.25 SEM images of **a** the pristine silica fiber and **b** hectorite–silica microfiber. **c** XRD pattern. **d** A cross-sectional TEM image of the hectorite–silica microfiber. Reprinted from Ref. [221]. Copyright 2016 Royal Society of Chemistry

9.8 Summary and Future Perspectives

Studies on layered materials as advanced adsorbents were summarized. Various useful phenomena for environmental purification or concentration of noble species have been found during the careful and extended studies on the adsorption of various species onto layered solids. Due to the natural abundance, the materials' variation and useful adsorption behavior toward various cationic species, the application of bentonites and smectite group of clay minerals is promising. In addition, some useful ion exchange properties such as the heavy metal concentration and the radioactive metal removal have been observed and the nature of the selectivity and efficiency has been investigated. The chemical modification of layered materials is also quite useful to tune the adsorption behavior. Due to the increased demands for the efficient and selective concentration of a target species from the environments, the materials' design will be conducted further along the line of careful syntheses of layered materials and their chemical modification.

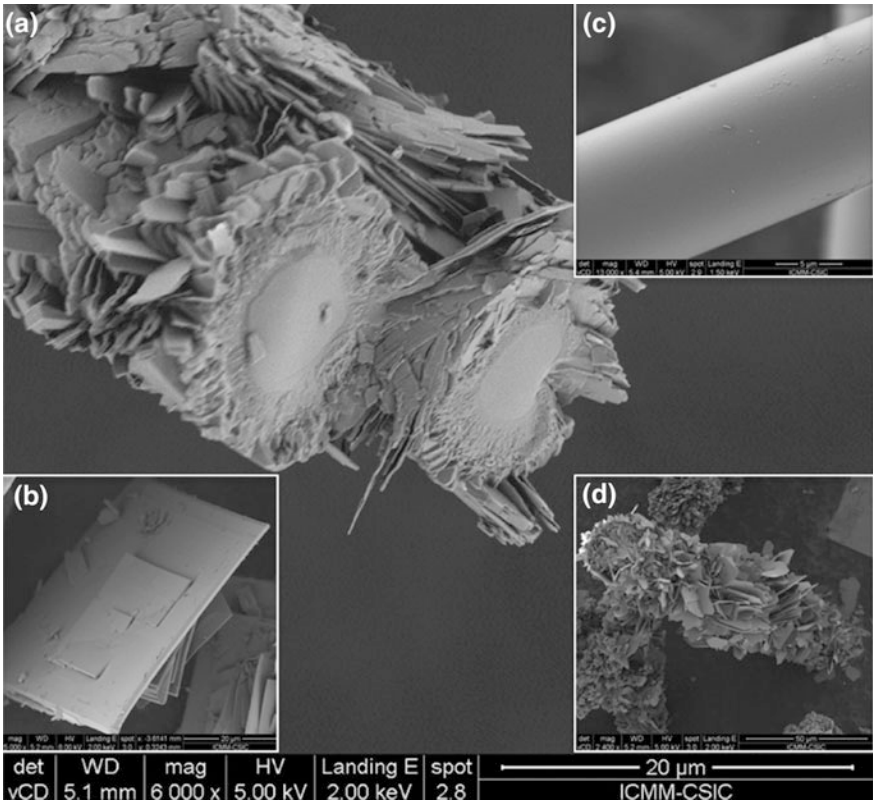

Fig. 9.26 FE-SEM images of **a** a cross-section of a titanosilicate (JDF-L1)-glass fiber hybrid where they observed the growth of the titanosilicate crystals radial to the glass fibers, **b** as-made JDF-L1, **c** naked glass fiber, and **d** the hybrid obtained after 4 days of reaction. Reprinted from Ref. [222]. Copyright 2013 American Chemical Society

Toward more specific targets (like huge amount of waste from industry and atomic power plant, very low concentration of biohazard etc.) the optimization of the materials design including process and production cost should be done.

References

1. Barrer RM (1978) Zeolites and clay minerals as sorbents and molecular sieves. Academic Press, London
2. Jordan JW (1950) J Phys Colloid Chem 54:294
3. Bergaya F, Theng BKG, Lagaly G (eds) (2006) Handbook of clay science. Elsevier Science, Amsterdam
4. (a) Maes A, Cremers A (1978) J Chem Soc Faraday Trans 174:1234: (b) Cremers A, Thomas HC (1968) Israel J Chem 6:949; c Martin H, Laudelout H (1963) J Chim Phys

60:1086; (d) Gast RG (1969) Soil Sci Soc Amer Proc 33:661; (e) Gast RG (1972) Soil Sci Soc Amer Proc 36:14
5. Sawhney L (1972) Clays Clay Miner 20:93
6. Scott AD, Smith SJ (1966) Clays Clay Miner 14:69
7. Komarneni S, Roy R (1988) Science 239:1286
8. Shimizu K, Hasegawa K, Nakamuro Y, Kodama T, Komarneni S (2004) J Mater Chem 14:1031
9. Coppin F, Berger G, Bauer A, Castet S, Loubet M (2002) Chem Geol 182:57
10. Okada T, Ehara Y, Ogawa M (2007) Clays Clay Miner 55:348
11. Lagaly G (1979) Adv Colloid Interface Sci 11:105
12. Lagaly G, Beneke K, Weiss A (1975) Am Mineral 60:642
13. Iler RK (1964) J Colloid Sci 19:648
14. Ide Y, Ochi N, Ogawa M (2011) Angew Chem Int Ed 50:654
15. Sasaki T, Komatsu Y, Fujiki Y (1986) J Radioanal Nucl 107:111
16. Komatsu Y, Fujiki Y (1980) Chem Lett 9:1525
17. Yang X, Makita Y, Hosokawa J, Sakane K, Ooi K (2005) Chem Mater 17:5420
18. Chitrakar R, Tezuka S, Sonoda A, Kakita H, Sakane K, Ooi K, Hirotsu T (2008) Ind Eng Chem Res 47:176
19. Kinomura N, Kumada N, Muto F (1985) J Chem Soc Dalton Trans 2349
20. Reichle WT (1986) Solid States Ionics 22:135
21. Miyata S (1983) Clays Clay Miner 31:305
22. Yamaoka T, Abe M, Tsuji M (1989) Mater Res Bull 24:1183
23. (a) Hines DR, Solin SA, Costantino U, Nocchetti M (2000) Phys Rev B 61:11348; (b) Iyi N, Matsumoto T, Kaneko Y, Kitamura K (2004) Chem Mater 16:2926; (c) Iyi N, Sasaki T (2008) J Colloid Interface Sci 322:237
24. Hayashi A, Nakayama H (2011) Chem Lett 40:276
25. Tezuka S, Chitrakar R, Sonoda A, Ooi K, Tomida T (2004) Green Chem 6:104
26. Chitrakar R, Tezuka S, Hosokawa J, Makita Y, Sonoda A, Ooi K, Hirotsu T (2010) J Colloid Interface Sci 349:314
27. Kaneko S, Ogawa M (2013) Appl Clay Sci 75–76:109
28. Ogawa M, Asai S (2000) Chem Mater 12:3253
29. Ogawa M, Inomata K (2005) Chem Lett 34:810
30. Aisawa S, Higashiyama N, Takahashi S, Hirahara H, Ikematsu D, Kondo H, Nakatama H, Narita E (2007) Appl Clay Sci 35:146
31. Thomas J, Bohor BF (1968) Clays Clay Miner 16:83
32. Fripiat JJ, Cruz MI, Bohor BF, Thomas J Jr (1974) Clays Clay Miner 22:23
33. Hemmen H, Rolseth EG, Fonseca DM, Hansen EL, Fossum JO, Plivelic TS (2012) Langmuir 28:1678
34. Michels L, Fossum JO, Rozynek Z, Hemmen H, Rustenberg K, Sobas PA, Kalantzopoulos GN, Knudsen KD, Janek M, Plivelic TS, de Sliva GJ (2015) Sci Rep 5:8775
35. Loring JS, Schaef HT, Turcu RVF, Thompson CJ, Miller QRS, Martin PF, Hu J, Hoyt DW, Qafoku O, Ilton ES, Felmy AR, Rosso KM (2012) Langmuir 28:7125
36. Loring JS, Ilton ES, Chen J, Thompson CJ, Martin PF, Benezeth P, Rosso KM, Felmy AR, Schaef HT (2014) Langmuir 30:6120
37. Cygan RT, Romanov VN, Myshakin EM (2012) J Phys Chem C 116:13079
38. Botan A, Rotemberg B, Marry V, Turq P, Noetinger B (2010) J Phys Chem C 114:14962
39. Myshakin EM, Saidi WA, Romanov VN, Cygan RT, Jordan KD (2013) J Phys Chem C 117:11028
40. Lee MS, McGrail BP, Glezakou V-M (2014) Environ Sci Technol 48:8612
41. Sena MM, Morrow CP, Kirkpatrick RJ, Krishnan M (2015) Chem Mater 27:6946
42. Cygan RT, Liang J-J, Kalinichev AG (2004) J Phys Chem B 108:1255
43. Miyata S, Hirose T (1978) Clays Clay Miner 26:441
44. Hutson ND, Speakman SA, Payzant EA (2004) Chem Mater 16:4135
45. Reddy MK, Xu ZP, Lu GQ, Diniz JC (2006) Ind Eng Chem Res 45:7504

46. Wang Q, Gao Y, Luo J, Zheng Z, Borgna A, Guo Z, O'Hare D (2013) RSC Adv 3:3414
47. Gao Y, Zhang Z, Wu J, Yi X, Zheng A, Umar A, O'Hare D, Wang Q (2013) J Mater Chem A 1:12782
48. Ishihara S, Sahoo P, Deguchi K, Ohki S, Tansho M, Shimizu T, Labuta J, Hill JP, Ariga K, Watanabe K, Yamauchi Y, Suehara S, Iyi N (2013) J Am Chem Soc 135:18040
49. Sahoo P, Ishihara S, Yamada K, Deguchi K, Ohki S, Tansho M, Shimizu T, Eisaku N, Sasai R, Labuta J, Ishikawa D, Hill JP, Ariga K, Prasad B, Bastakoti P, Yamauchi Y, Iyi N, Appl ACS (2014) Mater Interfaces 6:18352
50. Constantino VRL, Pinnavaia TJ (1995) Inorg Chem 34:883
51. Theng BKG (1974) The chemistry of clay-organic reactions. Adam Hilger, London
52. Ogawa M, Kuroda K (1997) Bull Chem Soc Jpn 70:2593
53. Okada T, Ide Y, Ogawa M (2012) Chem–Asian J 7:1980
54. Okada T, Seki Y, Ogawa M (2014) J Nanosci Nanotech 14:2121
55. Ogawa M, Kuroda K, Kato C (1989) Chem Lett 18:1659
56. Ogawa M, Hirata K, Kuroda K, Kato C (1992) Chem Lett 21:365
57. Lagaly G (1981) Clay Miner 16:1
58. Izawa H, Kikkawa S, Koizumi M (1983) Polyhedron 2:741
59. Lagaly G, Beneke K (1976) J Inorg Nucl Chem 38:1513
60. Jones TR (1983) Clay Miner 18:399
61. Meyn M, Beneke K, Lagaly G (1990) Inorg Chem 29:5201
62. Morioka S, Tagaya H, Karasu M, Kadokawa J, Chiba K (1995) J Solid State Chem 117:337
63. Chiou CT, Peters LJ, Freed VH (1979) Science 207:831
64. Boyd SA, Lee JF, Mortland MM (1988) Nature 333:345
65. Xu S, Sheng G, Boyd SA (1997) Adv Agron 59:25
66. Jaynes WF, Boyd SA (1991) Soil Sci Soc Am J 55:43
67. Mortland MM, Shaobai S, Boyd SA (1986) Clays Clay Miner 34:581
68. Barriga C, Gaitan M, Pavlovic I, Ulbarri MA, Hermonsin MC, Cornejo J (2002) J Mater Chem 12:1027
69. Klumpp E, Ortegac CC, Klahrea P, Tinoa FJ, Yapard S, Prtilloc C, Stegenc S, Queiroloc F, Schwuger MJ (2004) Colloids Surf A 230:111
70. Chuang YH, Tzou YM, Wang MK, Liu CH, Chiang PN (2008) Ind Eng Chem Res 47:3813
71. Nakato T, Miyashita H, Yakabe S (2003) Chem Lett 32:72
72. Wei Q, Nakato T (2006) Microporous Mesoporous Mater 96:84
73. Hayashi A, Nakayama H (2003) Bull Chem Soc Jpn 76:2315
74. Jaynes WF, Vance GF (1999) Clays Clay Miner 47:358
75. Okada T, Morita T, Ogawa M (2004) Clay Sci 12:277
76. Okada T, Ogawa M (2002) Chem Lett 812
77. Okada T, Ogawa M (2003) Chem Commun 1378
78. Seki Y, Ogawa M (2010) Bull Chem Soc Jpn 83:712
79. Seki Y, Ide Y, Okada T, Ogawa M (2015) Appl Clay Sci 109–110:64
80. Rutherford D, Chiou CT, Eberl DD (1997) Clays Clay Miner 45:534
81. Ogawa M (2004) Photoprocesses in clay-organic complexes. In: Auerbach SM, Carrado KA, Dutta PK (eds) Handbook of layered materials handbook of layered materials. Marcel Dekker, New York, pp 191–259
82. Barrer RM (1989) Clays Clay Miner 37:385
83. Smith JA, Jaffe PR (1991) Environ Sci Technol 25:2054
84. Lao H, Latieule S, Detellier C (1991) Chem Mater 3:1009
85. Seki Y, Okada T, Ogawa M (2009) Microporous Mesoporous Mater 129:30
86. Lee JF, Mortland MM, Chiou CT, Kile DE, Boyd SA (1990) Clays Clay Miner 38:113
87. Lawrence MAM, Kukkadapu RK, Boyd SA (1998) Appl Clay Sci 13:13
88. Okada T, Morita T, Ogawa M (2005) Appl Clay Sci 29:45
89. Ogawa M, Kuroda K (1995) Chem Rev 95:399
90. Ogawa M (1998) Ann Rep (Sec. C) 94:209

91. Thomas JK (1988) Acc Chem Res 21:275
92. Yamagishi A (1987) J Coord Chem 16:131
93. Traynor MF, Mortland MM, Pinnavaia TJ (1978) Clays Clay Miner 26:318
94. (a) Yamagishi A, Taniguchi M, Imamura Y, Sato H (1996) Appl Clay Sci 11:1; (b) Fujita S, Sato H, Kakegawa N, Yamagishi A (2006) J Phys Chem B 110:2533
95. Breu J, Stoll A, Lange KG, Probst T (2001) Phys Chem Chem Phys 3:1232
96. Mermut AR (ed) (1994) Layer charge characteristics of 2:1 silicate clay minerals. CMS workshop lectures, vol 6. Clay Minerals Society
97. Hofmann U, Klemen RZ (1950) Anorg Allg Chem 262:95
98. Jaynes WF, Traina SJ, Bigham JM, Johnston CT (1992) Clays Clay Miner 40:397
99. Jaynes WF, Boyd SA (1991) Clays Clay Miner 39:428
100. Herling MM, Kalo H, Seibt S, Schobert R, Breu J (2012) Langmuir 28:14713
101. Ogawa M, Matsutomo T, Okada T (2008) J Ceram Soc Jpn 116:1309
102. Okada T, Matsutomo T, Ogawa M (2010) J Phys Chem C 114:539
103. (a) Stöcker M, Seidl W, Seyfarth L, Senker J, Breu J (2008) Chem Commun 629; (b) Stöcker M, Seyfarth L, Hirsemann D, Senker J, Breu J (2010) Appl Clay Sci 48:146; (c) Mariychuk R, Baumgartner A, Wagner FE, Lerf A, Dubbe A, Moos R, Breu J (2007) Chem Mater 19:5377; (d) Baumgartner A, Sattler K, Thun J, Breu J (2008) Angew Chem Int Ed 47:1640
104. Breu J, Seidl W, Stoll AJ, Lange KG, Probst TU (2001) Chem Mater 13:4213
105. Ruiz-Hitzky E, Rojo JM (1980) Nature 287:28
106. Takahashi N, Kuroda K (2011) J Mater Chem 21:14336
107. Toriya S, Kobayashi S, Takei T, Fuji M, Watanabe T, Chikazawa M (2003) Colloid Polym Sci 281:1121
108. Ogawa M, Okutomo S, Kuroda K (1998) J Am Chem Soc 120:7361
109. Okutomo S, Kuroda K, Ogawa N (1999) Appl Clay Sci 15:253
110. Fujita I, Kuroda K, Ogawa M (2003) Chem Mater 15:3134
111. Fujita I, Kuroda K, Ogawa M (2005) Chem Mater 17:3717
112. Ide Y, Ogawa M (2007) Angew Chem Int Ed 46:8449
113. Ide Y, Iwasaki S, Ogawa M (2011) Langmuir 27:2522
114. Malla PB, Ravindranathanm P, Komarneni S, Roy R (1991) Nature 351:555
115. Ide Y, Fukuoka A, Ogawa M (2007) Chem Mater 19:964
116. Ide Y, Nakasato Y, Ogawa M (2008) Bull Chem Soc Jpn 81:757
117. Ide Y, Matsuoka M, Ogawa M (2010) J Am Chem Soc 132:16762
118. Kim TW, Hwang S-J, Jhung SH, Chang J-S, Park H, Choi W, Choy J-H (2008) Adv Mater 20:539
119. (a) Pinnavaia TJ (1983) Science 220:365; (b) Ohtsuka K (1997) Chem Mater 9:2039
120. Michot LJ, Barres O, Hegg EL, Pinnavaia TJ (1993) Langmuir 9:1794
121. Galarneau A, Barodawalla A, Pinnavaia TJ (1995) Nature 374:529
122. Nakatsuji M, Ishii R, Wang Z-M, Ooi K (2004) J Colloid Interface Sci 272:158
123. Németh J, Rodríguez-Gattorno G, Díaz D, Vázquez-Olmos AR, Décany I (2004) Langmuir 20:2855
124. Michot LJ, Pinnavaia TJ (1991) Clays Clay Miner 39:634
125. Landis ME, Aufdembrink BA, Chu P, Johnson ID, Kirker GW, Rubin MK (1991) J Am Chem Soc 113:3189
126. Anderson MW, Klinowski J (1990) Inorg Chem 29:3260
127. Ide Y, Nakasato Y, Ogawa M (2010) J Am Chem Soc 132:3601
128. Norrish K (1954) Discuss Faraday Soc 18:120
129. Mooney RW, Keenan AG, Wood LA (1952) J Am Chem Soc 74:1371
130. Ferrage E, Lanson B, Michot LJ, Robert J-L (2010) J Phys Chem C 114:4515
131. Tenorio RP, Alme LR, Engelsberg M, Fossum JO, Hallwass F (2008) J Phys Chem C 112:575
132. Malikova N, Cadene A, Dubois E, Marry V, Durand-Vidal S, Turq P, Breu J, Longeville S, Zanotti J-M (2007) J Phys Chem C 111:17603

133. Sasai R, Matsuoka Y, Sato H, Moriyoshi C, Kuroiwa Y (2013) Chem Lett 42:1285
134. Emiel EJM, Hensen B (2002) J Phys Chem B 106:12664
135. Young DA, Smith DE (2000) J Phys Chem B 104:9163
136. Boek ES, Coveney PV, Skipper NT (1995) J Am Chem Soc 117:12608
137. Morrow CP, Yazaydin AO, Krishnan M, Bowers GM, Kalinichev AG, Kirkpatrick RJ (2013) J Phys Chem C 117:5172
138. Dazas B, Lanson B, Delville A, Robert J-L, Komarneni S, Michot LJ, Ferrage E (2015) J Phys Chem C 119:4158
139. Wang J, Kalinichev AG, Kirkpatrick RJ, Hou X (2001) Chem Mater 13:145
140. (a) Stöcker M, Kunz D, Schmidt M, Hirsemann D, Kalo H, Putz B, Senker J, Breu J (2013) Langmuir 29:1280; (b) You S, Kunz D, Stöcker M, Kalo H, Putz B, Breu J, Talyzin AV (2013) Angew Chem Int Ed 52:3891
141. Okada T, Oguchi J, Yamamoto K, Shiono T, Fujita M, Iiyama T (2015) Langmuir 31:180
142. Rau H (1990) In: Dürr H, Bouas-Laurent H (eds) Studies in organic chemistry: photochromism, molecules and systems, vol. 40. Elsevier, Amsterdam, pp 165–192
143. Ogawa M, Ishii T, Miyamoto N, Kuroda K (2001) Adv Mater 13:1107
144. Ogawa M, Ishii T, Miyamoto N, Kuroda K (2003) Appl Clay Sci 22:179
145. Ogawa M, Ishikawa A (1998) J Mater Chem 8:463
146. Ogawa M, Goto R, Kakegawa N (2000) Clay Sci 11:231
147. Ogawa M (1996) Chem Mater 8:1347
148. Ogawa M, Yamamoto M, Kuroda K (2001) Clay Miner 36:263
149. Heinz H, Vaia RA, Koerner H, Farmer BL (2008) Chem Mater 20:6444
150. Tong ZW, Takagi S, Shimada T, Tachibana H (2006) Inoue J Am Chem Soc 128:684
151. Tong ZW, Sasamoto S, Shimada T, Takagi S, Tachibana H, Zhang XB, Tryk DA, Inoue H (2008) J Mater Chem 18:4641
152. Nabetani Y, Takamura H, Hayasaka Y, Shimada T, Takagi S, Tachibana H, Masui D, Tong Z, Inoue H (2011) J Am Chem Soc 133:17130
153. Han J, Yan D, Shi W, Ma J, Yan H, Wei M, Evans DG, Duan X (2010) J Phys Chem B 114:5678
154. Okada T, Watanabe Y, Ogawa M (2004) Chem Commun 320
155. Okada T, Watanabe Y, Ogawa M (2005) J Mater Chem 15:987
156. Okada T, Sakai H, Ogawa M (2008) Appl Clay Sci 40:187
157. Van Olphen H (1977) An introduction to clay colloid chemistry, 2nd edn. Wiley-Interscience, New York, pp 174–181
158. Ruehrwein RA, Ward DW (1952) Soil Sci 73:485
159. Warkentin BP, Miller RD (1958) Soil Sci 85:14
160. Garwood GA, Mortland MM, Pinnavaia TJ (1983) J Mol Catal 22:153
161. Boyd SA, Mortland MM (1986) J Mol Catal 34:1
162. Ogawa M, Tsujimura M, Kuroda K (2000) Langmuir 16:4202
163. Kakegawa N, Ogawa M (2004) Langmuir 20:7004
164. Sohmiya M, Omata S, Ogawa M (2012) Polym Chem 3:1069
165. Letaïef S, Ruiz-Hitzky E (2003) Chem Commun 24:2996
166. Letaïef S, Martín-Luengo MA, Aranda P, Ruiz-Hitzky E (2006) Adv Funct Mater 16:401
167. Yoneyama H, Haga S, Yamanaka S (1989) J Phys Chem 93:4833
168. Mogyorósi K, Dékány I, Fendler JH (2003) Langmuir 19:2938
169. Enea O, Bard AJ (1986) J Phys Chem 90:301
170. Stramel RD, Nakamura T, Thomas JK (1986) Chem Phys Lett 130:423
171. Bradford S, Simunek J, Bettahar M, Van Genuchten MT, Yates SR (2003) Environ Sci Technol 37:2242
172. Sauer JE, Davis EJ (1994) Environ Sci Technol 28:737
173. Zevi Y, Dathe A, McCarthy JF, Richards BK, Steenhuis TS (2005) Environ Sci Technol 39:7055
174. Ogawa M, Kaneko S (2013) Langmuir 29:14469

175. Nakamura Y, Yamagishi A, Matsumoto S, Tohkubo K, Ohtsu Y, Yamaguchi M (1989) J Chromatogr 482:165
176. Call F (1953) Nature 172:126
177. Nakazawa H, Yamada H, Fujita T, Ito Y (1987) Clay Sci 6:269
178. Okada T, Kato T, Yamaguchi T, Sakai T, Mishima S (2013) Ind Eng Chem Res 52:12018
179. Ogawa M, Takahashi M, Kato C, Kuroda K (1994) J Mater Chem 4:519
180. Sasai R, Iyi N, Fujita T, Arbeloa LF, Martinez MV, Takagi K, Itoh H (2004) Langmuir 20:4715
181. Ishida Y, Kulasekharan R, Shimada T, Takagi S, Ramamurthy V (2013) Langmuir 29:1748
182. Inukai K, Hotta Y, Taniguchi M, Tomura S, Yamagishi A (1994) J Chem Soc Chem Commun 959
183. Kleinfeld ER, Ferguson GS (1994) Science 265:370
184. Lvov Y, Ariga K, Ichinose I, Kunitake T (1996) Langmuir 12:3038
185. Lotsch BV, Ozin GA (2008) Adv Mater 20:4079
186. Lotsch BV, Ozin GA (2008) ACS Nano 10:2065
187. Takagi S, Shimada T, Masui D, Tachibana H, Ishida Y, Tryk DA, Inoue H (2010) Langmuir 26:4639
188. Mously C (2004) Appl Clay Sci 27:159
189. Yan Y, Bein T (1993) Chem Mater 5:905
190. Ogawa T, Ohtsu T, Yamaguchi M (1992) Kuromatogurafi (Japanese) 13:315
191. Hirose K, Asada K, Darwish I, Akizawa T, Yoshioka M (1997) J Pharam Biomed Anal 1241
192. Hirose K, Akizawa T, Yoshioka M (1998) Anal Chim Acta 129
193. Yamagishi A, Soma M (1981) J Am Chem Soc 103:4640
194. Yamagishi A (1985) J Am Chem Soc 107:732
195. Yamagishi A, Taniguchi M, Imamura Y, Sato H (1996) Appl Clay Sci 11:1
196. Yamagishi A (1983) J Chromatogr A 262:41
197. Yamagishi A (1985) J Chromatogr A 319:299
198. Sato H, Yamagishi A, Kato S (1992) J Am Chem Soc 114:10933
199. Miyamoto N, Kuroda K, Ogawa M (2001) J Am Chem Soc 123:6949
200. Gasperin M, Bihan MTL (1982) J Solid State Chem 43:346
201. Nassau K, Shiever JW, Bernstein JL (1969) J Electrochem Soc 116:348
202. Ogawa M, Iwata D (2010) Cryst Growth Des 10:2068
203. Endo K, Sugawara Y, Kuroda K (1994) Bull Chem Soc Jpn 67:3352
204. Ogawa M, Inomata K (2011) Clay Sci 15:131
205. Li L, Ma R, Ebina Y, Iyi N, Sasaki T (2005) Chem Mater 17:4386
206. Liu Z, Ma R, Osada M, Iyi N, Ebina Y, Takada K, Sasaki T (2006) J Am Chem Soc 128:4872
207. Ogawa M, Kaiho H (2002) Langmuir 18:4240
208. Kayano M, Ogawa M (2006) Clays Clay Miner 54:382
209. Kayano M, Ogawa M (2006) Bull Chem Soc Jpn 79:1988
210. Arai Y, Ogawa M (2009) Appl Clay Sci 42:601
211. (a) Nitoh K, Ayral A, Ogawa M (2010) Chem Lett 39:1018; (b) Naito S, Nitoh K, Ayral A, Ogawa M (2012) Ind Eng Chem Res 51:14414
212. Kuroda Y, Miyamoto Y, Hibino M, Yamaguchi K, Mizuno N (2013) Chem Mater 25:2291
213. Chen H, Zhang F, Fu S, Duan X (2006) Adv Mater 18:3089
214. Zhang F, Zhan L, Chen H, Xu S, Evans DG, Duan X (2008) Angew Chem Int Ed 47:2466
215. Zhang T, Zhou Y, He M, Zhu Y, Bu X, Wang Y (2013) Chem Eng J 219:278
216. Zhang T, Zhou Y, Bu X, Xue J, Hu J, Wang Y, Zhang M (2014) Microporous Mesoporous Mater 188:37
217. Okada T, Yoshido S, Miura H, Yamakami T, Sakai T, Mishima S (2012) J Phys Chem C 116:21864
218. Okada T, Suzuki A, Yoshido S, Minamisawa MH (2015) Microporous Mesoporous Mater 215:168
219. Okada T, Suzuki A (2015) Clay Sci 19:45

220. Okada T, Sueyoshi M, Minamisawa HM (2015) Langmuir 31:13842
221. Okada T, Shimizu K, Yamakami T (2016) RSC Adv 6:26130
222. Pérez-Carvajal J, Aranda P, Berenguer-Murcia A, Cazorla-Amorós D, Coronas J, Ruiz-Hitzky E (2013) Langmuir 29:7449
223. Okada T, Kumasaki A, Shimizu K, Yamagishi A, Sato H (2016) J Chromatogr Sci 54:1238

Chapter 10
Sensors

Takuya Fujimura and Ryo Sasai

10.1 Introduction

Sensors are defined as devices that can detect changes in various physical quantities. Multiple sensor devices are utilized in our daily lives and various industries, such as thermometers, hygrometers, barometers, gas sensors, thermistors, calorimeters, magnetic sensors, strain sensors, and optical sensors. Recently, the demand for new sensors with higher sensitivity, speed of response, and stability has increased. In particular, gas sensors with the ability to detect a specific molecule, such as ammonia, nitrogen oxides, sulfur oxides, carbon monoxide, and volatile organic compounds (VOCs), are essential for maintaining our safety and comfortable lives because multiple chemical sensitivity and sick building syndrome have become serious social issues in recent years. There are four major types of practical gas sensors: (i) semiconductor-based sensors, which exhibit a change in electrical resistivity that is induced by the adsorption of target molecules on the semiconductor surface; (ii) electrochemical sensors, which exhibit a change in the conductance or potential of the electrochemical cell in the absence and presence of target molecules; (iii) catalytic combustion-type sensors, which exhibit a temperature change that is induced by the combustion of target molecules adsorbed on the catalyst; and (iv) colorimetric sensors, which exhibit a color change that is caused by the interaction between a colorimetric reagent and the target molecules. These practical sensors exhibit sufficient sensitivity to detect gas molecules, but insufficient selectivity because the adsorption of target molecules on a sensor surface is a physical process, thus it is difficult to realize the selective adsorption of a target molecule. Thus, many researchers have vigorously investigated and developed

T. Fujimura · R. Sasai (✉)
Department of Physics and Materials Science, Interdisciplinary Graduate School of Science and Engineering, Shimane University, 1060 Nishikawatsu-Cho, Matsue, Shimane 690-8504, Japan
e-mail: rsasai@riko.shimane-u.ac.jp

T. Nakato et al. (eds.), *Inorganic Nanosheets and Nanosheet-Based Materials*, Nanostructure Science and Technology, DOI 10.1007/978-4-431-56496-6_10

novel sensors with higher selectivities and sensitivities toward specific gas molecules [1–14]. In addition, these novel sensors require faster response times to realize the real-time monitoring of target molecules in media. Charged inorganic nanosheets, which are a component of ion-exchangeable and layered inorganic compounds, have attracted much attention as a promising material for achieving novel molecular sensors that possess higher selectivities and sensitivities toward specific molecules. In this chapter, the authors will discuss the recent developments concerning sensor materials based on charged inorganic nanosheets.

10.2 Sensing Gas Molecules

The allowable concentrations of various toxic gases in the air are set by organization of all nationalities, such as the World Health Organization and environmental agencies, for the purposes of environmental conservation and the maintenance of good public health. In particular, real-time monitoring of the lower concentrations of VOCs is very important because they can induce health issues. However, it is hard to detect VOCs in air selectively with the current generation of semiconductor-based sensors, such as devices based on tin dioxide. Thus, novel high-performance gas sensors with higher sensitivities and selectivities towards VOCs in air are strongly desired [15–17]. Ito et al. [18–21] reported the VOC-sensing properties of thin solid films of layered sodium molybdate that had the interlayer spaces filled with poly(*o*-anisidine) (PoANIS), as shown in Fig. 10.1. This layered molybdate/PoANIS hybrid film can detect aldehydes at a parts-per-billion level through changes in the electrical resistivity of the film, which are induced by the adsorption of aldehydes into the interlayer spaces. In addition, Ito et al. reported that the adsorption of aldehydes into the hybrid film can be controlled by changing the polycations. The results of this study suggest that the selective detection of target molecules can be controlled by modifying the interlayer spacing and/or surface of the charged inorganic nanosheets with various organic compounds. Furthermore, these results indicate that the interlayer spaces and surfaces of layered materials can be utilized as not only regions for adsorption, but also for the detection of the target molecules.

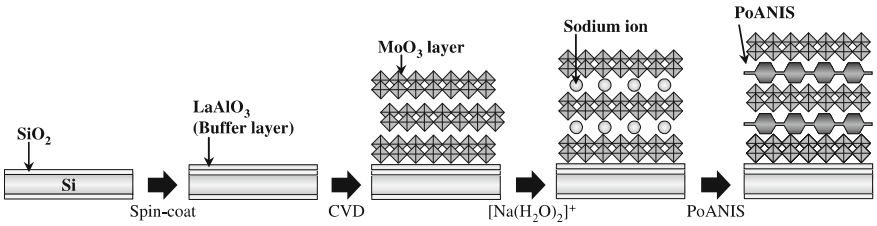

Fig. 10.1 Schematic diagram showing the preparation of hybrid thin films composed of layered molybdenum trioxide and PoANIS. Reprinted with permission from Ref. [20]. Copyright 2007, The Chemical Society of Japan

Shiratori et al. [22–24] reported that the concentration of target molecules in air could be quantitatively measured by monitoring the weight of thin solid films of polyelectrolytes hybridized with cation-exchangeable clay or layered zirconium phosphate via the quartz-crystal microbalance method. To detect a specific compound in air with this simple system, it is very important to construct an adsorption field with a high affinity for the specific molecule. However, the sensitivity of this sensing system is solely dependent on the precision of the mass-measuring device.

Electrochemical responses can also be utilized for molecular sensing, e.g., changes in the current and/or potential of electrochemical cells that are induced by molecular adsorption on electrodes modified with layered inorganic compounds or layered inorganic/organic hybrids. Pinnavaia et al. demonstrated that 2,4-dichlorophenoxyacetic acid and 2,4-dichlorophenol can be detected by using the electrochemical response of clay-modified electrodes containing amphipathic compounds. [25, 26] Furthermore, the detection ability of this electrochemical sensor can be adjusted by altering the concentration of the amphipathic modifier. The results of these studies indicate that the electrochemical response is more sensitive when sodium ions inhabit the interlayer spaces with amphipathic modifier because the dissociation reactions of sodium ions promote the electrochemical response. Sekine et al. [27] prepared an electrode modified with a cobalt porphyrin/clay complex, silver colloid, and polymer, and demonstrated that an electrochemical cell using this modified electrode can work as an oxygen sensor. The authors also reported that the application of montmorillonite and vermiculite clays improved the stability of this hybrid system.

Various researchers have proposed other approaches for developing sensing devices that utilize nanosheets or hybrid compounds composed of nanosheets and organic molecules [28–34]. The nanosheets of Zinc oxide [35–38], molybdenum sulfide [39], indium oxide [40], tungsten oxide [41], tricobalt tetraoxide [42], and copper oxide [43] have been investigated. The target molecules are detected through changes in the semiconductor properties of the layered materials. To improve the sensitivity of such materials, porous and petaloid structures with large specific surface areas were tested, which were composed of various nanosheets. These studies reported that various gases, such as VOCs [35], carbon monoxide [38], alcohols [37], nitrogen oxides [39–41], acetone [42], and hydrogen sulfide [36], can be detected with such systems.

To create sensing devices that can detect target molecules in air, the authors of this chapter have also developed hybrid materials that incorporate luminous dyes and surfactants into the interlayer spaces of ion-exchangeable layered materials, e.g., laponite [44], titanate nanosheets (TNSs) [45], and layered double hydroxides (LDHs) [46, 47]. The effects of molecular adsorption on the luminous properties of these hybrid materials were investigated. The quantum yield (ϕ) of alkyltrimethylammonium (CnTMA) and rhodamine 6G (R6G) hybridized with laponite, a cation-exchangeable clay, is reversibly changed by variations in the relative humidity (RH), as shown in Table 10.1. In addition, shifts in the peak of the fluorescence spectrum of the hybrid material occur, as shown in Fig. 10.2. Moreover, the responsivity of ϕ to changes in RH can be affected by altering the

Table 10.1 Luminescence quantum yield (ϕ, units = %) of the laponite/CnTMA/R6G hybrid materials

Surfactant	Dry	Wet
None	40.3	20.8
$(CH_3)_3N(CH_2)_{15}CH_3Br$	45.3	20.0
$(CH_3)_3N(CH_2)_5CH_3Br$	66.8	66.5

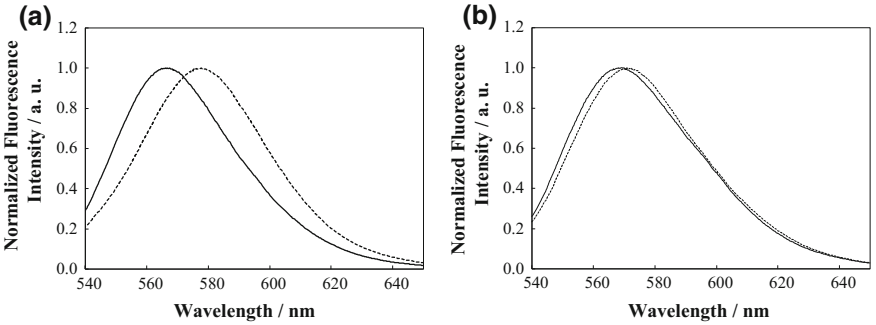

Fig. 10.2 Normalized fluorescence spectra of **a** laponite/C6TMA/R6G and **b** laponite/C16TMA/R6G complexes (*solid line* dry conditions, *broken line* wet conditions)

alkyl-chain length of CnTMA, as shown in Table 10.1. This behavior is ascribed to the reorganization and dissociation of aggregated R6G in the interlayer spaces of laponite, both of which are induced by the adsorption and desorption of interlayer water.

In addition, hybrid materials composed of TNSs, rhodamine 3B (R3B), and decyltrimethylammonium (C10TMA) exhibit interesting properties, such as a reversible color change (chromism) depending on the RH and emission quenching in the presence of ammonia gas under a high RH. The chromism of these R3B-based hybrid materials is ascribed to a decrease of electrostatic interactions between the R3B molecules and TNSs because the distance between the R3B molecules and TNSs increases when water is adsorbed between the TNSs and R3B (Fig. 10.3). The color of these R3B-based hybrid materials under a high RH is the same as that of an R3B solution, which supports the above mechanism.

The luminescence quenching of the R3B-based hybrid materials is ascribed to an intramolecular cyclization reaction of R3B that is preceded by the adsorption of ammonia molecules in the interlayer spaces that contain adsorbed water molecules. Moreover, the resulting nonionic and cyclized R3B molecules move to be stabilized by the hydrophobic regions formed by C10TMA. The yield of the intramolecular cyclization reaction is dependent upon the concentration of ammonia in the air, and thus, a quantitative response against ammonia gas can be obtained, as shown in Fig. 10.4. Furthermore, when benzyldecyldimethylammonium is used instead of C10TMA in this titanate/R3B-based hybrid material, the resulting material can be used to identify the presence of toluene and benzene by measuring the spectral shift of the luminescence, as shown in Fig. 10.5.

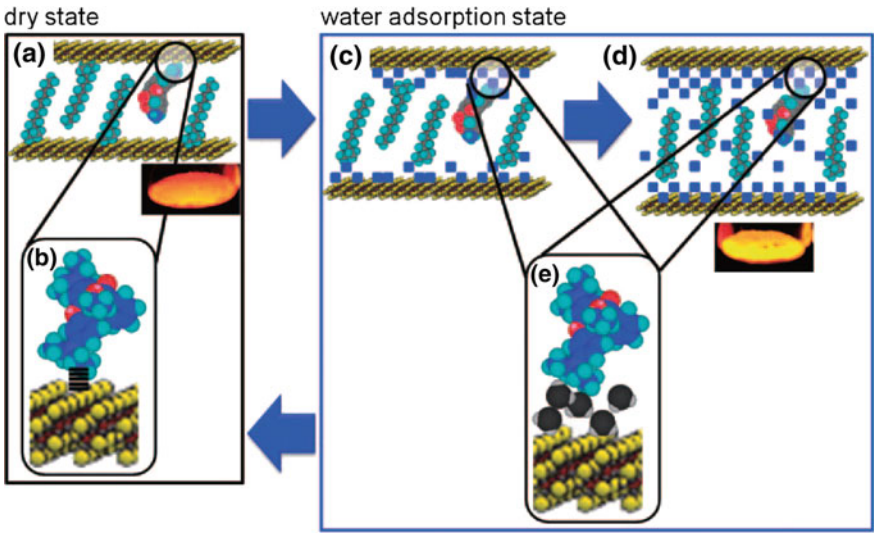

Fig. 10.3 Suggested mechanism model of the structural and spectroscopic response of TNS/C10TMA/R3B hybrids to water adsorption. The inserted photographs show the luminescence of a sample under a black lamp (356 nm). **a** Overall structure of the dry TNS/C10TMA/R3B material. **b** Enlarged view of the region around an R3B molecule and TNS surface under dry conditions. **c, d** Overall structure of the TNS/C10TMA/R3B material under **c** low RH (<20%) and **d** high RH (>20%). **e** Enlarged view of the region around an R3B molecule and TNS surface under wet conditions. Reprinted with permission from Ref. [45]. Copyright 2011, The Chemical Society of Japan

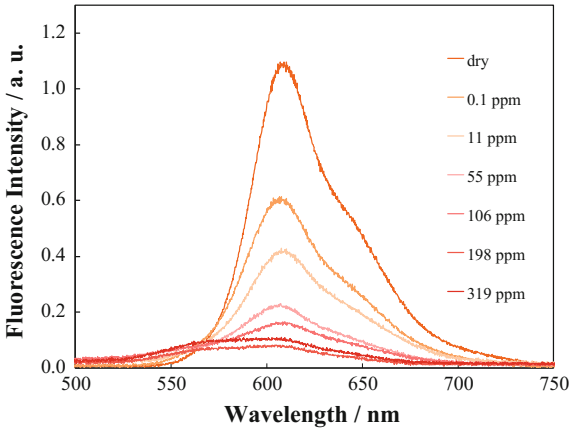

Fig. 10.4 Fluorescence spectra of the TNS/C10TMA/R3B hybrid material under various ammonia concentrations. Legend shows the concentrations of ammonia tested

The molecular sensing of gases by hybrid systems composed of nanosheets, a surfactant, and an emission dye suggests that the adsorption behavior of target molecules and emission properties of the dye can be controlled by using different surfactants to modify the interlayer spacing of the nanosheets.

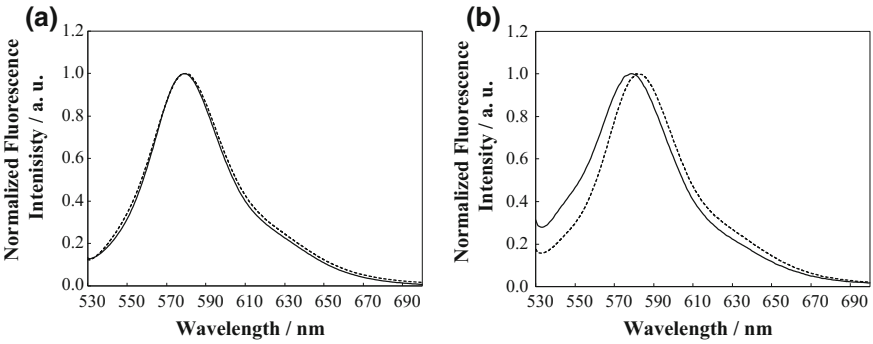

Fig. 10.5 Luminescence spectra of the **a** TNS/C10TMA/R3B and **b** TNS/benzyldecyldimethylammonium/R3B hybrid materials (*solid line* toluene, *broken line* benzene)

The authors of this chapter have also demonstrated the luminous properties of hybrid materials composed of an LDH, butanesulfonate (C4S), and anionic fluorescein dye (AFD), which exhibit changes in luminescence upon the adsorption of water or basic molecules, such as ammonia and amines. [46, 47] In the case of LDH/C4S/AFD hybrids, the luminescence intensity increases when the RH or concentration of ammonia in wet air increases. Under dry conditions, the lactone form of the fluorescein molecule, which is a nonionic molecule with no luminous ability, is stabilized by the hydrophobic regions formed by the C4S molecules in the interlayer spaces of the LDH. When water molecules are adsorbed by the dry hybrids, there is an increase in the concentration of dianionic fluorescein molecules, which are yellowish in color and exhibit strong luminescence in the visible spectrum, while the concentration of the lactone form of fluorescein decreases. Thus, an absorption band appears in the visible spectrum and luminescence occurs. Furthermore, when ammonia molecules are adsorbed by the wet interlayer space (dissolved in interlayer water), the pH value of the interlayer spaces of the LDH/C4S/AFD hybrid material increases. The LDH/C4S/AFD hybrid material then produces remarkable luminescence because the chemical equilibrium between the dianion and lactone forms of fluorescein is shifted by the basic conditions (Fig. 10.6).

Therefore, the studies discussed in this section have shown that selective molecular recognition and/or a high sensitivity can be achieved by using hybrid materials that contain layered inorganic materials. Furthermore, by considering the modifiable two-dimensional spaces provided by layered materials, the development of sensing devices that exhibit higher sensitivities and selectivities is expected.

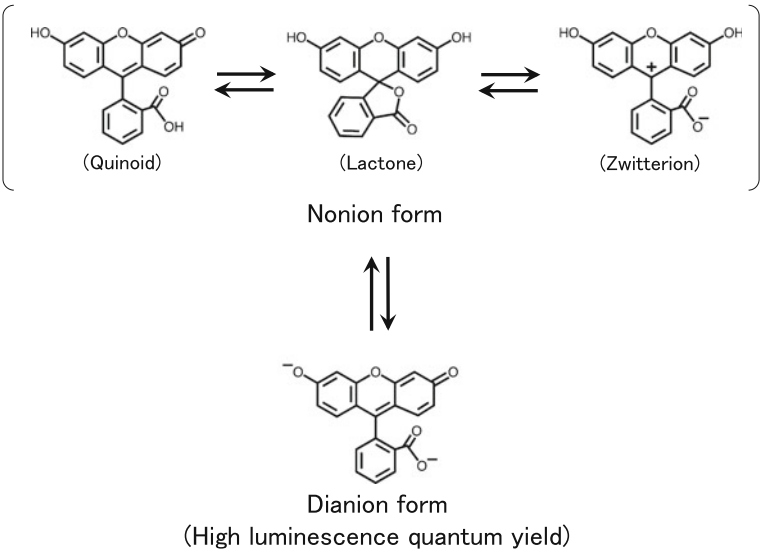

Fig. 10.6 Structures and formation routes of the various forms of fluorescein. The formation of the dianionic form is promoted under basic conditions

10.3 Sensing Dissolved Molecules

It is also necessary to monitor the aquatic environment and management of wastewater produced by various industries and sewage-treatment plants. Over the past few decades, it has been revealed that some chemical compounds, such as endocrine-disrupting chemicals and heavy metal ions, can affect the environment and wildlife, even at low concentrations. Thus, the development of novel sensors that can selectively detect various toxic chemicals and ions is required [48–54].

The development of sensors that can monitor the concentrations of heavy metal ions in water, the presence of which can be indicative of water pollution, has attracted much attention. One of the routes to create such sensors is the application of electrodes modified with clay and clay/organic hybrids in electrochemical sensors. Celi et al. [55] reported that clay modified with a thiol-containing organosilanol can adsorb mercury, lead, and zinc ions (Fig. 10.7). Fiho et al. [56] evaluated the adsorption properties of a hexadecyltrimethylammonium/montmorillonite hybrid that incorporated dithiol species into the interlayer spaces. The authors also reported that an electrode modified with this hybrid material can electrochemically detect mercury ions in water with a high selectivity. Sun et al. [57] reported that hybrid materials composed of an LDH and aminonaphthol disulfonate can be used to detect mercury ions in solution by measuring the change in spectral characteristics.

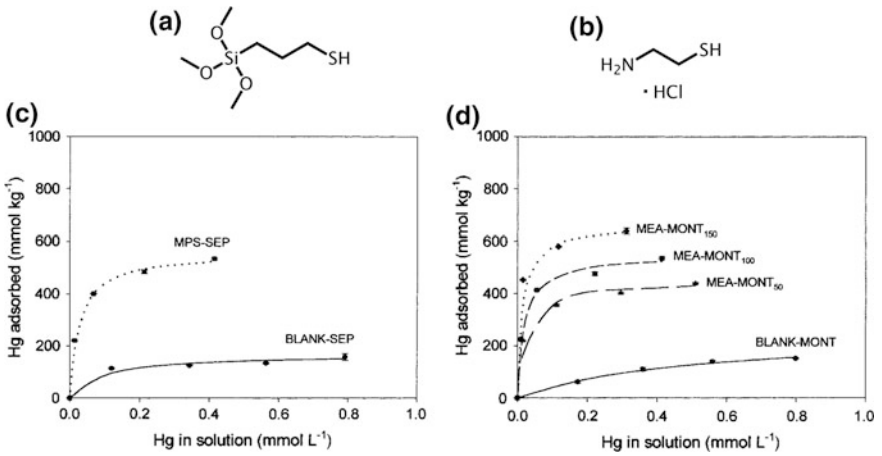

Fig. 10.7 **a, b** Molecular structures of the grafted molecules used in the studies performed by Celi et al.: **a** 3-mercaptopropyltrimethoxysilane and **b** 2-aminoethanethiol hydrochloride. **c, d** Mercury absorption isotherms of **c** sepiolite modified with 3-mercaptopropyltrimethoxysilane and **d** montmorillonite modified with 2-mercaptoethylammonium. Reprinted with permission from Ref. [55]. Copyright 2000 American chemical society

It is also important to develop devices that can sense toxic organic compounds dissolved in aqueous media, such as endocrine disruptors and agricultural chemicals. Zen et al. [58] reported that uric acid (≥ 0.2 μM) and dopamine (≥ 2.7 nM) can be selectively detected with an electrochemical method involving a glassy carbon electrode modified with Nafion and nontronite. In addition, Kröning et al. [59, 60] reported the detection of nitrogen oxides with an electrode modified with a clay/myoglobin complex, while Tonle et al. reported the detection of methylene blue with an electrode modified with an organoclay. Furthermore, Yin et al. [61] reported the electrochemical detection of nanomolar concentrations of bisphenol A by utilizing a glassy carbon electrode modified with an LDH.

These examples show that a wide range of clay-modified electrodes have been developed for electrochemical sensors. The advantage of combining electrochemical sensors with clay-modified electrodes is that the selectivity can be altered by modifying the surfaces and/or interlayer spaces of the clay with functional molecules. Further developments relating to electrochemical sensors that utilize clay-modified electrodes are expected in the future. Moreover, optical sensors for various chemicals, such as the optical pH sensor reported by Shi et al. [62] are also being developed by many researchers. Thus, the development of novel sensors that utilize hybrid materials composed of functional dyes and layered inorganic materials is expected to continue.

10.4 Summary

In this chapter, the authors discussed various studies regarding the research and development of sensors that can detect various target chemicals in air and aqueous media, with a focus on sensing materials based on ion-exchangeable and layered inorganic compounds. The development of such sensing devices is necessary for maintaining our safety and health, and for securing safe water supplies. However, most of the studies discussed in this chapter were performed under ideal conditions, e.g., tests were performed in dry nitrogen atmospheres, which are very different from real-world conditions, i.e., the atmosphere contains exhaust gases, air, environmental water, and pollution. Under real-world conditions, it is crucial to suppress the interference of coexisting substances. Most of the recent studies on molecular sensing with layered materials have focused on the properties of hybrid materials, with only a few studies reporting the development of sensing devices that can be used in real-world conditions. However, as described in this chapter, the nanospaces provided by layered materials can be modified with various functional compounds, and this property is a crucial advantage for enhancing the selectivity of sensors. By considering this advantage, it is expected that sensors based on hybrid systems will achieve the high sensitivity and selectivity that is needed for the next generation of sensors. The application of layered materials in sensors is a relatively recent area of research, and it is expected that further advances towards the development of high-performance sensors will occur as interest in this area of research grows.

References

1. Yamazoe N (2005) Toward innovations of gas sensor technology. Sens Actuators, B 108(1–2): 2–14. doi:10.1016/j.snb.2004.12.075
2. Utriainen M, Kärpänoja E, Paakkanen H (2003) Combining miniaturized ion mobility spectrometer and metal oxide gas sensor for the fast detection of toxic chemical vapors. Sens Actuators, B 93(1–3):17–24. doi:10.1016/s0925-4005(03)00337-x
3. Timmer B, Olthuis W, Berg AVD (2005) Ammonia sensors and their applications—a review. Sens Actuators, B 107(2):666–677. doi:10.1016/j.snb.2004.11.054
4. Sun B, Horvat J, Kim HS, Kim W-S, Ahn J, Wang G (2010) Synthesis of mesoporous & α-Fe2O3 nanostructures for highly sensitive gas sensors and high capacity anode materials in lithium ion batteries. J Phys Chem C 114(44):18753–18761. doi:10.1021/jp102286e
5. Schedin F, Geim AK, Morozov SV, Hill EW, Blake P, Katsnelson MI, Novoselov KS (2007) Detection of individual gas molecules adsorbed on graphene. Nat Mater 6(9):652–655. doi:10.1038/nmat1967
6. Miasik JJ, Hooper A, Tofield BC (1986) Conducting polymer gas sensors. J Chem Soc, Faraday Trans 1 82(4):1117–1126. doi:10.1039/f19868201117
7. Lu Y, Partridge C, Meyyappan M, Li J (2006) A carbon nanotube sensor array for sensitive gas discrimination using principal component analysis. J Electroanal Chem 593(1–2): 105–110. doi:10.1016/j.jelechem.2006.03.056

8. Li Z, Zhao Q, Fan W, Zhan J (2011) Porous SnO_2 nanospheres as sensitive gas sensors for volatile organic compounds detection. Nanoscale 3(4):1646–1652. doi:10.1039/c0nr00728e
9. Jang J, Bae J (2007) Carbon nanofiber/polypyrrole nanocable as toxic gas sensor. Sens Actuators, B 122(1):7–13. doi:10.1016/j.snb.2006.05.002
10. Honeybourne CL, Ewen RJ, Hill CAS (1984) Use of thin films of conjugated organic macrocycles as the active elements in toxic-gas sensors operating at room temperature. J Chem Soc, Faraday Trans 1 80(4):851–863. doi:10.1039/f19848000851
11. Feng L, Musto CJ, Kemling JW, Lim SH, Suslick KS (2010) A colorimetric sensor array for identification of toxic gases below permissible exposure limits. Chem Commun 46(12): 2037–2039. doi:10.1039/b926848k
12. Du N, Zhang H, Chen BD, Ma XY, Liu ZH, Wu JB, Yang DR (2007) Porous indium oxide nanotubes: layer-by-layer assembly on carbon-nanotube templates and application for room-temperature NH_3 gas sensors. Adv Mater 19(12):1641–1645. doi:10.1002/adma.200602128
13. Barea E, Montoro C, Navarro JA (2014) Toxic gas removal—metal-organic frameworks for the capture and degradation of toxic gases and vapours. Chem Soc Rev 43(16):5419–5430. doi:10.1039/c3cs60475f
14. Zeng W, Liu T, Wang Z (2012) Enhanced gas sensing properties by SnO_2 nanosphere functionalized TiO_2 nanobelts. J Mater Chem 22(8):3544–3548. doi:10.1039/c2jm15017d
15. Yoon J, Chae SK, Kim JM (2007) Colorimetric sensors for volatile organic compounds (VOCs) based on conjugated polymer-embedded electrospun fibers. J Am Chem Soc 129(11): 3038–3039. doi:10.1021/ja067856+
16. Wang J, Zhang P, Qi J-Q, Yao P-J (2009) Silicon-based micro-gas sensors for detecting formaldehyde. Sens Actuators, B 136(2):399–404. doi:10.1016/j.snb.2008.12.056
17. Nguyen H, El-Safty SA (2011) Meso- and macroporous Co_3O_4 nanorods for effective VOC gas sensors. J Phys Chem C 115(17):8466–8474. doi:10.1021/jp1116189
18. Itoh T, Matsubara I, Shin W, Izu N, Nishibori M (2008) Preparation of layered organic-inorganic nanohybrid thin films of molybdenum trioxide with polyaniline derivatives for aldehyde gases sensors of several tens ppb level. Sens Actuators, B 128(2):512–520. doi:10.1016/j.snb.2007.07.059
19. Wang J, Matsubara I, Itoh T, Murayama N, Shin W, Izu N (2006) Preparation of polystyrene and surfactant co-intercalated MoO_3 nano hybrids and their VOC gas sensing properties. IEEJ Trans Sens Micromachines 126(10):548–552. doi:10.1541/ieejsmas.126.548
20. Itoh T, Matsubara I, Shin W, Izu N (2007) Preparation and characterization of a layered molybdenum trioxide with poly(o-anisidine) hybrid thin film and its aldehydic gases sensing properties. Bull Chem Soc Jpn 80(5):1011–1016. doi:10.1246/bcsj.80.1011
21. Itoh T, Matsubara I, Shin W, Izu N, Nishibori M (2007) Highly aldehyde gas-sensing responsiveness and selectivity of layered organic-guest/MoO_3-host hybrid sensor. J Ceram Soc Jpn 115(1347):742–744. doi:10.2109/jcersj2.115.742
22. Kikuchi M, Omori K, Shiratori S (2004) The 3rd IEEE Conference on Sensors, Oct. 24–27
23. Kushida S, Shiratori S (2002) Proceedings of the 19th Sensor Symposium. p 145–150
24. Ushimi Y, Ito Y, Horiuchi H, Kadota M, Nozaki Y, Hotta Y, Shiratori S (2015) Quartz crystal microbalance sensor for NH_3 gas with compensation of humidity drift. Electron Commun Jpn 98(6):1–7. doi:10.1002/ecj.11653
25. Ozkan D, Kerman K, Meric B, Kara P, Demirkan H, Polverejan M, Pinnavaia TJ, Ozsoz M (2002) Heterostructured fluorohectorite clay as an electrochemical sensor for the detection of 2,4-dichlorophenol and the herbicide 2,4-D. Chem Mater 14(4):1755–1761. doi:10.1021/cm011529d
26. Ozsoz M, Erdem A, Ozkan D, Kerman K, Pinnavaia TJ (2003) Clay/sol-gel-modified electrodes for the selective electrochemical monitoring of 2,4-dichlorophenol. Langmuir 19(11):4728–4732. doi:10.1021/la034116v
27. Yuasa M, Nagaiwa T, Kato M, Sekine I, Hayashi S (1995) Electrochemical properties of metalloporphyrin-clay complex-modified electrode systems: investigation as oxygen sensors. J Electrochem Soc 142(8):2612–2617. doi:10.1149/1.2050062

28. Zeng Z, Yin Z, Huang X, Li H, He Q, Lu G, Boey F, Zhang H (2011) Single-layer semiconducting nanosheets: high-yield preparation and device fabrication. Angew Chem Int Ed 50(47):11093–11097. doi:10.1002/anie.201106004
29. Basu S, Bhattacharyya P (2012) Recent developments on graphene and graphene oxide based solid state gas sensors. Sens Actuators, B 173:1–21. doi:10.1016/j.snb.2012.07.092
30. Kannan PK, Late DJ, Morgan H, Rout CS (2015) Recent developments in 2D layered inorganic nanomaterials for sensing. Nanoscale 7(32):13293–13312. doi:10.1039/c5nr03633j
31. Kou L, Frauenheim T, Chen C (2014) Phosphorene as a superior gas sensor: selective adsorption and distinct I–V response. J Phys Chem Lett 5(15):2675–2681. doi:10.1021/jz501188k
32. Li J, Fan H, Jia X (2010) Multilayered ZnO nanosheets with 3D porous architectures: synthesis and gas sensing application. J Phys Chem C 114(35):14684–14691. doi:10.1021/jp100792c
33. Okada T, Ide Y, Ogawa M (2012) Organic-inorganic hybrids based on ultrathin oxide layers: designed nanostructures for molecular recognition. Chem—Asian J 7(9):1980–1992. doi:10.1002/asia.201101015
34. Okada T, Ogawa M (2002) Adsorption of phenols onto 1,1′-dimethyl-4,4′-bipyridinium-smectites. Chem Lett 31(8):812–813. doi:10.1246/cl.2002.812
35. Meng F, Hou N, Ge S, Sun B, Jin Z, Shen W, Kong L, Guo Z, Sun Y, Wu H, Wang C, Li M (2015) Flower-like hierarchical structures consisting of porous single-crystalline ZnO nanosheets and their gas sensing properties to volatile organic compounds (VOCs). J Alloys Compd 626:124–130. doi:10.1016/j.jallcom.2014.11.175
36. Zhu Y, Wang Y, Duan G, Zhang H, Li Y, Liu G, Xu L, Cai W (2015) In situ growth of porous ZnO nanosheet-built network film as high-performance gas sensor. Sens Actuators, B 221:350–356. doi:10.1016/j.snb.2015.06.115
37. Yuliarto B, Julia S, Wulan SNL, Iqbal M, Ramadhani MF, Nugraha N (2015) The effect of tin addition to ZnO nanosheet thin films for ethanol and isopropyl alcohol sensor applications. J Eng Technol Sci 47(1):76–91. doi:10.5614/j.eng.technol.sci.2015.47.1.6
38. Zeng Y, Qiao L, Bing Y, Wen M, Zou B, Zheng W, Zhang T, Zou G (2012) Development of microstructure CO sensor based on hierarchically porous ZnO nanosheet thin films. Sens Actuators, B 173:897–902. doi:10.1016/j.snb.2012.05.090
39. Cui S, Wen Z, Huang X, Chang J, Chen J (2015) Stabilizing MoS_2 nanosheets through SnO_2 nanocrystal decoration for high-performance gas sensing in air. Small 11(19):2305–2313. doi:10.1002/smll.201402923
40. Gao L, Cheng Z, Xiang Q, Zhang Y, Xu J (2015) Porous corundum-type In_2O_3 nanosheets: synthesis and NO_2 sensing properties. Sens Actuators, B 208:436–443. doi:10.1016/j.snb.2014.11.053
41. Wang C, Li X, Feng C, Sun Y, Lu G (2015) Nanosheets assembled hierarchical flower-like WO_3 nanostructures: synthesis, characterization, and their gas sensing properties. Sens Actuators, B 210:75–81. doi:10.1016/j.snb.2014.12.020
42. Zhang Z, Wen Z, Ye Z, Zhu L (2015) Gas sensors based on ultrathin porous Co_3O_4 nanosheets to detect acetone at low temperature. RSC Adv. 5(74):59976–59982. doi:10.1039/c5ra08536e
43. Faisal M, Khan SB, Rahman MM, Jamal A, Umar A (2011) Ethanol chemi-sensor: evaluation of structural, optical and sensing properties of CuO nanosheets. Mater Lett 65(9):1400–1403. doi:10.1016/j.matlet.2011.02.013
44. Sasai R, Itoh T, Ohmori W, Itoh H, Kusunoki M (2009) Preparation and characterization of rhodamine 6G/alkyltrimethylammonium/laponite hybrid solid materials with higher emission quantum yield. J Phys Chem C 113(1):415–421. doi:10.1021/jp805201n
45. Sasai R, Iyi N, Kusumoto H (2011) Luminous change of rhodamine 3B incorporated into titanate nanosheet/decyltrimethylammonium hybrids under humid atmosphere. Bull Chem Soc Jpn 84(5):562–568. doi:10.1246/bcsj.20100343
46. Sasai R (2011) 3rd International Congress on Ceramics (ICC3): Hybrid and Nano-Structured Materials 18

47. Sasai R, Miyanaga H, Morita M (2013) Preparation and characterization of highly photoluminescent hybrid solids from anionic fluorescein dye, surfactant, and layered double hydroxide. Clay Sci. 17:35–40
48. Wu CS, Oo MKK, Fan X (2010) Highly sensitive multiplexed heavy metal detection using quantum-dot-labeled DNAzymes. ACS Nano 4(10):5897–5904. doi:10.1021/nn1021988
49. Oehme I, Wolfbeis OS (1997) Optical sensors for determination of heavy metal ions. Mikrochimi Acta 126(3–4):177–192. doi:10.1007/bf01242319
50. Nolan EM, Lippard SJ (2003) A "turn-on" fluorescent sensor for the selective detection of mercuric ion in aqueous media. J Am Chem Soc 125(47):14270–14271. doi:10.1021/ja037995g
51. Forzani ES, Zhang H, Chen W, Tao N (2005) Detection of heavy metal ions in drinking water using a high-resolution differential surface plasmon resonance sensor. Environ Sci Technol 39(5):1257–1262. doi:10.1021/es049234z
52. Ono A, Togashi H (2004) Highly selective oligonucleotide-based sensor for mercury(II) in aqueous solutions. Angew Chem Int Ed 43(33):4300–4302. doi:10.1002/anie.200454172
53. Ng SC, Zhou XC, Chen ZK, Miao P, Chan HSO, Li SFY, Fu P (1998) Quartz crystal microbalance sensor deposited with Langmuir-Blodgett films of functionalized polythiophenes and application to heavy metal ions analysis. Langmuir 14(7):1748–1752. doi:10.1021/la970296v
54. Campbell CG, Borglin SE, Green FB, Grayson A, Wozei E, Stringfellow WT (2006) Biologically directed environmental monitoring, fate, and transport of estrogenic endocrine disrupting compounds in water: a review. Chemosphere 65(8):1265–1280. doi:10.1016/j.chemosphere.2006.08.003
55. Celis R, HermosÍn MC, Cornejo J (2000) Heavy metal adsorption by functionalized clays. Environ Sci Technol 34(21):4593–4599. doi:10.1021/es000013c
56. Filho NLD, do Carmo DR (2006) Study of an organically modified clay: selective adsorption of heavy metal ions and voltammetric determination of mercury(II). Talanta 68(3):919–927. doi:10.1016/j.talanta.2005.06.028
57. Sun Z, Jin L, Zhang S, Shi W, Pu M, Wei M, Evans DG, Duan X (2011) An optical sensor based on H-acid/layered double hydroxide composite film for the selective detection of mercury ion. Anal Chim Acta 702(1):95–101. doi:10.1016/j.aca.2011.06.026
58. Zen J-M, Chen P-J (1997) A selective voltammetric method for uric acid and dopamine detection using clay-modified electrodes. Anal Chem 69(24):5087–5093. doi:10.1021/ac9703562
59. Kröning S, Scheller FW, Wollenberger U, Lisdat F (2004) Myoglobin-clay electrode for nitric oxide (NO) detection in solution. Electroanalysis 16(4):253–259. doi:10.1002/elan.200402780
60. Tonle IK, Ngameni E, Tcheumi HL, Tchieda V, Carteret C, Walcarius A (2008) Sorption of methylene blue on an organoclay bearing thiol groups and application to electrochemical sensing of the dye. Talanta 74(4):489–497. doi:10.1016/j.talanta.2007.06.006
61. Yin H, Cui L, Ai S, Fan H, Zhu L (2010) Electrochemical determination of bisphenol A at Mg–Al–CO_3 layered double hydroxide modified glassy carbon electrode. Electrochim Acta 55(3):603–610. doi:10.1016/j.electacta.2009.09.020
62. Shi W, He S, Wei M, Evans DG, Duan X (2010) Optical pH sensor with rapid response based on a fluorescein-intercalated layered double hydroxide. Adv Funct Mater 20(22):3856–3863. doi:10.1002/adfm.201001081

Chapter 11
Energy Storage Systems

Wataru Sugimoto and Dai Mochizuki

11.1 Introduction

Recent advances in structural and compositional control of two-dimensional nanomaterials have enabled fabrication of advanced electrode materials with controlled electrode/electrolyte interfaces leading to the design and tailoring of multiple functionalities. Interest in the application of such materials for electrochemical energy storage and conversion applications such as batteries, supercapacitors, and fuel cells has considerably risen in recent years.

Colloidal nanosheets are typically derived from layered inorganic materials via solution-based exfoliation processes and have been studied with clays and transition metal chalcogenides for decades and more recently, transition metal oxide nanosheets, graphite oxide nanosheets (graphene oxide), and MXene. Such two-dimensional nanosheets have been shown to possess distinctive physical and chemical functions unique to the structure and composition of the parent layered compounds. This section will focus mainly on the application of exfoliated nanosheets derived from layered transition metal oxides towards electrochemical energy storage, namely, supercapacitors and rechargeable batteries.

11.2 Requirements as Electrode Materials

Electrochemical reactions related to supercapacitors occur at the interface of the electrode material and electrolyte. Thus, high surface area leads to more active sites for electrosorption of ions and electrochemical reactions to occur, consequently leading to higher utilization. In the case of batteries, the major redox reaction is a

W. Sugimoto (✉) · D. Mochizuki
Center for Energy and Environmental Science, Shinshu University, Ueda, Nagano, Japan
e-mail: wsugi@shinshu-u.ac.jp

T. Nakato et al. (eds.), *Inorganic Nanosheets and Nanosheet-Based Materials*,
Nanostructure Science and Technology, DOI 10.1007/978-4-431-56496-6_11

bulk reaction, thus micro-sized particles have traditionally been used. In contrast, nanomaterials have attracted recent interest, as the small diffusion length is anticipated to be advantageous for high-power Li-ion batteries. General requirements for nanosheets to be used as a high-power electrode material include, high electrochemically active surface area, electrochemical stability in the electrolyte and working potential under interest, and sufficient electronic conductivity. The nanosheet should be tolerant against electrochemical dissolution in either aqueous or nonaqueous electrolytes and should not undergo structural changes (should have dimensional stability). A resistive electrode will lead to undesirable energy loss at high power, thus the electronic conductivity of the electrode is an important factor.

Although most exfoliated oxide nanosheets are insulating, a few have conductivity sufficient enough for use as electrode materials. These materials can be used in most nonaqueous and neutral aqueous electrolytes. Semiconducting materials such as manganese oxide nanosheets are often mixed with carbon as a conducting binder to cover for the low electronic conductivity. Ruthenium oxide nanosheets are one of the rare materials that have metallic conductivity and can be used in acidic and basic aqueous electrolytes.

11.3 Fabrication of Thin-Film Electrodes

One of the distinctive features of exfoliated nanosheets is that it is obtained as a stable colloid. Thus, wet-processing techniques commonly used by colloidal chemists can be applied for thin-film fabrication. The precursor for nanosheets is in most cases ion-exchangeable layered oxides with a general formula $A_xM_yO_z$, where A is an alkaline metal and M is a transition metal. The resulting nanosheets have a formal composition of $(M_yO_z)^{x-}$, thereby the exfoliated nanosheets intrinsically have a negative charge and can be considered as a two-dimensional macro-anion. The negatively charged nanosheets are stabilized by a counter cation in the solution, typically a tetrabutyl ammonium cation (TBA^+). Primary alkyl ammonium cations strongly interact with the nanosheet and tend to form layered compounds, thus are usually not good exfoliation agents. The long alkyl chain and the charge, being centered in the bulky TBA, weaken the interaction between the positively charged organic molecule and the negatively charged inorganic macro-anion. This leads to stabilization of the nanosheet as a colloid. The solution is typically basic with excess TBA^+ as-prepared, but exfoliation can also be induced by dispersing a pre-synthesized $TBA^+(M_yO_z)^{x-}$ intercalation compounds in water or organic solvents with high dielectric constant.

Common fabrication techniques of thin-film electrodes include (1) casting or spin-coating, (2) Langmuir–Blodgett (LB) technique, (3) electrostatic layer-by-layer (LbL) deposition, and (4) electrophoretic deposition (EPD). Casting or spin-coating (1) is the simplest method, involving dropping a colloidal solution onto a conducting substrate and drying. Advantageous of this method is that as long as the solid concentration of the colloid is known, the amount that is dropped onto

the electrode is known and can be controlled in microgram precision (does not apply for spin-coating). The interaction between the deposited nanosheet and substrate (current collector) is relatively weak, and thus films sometimes are easily detached from the substrate, especially for thick films. Techniques (2)–(4) utilize the negative charge of the nanosheets and thus the films are strongly bound to the substrate and is firm. The LB technique (2) affords high-quality flat thin films with accurate control of thickness. Nanosheets are spread out on the surface of a solution and transferred onto the current collector by immersion/emersion. Multilayers of nanosheets can be prepared by sequential deposition. The high quality of LB films allows deep understanding of the fundamental properties of nanosheet thin films. The strenuous process of the LB method (2) limits film thickness to the nanometer scale, typically up to 10 nanosheet layers thick. The electrostatic LbL deposition technique (3) makes use of the negative Zeta potential of the nanosheets and utilizes a counter polycation such as PDDA to sequentially deposit the inorganic macro-anion nanosheet and the organic polycation layer-by-layer. The quality of the films (flatness, coverage, etc.) is not as high as LB films, but multilayer deposition is less time consuming and finding optimal conditions is less laborious. Commercial apparatus for laboratory scale films can be acquired at a reasonable cost. The EPD technique (4) is suitable for fabricating thick films. By polarizing two electrodes in the colloid, the negatively charged nanosheets are deposited onto the positively polarized electrode. The method also allows microfabrication on micro-electrodes because deposition is restricted to the conducting regions. The EPD films are characterized by the absence of organic counter polycations. EPD films have rougher surfaces compared to LB and LbL films and are thus fit for preparing porous nanosheet films.

11.4 Pseudo-capacitive Properties of Exfoliated Oxide Nanosheet Electrodes

As a charge-storage device with fast charge/discharge capability and long cycle life, supercapacitors have attracted interest as an alternative to batteries for various applications. Most current commercial devices employ microporous activated carbon with a surface area of 1500–3000 m^2/g as the electrode material for both positive and negative electrodes. Such devices are called electrical double-layer capacitors (EDLC). As the charge is stored at the electrified electrode/electrolyte interface (electrical double layer), high surface area is a necessity. The electrode material should also have appreciable electronic conductivity in order to warrant low *iR* loss at high current density. In contrast to EDLCs which store charge by non-Faradaic reactions, pseudo-capacitor [also known as redox (super)capacitor] electrodes can utilize charge transfer due to surface redox processes in addition to the charge stored at the electrical double layer. The surface Faradaic process can increase the total amount of charge stored by up to a factor of ten compared to the

non-Faradaic electrical double-layer capacitance. Conducting oxide electrodes such as ruthenium oxide and manganese oxide have been studied as potential materials for such pseudo-capacitive electrodes. Note that the Faradaic processes utilized for such electrodes are confined to the surface or near surface of a few atomic layers, which is essential for the fast charging properties indispensable for supercapacitor applications. Thus, high surface area is an essential physical property for pseudo-capacitive electrodes. The difference between pseudo-capacitive and battery-type storage is that the latter is based on the electrochemically driven intercalation of ions into the bulk of the material, and hence is a slower, electrochemically irreversible process coupled with heat transfer.

Conducting nanosheets are promising for pseudo-capacitive electrodes owing to the large electrochemically active surface area. The two dimensionally extended structure should also be advantageous for transporting electrons. Exfoliated nanosheets of RuO_2 [1–4], MnO_2 [5–7], Co-LDH [8], have shown promising pseudo-capacitive properties. Literature outlined here will be limited to those that show reversible redox behavior. It is emphasized that calculating capacitance (unit of F/g) from non-linear galvanostatic charge/discharge curves or cyclic voltammograms that show irreversible redox process should be strictly avoided, as such electrochemical behavior is typical of bulk electrochemical reactions (battery-type reaction). The energy storage capability of such materials should be reported as capacity (unit of mAh/g). Readers are suggested to read literature [9, 10], for details of the differences between pseudo-capacitor like and battery-like behaviour.

11.4.1 Pseudo-capacitive Properties of RuO_2 Nanosheet Electrodes

The concept of using nanosheet electrodes for fast and reversible energy storage was first demonstrated with exfoliated $RuO_{2.1}$ nanosheets derived from a layered $K_{0.2}RuO_{2.1}{\cdot}nH_2O$ [11]. Later on, $RuO_{2.0}$ nanosheets were derived from $NaFeO_2$-type $Na_{0.2}RuO_{2.0}{\cdot}nH_2O$ [12]. These RuO_2 nanosheets show reversible redox behaviour and specific capacitance comparable to 1–2 nm sized RuO_2 nanoparticles. The mechanism of the pseudo-capacitive behaviour has been extensively studied. Although more work is necessary to fully understand the charge-storage mechanism, some important aspects can be emphasized.

(1) Nanosheet electrodes have about two times higher specific capacitance compared to its precursor material, layered ruthenic acid (Figs. 11.1 and 11.2) [11, 12]. The non-Faradaic electrical double-layer capacitance of layered ruthenic acid and its nanosheet derivative are the same, which indicates that the surface utilization (electrochemically active surface area) is the same. The higher specific capacitance is attributed to an increase in the surface redox (pseudo-capacitance), owing to the open-framework structure of the nanosheet electrode which allows facile penetration of ions into the porous structure.

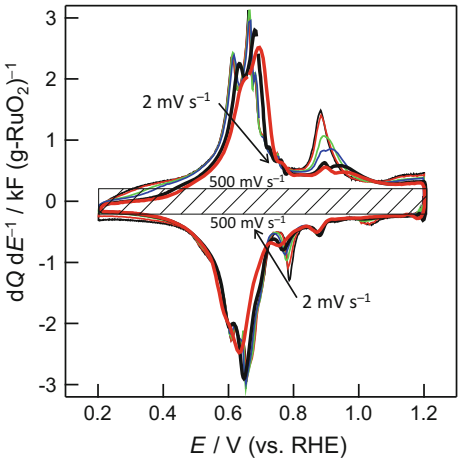

Fig. 11.1 Cyclic voltammograms (potential vs. differential capacitance) of $RuO_{2.1}$ nanosheets derived via exfoliation of layered $K_{0.2}RuO_{2.1}$ in 0.5 M H_2SO_4 (25 °C) at scan rates of 2–500 mV/s. The contribution from the electric double-layer capacitance is shown in the *shaded region*. Reproduced with permission from Ref. [11]. Copyright 2003, John Wiley and Sons

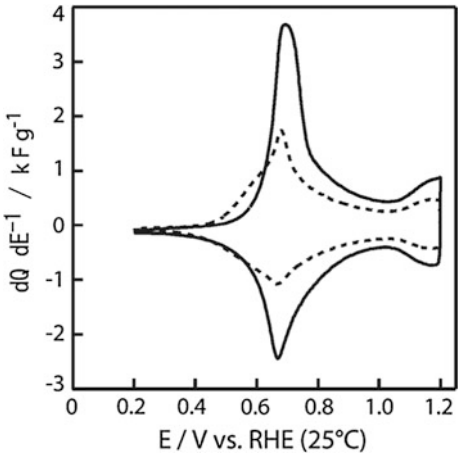

Fig. 11.2 Cyclic voltammograms (potential vs. differential capacitance) of $H_{0.2}RuO_{2.0}$ derived from α-$NaFeO_2$ type $NaRuO_{2.0}$ (*broken line*) and restacked $RuO_{2.0}$ nanosheets (*solid line*) at 2 mV/s in 0.5 M H_2SO_4 (25 °C). Reprinted with permission from Ref. [12]. Copyright 2010 American Chemical Society

(2) Protons are the active species for surface redox, although some contribution from anion adsorption/desorption should be present [1, 4, 13–17]. Thus, the largest specific capacitance is obtained with acidic electrolytes, where the contribution from surface Faradaic processes can account to as high as 60% of the total capacitance (Fig. 11.3) [14]. Alkaline and neutral electrolyte do not give a large contribution from redox process and the charge storage mainly originates from non-Faradaic electrical double-layer capacitance [13].

(3) The hydrated interlayer is important for the penetration of electrolyte into the porous structure [18–20] and the ionic conductivity dominates the power performance (Fig. 11.4) [21].

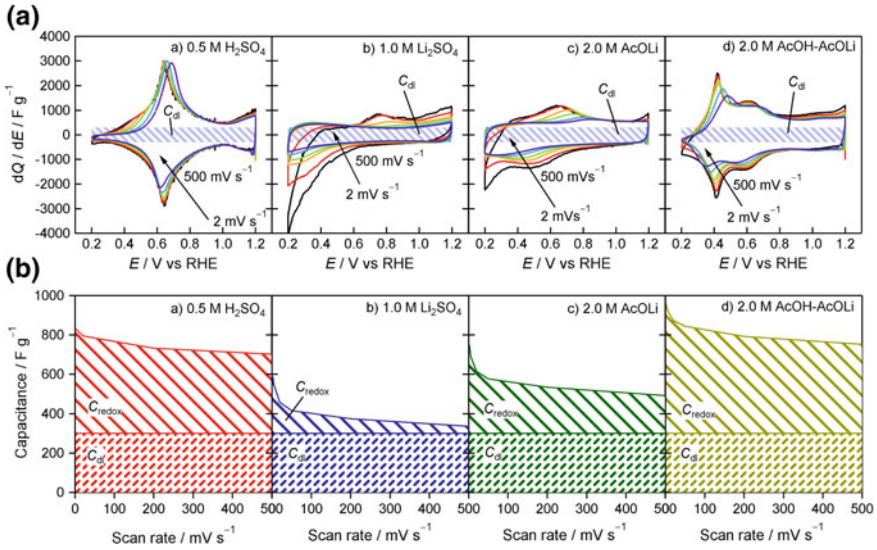

Fig. 11.3 **a** Cyclic voltammograms of $RuO_{2.0}$ nanosheets derived from α-$NaFeO_2$ type $NaRuO_{2.0}$ in 0.5 M H_2SO_4, 1.0 M Li_2SO_4, 2.0 M AcOLi, and 2.0 M AcOH–AcOLi with v = 2, 5, 20, 50, 200, and 500 mV/s (60 °C). **b** The overall capacitance deconvoluted into the electrical double-layer capacitance (C_{dl} = 300 F/g) and redox capacitance (C_{redox}). Reproduced with permission from Ref. [14]. Copyright 2003, The Electrochemical Society

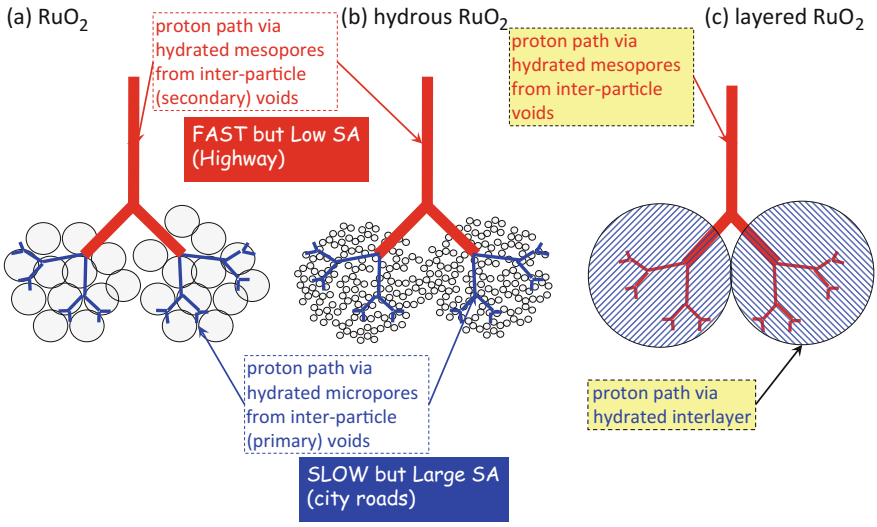

Fig. 11.4 Fractal tree-root model proposed for **a** anhydrous RuO_2, **b** hydrous RuO_2, and **c** layered $H_{0.2}RuO_{2.1}{\cdot}H_2O$ based on analysis of electrochemical impedance spectroscopy. Reproduced with permission from Ref. [15]. Copyright 2010 American Chemical Society

(4) High electronic conductivity is essential for fast charge storage with low *iR* loss. $RuO_{2.1}$ nanosheet derived from layered $K_{0.2}RuO_{2.1}{\cdot}nH_2O$ has electronic conductivity higher than reduced graphite oxide (chemical graphene) [22].

Interestingly, the capacitance of RuO_2 nanosheet electrodes in acetic acid-lithium acetate (AcOH–AcOLi) buffered solutions with near neutral pH is higher than that obtainable in acidic media (Fig. 11.3) [1]. Even bioelectrolytes such as phosphate buffered saline and fetal bovine serum exhibited high capacitance, paving the way for possible implantable bio-supercapacitors [14]. In addition to the excellent pseudo-capacitive properties of RuO_2 nanosheet given above, the colloidal properties of exfoliated nanosheets allow facile fabrication of various functional films. The drawback of oxide electrodes is its narrow electrochemical window. This drawback can be overcome using a Li or Li_xC_6 anode with a water stable, Li conducting solid electrolyte as the membrane. Such a configuration allows the use of aqueous catholytes with pseudo-capacitive oxide electrode and benefits from the low anode potential giving a cell voltage of $\sim$4 V and specific energy that can compete with present battery technology (Fig. 11.5) [1, 3].

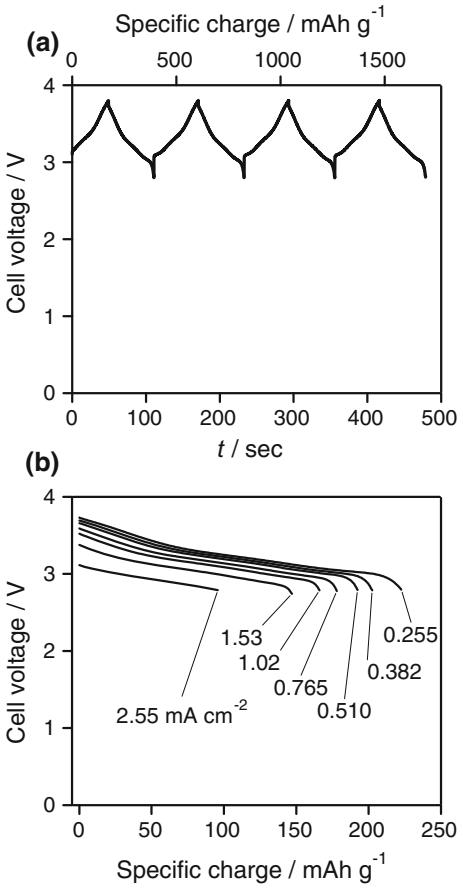

Fig. 11.5 **a** Charge/discharge curve at 0.255 mA/cm^2 and **b** discharge curves with various current densities of the hybrid capacitor using $RuO_{2.0}$ nanosheet positive electrode and multi-layered Li negative electrode in 5.0 M AcOH–AcOLi buffered electrolyte. Reproduced with permission from Ref. [1]. Copyright 2013 The Electrochemical Society of Japan

11.4.2 Pseudo-capacitive Properties of MnO_x and CoO_x Nanosheet Electrodes

Ruthenium is a platinum-group metal, and thus its abundance may limit application of RuO_2-based supercapacitors to small-scaled devices or high-end applications where flexible or translucent characteristics are desired [23, 24]. Less-expensive metal oxides, in particular manganese oxide, have been studied as alternatives [7, 25]. The pseudo-capacitive behaviour of manganese oxide in mild aqueous electrolytes (e.g., 2 M KCl) was first reported by Lee and Goodenough [26, 27]. Since then, a large number of studies have reported the charge-storage properties of MnO_x prepared by various synthetic methods, with a variety of crystal structures (amorphous, beta, gamma, etc.) and electrode structures (thin films, powders, composites, porous architectures). The pseudo-capacitance in mild aqueous electrolytes for MnO_x electrodes originates from the Mn^{3+}/Mn^{4+} redox couple and involves the injection/extraction of electrons into/from MnO_x based electrodes, accompanied by the insertion/intercalation of charge-compensating cations from the electrolyte [28]. Since MnO_x compounds are poor electronic conductors, and the redox active sites are at/near the surface, thin films generally afford higher specific capacitance. Thicker films, typically above 1 μm, tend to have capacitance lower than 300 F/g, even with conductive carbon additives (Fig. 11.6). Readers are suggested to refer to literature [28] for details of the mechanism of pseudo-capacitance in MnO_x compounds.

Among the various forms of manganese oxides, δ-MnO_2 (generally known by its mineral name, birnessite) has a layered structure and can be exfoliated into MnO_2 nanosheets. The exfoliation of birnessite dates back to the early 2000s [29–31]. Suzuki, Miyayama and co-workers have conducted a series of studies on the capacitive behaviour of exfoliated birnessite in neutral aqueous electrolytes, including size dependence [25, 32] and effect of metal-doping [33]. Capacitance ranging from a few hundred to a thousand F/g was reported. The general trend in electrochemical properties seems to follow other MnO_x materials; that is, the capacitive performance is highly dependent on the electrode microstructure with high capacitance observed for thin-film electrodes (low active material loadings).

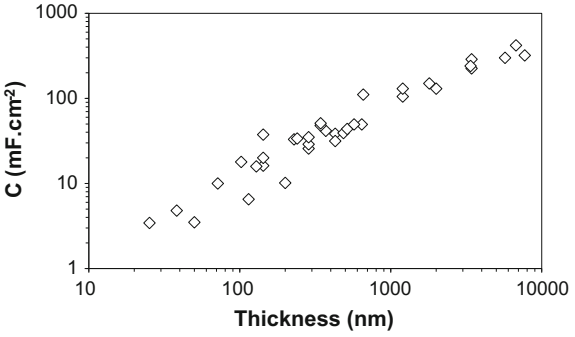

Fig. 11.6 Specific capacitance versus the thickness of MnO_2 layer. Reproduced with permission from Ref. [28]. Copyright 2017, Springer

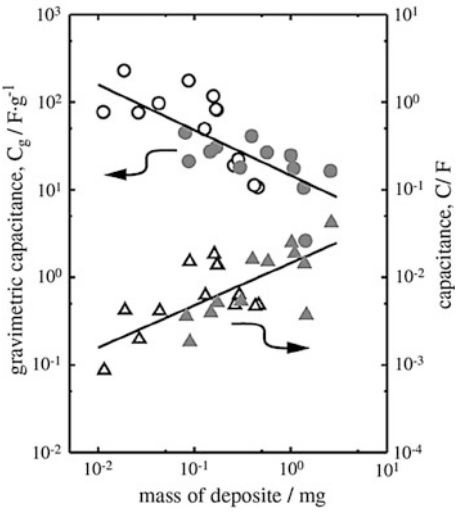

Fig. 11.7 Relationship between mass of deposit and capacitance for exfoliated birnessite nanosheet electrodes prepared by electrophoretic deposition. Open and filled markers represent birnessite nanosheets exfoliated from K- and Na-birnessite, respectivley. Reproduced with permission from Ref. [7]. Copyright 2008, The Ceramic Society of Japan

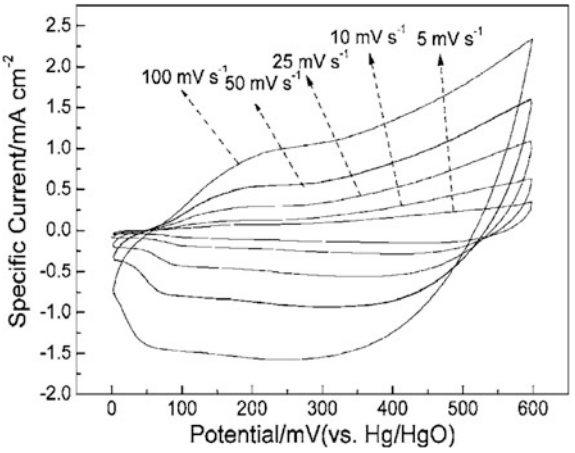

Fig. 11.8 Cyclic voltammograms of a Co–Al LDH nanosheet thin-film electrode in 1 M NaOH at different scan rates. Reproduced with permission from Ref. [40]. Copyright 2007, The Electrochemical Society

It was also shown that electrodes made from smaller size nanosheets had higher capacitance than that made from larger size ones, which the authors attributed to larger specific surface area and mesoporous volume.

An interesting relationship between mass loading versus the gravimetric and areal capacitance has been studied with a series of electrophoretically deposited exfoliated birnessite. The capacitance had a linear correlation to the deposited mass (Fig. 11.7). Other methods of preparing electrode materials composed of birnessite nanosheet include flocculation [5], pillaring [34], adsorption on carbon [35, 36], and layer-by-layer deposition with carbons or other nanosheets [6, 37–39].

Delaminated layered double hydroxides containing cobalt show pseudo-capacitive behaviour in alkaline electrolyte such as NaOH or KOH with capacitance of 600–800 F/g and a voltage window of 0.6 V (Fig. 11.8) [8, 40–42].

Despite the high specific capacitance, the electrochemical window is ~0.6 V, thus the energy density when used in a symmetric configuration is not high.

11.5 Oxide Nanosheets for Rechargeable Batteries

Ti, Mn, Mo, and Ru-based oxide nanosheets have been studied for rechargeable batteries by various groups. Freeze-dried lepidocrocite type $Ti_{0.92}O_2$ nanosheets give a discharge capacity of 165 mAh/g in 1 M $LiPF_6$/EC + DMC [43]. Tetratitanate thin films show fairly high capacity of 180 mAh/g in 1 M $LiClO_4$/PC, which is comparable to anatase TiO_2 or octatitanate synthesized by heat treatment of tetratitanate nanosheets [44]. Analysis of ultra-thin films composed of large- and small-sized tetratitanate nanosheet electrodes fabricated by layer-by-layer deposition showed that large-sized nanosheets exhibit mixed charge-transfer controlled and diffusion limited process with $b = 0.86$ for $i = av^b$ (where i is current, v is scan rate, and b is the slope of the log–log plot) at low scan rates (2–10 mV/s) and changes to diffusion limited process with $b = 0.52$ above 50 mV/s (Fig. 11.9). Interestingly, small-sized nanosheets exhibited mixed charge-transfer controlled

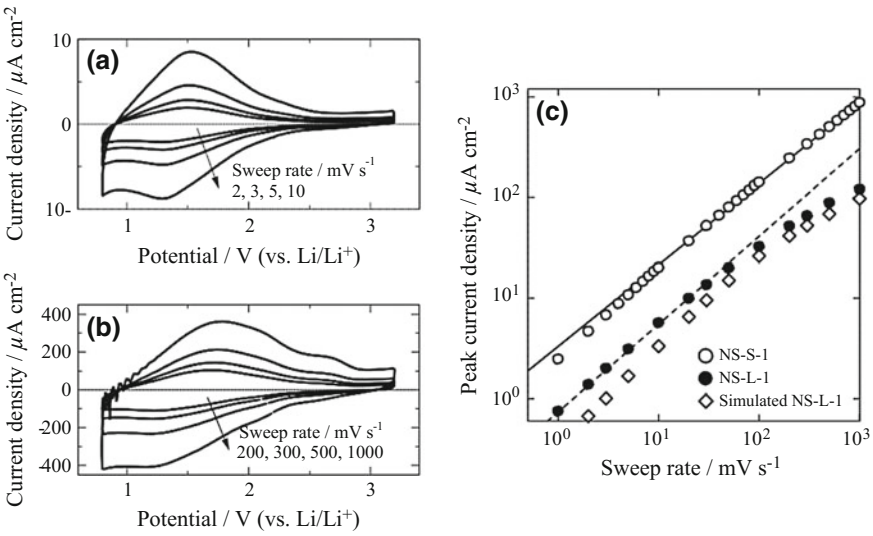

Fig. 11.9 **a, b** Cyclic voltammograms of a large-sized tetratitanate nanosheet electrode prepared by electrostatic deposition. **c** Relationships between the cathodic peak current density of tetratitanate nanosheet electrodes with large (NS-L-1) and small (NS-S-1) sized nanosheets and the sweep rate. Reproduced with permission from Ref. [45]. Copyright 2011, Elsevier

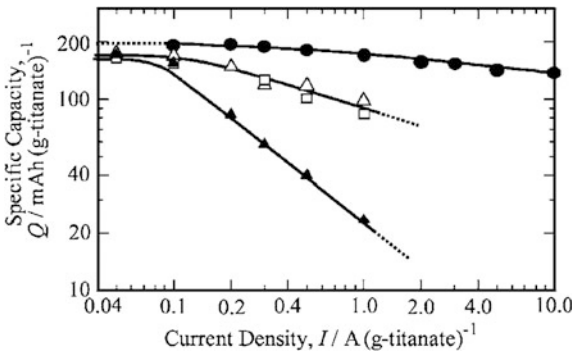

Fig. 11.10 Discharge capacity of reassembled-octatitanate composite with carbon fiber (RHT8/CF *filled circle*) and acetylene black (RHT8/AB *filled triangle*) as a function of current density compared with those of octatitanate $H_2Ti_8O_{17}$ (CHT8, *open circle*) and reassembled octatitanate (RHT8, *open triangle*). Reproduced with permission from Ref. [48]. Copyright 2007, The Electrochemical Society

and diffusion limited process with $b = 0.81$ up to 1000 mV/s, indicating the faster kinetics of the reaction compared with larger sized nanosheets. The lithium ion diffusion coefficient for tetratitanate nanosheets along the *b*-axis was estimated to be 3×10^{-10} cm^2/s [45]. A much thicker film prepared by electrophoretic deposition gave a diffusion coefficient of 6×10^{-14} cm^2/s. This value was 1/5000 of that along the in-plane direction of tetratitanate nanosheets (3×10^{-10} cm^2/s) [44].

Tetratitanate nanosheets can be converted to octatitanate $H_2Ti_8O_{17}$ [46–48], TiO_2(B) [49], and anatase [43]. Reassembled octatitanate showed higher reversible capacity of 175 (mA h)/g, higher energy efficiency, and a better cyclability than those of octatitanate without the nanosheet process [46]. The properties can be further increased by flocculation in the presence of carbon (Fig. 11.10) [47, 48]. TiO_2(B) derived from tetratitanate nanosheets exhibited enhanced performance compared to its non-exfoliated form with a high capacity of 253 mAh/g.

MnO_2 [50, 51] and MoO_2 [52] nanosheets are also capable of storing lithium. MnO_2 derived via exfoliation of $K_{0.45}MnO_2$ and subsequent flocculation with Li^+ gives 266 mAh/g, which is 93% of the theoretical capacity. The disordered structure was suggested to prevent irreversible conversion into the spinel structure, leading to better capacity retention. Restacked MoO_2 nanosheets show a very high capacity of 400 mAh/g, which is twice the theoretical capacity [52].

An interesting work involves the use of RuO_2 nanosheets as a carbon-free oxygen cathode catalyst for Li–O_2 battery [53]. The high conductivity coupled with adequate porosity and electrocatalytic activity allows stable charge/discharge of 1000 mAh/g with small overpotentials (Fig. 11.11).

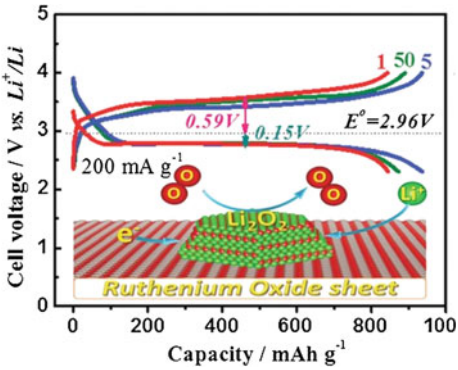

Fig. 11.11 Discharge–charge profiles of the Li–O_2 battery with a RuO_2 nanosheet cathode over 50 cycles at 200 mA/g. Reproduced with permission from Ref. [53]. Copyright 2015, The Royal Society of Chemistry

References

1. Makino S, Ban T, Sugimoto W (2013) Electrochemical capacitor behavior of RuO_2 nanosheets in buffered solution and its application to hybrid capacitor. Electrochemistry 81 (10):795–797
2. Deng L, Wang J, Zhu G, Kang L, Hao Z, Lei Z, Yang Z, Liu ZH (2014) RuO_2/graphene hybrid material for high performance electrochemical capacitor. J Power Sources 248:407–415
3. Makino S, Shinohara Y, Ban T, Shimizu W, Takahashi K, Imanishi N, Sugimoto W (2012) 4 V class aqueous hybrid electrochemical capacitor with battery-like capacity. RSC Adv 2(32):12144–12147
4. Sugimoto W, Yokoshima K, Murakami Y, Takasu Y (2006) Charge storage mechanism of nanostructured anhydrous and hydrous ruthenium-based oxides. Electrochim Acta 52(4):1742–1748
5. Song MMS, Lee KMKM, Lee YRYR, Kim IYIY, Kim TWTW, Gunjakar JLJL, Hwang SSJ (2010) Porously assembled 2D nanosheets of alkali metal manganese oxides with highly reversible pseudocapacitance behaviors. J Phys Chem C 114(50):22134–22140
6. Zheng H, Tang F, Jia Y, Wang L, Chen Y, Lim M, Zhang L, (Max) Lu G (2009) Layer-by-layer assembly and electrochemical properties of sandwiched film of manganese oxide nanosheet and carbon nanotube. Carbon N.Y. 47(6):1534–1542
7. Takei T, Yonesaki Y, Kumada N, Kinomura N (2008) Anodic electrodeposition of redoxable film from manganese oxide nanosheet. J Ceram Soc Japan 116(11):1222–1227
8. Wang Y, Yang W, Chen C, Evans DG (2008) Fabrication and electrochemical characterization of cobalt-based layered double hydroxide nanosheet thin-film electrodes. J Power Sources 184:682–690
9. Simon P, Gogotsi Y, Dunn B (2014) Where do batteries end and supercapacitors begin? Science 343(6176):1210–1211
10. Augustyn V, Simon P, Dunn B (2014) Pseudocapacitive oxide materials for high-rate electrochemical energy storage. Energy Environ Sci 7(5):1597–1614
11. Sugimoto W, Iwata H, Yasunaga Y, Murakami Y, Takasu Y (2003) Preparation of ruthenic acid nanosheets and utilization of its interlayer surface for electrochemical energy storage. Angew Chem Int Ed Engl 42(34):4092–4096
12. Fukuda K, Saida T, Sato J, Yonezawa M, Takasu Y, Sugimoto W (2010) Synthesis of nanosheet crystallites of ruthenate with an alpha-$NaFeO_2$-related structure and its electrochemical supercapacitor property. Inorg Chem 49(10):4391–4393
13. Sugimoto W, Iwata H, Murakami Y, Takasu Y (2004) Electrochemical capacitor behavior of layered ruthenic acid hydrate. J Electrochem Soc 151(8):A1181–A1187

14. Makino S, Ban T, Sugimoto W (2015) Towards implantable bio-supercapacitors: pseudocapacitance of ruthenium oxide nanoparticles and nanosheets in acids, buffered solutions, and bioelectrolytes. J Electrochem Soc 162(5):A5001–A5006
15. Sugimoto W, Iwata H, Yokoshima K, Murakami Y, Takasu Y (2005) Proton and electron conductivity in hydrous ruthenium oxides evaluated by electrochemical impedance spectroscopy: the origin of large capacitance. J Phys Chem B 109(15):7330–7338
16. Sugimoto W, Ohta T, Yokoshima K, Takasu Y (2007) Evaluation of the redox behavior of hydrous ruthenium oxides: effect of temperature and acid concentration on the electrochemical behavior of layered ruthenium oxide. Electrochemistry 75(8):645–648
17. Sugimoto W, Kizaki T, Yokoshima K, Murakami Y, Takasu Y (2004) Evaluation of the pseudocapacitance in RuO_2 with a RuO_2/GC thin film electrode. Electrochim Acta 49(2):313–320
18. Dmowski W, Egami T, Swider-Lyons KE, Love CT, Rolison DR (2002) Local atomic structure and conduction mechanism of nanocrystalline hydrous RuO_2 from X-ray scattering. J Phys Chem B 106(49):12677–12683
19. McKeown DA, Hagans PL, Carette LPL, Russell AE, Swider KE, Rolison DR (1999) Structure of hydrous ruthenium oxides: implications for charge storage. J Phys Chem B 103 (23):4825–4832
20. Ma Z, Zheng JP, Fu R (2000) Solid state NMR investigation of hydrous ruthenium oxide. Chem Phys Lett 331(1):64–70
21. Sugimoto W, Iwata H, Yokoshima K, Murakami Y, Takasu Y (2005) Proton and electron conductivity in hydrous ruthenium oxides evaluated by electrochemical impedance spectroscopy: the origin of large capacitance. J Phys Chem B 109(15):7330–7338
22. Sato J, Kato H, Kimura M, Fukuda K, Sugimoto W (2010) Conductivity of ruthenate nanosheets prepared via electrostatic self-assembly: characterization of isolated single nanosheet crystallite to mono- and multilayer electrodes. Langmuir 26(23):18049–18054
23. Arnold CB, Wartena RC, Swider-Lyons KE, Pique A (2003) Direct-write planar microultracapacitors by laser engineering. J Electrochem Soc 150(5):A571–A575
24. Sugimoto W, Yokoshima K, Ohuchi K, Murakami Y, Takasu Y (2006) Fabrication of thin-film, flexible, and transparent electrodes composed of ruthenic acid nanosheets by electrophoretic deposition and application to electrochemical capacitors. J Electrochem Soc 153(2):A255–A260
25. Jang H, Suzuki S, Miyayama M (2012) Self-reassembled MnO_2 nanosheets for electrochemical capacitors in neutral aqueous solution. J Electrochem Soc 159(9):A1425–A1430
26. Lee HY, Goodenough JB (1999) Supercapacitor behavior with KCl electrolyte. J Solid State Chem 144(1):220–223
27. Lee HY, Manivannan V, Goodenough JB (1999) Electrochemical capacitors with KCl electrolyte. C.R. Acad Sci, Ser IIc: Chim 2(11–13):565–577
28. Brousse T, Bélanger D, Chiba K, Egashira M, Favier F, Long J, Miller JR, Morita M, Naoi K, Simon P, Sugimoto W (2017) Materials for electrochemical Capacitors. In: Breitkopf C, Swider-Lyons K (eds) Springer handbook of electrochemical energy, 1st edn. Springer, Berlin, Heidelberg, pp 495–561
29. Liu ZH, Ooi K, Kanoh H, Tang WP, Tomida T (2000) Swelling and delamination behaviors of birnessite-type manganese oxide by intercalation of tetraalkylammonium ions. Langmuir 16(9):4154–4164
30. Gao Q, Giraldo O, Tong W, Suib SL (2001) Preparation of nanometer-sized manganese oxides by intercalation of organic ammonium ions in synthetic birnessite OL-1. Chem Mater 13(3):778–786
31. Omomo Y, Sasaki T, Wang L, Watanabe M (2003) Redoxable nanosheet crystallites of MnO_2 derived via delamination of a layered manganese oxide. J Am Chem Soc 125(12):3568–3575
32. Yano M, Suzuki S, Miyayama M, Ohgaki M (2013) Electrode properties and microstructures of MnO_2 nanosheet thin films as cathodes for electrochemical capacitors. Solid State Ionics 233:32–37

33. Yano M, Suzuki S, Miyayama M, Ohgaki M (2013) Effects of microstructure on electrode properties of nanosheet-derived Hx(Ni1/3Co1/3Mn1/3)O_2 for electrochemical capacitors. Nanomaterials 3:204–220
34. Yuan J, Liu Z-H, Qiao S, Ma X, Xu N (2009) Fabrication of MnO_2-pillared layered manganese oxide through an exfoliation/reassembling and oxidation process. J Power Sources 189(2):1278–1283
35. Kai K, Kobayashi Y, Yamada Y, Miyazaki K, Abe T, Uchimoto Y, Kageyama H (2012) Electrochemical characterization of single-layer MnO_2 nanosheets as a high-capacitance pseudocapacitor electrode. J Mater Chem 22(29):14691-14695
36. Lee YR, Kim IY, Kim TW, Lee JM, Hwang S-J (2012) Mixed colloidal suspensions of reduced graphene oxide and layered metal oxide nanosheets: useful precursors for the porous nanocomposites and hybrid films of graphene/metal oxide. Chem Eur J 18(8):2263–2271
37. Li Z, Wang J, Liu X, Liu S, Ou J, Yang S (2011) Electrostatic layer-by-layer self-assembly multilayer films based on graphene and manganese dioxide sheets as novel electrode materials for supercapacitors. J Mater Chem 21(10):3397–3403
38. Zhang X, Yang W, Evans DG (2008) Layer-by-layer self-assembly of manganese oxide nanosheets/polyethylenimine multilayer films as electrodes for supercapacitors. J Power Sources 184:695–700
39. Sakai N, Fukuda K, Omomo Y, Ebina Y, Takada K, Sasaki T (2008) Hetero-nanostructured films of titanium and manganese oxide nanosheets: photoinduced charge transfer and electrochemical properties. J Phys Chem C 112(13):5197–5202
40. Wang Y, Yang W, Yang J (2007) A Co–Al layered double hydroxides nanosheets thin-film electrode. Electrochem Solid-State Lett 10(10):A233-A236
41. Dong XX, Wang L, Wang D, Li C, Jin J (2011) Layer-by-Layer engineered Co–Al hydroxide nanosheets/graphene multilayer films as flexible electrode for supercapacitor. Langmuir 28 (1):293–298
42. Schneiderová B, Demel J, Pleštil J, Tarábková H, Bohuslav J, Lang K (2014) Electrochemical performance of cobalt hydroxide nanosheets formed by the delamination of layered cobalt hydroxide in water. Dalton Trans 43(27):10484–10491
43. Kijima N, Takahashi Y, Hayakawa H, Awaka J, Akimoto J (2008) Synthesis, characterization, and electrochemical properties of a thin flake titania fabricated from exfoliated nanosheets. J Phys Chem Solids 69(5–6):1447–1449
44. Suzuki S, Miyayama M (2012) Electrochemical intercalation of lithium into thin film of stacked tetratitanate nanosheets fabricated by electrophoretic deposition. J Electrochem Soc 160(2):A293–A296
45. Suzuki S, Miyayama M (2011) Ultra-thin film electrodes of tetratitanate nanosheets. Solid State Ionics 204–205:66–72
46. Suzuki S, Miyayama M (2006) Lithium intercalation properties of octatitanate synthesized through exfoliation/reassembly. J Phys Chem B 110(10):4731–4734
47. Suzuki S, Miyayama M (2011) Microstructural controls of titanate nanosheet composites using carbon fibers and high-rate electrode properties for lithium ion secondary batteries. J Power Sources 196(4):2269–2273
48. Suzuki S, Miyayama M (2007) Lithium intercalation properties of reassembled titanate/carbon composites. J Electrochem Soc 154(5):A438-A443
49. Jang H, Suzuki S, Miyayama M (2012) Synthesis of open tunnel-structured TiO_2(B) by nanosheets processes and its electrode properties for Li-ion secondary batteries. J Power Sources 203:97–102
50. Takada K, Kajiyama A, Onoda M, Michiue Y, Watanabe M, Sasaki T (2003) Synthesis of a Li–Mn-oxide with disordered layer stacking through flocculation of exfoliated MnO_2 nanosheets, and its electrochemical properties. Chem Mater 15(23):4508–4514
51. Sakai N, Ebina Y, Takada K, Sasaki T (2005) Inorganic multilayer films of manganese oxide nanosheets and aluminum polyoxocations: fabrication, structure, and electrochemical behavior. Chem Mater 17(6):1352–1357

52. Sugaya H, Fukuda K, Morita M, Murayama H, Matsubara E, Kume T, Uchimoto Y (2015) High-capacity lithium-ion storage system using unilamellar crystallites of exfoliated MoO_2 nanosheets. Chem Lett 44(11):1595–1597
53. Liao K, Wang X, Sun Y, Tang D, Han M, He P, Jiang X, Zhang T, Zhou H (2015) An oxygen cathode with stable full discharge–charge capability based on 2D conducting oxide. Energy Environ Sci 8(1):1992–1997

Chapter 12
Graphene Oxide Based Electrochemical System for Energy Generation

Kazuto Hatakeyama, Shinya Hayami and Yasumichi Matsumoto

12.1 Introduction

Graphene, a discreet monolayer of graphitic structure (Fig. 12.1) has very promising and unusual physical properties including very high electron mobility, thermal conductivity, and mechanical strength [1]. Because of these inventions, Geim and Novoselov won the Nobel Prize in Physics at 2010.

Graphene oxide (GO), the oxidized form of graphene, can be generated from several oxidation process [2]. Reduced graphene oxide (rGO) is the reduced form of GO. GO and rGO have a wide range of applications as they possess some very interesting properties including photoluminescence [3, 4], magnetism [5, 6], catalysis [7, 8], and molecular selectivity [9–11] Therefore, numerous researchers is trying to adopt GO in various fields, since Ruoff's groups produced GO for the first time at 2007 [12]. Remarkably, beyond 4000 research articles on GO have been published only in 2015. One of the major reasons for this huge study on GO is, it is easy and mass production process in low cost. High cost and high energy process such as CVD is usually necessary to produce large area graphene without defect. Contrastively, GO can be easily produced from abundant and inexpensive natural graphite by liquid-phase chemical treatment.

GO has many kind of functional groups and defects in its structure (Fig. 12.1). GO contains typical oxygenated functional sites, including epoxide, hydroxyl,

K. Hatakeyama · S. Hayami
Graduate School of Science and Technology Kumamoto University,
2-39-1 Kurokami, Chuo-Ku, Kumamoto 860-8555, Japan
e-mail: kazuto@kumamoto-u.ac.jp

S. Hayami
e-mail: hayami@sci.kumamoto-u.ac.jp

Y. Matsumoto (✉)
Kumamoto University, 2-39-1 Kurokami, Chuo-Ku, Kumamoto 860-8555, Japan
e-mail: yasumi@gpo.kumamoto-u.ac.jp

T. Nakato et al. (eds.), *Inorganic Nanosheets and Nanosheet-Based Materials*,
Nanostructure Science and Technology, DOI 10.1007/978-4-431-56496-6_12

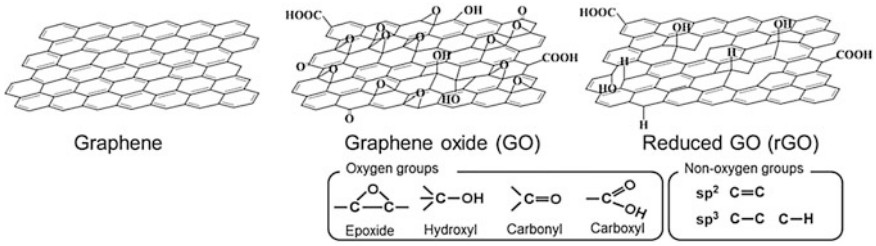

Fig. 12.1 Schematic for graphene, graphene oxide (GO) and reduced GO (rGO)

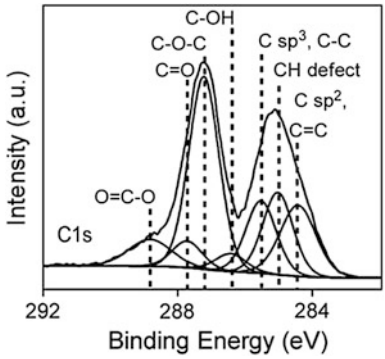

Fig. 12.2 C1s XPS spectrum of GO

carbonyl and carboxyl groups, where the epoxide groups are the major contributors (Fig. 12.2). The oxygen functional groups provide GO various functionalities. For example, GO is soluble in water because the polar oxygenated sites have partially minus charge, which allows GO for liquid-phase processing and applications. The oxygen functional groups also have huge effect on the electronic and photonic properties of GO.

Herein we would like to confine our discussion on the basic properties and applications of GO and rGO for electrochemical energy storing systems. GO is an electric insulator but a good proton conductor, while rGO is a good electric conductor with lower proton conductivity. Therefore, both the electrolyte and electrode can be fabricated by GO only.

12.2 Properties of GO

12.2.1 Structure of GO

On a single GO layer, there are chemically different regions such as hydrophobic π-conjugated sp [2] domains, hydrophilic sp [3] domains with hydrophilic oxygen functional groups and holes [13]. Schematic for nanostructure in GO is shown in

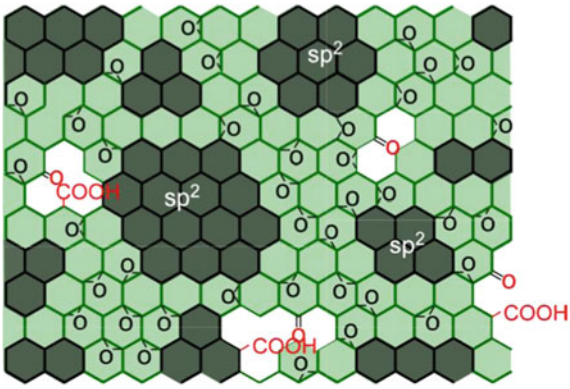

Fig. 12.3 Schematic of nanostructure in GO nanosheet. Reprinted from Ref. [16]. Copyright 2012 American Chemical Society

Fig. 12.3. As each domains have different properties, GO can exhibit multifunctionality. The unique properties of GO strongly depend on the extent of each domain area. The typical nature of each domain is described below.

sp [3] domains with oxygen functional groups and C–H bands account for a large area of GO. The minus charge of oxygen functional groups lead to hydrophilic property of GO. Therefore, GO is dispersible in water and forms composites with various positively charged materials such as metal cations, by electrostatic interaction. Electrons cannot move in a sp [3] domains, which causes electric insulation property in GO. But, the protons easily can move within a sp [3] domain, which leads to high proton conductivity of GO (explained in a later section).

sp [2] domains with a same honeycomb structure as graphene are scattered about in sp [3] matrix. Because electrons are free to move within the sp [2] domain, rGO with large and/or many sp [2] domains acts as good electric conductor (explained in a later section). As a sp [2] domain has a band gap corresponding to domain size due to the quantum confinement effect, the semiconducting properties of GO is not surprising [3, 4]. In addition, a network of sp [2] domain nanocapillaries formed within GO laminates allows low-friction flow of water [14].

There are few nanoscale sized holes in GO. Holes are generated during the release of CO and CO_2 during the oxidation and exfoliation processes of GO. Selective molecular sieving through a few layer GO was possible to avail due to the existence of these holes [10, 11]. In this case, a molecule transfers via holes corresponding to the kinetic diameter of that molecule. Additionally, it is well known that the zigzag edge surrounding a hole has localized spins [15]. Therefore, GO takes on ferromagnetic property by purposely making holes in GO [8].

The rate of domain areas and extent of oxygen functional groups can be tuned using oxidation and reduction processes. It is possible to produce GO with various oxygen functional groups by varying the amount of oxidant and time of reaction [16]. Control of GO structure within a wider range of oxygen content is feasible through the process of reduction or the strength of reducing agent. Also, different reduction process produces a wide variety of rGO; thermal reduction leads to increase sp [2] domains, while electrochemical reduction and photoreduction leads

to increased C–H groups and defects [17]. The rate of domain areas and content of oxygen functional groups directly affect the nature of GO. This means that properties of GO can be tuned using oxidation and reduction processes. For instance, various photoluminescence colors from GO are produced in controlled photoreduction [3].

12.2.2 Electric Conduction of GO

Graphene displays a remarkable electric conductivity of $\sim 10^6$ S/cm, which is higher than that of silver [18]. However, GO scarcely leads an electron current because contiguous π-conjugation bands are broken by sp [3] domains (explained above). The high electric conductivity is necessary for application in electrical devices. Therefore, a great deal of effort has been devoted to restore electric conduction of GO. The electric conduction of GO usually increase through reduction process. Before reduction, the electric conduction of GO occurred by tunneling and hopping through isolated sp [2] domains in sp [3] matrix. On the other hand, rGO shows a good electric conductivity because sp [2] domains gradually expand and finally a conduction path is generated at the percolation threshold by reduction process [19]. The electric conductivities of rGO reduced by typical method are summarized in Table 12.1.

Thermal reduction is the most popular process for recovering electric conduction GO. Mullen's group has reported GO annealed at a temperature of 1100 °C in Ar/H_2 shows a high conductivity as 727 S/cm [20]. Lopez et al. has reported that annealed GO in C_2H_4 atmosphere at 800 °C demonstrates conductivity of 10–350 S/cm, due to repair of defects in GO by CVD [21]. Similarly, Mullen's group demonstrated that GO treated in CH_4 plasma at 700 °C for a short time (20 s) exhibits an electric conductivity 345 S/cm [22]. Though thermal reduction provides

Table 12.1 Electric conductivities of rGO by various reduction methods

Reduction method	Conditions	Electric conductivity
Thermal reduction	1900 °C in UHV [30]	565 S/cm
	1100 °C in Ar/H_2 [20]	727 S/cm
	800 °C in C_2H_4 [21]	10–350 S/cm
	Plasma treatment as 700 °C in CH_4 [22]	345 S/cm
Chemical reduction	Hydrazine [12]	2 S/cm
	$NaBH_4$ [23]	0.045 S/cm
	Hydroiodic acid [24]	298 S/cm
Chemical + thermal reduction	500 °C in are after a hydrazine treatment [25]	351 S/cm
Photoreduction	UV irradiation [17]	10^{-4}–10^{-3} S/cm

pure rGO with high electric conductivity, the process is sometimes difficult, as is stipulated by technical necessity including UHV, H_2, and hydrocarbon atmospheres.

Chemicals reduction is another promising way to obtain rGO. Many chemicals such as hydrazine [12], $NaBH_4$ [23] and hydroiodic acid have been reported for reducing GO. Among chemical reductions, GO reduced by 55% hydroiodic acid for 1 h at 100 °C showed a high electric conductivity of 298 S/cm [24]. Also, annealed GO at a temperature of 500 °C after hydrazine treatment showed electric conductivity of 351 S/cm [25]. In chemical reduction, some heteroatoms are introduced into rGO and affect electrical properties of rGO.

Photoreduction is the simplest way for reduction of GO. In the earliest use of photoreduction, photocatalysts such as TiO_2 and ZnO were added for using the photoproduced electron [26, 27]. Subsequently, Matsumoto's group found that photoreduction of GO fully progresses without a photocatalyst [28].Also, photopatterning is possible using photomask or laser [28, 29]. However, the electric conductivity of photo-reduced rGO is relatively low as 10^{-4}–10^{-3} S/cm [17].

12.2.3 Proton Conduction of GO

Proton conduction plays important role in a wide range of electrochemical systems such as fuel cells and supercapacitors [31]. Proton conductor based on organic and coordination polymers, such as hydrocarbon ionomers, acid-doped polymers, inorganic/organic nanohybrid, superprotonic solid acids and acid/base ionic liquids have been reported and typical conductivity ranges for Nafion, phosphates, carboxylic acids and imidazoles are 10^{-1}–10^{-5}, 10^{-1}–10^{-4}, 10^{-5}–10^{-6}, and 10^{-6}–10^{-8} S/cm, respectively [32–37] Usually, proton conductors are constructed by a strong framework for maintaining the structure and proton transfer channel with hydrophilic property. From this perspective, GO with carbon framework and oxygen functional groups should act as a proton conductor.

Based on this issue, the proton conduction of GO has been researched extensively. Previously, the ion conduction of GO was measured by Ajayan et al. to apply GO film as solid electrolyte in all carbon-based supercapacitor [38]. Karim et al. demonstrated the proton conduction of GO using heavy water (D_2O) [39]. The conductivity of H_2O-humidified GO was ~1.25 times higher than that of D_2O-humidified GO, which clearly showed that the ionic species moving through GO nanosheet is the proton. The details about the proton conduction mechanism of GO was reported by Hatakeyama et al. using single-layer and multilayer GO [40]. Figure 12.4 shows the dependence of the proton conductivities of GO films in horizontal (in-plane) direction with various thicknesses and relative humidity (RH) at 25 °C. The results indicate five important phenomena about proton conduction of GO. (1) The proton conductivity of GO at 100% humidity was relatively high, nearly 10^{-3} S/cm. (2) The proton conductivity of a single nanosheet was much lower than those of multilayer films, meaning that protons move more frequently at the interlayers. (3) The conductivity increased with increasing film

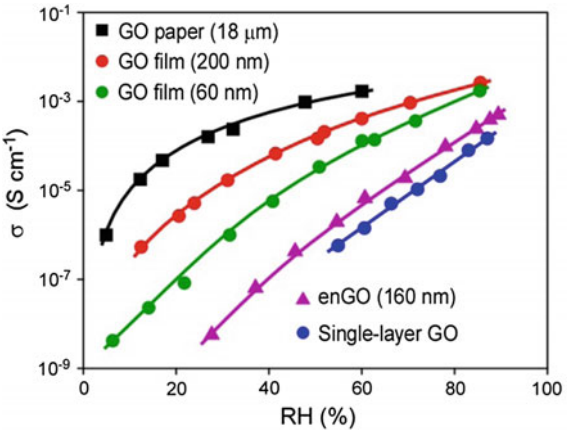

Fig. 12.4 Proton conductivities of GO films as a function of relative humidity; ethylene diamine (enGO). Reprinted with permission from Ref. [40]. Copyright (2014) WILEY-VCH Verlag GmbH & Co. KGaA, Weinheim

thickness. (4) Modification of epoxide groups with ethylenediamine leads to decreased proton conductivity, indicating that the hydrated epoxide groups are the major contributor for proton transportation. The activation energy (E_a) of proton transfer was found to be low (<0.3 eV) through measuring the slope of Arrhenius plot. The low E_a value implies that proton conduction in GO proceeds via the Grotthuss mechanism, where the protons move by hopping from an H_3O^+ ion to the nearest water molecule. Consequently, the faster proton movement in GO occurs via the interlayer water film interacting with the epoxy group.

The proton conductivity of GO under high RH condition is around 10^{-3} S/cm and is lower than that of the widely used Nafion (10^{-2}–10^{-1} S/cm) proton exchangers. Therefore, in order to improve proton conduction of GO to a competitive value of Nafion, numerous physical and chemical modification was attempted, which includes the formation of hybrids with Nafion [41, 42], sulfate ions and organosulfur compounds [43]. Among these methods, introducing sulfate ions into GO interlayers was found to be the fascicle cheap and most simple method for approaching to the Nafion conductivity [44]. The interlayer distance of multilayer GO intercalated by sulfate ion was possible to increase. In addition, during humidification the sulfate ions results in a layer of diluted H_2SO_4 at GO interlayer, which increases the proton conductivity dramatically.

The in-plane and through-plane proton conductivities of GO are significantly difference. The proton conductivity of in-plane is generally much higher than that of the through-plane [45]. In through-plane conduction, protons must transfer through a roundabout route, while protons can directly transfer along the basal plane of GO nanosheet in case of in-plane conduction. Therefore, protons moves larger distance in through-plane conduction and the conductivity is lower. However, compared with the in-plane one the through-plane proton conduction is more significant for practical applications because it is difficult to make a GO membrane where all the GO nanosheets are aligned perpendicularly. In order to increase the through-plane proton conductivity, several studies have been demonstrated [46].

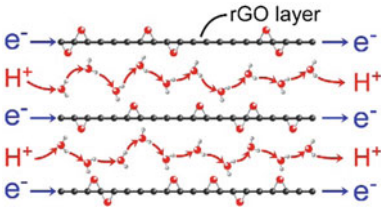

Fig. 12.5 Schematic model of electron and proton mixed conduction in rGO film

12.2.4 Electron and Proton Mixed Conduction of GO

Materials with relatively high electric and protonic conductivities (mixed conductor) are important for various applications such as fuel cells, supercapacitors, and gas separation membranes [47–49] The electric conductivity of GO dramatically increased by reduction as mentioned above. On the other hand, the proton conductivity decreased by a reduction process because oxygen functional groups and layer distance of GO decrease through reduction. Therefore, mixed electric and proton conducting in rGO can be easily produced by an optimized reduction process. Through controlled reduction of GO by UV irradiation and thermal annealing, Matsumoto's group has found the suitable degree of reduction for obtaining an optimized mixed conductor [17]. In this case, electrons transfer through rGO planes, while protons diffuse into the interlayer (Fig. 12.5). The proposed mixed conducting rGO showed the same electric and protonic conductivities of $\sim 10^{-4}$ S/cm at room temperature under 90% RH. Moreover, both conductivities were successfully enhanced by introducing sulfate ions into the rGO interlayers [50]. Among the mixed conductors reported, the enhanced rGO film exhibited the best performance at room temperature. Considering the good mixed conduction and its unique mechanism, rGO is suitable for electrode material in some batteries, fuel cell, and supercapacitor. rGO ensures an electrode with the large reactive site, which leads to high performance of battery (described in a following section).

12.3 Applications of GO/RGO in Electrochemical Devices

12.3.1 Fuel Cells

Fuel cells are one of the most important energy conversion devices that allow a promising way to convert chemical energy directly into electrical energy. Proton exchange membranes having high proton conduction, good mechanical strength, and gas barrier property are the key material for of the fuel cells. Because of the good mechanical strength, flexibility, and high proton conduction, GO membranes functions excellently as the solid electrolyte in fuel cells. In addition, it is reported that submicrometer-thick GO membranes can be completely impermeable to

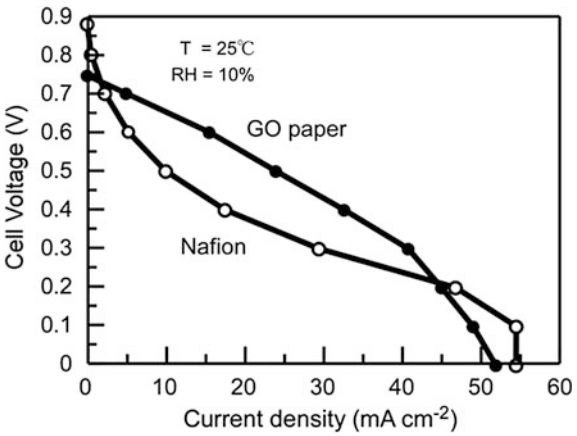

Fig. 12.6 The performance of the fuel cells using GO electrolyte (∼15 μm) with Pt/C electrodes. Reprinted with permission from Ref. [45]. Copyright (2013) The Electrochemical Society

liquids, vapors, and gases (even helium) [14]. Therefore, worldwide attempts for using GO as solid electrolyte in fuel cells is observed.

Previously, GO hybrid with Nafion [41, 42] and GO sulfonated by surfer based organic compounds [43] has been reported as the electrolyte for fuel cells. After that, Tateishi et al. demonstrated the performance of a simple H_2/O_2 fuel cell using a 100% GO membrane as electrolyte [45]. Figure 12.6 shows the performance of the fuel cells using GO electrolyte (∼15 μm) with Pt/C electrodes at low RH and room temperature. The open circuit voltage was ∼0.9 V, the highest short circuit current was ∼50 mA/cm, and the highest maximum power density was ∼13 mW/cm. Thus, the GO membrane exactly acted as the fuel cell electrolyte even at low RH and room temperature. Moreover, the fuel cell using GO electrolyte shows the better performance than that using Nafion with ∼150 μm thickness. This report indicated the possible application of GO membrane in fuel cells. Gao et al. [46] reported the through-plane proton conductivity of GO with its increased performance in fuel cell by the chemical modification through treating with ozone. This improvement was explained by an increase in the number of proton-hopping sites as well as the addition of pinholes and smaller sheet sizes due to the ozonation process.

The instability of GO is a major drawback for large-scale commercialization of GO electrolyte. The gradual degradation of oxygen functional groups, especially the epoxide groups in GO at room temperature [51] results in a short lifetime. The degradation is accelerated in harsh environments such as high temperature and exposure to UV irradiation [17]. The proton conductivity of GO decrease and the electron conductivity increases. As a result, short-circuiting of the electrodes results in and it becomes impossible to use GO electrolyte in fuel cells. Therefore, a great deal of efforts has been devoted to improve the stability of GO membrane for practical applications.

GO has also been applied to fuel cell cathodes. Usually, an expensive Pt-based catalyst is used as fuel cell cathodes due to its good catalytic activity towards the

oxygen reduction reaction (ORR). The high cost of Pt-based materials is inconvenient for the commercialization of fuel cells [52]. Therefore, GO-based noble-metal-free ORR electrocatalysts have been lively studied for decreasing the cost of fuel cells. Two major approaches have been noticed to produce a GO-based ORR electrocatalysts. The first attempt includes the doping of nonmetallic hetero atoms such as nitrogen and boron into rGO sheet by simple methods including thermal annealing and hydrothermal treatment. Some catalysts resulting from such method show better ORR catalytic activities compared with the Pt/C catalyst [53, 54]. The second way is the hybridization of rGO with metal-based nanostructures such as iron phthalocyanine (FePc) and Co_3O_4 [7, 55]. The advantage of this approach is that the electrocatalysts with high ORR activity can be obtained by simple solution process. The fuel cell using an ultrathin FePc layer self-assembled on rGO as cathode electrode was produced successfully and employed in fuel cell [45]. This result implies the possibility for fabrication of GO-based low cost fuel cell in near future.

12.3.2 Supercapacitors

A supercapacitor is an energy storage device, which stores energy by means of the electrical double layer effect. Because of their high power density, fast power delivery and a long life cycle, supercapacitors are expected to be important tools for consumer electronics, transportations and space technologies. A supercapacitor is composed of two parts; electrodes and electrolyte. It is desirable for electrodes to have high surface area and high electronic conductivity. As well, the electrolyte needs to have high ionic conductivity. rGO and GO possessing these respective properties comprises their perfect applications in supercapacitor.

Numerous carbon based electrodes including graphite, activated carbon, and carbon nanotube have been used as supercapacitor electrodes. Graphene theoretically has a specific surface area of 2.63×10^3 m^2/g and specific gravity capacitance of 550 F/g [56]. Considering the existence of large amount of defects and oxygen functional groups in rGO basal plane, higher specific surface area and specific gravity capacitance in rGO is expected. The first report about a supercapacitor using rGO electrode was published by Ruoff's group in 2008 [57]. In this report, super capacitor using rGO electrode reduced by hydrazine showed a specific gravity capacitance of 135 F/g. Since that initial report, porous [58, 59] and dimensionally controlled [60, 61] rGO electrodes have been reported to exhibit better supercapacitance. As the in-plane ion conduction is much higher than the through-plane one, it was observed that supercapacitors using rGO electrode oriented vertical to direction of ion transfer exhibited increased rate performance [22, 62].

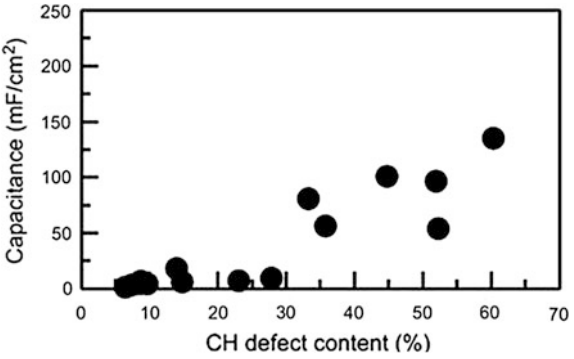

Fig. 12.7 Electrochemical capacitance as a function of CH defect content. Reprinted with permission from Ref. [65]. Copyright 2014 Elsevier Ltd

Pseudocapacitors possessing Faradic redox at the surface have been explored to improve the specific capacitances. Mullen's group observed enhanced supercapacitance performance in rGO electrode co-doped by N and B [63]. Dai's group reported a high specific gravity capacitance of ~1335 F/g in a hybrid system, where $Ni(OH)_2$ nanocrystals are grown on rGO [64]. The rGO electrode prepared by electrochemical reduction showed a high specific gravity capacitance of approximately 5000–10,000 F/g, a value much higher than that of other rGO-based electrodes mentioned above [65]. As a large number of CH groups are formed via electrochemical reduction, this extraordinary specific capacitance is attributed to redox reactions of CH groups ($CH \leftrightarrow C^- + H^+ + e^-$) during electrochemical charge–discharge. In fact, there is a strong correlation between the amount of CH groups and the capacitance; the capacitance increases with increasing the amount of CH groups (Fig. 12.7).

All carbon-based supercapacitors can be fabricated using GO and rGO as solid-state electrolyte and electrodes (Fig. 12.8). In such cases, GO and rGO functions as protonic and electronic conductor, respectively. The relevant report was published first time by Ajayan et al. in 2011. They fabricated micro-sized rGO electrodes on GO film by simple photoreduction method with laser irradiation patterning and confirmed that the device functions as a supercapacitor. They also found that the performance of the in-plane supercapacitor was higher than that of the conventional sandwich type supercapacitor. Higher in-plane proton conductivity is considered as the fact behind this observation. El-Kady et al. successfully produced more than 100 micro-supercapacitors on a single disk in 30 min or less by direct laser writing on GO films using a standard Light Scribe DVD burner [66]. All these carbon-based modifications are expected to decrease the production cost of supercapacitor. However, energy density of these GO-based supercapacitor are still lower than that of the conventional electrochemical supercapacitor. Therefore, it is necessary to improve the energy density of the solid-state GO supercapacitor for considering their practical application.

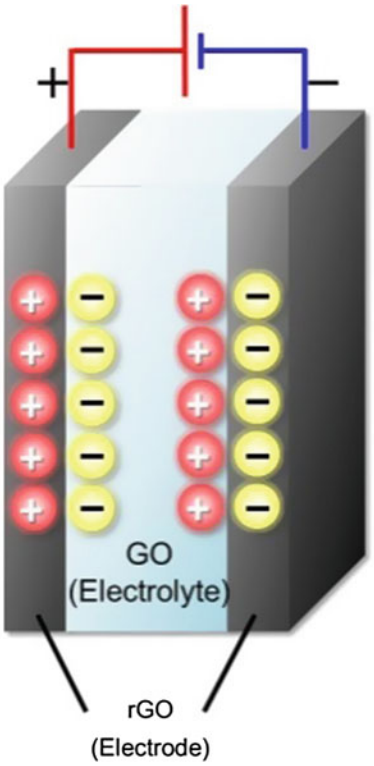

Fig. 12.8 Models of all carbon based supercapacitor using GO and rGO as the solid-state electrolyte and electrodes, respectively

12.3.3 Other Devices

GO has been introduced into the electrodes (especially at the anode) of lithium-ion battery. Transition metal oxides and Si nanoparticles are the promising candidate for an anode material in lithium-ion batteries because of their capable for the insertion/extraction of Li^+. However, these materials have the low electric conductivity and break into small clusters during the lithiation/delithiation process due to their huge volume change. rGO with good physical/chemical properties, mixed conduction, and high surface area have a great potential as additive in lithium electrode materials. Ruoff's group reported higher discharge and charge capacities with good cycling performance and rate capability in the composite of rGO with platelet/Fe_2O_3 nanoparticle [67]. Chang et al. [68] found that Si nanoparticle/rGO composite anode can exhibit excellent lithium storage performance with high specific capacity, fast rate capability, and superior capacity retention during cycling. In both examples, the cycling performance were much improved by adding rGO, which is attributed to the restriction on large volume change of Fe_2O_3 and Si nanoparticle by rGO coated on their surfaces. A significant number of novel

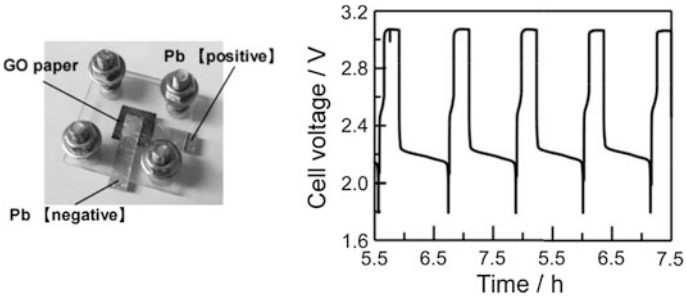

Fig. 12.9 Photograph and charge–discharge cycles of lead battery using GO electrolyte. Reprinted with permission from Ref. [75]. Copyright (2014) The Electrochemical Society

researches on rGO composites with TiO_2, SnO_2, and MoS_2 as the anode for lithium-ion battery were reported as well [69–71].

The excellent properties of rGO can also be employed for devising lithium-ion battery cathodes. For instance, Zhou et al. [72] has reported rGO modified $LiFePO_4$ composite as a lithium-ion battery cathode material exhibiting high-rate capability and cycling stability due to the expanded Li^+ diffusion channels and increased electric conductivity attributed by the rGO fragment. In the similar way, rGO has employed successfully as the electrode materials in sodium-ion battery and lithium-sulfur battery [73, 74].

Some batteries using GO electrolyte have been developed due to the excellent ion transfer properties of GO. Tateishi et al. [75] demonstrated that GO membrane, with high proton conductivity and sulfuric acid affinity, can be used as an electrolyte alternative to sulfuric acid in lead-acid batteries. This GO electrolyte based lead-acid battery possess low thickness ($\sim$2 mm), lightweight and stable charge–discharge cycles (Fig. 12.9). In a follow-up report, Huang et al. proposed a the possibility of a lithium-sulfur battery based on GO electrolyte [76]. GO membrane has the unique property for the small ions to be defused rapidly through it, while keeping the larger ions impermeable [9]. Lithium-ion can transfer between electrodes through GO electrolyte, while the shuttle of polysulfide, which induces capacity degradation and poor cycling stability, is blocked. Consequently, the lithium-sulfur battery exhibited the enhanced cycling performance.

References

1. Geim AK, Novoselov KS (2007) The rise of graphene. Nat Mater 6:183–191. doi:10.1038/nmat1849
2. Dreyer DR, Park S, Bielawski CW, Ruoff RS (2010) The chemistry of graphene oxide. Chem Soc Rev 39:228–240. doi:10.1039/b917103g
3. Chien CT, Li SS, Lai WJ et al (2012) Tunable photoluminescence from graphene oxide. Angew Chem Int Ed 51:6662–6666. doi:10.1002/anie.201200474

4. Eda G, Lin YY, Mattevi C et al (2010) Blue photoluminescence from chemically derived graphene oxide. Adv Mater 22: 505–+. doi:10.1002/adma.200901996
5. Wang Y, Huang Y, Song Y et al (2009) Room-temperature ferromagnetism of graphene. Nano Lett 9:220–224: doi:10.1021/nl802810g
6. Taniguchi T, Yokoi H, Nagamine M et al (2014) Correlated optical and magnetic properties in photoreduced graphene oxide. J Phys Chem C 118:28258–28265. doi:10.1021/jp509399x
7. Taniguchi T, Tateishi H, Miyamoto S et al (2013) A self-assembly route to an iron phthalocyanine/reduced graphene oxide hybrid electrocatalyst affording an ultrafast oxygen reduction reaction. Part Part Syst Charact 30:1063–1070. doi:10.1002/ppsc.201300177
8. Matsumoto Y, Koinuma M, Ida S et al (2011) Photoreaction of graphene oxide nanosheets in water. J Phys Chem C 115:19280–19286. doi:10.1021/jp206348s
9. Joshi RK, Carbone P, Wang FC et al (2014) Precise and ultrafast molecular sieving through graphene oxide membranes. Science 343:752–754. doi:10.1126/science.1245711
10. Li H, Song ZN, Zhang XJ et al (2013) Ultrathin, molecular-sieving graphene oxide membranes for selective hydrogen separation. Science 342:95–98. doi:10.1126/science.1236686
11. Kim HW, Yoon HW, Yoon SM et al (2013) Selective gas transport through few-layered graphene and graphene oxide membranes. Science 342:91–95. doi:10.1126/science.1236098
12. Stankovich S, Dikin DA, Piner RD et al (2007) Synthesis of graphene-based nanosheets via chemical reduction of exfoliated graphite oxide. Carbon 45:1558–1565. doi:10.1016/j.carbon.2007.02.034
13. Erickson K, Erni R, Lee Z et al (2010) Determination of the local chemical structure of graphene oxide and reduced graphene oxide. Adv Mater 22:4467–4472. doi:10.1002/adma.201000732
14. Nair RR, Wu HA, Jayaram PN, Grigorieva IV, Geim AK (2012) Unimpeded permeation of water through helium-leak-tight graphene-based membranes. Science 335:442–444. doi:10.1126/science.1211694
15. Nakada K, Fujita M, Dresselhaus G, Dresselhaus MS (1996) Edge state in graphene ribbons: Nanometer size effect and edge shape dependence. Phys Rev B 54:17954–17961. doi:10.1103/PhysRevB.54.17954
16. Koinuma M, Ogata C, Kamei Y et al (2012) Photochemical engineering of graphene oxide nanosheets. J Phys Chem C 116:19822–19827. doi:10.1021/jp305403r
17. Hatakeyama K, Tateishi H, Taniguchi T et al (2014) Tunable graphene oxide proton/electron mixed conductor that functions at room temperature. Chem Mater 26:5598–5604. doi:10.1021/cm502098e
18. Subrina S, Kotchetkov D (2008) Simulation of heat conduction in suspended graphene flakes of variable shapes. J Nanoelect Optoelect 3:249–269. doi:10.1166/jno.2008.303
19. Mattevi C, Eda G, Agnoli S et al (2009) Evolution of electrical, chemical, and structural properties of transparent and conducting chemically derived graphene thin films. Adv Funct Mater 19:2577–2583. doi:10.1002/adfm.200900166
20. Wang X, Zhi LJ, Mullen K (2008) Transparent, conductive graphene electrodes for dye-sensitized solar cells. Nano Lett 8:323–327. doi:10.1021/nl072838r
21. Lopez V, Sundaram RS, Gomez-Navarro C et al (2009) Chemical vapor deposition repair of graphene oxide: a route to highly conductive graphene monolayers. Adv Mater 21:4683–+. doi:10.1002/adma.200901582
22. Wu ZS, Parvez K, Feng XL, Mullen K (2013) Graphene-based in-plane micro-supercapacitors with high power and energy densities. Nat Commun 4. doi:10.1038/ncomms3487
23. Shin HJ, Kim KK, Benayad A et al (2009) Efficient reduction of graphite oxide by sodium borohydride and its effect on electrical conductance. Adv Func Mater 19:1987–1992. doi:10.1002/adfm.200900167
24. Pei SF, Zhao JP, Du JH, Ren WC, Cheng HM (2010) Direct reduction of graphene oxide films into highly conductive and flexible graphene films by hydrohalic acids. Carbon 48:4466–4474. doi:10.1016/j.carbon.2010.08.006

25. Chen H, Muller MB, Gilmore KJ, Wallace GG, Li D (2008) Mechanically strong, electrically conductive, and biocompatible graphene paper. Adv Mater 20:3557–+. doi:10.1002/adma.200800757
26. Williams G, Seger B, Kamat PV (2008) TiO_2-graphene nanocomposites. UV-assisted photocatalytic reduction of graphene oxide. ACS Nano 2:1487–1491. doi:10.1021/nn800251f
27. Akhavan O (2011) Photocatalytic reduction of graphene oxides hybridized by ZnO nanoparticles in ethanol. Carbon 49:11–18. doi:10.1016/j.carbon.2010.08.030
28. Matsumoto Y, Koinuma M, Kim SY et al (2010) Simple photoreduction of graphene oxide nanosheet under mild conditions. ACS Appl Mater Interfaces 2:3461–3466. doi:10.1021/am100900q
29. Zhang YL, Guo L, Wei S et al (2010) Direct imprinting of microcircuits on graphene oxides film by femtosecond laser reduction. Nano Today 5:15–20. doi:10.1016/j.nantod.2009.12.009
30. Jin MH, Kim TH, Lim SC et al (2011) Facile physical route to highly crystalline graphene. Adv Funct Mater 21:3496–3501. doi:10.1002/adfm.201101037
31. Kreuer KD (1996) Proton conductivity: materials and applications. Chem Mater 8:610–641. doi:10.1021/cm950192a
32. Bose S, Kuila T, Thi XLN et al (2011) Polymer membranes for high temperature proton exchange membrane fuel cell: Recent advances and challenges. Prog Polym Sci 36:813–843. doi:10.1016/j.progpolymsci.2011.01.003
33. Yang L, Tang J, Li L et al (2012) High quality pristine perfluorosulfonated ionomer membranes prepared from perfluorinated sulfonyl fluoride solution. RSC Adv 2:5950–5953. doi:10.1039/c2ra20318a
34. Vilciauskas L, Tuckerman ME, Bester G, Paddison SJ, Kreuer K-D (2012) The mechanism of proton conduction in phosphoric acid. Nat Chem 4:461–466. doi:10.1038/nchem.1329
35. Woundenberg RC, Yavuzcetin O, Tuominen MT, Coughlin EB (2007) Intrinsically proton conducting polymers and copolymers containing benzimidazole moieties: glass transition effects. Solid State Ion 178:1135–1141. doi:10.1016/j.ssi.2007.05.006
36. McKeen JC, Yan YS, Davis ME (2008) Proton conductivity of acid-functionalized zeolite beta, MCM-41, and MCM-48: effect of acid strength. Chem Mater 20:5122–5124. doi:10.1021/cm801418r
37. Kreuer KD (2001) On the development of proton conducting polymer membranes for hydrogen and methanol fuel cells. J Membr Sci 185:29–39. doi:10.1016/s0376-7388(00)00632-3
38. Gao W, Singh N, Song L et al (2011) Direct laser writing of micro-supercapacitors on hydrated graphite oxide films. Nat Nanotechnol 6:496–500. doi:10.1038/nnano.2011.110
39. Karim MR, Hatakeyama K, Matsui T et al (2013) Graphene oxide nanosheet with high proton conductivity. J Am Chem Soc 135:8097–8100. doi:10.1021/ja401060q
40. Hatakeyama K, Karim MR, Ogata C et al (2014) Proton conductivities of graphene oxide nanosheets: single, multilayer, and modified nanosheets. Angew Chem Int Ed 53:6997–7000. doi:10.1002/anie.201309931
41. Zarrin H, Higgins D, Jun Y, Chen ZW, Fowler M (2011) Functionalized graphene oxide nanocomposite membrane for low humidity and high temperature proton exchange membrane fuel cells. J Phys Chem C 115:20774–20781. doi:10.1021/jp204610j
42. Lee DC, Yang HN, Park SH, Kim WJ (2014) Nafion/graphene oxide composite membranes for low humidifying polymer electrolyte membrane fuel cell. J Membr Sci 452:20–28. doi:10.1016/j.memsci.2013.10.013
43. Ravikumar, Scott K (2012) Freestanding sulfonated graphene oxide paper: a new polymer electrolyte for polymer electrolyte fuel cells. Chem Commun 48:5584–5586. doi:10.1039/c2cc31771k
44. Hatakeyama K, Karim MR, Ogata C et al (2014) Optimization of proton conductivity in graphene oxide by filling sulfate ions. Chem Commun 50:14527–14530. doi:10.1039/c4cc07273a
45. Tateishi H, Hatakeyama K, Ogata C et al (2013) Graphene oxide fuel cell. J Electrochem Soc 160:F1175-F1178. doi:10.1149/2.008311jes

46. Gao W, Wu G, Janicke T et al (2014) Ozonated graphene oxide film as a proton-exchange membrane. Angew Chem Int Ed 53:3588–3593. doi:10.1002/anie.201310908
47. Tripathi BP, Schieda M, Shahi VK, Nunes SP (2011) Nanostructured membranes and electrodes with sulfonic acid functionalized carbon nanotubes. J Power Sources 196:911–919. doi:10.1016/j.jpowsour.2010.08.110
48. Rolison DR, Hagans PL, Swider KE, Long JW (1999) Role of hydrous ruthenium oxide in Pt-Ru direct methanol fuel cell anode electrocatalysts: the importance of mixed electron/proton conductivity. Langmuir 15:774–779. doi:10.1021/la9807863
49. Escolastico S, Somacescu S, Serra JM (2014) Solid state transport and hydrogen permeation in the system $Nd_{5.5}W_{1-x}Re_xO_{11.25-delta}$. Chem Mater 26:982–992. doi:10.1021/cm402821w
50. Hatakeyama K, Islam MS, Michio K et al (2015) Super proton/electron mixed conduction in graphene oxide hybrids by intercalating sulfate ions. J Mater Chem A 3:20892–20895. doi:10.1039/c5ta05653e
51. Kim S, Zhou S, Hu YK et al (2012) Room-temperature metastability of multilayer graphene oxide films. Nat Mater 11:544–549. doi:10.1038/nmat3316
52. Morozan A, Jousselme B, Palacin S (2011) Low-platinum and platinum-free catalysts for the oxygen reduction reaction at fuel cell cathodes. Energy Environ Sci 4:1238–1254. doi:10.1039/c0ee00601g
53. Lin ZY, Song MK, Ding Y et al (2012) Facile preparation of nitrogen-doped graphene as a metal-free catalyst for oxygen reduction reaction. Phys Chem Chem Phys 14:3381–3387. doi:10.1039/c2cp00032f
54. Wang SY, Zhang LP, Xia ZH et al (2012) BCN graphene as efficient metal-free electrocatalyst for the oxygen reduction reaction. Angew Chem Int Ed 51:4209–4212. doi:10.1002/anie.201109257
55. Liang YY, Li YG, Wang HL et al (2011) Co_3O_4 nanocrystals on graphene as a synergistic catalyst for oxygen reduction reaction. Nat Mater 10:780–786. doi:10.1038/nmat3087
56. El-Kady MF, Strong V, Dubin S, Kaner RB (2012) Laser scribing of high-performance and flexible graphene-based electrochemical capacitors. Science 335:1326–1330. doi:10.1126/science.1216744
57. Stoller MD, Park SJ, Zhu YW, An JH, Ruoff RS (2008) Graphene-based ultracapacitors. Nano Lett 8:3498–3502. doi:10.1021/nl802558y
58. Zhu YW, Murali S, Stoller MD et al (2011) Carbon-based supercapacitors produced by activation of graphene. Science 332:1537–1541. doi:10.1126/science.1200770
59. Kim T, Jung G, Yoo S, Suh KS, Ruoff RS (2013) Activated graphene-based carbons as supercapacitor electrodes with macro- and mesopores. ACS Nano 7:6899–6905. doi:10.1021/nn402077v
60. Miller JR, Outlaw RA, Holloway BC (2010) Graphene double-layer capacitor with ac line-filtering performance. Science 329:1637–1639. doi:10.1126/science.1194372
61. Yoo JJ, Balakrishnan K, Huang JS et al (2011) Ultrathin planar graphene supercapacitors. Nano Lett 11:1423–1427. doi:10.1021/nl200225J
62. Yoon Y, Lee K, Kwon S et al (2014) Vertical alignments of graphene sheets spatially and densely piled for fast ion diffusion in compact supercapacitors. ACS Nano 8:4580–4590. doi:10.1021/nn500150j
63. Wu ZS, Winter A, Chen L et al (2012) Three-dimensional nitrogen and boron co-doped graphene for high-performance all-solid-state supercapacitors. Adv Mater 24:5130–5135. doi:10.1002/adma.201201948
64. Wang HL, Casalongue HS, Liang YY, Dai HJ (2010) $Ni(OH)_2$ Nanoplates grown on graphene as advanced electrochemical pseudocapacitor materials. J Am Chem Soc 132:7472–7477. doi:10.1021/ja102267j
65. Tateishi H, Koinuma M, Miyamoto S et al (2014) Effect of the electrochemical oxidation/reduction cycle on the electrochemical capacitance of graphite oxide. Carbon 76:40–45. doi:10.1016/j.carbon.2014.04.034

66. El-Kady MF, Kaner RB (2013) Scalable fabrication of high-power graphene micro-supercapacitors for flexible and on-chip energy storage. Nat Commun 4. doi:10.1038/ncomms2446
67. Zhu XJ, Zhu YW, Murali S, Stollers MD, Ruoff RS (2011) Nanostructured reduced graphene oxide/Fe_2O_3 composite as a high-performance anode material for lithium ion batteries. ACS Nano 5:3333–3338. doi:10.1021/nn200493r
68. Chang JB, Huang XK, Zhou GH et al (2014) Multilayered Si nanoparticle/reduced graphene oxide hybrid as a high-performance lithium-ion battery anode. Adv Mater 26:758–764. doi:10.1002/adma.201302757
69. Li YM, Lv XJ, Lu J, Li JH (2010) Preparation of SnO_2-nanocrystal/graphene-nanosheets composites and their lithium storage ability. J Phys Chem C 114:21770–21774. doi:10.1021/jp1050047
70. Xin X, Zhou XF, Wu JH, Yao XY, Liu ZP (2012) Scalable synthesis of TiO2/Graphene nanostructured composite with high-rate performance for lithium ion batteries. ACS Nano 6:11035–11043. doi:10.1021/nn304725m
71. Chang K, Chen WX (2011) L-Cysteine-assisted synthesis of layered MoS_2/graphene composites with excellent electrochemical performances for lithium ion batteries. ACS Nano 5:4720–4728. doi:10.1021/nn200659w
72. Zhou XF, Wang F, Zhu YM, Liu ZP (2011) Graphene modified $LiFePO_4$ cathode materials for high power lithium ion batteries. J Mater Chem 21:3353–3358. doi:10.1039/c0jm03287e
73. Qu BH, Ma CZ, Ji G et al (2014) Layered SnS_2-reduced graphene oxide composite—a high-capacity, high-rate, and long-cycle life sodium-ion battery anode material. Adv Mater 26:3854–3859. doi:10.1002/adma.201306314
74. Wang HL, Yang Y, Liang YY et al (2011) Graphene-wrapped sulfur particles as a rechargeable lithium-sulfur battery cathode material with high capacity and cycling stability. Nano Lett 11:2644–2647. doi:10.1021/nl200658a
75. Tateishi H, Koga T, Hatakeyama K et al (2014) Graphene oxide lead battery (GOLB). ECS Electrochem Lett 3:A19-A21. doi:10.1149/2.002403ee1
76. Huang JQ, Zhuang TZ, Zhang Q et al (2015) Permselective graphene oxide membrane for highly stable and anti-self-discharge lithium-sulfur batteries. ACS Nano 9:3002–3011. doi:10.1021/nn507178a

Chapter 13
Nanosheet-Based Electronics

Minoru Osada

13.1 Introduction

Two-dimensional (2D) materials with atomic or molecular thickness are emerging as a new frontier of materials science. These 2D nanosheets are now considered to be excellent candidates for future electronic applications. Graphene is one of the most promising materials being researched today [1–3]; it has many amazing functionalities, such as high electron mobility and quantum Hall effects, prompting researchers to suggest that graphene will one day replace silicon in electronic devices. However, graphene is a conductor, and electronic technology also requires insulators and semiconductors. Along with graphene, 2D inorganic nanosheets have increasingly attracted fundamental research interest because of their diversity in physical properties. Many efforts have been devoted to synthesizing 2D nanosheets of various inorganic materials, including metal chalcogenides, nitrides, oxides, hydroxides, as well as primarily investigating their unique electronic structures and physical properties [3–10].

Among the type of 2D inorganic nanosheets, oxide nanosheets are important, fascinating research targets to be pursued because of the virtually infinite varieties of layered oxide materials with interesting functional properties [4–6, 8, 11]. These oxide nanosheets are exceptionally rich in structural diversity and electronic properties; oxide nanosheets exist in a whole class of functional materials, including metals, semiconductors, insulators (dielectrics), and magnetic materials. Oxide nanosheets also have remarkable potential as building blocks for tailoring new artificial materials combined with a wide range of foreign materials, such as organic molecules, gels, polymers, and inorganic nanoparticles [6, 12].

M. Osada (✉)
International Center for Materials Nanoarchitectonics (WPI-MANA), National Institute for Materials Science (NIMS), Tsukuba, Ibaraki 305-0044, Japan
e-mail: OSADA.Minoru@nims.go.jp

T. Nakato et al. (eds.), *Inorganic Nanosheets and Nanosheet-Based Materials*, Nanostructure Science and Technology, DOI 10.1007/978-4-431-56496-6_13

Here, we review electronic properties of 2D oxide nanosheets, highlighting emerging functionalities in electronic applications. We also present a perspective on the advantages offered by nanosheet architectures for various applications in electronics, spinelectronics, energy, and environment technologies.

13.2 Electronic Properties of 2D Oxide Nanosheets

The development of 2D oxide nanosheets with a wide range of physical properties is very important in the design of nanodevices with sophisticated functionality. A variety of oxide nanosheets have been synthesized by delaminating the precursors of layered oxides into their elemental layers (Table 13.1; Fig. 13.1). These oxide nanosheets have distinct differences and advantages compared with graphene and other 2D materials because of their potential to be used as insulators, semiconductors, and even conductors, depending on their chemical composition and structures of the parent layered compounds. Oxide nanosheets thus present a tantalizing prospect of scaling all electronic technology down to a truly atomic scale.

Most oxide nanosheets synthesized to date are so-called d^0 transition-metal oxides (with Ti^{4+}, Nb^{5+}, Ta^{5+}, W^{6+}) [8]. Such d^0 oxide nanosheets are typically

Table 13.1 Library of 2D oxide nanosheets

Material		Property
Ti	$Ti_{0.91}O_2$, $Ti_{0.87}O_2$, Ti_4O_9, Ti_5O_{11}	Semiconducting, dielectric, photocatalytic
	$Ti_{0.8}Co_{0.2}O_2$, $Ti_{0.6}Fe_{0.4}O_2$, $Ti_{(5.2-2x)/6}Mn_{x/2}O_2$ ($0 \leq x \leq 0.4$), $Ti_{0.8-x/4}Fe_{x/2}Co_{0.2-x/4}O_2$ ($0 \leq x \leq 0.8$)	Ferromagnetic
Mn	MnO_2	Redoxable
Co	CoO_2	Conducting
Cu	$Bi_2Sr_2CaCu_2O_8$[a]	Superconducting
Nb, Ti-Nb	Nb_3O_8, Nb_6O_{17}, $TiNbO_5$, Ti_2NbO_7, Ti_5NbO_{14}	Photocatalytic dielectric
Ta	TaO_3	Electrolyte
Perovksite	$LaNb_2O_7$, $(Ca,Sr)_2Nb_3O_{10}$, $(Ca,Sr)_2Ta_3O_{10}$, $Ca_2Na_{m-3}Nb_mO_{3m+1}$ (m = 3–6), $SrTa_2O_7$, $Bi_2SrTa_2O_9$, $Bi_4Ti_3O_{12}$	Photocatalytic, dielectric
	$La_{0.9}Eu_{0.05}Nb_2O_7$, $La_{0.7}Tb_{0.3}Ta_2O_7$, $Eu_{0.56}Ta_2O_7$, $Gd_{1.4}Eu_{0.6}Ti_3O_{10}$, $Bi_2SrTa_2O_9$	Luminescence
Mo	MoO_2, MoO_3[a]	Conducting
Ru	$RuO_{2.1}$, RuO_2	Conducting, redoxable
W	W_2O_7, $Cs_4W_{11}O_{36}$, WO_3[a]	Redoxable, photochromic

[a]Nanosheet derived from mechanical exfoliation

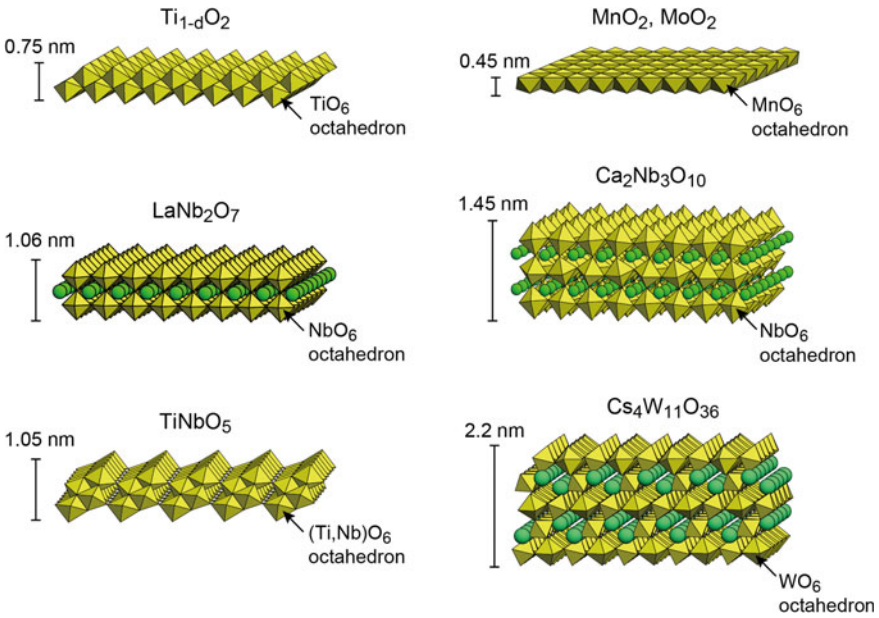

Fig. 13.1 Structures of selected oxide nanosheets

wide bandgap semiconductors, enabling their potential as a semiconducting host, photocatalyst, high-k dielectric, etc. For example, Ti-based oxide ($Ti_{1-\delta}O_2$, $TiNbO_5$, Ti_2NbO_7) and $Ca_2Nb_3O_{10}$ nanosheets offer excellent photochemical and dielectric properties [13–15]. Nanosheets, such as MnO_2, MoO_2, $RuO_{2.1}$, RuO_2, and $Cs_4W_{11}O_{36}$ undergo electrochemically reversible redox reactions [16–19]. Among the redox nanosheets, $RuO_{2.1}$ nanosheets exhibited highly electronic conducting with 10^{-4} Ω cm, a value being similar to that of transparent conducting oxide films (such as ITO) [17, 20].

There have been several works on magnetic properties of oxide nanosheets. Recent interests in room temperature (RT) ferromagnetic semiconductors and low-dimensional magnetic nanostructures have stimulated research in the synthesis and characterization of nanosheet-based ferromagnets. Such RT ferromagnetic properties in oxide nanosheets were first observed in $Ti_{0.8}Co_{0.2}O_2$, prepared by delaminating a corresponding layered titanate ($K_{0.8}Ti_{1.6}Co_{0.4}O_4$) [21, 22]. The magnetization of $Ti_{0.8}Co_{0.2}O_2$ nanosheet is anisotropic due to the 2D nature, and the spin moment of 1 μ_B/Co expected for the low-spin ($S = 1/2$) state of Co^{2+}. Similar ferromagnetic properties have also been reported in other 3d transition-metal oxide nanosheets, including $Ti_{1-x}Co_xO_2$ ($x \leq 0.2$), $Ti_{1-x}Fe_xO_2$ ($x \leq 0.4$), $Ti_{1-x}Mn_xO_2$ ($x \leq 0.4$) [23].

To date, these oxide nanosheets are mainly produced by delaminating the intrinsic layered structures of their bulk counterparts. To expand the utility of oxide nanosheets, lattice engineering, and/or doping process have recently been utilized

for tailoring electronic properties. In this context, the exfoliation technique of layered compounds is very helpful for rationally designing oxide nanosheets with various functionalities. The composition of oxide nanosheets can be intentionally modified and tuned by substitution and incorporation of other elements into designated sites during solid-state synthesis of layered compounds. Such lattice engineering and/or doping process are indeed useful for designing dielectric [15, 24, 25], ferromagnetic [21–23, 26, 27] and photoluminescent properties [28–30] in oxide nanosheets. In semiconducting $Ti_{1-\delta}O_2$ nanosheets (Fig. 13.2), controlled doping with Fe/Co ions offers exquisite control of the electronic properties, including the position of impurity bands, the Fermi energy, and ferromagnetic properties [27]. This band engineering transforms the $Ti_{1-x-y}Fe_xCo_yO_2$ nanosheet into a room temperature half-metallic ferromagnet, thus accomplishing the main requirements for future spinelectronics.

In addition to these chemically derived nanosheets, some of oxide nanosheets ($Bi_2Sr_2CaCu_2O_8$, MoO_3, WO_3, TiO_{2-x}, etc.) can be prepared by mechanical separation with adhesive tapes [31]. Other bottom-up synthetic protocols have also been explored to obtain oxide nanosheets. For example, MnO_2 nanosheets are directly obtained by one-pot synthesis route involving chemical oxidation of Mn^{2+} in a tetramethylammonium aqueous solution [32]. However, these nanosheets are

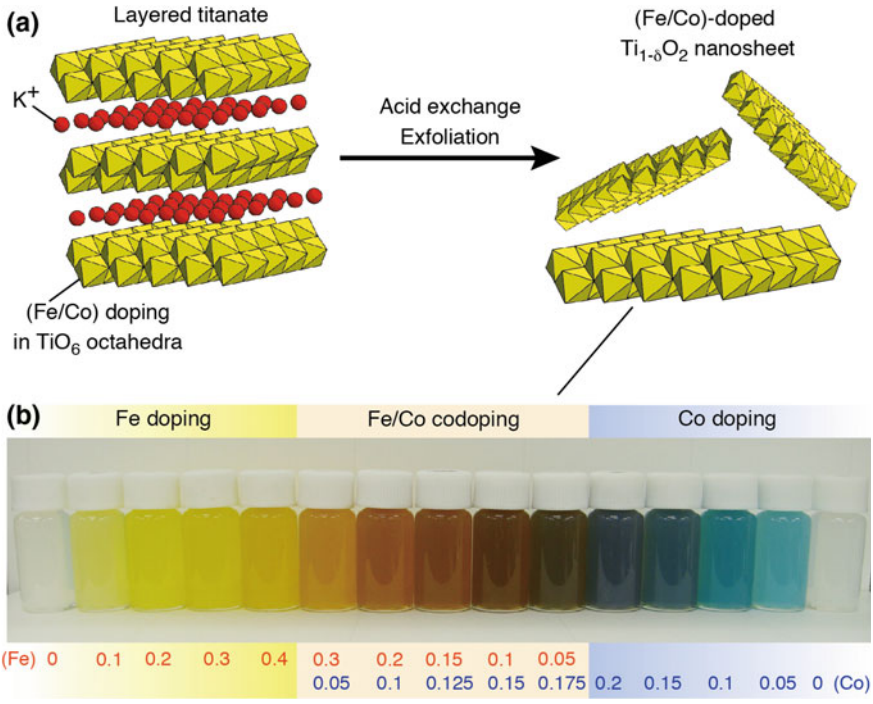

Fig. 13.2 Controlled doping in magnetic nanosheets ($Ti_{1-x-y}Fe_xCo_yO_2$)

usually quite small with the lateral dimension less than 100 nm. Also, the nanosheets, derived from mechanical separation and growth techniques, are formed on the substrate and thus not applicable as precursors for device assembly.

13.3 Electronic Devices Based on 2D Oxide Nanosheets

There is enormous interest in building electronic devices based on 2D materials. Thin-film device architectures based on 2D materials have attracted considerable interest in recent years because of intriguing physical properties and synergistic effects resulting from different 2D nanosheets. Van der Waals heterostructures based on graphene and other 2D analogs are one of the hot topics in materials science [3]. A particular focus is on establishing nanoarchitectures of 2D nanosheets through finely controlled synthesis, hierarchically structured assembly and device design. The resulting stack represents new artificial material assembled in a chosen sequence—as in building with LEGO—with blocks defined with one atomic layer precision.

2D oxide nanosheets have recently become a unique playground for such LEGO-like games. An important aspect of oxide nanosheets is that various nanostructures can be fabricated using them as 2D building blocks [6, 12, 33]. In practice, colloidal nanosheets can be organized into various nanostructures or combined with a range of foreign materials at the nanometer scale by applying solution-based synthetic techniques involving layer-by-layer assembly and Langmuir–Blodgett deposition (Fig. 13.3). It is even possible to tailor superlattice-like assemblies by fusing and/or assembling with a wide range of materials, such as organic molecules, gels, polymers, and inorganic nanoparticles. Such soft-chemical protocols relying on the use of 2D building blocks and operating at room temperature open up pathways to create new artificial materials and devices with kinetically controlled, hierarchical nanoarchitectures, and tailored properties.

Various interesting and useful properties have been developed by organizing or assembling 2D oxide nanosheets into hybrid materials or multilayer films. Sophisticated functionalities or nanodevices can be designed through the selection of nanosheets and combining materials, and precise control over their arrangement at a molecular scale. Those include high-*k* nanocapacitors, all nanosheet field-effect transistors (FETs), artificial Pb-free ferroelectrics, magnetic superlattices (spin-electronic devices), plasmonic metamaterials, Li-ion batteries, supercapacitors, photovoltaics, photon-harvesting systems, etc.

In the nanosheets, 2D structures created by lateral confinement can potentially lead to not only the modification of electronic structures but also the modulation of electron-transport phenomena that arise from the quantum confinement effect. Unlike the gapless nature of graphene, most oxide nanosheets (with Ti^{4+}, Nb^{5+}, Ta^{5+}, W^{6+}) are have wide bandgap (3–4 eV) [34–36], and thus present a tantalizing prospect of scaling all oxide semiconductor technology down to a truly atomic

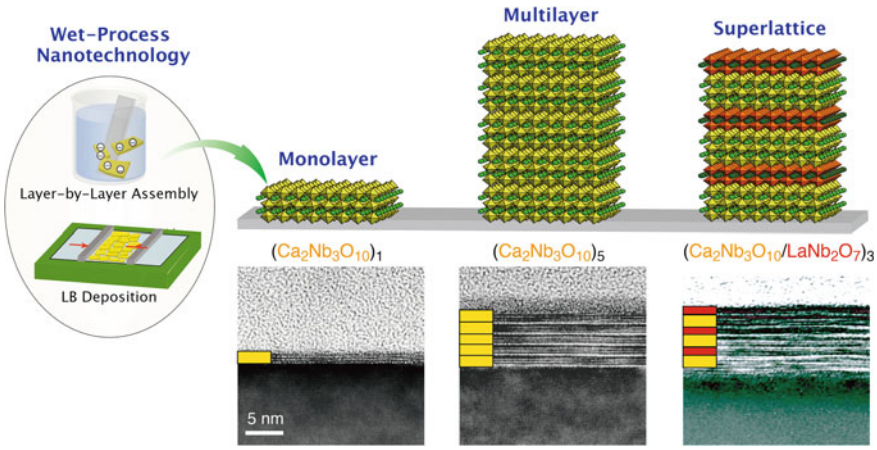

Fig. 13.3 Solution-based layer-by-layer assembly of oxide nanosheets

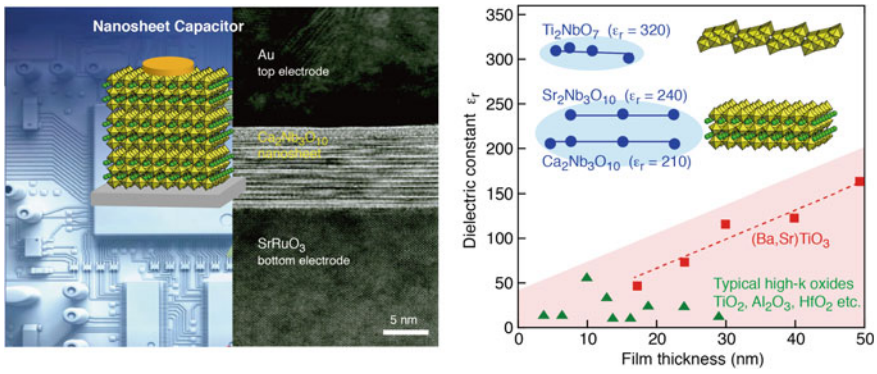

Fig. 13.4 (*Left*) Schematic illustration and TEM image of nanosheet-based capacitor (*Right*) Dielectric properties of oxide nanosheets and typical high-*k* films

scale. The availability of semiconduting nanosheets opens up possibilities for designing more complex nanodevices, such as photoconducting cells [37], *p-n* junctions [38], and FETs [5].

d^0 oxide nanosheets (with Ti^{4+}, Nb^{5+}, Ta^{5+}, W^{6+}) can also be utilized as high-*k* dielectrics, which are essential for many electronic devices, such as memories, capacitors, and gate insulators. Despite significant advances in graphene-like 2D nanosheets, it remains a challenge to explore high-*k* dielectric counterparts, which have great potential in new 2D electronics. Oxide nanosheets may be the perfect solution as a new era unfolds in 2D dielectrics and post-graphene technology [2, 8–10]. For example, titania- or perovskite-based nanosheets (Ti_2NbO_7, $(Ca,Sr)_2Nb_3O_{10}$) exhibited the highest permittivity (ε_r = 200–320) ever realized in all known dielectrics in the ultrathin region (<10 nm) (Fig. 13.4) [14, 15]. These nanosheets

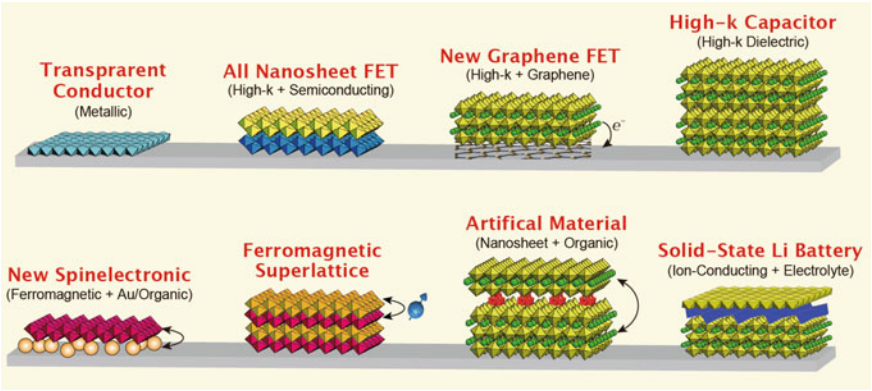

Fig. 13.5 LEGO-like game for materials design via 2D nanosheet architectonics

also retained both size-free high-ε_r characteristic (>200) and high insulation resistance ($\sim 10^{-7}$ A/cm^2) at high temperatures up to 250 °C [39, 40]. Notably, nanosheet-based capacitors exhibited an unprecedented capacitance density (~ 100 μF/cm^2), which was 1000 times higher than that of state-of-the art ceramic condensers [41]. The simultaneous improvement of ε_r and thermal stability in high-*k* nanodielectrics is of critical technological importance, and high-*k* nanosheest have great potential for a rational design and construction of high-temperature capacitors and energy storage devices. Another enticing possibility using high-*k* dielectric nanosheets is the layer-by-layer engineering of FET devices combined with graphene and semiconducting nanosheets [5, 42]. Such a superlattice allows the rational design of high-performance FET devices, which realize mobility enhancement by dielectric screening. These topics are an important target for "More & Beyond Moore" technology promoted by the International Technology Roadmap for Semiconductors.

Controlled assembly of 2D oxide nanosheets is useful for control of interlayer physical interactions and immobilization of functional nanostructures on device architectures (Fig. 13.5). Combining different nanosheets into desired superlattice structures can produce new electronic states at the interface and the opportunity to create artificial materials with novel properties.

Some examples with these advantages were demonstrated by superlattices of ferromagnetic and dielectric nanosheets. Superlattices of ferromagnetic nanosheets ($Ti_{0.8}Co_{0.2}O_2$, $Ti_{0.6}Fe_{0.4}O_2$) exhibited a gigantic magneto-optical response ($\sim 3 \times 10^5$ deg/cm) in the visible-wavelength region, which stems from the interlayer *d*–*d* transitions (Co^{2+}–Fe^{3+}) between adjacent nanosheets [22, 43]. This superlattice is thus regarded as an artificially constructed ferromagnet, where the charge, spin, and orbital degree of freedoms might be strongly coupled at the interface. Layering combinations can be created with infinite varieties and artificial layered structures with enhanced interface interactions can be formed with a great freedom of design. Such an architectonics concept can be utilized for designing

nanostructured ferroelectrics [44]. We fabricated an artificial superlattice by alternately stacking of two different dielectric nanosheets ($Ca_2Nb_3O_{10}$, $LaNb_2O_7$). By such an artificial structuring, we found that the ($Ca_2Nb_3O_{10}$/$LaNb_2O_7$) superlattice possesses a new form of interface coupling, which gives rise to ferroelectricity at room temperature. This artificial superlattice exhibited a robust ferroelectric property even at several nanometer thicknesses, which is essentially required for future memories.

The growing interest in nanosheet architectonics is not limited to electronic devices, but also proves a new route to energy and environment technologies. Important and attractive topics include: (i) Pb-free ferroelectrics [44, 45], (ii) nanosheet supercapacitors [17, 46], (iii) solid-state Li-ion batteries [47] and (iv) plasmonic photovoltaics [48], sensors [49]. For example, we recently developed new magneto-plasmonic nanoarchitectures consisted of 1-nm thick ferromagnetic nanosheets ($Ti_{0.8}Co_{0.2}O_2$) and Au nanoparticles [49]. This magneto-plasmonic nanosystem showed surface-plasmon-resonance on magneto-optical activity, which is appealing for new applications in all-optical magnetic data storage and nano-sensing. Further integration including photocataytic, photochromic, redoxable, and photoluminescent nanosheets could lead to unified optoelectronic and photon-harvesting systems [33, 50], such as visible-active photocatalysts, photon-harvesting systems, light-emitting devices, etc.

13.4 Conclusion and Outlook

We overviewed recent research on 2D oxides nanosheets and their architectonics for innovative materials and electronic devices. The virtually infinite varieties of oxide nanosheets, which can be used to assemble various nanoarchitectures, suggest that our nanosheet technology will contribute to striking progress in materials science, electronics, and energy/environmental technologies. Some examples indicate the potential importance of nanosheet architectonics for designing new artificial materials with tailored electronic properties. Artificially structured layered materials are capable of expressing totally novel properties based on the creation of new interfaces and layer interactions. In terms of technological applications, we focused only on some examples of electronic applications. However, considering the limitless combination of possibilities between nanosheets and other modules, we foresee developing fusion materials and more complex devices exhibiting a wide range of new and sophisticated functions. We hope that all aspects described here demonstrate the great potential of oxide nanosheets, introducing more exciting properties and wide-ranging applications in the future.

References

1. Geim AK, Novoselov KS (2007) Nat Mater 6:183–191
2. Geim AK (2009) Science 324:1530–1534
3. Geim AK, Grigorieva IV (2013) Nature 499:419–425
4. Sasaki T (2007) J Ceram Soc Jpn 115:9–16
5. Osada M, Sasaki T (2009) J Mater Chem 19:2503–2511
6. Ma R, Sasaki T (2010) Adv Mater 22:5082–5104
7. Mas-Balleste R, Gomez-Navarro C, Gomez-Herrero J, Zamora F (2011) Nanoscale 3:20–30
8. Osada M, Sasaki T (2012) Adv Mater 24:210–228
9. Chhowalla M, Shin HS, Eda G, Li LJ, Loh KP, Zhang H (2013) Nat Chem 5:263–275
10. Butler SZ, Hollen SM, Cao L, Cui Y, Gupta JA, Gutiérrez HR, Heinz TF, Hong SS, Huang J, Ismach AF, Johnston-Halperin E, Kuno M, Plashnitsa VV, Robinson RD, Ruoff RS, Salahuddin S, Shan J, Shi L, Spencer MG, Terrones M, Windl W, Goldberger JE (2013) ACS Nano 7:2898–2926
11. Wang L, Sasaki T (2014) Chem Rev 114:9455–9486
12. Osada M, Sasaki T (2015) Polym J 47:89–98
13. Osada M, Ebina Y, Funakubo H, Yokoyama S, Kiguchi T, Takada K, Sasaki T (2006) Adv Mater 18:1023–1027
14. Osada M, Akatsuka K, Ebina Y, Funakubo H, Ono K, Takada K, Sasaki T (2010) ACS Nano 4:5225–5232
15. Osada M, Takanashi G, Li BW, Akatsuka K, Ebina Y, Ono K, Funakubo H, Takada K, Sasaki T (2011) Adv Funct Mater 21:3482–3487
16. Omomo Y, Sasaki T, Wang LZ, Watanabe M (2003) J Am Chem Soc 125:3568–3575
17. Sugimoto W, Iwata H, Yasunaga Y, Murakami Y, Takasu Y (2003) Angewandte Chemie-Int Ed 42:4092–4096
18. Fukuda K, Akatsuka K, Ebina Y, Ma R, Takada K, Nakai I, Sasaki T (2008) ACS Nano 2:1689–1695
19. Fukuda K, Akatsuka K, Ebina Y, Osada M, Sugimoto W, Kimura M, Sasaki T (2011) Inorg Chem 51:1540–1543
20. Sato J, Kato H, Kimura M, Fukuda K, Sugimoto W (2010) Langmuir 26:18049–18054
21. Osada M, Ebina Y, Fukuda K, Ono K, Takada K, Yamaura K, Takayama-Muromachi E, Sasaki T (2006) Phys Rev B 73:153301
22. Osada M, Ebina Y, Takada K, Sasaki T (2006) Adv Mater 18:295–299
23. Dong XP, Osada M, Ueda H, Ebina Y, Kotani Y, Ono K, Ueda S, Kobayashi K, Takada K, Sasaki T (2009) Chem Mater 21:4366–4373
24. Osada M, Sasaki T (2012) Int J Appl Ceram Technol 9:29–36
25. Ebina Y, Akatsuka K, Fukuda K, Sasaki T (2012) Chem Mater 24:4201–4208
26. Osada M, Itose M, Ebina Y, Ono K, Ueda S, Kobayashi K, Sasaki T (2008) Appl Phys Lett 92:253110
27. Osada M, Yoguchi S, Itose M, Li BW, Ebina Y, Fukuda K, Kotani Y, Ono K, Ueda S, Sasaki T (2014) Nanoscale 6:14227–14236
28. Ozawa TC, Fukuda K, Akatsuka K, Ebina Y, Sasaki T (2007) Chem Mater 19:6575–6580
29. Ozawa TC, Fukuda K, Akatsuka K, Ebina Y, Sasaki T, Kurashima K, Kosuda K (2008) J Phys Chem C 112:17115–17120
30. Ida S, Ogata C, Eguchi M, Youngblood WJ, Mallouk TE, Matsumoto Y (2008) J Am Chem Soc 130:7052–7059
31. Novoselov KS, Jiang D, Schedin F, Booth TJ, Khotkevich VV, Morozov SV, Geim AK (2005) Proc National Acad Sci U S A 102:10451–10453
32. Kai K, Yoshida Y, Kageyama H, Saito G, Ishigaki T, Furukawa Y, Kawamata J (2008) J Am Chem Soc 130:15938–15943
33. Gunjakar JL, Kim IY, Lee JM, Jo YK, Hwang S-J (2014) J Phys Chem C 118:3847–3863
34. Sasaki T, Watanabe M (1997) J Phys Chem B 101:10159–10161

35. Sakai N, Ebina Y, Takada K, Sasaki T (2004) J Am Chem Soc 126:5851–5858
36. Akatsuka K, Takanashi G, Ebina Y, Haga M, Sasaki T (2012) J Phys Chem C 116:12426–12433
37. Sakai N, Fukuda K, Omomo Y, Ebina Y, Takada K, Sasaki T (2008) J Phys Chem C 112:5197–5202
38. Sato H, Okamoto K, Tamura K, Yamada H, Saruwatari K, Kogure T, Yamagishi A (2008) Appl Phys Express 1:035001
39. Li B-W, Osada M, Ebina Y, Akatsuka K, Fukuda K, Sasaki T (2014) ACS Nano 8:5449–5461
40. Kim YH, Kim HJ, Osada M, Li BW, Ebina Y, Sasaki T (2014) ACS Appl Mater Interfaces 6:19510–19514
41. Wang C, Osada M, Ebina Y, Li BW, Akatsuka K, Fukuda K, Sugimoto W, Ma R, Sasaki T (2014) ACS Nano 8:2658–2666
42. Li W, Li S-L, Komatsu K, Aparecido-Ferreira A, Lin Y-F, Xu Y, Osada M, Sasaki T, Tsukagoshi K (2013) Appl Phys Lett 103:023113
43. Osada M, Sasaki T, Ono K, Kotani Y, Ueda S, Kobayashi K (2011) ACS Nano 5:6871–6879
44. Li B-W, Osada M, Ozawa TC, Ebina Y, Akatsuka K, Ma R, Funakubo H, Sasaki T (2010) ACS Nano 4:6673–6680
45. Li BW, Osada M, Akatsuka K, Ebina Y, Ozawa TC, Sasaki T (2011) Jpn J Appl Phys 50:09NA10
46. Makino S, Shinohara Y, Ban T, Shimizu W, Takahashi K, Imanishi N, Sugimoto W (2012) RSC Adv 2:12144–12147
47. Xu X, Takada K, Fukuda K, Ohnishi T, Akatsuka K, Osada M, Hang BT, Kumagai K, Sekiguchi T, Sasaki T (2011) Energy Environ Sci 4:3509–3512
48. Sakai N, Sasaki T, Matsubara K, Tatsuma T (2010) J Mater Chem 20:4371–4378
49. Osada M, Hajduková-Šmídová N, Akatsuka K, Yoguchi S, Sasaki T (2013) J Mater Chem C 1:2520
50. Luo B, Liu G, Wang L (2016) Nanoscale 8:6904–6920

Chapter 14
Photoenergy Conversion

Yohei Ishida and Shinsuke Takagi

14.1 Introduction

Inorganic nanosheets are utilized for converting or harvesting energy. The modern world is reliant on the use of energy in various forms, including photo, electrical, chemical, potential, mechanical, nuclear, and thermal energy. Efficient interconversion among these energy forms is crucial to the functioning of today's society. This chapter will focus on the conversion of photoenergy into other forms of energy using inorganic nanosheets. Inorganic nanosheet-based photoenergy conversion materials have an advantage due to their unique properties, such as highly crystalline two-dimensional surfaces, high aspect ratios, and the separation of the front and back sides by atomically thin surfaces. Inorganic nanosheet-based photoenergy conversion has been reported in various fields, and this chapter briefly reviews the conversion of photoenergy into chemical, electrical, and mechanical energy, as well as other photoenergies (wavelength conversion or light harvesting).

Y. Ishida
Division of Material Science and Engineering, Faculty of Engineering,
Hokkaido University, Kita 13, Nishi 8, Kita-Ku, Sapporo, Hokkaido 060-8628, Japan

S. Takagi (✉)
Department of Applied Chemistry, Graduate Course of Urban Environmental Sciences,
Tokyo Metropolitan University, Minami-Ohsawa 1-1, Tokyo 192-0397, Japan
e-mail: takagi-shinsuke@tmu.ac.jp

T. Nakato et al. (eds.), *Inorganic Nanosheets and Nanosheet-Based Materials*,
Nanostructure Science and Technology, DOI 10.1007/978-4-431-56496-6_14

14.2 Conversion of Photoenergy into Chemical Energy

Photocatalysis, the general process of converting photoenergy into chemical energy, has been extensively investigated since Fujishima and Honda first reported photocatalytic water splitting using a titanium dioxide (TiO_2) semiconductor [1]. TiO_2 photocatalysis has been developed for use in both organic pollutant degradation and hydrogen generation via water splitting.

Among various oxide semiconductor photocatalysts [2], TiO_2 has proven the most suitable for widespread use in solar energy conversion and environmental applications due to its chemical inertness, strong oxidizing power, low cost, and long-term stability. Moreover, exfoliated titanium oxide nanosheets have received considerable attention [3].

As exfoliated nanosheets in suspension provide almost infinite available spaces for guest species to homogeneously adsorb the nanosheet surfaces, nanosheet-based photocatalysts are expected to have unique characteristics.

The photocatalytic decomposition of harmful organic compounds in water or air is a promising process for environmental remediation and has been studied using titania nanosheet photocatalysts under UV irradiation. For example, the nanocomposite prepared by pillaring $Ti_{0.91}O_2^{0.36-}$ nanosheets with TiO_2 nanoparticles via an exfoliation-reassembly process efficiently decomposed organic pollutants such as methylene blue and 4-chlorophenol under UV light irradiation [4].

Photocatalytic water splitting for hydrogen generation using titania nanosheets has also been reported. As the conduction band minimum position of layered titanate is only slightly higher than the redox couple potential of H^+/H_2, titania nanosheets do not provide strong reduction for water splitting. For example, nitrogen-doped titanate exhibited apparent visible-light absorption up to 450 nm [5], whereas its performance in water splitting for hydrogen generation was nearly negligible. Osterloh and co-workers systematically studied the change in the optical, vibrational, electronic, and photocatalytic properties of multi-layered titanates $A_2Ti_4O_9$ (A = K, H, TBA) [6]. The catalytic activity of all titanates was limited by the potential of the conduction band edge, which is too low for efficient H_2 evolution in a neutral solution (Fig. 14.1). With the assistance of cocatalysts, such as Pt metal, $Ti_{0.91}O_2^{0.36-}$ exhibited a moderate hydrogen production yield. Loading with Pt shifted the band edge of all titanates toward oxidizing potentials (Fig. 14.1), which was attributed to Fermi level equilibration across the titanate-platinum interface.

Layered niobate is one of the other examples of a nanosheet-based photocatalyst, although Nb_2O_5 is not a photocatalyst under UV irradiation [7]. Chemical exfoliation of $K_4Nb_6O_{17}$ and the similarly structured Dion–Jacobsen phase $KCa_2Nb_3O_{10}$ produces 1 nm thin single-crystalline nanosheets or scrolls. The crystalline nanosheets and their Pt and IrO_2-modified derivatives showed photocatalytic activity in water splitting [7–9].

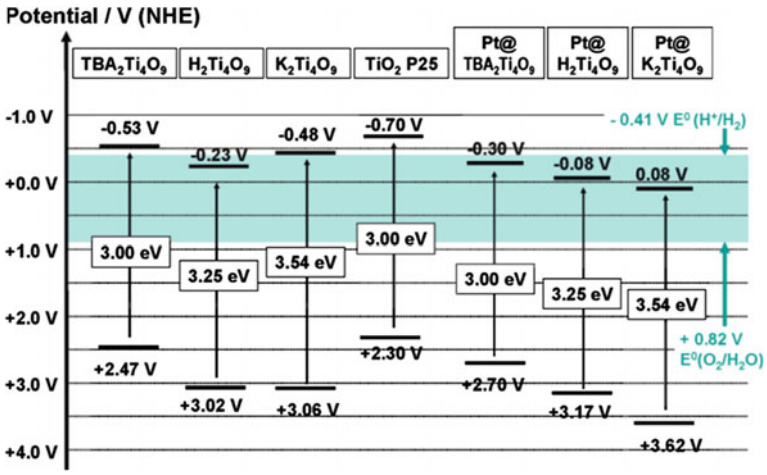

Fig. 14.1 Band gap potentials of various layered titanate and $Ti_4O_9^{2-}$ nanosheets determined by optical and photoelectrochemical measurements. Experimental data for TiO_2 P25 nanoparticles are included for comparison. Reprinted with permission from Ref. [6] (copyright 2010, American Chemical Society)

14.3 Conversion of Photoenergy into Electrical Energy

Devices used to convert photoenergy into electrical energy are generally called photovoltaic devices. Several types of efficient and mature photovoltaic devices have been developed, and can be distinguished according to their content and structure. Well-established photovoltaic materials on inorganic bases include silicon, III-V and II-VI PN junctions, and copper-indium-gallium-selenium (CIGS) photovoltaic devices [2].

As described in the previous chapter, TiO_2 is the most common semiconductor photocatalyst, but it is also widely used in photovoltaic devices [2, 3]. The rapid transport and transfer of photogenerated electrons in these TiO_2 films is pivotal to improving the conversion efficiency from photoenergy to electrical energy. Generally, TiO_2 nanoparticles with a diameter of 10–20 nm were used; hence, the obtained film was usually transparent with little light scattering. The incorporation of relatively large particles (above 100 nm) has been employed at light-scattering centers to increase the optical length of the film, and enhanced light harvesting has been demonstrated [10]. The use of two-dimensional nanosheets with sizes approaching 100 nm should have a similar effect. As a result, such materials are expected to exhibit high light-harvesting efficiency and fast charge carrier motion due to the 2D crystalline surfaces.

To this end, Haga and co-workers reported novel photoelectrochemical devices using titania nanosheets with Zn porphyrin molecules fabricated by layer-by-layer techniques (Fig. 14.2) [11]. Closely packed titania nanosheet ($Ti_{0.91}O_2$) monolayers on indium tin oxide (ITO), mica, and quartz surfaces strongly adsorbed cationic

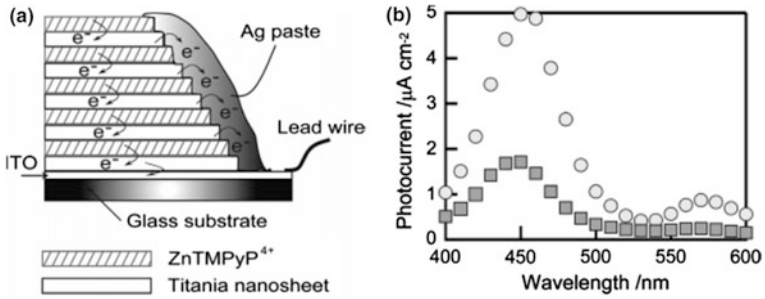

Fig. 14.2 **a** Schematic illustration of graduated multilayer film with Ag paste on an ITO electrode, **b** photocurrent action spectra of [($ZnTMPyP^{4+}$/titania nanosheet)$_5$/ITO] + Ag paste (*circle*) and ($ZnTMPyP^{4+}$/titania nanosheet)$_5$/ITO (*square*). Reprinted with a slight modification with permission from ref [11] (copyright 2007, American Chemical Society)

[5,10,15,20-tetrakis(1-methylpyridinium-4-yl)porphyrinatozinc]$^{4+}$ ($ZnTMPyP^{4+}$) via electrostatic interactions.

The visible-light irradiation of this multilayer film on an ITO electrode in the presence of triethanolamine as an electron donor resulted in an anodic photocurrent. The quantum yield for photocurrent generation by this two-layer film, with the electrode structure ITO/titania nanosheet/$ZnTMPyP^{4+}$, was estimated to be 8.63%. The titania nanosheet itself has a wide band gap (3.8 eV) due to the 2D quantum size effect. This caused vertical electron transport efficiency, through the alternately layered titania nanosheets and organic dyes such as $ZnTMPyP^{4+}$ on the solid surface, to lower as the number of layers increased due to the succession of vertical energy barriers. To overcome this limitation, the use of a lateral interlayer connection of all titania nanosheets with Ag paste was also examined, resulting in a significant improvement in photocurrent density compared with the bare titania nanosheet-$ZnTMPyP^{4+}$ system. Other types of inorganic nanosheets, such as $Ca_2Nb_3O_{10}^-$, $TiNbO_5^-$, $Ti_2NbO_7^-$, and $Ti_5NbO_{14}^{3-}$, have also been reported as novel photovoltaic materials [12].

14.4 Conversion of Photoenergy into Mechanical Energy

Photoresponsive mechanical materials are usually defined as having macroscopic-scale morphologies that are reversibly changed by photoirradiation. These materials are promising for applications in light-driven actuators and artificial muscles that are able to convert the photoenergy into mechanical energy. Many excellent photoresponsive mechanical materials have been reported, such as molecular single crystals [13], and liquid crystal polymers [14].

For this purpose, Inoue and co-workers focused on the use of inorganic nanosheets [15, 16]. They reported that upon photoirradiation of layered $K_4Nb_6O_{17}$

intercalated with a polyfluoroalkyl azobenzene surfactant, a very large magnitude lateral movement (sliding) of the nanosheets was reversibly induced. Nanosheet sliding has been clearly observed in a cross section of layered hybrid film, as a result of concomitant reversible *cis-trans* isomerization of the azobenzene moiety. Using photoirradiation at 368 and 463 nm, the total reversible sliding motion of the layered hybrid film reached ~1500 nm in the lateral direction. Furthermore, the thickness of the hybrid film (~450 nm) was reversibly changed by up to ±18 nm as each interlayer space shrank and expanded due to photoisomerization of the intercalated azobenzene derivative. This work shows that nanosheet-based photoinduced mechanical materials have an advantage due to their large two-dimensional surfaces and high aspect ratios.

14.5 Wavelength Conversion of Photoenergy and Light Harvesting

14.5.1 Theory of Förster Resonance Energy Transfer

Förster (or fluorescence) resonance energy transfer (FRET) is the transfer of photoexcitation energy from a donor fluorophore to an acceptor [17–19].

$$A^* + B \rightarrow A + B^* \tag{14.1}$$

Here, * denotes the electrically excited state, A and B denote energy donor and energy acceptor molecules, respectively.

The reaction rate constant for FRET is expressed as shown in Eq. 14.2,

$$k_{ET} = \frac{9\phi_D \kappa^2 ln10}{128\pi^5 n^4 N_A \tau_D R^6} \int f_D(v)\varepsilon_A(v)\frac{dv}{v^4} \tag{14.2}$$

where ϕ_D is the fluorescence quantum yield of the donor, n is the refractive index of the medium, N_A is Avogadro's number, κ^2 is the dipole orientation factor, τ_D is the excited lifetime of the donor in the absence of an acceptor, R is the distance between the donor and the acceptor, and the integral part represents the spectral overlap between the absorption spectrum of the energy acceptor and fluorescence spectrum of the energy donor. As can be seen from Eq. 14.2, the energy-transfer rate constant is inversely proportional to the sixth power of R. A large spectral overlap integral between the absorption spectrum of the energy acceptor and the fluorescence spectrum of the energy donor is necessary for efficient energy transfer. Moreover, a parallel arrangement of the transition dipoles enhances the FRET efficiency and a perpendicular orientation prevents FRET (expressed as κ^2 in Eq. 14.2) [20]. Generally, FRET phenomena are observable at donor–acceptor distances of around 20–60 Å when the spectral overlap is large enough [21–27].

Since FRET is a highly sensitive spectroscopic measurement technique for processes occurring on the nanometer and sub-nanometer scale, it has been widely used for qualitative and quantitative biochemical applications, such as DNA sequencing [28]. Moreover, a light-harvesting antenna in natural photosynthetic bacteria realizes highly efficient photoexcited energy-transfer processes for photosynthesis [29]. This has strongly encouraged researchers to study synthetic molecular or supramolecular FRET systems for artificial photosynthesis and artificial light-harvesting systems.

While research on FRET has been mainly focused on synthetic molecular systems, supramolecular biosystems (with DNA, peptides, etc.), or quantum dots, nanosheets have been well used in the twenty-first century [30]. The methodologies of using nanosheets can be categorized into two series: (1) the use of nonphotofunctional nanosheets as FRET reaction fields for organic guests, and (2) the use of photofunctional nanosheets as a FRET donor or acceptor. The advantages of such FRET research on 2D nanosheets are (i) effective control of κ^2 according to the 2D reaction field [20], (ii) ease of handling the materials due to their large size (several tens to thousands of nm), (iii) additionally, the photophysical characteristics of organic guests such as fluorescence quantum yields or lifetimes are sometimes enhanced [31, 32] by adsorption onto atomically flat 2D surfaces. Recent results on 2-dimensional FRET utilizing nanosheets will be reviewed.

14.5.2 *Nonphotofunctional Nanosheets as FRET Reaction Fields for Organic Guests*

Typical, anionic charged-clay minerals are useful materials for nonphotofunctional nanosheets because of their chemical stability, optical transparency in the visible region, and ease of handling [33]. Cationic guest molecules can form stable complexes through electrostatic interactions (and through hydrophobic interactions when applied in aqueous solution).

From the various types of anionic clay minerals, saponite (of the smectite group) is the focus of this chapter due to its suitable charge density. The typical chemical formula of saponite clay is expressed as $[(Si_{7.20}Al_{0.80})\text{-}(Mg_{5.97}Al_{0.03})O_{20}(OH)_4]^{-0.77}(Na_{0.77})^{+0.77}$. The experiments presented here have been carried out using an aqueous suspension of exfoliated single saponite nanosheets at low concentrations.

It is well known that organic molecules tend to aggregate and/or segregate on inorganic surfaces, mainly because of hydrophobic interactions and Van der Waals interactions between the organic molecules [34, 35]. Since H-aggregation and irregular aggregation drastically decrease the excited-state lifetime, efficient photochemical reactions such as FRET had been considered difficult in clay/dye complexes.

Uniform molecular adsorption on saponite surfaces was realized in the pioneering work by Takagi and Inoue in 2002 (Fig. 14.3) [36, 37]. Systematic experiments using numerous cationic porphyrin derivatives showed that a porphyrin molecule, which has a specific molecular structure, can be adsorbed on clay surfaces without concomitant aggregation, even under high-density conditions. Such nonaggregated alignment results from distance matching due to guest—host Coulombic interactions between the positively charged dye molecules and the negatively charged-clay surface. This effect was termed the "size-matching effect." The average center-to-center intermolecular distance was determined to be 2.4 nm under saturated adsorption conditions based on a hexagonal array. This value is most interesting from the viewpoint of photochemistry, because the interaction between the transition moments of adjacent porphyrin molecules (aggregation) is negligible; however, interactions in the excited state are possible. Thus, efficient photochemical reactions such as FRET are expected.

FRET between two different kinds of porphyrins (*m*-TMPyP(D) and *p*-TMPyP (A)) was investigated by steady-state and time-resolved fluorescence measurements [38]. A decrease in donor fluorescence and an increase in acceptor fluorescence were observed as the dye loading increased (Fig. 14.4 left). Clear isoemissive points were observed, as indicated by the arrows in the figure.

In Fig. 14.4 right, the energy-transfer efficiencies (η_{ET}) are plotted against the porphyrin loading levels. η_{ET} increased with increasing porphyrin loading levels, because the average intermolecular distance between the porphyrins decreased. Notably, the maximum η_{ET} reached $\sim$100% at higher acceptor ratios and dye loadings. The mechanism of the FRET process has been investigated by time-resolved fluorescence spectroscopy.

In spite of the advantages of saponite–porphyrin systems, a limitation is that anionic clay nanosheets could only be used as hosts for cationic adsorbent molecules. Neutral molecules, such as aromatics, do not adsorb on these surfaces. A new strategy has been developed to overcome this problem. The strategy involved a supramolecular approach in which a cationic organic host system, which included a neutral guest molecule, was adsorbed on anionic saponite surfaces [39, 40].

A cavitand containing eight ammonium groups (octaamine, OAm [41]) was used as the host for neutral organic molecules (Fig. 14.5). Strong Coulombic attractions

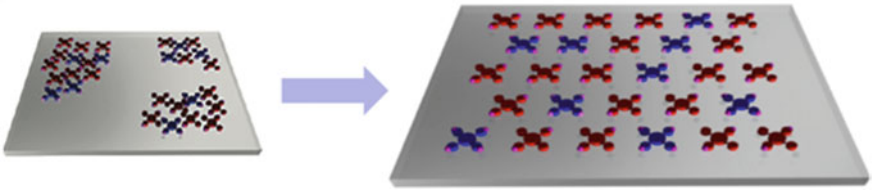

Fig. 14.3 Schematic representation of a saponite/porphyrin supramolecular complex. The guest porphyrins adsorb on the saponite surface as monomers without aggregation through the "size-matching effect." Reprinted with permission from Ref [38] with a slight modification (copyright 2011, American Chemical Society)

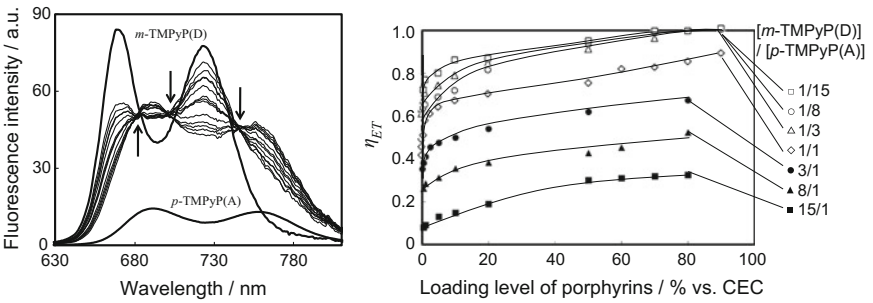

Fig. 14.4 *Left.* The fluorescence spectra for *m*-TMPyP(D)/*p*-TMPyP(A)/saponite complexes. The *thick lines* are the individual fluorescence spectra of the *m*-TMPyP(D)/saponite and *p*-TMPyP(A)/saponite complexes. The *arrows* indicate isoemissive points. *Right.* The energy-transfer efficiencies at various loading levels and ratios of porphyrins. Reprinted with permission from Ref. [38] (copyright 2011, American Chemical Society)

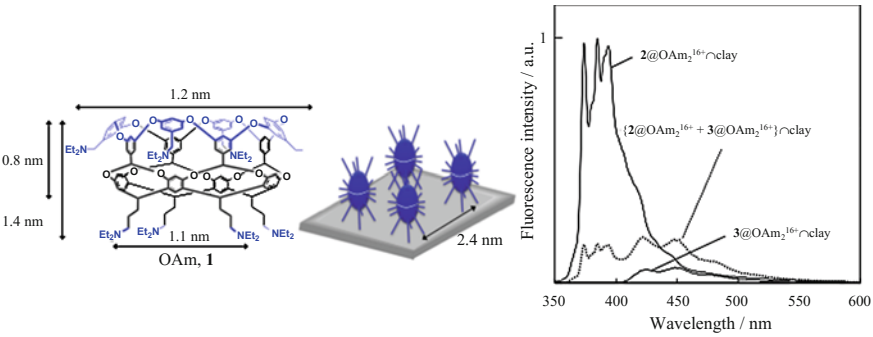

Fig. 14.5 Structure of octaamine cavitand (OAm, **1**), a plausible adsorption structure model of guest@OAm_2^{16+} on saponite surfaces under maximum adsorption conditions, and fluorescence spectra for the {**2**@OAm_2^{16+} + **3**@OAm_2^{16+}} ∩ clay complex and respective **2**@OAm_2^{16+} ∩ clay and **3**@OAm_2^{16+} ∩ clay complexes. Reprinted with permission from Ref. [40] with a slight modification (copyright 2013, American Chemical Society)

between the ammonium groups and the anionic saponite anchored OAm to the nanosheets. Since OAm forms capsular assemblies with neutral organic guest molecules, energy transfer between two OAm capsules, one containing a donor molecule (pyrene, **2**) and the other encapsulating an acceptor molecule (2-acetylanthracene, **3**), adsorbed on saponite surfaces was investigated [40]. The efficient FRET between **2**@OAm_2^{16+} (pyrene encapsulated within two OAm^{8+} species) and **3**@OAm_2^{16+} adsorbed on saponite nanosheets was demonstrated by monitoring the fluorescence intensities and lifetimes. With increased loading levels of guests, the fluorescence intensity of donor **2** decreased, while that of acceptor **3** increased (Fig. 14.5 right). This suggested the possibility of FRET in the current system. η_{ET} was determined to be 85%. As expected, owing to the decreased intermolecular distance, η_{ET} increased with the loading level. By the detailed

time-resolved fluorescence measurement, FRET rate constant was calculated to be $1.4 \times 10^7\ s^{-1}$.

As summarized above, supramolecular surface photochemistry has undergone significant development recently [37, 38, 42–44]. Recent developments and understandings of molecular attitudes on inorganic surfaces greatly encourage the application of these nanosheet–dye systems in photonics fields.

14.5.3 Photofunctional Nanosheets as FRET Donor/Acceptors

Some photofunctional nanosheets, such as graphene oxide or transition metal dichalcogenides, have been used as FRET donor or acceptors in combination with other organic dyes or quantum dots. In this chapter, FRET phenomena utilizing the excited state of nanosheet materials will be reviewed.

Graphene is a one-atom-thick planar sheet of sp^2-bonded carbon atoms ordered in a two-dimensional honeycomb lattice [45]. Graphene oxide (GO) consists of a similar atomically thin structural lattice, but possesses oxygen-containing functional groups [46]. Consequently, GO possesses recombined electron–hole pairs localized within a small sp^2 carbon domain embedded in a sp^3 matrix, and displays photoluminescence properties. Due to its heterogeneous structure containing various densities and distributions of carboxyl or hydroxyl groups, predominantly arising from differences in synthesis processes, GO can be fluorescent over a broad range of wavelengths from the near IR to UV regions. Thus, GO can be used as a FRET donor or acceptor when its emission wavelength is properly controlled [47–49].

Dong and co-workers demonstrated the first efficient FRET between quantum dots (QDs) and GO for biosensing applications [50]. Specifically, CdTe QDs, conjugated with a molecular beacon (MB), were used to detect DNA concentration and sequence, as well as to detect proteins such as thrombin. By the surface modification of QDs with a MB, the FRET between QDs and GO and the strong interaction between the ssDNA of the MB loop structure and GO were combined to develop a novel sensitive and selective platform for fluorescence quenching detection of DNA. Upon recognition of the MB to the target, the increasing QD-GO distance and the weakened DNA-GO interaction significantly hindered the FRET, and thus, increased the fluorescence of the QDs (Fig. 14.6 left).

The specificity of the MB-QD probe was studied using three kinds of DNA sequences, including a perfectly complementary target, a single-base mismatched strand, and a three-base mismatched strand. Specifically, the MB-QD probe differentiated between the perfectly complementary target, single-base mismatched strand (signal was 40% of that of the perfectly complementary target), and three-base mismatched strand (signal was 15%). Moreover, the quenching efficiency was much higher for MB-QDs than the typical efficiency seen in MB-based detection, which helped to improve the achievable sensitivity and dynamic range.

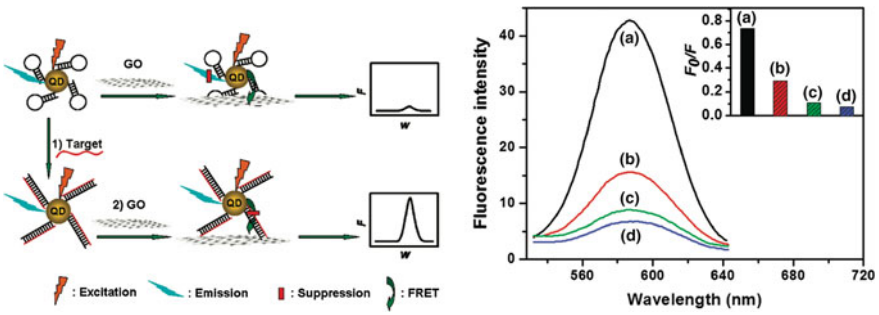

Fig. 14.6 Left: Schematic representation of GO-induced fluorescence quenching of MB-QDs and the biosensing mechanism through FRET. *Right* Fluorescence spectra of MB-QDs after incubation with **a** target, **b** single-base mismatch stand, **c** three-base mismatch stand, and **d** no target, followed by addition of GO for 5 min. Inset: fluorescence intensity ratio F_0/F. Reprinted with permission from ref [50] (copyright 2010, American Chemical Society)

These results demonstrated that the proposed approach could effectively detect the target with high specificity and had potential applications in single nucleotide polymorphism analysis.

Single- or several-layered transition metal dichalcogenides (TMDs) are another example of photofunctional–nanosheet-based FRET [51, 52]. TMDs are generally expressed as MX_2, where M is a transition metal of groups 4–10 and X is a chalcogen. Exfoliation of the bulk TMDs into mono- or few-layer structures largely preserves their properties, and also leads to additional characteristics due to confinement effects.

Molybdenum disulfide (MoS_2) is a widely known layered TMD. It is an indirect-band-gap semiconductor with an energy gap of $\sim$1.29 eV in the bulk form (although it does not show virtual emission) and has also attracted interest as a photovoltaic and photocatalytic material. The band gap of MoS_2 increases on decreasing crystal thickness below 100 nm due to quantum confinement effects, and the quantum yield drastically increases from the bulk form. In addition to the increase in its size, the nature of the band gap also changes from indirect to direct when the thickness reaches a single monolayer. Recent success in isolating MoS_2 monolayers has allowed the observation of strong photoluminescence that can be attributed to the direct-gap electronic structure of monolayer MoS_2 [53].

Prins and co-workers have recently reported systematic FRET phenomena from colloidal quantum dots to exfoliated monolayer and few-layer MoS_2 [54]. They used CdSe/CdZnS core/shell QDs, whose emission spectrum overlaps with the direct excitonic absorption of MoS_2. Monolayer and few-layer MoS_2 nanosheets were deposited on Si/SiO_2 substrates, and QDs were deposited by spin-coating to form a submonolayer that is uniformly $\leq$1-QD thick.

Figure 14.7a shows a bright-field optical micrograph of a MoS_2 flake prior to the deposition of QDs. The different colors indicate that there are several thicknesses present. For the observed region in Fig. 14.7a, the thickness was identified by micro-Raman measurements as bulk-like thickness (>8 layers) down to monolayer

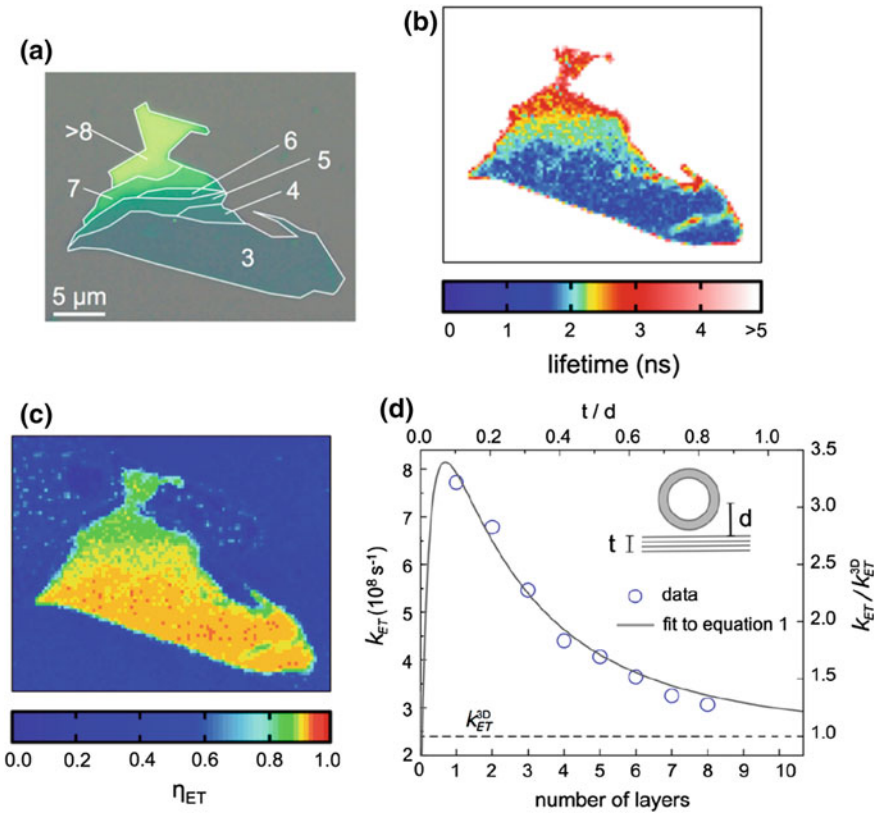

Fig. 14.7 **a** Optical micrograph of a mechanically exfoliated MoS_2 flake with indicated layer thicknesses of the different facets. **b** QD fluorescence lifetime map of the same flake with a saturated color scale to emphasize the lifetime variations within the flake area. **c** Energy-transfer efficiency map of the same flake. Scale bar is identical for all three panels. **d** Energy-transfer rate as a function of the number of MoS_2 layers. The *dashed line* represents the energy-transfer rate to thick, bulk-like MoS_2, and the *circles* indicate experimental data. Inset: schematic representation of the definition of the thickness (t) and distance (d) parameters. Reprinted with permission from Ref. [54] with a slight modification (copyright 2014, American Chemical Society)

thickness (depicted as numbers in the Figure). Fluorescence lifetime decays of QDs were observed by laser-scanning microscopy (Fig. 14.7b). The fluorescence lifetime of QDs located away from the flake was close to their native lifetime of 20.4 ns, while those of the QDs on top of the MoS_2 were significantly shortened, indicating the strong quenching of the QD excited state by FRET to the MoS_2 nanosheets. Interestingly, the lifetime was dependent on flake thickness, with the strongest QD quenching occurring for the thinnest regions of MoS_2. The differences in QD lifetimes and calculated energy-transfer efficiencies on layered MoS_2 with varying thicknesses can be expressed as 2D mapping images, as shown in Fig. 14.7b and c, respectively. As a result of systematic experiments, the energy-

transfer rates corresponding to the different thicknesses ranging from 1 to 8 layers were determined with the energy-transfer rate in the bulk limit (Fig. 14.7d).

Similarly, organic nanosheets, such as graphitic carbon nitrides [55], hexagonal boron nitrides [56], synthetic 2D polymers [57], and supramolecular metal-complex nanosheets [58], are also promising as novel 2D FRET systems.

FRET is now a promising tool due to its distance dependence; $k_{ET} \propto R^{-6}$ (Eq. 14.2), especially for biological nanoscale analyzes. Moreover, 2D FRET is a promising candidate for accomplishing artificial photosynthesis; an artificial light-harvesting system (which generally requires stepwise efficient FRET processes) and an artificial reaction center complex, a leading candidate in renewable energy production. Hence, nanosheet-based efficient FRET or other photophysical processes are greatly encouraged for future energy and environmental applications.

14.6 Summary

In this chapter, inorganic nanosheet-based photoenergy conversion systems have been briefly reviewed. Some representative works have already reported efficient photoenergy conversion as well as the effective utilization of unique advantages of two-dimensional nanosheets. Novel and more efficient photoenergy conversion systems using inorganic nanosheets with a help of molecules, nanoparticles or other kinds of inorganic nanosheets are highly desired in order to realize future sustainable society.

References

1. Fujishima A, Honda K (1972) Electrochemical photolysis of water at a semiconductor electrode. Nature 238:37–38
2. Osterloh FE (2013) Inorganic nanostructures for photoelectrochemical and photocatalytic water splitting. Chem Soc Rev 42:2294–2320
3. Wang L, Sasaki T (2014) Titanium oxide nanosheets: graphene analogues with versatile functionalities. Chem Rev 114:9455–9486
4. Paek S-M, Jung H, Lee Y-J, Park M, Hwang S-J, Choy J-H (2006) Exfoliation and reassembling route to mesoporous titania nanohybrids. Chem Mater 18:1134–1140
5. Liu G, Wang L, Sun C, Chen Z, Yan X, Cheng L et al (2009) Nitrogen-doped titania nanosheets towards visible light response. Chem Commun 1383–1383
6. Allen MR, Thibert A, Sabio EM, Browning ND, Larsen DS, Osterloh FE (2010) Evolution of physical and photocatalytic properties in the layered titanates $A_2Ti_4O_9$ (A = K, H) and in nanosheets derived by chemical exfoliation. Chem Mater 22:1220–1228
7. Domen K, Kudo A, Shibata M, Tanaka A, Maruya KI, Onishi T (1986) Novel photocatalysts, ion-exchanged $K_4Nb_6O_{17}$, with a layer structure. J Chem Soc Chem Commun 1706–1712
8. Sayama K, Tanaka A, Domen K (1991) Photocatalytic decomposition of water over platinum-intercalated potassium niobate ($K_4Nb_6O_{17}$). J Phys Chem 95:1345–1348

9. Compton OC, Mullet CH, Chiang S, Osterloh FE (2008) A building block approach to photochemical water-splitting catalysts based on layered niobate nanosheets. J Phys Chem C 112:6202–6208
10. Tan B, Wu Y (2006) Dye-sensitized solar cells based on anatase TiO_2 nanoparticle/nanowire composites. J Phys Chem B 110:15932–15938
11. Akatsuka K, Ebina Y, Muramatsu M, Sato T, Hester H, Kumaresan D et al (2007) Photoelectrochemical properties of alternating multilayer films composed of titania nanosheets and Zn porphyrin. Langmuir 23:6730–6736
12. Akatsuka K, Takanashi G, Ebina Y, Haga M-A, Sasaki T (2012) Electronic band structure of exfoliated titanium- and/or niobium-based oxide nanosheets probed by electrochemical and photoelectrochemical measurements. J Phys Chem C 116:12426–12433
13. Irie M, Kobatake S, Horichi M (2001) Reversible surface morphology changes of a photochromic diarylethene single crystal by photoirradiation. Science 291:1769–1772
14. Yu Y, Nakano M, Ikeda T (2003) Directed bending of a polymer film by light. Nature 425:145–145
15. Nabetani Y, Takamura H, Hayasaka Y, Shimada T, Takagi S, Tachibana H et al (2011) A photoactivated artificial muscle model unit: reversible, photoinduced sliding of nanosheets. J Am Chem Soc 133:17130–17133
16. Nabetani Y, Takamura H, Hayasaka Y, Sasamoto S, Tanamura Y, Shimada T et al (2013) An artificial muscle model unit based on inorganic nanosheet sliding by photochemical reaction. Nanoscale 5:3182
17. Perrin JB (1924) Fluorescence et lois générales relatives aux vitesses de réaction. Comptes rendus hebdomadaires des séances de l'Académie des Sci 178:1401–1406
18. Förster Th (1946) Energiewanderung und Fluoreszenz. Naturwissenschaften 6:166–175
19. Förster Th (1948) Zwischenmolekulare Energiewanderung und Fluoreszenz. Ann Phys 1–2:55–75
20. Baumann J, Fayer MD (1986) Excitation transfer in disordered two-dimensional and anisotropic three-dimensional systems: effects of spatial geometry on time-resolved observables. J Chem Phys 85:4087
21. Kelley RF, Lee SJ, Wilson TM, Nakamura Y, Tiede DM, Osuka A et al (2008) Intramolecular energy transfer within butadiyne-linked chlorophyll and porphyrin dimer-faced, self-assembled prisms. J Am Chem Soc 130:4277–4284
22. Hoffman JB, Choi H, Kamat PV (2014) Size-dependent energy transfer pathways in cdse quantum dot-squaraine light-harvesting assemblies: förster versus dexter. J Phys Chem C 118:18453–18461
23. Zhang X, Marocico CA, Lunz M, Gerard VA, Gun'ko YK, Lesnyak V et al (2014) Experimental and theoretical investigation of the distance dependence of localized surface plasmon coupled förster resonance energy transfer. ACS Nano 8:1273–1283
24. Becker K, Lupton JM, Müller J, Rogach AL, Talapin DV, Weller H et al (2006) Electrical control of Förster energy transfer. Nat Mater 5:777–781
25. Inagaki S, Ohtani O, Goto Y, Okamoto K, Ikai M, Yamanaka K-I et al (2009) Light harvesting by a periodic mesoporous organosilica chromophore. Angew Chem Int Ed 48:4042–4046
26. Hildebrandt N, Wegner KD, Algar WR (2014) Luminescent terbium complexes: superior Förster resonance energy transfer donors for flexible and sensitive multiplexed biosensing. Coord Chem Rev 273–274:125–138
27. Frischmann PD, Mahata K, Würthner F (2013) Powering the future of molecular artificial photosynthesis with light-harvesting metallosupramolecular dye assemblies. Chem Soc Rev 42:1847–1870
28. Silvi S, Credi A (2015) Luminescent sensors based on quantum dot-molecule conjugates. Chem Soc Rev 44:4275–4289
29. McDermott G, Prince SM, Freer AA, Hawthornthwaite-Lawless AM, Papiz MZ, Cogdell RJ et al (1995) Crystal structure of an integral membrane light-harvesting complex from photosynthetic bacteria. Nature 374:517–521

30. Takagi S, Tryk DA, Inoue H (2002) Photochemical energy transfer of cationic porphyrin complexes on clay surface. J Phys Chem B 106:5455–5460
31. Ishida Y, Shimada T, Takagi S (2014) Surface-fixation induced emission of porphyrazine dye by a complexation with inorganic nanosheets. J Phys Chem C 118:20466–20471
32. Villemure G, Detellier C, Szabo AG (1986) Fluorescence of clay-intercalated methylviologen. J Am Chem Soc 108:4658–4659
33. Shichi T, Takagi K (2000) Clay minerals as photochemical reaction fields. J Photochem Photobiol C Photochem Rev 1:113–130
34. Bujdák J (2006) Effect of the layer charge of clay minerals on optical properties of organic dyes. A review. Appl Clay Sci 34:58–73
35. Ghosh PK, Bard AJ (1984) Photochemistry of tris (2, 2′-bipyridyl) ruthenium (II) in colloidal clay suspensions. J Phys Chem 88:5519–5526
36. Takagi S, Shimada T, Eguchi M, Yui T, Yoshida H, Tryk DA et al (2002) High-density adsorption of cationic porphyrins on clay layer surfaces without aggregation: the size-matching effect. Langmuir 18:2265–2272
37. Takagi S, Shimada T, Ishida Y, Fujimura T, Masui D, Tachibana H et al (2013) Size-matching effect on inorganic nanosheets: control of distance, alignment, and orientation of molecular adsorption as a bottom-up methodology for nanomaterials. Langmuir 29:2108–2119
38. Ishida Y, Shimada T, Masui D, Tachibana H, Inoue H, Takagi S (2011) Efficient excited energy transfer reaction in clay/porphyrin complex toward an artificial light-harvesting system. J Am Chem Soc 133:14280–14286
39. Ishida Y, Kulasekharan R, Shimada T, Ramamurthy V, Takagi S (2014) Supramolecular-surface photochemistry: supramolecular assembly organized on a clay surface facilitates energy transfer between an encapsulated donor and a free acceptor. J Phys Chem C 118:10198–10203
40. Ishida Y, Kulasekharan R, Shimada T, Takagi S, Ramamurthy V (2013) Efficient singlet-singlet energy transfer in a novel host-guest assembly composed of an organic cavitand, aromatic molecules, and a clay nanosheet. Langmuir 29:1748–1753
41. Kulasekharan R, Ramamurthy V (2011) New water-soluble organic capsules are effective in controlling excited-state processes of guest molecules. Org Lett 13:5092–5095
42. Ishida Y, Shimada T, Takagi S (2013) Artificial light-harvesting model in a self-assembly composed of cationic dyes and inorganic nanosheet. J Phys Chem C 117:9154–9163
43. Ishida Y, Shimada T, Tachibana H, Inoue H, Takagi S (2012) Regulation of the collisional self-quenching of fluorescence in clay/porphyrin complex by strong host-guest interaction. J Phys Chem A 116:12065–12072
44. Ishida Y, Fujimura T, Masui D, Shimada T, Tachibana H, Inoue H et al (2011) What lowers the efficiency of an energy transfer reaction between porphyrin dyes on clay surface? Clay Sci 15:169–174
45. Rao CNR, Sood AK, Subrahmanyam KS, Govindaraj A (2009) Graphene: the new two-dimensional nanomaterial. Angew Chem Int Ed 48:7752–7777
46. Morales-Narváez E, Merkoçi A (2012) Graphene oxide as an optical biosensing platform. Adv Mater 24:3298–3308
47. Piao Y, Liu F, Seo TS (2011) The photoluminescent graphene oxide serves as an acceptor rather than a donor in the fluorescence resonance energy transfer pair of Cy3.5-graphene oxide. Chem Commun 47:12149–12151
48. Liu F, Choi JY, Seo TS (2010) Graphene oxide arrays for detecting specific DNA hybridization by fluorescence resonance energy transfer. Biosens Bioelectron 25:2361–2365
49. Balapanuru J, Yang J-X, Xiao S, Bao Q, Jahan M, Polavarapu L et al (2010) A graphene oxide-organic dye ionic complex with DNA-sensing and optical-limiting properties. Angew Chem Int Ed 49:6549–6553
50. Dong H, Gao W, Yan F, Ji H, Ju H (2010) Fluorescence resonance energy transfer between quantum dots and graphene oxide for sensing biomolecules. Anal Chem 82:5511–5517

51. Zhu C, Zeng Z, Li H, Li F, Fan C, Zhang H (2013) Single-layer MoS_2-based nanoprobes for homogeneous detection of biomolecules. J Am Chem Soc 135:5998–6001
52. Ha HD, Han DJ, Choi JS, Park M, Seo TS (2014) Dual role of blue luminescent MoS_2 quantum dots in fluorescence resonance energy transfer phenomenon. Small 10:3858–3862
53. Scheuschner N, Ochedowski O, Kaulitz A-M, Gillen R, Schleberger M, Maultzsch J (2014) Photoluminescence of freestanding single- and few-layer MoS_2. Phys Rev B 89:125406
54. Prins F, Goodman AJ, Tisdale WA (2014) Reduced dielectric screening and enhanced energy transfer in single- and few-layer MoS_2. Nano Lett 14:6087–6091
55. Wang Q, Wang W, Lei J, Xu N, Gao F, Ju H (2013) Fluorescence quenching of carbon nitride nanosheet through its interaction with DNA for versatile fluorescence sensing. Anal Chem 85:12182–12188
56. Song L, Ci L, Lu H, Sorokin PB, Jin C, Ni J et al (2010) Large scale growth and characterization of atomic hexagonal boron nitride layers. Nano Lett 10:3209–3215
57. Sakamoto J, van Heijst J, Lukin O, Schlüter AD (2009) Two-dimensional polymers: just a dream of synthetic chemists? Angew Chem Int Ed 48:1030–1069
58. Sakamoto R, Takada K, Sun X, Pal T, Tsukamoto T, Phua EJH et al (2016) The coordination nanosheet (CONASH). Coordin Chem Rev 320–321:118–128

Chapter 15
Photofunctional Nanosheet-Based Hybrids

Jayavant L. Gunjakar, In Young Kim and Seong-Ju Hwang

15.1 Introduction

One of the key challenges in material science is the design and development of novel functional materials with tailored architectures and unique functionalities. It is not easy to predict the ultimate properties of the obtained materials due to their structural and electronic complexity. Over the past decade, hybridization between different chemical species attracts a great deal of research activity because of its effectiveness not only in controlling the physicochemical properties of each component but also in creating unexpected functionality via synergistic coupling between the components [1–5]. This hybridization strategy provides an effective way to optimize the properties of the functional materials, which is far superior over the conventional design of materials using single component. Diverse nanostructured materials with expanded surface areas such as 0D quantum dots, 1D nanowires/nanotubes, 2D nanosheets, and 3D porous matrices become promising building blocks for the synthesis of hybrid materials, since chemical interaction between hybridized components occurs at their interface. Current progress in the research fields of 2D nanostructured materials makes possible the synthesis of diverse family of well-defined 2D nanosheets with highly anisotropic crystal structure and morphology, and subnanometer-level thickness [6–9]. In comparison with other nanostructured materials, the 2D nanosheets are more useful candidates for the synthesis of nanohybrid materials with emerging physicochemical properties

J.L. Gunjakar · I.Y. Kim · S.-J. Hwang (✉)
Department of Chemistry and Nanoscience College of Natural Sciences,
Ewha Womans University, Seoul 03760, Korea
e-mail: hwangsju@ewha.ac.kr

J.L. Gunjakar
e-mail: jlgunjakar@gmail.com

I.Y. Kim
e-mail: thinkgood04@gmail.com

T. Nakato et al. (eds.), *Inorganic Nanosheets and Nanosheet-Based Materials*,
Nanostructure Science and Technology, DOI 10.1007/978-4-431-56496-6_15

since all the component ions of the 2D nanosheets are exposed to their surface and thus can be remarkably modified by the hybridization with hybridized foreign species [1, 2, 10–15]. Over the past decades, reduced graphene oxide (rG-O) nanosheets prepared by the exfoliation of graphite oxide, and their nanohybrids receive intense research interest because of their unique physicochemical properties and valuable functionalities. Currently research interest on the rG-O is extended to 2D nanostructured inorganic solids with diverse crystal structures, chemical compositions, and surface properties [1, 2]. As inorganic analogs of graphene, the exfoliated 2D inorganic nanosheets can be synthesized by soft-chemical exfoliation reaction of the pristine layered inorganic solids. The resulting 2D nanosheets of inorganic solids show a broad spectrum of physicochemical properties from insulating to metallic and from diamagnetic to ferromagnetic. More importantly, their properties are tunable by changing the chemical composition and crystal structure of the pristine compound [1, 6, 16–19]. This fact opens up a new paradigm of 'hybrid materials on demand' by providing unique opportunities for the hybridization of 2D nanosheet with practically unlimited guest species including inorganic, organic, polymeric, and bio molecules/nanostructures [1, 11]. Such a hybridization approach using 2D inorganic nanosheets as platforms furnishes various hybrid structures with diverse physicochemical properties. On the basis of the investigation of the properties of 2D nanosheets, it is possible to design and synthesize novel nanosheet-based hybrid materials with versatile structural, electronic, optical, mechanical and physicochemical properties. The application of 2D inorganic nanosheets as building blocks leads to the formation of highly porous structure and controlled modification of electronic structure, which are attributable to the house-of-cards-type stacking of sheet-like crystallites and an electronic coupling between the hybridized components, respectively [13–15, 20–26]. In comparison with graphene, inorganic 2D nanosheets boast more versatile properties and wider range of applications from nanoelectronics to energy sector [27, 28]. The physicochemical properties and applicability of these 2D nanosheets can be further tailored by hybridization with foreign species. The resulting nanosheet-based hybrid materials can be utilized as core materials for diverse technologies such as energy storage and conversion, heterogeneous catalysts, porous electrode materials, electrochemical sensors, biomolecule/drug reservoirs, inorganic/polymer composite films, high-T_c superconductor, and ferromagnetic/ferroelectric films [1, 2, 11, 18, 19, 29, 30]. Recently several review articles and special themed issues are devoted for the 2D nanosheets and their hybrid materials [1, 2, 11, 28].

Among many application fields of nanosheet-based hybrid materials, harnessing solar energy attracts intense research interest because of its promising potential to replace fossil fuels and to fulfill a rising global demand for sustainable energy. One of the most important issues in this technology is a conversion of solar energy to electrical energy and also to chemical energy in the form of solar fuels such as H_2, CH_3OH, HCOOH, and CH_4 [21–33]. The photoexcitation of semiconductors by a light source of photon energy greater than their bandgap energies induces an electronic excitation from valence band (VB) to the conduction band (CB), leading to the creation of excited electrons and holes (h^+) [31]. The photoinduced electrons

and holes can migrate to the surface sites for inducing the photocatalytic reaction in the vicinity of the semiconductor surface. Since the recombination between the photoinduced electrons and holes leads to the emission of photoluminescence (PL) instead of photocatalysis, the efficient separation of these charged species across the semiconductor interface is one of the key factors for determining the conversion efficiency of light energy into electrical or chemical energies. An effective separation of photoinduced charges can be effectively achieved by a strong electronic coupling between semiconductor 2D nanosheets and guest species [10, 15, 16, 22–26].

Several review articles and few special themed issues highlighted the synthetic strategies, properties, and applications of 2D nanosheets and their hybrids [1, 2, 11, 28]. However, none of the review article or book chapter is specially designed for the specific application of the photofunctional nanosheet-based hybrid materials. In this chapter, hybridization of 2D inorganic nanosheets with diverse inorganic, organic, bio-, and polymer molecules/nanostructures is described together with their photofunctional applications. The unique interaction between nanosheet and guest species enables to optimize the physicochemical properties and photofunctionalities of the resulting nanohybrid materials. Various synthetic techniques for the 2D nanosheet-based hybrids are discussed together with their unique synergistic properties. In order to meet strict requirements as per the environmental friendly and green energy creation systems, special emphasis is put forward on photofunctional 2D nanosheets based hybrids.

15.2 Properties of Nanosheet-Based Hybrids

Extremely thin thickness: The exfoliated 2D nanosheets of inorganic solids show monolayer morphology with ultrathin thickness in the range of 0.5–2.0 nm. Therefore all of the constituent elements are practically exposed to the surfaces of the nanosheet. The surface exposition of component ions is crucial in achieving a strong chemical interaction and electronic coupling with hybridized species, leading to the improvement of the functionality of components through synergistic coupling [2, 7, 9, 10, 18].

Flexibility of composition control: The exfoliated 2D nanosheets of inorganic solids can possess a variety of crystal structures and chemical compositions depending on the structure types and formulas of the pristine host materials for exfoliation reaction; layered double hydroxide with brucite structure, layered metal oxides with rocksalt-type layered structure ($LiCoO_2$, $Li[Mn_{1/3}Co_{1/3}Ni_{1/3}]O_2$, $K_{0.45}MnO_2$, etc.), layered Perovskite structure (Dion–Jacobson phase, $KCa_2Nb_3O_{10}$, $KSr_2Nb_3O_{10}$, $KCa_2Ta_3O_{10}$, $KSr_2Ta_3O_{10}$, $KLaNb_2O_7$, $K(Ca,Sr)_2Nb_3O_{10}$, etc.), and so on. Since most of the layered metal oxide structures are stable enough to provide lattice sites for the substitution of diverse cations and anions, the control of the

chemical compositions of 2D nanosheets can be easily achieved by the exfoliation of the chemically substituted derivatives of layered materials [6, 16].

Anisotropic morphology and flexibility: The exfoliated 2D nanosheets of inorganic solids have extremely high anisotropic 2D morphology like graphene. Also these 2D materials demonstrate high flexibility with scrolling behavior along certain crystallographic axis. These characteristics of the inorganic nanosheets render these materials effective building blocks for the inorganic nanotubes and husk in peapod type nanostructures [34–36].

Sufficient surface charge: Since most of layered inorganic solids contain charge-compensating ionic species in their interlayer spaces, the exfoliated inorganic nanosheets possess distinct surface charge [9, 37]. The presence of surface charge minimizes the self-agglomeration of the exfoliated inorganic nanosheets, endowing high chemical stability for their colloidal suspensions. The electrostatic interaction between the exfoliated inorganic nanosheets and oppositely charged guest species makes it easier to synthesize nanosheet-based hybrid materials with well-ordered heterostructure.

Expanded surface area: Due to the highly anisotropic 2D morphology of the exfoliated nanosheets [7, 9, 18], these 2D materials boast wide surface area, which can be easily functionalized by anchoring diverse functional groups. This characteristic of the exfoliated nanosheets makes possible the flexible control of their surface property, which opens up great possibility to tailor the functionality of nanosheet-based hybrid materials.

Photoinduced hydrophilicity: Unilamellar exfoliated nanosheets of semiconducting metal oxides such as $TiNbO_5$, Ti_2NbO_7, Ti_5NbO_{14}, and Nb_3O_8 show photoinduced superhydrophilic property. This unique feature highlights the usefulness of these nanosheets as photocatalytic self-cleaning and antifogging coatings. This property of the exfoliated nanosheet enlightens the origin and mechanism of the photogenerated superhydrophilic state of oxide surface, which has long been a matter of argument and speculation [38].

15.3 Photofunctional Applications of Nanosheet-Based Hybrids

Many of inorganic nanosheets have potential availability as building blocks for photofunctional hybrid materials and devices, since they are semiconducting with variable band structures. The photofunctional application fields of these nanosheet-based hybrid materials include the photocatalytic degradation of toxic organic/inorganic pollutants, photocatalytic water splitting, CO_2 photoreduction, photovoltaics, photoluminescence, and photoinduced biological properties. As highlighted in the introduction section, the harnessing of solar energy is one of the promising ways to replace fossil fuels and fulfill the rising global demand for sustainable energy.

Among many semiconducting inorganic solids, titanium oxide is one of the most intensively investigated photocatalysts because of its high stability, low price, low toxicity, and rich abundance. This material however suffers from wide bandgap separation, low quantum yield, and high recombination rate of excitons [32]; its wide bandgap semiconducting nature limits the light absorption profile to the UV region of the solar spectrum, which constitutes only 4% of the total solar energy. As an efficient method to overcome these hurdles of wide bandgap semiconductors, the hybridization with narrow bandgap semiconducting species receives prime attention because it enables the precise engineering of band structure to improve the conversion efficiency of solar energy to chemical/electrical energy. To date, many attempts have been made to combine wide bandgap semiconductors with visible light active photocatalyst. As a result of very thin thickness of 2D nanosheet, the hybridization of this nanostructured material with other semiconducting species gives rise to a formation of new electronic structure via a coupling between two kinds of semiconductors with different electronic structures.

Depending on the band alignment of component semiconductors, newly evolved electronic structure of the hybrid material can be classified into three types, straddling gap (type I), staggered gap (type II), and broken gap (type III) [2]. The hybrid materials with type II electronic structure are of prime importance since they show a significant extension of the lifetime of photoinduced electrons and holes via an internal charge transfer with improved harvesting ability of visible light. The band structures of exfoliated metal oxides are strongly dependent on their chemical compositions. The 2D nanosheets of layered titanium and niobium oxide ($Ti_{0.91}O_2^{0.36-}$, $Nb_3O_8^{3-}$, $Ca_2Nb_3O_{10}^-$, $TiNbO_5^-$, $Ti_2NbO_7^-$, and $Ti_5NbO_{14}^{3-}$) are wide bandgap semiconductor with an indirect bandgap of 3.4 − 3.7 eV. There occurs the increase of bandgap energy upon the exfoliation, which is attributable to the quantum size effect of subnanometer-thick nanosheet [39]. The band positions of $Ti_{0.91}O_2^{0.36-}$, $Nb_3O_8^{3-}$, $Ca_2Nb_3O_{10}^-$, $TiNbO_5^-$, $Ti_2NbO_7^-$, and $Ti_5NbO_{14}^{3-}$ nanosheets are estimated from the onset values of photocurrent with conduction band-edge potential at −1.27, −1.32, −1.12, −1.33, −1.30, and −1.29 V versus Ag/Ag^+, respectively. These nanosheets are suitable for type II-hybridization, which is fairly useful not only in extending the lifetime of photoinduced electrons and holes but also in improving the light-harvesting ability [39]. Such metal oxide nanosheets can be used as functional building blocks for various photoenergy harvesting devices.

15.3.1 Photocatalytic Degradation of Toxic Organic Pollutants

In the last few decades, an increasing threat of environmental pollution and global climate change evokes a great deal of research interest about purification technologies for relieving the emission of toxic industrial waste. Semiconductor-assisted

photocatalytic degradation of harmful pollutants has received special attention because of its usefulness as an economic and eco-friendly option for reducing the deepening threat of environmental pollution. The exfoliated metal oxide nanosheets have been applied as building blocks for novel porous hybrid-type photocatalysts showing high activity for the surface adsorption and photodegradation of organic pollutants. Many type of layered metal oxide nanosheet-based hybrid materials such as guest-layered metal oxide nanohybrids (guest = metal, metal hydroxide, and quantum dots; layered metal oxide = titanate and niobates) are synthesized by employing several synthetic methodologies including an electrostatically derived reassembling and the growth of nanoclusters/nanoparticle on exfoliated 2D metal oxide nanosheets. In terms of an electrostatic interaction between negatively charged titanate nanosheets and positively charged nanospecies, the lepidocrocite-structured $Ti_{0.91}O_2{}^{0.36-}$ nanosheets can be effectively hybridized with many guest species such as TiO_2 nanosol, zinc hydroxide nanosol, polyethylenimine (PEI)-modified Pt nanoparticles, K^+ ions, and Zr^{4+} ions, yielding a series of UV-active hybrid photocatalysts with expanded surface area and enhanced photocatalytic activity for degradation of organic pollutants [13–15, 40, 41].

According to the powder X-ray diffraction (XRD) analysis, these cationic guest species are intercalated into the interlayer space of layered titanate nanosheets, leading to the formation of highly ordered layer-by-layer-ordered structure, as illustrated in Fig. 15.1A [13]. The resulting nanohybrids demonstrate remarkable expansion of surface area and the formation of mesopores upon hybridization. The porosities of these materials are tunable by the control of chemical compositions and heat treatment at elevated temperature. In the case of the TiO_2 nanosol-layered titanate nanohybrid, the ratio of TiO_2 nanoparticle/layered titanate nanosheet is carefully tuned from 1.5 to 5.0 to optimize the porosity of the resulting nanohybrids. These materials are denoted as nanohybrid-I and nanohybrids-II, respectively. Among the present materials, the TiO_2 nanosol-layered titanate nanohybrid (i.e., nanohybrid-I) displays the greatest porosity (Fig. 15.1B [13]; S_{BET} = 190 m^2/g, pore size = 6 nm), which are greater than those of K^+-layered titanate nanohybrid (S_{BET} = 8 m^2/g, pore size = 5.2 nm), ZnO-layered titanate nanohybrid (S_{BET} = 134 m^2/g, pore size = 3.5 nm), Pt-layered titanate nanohybrid (S_{BET} = 67 m^2/g, pore size = 14 nm), and zirconium-layered titanate nanohybrid (S_{BET} = 176 m^2/g, pore size = 3.9 nm). The specific surface areas of these reassembled nanohybrids are much larger than that of the pristine protonated titanate (13 m^2/g), underscoring the usefulness of the exfoliation-reassembling in increasing the porosity of the layered inorganic solids. These titanate nanosheet-based hybrid materials are applied as photocatalysts for the photodegradation of organic pollutants such as 4-chlorophenol (4-CP), methylorange (MO), and methyleneblue (MB). As plotted in Fig. 15.1C [13], after 4 h of UV irradiation, 99% of 4-CP in an aqueous suspension was degraded by the TiO_2-layered titanate nanohybrid, highlighting the high photocatalytic activity of this material. It is therefore concluded that the exfoliation-reassembling method is very efficient in exploring mesoporous hybrid-type photocatalysts with enhanced photocatalytic activity and optimized pore structure.

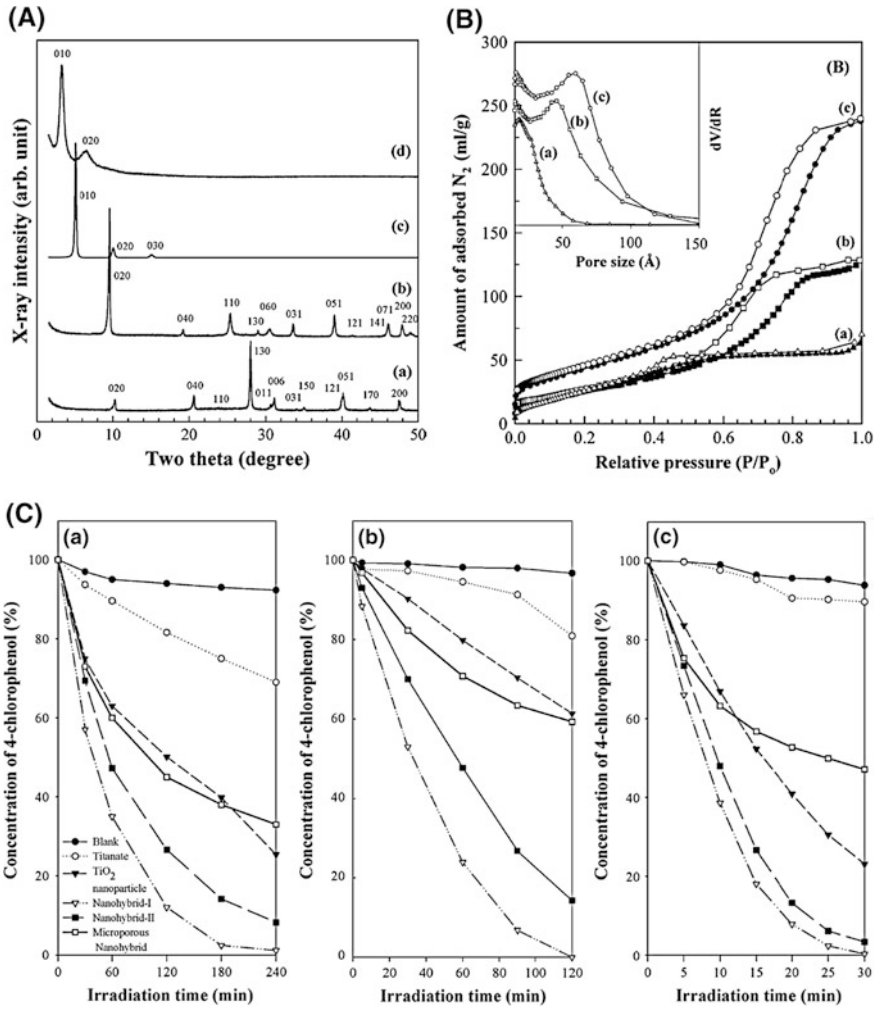

Fig. 15.1 **A** XRD patterns for *a* the layered cesium titanate, *b* layered protonic titanate, *c* tetrabutylammonium (TBA)-intercalated layered titanate, and *d* microporous titanate nanosheet-TiO_2 hybrid. **B** Nitrogen adsorption-desorption isotherms for *a* TiO_2 nanoparticles, *b* nanohybrid-II, and *c* nanohybrid-I. The *inset* indicates the pore size distribution curves, respectively. **C** Nanohybrid-assisted photocatalytic degradation of *a* 4-CP, *b* MO, and *c* MB. (Reprinted with Permission from Ref. [13]) Copyright 2006 ACS Publication

On the basis of the same synthetic strategy, visible light active hybrid-type photocatalysts are synthesized by the reassembling of exfoliated titanate nanosheets with narrow bandgap semiconducting species such as chromium oxide, nickel oxide, iron oxide, copper oxide, and silver oxosalts [20, 23, 25, 26, 42]. As a result of the electronic coupling between the hybridized components, a distinct red-shift of absorption edge to visible light region is observed upon the hybridization, together

with the weakening of PL signal reflecting the depression of electron–hole recombination. All of the nanohybrids show the remarkable expansion of surface area and the formation of micro-/mesopores, which are ascribable to the house-of-cards-type stacking structure of titanate nanosheets. Additionally, the hybridization of layered titanate nanosheet with guest species induces a unique phenomenon via a strong chemical interaction originating from the very thin thickness of titanate nanosheet. In one instance, the copper oxide-layered titanate nanohybrid demonstrates the unique phase transformation behavior from rutile TiO_2 to anatase TiO_2 [23]. This is a result of intimate hybridization of titanium oxide with copper oxide. In addition to the unprecedented phase transition, the remarkable variation of optical property upon the heat treatment is observed upon the hybridization with copper oxide. As illustrated in Fig. 15.2A, the as-prepared copper oxide-layered titanate nanohybrid shows distinct absorption edge, indicative of its semiconducting nature with bandgap of 2.0 eV. The absorption edge at 2.0 eV remains unchanged after calcination at 200 °C, which is due to the nanometer-level structural coherence of guest copper oxide causing a quantum confinement effect. A further heat treatment at elevated temperature causes a marked red-shift of edge energy to below 1.4 eV, indicating the formation of CuO phase.

The as-prepared copper oxide-layered titanate nanohybrid and its calcined derivative at 200 °C can induce a distinct photodegradation of organic substrate molecules under illumination of visible light ($\lambda > 420$ nm), see Fig. 15.2B. The observed visible light photocatalytic activity of copper oxide-layered titanate nanohybrid is much stronger than those of copper oxide and the pristine layered titanate, indicating the beneficial effect of hybridization on the photocatalytic activity of component metal oxides. The calcination at higher temperatures of 300–500 °C results in a remarkable deactivation of the photocatalytic activity of the nanohybrids, which is ascribable to the phase separation between titanium oxide and copper oxide and also to the collapse of porous stacking structure with decrease of surface area. This result clearly demonstrates that the improved photocatalytic activity of nanosheet-based hybrid material originates from the expansion of surface area and the enhancement of visible light absorption upon the nanoscale hybridization. In addition to this copper oxide-titanate nanohybrid, many other nanosheet-based hybrid photocatalysts such as CdS-titanate, ZnO-Fe-doped titanate, α-Fe_2O_3-titanate, Co-tetratitanate, SnO_2-tetratitanate, TiO_2-MoO_3, SnO_2-hexaniobate, graphene-hexaniobate, TiO_2-Bi-doped hexaniobate, TiO_2-$HTaWO_6$, $Mn(H_2O)_x$-$TaWO_6$ can be synthesized by the electrostatically derived reassembling between exfoliated metal oxide nanosheets and cationic guest species [43–54].

In addition to the reassembling strategy, the direct crystal growth of semiconductor nanoparticle on the surface of the 2D metal oxide nanosheet is also employed to synthesize nanosheet-based hybrid photocatalysts. In one instance, an efficient visible light photocatalyst of Ag_2CO_3/Ag-Ti_5NbO_{14} nanohybrid can be synthesized by the growth of Ag_2CO_3/Ag nanoparticle on the exfoliated 2D Ti_5NbO_{14} nanosheets [42]. To probe the effect of chemical composition on the physicochemical properties of Ag_2CO_3/Ag-Ti_5NbO_{14} nanohybrids, two different Ag_2CO_3/Ti_5NbO_{14} ratios of 0.5 and 1 are applied. (The resulting materials are

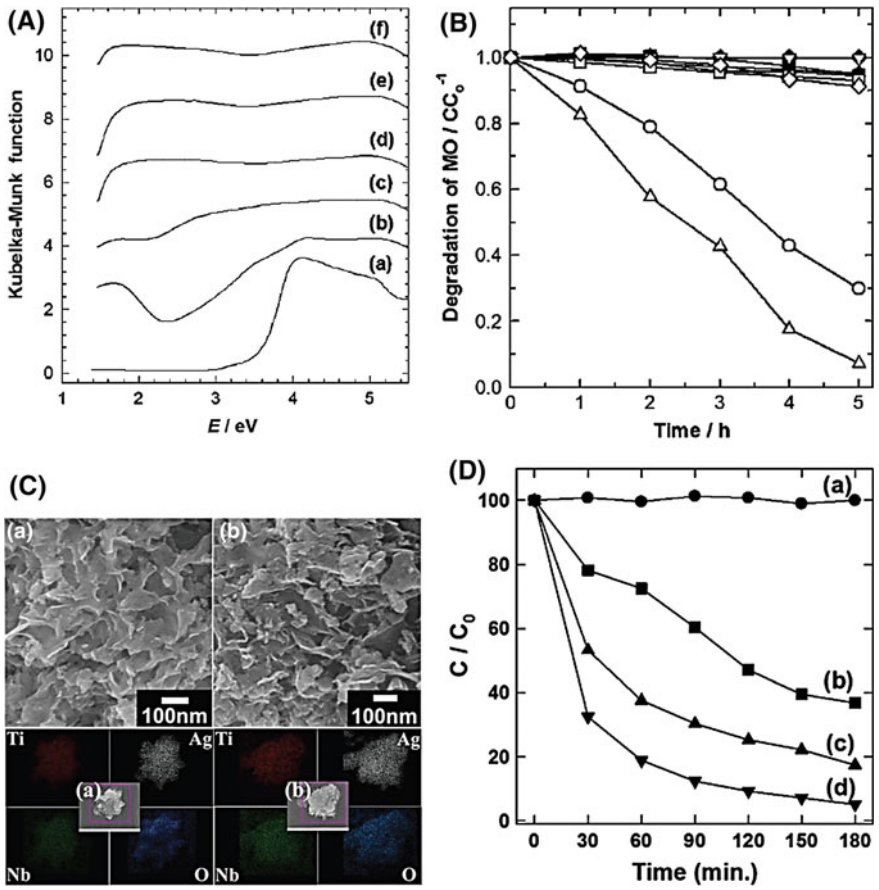

Fig. 15.2 **A** Diffuse reflectance UV–vis spectra for *a* pristine cesium titanium oxide, *b* as-prepared copper oxide-layered titanate nanohybrid and its derivatives calcined at *c* 200, *d* 300, and *e* 500 °C, and *f* the reference CuO. **B** The time-dependent profiles of the methyl orange concentration upon photocatalytic degradation under visible radiation ($\lambda > 420$ nm) with the as-prepared copper oxide-layered titanate nanohybrid (*open circles*) and its derivatives calcined at 200 (*open triangles*), 300 °C (*open squares*) and 500 °C (*open diamonds*), the pristine cesium titanium oxide (*open inverse triangles*), CuO (*closed squares*), Cu_2O (*closed diamonds*), P-25 (*closed triangles*), and blank test (*closed circles*). **C** *Top* FE-SEM images and *Bottom* elemental maps and *center* FE-SEM images of *a* **AT1** and *b* **AT2**. **D** Time profiles of photocatalytic degradation of 4-CP by *a* the pristine $K_3Ti_5NbO_{14}$, *b* Ag_2CO_3, *c* **AT1**, and *d* **AT2** under the irradiation of visible light ($\lambda > 420$ nm). (Reprinted with Permission from Refs. [23, 42]) Copyright 2006 ACS Publication and 2014 Royal Society Chemistry

denoted as **AT1** and **AT2**, respectively.) According to the field emission-scanning electron microscopy (FE-SEM), both the Ag_2CO_3/Ag-Ti_5NbO_{14} nanohybrids exhibit mesoporous stacking morphology of the reassembled nanosheets with surface-adsorbed nanoparticles of silver and silver carbonate (Fig. 15.2C). The energy dispersive spectrometry (EDS)-elemental mapping analysis clearly

demonstrates the homogeneous distribution of Ag, Ti, Nb, and O elements in entire parts of the nanohybrid, confirming the uniform hybridization between silver species and titanoniobate nanosheets. As plotted in Fig. 15.2D, both the Ag_2CO_3/Ag-Ti_5NbO_{14} nanohybrids display the promising photocatalytic activity for the visible light-induced degradation of 4-CP molecule, which is higher than those of the Ag_2CO_3. The enhanced photocatalytic activity of the present nanohybrids can be understood as a result of strong electronic coupling between Ag_2CO_3/Ag nanocrystals and Ti_5NbO_{14} nanosheets. The present result provides clear evidence for the usefulness of the crystal growth strategy as an alternative route to nanosheet-based hybrid photocatalysts.

Also an electrophoretic deposition method is employed to deposit photoactive thin films composed of titania nanosheets intercalated with methyl viologen (MV^{2+}) [55]. Upon the irradiation of UV light, the obtained titania-MV^{2+} thin films show blue coloring due to the formation of reduction product from MV^{2+}, clearly demonstrating the photocatalytic activity of the films.

15.3.2 Photocatalytic Water Splitting and CO_2 Reduction

The increasing need of energy caused by fast urbanization and industrialization causes the large-scale emission of CO_2 resulting in global climate change. The deepen crisis of climate change evokes a great deal of research for developing renewable energy resources. Among various renewable energy resources, solar energy occupies the first place due to its rich abundance and environmental benignity. A less than 0.02% of total solar energy falling on the earth is enough to substitute the total energy consumption of conventional fuel. In addition to photovoltaics, the conversion of solar energy to chemical energy attracts intense research interest. The transformation of solar energy to chemical energy can be achieved by the photocatalytic production of H_2 from water and the photoreduction of CO_2 to hydrocarbon molecules. Of prime importance is that hydrogen receives intense research interest as a zero-emission fuel to meet the future energy demands.

Currently a majority of hydrogen energy comes from the cracking process of petroleum [56]. In comparison with this fossil fuel-dependent method, the photocatalytic water splitting provides much cleaner and safer options for the production of hydrogen. However, there are only a few examples of visible light active photocatalyst efficient for pure water splitting [32]. Instead of single component photocatalysts, hybrid-type photocatalysts composed of intimately coupled two different photocatalysts are more promising for water photosplitting because of their high level of flexibility to control the electronic structures, crystal morphologies, and photocatalyst performances [1, 2].

Like the photocatalysts for the degradation of harmful pollutants, the efficient photocatalysts for visible light-induced generation of H_2 and O_2 can be synthesized by the reassembling between exfoliated metal oxide nanosheets and nanostructured semiconductors. In one instance, the hybridization between negatively charged

titanate nanosheets and positively charged CdS QDs yields the mesoporous nanohybrids of CdS-layered titanate [43]. The chemical composition of the CdS-layered titanate nanohybrids is controlled by adopting two different mixing ratios of Cd/Ti of 5 and 2.5 (the resulting nanohybrids are denoted as CdTi-1 and CdTi-2, respectively.). As illustrated in Fig. 15.3A, B the strong electronic coupling between titanate and CdS leads to the marked narrowing of bandgap energy caused by direct electron transition between the hybridized components and also to the remarkable depression of electron–hole recombination. As a consequence, the resulting CdS-layered titanate nanohybrids show high photocatalytic activity for visible light-induced H_2 generation without the help of Pt cocatalyst (see Fig. 15.3C). The photocatalyst performance of CdS-layered titanate nanohybrid can be further improved by the partial substitution of Rh for the layered titanate [16]. The application of Rh-substituted layered titanates as host materials for exfoliation

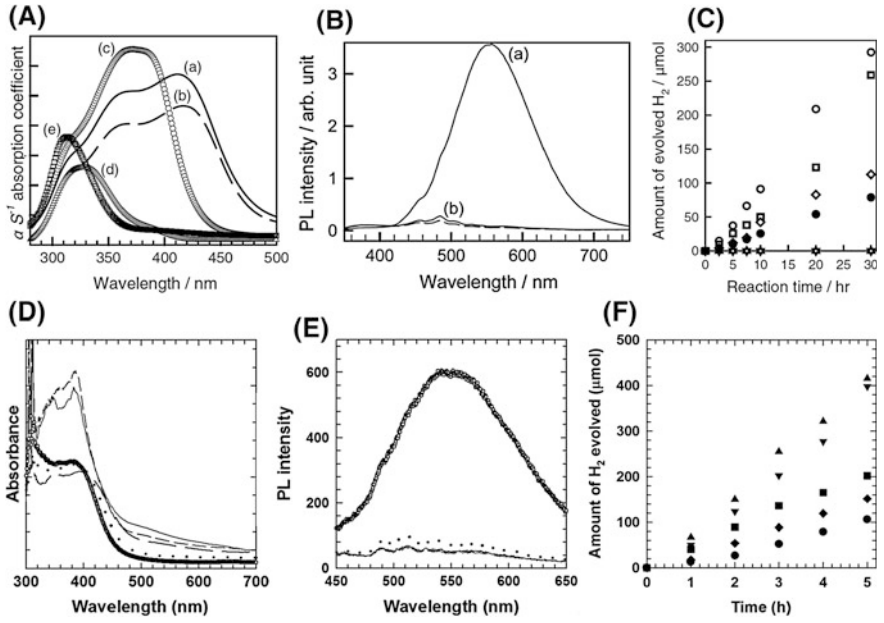

Fig. 15.3 **A** Diffuse reflectance UV–vis spectra for *a* **CdTi-1** and *b* **CdTi-2**, *c* CdS QDs, *d* protonated layered titanate, and *e* TBA-intercalated layered titanate. **B** PL spectra of *a* the CdS QDs, and *b* the as-prepared nanohybrids of **CdTi-1** (*solid lines*), and **CdTi-2** (*dashed lines*). **C** Visible-light-induced ($\lambda > 420$ nm) production of H_2 gas by the as-prepared nanohybrids of **CdTi-1** (*squares*) and **CdTi-2** (*open circles*), the CdS QDs (*diamonds*), the nonporous composite of CdS and layered titanate (*closed circles*), protonated titanate (*triangles*), and TBA-intercalated titanate (*inverse triangles*). **D.** Diffuse reflectance UV–vis spectra and E. PL spectra of the CdS-$Ti_{(5.2-x)/6}Rh_{x/2}O_2$ nanohybrids with $x = 0$ (*dot*), 0.025 (*long dash*), 0.5 (*short dash*), and 0.1 (*solid*), and reference CdS QD (*circle*). **F** Visible-light-induced ($\lambda > 420$ nm) H_2 production by the CdS-$Ti_{(5.2-x)/6}Rh_{x/2}O_2$ nanohybrid with $x = 0$ (*diamonds*), 0.025 (*squares*), 0.05 (*triangles*), and 0.1 (*inverse triangles*), with the reference CdS QDs (*circles*) and P25 TiO_2–CdS (*hexagons*). (Reprinted with Permission from Refs. [16, 43] Copyright 2011 and 2015 Wiley VCH)

leads to the synthesis of Rh-substituted titanate nanosheets with tunable electronic structure and optical property. As illustrated in Fig. 15.3D, the Rh-substituted CdS-layered titanate nanohybrids show red-shift upon the hybridization with CdS, confirming the enhancement of visible light absorptivity. The strong PL signal of CdS QD becomes remarkably depressed by the hybridization with the Rh-substituted titanate nanosheet, indicating the depression of electron–hole recombination and the elongation of lifetime of charge carriers (see Fig. 15.3E). The partial replacement of Ti with Rh is quite effective in improving the electronic coupling between layered titanate nanosheets and CdS QDs. The resulting Rh-substituted CdS-layered titanate nanohybrids exhibit much higher photocatalytic activity and better photostability than the unsubstituted homologue, underscoring the effectiveness of Rh-substituted layered titanate nanosheet as a building block for synthesizing highly efficient hybrid-type photocatalysts (see Fig. 15.3F). This result underscores the high flexibility of the chemical composition of exfoliated nanosheets provides a powerful tool to explore highly efficient photocatalyst materials through the hybridization.

In addition to H_2 evolution photocatalysts, efficient nanohybrids for visible light-induced O_2 generation can be synthesized via the hybridization with exfoliated inorganic nanosheets. The hybridization of layered titanate nanosheets with Ag_3PO_4 nanocrystals gives rise to the synthesis of highly efficient photocatalysts for O_2 generation [10]. In comparison with TiO_2 nanoparticles, the exfoliated titanate nanosheet experiences strong modifications of chemical bonds and electronic structures upon the hybridization with Ag_3PO_4, indicating the remarkable advantage of very thin 2D nanosheet morphology in maximizing the electronic coupling with hybridized species. As illustrated in Fig. 15.4A, 0D TiO_2-Ag_3PO_4 (**0D-TOAP**) nanohybrids show the Bragg reflections of anatase- and rutile-structured TiO_2 as well as those of Ag_3PO_4, indicating the hybridization of P25 with silver phosphate. Conversely, only the XRD peaks of the Ag_3PO_4 phase are discernible for the 2D TiO_2-Ag_3PO_4 (**2D-TOAP**) nanohybrids without those of the lepidocrocite titanium oxide phase. The absence of layered TiO_2-related peaks strongly suggests the homogeneous and disordered dispersion of titanium oxide nanosheets in the **2D-TOAP** nanohybrid without the formation of segregated layered titanium oxide phase. The resulting **2D-TOAP** nanohybrid shows very high photocatalytic activity for visible light-induced O_2 generation than does the **0D-TOAP** homologue, see Fig. 15.4C.

New type of 2D hybrid photocatalysts of layered titanate-Zn-Cr-LDH can also be synthesized by an electrostatically derived interstratification of two oppositely charged component nanosheets [22]. Similarly to the Ag_3PO_4-layered titanate nanohybrid, the strong electronic coupling between subnanometer-thick nanosheets of layered titanate and Zn-Cr-LDH is quite useful in optimizing the photocatalytic activity of the hybridized semiconductors through the depression of electron–hole recombination and the enhancement of visible light absorption [22]. The resulting titanate-Zn-Cr-LDH nanohybrid demonstrates enhanced O_2 evolution activity due to the nanoscale hybridization between Zn-Cr-LDH and titanate nanosheets. Similarly an electrostatically derived reassembling between 2D

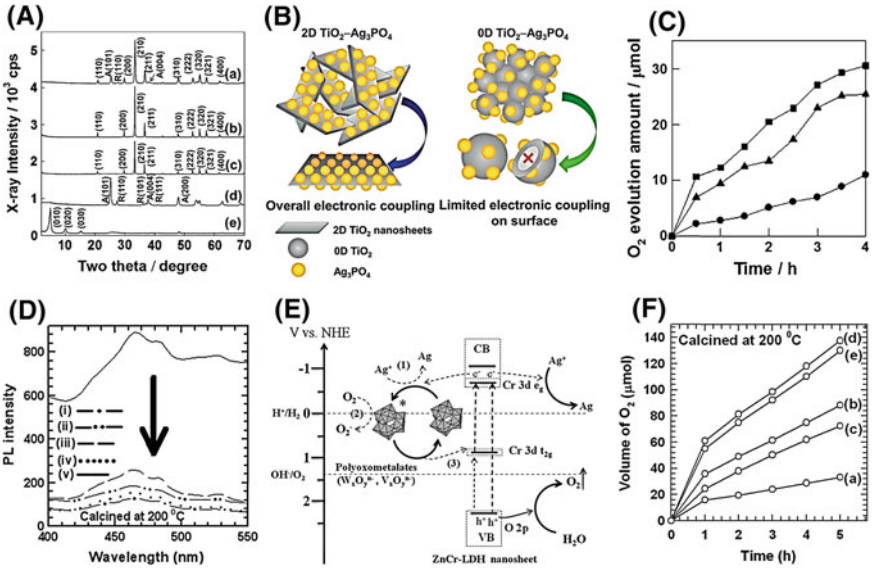

Fig. 15.4 **A** Powder XRD patterns of *a* **0D-TOAP** nanohybrids, *b* **2D-TOAP** nanohybrids, *c* nanocrystalline Ag_3PO_4, *d* P25 TiO_2 nanocrystals, and *e* freeze-dried TiO_2 nanosheets. In *a* and *d*, the miller indices with A and R denote the peaks of anatase and rutile TiO_2 phase, respectively. **B** Schematic models for the crystal dimension and electronic coupling in the 0D-**TOAP** and 2D-**TOAP** nanohybrids. **C** Visible light ($\lambda > 420$ nm)-induced O_2 generation by nanocrystalline Ag_3PO_4 (*circles*), 0D-TOAP nanohybrids (*triangles*), and 2D-TOAP nanohybrids (*squares*). **D** PL spectra of the **ZCW-1** (*dot–dashed lines*), **ZCW-2** (*dot–dot–dashed lines*), **ZCV-1** (*dashed lines*), **ZCV-2** (*dotted lines*), and pristine Zn-Cr-LDH (*solid lines*). **E** Schematic illustration for internal electron transfer in the present Zn-Cr-LDH–POM nanohybrids. **F** Time-dependent photoproduction of O_2 gas under visible light illumination ($\lambda > 420$ nm). *a* The pristine Zn-Cr-LDH and the Zn-Cr-LDH–POM nanohybrids of *b* **ZCV-1**, *c* **ZCW-2**, *d* **ZCW-1**, and *e* **ZCW-2**. (Reprinted with Permission from Refs. [10, 24]) Copyright 2014 Wiley VCH and 2013 Nature Publishing Group

Zn-Cr-LDH nanosheets and 0D polyoxometalate (POM) nanoclusters yields porous hybrid photocatalysts highly efficient for O_2 photogeneration [24]. Two kinds of the Zn−Cr-LDH−$W_7O_{24}^{6-}$ nanohybrids are synthesized with a charge balanced ratio (POM:Zn–Cr-LDH = 1:2.57) and a threefold POM excess ratio (POM:Zn–Cr-LDH = 1:7.71) (these materials are denoted as ZCW-1and ZCW-2, respectively.). Similarly the Zn−Cr-LDH−$V_{10}O_{28}^{6-}$ nanohybrids (ZCV-1 and ZCV-2) are synthesized with the molar ratio of POM:Zn–Cr-LDH = 1:1.81 and 1:5.64, respectively. As shown in Fig. 15.4D, the PL signal of the pristine Zn–Cr-LDH becomes nearly quenched after hybridization with POM nanoclusters, indicating a significant depression of electron–hole recombination. The observed remarkable depression of PL peaks upon the hybridization with POM can be understood by the internal charge transfer between Zn–Cr-LDH and POM component, as illustrated in Fig. 15.4E. The Zn–Cr-LDH-POM nanohybrid demonstrates enhanced photocatalytic activity for visible light-induced O_2 generation than pristine Zn–Cr-LDH, see Fig. 15.4F. Summarizing the present results, the

nanoscale hybridization between exfoliated metal oxide nanosheets and other nanostructured semiconductor with appropriate electronic structure can provide a powerful methodology to explore novel hybrid-type photocatalysts efficient for visible light-induced H_2 and O_2 evolutions.

15.3.3 Solar Cells

The increase in energy consumption by the modern society results in the depletion of fossil energy, and simultaneously the increase of atmospheric CO_2 concentration with significant global warming. As described above, the rich abundance of solar energy makes it the most promising renewable energy source to replace fossil fuel. A direct conversion of solar energy to electrical energy can be achieved by using photovoltaic devices. High production cost of silicon-based solar cell restricts the large-scale application of this conventional photovoltaics.

As alternative photovoltaics with economic and ecological merits, several types of solar cells have been intensively investigated. One of the most promising next-generation devices is dye sensitized solar cells (DSSCs) [57, 58]. In DSSCs, incident light is harvested by dye molecules adsorbed on nanocrystalline semiconductors acting as electron transporting agent. Many kinds of metal oxide semiconductors such as TiO_2, SnO_2, ZnO, Nb_2O_5, CeO_2, and $SrTiO_3$ have been employed as electrode materials for the DSSC. Among them, TiO_2 is the most promising electrode material in terms of high efficiency, rich abundance, and low production cost. However, the use of polymer binder for TiO_2 electrode leads to the decrease of surface area and the aggregation of particles after thermal treatment of TiO_2-polymer mixture, which can be reduced by the fabrication of porous stacking structure of TiO_2 nanoparticles. The porosity of TiO_2 electrode can be effectively enhanced by the reassembling of positively charged anatase TiO_2 nanocrystals with negatively charged layered titanate nanosheets [59]. The resulting titanium oxide material possesses greater surface roughness and porosity than do the conventional TiO_2 nanoparticles, see Fig. 15.5A. As a result of enhanced roughness and porosity, the resulting titanium oxide electrode composed of house-of-cards-type stacked nanosheets and nanocrystals absorbs a larger amount of dye molecules (1.73×10^{-8} mol/cm^2) than does conventional TiO_2 nanoparticles absorbing 7.8×10^{-9} mol/cm^2. As a consequence, the obtained mesoporous TiO_2 hybrid electrode shows a high photocurrent and solar-to-electrical conversion efficiency, see Fig. 15.5B.

On the basis of layer-by-layer deposition method, the multilayer film of polyaniline (PANI) and layered titanate can be fabricated on the basis of the electrostatic interaction between positively charged PANI and negatively charged layered titanate nanosheet [60]. By varying the potential applied, PANI can be switched from n-type to p-type semiconductor, leading to the systematic change of photocurrents. This result highlights the usefulness of the layer-by-layer assembly of titanate nanosheets and PANI as potential photoelectrodes.

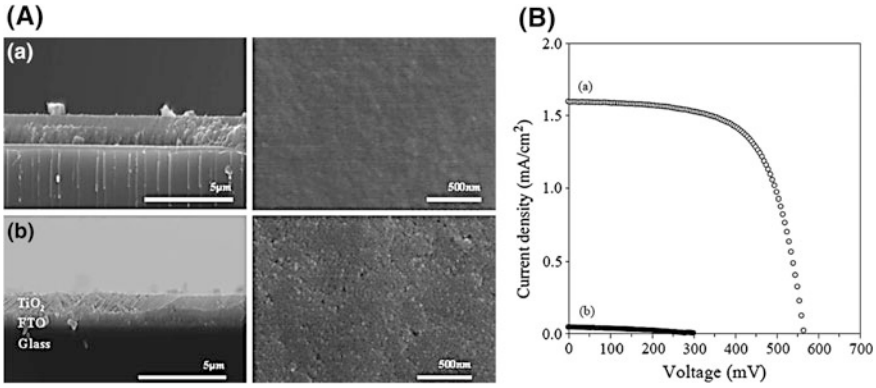

Fig. 15.5 **A** SEM images for *a* TiO_2 nanoparticles and *b* the titanate nanosheet-TiO_2 nanohybrid: the *cross-sectional view* (*left*) and the *top view* (*right*). **B** Photocurrent–voltage curves of DSSC with (*a*) and without (*b*) the incorporation of a layered titanate. Measurements were performed using a Keithley Model 2400 source measure unit, where a 1000 W Xenon lamp (Oriel, 91193) served as a light source. The light was adjusted with a NREL-calibrated Si solar cell (PV Measurements, Inc.) for approximating one sun light intensity (100 mW/cm^2) under AM 1.5 radiation. (Reprinted with Permission from Ref. [59]) Copyright 2006 Elsevier Sciences

15.3.4 Photoluminescence

As highlighted in introduction section, the recombination of photoexcited electrons and holes induces the emission of light, i.e., luminescence. The material or thin films which emit light when excited by radiation are called phosphors and are usually designed to provide visible color emission. Due to their enormous electro-optical applicabilities for light-emitting diodes (LEDs), field-effect transistors, photovoltaic cells, luminescent sensors and switches, optical brighteners, emission displays, projection televisions (PTV), plasma display panels (PDP), thousands of phosphors are prepared and some of them are widely used. The rare earth element-activated metal oxide phosphors are of particular interest due to their superior chemical and physical stability, as compared with other types of hosts like chalcogenides, halides, and organic molecules. There are several reports about photoluminescent 2D metal oxide nanosheets such as $La_{0.90}Eu_{0.05}Nb_2O_7$, $Eu_{0.56}Ta_2O_7$, $(K_{1.5}Eu_{0.5})Ta_3O_{10}$, $Gd_{1.4}Eu_{0.6}Ti_3O_{10}^-$, $La_{0.7}Tb_{0.3}Ta_2O_7^-$, $Bi_2SrTa_2O_9$ and $La_{0.90}Sm_{0.05}Nb_2O_7$ [61–66]. These nanosheets of metal oxide with extremely high anisotropic morphology offer great advantages over their bulk counterparts, since the 2D nanosheet morphology is advantageous for efficient absorption of excitation energy. The emission color for various applications can be finely adjusted by sequential depositions of nanosheet phosphors with different emission colors while avoiding the cross-relaxation interactions of photoactivators in different nanosheet hosts.

Another class of nanosheet-based phosphors can be synthesized by the hybridization of photoluminescent guest ions with transition metal oxide

nanosheets. This type of phosphors includes the intercalation compounds of layered metal oxides with the guests of Eu^{3+}, Tb^{3+}, Hydrated Eu^{3+}, $Eu(phen)_2Cl_3{\cdot}2H_2O$, and $Tb(phen)_2Cl_3{\cdot}2H_2O$ (phen = 1,10-phenanthroline) [67–71]. The high layer charge and variable crystal structure of exfoliated metal oxide nanosheets enable to accommodate high concentrations of photoactivators in the 2D nanosheet lattice without quenching the luminescence, as predicted by the percolation model. The large surface areas of these nanosheet-based hybrid materials formed by the stacking structure of nanosheets are definitely advantageous in effectively receiving excitation energy. However, along with the guest of lanthanide ions or lanthanide complexes, these phosphors frequently contain co-intercalated species such as H_2O and hydronium ions, which act as energy transfer mediators to quench photoluminescence. Therefore, the incorporation of lanthanide activator into the lattice of metal oxide nanosheet sites is more effective than the intercalation of phosphores in between the metal oxide nanosheets in terms of efficient energy transfer from the host nanosheet to the photoactivators. In these phosphor systems, the increase of photoactivator concentration up to Pc (critical concentration limit) is trivial for the enhancement of PL property. In one instance, the $Eu_{0.56}Ta_2O_7$ nanosheet with high photoactivating lanthanide concentration can be obtained by the soft-chemical exfoliation reaction of the layered perovskite $Li_{2-x}H_xEu_{0.56}Ta_2O_7$ [62]. Nearly optimum concentration of Eu^{3+} activator (50%) is achieved in the $Eu_{0.56}Ta_2O_7$ nanosheet. As illustrated in Fig. 15.6A, B, among many allowed direct excitation transitions of Eu^{3+} ion, only a very weak and broad peak is observed at around 402 nm, which is attributed to the convolution of the $^7F_0 \rightarrow {}^5L_6$ and $^7F_0 \rightarrow {}^5D_3$ transitions. Conversely, the host excitation peak at 276 nm is quite intense, which is assigned as the $^5D_0 \rightarrow {}^7F_2$ transition of Eu^{3+} ion.

Red and green luminescences are commonly observed in lanthanide-intercalated nanosheet phosphors, while blue is rarely observed. On the other hand, the exfoliated 2D nanosheet derived from layered perovskite $Bi_2SrTa_2O_9$ (BST) shows blue PL [65]. As shown in Fig. 15.6C, ethylamine intercalated BST (EA-BST) displays strong blue emission than do the pristine BST and protonated $H_{1.67}Bi_{0.21}Sr_{0.85}Ta_2O_7$ (H-BST). In the PL spectrum of the suspension of the BST-nanosheet, a prominent visible blue emission with a peak at 475 nm is induced with the 285 nm excitation, see Fig. 15.6D. The present finding clearly highlights the role of metal oxide nanosheet as an efficient phosphor for the development of new PL device constituted of luminescent nanosheets with all colors.

Layer-by-layer deposition technique is adopted for the deposition of multilayer photoluminescent thin films via the sequential deposition of TiO–Eu^{3+}–TiO–Tb^{3+}–NbO–Tb^{3+}–NbO–Eu^{3+} units, see Fig.15.7 [70]. The PL properties of the obtained multilayer films are strongly dependent on the combination of nanosheets with red and green luminescence. Also, the films show humidity-dependent color change of PL emission.

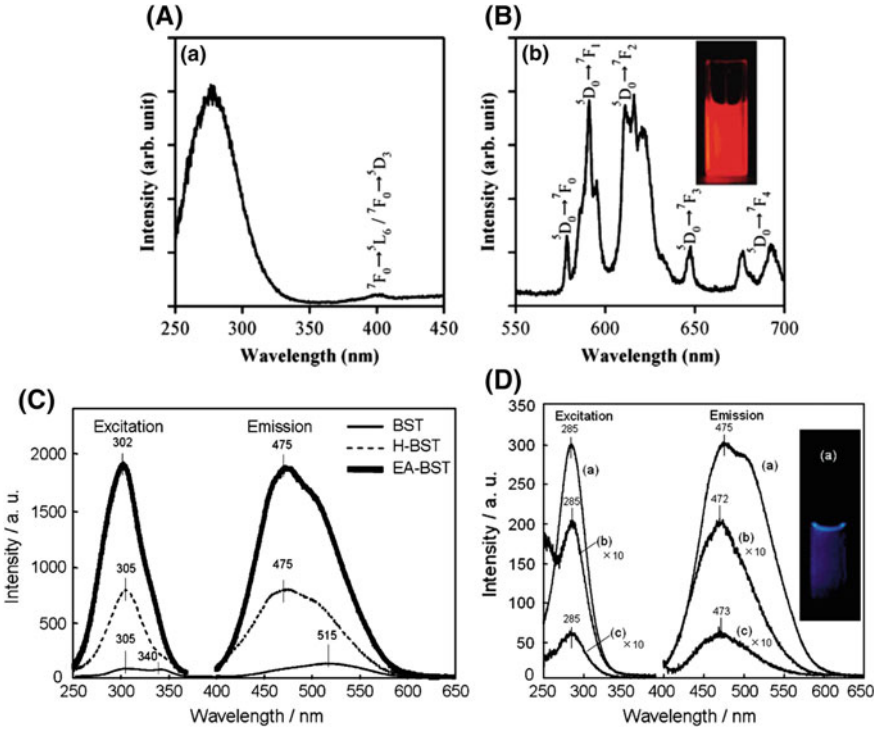

Fig. 15.6 PL **A** excitation and **B** emission spectra of $Eu_{0.56}Ta_2O_7$ nanosheets. The excitation spectra are monitored at 616 nm emission, and the emission spectra are obtained by exciting at 276 nm. **C** Excitation and emission spectra of BST, H-BST, and EA-BST powders (λ_{ex} = 300 nm, λ_{em} = 475 nm). **D** Excitation and emission spectra of *a* BST-nanosheet solution, *b* monolayer LBL film of BST-nanosheet in 0.1 M NaOH solution, and *c* monolayer LBL film of BST-nanosheet in 0.1 M HCl solution (λ_{ex} = 285 nm, λ_{em} = 475 nm). The *inset* shows *red* and *blue* luminescences of the $Eu_{0.56}Ta_2O_7$ and $Bi_2SrTa_2O_9$ nanosheets. (Reprinted with Permission from Refs. [62, 65] Copyright 2008 and 2007 ACS Publication

15.4 Conclusions and Outlook

The essence of this chapter is the comprehensive overview on 2D inorganic nanosheet-based hybrid materials and their photofunctional application. The synthetic condition strongly affects the optical and electronic properties of the 2D nanosheets and their nanohybrids. The 2D nanosheets derived from the chemical exfoliation can be used as a basic building block for the nanohybrid. Varity of guest species can be hybridized with the exfoliated inorganic 2D nanosheets by the soft-chemical reassembling strategy, yielding mesoporous nanosheet-based hybrid materials. The very thin thickness of the exfoliated nanosheets makes possible an unusually strong electronic coupling with hybridized species, leading to the remarkable enhancement of the functionalities of hybridized species and also to the

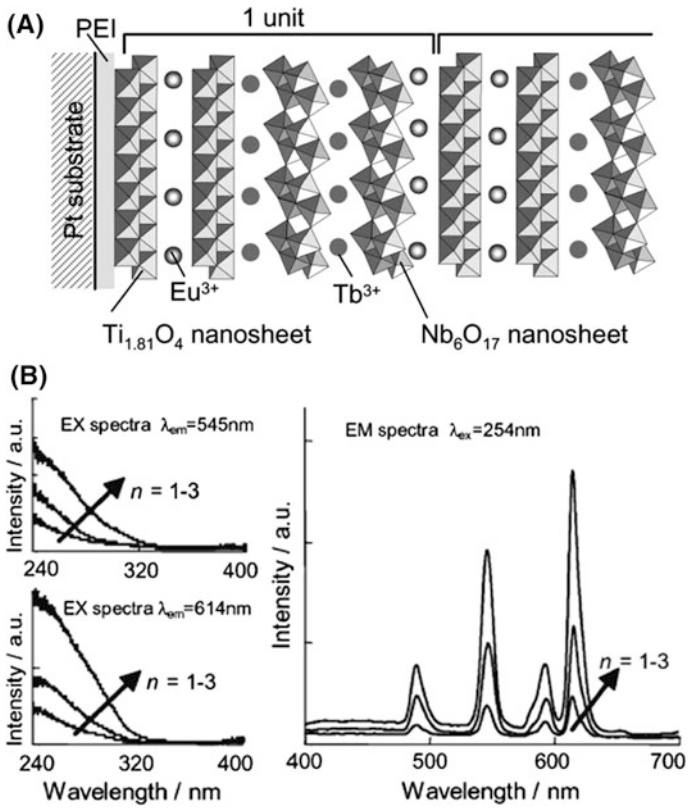

Fig. 15.7 **A** Structure of the multilayer film intercalated with Eu^{3+} and Tb^{3+} ions. **B** Excitation and emission spectra of $[Eu–Tb–multisheet]_n$ (n = 1–3). (Reprinted with Permission from Ref. [70]) Copyright 2006 Royal Society Chemistry

creation of unexpected unique properties. The remarkably enhanced electronic coupling in the 2D nanosheet-based nanohybrids relies on the fact that all the component ions are exposed on the surface of very thin 2D nanosheets and can be strongly modified by the interaction with hybridized species. The unprecedented efficient interaction in the 2D nanosheet-based hybrid materials provides useful opportunity to effectively tailor their electronic, optical, and morphological properties, which are closely related to the photofunctionalities of these hybrid materials. Additionally the high flexibility of the chemical composition of nanosheet allows us to optimize the photofunctionalities of the 2D nanosheet-based materials. Since it is possible to replace the cationic and anionic components of 2D nanosheet with substituent ions, the band structure of this material including bandgap energy and the positions of VB and CB can be finely tailored. The fine-tuning of the band structure of nanosheet makes it possible to control the internal electron transfer in the 2D nanosheet-based hybrids and thus to optimize their photofunctionalities. Although there are plenty of 2D metal oxide nanosheets

available as a building block for the advanced nanohybrid architecture, only a few metal oxide nanosheets such as titanate, niobate, and tantalate are explored in the context of photofunctional hybridization. Taking into account rich opportunities in designing and tailoring the chemical and physical properties of the exfoliated 2D nanosheets, the hybridization strategy using the 2D inorganic nanosheets leads to the exploration of diverse novel photofunctional materials with unexpected or remarkably improved functionality.

References

1. Gunjakar JL, Kim IY, Lee JM et al (2014) Exploration of nanostructured functional materials based on hybridization of inorganic 2D nanosheets. J Phys Chem C 118:3847–3863
2. Kim IY, Jo YK, Lee JM et al (2014) Unique advantages of exfoliated 2D nanosheets for tailoring the functionalities of nanocomposites. J Phys Chem Lett 5:4149–4161
3. Tran PD, Wong LH, Barber J et al (2012) Recent advances in hybrid photocatalysts for solar fuel production. Energy Environ Sci 5:5902–5918
4. Kim H, Kim J, Kim W et al (2011) Enhanced photocatalytic and photoelectrochemical activity in the ternary hybrid of $CdS/TiO_2/WO_3$ through the cascadal electron transfer. J Phys Chem C 115:9797–9805
5. Sekizawa K, Maeda K, Domen K et al (2013) Artificial Z-scheme constructed with a supramolecular metal complex and semiconductor for the photocatalytic reduction of CO_2. J Am Chem Soc 135:4596–4599
6. Kim S-J, Kim IY, Patil SB et al (2014) Composition-tailored 2D $Mn_{1-x}Ru_xO_2$ nanosheets and their reassembled nanocomposites: improvement of electrode performance upon Ru substitution. Chem Eur J 20:5132–5140
7. Oh E-J, Kim TW, Lee KM et al (2010) Unilamellar nanosheet of layered manganese cobalt nickel oxide and its heterolayered film with polycations. ACS Nano 4:4437–4444
8. Ataca C, Sahin H, Ciraci S (2012) Stable, single-layer MX_2 transition-metal oxides and dichalcogenides in a honeycomb-like structure. J Phys Chem C 116:8983–8999
9. Sasaki T, Watanabe M (1998) Osmotic swelling to exfoliation. Exceptionally high degrees of hydration of a layered titanate. J Am Chem Soc 120:4682–4689
10. Jo YK, Kim IY, Gunjakar JL et al (2014) Unique properties of 2D layered titanate nanosheets as a building block for the optimization of the photocatalytic activity and photostability of TiO_2-based nanohybrids. Chem Eur J 20:10011–10019
11. Park D-H, Hwang S-J, Oh J-M et al (2013) Polymer–inorganic supramolecular nanohybrids for red, white, green, and blue applications. Prog Polym Sci 38:1442–1486
12. Choy J-H (2004) Intercalative route to heterostructured nanohybrids. J Phys Chem Sol 65:373–383
13. Paek SM, Jung H, Lee YJ et al (2006) Exfoliation and reassembling route to mesoporous titania nanohybrids. Chem Mater 18:1134–1140
14. Kim IY, Lee KY, Kim TW et al (2011) Porous zirconium complex-layered titanate nanohybrids with gas adsorption and photocatalytic activity. Mater Lett 65:894–896
15. Kim TW, Hwang SJ, Park Y et al (2007) Chemical bonding character and physicochemical properties of mesoporous zinc oxide-layered titanate nanocomposites. J Phys Chem C 111:1658–1664
16. Lee JM, Jin HB, Kim IY et al (2015) A crucial role of Rh substituent ion in photoinduced internal electron transfer and enhanced photocatalytic activity of CdS-$Ti_{(5.2-x)/6}Rh_{x/2}O_2$ nanohybrids. Small 11:5771–5780

17. Liu G, Wang L, Sun C et al (2009) Nitrogen-doped titania nanosheets towards visible light response. Chem Commun 1383–1385
18. Osada M, Takanashi G, Li B-W et al (2011) Controlled polarizability of one-nanometer-thick oxide nanosheets for tailored, high-k nanodielectrics. Adv Funct Mater 21:3482–3487
19. Osada M, Sasaki T, Ono K et al (2011) Orbital reconstruction and interface ferromagnetism in self-assembled nanosheet superlattices. ACS Nano 5:6871–6879
20. Kim TW, Hur SG, Hwang SJ et al (2007) Heterostructured visible-light-active photocatalyst of chromia-nanoparticle-layered titanate. Adv Funct Mater 17:307–314
21. Kim TW, Hur SG, Hwang S-J et al (2006) Layered titanate-zinc oxide nanohybrids with mesoporosity. Chem Commun 220–222
22. Gunjakar JL, Kim TW, Kim HN et al (2011) Mesoporous layer-by-layer ordered nanohybrids of layered double hydroxide and layered metal oxide: highly active visible light photocatalysts with improved chemical stability. J Am Chem Soc 133:14998–15007
23. Kim TW, Ha H-W, Paek M-J et al (2010) Unique phase transformation behavior and visible light photocatalytic activity of titanium oxide hybridized with copper oxide. J Mater Chem 20:3238–3245
24. Gunjakar JL, Kim TW, Kim IY et al (2013) Highly efficient visible light-induced O_2 generation by self-assembled nanohybrids of inorganic nanosheets and polyoxometalate nanoclusters. Sci Rep 3:2080
25. Kim TW, Hwang SJ, Jhung SH et al (2008) Bifunctional heterogeneous catalysts for selective epoxidation and visible light driven photolysis: nickel oxide-containing porous nanocomposite. Adv Mater 20:539–542
26. Kim TW, Ha HW, Paek M-J et al (2008) Mesoporous iron oxide-layered titanate nanohybrids: soft-chemical synthesis, characterization, and photocatalyst application. J Phys Chem C 112:14853–14862
27. Osada M, Sasaki T (2012) Two-dimensional dielectric nanosheets: novel nanoelectronics from nanocrystal building blocks. Adv Mater 24:210–228
28. Wang L, Sasaki T (2014) Titanium oxide nanosheets: graphene analogues with versatile functionalities. Chem Rev 114:9455–9486
29. Jang ES, Chang JJ, Gwak J et al (2007) Asymmetric high-T_c superconducting gas separation membrane. Chem Mater 19:3840–3844
30. Fukuda K, Sato J, Saida T et al (2013) Fabrication of ruthenium metal nanosheets via topotactic metallization of exfoliated ruthenate nanosheets. Inorg Chem 52:2280–2282
31. Walter MG, Warren EL, McKone JR et al (2010) Solar water splitting cells. Chem Rev 110:6446–6473
32. Kudo A, Miseki Y (2009) Heterogeneous photocatalyst materials for water splitting. Chem Soc Rev 38:253–278
33. Osterloh FE (2013) Inorganic nanostructures for photoelectrochemical and photocatalytic water splitting. Chem Soc Rev 42:2294–2320
34. Schaak RE, Mallouk TE (2000) Prying apart ruddlesden-popper phases: exfoliation into sheets and nanotubes for assembly of perovskite thin films. Chem Mater 12:3427–3434
35. Rostamzadeh T, Adireddy S, Wiley JB (2015) Formation of scrolled silver vanadate nanopeapods by both capture and insertion strategies. Chem Mater 27:3694–3699
36. Yao Y, Chaubey GS, Wiley JB (2012) Fabrication of nanopeapods: scrolling of niobate nanosheets for magnetic nanoparticle chain encapsulation. J Am Chem Soc 134:2450–2452
37. Ma R, Liu Z, Li L et al (2006) Exfoliating layered double hydroxides in formamide: a method to obtain positively charged nanosheets. J Mater Chem 16:3809–3813
38. Shibata T, Takanashi G, Nakamura T et al (2011) Titanoniobate and niobate nanosheet photocatalysts: superior photoinduced hydrophilicity and enhanced thermal stability of unilamellar Nb_3O_8 nanosheet. Energy Environ Sci 4:535–542
39. Akatsuka K, Takanashi G, Ebina Y et al (2012) Electronic band structure of exfoliated titanium- and/or niobium-based oxide nanosheets probed by electrochemical and photoelectrochemical measurements. J Phys Chem C 116:12426–12433

40. Jung TS, Kim TW, Hwang SJ (2009) Mesoporous assembly of layered titanate with well-dispersed Pt cocatalyst. Bull Korean Chem Soc 30:449–453
41. Kim TW, Kim IY, Im JH et al (2009) Improved photocatalytic activity and adsorption ability of mesoporous potassium-intercalated layered titanate. J Photochem Photobiol A: Chem 205:173–178
42. Park S, Lee JM, Jo YK et al (2014) A facile exfoliation-crystal growth route to multicomponent Ag_2CO_3/Ag-Ti_5NbO_{14} nanohybrids with improved visible light photocatalytic activity. Dalton Trans 43:10566–10573
43. Kim HN, Kim TW, Kim IY et al (2011) Cocatalyst-free photocatalysts for efficient visible-light-induced H_2 production: porous assemblies of CdS quantum dots and layered titanate nanosheets. Adv Funct Mater 21:3111–3118
44. Fu J, Li G, Xi F et al (2012) Hybrid nanocomposite with visible-light photocatalytic activity: CdS–pillared titanate. Chem Engineer J 180:330–336
45. Zhang KZ, Lin BZ, Chen YL et al (2011) Fe-doped and ZnO-pillared titanates as visible-light-driven photocatalysts. J Colloid Interface Sci 358:360–368
46. Chen ZJ, Linn BZ, Chen YL et al (2010) Pillaring and photocatalytic properties of mesoporous α-Fe2O3/titanate nanocomposites via an exfoliation and restacking route. J Phys Chem Solids 71:841–847
47. Liu H, Lin B, He L et al (2013) Mesoporous cobalt-intercalated layered tetratitanate for efficient visible-light photocatalysis. Chem Engineer J 215–216:396–403
48. Li B, Lin BZ, Zhang O et al (2012) Heterostructured tin oxide-pillared tetratitanate with enhanced photocatalytic activity. J Colloid Interface Sci 386:1–8
49. Kang JH, Yeo HJ, Jeong JH (2012) Titania-pillared molybdenum oxide as a new nanoporous photocatalyst. J Phys Chem Solids 73:1469–1472
50. Wang Q, Lin BZ, Xu BH et al (2010) Preparation and photocatalytic properties of mesoporous SnO_2–hexaniobate layered nanocomposite. Microporous Mesoporous Mater 130:344–351
51. Li X, Zhang T, Gu S et al (2013) Reduced graphene oxide/potassium niobate composite nanoscrolls with enhanced photocatalytic activity for dye degradation. Sep Purif Technol 108:139–142
52. Lin BZ, Li XL, Xu BH et al (2012) Improved photocatalytic activity of anatase TiO_2-pillared $HTaWO_6$ for degradation of methylene blue. Microporous Mesoporous Mater 155:16–23
53. Pian XT, Lin BZ, Chen YL et al (2011) Pillared nanocomposite TiO_2/Bi-doped hexaniobate with visible-light photocatalytic activity. J Phys Chem C 115:6531–6539
54. Lin B, He L, Zhu B et al (2012) Visible-light photocatalytic activity of mesoporous nanohybrid assembled by tantalotungstate nanosheets and manganese ions. Catal Commun 29:166–169
55. Yui T, Mori Y, Tsuchino T et al (2005) Synthesis of photofunctional titania nanosheets by electrophoretic deposition. Chem Mater 17:206–211
56. Haryanto A, Fernando S, Murali N (2005) Current status of hydrogen production techniques by steam reforming of ethanol: a review. Energy Fuel 19:2098–2106
57. Kochuveedu ST, Jang YH, Kim DH (2013) A study on the mechanism for the interaction of light with noble metal-metal oxide semiconductor nanostructures for various photophysical applications. Chem Soc Rev 42:8467–8493
58. Gong J, Liang J, Sumathy K (2012) Review on dye-sensitized solar cells (DSSCs): fundamental concepts and novel materials. Renew Sustain Energy Rev 16:5848–5860
59. Paek SM, Jung H, Lee YJ et al (2006) Nanostructured TiO_2 films for dye-sensitized solar cells. J Phys Chem Solids 67:1308–1311
60. Seger B, McCray J, Mukherji A et al (2013) An n-type to p-type switchable photoelectrode assembled from alternating exfoliated titania nanosheets and polyaniline layers. Angew Chem Int Ed 52:6400–6403
61. Ozawa TC, Fukuda K, Akatsuka K et al (2006) Preparation and characterization of the Eu^{3+} doped perovskite nanosheet phosphor: $La_{0.90}Eu_{0.05}Nb_2O_7$. Chem Mater 19:6575–6580

62. Ozawa TC, Fukuda K, Akatsuka K et al (2008) $Eu_{0.56}Ta_2O_7$: A new nanosheet phosphor with the high intrananosheet site photoactivator concentration. J Phys Chem C 112:1312–1315
63. Ozawa TC, Fukuda K, Akatsuka K et al (2008) $(K_{1.5}Eu_{0.5})Ta_3O_{10}$: a far-red luminescent nanosheet phosphor with the double perovskite structure. J Phys Chem C 112:17115–17120
64. Ida S, Ogata C, Eguchi M et al (2008) Photoluminescence of perovskite nanosheets prepared by exfoliation of layered oxides, $K_2Ln_2Ti_3O_{10}$, $KLnNb_2O_7$, and $RbLnTa_2O_7$ (Ln: Lanthanide Ion). J Am Chem Soc 130:7052–7059
65. Ida S, Ogata C, Unal U et al (2007) Preparation of a blue luminescent nanosheet derived from layered perovskite $Bi_2SrTa_2O_9$. J Am Chem Soc 129:8956–8957
66. Ozawa TC, Fukuda K, Akatsuka K et al (2009) Enhancement of host excitation-mediated photoluminescence and preferential quenching of direct photoactivator excitation-mediated photoluminescence by exfoliation of layered $KLa_{0.90}Sm_{0.05}Nb_2O_7$ into $La_{0.90}Sm_{0.05}Nb_2O_7$ Nanosheets. J Phys Chem C 113:8735–8742
67. Xin H, Ma R, Wang L et al (2004) Photoluminescence properties of lamellar aggregates of titania nanosheets accommodating rare earth ions. Appl Phys Lett 85:4187–4189
68. Xin H, Ebina Y, Ma R et al (2006) Thermally stable luminescent composites fabricated by confining rare earth complexes in the two-dimensional gallery of titania nanosheets and their photophysical properties. J Phys Chem B 110:9863–9868
69. Matsumoto Y, Unal U, Kimura Y et al (2005) Synthesis and photoluminescent properties of titanate layered oxides intercalated with lanthanide cations by electrostatic self-assembly methods. J Phys Chem B 109:12748–12754
70. Ida S, Araki K, Unal U et al (2006) Photoluminescence properties of multilayer oxide films intercalated with rare earth ions by the layer-by-layer technique. Chem Commun 3619–3621
71. Ida S, Unal U, Izawa K et al (2006) Photoluminescence spectral change in layered titanate oxide intercalated with hydrated Eu^{3+}. J Phys Chem B 110:23881–23887

Chapter 16
Efficient Photocatalytic Systems Integrated with Layered Materials Promoters

Yusuke Ide

16.1 Introduction

Enhancement of the photocatalytic efficiency of semiconductor photocatalysts has actively been investigated for the efficient utilization of solar energy for environmental purification, fuel production and fine chemical syntheses. In the photocatalytic reactions of semiconductors, electron-hole pairs generated by their band gap excitation in the bulk are transferred to the surface adsorbed molecules with competition of charge recombination; the photocatalytic efficiency therefore depends largely on their charge separation efficiency, surface areas, and so on. Layered materials composed of semiconducting nanosheets, such as layered titanates and niobates, have been expected as promising photocatalysts, because of potential in prompt carrier migration to the surface and large surface area based on ultrathin thickness of nanosheets [1–5]. Since the discovery of exfoliation and restacking of layered semiconductors [6, 7], a great number of research has been carried out to enhance the photocatalytic efficiency by enhanced charge separation at host-guest interfaces and increase in surface area upon pillaring of interlayer spaces through hybridization with various functional units including nanoparticles and even other kinds of nanosheets [8–13]. These progresses are also well-reviewed by Prof. Hwang et al. in the previous chapter of this book.

Layered materials, such as smectite of clay minerals, have been investigated as supports of semiconductor photocatalysts [14–16]. In these studies, photocatalyst particles are immobilized in the interlayer spaces or on the particle outer surface of

Y. Ide (✉)
International Center for Materials Nanoarchitectonics (MANA),
National Institute for Materials Science (NIMS), Tokyo, Japan
e-mail: IDE.Yusuke@nims.go.jp

Y. Ide
Graduate School of Creative Science and Engineering,
Waseda University, Shinjuku, Japan

T. Nakato et al. (eds.), *Inorganic Nanosheets and Nanosheet-Based Materials*,
Nanostructure Science and Technology, DOI 10.1007/978-4-431-56496-6_16

layered materials, which mainly act to (i) avoid the aggregation of photocatalyst particles, (ii) make their recovery from reaction media more easily, and (iii) concentrate reactant molecules near photocatalysts by the adsorption to enhance the decomposition of the reactants. A good example is the enhanced photocatalytic decomposition of aqueous phenols over TiO_2 particles deposited on montmorillonite whose interlayer was modified with a long-chain alkylammonium cation to adsorb phenols [14]. Similar phenomena were observed for a layered niobate exchanged with a long-chain alkylammonium cation [17].

In this chapter, the author focus on integration of semiconductor photocatalysts with layered materials producing unusual photocatalytic systems. In these systems, photocatalysts particles are not intercalated/deposited in/on the layered materials and are mixed with layered materials at more macroscopic level. For examples, because some layered materials show unique charge transfer, they can enhance the charge separation efficiency of semiconductor photocatalysts even when the two kinds of particles are mixed (and interacted each other) in reaction media. On the other hand, since molecular recognition ability of layered materials can be controlled as well-reviewed by Prof. Okada and Prof. Ogawa in the previous chapter of this book, they can alter the distribution of products and by-products during photocatalytic reactions, increasing the yield and selectivity of desired products. Herein, the author summarize such unusual photocatalytic systems by emphasizing how the properties and functions of layered materials play a role to enhance the photocatalytic efficiency.

16.2 Charge Transfer Promoters

Graphene has attracted a lot of attention as supports of semiconductor photocatalysts due to its high electron conductivity [18] since the pioneering work by Kamat and co-workers, who had reported the synthesis TiO_2/graphene hybrid and the feasibility of using graphene as an electron-transfer medium to enhance the charge separation efficiency of TiO_2 [19]. Hexagonal-BN (h-BN), a structural analogue of graphite, has been known as an insulator with a wide band gap (up to 7 eV) [20, 21]. However, some recent studies have demonstrated that nanostructured h-BN, depending on its morphology (nanoribbons, monolayer-nanosheets, and so on), shows electronic transport comparable to metals or metal oxides [22] or semiconducting properties [23], [24]. Indeed, hybridization of semiconductor photocatalysts with h-BN to enhance the photocatalytic efficiency has been reported [25–27]. As a pioneering work, Tang et al. [25] synthesized h-BN nanotube/TiO_2 (rutile) hybrid by deposition of rutile on h-BN nanotube surface from $TiCl_3$ solution. This hybrid showed a remarkable photocatalytic activity with respect to reduction of Ni^{2+} in water, while a commercial TiO_2 scarcely showed the activity under the identical condition. The proposed mechanism involved the enhanced charge separation via transfer of photogenerated holes on rutile to h-BN due to the intrinsic electrostatic field of h-BN nanotube surface.

When compared to hybridization described above, particle-level mixing of semiconductor photocatalysts and h-BN materials can be more simple, effective and versatile. Fu et al. prepared a composite of h-BN/TiO_2 by ball-milling of commercial h-BN and TiO_2 (mainly composed of anatase) particles [28]. The composites containing 0.5 wt% of h-BN showed the enhanced activity by up to 15 times with respect to the degradation of cationic organic dyes in water. It was proposed that transfer of photogenerated holes in the bulk of the TiO_2 component to the surface was promoted by the adjacent h-BN that had become negatively charged because of the formation of N defects originated from the reconstruction and deterioration of the original h-BN during the ball milling process.

We recently reported that Au nanoparticle-loaded TiO_2(Au/TiO_2), a widely investigated visible light-responsive TiO_2 [29, 30], showed considerably enhanced activity when simply mixed with h-BN nanosheets in the photocatalytic reaction medium [31]. The activity of Au nanoparticle-loaded P25 (Au/P25), one of the most active Au/TiO_2 for oxidations [32], evaluated by the oxidative decomposition of formic acid in water into CO_2 under visible light irradiation, was enhanced up to 3 times depending on the added amount of h-BN nanosheets (Fig. 16.1). We could conclude that electrons, injected from Au nanoparticle to the conduction band of P25, were transferred to the h-BN nanosheets to be consumed by reducing O_2 into O_2^-, retarding charge recombination efficiently.

It was worth noting that a hybrid of Au/TiO_2 and h-BN nanosheets (Au/TiO_2/BN), synthesized by the deposition of anatase particles on h-BN nanosheets from $TiCl_3$ solution and subsequent selective deposition of Au nanoparticles on the TiO_2 moiety [27], showed considerably lower activity than the Au/P25-BN mixture and lower activity than Au/P25 alone with the same amount of photocatalysts (Fig. 16.1). This stems from that Au/P25 shows considerably higher activity than

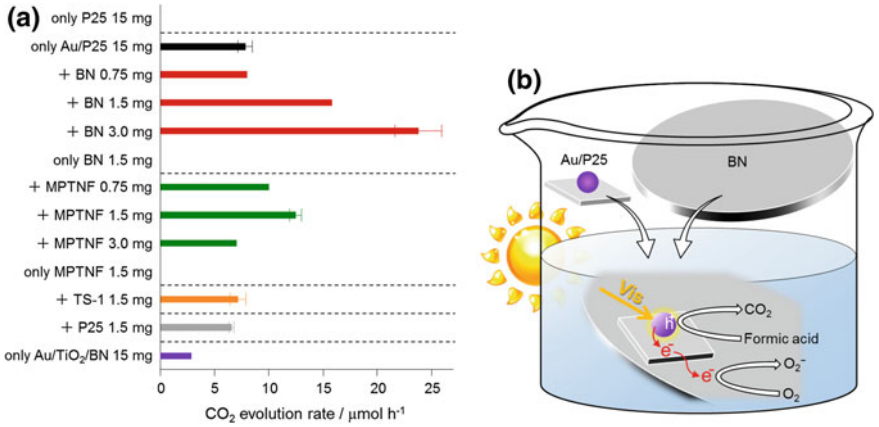

Fig. 16.1 **a** Photocatalytic activity for oxidation of formic acid in water to CO_2 over different samples under visible light irradiation ($\lambda > 420$ nm). **b** Scheme for enhanced photocatalytic activity of Au/P25-BN mixture

the Au/TiO_2 (anatase) phase in Au/TiO_2/BN hybrid due to the higher charge separation effciency[32] and that Au/TiO_2/BN contains only a small amount (ca. 5 wt%) of Au/TiO_2. It is quite difficult to deposit P25 particles and a larger amount of anatase fine particles on h-BN nanosheets for synthesizing Au/TiO_2/BN hybrids with enhanced activity. It is also difficult to use a larger amount of Au/TiO_2/BN for photocatalytic reactions in aqueous solutions because of its bulkiness (lightness) and resistance to wetting with water. Therefore, the availability of the highly active Au/P25 in adequate amounts is a great advantage of this simple method of mixing with h-BN nanosheets over the hybridization approach. In the consideration of the fact the band gap of h-BN materials are controlled even to sensitize TiO_2 [24], h-BN can be a new type of promoters of semiconductor photocatalysts alternative to graphene.

Very recently, we have found that a simple mixture of P25 TiO_2 and a layered titanate (the proton-exchanged form of $K_{0.8}Ti_{1.73}Li_{0.27}O_4$, named HTO) shows considerably higher photocatalytic activity for the oxidative decomposition of formic acid in water and H_2 production from water under simulated solar light than P25, a bench mark photocatalyst [33]. In this case, HTO, which scarcely shows a photocatalytic activity probably due to the rapid charge recombination, showed remarkably enhanced photocatalytic activity upon mixing with P25 as a result of retardation of charge recombination through transfer of photoexcited electrons from HTO to P25 (Fig. 16.2). It was indicated that interparticle electrostatic interactions and conduction band potentials of P25 and HTO were important for such electron transfer. Remarkably, the activity of the HTO/P25mixture was higher than that of HTO modified with Pt nanoparticles, a widely used co-catalyst. Given rich intercalation

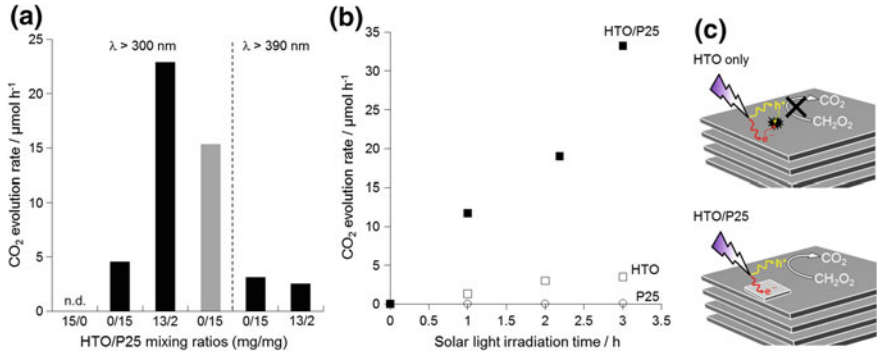

Fig. 16.2 **a** CO_2 evolution rates at different HTO/P25 (mg/mg) mixing ratios under full-spectrum simulated solar light and simulated solar light with a wave length of $\lambda > 390$ nm at which HTO is not excited but P25 is. The gray bar indicates the CO_2 evolution rate for Pt nanoparticle-loaded HTO. **b** Time courses of H_2 evolution from water containing methanol on P25, HTO and HTO/P25 mixture under full-spectrum simulated solar light. **c** Scheme for photocatalytic reactions on HTO and HTO/P25 mixture

chemistry of layered titanates and other layered semiconductors, this findings will make their photocatalytic applications more effective and feasible.

Such simple mixing in reaction media of two kinds of semiconductors particles has been used also for visible light-induced photocatalytic water splitting into H_2 and O_2 by a two-step photoexcitation system, so-called Z scheme, using H_2-evolving and O_2-evolving photocatalysts and shuttle redox couple between them [34]. In this system, photoexcited electrons on H_2-evolving photocatalyst reduce water to H_2, and holes generated oxidize a reductant to an oxidant. The oxidant generated is then reduced back to the reductant by the photoexcited electrons on O_2-evolving photocatalyst where holes oxidize water to O_2. Applying Z-scheme systems can thus lower the energy required to drive each photocatalysis process, enabling us to utilize a wider range of visible light than in single visible light-responsive photocatalysts having sufficient potentials for overall water splitting [34]. Abe and co-workers achieved efficient and long-life time water splitting by using layered niobates ($H_4Nb_6O_{17}$) sensitized with organic dyes such as coumarin and carbazole having the interlayer Pt nanoparticles as H_2-evolving photocatalyst, IrO_2 and Pt nanoparticles-loaded WO_3 as an O_2-evolving photocatalyst, and I_3^-/I^- redox couple (Fig. 16.3) [35]. In this system, the attached dyes stably generated H_2 and I_3^- from an aqueous KI solution and the IrO_2 and Pt-loaded WO_3 oxidized water to O_2 and reduced the I_3^- back to I^-. The use of the layered niobate effectively suppressed the backward reduction of I_3^- to I^- because it was hard for I_3^- anions to access the Pt particles inside due to the electrostatic repulsion between I_3^- and negatively charged niobate layers [2]. The introduction of oligothiophene moiety in the sensitizers was also important because the oxidized states of the dye molecules were relatively stable even in water to exhibit long-lifetime reversible oxidation/reduction cycles.

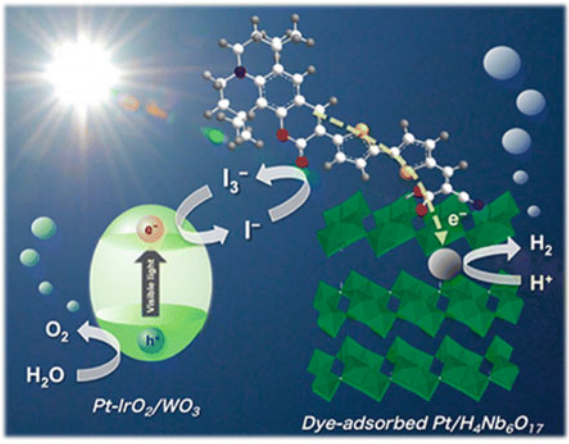

Fig. 16.3 Scheme for overall water splitting using dye-sensitized $H_4Nb_6O_{17}$ with interlayer Pt nanoparticles as H_2-evolving photocatalyst and Pt and IrO_2 nanoparticles co-modified WO_3 as H_2-evolving photocatalyst. Reprinted with permission from Ref. [35]

16.3 Molecular Recognition

Molecular recognition ability of layered materials can also play important roles in photocatalytic reactions. Partial oxidation of organic molecules with molecular O_2 by photocatalysis has long been investigated for green fine chemical synthesis. Semiconductor photocatalyst such as TiO_2 easily overoxidize organic substrates to undesired by-products such as CO_2, however, due to the presence of highly oxidizing radical species when used as photocatalyst for partial oxidation. Developing new photocatalysts has thus been investigated extensively for enhancing yields and selectivity of partially oxidized products [36]. On the other hand, we have reported that when the partial oxidation of benzene to phenol (direct benzene oxidation), which is one of the most desired and challenging reactions in industry, is conducted using a commercial TiO_2 in the presence of a layered silicate adsorbent, phenol can be recovered in a high yield (recovery) and selectivity (purity) [37]. The H^+-exchanged form (H-mag) of a layered silicate, magadiite (Na-mag), was used to adsorb phenol rapidly and selectively by hydrogen-bonding interactions from water containing benzene (Fig. 16.4a, b). During the photocatalytic reaction, phenol was scarcely detected in the liquid phase (Fig. 16.4c). These results indicate that photocatalytically generated phenol was rapidly, selectively and efficiently captured by H-mag not to be overoxidized, after which the captured phenol could be easily eluted by simple washing (Fig. 16.4d).

Recently, we successfully extended this strategy to synthesize another partially oxidized product, catechol, not but phenol (Fig. 16.5a) [38]. In this case, we used a layered silicate, Hiroshima University Silicate 7 (HUS-7, Fig. 16.5b), that can recognize catechol, not but phenol (Fig. 16.5c, d). This silicate has hydrophilic (silanol groups and water molecules) and hydrophobic (benzene rings) functionalities in the interlayer space. Catechol, with a balanced hydrophilic and hydrophobic nature, may thus adsorb selectively and effectively on HUS-7 over benzene, phenol and other hydroxyl phenols. A wide variety of layered materials with tailor-made molecular recognition abilities is available [39], semiconductor photocatalysts and layered materials can thus be the best combination for versatile and green fine chemical syntheses.

If layered material adsorbents that recognize CO_2 are integrated with photocatalytic systems for decomposition of organic compounds in water into CO_2 (complete oxidation), we can enhance the photocatalytic activity. We had preliminary found that the photocatalytic decomposition of organic compounds in water on semiconductor photocatalysts such as TiO_2 was enhanced when the reactions were conducted with conventional CO_2 adsorbents including amino group-modified SBA-15 mesoporous silica (NH_2-SBA) placed in the gas phase of the reaction container [40]. Although the mechanism was not clear, the decomposition rates depended on the performances of CO_2 adsorbents placed. We have therefore designed a new CO_2 adsorbent, magadiite with the interlayer amino and octadecyl groups (NH_2-C_{18}-mag), exhibiting better performance [41]. Figure 16.6 shows adsorption isotherms of CO_2, N_2 and H_2O vapor on NH_2-C_{18}-mag, together with

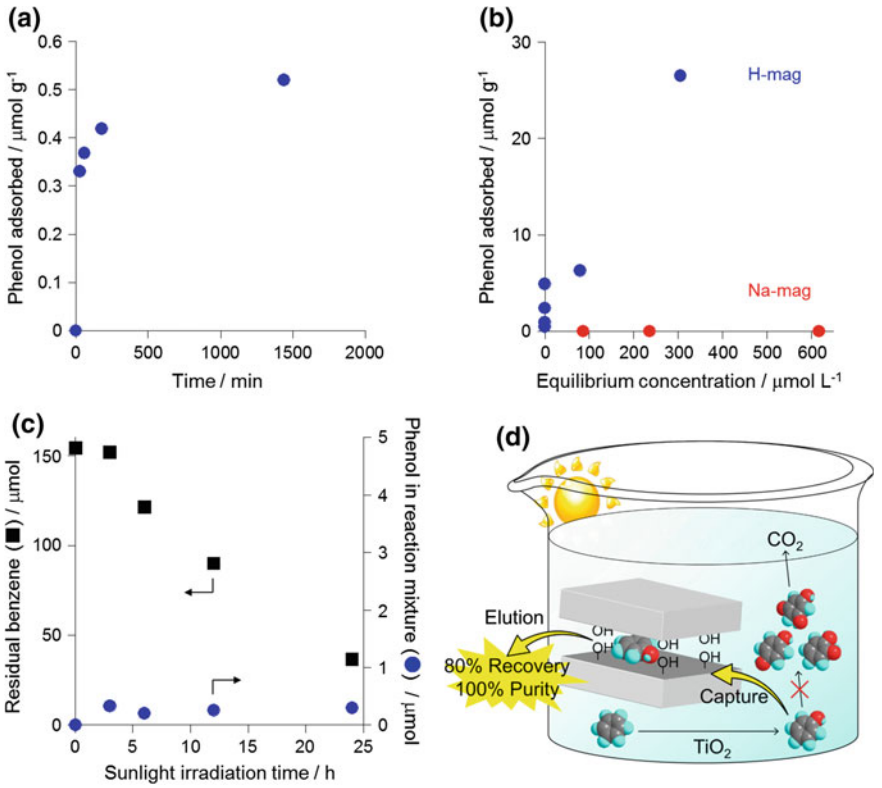

Fig. 16.4 **a** Time course of adsorption of phenol on H-mag from water containing benzene. **b** Adsorption isotherms of phenol on H-mag and Na-mag from water containing benzene. **c** Concentration of benzene and phenol during the photocatalytic reaction. **d** Scheme for photocatalytic oxidation of benzene to phenol over TiO_2 in the presence of the phenol-philic adsorbent

those on NH_2-SBA and magadiite modified with one of the two functional groups (NH_2-mag and C_{18}-mag). NH_2-C_{18}-mag effectively adsorbed CO_2 like conventional NH_2-SBA, and more selectively adsorbed CO_2 over N_2 and H_2O vapor than NH_2-SBA (these gases are the headspace components of photocatalytic decomposition of organic compounds in water, as well as main components of flue gases). Such effective and selective CO_2 adsorption was not observed for NH_2-mag and C_{18}-mag. We thus considered the main reasons for the high CO_2 adsorption performance of NH_2–C_{18}–mag as follows: (i) the narrow but amine-modified expandable interlayer space which limits N_2 adsorption but allows CO_2 and H_2O adsorption (the attached octadecyl groups may not only initiate CO_2 and H_2O adsorption as pillars but also control H_2O uptake due to the hydrophobicity), (ii) the closely arranged amine and co-adsorbed H_2O that are favorable for efficient CO_2 binding

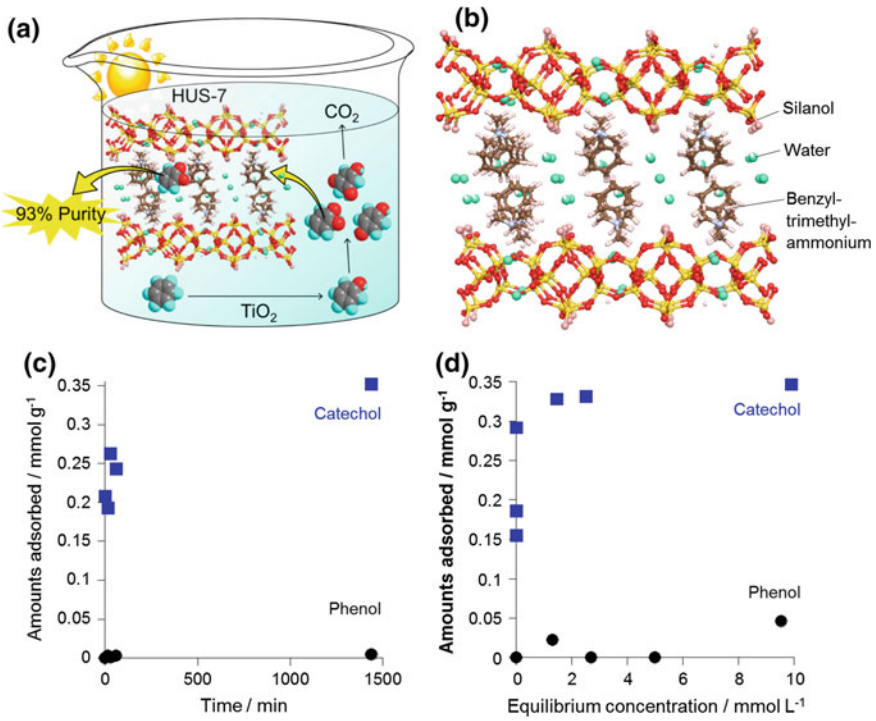

Fig. 16.5 **a** Scheme for photocatalytic oxidation of benzene to catechol over TiO_2 in the presence of the catechol-philic adsorbent. **b** Structure of HUS-7. **c** Time course of adsorption of catechol and phenol on HUS-7 from acetonitrile containing benzene, phenol and catechol. **d** Adsorption isotherms of catechol and phenol on HUS-7 from acetonitrile containing benzene, phenol and catechol

(theoretically 2 mol of amine can react with 1 mol of CO_2 under dry conditions, whereas the reaction stoichiometry changes to 1:1 in the presence of H_2O).

As expected, NH_2-C_{18}-mag was better additive of photocatalytic decomposition of organic compounds in water [41]. Figure 16.7 shows the visible light-induced photocatalytic decomposition of formic acid in water into CO_2 by Au nanoparticle-loaded CeO_2 (Au/CeO_2) [42] at different conditions. The decomposition rate really depended on the CO_2 adsorption efficiency and selectivity of the studied CO_2 adsorbents and NH_2–C_{18}-mag gave the best result. It should be noted here that the photocatalytic formic acid decomposition was scarcely enhanced when the reaction was conducted in air, namely an open system. These results indicate the importance of factitious and efficient removal of CO_2 by CO_2 adsorbents to enhance the efficiency of photocatalytic organic pollutant removal.

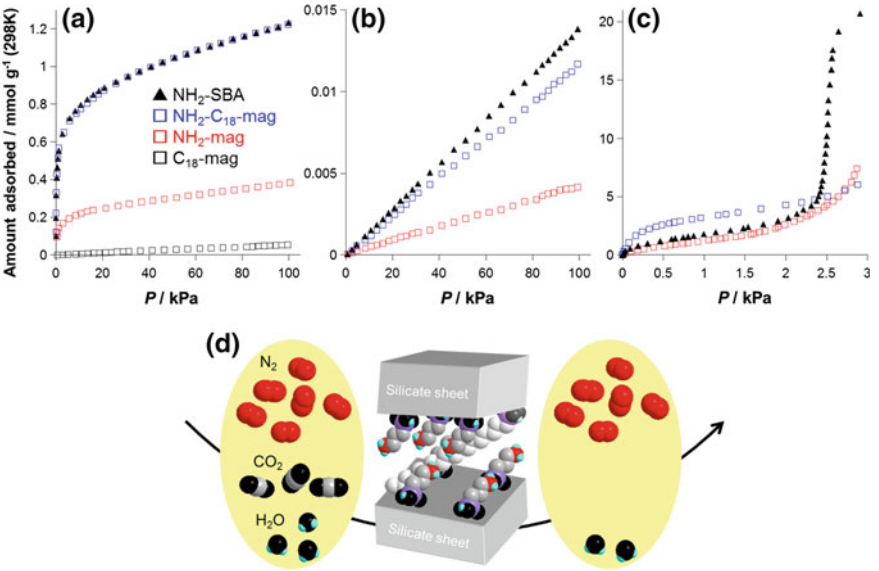

Fig. 16.6 Adsorption isotherms at 298 K of **a** CO_2, **b** N_2 and **c** H_2O vapor on different materials **d** scheme for selective CO_2 uptake by NH_2-C_{18}-mag

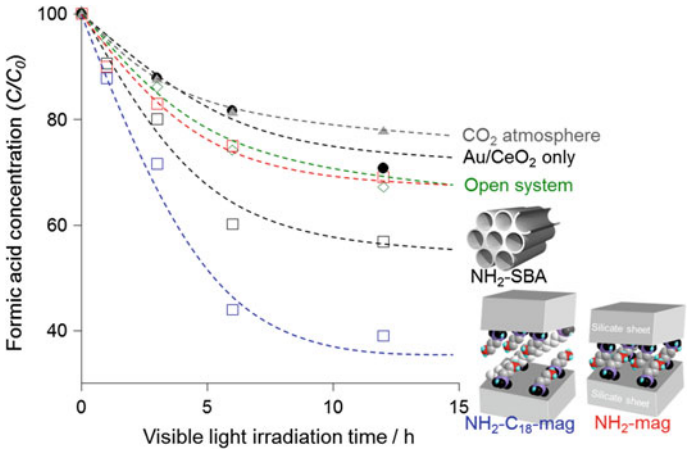

Fig. 16.7 Time course of photocatalytic oxidation of formic acid in water to CO_2 by Au/CeO_2 under different conditions. *Inset* shows the schematic structures of CO_2 adsorbents placed in the gas phase of the reactions

16.4 Others

In rare case, clays unusually affect photocatalytic reactions. Ogawa and co-workers reported the enhanced photocatalytic oxidation of benzene by P25 TiO_2 in clay suspensions [43]. As shown in Fig. 16.8, the benzene consumption rate in aqueous suspensions of a swelling clay, synthetic saponite (Sumecton SA), was faster than that in water and depending on the added amount of saponite. The partially oxidized products, phenol, catechol, and 1,2,4-trihydroxybenzene were detected during the reactions and a smaller amount of phenol and catechol, and larger amount of 1,2,4-trihydroxybenzene formed when a larger amount of saponite was used. In consideration of the fact that benzene is oxidized to phenol and phenol is then oxidized to phenols such as catechol and 1,2,4-trihydroxybenzen to be completely oxidized to CO_2, it is thought that saponite suspensions enhance the photocatalytic oxidation of benzene over P25. Similar results were observed when other swelling clay, montmorillonite, and a non-swelling clay, talc, were used. The fact that even talc dispersion enhanced the photocatalytic activity implies that the adsorption of benzene on the clays themselves scarcely contributes to the photocatalytic reactions. The properties of clay suspensions or dispersions such as hydrophilicity were proposed as possible factors of the enhanced photocatalytic activity.

Ogawa et al. also reported the visible light-induced photocatalytic oxidation of aqueous benzene over tris(2,2'-bipyridine)ruthenium(II) complex-intercalated synthetic saponite simply mixed or hybridized with anatase TiO_2 nanoparticles [44, 45]. The photostability of the organic dye in the photocatalytic systems was improved, probably due to the separation of the organic dye from the TiO_2 surface by the thin clay layer (Fig. 16.9). The fact that the photocatalytic reaction proceeded even in the absence of molecular O_2 implied the enhanced charge separation

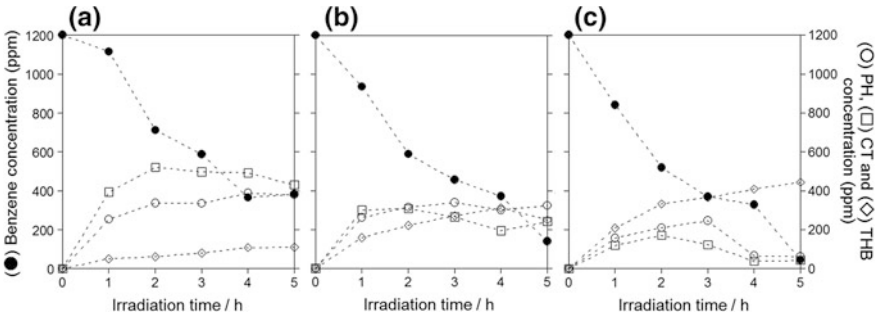

Fig. 16.8 Photocatalytic oxidation of benzene over P25 in **a** water and in water containing **b** 0.2 wt% and **c** 1 wt% of saponite. PH, CT and THB indicate phenol, catechol and 1,2,4-trihydroxybenzene, respectively

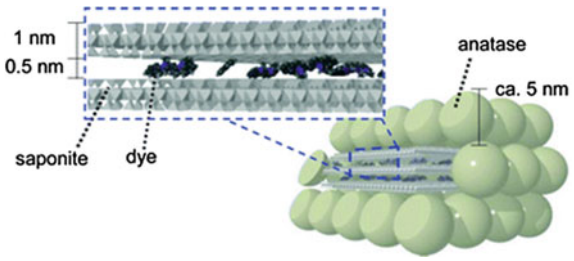

Fig. 16.9 Schematic drawing of the dye-clay intercalation compound hybridized with anatase TiO_2 nanoparticles. Reprinted with permission from Ref. [44]

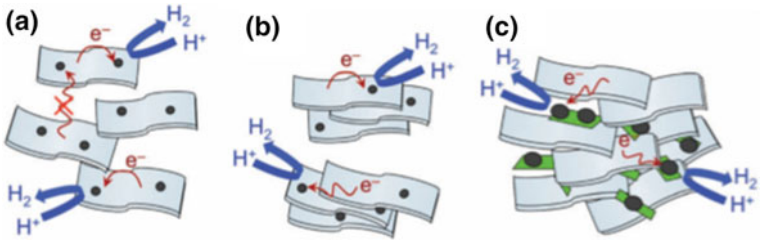

Fig. 16.10 Schematic representation of the effective photocatalytic H_2 evolution from water in $K_4Nb_6O_{17}$ and clay nanosheets systems. In the Pt-loaded niobate nanosheet colloid, the Pt co-catalyst on each nanosheet promotes the H_2 evolution but interparticle electron transfer is not allowed (**a**). If NaCl is added to this colloid, the nanosheets are stacked to facilitate the electron transfer between different nanosheets but the internal surfaces are unavailable to the reaction (**b**). In the mixture of the niobate nanosheets, Pt-loaded clay particles, and NaCl, poorly ordered restacking of the niobate nanosheets with the aid of the clay particles and NaCl allows both the interparticle electron transfer and high surface area (**c**). Reprinted with permission from Ref. [46]

on the organic dye via electron transfer from the excited dye to the TiO_2 by the presence of the thin clay layer, promoting benzene oxidation by the organic dye.

Nakato et al. [46] reported that photocatalytic H_2 evolution from water by $K_4Nb_6O_{17}$ nanosheets was greatly enhanced in the presence of clay (synthetic hectorite, Laponite) nanosheets. They systematically investigated effects of Pt co-catalyst and electrolytes on the photocatalytic activity and found that a mixture of the niobates nanosheets, Pt-loaded clay nanosheets and NaCl gave the best result. It was proposed that the clay nanosheets suppressed the regular layer stacking of the niobates nanosheets by the electrolyte to facilitate irregular layer staking of the niobates nanosheets, both increasing the surface area to expose to the reactants and enhancing charge separation through interparticle electron transfer (Fig. 16.10).

16.5 Conclusions

Examples on semiconductor photocatalytic systems integrated with layered materials promoters have been summarized. By designing physicochemical properties and functions of layered materials, the reaction efficiency of semiconductor photocatalysts with respect to variety of reactions including organic pollutant removal, H_2 evolution from water and fine chemical synthesis were successfully enhanced, whereas there were several examples in which roles of layered materials were not clear. Recent progresses on layered materials syntheses (e.g. band gap tuning, controlled particle morphology, complicated and precise interlayer modifications) will such integration more effective and sophisticated, developing realistic photocatalytic systems.

References

1. Kudo A, Tanaka A, Domen K, Maruya K, Aika K, Onishi T (1988) J Catal 111:67
2. Kim YI, Salim S, Huq MJ, Mallouk TE (1991) J Am Chem Soc 113:9561
3. Ebina Y, Tanaka A, Kond JN, Domen K (1996) Chem Mater 8:2534
4. Compton OC, Carroll EC, Kim JY, Larsen DS, Osterloh FE (2007) J Phys Chem C 111:14589
5. Okamoto Y, Ida S, Hyodo J, Hagiwara H, Ishihara T (2011) J Am Chem Soc 133:18034
6. Keller SW, Kim HN, Malloluk TE (1994) J Am Chem Soc 131:8817
7. Sasaki T, Watanabe M, Hashizume H, Yamada H, Nakazawa H (1996) J Am Chem Soc 118:8329
8. Gunjakar JL, Kim IY, Lee JM, Jo YK, Hwang SJ (2014) J Phys Chem C 114:3847
9. Kim TW, Hur SG, Hwang SJ, Park H, Choi W, Choy JH (2007) Adv Mater 17:304
10. Oshima T, Lu D, Ishitani O, Maeda K (2015) Angew Chem Int Ed 54:2698
11. Gunjakar JL, Kim TW, Kim HN, Kim IY, Hwang SJ (2011) J Am Chem Soc 133:14998
12. Mochizuki D, Kumagai K, Maitani MM, Wada Y (2012) Angew Chem Int Ed 51:5452
13. Ida S, Takashiba A, Koga S, Hagiwara H, Ishihara T (2014) J Am Chem Soc 136:1872
14. Ilisz I, Dombi A, Mogyorósi K, Farkas A, Dékány I (2002) Appl Catal B 39:247
15. Aranda P, Kun R, Martín-Luengo MA, Letaïef S, Dékány I, Ruiz-Hitzky E (2008) Chem Mater 20:84
16. Liu J, Zhang G (2014) Phys Chem Chem Phys 16:8178
17. Wei Q, Nakamura K, Endo Y, Kameyama M, Nakato T (2008) Chem Lett 37:152
18. Xiang Q, Yu J, Jaroniec M (2012) Chem Soc Rev 41:782
19. Williams G, Seger B, Kamat PV (2008) ACS Nano 2:1487
20. Golberg D, Bando Y, Huang Y, Terao T, Mitome M, Tang C, Zhi C (2010) ACS Nano 4:2979
21. Solozhenko VL, Lazarenko AG, Petitet JP, Kanaev AV (2001) J Phys Chem Solids 62:1331 and references therein
22. Lyalin A, Nakayama A, Uosaki K, Taketsugu T (2013) J Phys Chem C 117:21359
23. Zeng HB, Zhi CY, Zhang ZH, Wei XL, Wang XB, Guo WL, Bando Y, Golberg D (2010) Nano Lett 10:5049
24. Weng Q, Ide Y, Wang X, Zhang C, Jiang X, Xue Y, Dai P, Komaguchi K, Bando Y, Golberg D (2015) Nano Energy 16:19 and references therein
25. Tang C, Li J, Bando Y, Zhi C, Golberg D (2010) Chem Asian J 5:1220
26. Wang M, Li M, Xu L, Wang L, Ju Z, Li G, Qian Y (2011) Catal Sci Technol 1:1159

27. Ide Y, Liu F, Zhang J, Kawamoto N, Komaguchi K, Bando Y, Golberg D (2014) J Mater Chem A 2:4150
28. Fu X, Hu Y, Yang Y, Liu W, Chen S (2013) J Hazardous Mater 244–245:102
29. Tian Y, Tatsuma T (2005) J Am Chem Soc 127:7632
30. Cheng H, Fuku K, Kuwahara Y, Mori K, Yamashita H (2015) J Mater Chem A 3:5244
31. Ide Y, Nagao K, Komaguchi K, Fuji R, Kogure A, Sugahara Y, Bando Y, Golberg D (2016) Phys Chem Chem Phys 18:79
32. Tsukamoto D, Shiraishi Y, Sugano Y, Ichikawa S, Tanaka S, Hirai T (2012) J Am Chem Soc 134:6309
33. Saito K, Kozeni M, Sohmiya M, Komaguchi K, Ogawa M, Sugahara Y, Ide Y (2016) Phys Chem Chem Phys 18:30920
34. Abe R (2010) J Photochem Photobiol C Photochem Rev 11:179
35. Abe R, Shinmei K, Koumura N, Hara K, Ohtani B (2013) J Am Chem Soc 135:16872
36. Shiraishi Y, Hirai T (2008) J Photochem Photobiol C Photochem Rev 9:157
37. Ide Y, Torii M, Sano T (2013) J Am Chem Soc 135:11784
38. Ide Y, Torii M, Tsunoji N, Sano T (2015) Clay Sci 19:59
39. Okada T, Ide Y, Ogawa M (2012) Chem Asian J 7:1980
40. Ide Y, Kagawa N, Ogo S, Sadakane M, Sano T (2012) Chem Commun 48:5521
41. Ide Y, Kagawa N, Sadakane M, Sano T (2013) Chem Commun 49:9027
42. Kominami H, Tanaka A, Hashimoto K (2010) Chem Commun 46:1287
43. Ide Y, Matsuoka M, Ogawa M (2012) Chem Cat Chem 4:628
44. Ogawa M, Sohmiya M, Watase Y (2011) Chem Commun 47:8602
45. Goto T, Ogawa M (2016) RSC Adv 6:23794
46. Nakato T, Fujita T, Mouri E (2015) Phys Chem Chem Phys 17:5547

Chapter 17
Semiconductor Nanosheets

Shintaro Ida

17.1 Band Structures of Nanosheets

Various types of nanosheet have been reported, which are prepared by exfoliation of layered compound [1–18] or hydrothermal method [19–22]. Nanosheets can be mainly calcified into three types: conductive nanosheet, semiconducting nanosheet, and insulating nanosheet. Especially, semiconducting nanosheets have attracted a lot attention in various fields, such as electric device, solar cell, emitting device, phosphor, and photocatalyst. Although, it is difficult to clarify distinguish the difference between semiconducting and insulating nanosheets, in this section, nanosheet with a bandgap of 4 eV or less is described as a semiconducting nanosheet. To design devises or photocatalyst, information of band structure such as conduction and valence band positions is important. For the preparation of photocatalyst for water splitting, the conduction band positon should be more negative than 0 V versus HNE at least, and then conduction band position should be more positive than 1.23 V versus NHE. In most cases, the band structure of the nanosheet is largely different from the parent layered compound, which might be due to the quantum size effect accompanying structure change from 3D bulk structure to 2D structure. In general, the bandgap of the nanosheet prepared by exfoliation of layered compound is larger than that of the parent layered compound [23]. Akatsuka et al. reported the detailed band structures for several types of oxide nanosheet as shown in Fig. 17.1 [24]. Recently, various types of nanoplate and nanosheet are prepared by one-pot hydrothermal method [19–22] or heat treatment of hydroxide nanosheet [25]. These nanosheets have been studied for the

S. Ida (✉)
Department of Applied Chemistry, Faculty of Engineering, Kyushu University,
744 Motooka, Nishi-ku, Fukuoka 819-0395, Japan
e-mail: s-ida@cstf.kyushu-u.ac.jp

T. Nakato et al. (eds.), *Inorganic Nanosheets and Nanosheet-Based Materials*,
Nanostructure Science and Technology, DOI 10.1007/978-4-431-56496-6_17

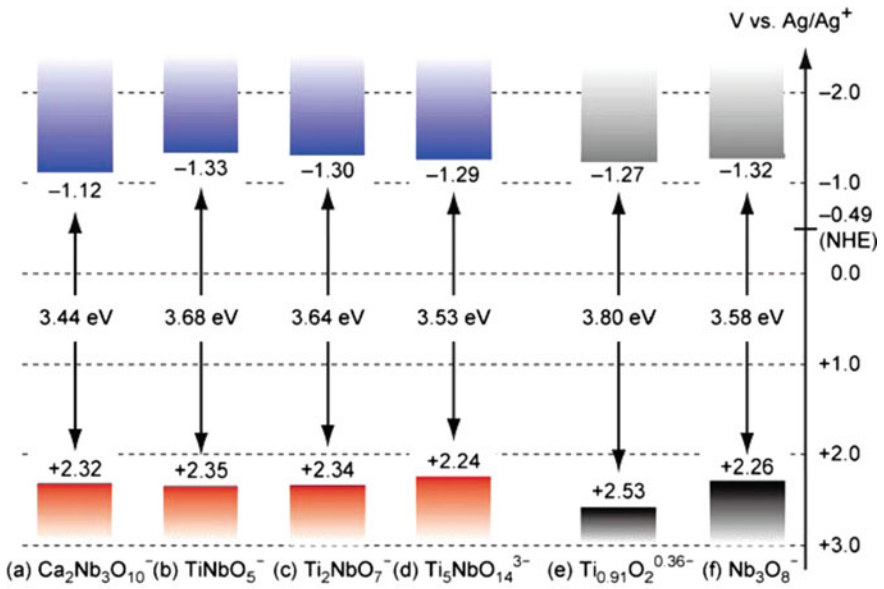

Fig. 17.1 Energy diagram depicting the conduction band edges, valence band edges, and bandgap energy for **a** $Ca_2Nb_3O_{10}^-$, **b** $TiNbO_5^-$, **c** $Ti_2NbO_7^-$, **d** $Ti_5NbO_{14}^{3-}$, **e** $Ti_{0.91}O_2^{0.36-}$, **f** $Nb_3O_8^-$ nanosheets. (Reprinted from Ref. [24] reported by Akatsuka et al.)

preparation of ultrathin devise or photocatalyst. The information of the band structures of the various types nanosheet and nanoplate are summarized in Table 17.1.

17.2 Nanosheet pn-Junction

The creation of an ultrathin p–n junction using nanosheet is one of initial challenges to apply nanosheet to electronic devises. In the field of chemistry, the preparation of pn-junction is a strategy to improve photocatalytic activity for water splitting, since it is considered that the potential gradient generated by formation of a p–n junction can act to suppress the recombination reaction of the photoexcited electrons and holes generated by bandgap excitation [26–35]. These potential gradient in the pn-junction is generated by the diffusion of free charge carriers between n-type and p-type semiconducting materials, which is expected to function as a driving force for the photoexcited holes and electrons to move to their respective reduction and oxidation sites: photoexcited electrons and holes move to n-type and p-type sides, respectively as shown in Fig. 17.2 In the case of photocatalyst for water splitting, the photoexcited electron reduces water to hydrogen, and the photoexcited hole

Table 17.1 Band structures of the various types nanosheets and nanoplates

Nanosheet or nanoplate	Conduction band position [V] versus NHE	Valence band position [V] versus NHE	Bandgap [eV]	References
C_3N_4 nanosheet	–	–	2.97–2.79	[37, 38]
MoS_2 nanosheet	−0.12	1.78	1.90	[39]
SnS	0	+1.3	1.3	[19]
$Bi_{24}O_{31}Cl_{10}$	−0.91	+1.80	2.71	[21]
BiOCl	−0.81	+2.53	3.34	[22]
CuS	−1.7	+0.7	2.4	[20]
WO_3 nanosheet	+0.23	+3.13	2.88	[40]

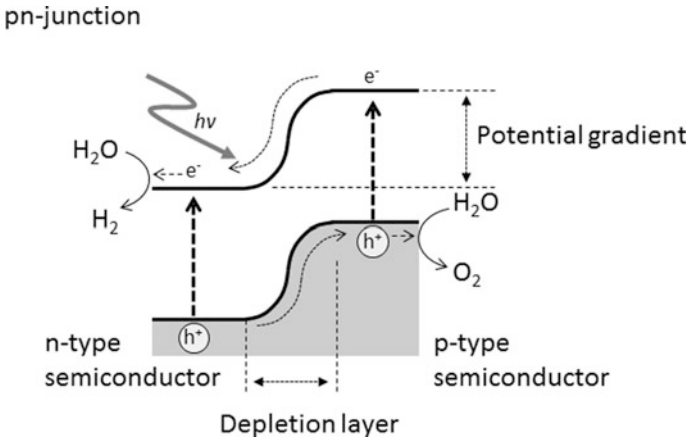

Fig. 17.2 Reaction model for photocatalytic water splitting on pn-junction photocatalyst

oxidizes water to oxygen. These carrier dynamics is similar to the photoexcited carriers in the solar cell.

However, the study on the ultrathin pn-junction has several problems such as the difficulty in the preparation and evaluation of such junction structures. The preparation of ultrathin p–n junctions using two materials with a large lattice mismatch by chemical vapor deposition (CVD) is generally difficult, since crystal lattice strain or a decrease in crystallinity is generated in the interface between pn-junction during the CVD process. Therefore, it is still unclear whether the formation of an ultrathin pn-junction is effective for improvement of photocatalytic activity. Furthermore, in general, it is said that sufficient thickness (space) is essential to create potential gradient in the depletion layer, since the space where the free charge carriers diffuse gives the depletion region (potential gradient). That is, in

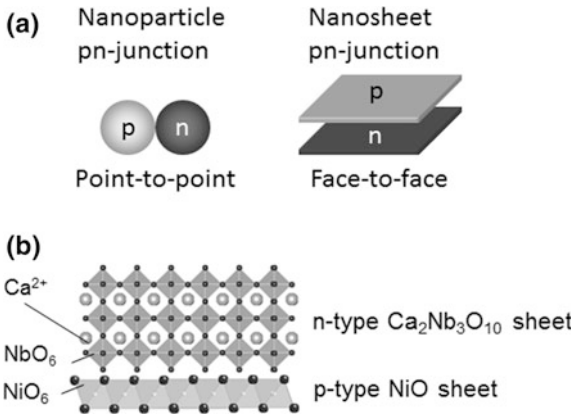

Fig. 17.3 **a** Preparation of pn-junction from nanoparticles or nanosheets and **b** structural model of p-NiO nanosheet/n-type $Ca_2Nb_3O_{10}$ nanosheet pn-junction

the case of an ultrathin pn-junction, there might be not enough space to form the depletion region. Nanosheets are a candidate material to provide an answer to the issue mentioned above. An ideal pn-junction without an amorphous layer between different p-type and n-type semiconductor materials with different crystal phases can be prepared by stacking of p-type and n-type semiconductor nanosheets. The p-type and n-type nanocrystals (nanoparticles) without inner defect may be potential materials, however, in the case of nanoparticle, the connection between them is point-to-point, while in a nanosheet, the connection is face-to-face as shown in Fig. 17.3a. This is an advantage of nanosheets in the evaluation of pn-junctions. In this section, our approach for the preparation of ultrathin pn-junction using p-type NiO and $Ca_2Nb_3O_{10}$ nanosheets is introduced below [26].

Figure 17.3b shows structural models of p-type NiO nanosheet/$Ca_2Nb_3O_{10}$ nanosheet pn-junction. The NiO nanosheet has the same crystal structure as a one-NiO_6-unit layer of the (111) plane in bulk NiO. The $Ca_2Nb_3O_{10}$ nanosheet has a perovskite structure with A-site Ca^{2+} and B-site Nb^{5+}, and has two perovskite units thick. The theoretical thickness of the NiO and $Ca_2Nb_3O_{10}$ nanosheet are 0.3 nm and 1.3 nm, respectively.

The $Ca_2Nb_3O_{10}$ nanosheet can be prepared by exfoliation of $HCa_2Nb_3O_{10,}$ [36] and the NiO sheet is prepared by the dehydration reaction of a $Ni(OH)_{2-\delta}$ nanosheet that is obtained by exfoliation of a layered nickel hydroxide intercalated with dodecyl sulfate ion [11, 25]. Figure 17.4 shows the AFM image and cross-sectional profile of the p–n junction region of p-NiO crystals on n-$Ca_2Nb_3O_{10}$crystals in the image. The hexagonal and polygonal shapes correspond to NiO and $Ca_2Nb_3O_{10}$ nanosheets, respectively.

The thickness of the p-NiO crystal estimated from the AFM image is ca. 0.3–0.4 nm and that of the n-$Ca_2Nb_3O_{10}$ crystal is 1.4–1.7 nm, and then the total thickness of the p–n junction is around 2.0 nm. The selected area electron diffraction pattern of the p–n (NiO/$Ca_2Nb_3O_{10}$) junction region had two types of diffraction patterns assigned to the [001]-oriented $Ca_2Nb_3O_{10}$ crystal and

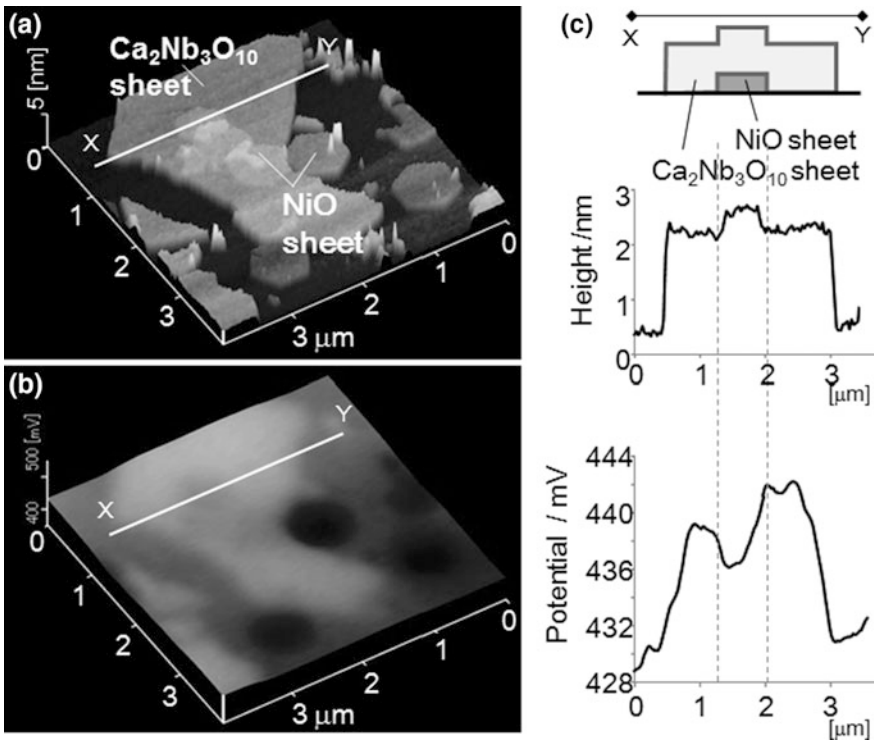

Fig. 17.4 **a** AFM image, **b** KPFM image, and **c** cross-sectional profile between *X* and *Y* of the $Ca_2Nb_3O_{10}$/NiO (n–p) junction film under vacuum conditions (Reproduced from Ref. [26])

[111]-oriented NiO crystal. An ideal p–n junction structure consisting of only single crystals can be obtained by stacking of the nanosheet.

Potential gradient in the pn-junction can be measured using Kelvin probe force microscopy (KPFM). Figure 17.4b shows the KPFM image of nanosheet pn-junciton. The KPFM image shows light (high surface potential) and dark (low surface potential) areas, which indicate shallow and deep Fermi levels, respectively. Considering the difference in the surface potential between the $Ca_2Nb_3O_{10}$ and NiO crystals, the sections consisting of only NiO crystals are darker than those of only $Ca_2Nb_3O_{10}$ crystals. This image provides information regarding the relationship between the Fermi levels of n-$Ca_2Nb_3O_{10}$ and p-NiO crystals. Figure 17.4c shows a cross-sectional profile of the junction in the AFM and KPFM images. The surface potential of the $Ca_2Nb_3O_{10}$/NiO junction is higher than that of the NiO crystals and lower than that of the $Ca_2Nb_3O_{10}$ crystals. It should be noted that the surface potential is not affected by the height of the material, but is affected by the underlying material (junction structure). In general, the diffusion of carriers continues until the drift current balances the diffusion current. In the case of an ultrathin film, there is not enough space to form the depletion region, which is formed in a general p–n junction device. However, the electrons and holes diffuse across the

junction into the p-type NiO/n-type $Ca_2Nb_3O_{10}$ nanosheets to balance the Fermi level as long as carriers such as electrons and holes exist in *n*-type $Ca_2Nb_3O_{10}$ and p-NiO nanosheets. Therefore, in the region of the ultrathin p–n junction (2 nm), it is assumed that all donors and acceptors are fully ionized. This means that the carrier concentration in the $Ca_2Nb_3O_{10}$ and NiO sheets decreases in the ultrathin p–n junction region. It is known that the position of the Fermi level varies as a function of carrier concentration and obeys the following equations:

$$n\text{ - type semiconductor}: E_F = E_C + k_b T \ln(n_0/N_C) \tag{17.1}$$

$$p\text{ - type semiconductor}: E_F = E_V - k_b T \ln(p_0/N_V) \tag{17.2}$$

where E_F is Fermi level, E_C is conduction band level, E_V is valence band level, k_b is Boltzmann constant, N_C is effective density of conduction band states, N_V is effective density of valence band states, n_0 is thermal-equilibrium concentrations of electrons, p_0 is thermal-equilibrium concentrations of holes, and T is temperature. When the carrier concentration in the $Ca_2Nb_3O_{10}$/NiO junction part decreases, the position of the Fermi level in the ultrathin p–n junction becomes lower than that of $Ca_2Nb_3O_{10}$ and higher than that of NiO. Thus, the position of the Fermi level in the ultrathin p–n junction identifies the positions between the Fermi levels of $Ca_2Nb_3O_{10}$ and NiO nanosheets. The difference in the surface potentials (position of Fermi level) obtained from KFM images of $Ca_2Nb_3O_{10}$/NiO substrates as shown in Fig. 17.4b corresponds to the position of the Fermi level obtained from the theory on Fermi levels.

In the case of the $Ca_2Nb_3O_{10}$/NiO junction film, most parts of the surface are $Ca_2Nb_3O_{10}$ crystals. However, there are high and low surface potential areas in the same surface of $Ca_2Nb_3O_{10}$ crystals, because there are junction and non-junction regions. Thus, potential gradients are generated on the same surface of the $Ca_2Nb_3O_{10}$ crystals. It is possible that these potential gradients result in spatially separated reaction sites (oxidation and reduction sites), which may suppress the recombination reaction.

We next turned our attention to the reaction site in this system. There is no special adsorption site such as a co-catalyst and no differences in the chemical composition and crystal face between $Ca_2Nb_3O_{10}$ (top layer)/NiO junction and non-junction (only $Ca_2Nb_3O_{10}$) regions. Thus, it is likely that the difference in the surface potential is the only driving force to separate electrons and holes. The separated electrons and holes reduce or oxidize water in the photocatalytic reaction. However, there have been no direct confirmations of where the hydrogen and oxygen evolution sites are. One reason for this is that hydrogen and oxygen are gases. If the product derived from the photocatalytic reaction is a solid material deposited by oxidation or reduction of metal ions, the reaction sites can be identified by observing the solid deposition sites after the photocatalytic reaction. Although such photodeposition is a good method for investigation of the reaction site, it should be noted that the photodeposition reaction is strongly influenced by the interactions between the metal ion and the deposition site, such as adsorption

and electrostatic energy, and the crystal face of the deposition site. Thus, in general, it is difficult to distinguish which factors contribute to the separation of the reaction sites. Therefore, the surface composition and crystal face of the surface should be confirmed in order to evaluate the reaction sites using the photodeposition reaction of a metal ion. However, in the case of nanosheet pn-junction, for example, the $Ca_2Nb_3O_{10}$/NiO n–p junction surface as shown in Fig. 17.4 has one ideal surface for evaluation of the reaction site. The surface contains n–p junction and non-junction regions. In the n–p junction, the NiO sheet is located under the $Ca_2Nb_3O_{10}$ sheet. Therefore, the surface condition of the $Ca_2Nb_3O_{10}$/NiO junction is exactly the same as that of the $Ca_2Nb_3O_{10}$ part. In addition, the $Ca_2Nb_3O_{10}$ surface has the same crystal face, because $Ca_2Nb_3O_{10}$ is a single crystal.

Actually, after the photodeposition reaction of MnO_x and Ag in 0.1 M $AgNO_3$ and 0.1 M $MnSO_4$ aqueous solutions was performed to confirm which parts of the junction films are photooxidation and photoreduction sites, Ag particles were deposited on $Ca_2Nb_3O_{10}$ in the non-junction region, while MnO_x particles were deposited on junctions and/or their edges. There was no material deposited on NiO in the non-junction region. In this reaction, Mn^{2+} is oxidized to Mn_2O_3 or MnO_2 by photogenerated holes, while Ag^+ is reduced to Ag by photogenerated electrons. MnO_x and Ag are deposited at the oxidation and reduction sites during the photocatalytic reaction. These results indicate that the $Ca_2Nb_3O_{10}$/NiO junctions are the photooxidation sites, while the non-junction regions and/or their edges are the photoreduction sites.

Figure 17.5 shows a proposed mechanism for the photodeposition reactions of Ag and MnO_x on the $Ca_2Nb_3O_{10}$/NiO junction surface. In the region of the ultrathin p–n junction (2 nm), it is possible to assume that all donors and acceptors are fully ionized. In addition, ionized donors remain in the narrow region of the non-junction region close to the junction edge due to the diffusion of carriers as shown in Fig. 17.5a. These ionized donors and acceptors create a difference in the space charge density around the edge of the junction, while the space charge density of the junction in the direction horizontal to the substrate is zero because the charges of the ionized donors and acceptors in the junction spatially compensate each other as shown in Fig. 17.5b. The two regions of immobile positive and negative charges around the edge of the junction might result in an electric field and band bending in the same $Ca_2Nb_3O_{10}$ nanosheet as shown in Fig. 17.5c. The photoexcited electrons and holes in the $Ca_2Nb_3O_{10}$ nanosheet are separated by the intra band bending. The photoexcited electrons move to the non-junction region (photoreduction site), and the photoexcited holes move to the junction (photooxidation site). The band structure proposed in Fig. 17.5c is in good agreement with the surface potential image (KPFM image) of the $Ca_2Nb_3O_{10}$/NiO junction (Fig. 17.4b). Although only one example is discussed here, effective use of nanosheets will aid in the elucidation of the mechanism of the photocatalytic reaction. These results indicate that material design to control the potential gradient on the catalyst surface is necessary to obtain highly efficient photocatalysts. It is expected that the evaluation method and results presented here will contribute to the development of ultrathin devise and photocatalyst using pn-junction and understanding of the reaction mechanism.

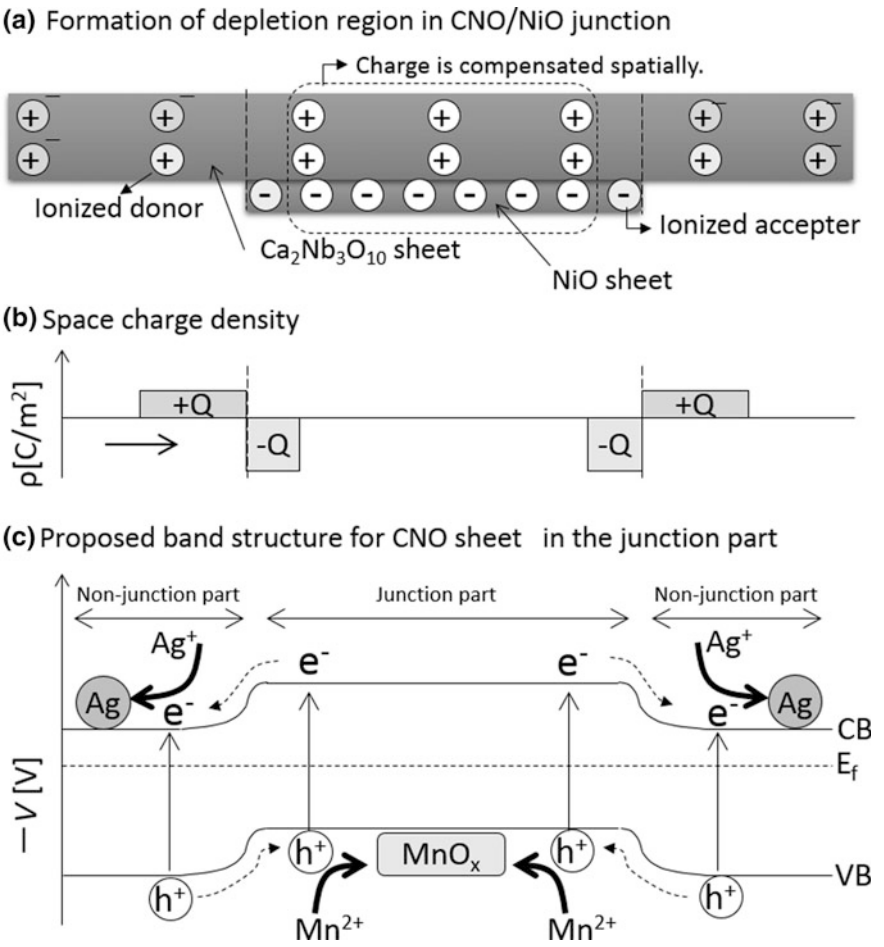

Fig. 17.5 Proposed band structure model in horizontal direction to the $Ca_2Nb_3O_{10}$/NiO junction surface; **a** formation of depletion region in the $Ca_2Nb_3O_{10}$/NiO junction, **b** space charge density remaining in the $Ca_2Nb_3O_{10}$/NiO junction surface, **c** model of band structure for $Ca_2Nb_3O_{10}$ sheet in the junction and non-junction regions (Reproduced from Ref. [26])

References

1. Abe R, Shinohara K, Tanaka A, Hara M, Kondo JN, Domen K (1997) Chem Mater 9:2179–2184
2. Sasaki T, Watanabe M (1998) J Am Chem Soc 120:4682–4689
3. Schaak RE, Mallouk TE (2000) Chem Mater 12:3427–3434
4. Ebina Y, Sasaki T, Harada M, Watanabe M (2002) Chem Mater 14:4390–4395
5. Schaak RE, Mallouk TE (2002) Chem Commun 706–707

6. Miyamoto N, Nakato T (2004) J Phys Chem B 108:6152–6159
7. Ma R, Liu Z, Li L, Iyi N, Sasaki T (2006) J Mater Chem 16:3809–3813
8. Ida S, Ogata C, Unal U, Izawa K, Inoue T, Altuntasoglu O, Matsumoto Y (2007) J Am Chem Soc 129:8956–8957
9. Ozawa TC, Fukuda K, Akatsuka K, Ebina Y, Sasaki T (2007) Chem Mater 19:6575–6580
10. Ida S, Ogata C, Eguchi M, Youngblood WJ, Mallouk TE, Matsumoto Y (2008) J Am Chem Soc 130:7052–7059
11. Ida S, Shiga D, Koinuma M, Matsumoto Y (2008) J Am Chem Soc 130:14038–14039
12. Matsumoto Y, Koinuma M, Kim SY, Watanabe Y, Taniguchi T, Hatakeyama K, Tateishi H, Ida S, Appl ACS (2010) Mater Interfaces 2:3461–3466
13. Sugiyama Y, Okamoto H, Mitsuoka T, Morikawa T, Nakanishi K, Ohta T, Nakano H (2010) J Am Chem Soc 132:5946–5947
14. Matsumoto Y, Koinuma M, Ida S, Hayami S, Taniguchi T, Hatakeyama K, Tateishi H, Watanabe Y, Amano S (2011) J Phys Chem C 115:19280–19286
15. Okamoto Y, Ida S, Hyodo J, Hagiwara H, Ishihara T (2011) J Am Chem Soc 133: 18034–18037
16. Ida S, Okamoto Y, Matsuka M, Hagiwara H, Ishihara T (2012) J Am Chem Soc 134: 15773–15782
17. Ida S, Okamoto Y, Koga S, Hagiwara H, Ishihara T (2013) RSC Adv 3:11521–11524
18. Zhang X, Xie X, Wang H, Zhang J, Pan B, Xie Y (2013) J Am Chem Soc 135:18–21. doi:10.1021/ja308249k
19. Hori S, Suzuki T, Suzuki T, Suzuki T, Nonomura S (2014) Jap J Appl Phys, 53. doi. 10.7567/JJAP.53.021801
20. Lei H, Fang G, Cheng F, Ke W, Qin P, Song Z, Zheng Q, Fan X, Huang H, Zhao X (2014) Sol Energy Mater Sol Cells 128:77–84. doi:10.1016/j.solmat.2014.05.021
21. Jin X, Ye L, Wang H, Su Y, Xie H, Zhong Z, Zhang H (2015) Appl Cat B: Environ 165: 668–675. doi:10.1016/j.apcatb.2014.10.075
22. Myung Y, Wu F, Banerjee S, Park J, Banerjee P (2015) Chem Commun 51:2629–2632. doi:10.1039/c4cc09295c
23. Sakai N, Ebina Y, Takada K, Sasaki T (2004) J Am Chem Soc 126:5851–5858. doi:10.1021/ja0394582
24. Akatsuka K, Takanashi G, Ebina Y, Haga MA, Sasaki T (2012) J Phys Chem C 116: 12426–12433
25. Ida S, Takashiba A, Ishihara T (2013) J Phys Chem C 117:23357–23363
26. Ida S, Takashiba A, Koga S, Hagiwara H, Ishihara T (2014) J Am Chem Soc 136:1872–1878
27. Meng F, Li J, Cushing SK, Zhi M, Wu N (2013) J Am Chem Soc 135:10286–10289
28. Lee JK, Lee W, Yoon TJ, Park GS, Choy JH (2002) J Mater Chem 12:614–618
29. Chen Y, Crittenden JC, Hackney S, Sutter L, Hand DW (2005) Environ Sci Tech 39: 1201–1208
30. Long M, Cai W, Cai J, Zhou B, Chai X, Wu Y (2006) J Phys Chem B 110:20211–20216
31. Kim HG, Borse PH, Jang JS, Jeong ED, Jung OS, Suh YJ, Lee JS (2009) Chem Commun 5889–5891
32. Chen C, Cai W, Long M, Zhou B, Wu Y, Wu D, Feng Y (2010) ACS Nano 4:6425–6432
33. Yang L, Luo S, Li Y, Xiao Y, Kang Q, Cai Q (2010) Environ Sci Tech 44:7641–7646
34. Yu J, Wang W, Cheng B (2010) Chem Asian J 5:2499–2506
35. Zhang Z, Shao C, Li X, Wang C, Zhang M, Liu Y, Appl ACS (2010) Mater Interfaces 2:2915–2923
36. Ebina Y, Sakai N, Sasaki T (2005) J Phys Chem B 109:17212–17216
37. Niu P, Yang Y, Yu JC, Liu G, Cheng HM (2014) Chem Commun 50:10837–10840. doi:10.1039/c4cc03060e

38. Lin Q, Li L, Liang S, Liu M, Bi J, Wu L (2015) Appl Cat B: Environ 163:135–142. doi:10.1016/j.apcatb.2014.07.053
39. Wang F, Shifa TA, Zhan X, Huang Y, Liu K, Cheng Z, Jiang C, He J (2015) Nanoscale 7:19764–19788. doi:10.1039/C5NR06718A
40. Waller MR, Townsend TK, Zhao J, Sabio EM, Chamousis RL, Browning ND, Osterloh FE (2012) Chem Mater 24:698–704. doi:10.1021/cm203293j

Chapter 18
Hybrids with Functional Dyes

Juraj Bujdák

Abbreviations

$^1\Delta_g$	Singlet oxygen
CEC	Cation exchange capacity
ED	Energy donor
EA	Energy acceptor
FRET	Förster resonance energy transfer
Hec	Hectorite
Lap	Laponite
LB	Langmuir–Blodgett
LbL	Layer-by-layer
LDH	Layered double hydroxide(s)
LNb	Layered niobate(s)
LSil	Layered silicate(s)
LTi	Layered titanate(s)
MB	Methylene blue
Mmt	Montmorillonite(s)
NLO	Nonlinear optical (or nonlinear optics)
RCMs	Reduced-charge montmorillonites
Rh	Rhodamine
ROS	Reactive oxygen species
Sap	Saponite
UV	Ultraviolet

J. Bujdák (✉)
Faculty of Natural Sciences, Department of Physical and Theoretical Chemistry, Comenius University in Bratislava, 842 15 Bratislava, Slovakia
e-mail: bujdak@fns.uniba.sk

J. Bujdák
Institute of Inorganic Chemistry, Slovak Academy of Sciences, Bratislava, Slovakia

T. Nakato et al. (eds.), *Inorganic Nanosheets and Nanosheet-Based Materials*, Nanostructure Science and Technology, DOI 10.1007/978-4-431-56496-6_18

18.1 Introduction

Hybrid materials are composed of at least two constituents and structurally built at the nanometer or molecular scale. The constituents may include molecules, functional groups, molecular fragments, polymeric chains, nanosheets, nanotubes, or other types of nanoparticles. Hybrid materials often exhibit multifunctional properties and have potential for various applications. Hybrids with organic dyes adsorbed on the surface of nanosheets or embedded in the crystals of layered compounds involve a very broad range of material types with variable structures, functionalities, and properties. Probably, the oldest hybrid material of this type is Maya blue, the pigment used by the Maya and Aztec civilizations in the era of pre-Columbian America. Maya blue is composed from indigo dye from the plant *Indigofera suffruticosa* intercalated in a clay mineral, palygorskite. The host particles of palygorskite do not contribute to the color of the pigment, but play an active role in the chemical stabilization of the dye. It is remarkable how long Maya blue paintings have lasted, despite the paints being exposed to harsh climatic conditions, high temperature and humidity. The properties of Maya blue inspired scientists, who tried to mimic its nature by developing similar types of materials [1–3]. In the modern era, the paint industry was probably one of the first branches to develop pigments based on composites of inorganic compounds with organic dyes. Inorganic solids were often used as the carriers of dye molecules, fillers, or pigment additives. Hybrid materials and nanomaterials incorporating organic dyes have only been extensively developed over the last few decades. In numerous cases, nanosheets and layered nanoparticles exhibit important functionalities and contribute to the materials' photophysical and photochemical properties. Examples include graphene and related compounds, layered semiconductors (metal oxides, hydroxides, sulfides), luminescent rare earth metal hydroxides, layered perovskites, etc. This chapter focuses on hybrid materials based on organic dyes representing the key components in terms of the materials' functionality. The dyes play primary roles in terms of the materials' optical and photofunctional properties. The inorganic components play mostly a passive role. On the other hand, inorganic layered compounds are able to significantly affect the properties of dye molecules. The inorganic layered compounds primarily include layered silicates (LSil), layered double hydroxides (LDH), but also other types. Hybrid materials with active organic dyes have been the focus of a lot of deserved attention for a few decades now. One of the first breakthrough review articles dealing with the photochemistry of such materials was published about 20 years ago [4]. This review was an inspiration for many researchers, providing original and critical perspectives on various aspects of materials of this type. Since then, thousands of papers, dozens of reviews [5–15] and several monographs and chapters [16–18] analyzing current knowledge of the topic have been published. This chapter emphasizes the

importance of the inorganic constituents in the properties of adsorbed or embedded organic dye molecules, analyzing primarily the latest knowledge published over the last decade. This chapter also explains the principles of the routes for the synthesis of active hybrid material and summarizes the phenomena occurring in these hybrid systems. Last but not least, it highlights the current state and promise of potential applications.

18.1.1 Basic Features of the Hybrids with Photoactive Dyes

Hybrids with photoactive nanosheets have received a lot of attention. However, using inert layered substrates can be advantageous in many cases. The photoactive inorganic compounds can initialize the photodecomposition of organic dyes. For example, layered titanates (LTi) are more efficient photocatalysts than standard commercial materials based on TiO_2 [19]. Some organic dyes are efficiently protected by the inert particles of LSil, whereas they decompose in the presence of photoactive layered niobates (LNb) [20]. Even mixtures of active and nonactive layered nanoparticles can significantly improve the protection of dye molecules compared to the pure semiconductor colloids. Examples are mixtures of exfoliated particles of LNb or LTi with LSil [21, 22].

The parameters of both the dyes and nanoparticle components are important to successfully design hybrid materials. The most important parameters of dye molecules include their molecular geometry and shape, charge and the distribution of functional and ionic groups, and hydrophobic or hydrophilic properties. The parameters of nanoparticles are more complex, depending on the type of layered compound, particle structure, surface reactivity, and topography. The presence of particle surface charge creates an electrostatic field affecting the orientation of polar molecules and controls the arrangement and distribution of charged ions. Ion exchange reactions have been traditionally used for the synthesis of hybrid materials of LSil and LDH. Organic counterions are irreversibly adsorbed onto the surface of nanoparticles. The binding coefficients of cationic organic dyes on the surface of LSil are several orders of magnitude larger than those of inorganic cations [23]. The dye adsorption often exceeds the cation exchange capacity (*CEC*). Molecular orientation depends on the degree of dye loading, on the size and molecular shape of dye molecules, and the presence of ionic groups. Anisotropy is one of the most important properties which can be implemented for anisotropic materials applicable in optical devices. Interesting properties can be expected based on the specific host–guest interactions leading to significant changes in dye properties. This might result from dye molecular aggregation, or can relate to the changes in dye geometry or electronic properties. Photophysical phenomena occurring in hybrid systems, such as resonance energy transfer or nonlinear optical (NLO) properties increase the attractiveness of such hybrid materials.

18.2 Surface and Structural Parameters of Inorganic Nanolayered Compounds

There is a large spectrum of inorganic layered compounds which are potential sources for nanosheets or layered particles for hybrids with functional dyes. They involve graphene, LSil, LDH, hydroxides, LTi, LNb, layered oxides, vanadates, phosphates, phosphonates, sulfides, nitrides, and others. Some basic information on these compounds is available in the literature (e.g. [24–26]). A typical example of nanolayered compounds with chemically inert surfaces are expandable LSil. They include smectites, which are expandable clay minerals such as montmorillonite (Mmt), saponite (Sap), hectorite (Hec), and related synthetic materials, such as Laponite (Lap). The particles of expandable LSil are about 0.96 nm thick, with diameters ranging from several tens to several hundreds of nm, up to a few μm. The individual layered particles of LSil are built from sheets of octahedrons and tetrahedrons linked together by covalent bonds. The octahedral sheet is based mostly on Al^{III}, Fe^{III}, Fe^{II}, Mg^{II} or Li^{I} central atoms, and O^{II-}, OH^-, F^- ligands. The occupancy in the octahedral sheets positions may lead to either a dioctahedral or trioctahedral structure. Tetrahedrons are occupied by predominantly Si^{IV} and Al^{III} central atoms. One octahedral sheet is sandwiched between two covalently bound sheets of tetrahedrons to form an individual layer. Nonequivalent isomorphous substitutions and vacancies in both the octahedral or tetrahedral sheets create a net negative charge, which is balanced by mobile exchangeable cations. The layer charge controls the distribution of exchangeable cations and plays key roles in various properties of the material. In the systems with cationic dyes, charge distribution sensitively controls the molecular aggregation [12, 27, 28] (see Sect. 18.4.3) and orientation of dye cations [29, 30] (see Sect. 18.5.1). Whereas LSil nanoparticles are built from three sheets of polyhedrons, LDH or layered hydroxides are composed of single sheets of polyhedrons of individual particles (Fig. 18.1). The topography of the particle surface at the atomic level and the presence of functional groups at the surface are very important in terms of adsorption and surface activity. One example is the specific orientation of rhodamine (Rh) and oxazine dyes in LSil hybrid films, where the inclination angle of the dyes with respect to the surface depends on the type of amine groups ($–NH_2$, –NHR, $–NR_2$, where R=methyl or ethyl). The largest orientation angles were observed for dye cations with –NHR groups (60–70°) [29–33]. It is assumed that the interaction of –NHR groups carrying a positive charge is influenced by the topography of the LSil basal surface: Probably the –NHR groups specifically interact at the surface, rearranging themselves according to pseudohexagonal cavities in the surface and causing molecules to be more inclined with respect to the plane of the surface. The smaller $–NH_2$ groups give more freedom of orientation, whereas the bulkier $–NR_2$ groups do not fit into the cavities at all. There have been no systematic studies focused on dye orientation related to different topographies of variable layered compounds.

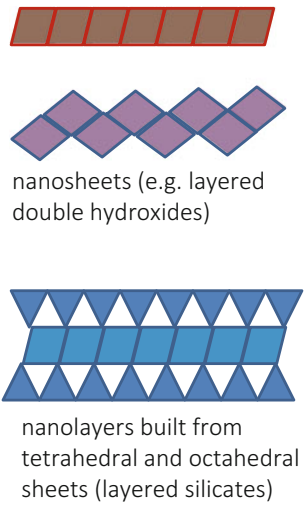

Fig. 18.1 Nanoparticles based on nanosheets or nanolayers composed from three sheets of polyhedrons

18.3 Material Types and Strategies for the Synthesis of Hybrid Materials

18.3.1 Colloids

The majority of the synthesis routes leading to hybrid materials proceeds via colloid systems with finely dispersed nanoparticles. The properties of the colloid precursors may crucially affect the quality of solid hybrid materials. The main parameter affecting the stability of colloidal systems is surface charge, which is compensated by the counterions of either an inorganic or organic type. The properties of the ions significantly affect swelling, interparticle associations, and particle exfoliation. LSil with Na^+ or Li^+ counterions swell macroscopically, forming finely dispersed individual nanoparticles [11]. Alkylammonium cations with short alkyl chains or bulky shapes are efficient swelling agents for some layered compounds with larger charge densities [20, 34]. LDH with the particles bearing a positive charge are accessible in the form with CO_3^{-2} anions, which, however, do not form stable colloids. The swelling of LDH can be achieved in organic polar solvents with NO_3^- or ClO_4^- counterions [35, 36]. However, the replacement of CO_3^{-2} anions is not easy [37, 38], and LDHs saturated with NO_3^- or ClO_4^- anions are unstable due to the presence of CO_2. The modification of LDH with organic anions of carboxylic acids, amino acids, organic sulfates can improve the stability of colloids [37]. Colloid properties are in general influenced by ionic strength, temperature, particle size, shape, and surface modification. More complex nonaqueous ternary colloidal systems sometimes including polymers or ionic surfactants have attracted a lot of attention. Premodification with large alkylammonium cations is an optimal step

toward altering surface properties, thus enhancing the stability of the colloids in organic solvents [39].

18.3.2 Surface Modification of Inorganic Nanoparticles

Premodification of the nanoparticle surface is frequently applied. There are several reasons why particle modification is performed:

- To improve colloid stability and alter particle surface properties
- To control or regulate dye adsorption
- To prevent or reduce dye molecular aggregation

Surface modification for the reduction of dye molecular aggregation is analyzed in Sect. 18.4.5. Improvements in colloid stability are often related to the modification of surface charge or the exchange of counterions. Surface grafting with molecules bearing ionic groups attached to the surface via covalent bonding can lead to significant changes in surface properties (see Sect. 18.3.4). In principle, dye adsorption itself also leads to a modification of surface properties. Thus the selection of an appropriate dye can be an alternative way to improve surface properties and achieve high colloid stability. For example, the adsorption of zwitterionic porphyrin, carrying both the cationic pyridinium and anionic carboxyl groups in the molecule, led to a significant stabilization of Mmt colloids [40]. Even the large-scale adsorption of this dye beyond the *CEC* value did not lead to particle flocculation.

The adsorption of organic ions of the opposite charge to that of the surface is often an irreversible process. However, the repulsive forces would prevent the adsorption of dye ions with the same charge. In such cases, surface modification is necessary and often realized by using ionic surfactants. The most typical examples are LSil modified with alkylammonium cations. The formed materials exhibit enhanced surface activity, and are able to absorb cations, neutral molecules as well as anions. For example, such modifications applied to Mmt turned this material into an efficient adsorbent of the anionic dye methyl orange [41]. Another type of surface modification involves surface activation with polyelectrolytes. The adsorption of organic polycations onto nanoparticles with a negative surface charge can significantly reduce or even reverse the original charge to positive values, thus creating an adsorption capacity for anionic organic dyes [42]. Applying the modification of Mmt surface with the polycation led to an increased adsorption of anionic dyes, but also retained the properties for an efficient adsorption of cations [43]. The efficient adsorption of anionic dyes on LSil can be achieved via modification with inorganic polycations or oligomeric cationic species, such as the *Keggin cation*, $Al_{13}O_4(OH)_{24}(H_2O)_{12}^{7+}$. The modification of smectites leads to materials called *pillared clays,* which exhibit enhanced porosity and interesting adsorption properties. Al^{III}-pillared clay (with *Keggin cations*) exhibited an

improved adsorption of Acid Turquoise Blue [44]. A similar trend was observed for the adsorption of orange II on silane-activated Al^{III}-pillared Mmt [45]. Besides the adsorption of anionic species, pillared clays are still able to also readily absorb cationic dyes [46], which is a similar feature to the materials modified with organic polyelectrolytes. There are some other interesting properties which have been observed for these materials: The adsorption of the cationic dye methylene blue (MB) on Fe^{III}-pillared LSil could be controlled by an external magnetic field [46]. In another study, surface modification with oligomeric cationic species led to enhanced fluorescence compared to non-pillared LSil [47].

18.3.3 Hybrids with Neutral, Insoluble, and Hydrophobic Dyes

The poor solubility of neutral and hydrophobic dyes sometimes complicates their application. Furthermore, organic nonpolar dyes which are poorly soluble in water exhibit low photoactivity in aqueous solutions. As was mentioned above, the modification of the particles with surfactants may significantly increase the adsorption of neutral dye molecules. The synthesis of hybrid materials with hydrophobic dyes must be often performed in organic solvents and/or under specific conditions to enhance dye's solubility. However, there were some recent studies which applied layered nanoparticles for dye solubilization. For example, synthetic LSil of a Lap type was used to solubilize the neutral dyes Nile red and coumarin 153 (Fig. 18.2) [48]. The co-adsorption of organic quaternary ammonium

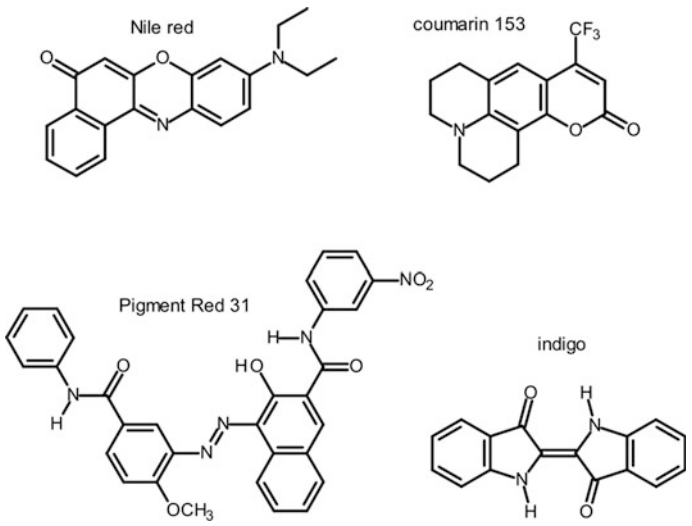

Fig. 18.2 Molecular formulas of neutral dyes used in hybrid materials

ions further enhanced dye luminescence. The small size of Lap particles guaranteed the high transparency of hybrid colloids. The stability of the hybrid dispersions remained even at higher concentrations, which indicated this material to be applicable in biophotonics [48]. The mechanism of dye solubilization in the presence of nanoparticles has not been explained yet. Theoretically there could be two different mechanisms:

1. The neutral molecule could hydrolyze, and ionized forms can be adsorbed onto the surface of opposite charge. One possible example is the reaction of the dye molecule as a Brønstedt base:

$$\mathrm{Dye\,(s) + H_2O\,(l) \rightleftarrows HDye^+\,(aq) + OH^-(aq)}$$

The cations formed would be significantly more soluble than the neutral molecules and would be selectively adsorbed on the particles with negative surface charge ($Surf^-$):

$$\mathrm{Surf^-(s) + HDye^+\,(aq) \rightleftarrows Surf^- - HDye^+\,(s)}$$

2. Poorly soluble dyes in their neutral molecular form can be stabilized in the adsorbed state to reduce hydrophobic interactions with water molecules. Thus, the stabilization of dye molecules by adsorption would be in principle the same as the precipitation of the insoluble dye molecules. Besides van der Waals forces, H-bond formation can be very important as was proven for indigo bonding in the Maya blue pigment [49]. Inspired by Maya blue, an aqueous colloid of synthetic Sap was used to dissolve the hydrophobic dye Pigment Red 31 (Fig. 18.2) [50]. The dye was bound onto the external surface via van der Waals and H-bonds but also hydrophobic interactions between the dye molecules were observed. Although no measurable intercalation of the dye was detected, the hybrid pigments were highly dispersible in water, thermally stable, and resistant to ultraviolet (UV) radiation [50]. For larger polymeric pigments, a basic solubilization route may not be efficient and special methods had to be developed. One example is a red pigment based on the large protein complex naturally occurring in red algae, called phycoerythrin. Salt-assisted adsorption promoted the fixation of phycoerythrin onto a Mmt surface [51]. In summary, the solubilization by nanoparticles seems to be very efficient for common hydrophobic dyes. This procedure can expand the use of the majority of dyes based on neutral molecules for photonic applications [52].

18.3.4 Sol–Gel Processes and Covalently Attached Dye Molecules

Hybrid materials are mostly prepared starting from the systems of both the components: Layered nanoparticles and organic dyes. However, in some cases, the syntheses of hybrid material and the formation of nanoparticles is realized in a single-step procedure. The accommodation of organic dye molecules proceeds at the same time or immediately after the formation of nanoparticles. This can be achieved relatively simply by including organic dye molecules in the mixture for nanoparticle synthesis. The earliest work using this strategy reported the formation of the hybrids based on Lap and LDH [53]. The hybrid materials with Lap particles were prepared in the course of Lap hydrothermal synthesis starting with SiO_2, $Mg(OH)_2$, LiF, and including either cationic dye alcian blue or neutral molecules of 15-crown-5-tetra-substituted phthalocyanine. The hybrids with LDHs were prepared via the hydrolysis of solutions containing $Al(NO_3)_3$, $Mg(NO_3)_2$, and NaOH, together with Cu^{II}-phthalocyanine anions. The syntheses of hybrid intercalation compounds were successful and the properties of the products were similar to those prepared by the conventional method based on ion exchange reactions [53]. The sol-gel processes are suitable routes for the incorporation of reactive dye species in hybrid materials. The dye moieties can be directly incorporated in the hybrid structure or linked via covalent bonds to nanoparticles. Trioctahedral synthetic LSil was synthesized from SiO_2, $Mg(OH)_2$, and LiF solutions together with a reactive silane molecule, carrying a coumarin dye moiety [54]. The incorporation of the coumarin fluorophores was proved by spectroscopy methods. In a similar approach, palygorskite modified with 3-aminopropyl triethoxysilane was applied as an efficient substrate, binding to specific reactive dyes [55]. In another study, a hybrid material carried two different dyes; each dye component was bound in a different way [56]. One was incorporated into the silicate matrix by hydrothermal synthesis as described in a previous work [54], and the second dye was additionally integrated by an ion exchange reaction. Förster resonance energy transfer (FRET) between these two dyes indicated a homogeneous distribution of the fluorophores in the matrix of the hybrid material [56, 57].

LSil are a typical example of the materials based on inert and chemically very stable particles. The particles edges represent a very small fraction, but with relatively reactive sites of hydrolyzed broken bonds. The high reactivity of the edge sites was utilized in another strategy for hybrid materials' preparation. The edges of LSil particles were selectively modified with reactive silane molecules bearing fluorophoric groups (Fig. 18.3) [58]. Since the particle edges represent only a minor fraction of the total surface, their modification did not significantly influence the colloid properties of the materials. On the other hand, the modification of the edges led to solid materials exhibiting relatively strong luminescence. Specific localization of the fluorophoric groups could be observed by confocal fluorescence spectroscopy only with the hybrids derived from LSi with relatively large-diameter particles [58]. Kaolinite is an LSil which neither swells nor forms stable colloids in

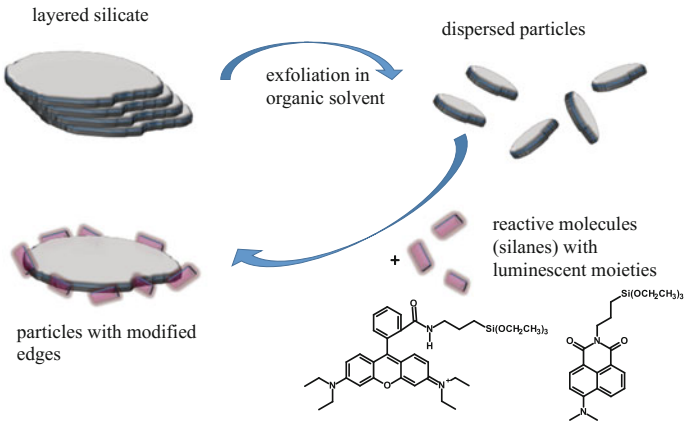

Fig. 18.3 Selective modification of particle edges with luminescent molecules. (According to reference [58])

water. Its particles do not carry any charge, so modification via ion exchange reaction cannot be applied. Therefore, hybrid materials based on kaolinite and organic dyes are rather very rare. It was reported that the microwave activation of kaolinite led to a material which exhibited better adsorption for tartrazine dye [59]. However, modification with reactive organic dyes seems to be the most affordable way [60]. After the pre-expansion of kaolinite with an organic polar solvent, the luminescent silane molecules reacted with surface OH groups leading to a unique photoactive material [60]. A very interesting but structurally complex type of hybrid material was synthesized from spherical silica particles of a submicrometer size [61]. Hydrothermal treatment with LiF and $MgCl_2$ created LSil particles attached by their edges to the silica surface. Extraordinary colloidal properties were controlled rather by the properties of silica spheres, but their adsorption properties were significantly influenced by the attached LSil particles. The modified spheres were active in the adsorption of cationic surfactant and organic dye, MB (Fig. 18.4). The colloidal stability was kept unchanged even under conditions of complete saturation with the dye cations. Under identical conditions basic hybrid MB/LSil colloids would be very unstable and completely flocculated [61].

18.3.5 Thin Solid Films

Films of hybrid materials can be used as the components in optical devices or for other numerous applications and therefore have received a lot of attention. The films based on the layered nanoparticles with organic dyes can be prepared in various ways. The simplest method is based on casting the colloids of nanoparticles on some sort of flat substrate and let the solvent evaporate out. The particles can be

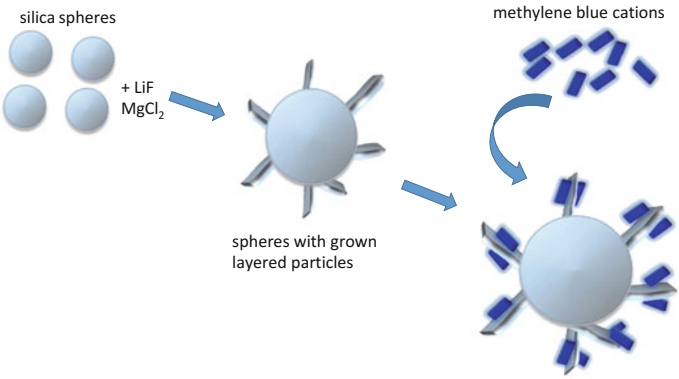

Fig. 18.4 Particles of layered silicate attached to silica *spheres* and methylene *blue* adsorption. (According to reference [61])

modified with dye molecules either already in the colloids, or in the latter step via the intercalation into the film. The most important properties which are usually required for hybrid optical films are optical homogeneity and transparency. These requirements initiated the development of various more sophisticated techniques. A spin coating and film formation via a vacuum filtration method [62] can be used for the preparation of relatively thick, but optically homogeneous and transparent films. In these cases particle size plays a significant role. Special types of films have been developed in order to precisely control composition, film thickness, structure, arrangement, and order of the discrete layers and components. These include Langmuir–Blodgett (LB) films and layer-by-layer (LbL) assemblies. Thin layers of monomolecular assemblies of amphiphilic molecules with well-defined structure and composition are basic building blocks for LB films. The assemblies are formed at an air/solution interface, from where they are deposited onto the substrate by dip coating. It is relatively simple to incorporate layered nanoparticles into LB films. Most frequently nanoparticles are modified with amphiphilic surfactant counterions; the same surfactants which are used for common LB films. The incorporation of organic dyes into LB films can be achieved in two different ways (Fig. 18.5): 1. Dye molecules are adsorbed onto the active surface of modified nanoparticles [63]. 2. Another way is to incorporate dyes molecules or ions with long alkyl chains instead of a fraction of the surfactant molecules during LB assembly. Octadecyl-Rh B or 3,3′-dioctadecyl oxacarbocyanine dye are examples of amphiphilic cations having chromophoric cationic groups, which have been applied in the production of LB films with LSil [64]. The structure of surfactant assemblies and the orientation of surfactant molecules in a hybrid LB film are similar to the films built from surfactant molecules alone (Fig. 18.5). The self-assembly of surfactant molecules and formation of dye molecular aggregates play significant roles, affecting the

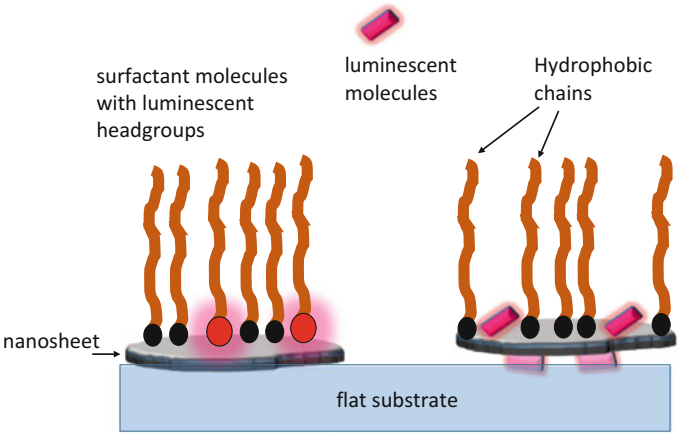

Fig. 18.5 Types of Langmuir–Blodgett films with organic dyes

optical properties of the films [65]. The influence of the surface charge density of LSil on the properties of hybrid LB films was also reported [64].

The LbL assemblies consisting of multilayers with alternating charge were discovered relatively recently. They are built via a step-by-step routine, through the deposition of a single monomolecular layer in each deposition step. The new layer with the opposite charge to the outer layer of the substrate is deposited from solution and the excess of molecules or particles is washed out after each deposition step. Coulombic forces play a key role, but other types of chemical bonds can also take a part. LbL assemblies are built by full control over the composition and order of the layers. Although the LbL technique was originally developed for the deposition of electrolytes, charged layered nanoparticles are ideal components for the multilayers of this type. The choice of the components can significantly affect the photoactivity of embedded dye molecules. For example, the dimerization of acridine orange incorporated in LbL films was significantly reduced when Lap was included in the films [66]. A detailed study utilizing chemometric analysis of the spectral data recorded after each deposition step could identify variable phenomena occurring during LbL assembly formation [67]. The outer surface with the adsorbed dye molecules exhibited significant changes upon the formation of a new layer. There was a partial desorption and conversion of dye molecules to an aggregated form. Complex and specifically designed LbL films were prepared for the purpose of investigating FRET between layers [67]. In another study, chromophoric groups were part of the polyelectrolyte chains used as the components in LbL assemblies [68]. They formed the J-aggregates exhibiting the properties of light-harvesting and excitation energy transfer systems.

18.3.6 Nanocomposites with Polymers and Other Complex Systems

More complex hybrid materials including industrial polymers were also developed. Nanocomposites of LSil particles with poly(styrene) and Rh 6G were synthesized in a two-step process [69]: First, the dye and radical initiator 2,2,6,6-tetramethyl-1-piperidyloxy (TEMPO) were intercalated in LSil. The addition of styrene and TEMPO-initiated polymerization led to polymeric nanocomposites that stabilized incorporated Rh molecules [69]. Spherical particles of poly (*N*-isopropylactylamide) hydrogels containing layered particles of Sap were used for the immobilization of various cationic species, including organic dyes [70]. Oligomeric silsesquioxane with a covalently attached chromophoric group of luminescent cyanine dye was intercalated in synthetic Sap. The hybrid material exhibited a high luminescence quantum yield and improved thermal and photochemical stability. The hybrid exhibited superior properties with respect to the luminescent oligomer or dye molecule alone [71]. In another study, hybrid mesoporous materials with high surface area were synthesized from LSil and poly (ethylene glycol) grafted sol–gel silica. The aerogel formed by evaporating the solvent exhibited hydrophobic properties, but with high capacities for the adsorption of ionic organic dyes, MB and malachite green [72]. Very interesting optical materials were developed when incorporating gold nanoparticles in LDH, exhibiting superior properties to adsorb methyl orange [73].

18.4 Molecular Aggregation and Photoactivity of Hybrid Materials

18.4.1 Metachromasy and Dye Molecular Aggregation

The discovery of dye molecular aggregation represents one of the most important milestones in the physical chemistry of organic dyes. The molecular aggregation of some organic dyes causes metachromasy, which was originally defined as significant color change induced by changing conditions, such as temperature, ionic strength, concentration, adsorption, etc. For the first time metachromasy was visually observed by optical microscopy in biological tissues stained with metachromatic dyes. The spectral changes often cover the complete range of the visible spectrum, sometimes representing spectral shifts of several thousand cm^{-1}. Exciton theory describes the spectral changes as the result of the electrostatic coupling between transition dipoles of dye molecules. It significantly alters the electronic properties of the dye molecules, namely the energies of their excited states. The dipole coupling depends significantly on the geometry of the aggregates

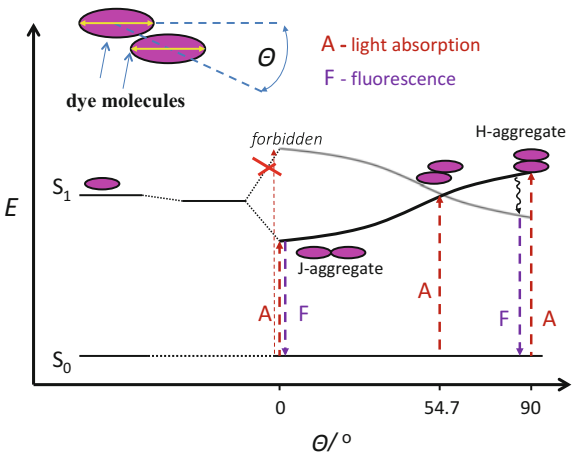

Fig. 18.6 Exciton splitting of the electronic excited states of dye molecular aggregates

(Fig. 18.6). The H-aggregates with the geometry characterized with a sandwich-type arrangement exhibit absorption bands shifted to lower wavelengths. The H-aggregates are mostly nonluminescent and nonactive species and often exhibit the properties of fluorescence quenchers. J-aggregates represent the type of molecular assemblies with a head-to-tail intermolecular association. They are characterized by light absorption at longer wavelengths, narrow absorption bands, and exhibit relatively small Stokes shifts. The J-aggregates represent interesting supramolecular systems with a broad spectrum of potential applications [74]. The formation of dye molecular aggregates on layered nanoparticles is a relatively common phenomenon. Probably one of the first papers reporting dye molecular aggregation in such systems was on MB in Mmt colloids [75]. The main driving force for dye aggregation is hydrophobic effect and enhanced concentration at liquid/solid interface. There are two main types of sites for dye aggregation: 1. The zones of the diffuse electric double layer surrounding colloid particles. 2. Sites at the particle surface. The zones with enhanced electrolyte concentration and ionic strength promote initial dye aggregation. The thickness of the zones and electric field characteristics depend on the charge of the particles and electrolyte type and concentration. Particle edges do not seem to play a significant role in dye adsorption and molecular aggregation, since they are a minor part of the total surface. The chemical modification of LSil particle edges with reactive silanes did not produce different tendencies in MB aggregation, although the properties of the colloids were significantly altered [76]. The planar surfaces of layered particles can exhibit variable properties, specific charge, topography, and chemical activity. Therefore the mechanism of dye aggregation is relatively complex, including fast adsorption and slow processes of the transformation of initially formed metastable dye aggregates [27, 77–79].

18.4.2 Molecular Aggregation and Photoactivity

Dye aggregation significantly affects the photoactivity of the molecules. As was mentioned above, most common aggregates are sandwich-type assemblies exhibiting low photoactivities. Therefore, the adsorption of dye molecules onto layered particles often leads to a decline in their photophysical properties. This phenomenon has been described in numerous articles and reviews [9, 12, 15, 80, 81]. However, there have been a few reports of an opposite trend. This may occur if the dye adsorption does not lead to molecular aggregation. Rarely dye adsorption can even suppress the formation of dye aggregates. This phenomenon occurs for organic dyes of specific molecular structure and the distribution of ionic groups in their molecules. For example, the aggregation of Sb^{V}-porphyrin was suppressed and fluorescence increased in the complexes with LSil. This effect was observed even at high loadings of the porphyrin dye [82]. In a few cases, the formed aggregates can be photoactive (e.g., J-aggregates or other specific types) (see Sect. 18.4.4). For example, the aggregation of cationic p-phenylene ethynylenes on Lap particles led to an enhanced fluorescence. The effect of the layered particles was to minimize the interactions of the dye molecules with water [83]. In some cases, the bonding between the adsorbed dye molecules and particle surface suppresses the mobility of dye molecules, thus reducing their quenching via collision frequency and other unfavorable relaxation pathways [84]. For example, the adsorption of cationic porphyrazine dye on inorganic nanosheets with negative charge led to a strong enhancement of their fluorescence quantum yields and lifetimes of their excited states. The phenomenon was named "*Surface-Fixation Induced Emission*" [85]. Another example is diarylmethane dye, auramine O, which exhibited enhanced fluorescence in Mmt colloids. The adsorption of this dye led to minimizing relaxation pathways via restriction of the torsional molecular motion [86, 87]. In the strategy to reduce molecular aggregation, layered particles were compared with other substrates. Nanosheets, being more rigid substrates, in some cases exhibit better properties for reducing dye aggregation than polymeric compounds [88]: Cyanine dye exhibited strong aggregation on negatively charged polymeric templates such as substituted amylose and cellulose. Substantially less aggregation was observed in the systems with lower negatively charged templates such as hyaluronic acid. Adsorption on Lap particles did not lead to dye aggregation, thus exhibiting optimal properties [88]. In rare cases, H-aggregates exhibit strong luminescence. One example is the H-aggregates of 3,3-dioctadecyl oxacarbocyanine dye formed in Lap colloids. The dye aggregates exhibited high activity in energy transfer processes [89]. The adsorption taking place in aqueous colloids of layered nanoparticles often leads to increasing solubility of poorly soluble, hydrophobic and nonionic dyes as has been discussed above (see Sect. 18.3.3). Neutral dye adsorption also leads to the reduction of dye molecular aggregation [48, 90, 91].

18.4.3 *Effect of Layer Charge*

The molecular aggregation of organic dyes significantly depends on the charge distribution on the nanoparticle surface [12]. For the first time, the effect of the layer charge was observed for MB using reduced-charge montmorillonites (RCMs) [27]. The series of RCMs was prepared from a single parent material saturated with Li^+ cations. The charge was reduced upon the fixation of Li^+ cations in layers by heating. The extent of the charge reduction was proportional to the temperature used in the thermal treatment. The samples of RCMs in a single series are very similar in structure, composition, and particle size and shape, but different in the layer charge and related properties. It is interesting that only very small, almost negligible changes in the layer charge led to significant changes in molecular aggregation [27, 92, 93]. With decreasing layer charge, H-aggregation decreases in favor of monomers, H-dimers and J-aggregates. There could be two interpretations of this phenomenon:

1. Low charge density on the particle surface induces larger distances between the adsorbed neighboring dye cations. This would suppress dye aggregation. High-charge density is reflected in small distances between adsorbed dye cations balancing the surface charge. This would promote the formation of H-aggregates.
2. Layer charge affects the electric double layer in the vicinity of the particle surface. High-charge density induces a high concentration of ions on the surface, and a high ionic strength which contributes to the increase in electric field. The increase in the ionic strength and high concentration of electrolyte ions would support the formation of dye molecular assemblies. The effect of ionic strength was proved in MB aggregation in Mmt and Lap aqueous colloids [94], and has also been observed for the dye aggregation in solutions.

The trend of the effect of the layer charge observed with the series of RCM samples was later confirmed with a series of various LSil, including samples of both natural origin and synthetic materials, of di- and trioctahedral structure, with the location of the charge due to substitutions in the octahedral or tetrahedral sheets [12, 28, 87, 95, 96]. The high sensitivity of the dye molecular aggregation to the layer charge was taken advantage of in layer charge probing. The method was successfully used to measure charge reduction due to cation fixation or induced by acid treatment [28, 97]. The effect of the layer charge is a general phenomenon, regardless the type of organic dye. It has been observed for the aggregation of MB, other phenothiazines, triphenylmethane and xanthene dyes, and oxazines. There is no simple model to describe the effect of the layer charge on the formation of J-aggregates [98]. These assemblies are structurally relatively variable and their formation is predominantly influenced by the dye molecular structure. J-aggregates are preferentially formed with dyes with a complex molecular shape, nonsymmetric position of the charged and polar groups, etc. (see Sect. 18.4.4).

An appropriate selection of layered templates, preferably with a low layer charge, is a basic precondition to avoid or at least to reduce dye molecular aggregation in hybrid materials. The appropriate choice of organic dye without metachromatic properties is another strategy being widely applied. Takagi and his coworkers elaborated on the optimal selection of suitable porphyrin dye/LSil pairs to obtain materials with optimal photophysical properties and high photoactivity. Both the dye and LSil templates were selected to match the charge distribution in both the components, so that the dye molecules would form a dense occupation on the host surface, but avoiding any molecular aggregation. There are specific guidelines which can be useful for selecting appropriate components and designing the composition of active and functional hybrid materials. These guidelines are called the *Size-matching rules* [40, 99–101] and reflect the matching the structural properties of both the dye and layered substrate.

18.4.4 J-Aggregates

A lot of attention has been devoted to J-aggregates due to their unique properties [74]. Their formation is not as rare and depends greatly on the conditions and dye molecular structure. The J-aggregation of cationic dyes has been studied more frequently, but it has been also observed for anionic dyes (e.g., [102]). As was mentioned above, J-aggregates are recognized by light absorption at lower energies. However, the adsorption of organic dye molecules itself is frequently accompanied by the same spectral shift [103]. Also conformational isomerization in the molecules occurring upon dye adsorption causes the same spectral changes [104] (see Sect. 18.5.2). J-aggregation was frequently also confused with the protonation of dye molecules [12]. Therefore, it is sometimes difficult to recognize if the spectral changes are due to J-aggregation. Rh dyes are a typical example [79], since there is only a small energy difference between the transitions of the monomeric form and J-dimers. Nevertheless, there is clear evidence of the formation of J-aggregates in numerous hybrid systems. J-aggregates are easily formed with dyes which have molecular shapes inappropriate for the formation of sandwich-type molecular assemblies. These mostly include cyanine dyes with side chains near the molecular center or porphyrins with a specific molecular shape and distribution of ionic groups [98, 105–107]. There are two types of J-aggregates. Ideal J-aggregates with a perfect head-to-tail association exhibit light absorption at lower energies, whereas so-called oblique aggregates are characterized by both H- and J- spectral bands. Both types of J-aggregates can coexist in some systems. An example is the two types of J-aggregates of pseudoisocyanine dye recognized in LSil films [107]. J-aggregation can be easily achieved for dyes whose molecules bear both positively and negatively charged groups. The charge distribution in zwitterionic molecules prevents a sandwich-type stacking. Examples are porphyrins with cationic pyridinium and anionic carboxyl groups in their molecules [40]. The formation of

J-aggregates can be significantly influenced by the third components in more complex systems, such as in LbL assemblies [67] or in systems with polymers [108].

18.4.5 Reduction of Dye Molecular Aggregation by Using Surfactants

The purpose of using surfactants is to dilute the adsorbed dye molecules and thus to achieve the suppression of dye molecular aggregation. There are several works providing evidence on the important role of ionic surfactants in improving the photophysical properties of hybrid materials. Cationic surfactants are used for nanoparticles with a surface negative charge [33, 109]. For the modification of nanoparticles with a positive charge, anionic surfactants are used [110, 111]. A series of materials based on LDH, anionic dye (1-anilinonaphthalene-8-sulfonate), and alkylsulfonate surfactants with variable length of alkyl chains were prepared and characterized [111]. Their luminescence depended on the structure of the formed assemblies, which sensitively reflected the properties of the surfactant used. Optimal conditions were found by combining the appropriate dye loading and proper selection of surfactant. Under optimal conditions, no apparent quenching took place for dye loading up to 20% of the anion exchange capacity of LDH [111]. Much lower dye concentrations were needed to completely avoid dye aggregation in the hybrid materials of Mmt modified with cationic alkylammonium surfactants. Optimal Rh dye loadings were only 0.1-0.5% of *CEC,* but fluorescence quantum yields achieved up to 80% under the optimal conditions [112, 113]. The properties of the molecular aggregates formed at higher dye loadings were also improved. They exhibited significant luminescence, in contrast to the aggregates formed in the absence of the cationic surfactants [114, 115]. The use of the surfactants does not always guarantee improved properties. In some cases, the modification with surfactants leads to an increase in molecular aggregation. For example, the interactions of anionic Merocyanine 540 in bentonite premodified with cetyltrimethylammonium cations led to the formation of H-aggregates with reduced photoactivity [116]. In another study, a higher fluorescence of hybrid films was achieved without a surfactant [117]. On the other hand, aqueous colloids of the same components exhibited an opposite trend. The effect of the surfactants probably depends significantly on the procedure used for hybrid material synthesis and on the type of material. There are several possible explanations for the opposite effect of alkylammonium cations. One is based on the phenomenon of molecular segregation. The formation of a segregated phase of alkylammonium cations reduces the surface available for the segregated dye molecules. As a consequence, the segregation leads to a locally increased concentration of dye molecules, thus promoting their aggregation [118]. This segregation was also proven for systems based on a mixture of different organic dyes. An example is a mixture of porphyrin and viologen dye co-adsorbed on Sap particles [119]. The fractions of each dye formed segregated phases, each

composed of a single type of molecules. The different structures of porphyrin and viologen molecules contributed to the increased stabilities of the segregated phases and prevented the formation of the mixed phase. The segregation was proven by energy transfer experiments. Part of the segregated porphyrin molecules remained luminescent and could not participate in the FRET process that would quenched their fluorescence with viologen [119]. The segregation can also be induced by reaction conditions affecting the properties of hybrid systems with ionic surfactants. For example, the effect of alkylammonium cations in solid hybrid systems depends significantly on the ambient humidity, as was observed for Rh 3B intercalated in LTi [120]. Water adsorption leads to the formation of dye molecular aggregates and significantly reduces the material's luminescence. The effect of humidity can be explained by a hydrophobic effect which arises with increasing water content. The presence of water molecules contributed to the self-assembly of alkyl chains forming a compact, isolated phase, thus pressuring the dye molecules to segregate from the alkylammonium phase.

18.4.6 Molecular Aggregation in Other Systems

Another strategy to prevent molecular aggregation was based on using a type of organic compound with 'container-shaped' molecules, called cavitands. Cavitand molecules have cavities which can accommodate single dye molecules inside, thus preventing their association. Dye/cavitand complexes could be adsorbed onto layered nanoparticles in similar ways to dye molecules alone. The effectiveness of the strategy to minimize molecular aggregation has already been proved. Cationic Zn^{II}-porphyrin, and 2-acetylanthracene encapsulated within a cationic organic cavitand were adsorbed on LSil particles. The hybrid exhibited high photoactivity, and the FRET efficiency between the dye components reached almost 100%. It proved a uniform and nonsegregated distribution of porphyrin cations and cavitand complexes [121]. In a similar way, cyclodextrine molecules with cavities which can accommodate luminescent dye molecules were also applied in hybrid films to prevent molecular aggregation [122]. There are several papers reporting the influence of polymeric substances on dye molecular aggregation. For example, interesting materials were prepared from oxazine 1 and in situ formed poly(norbornane) and fluoromica nanoparticles [108]. The co-adsorption of polar copolymers of poly (ethylene oxide) and poly(propylene oxide) on Lap led to enhanced dye aggregation. It is likely that segregation occurred between the polymer molecules and dye cations. Interestingly, the dye adsorption on Lap without polymers led to lower dye aggregation [123]. However, an opposite trend was observed for the particles modified with water-soluble chitosan. The presence of the polymer changed the dielectric properties near the adsorption sites, thus reducing molecular aggregation and increasing the fluorescence of the hybrid material [124]. Enhanced fluorescence was also achieved in the hybrid materials modified with the cationic polyelectrolyte [125].

18.5 Phenomena and Properties of Hybrid Materials

18.5.1 Optical Anisotropy and Dye Molecular Orientation

The term *anisotropy* refers to material's properties which are directionally dependent. Optical anisotropy defines the optical property of a substance that depends on the direction of light propagation or polarization. Nanosheets or nanolayers are anisotropic materials which result directly from the structure and shape of the particles. The aspect ratio of these materials is a parameter which quantifies the geometric shape of the nanoparticles, and is defined as the ratio of the particles' diameter to the thickness of an individual particle. The layer thickness is mostly well defined, resulting from the structure of a specific compound and generally does not exceed a few nm. There is a large variation in the diameter of the particles, being in the range from tens to hundreds of nm. Nevertheless, the aspect ratios of the particles of layered compounds is mostly well above 10, which significantly affects the association of the particles in colloids or in the solid state. Face-to-face assemblies with the particles aligned in a parallel fashion are preferentially formed in the solid state. The nanoparticles forming films are oriented in a parallel fashion with respect to the substrate surface plane. Such an orientation has a high impact on the material's optical anisotropy. The molecular orientation of dye cations depends on many parameters and conditions, such as molecular shape and the distribution of ionic and polar groups [126, 127], concentration [33, 126], and molecular aggregation [12, 93], which is controlled by the surface properties of the nanoparticles [30]. The probability of the absorption of electromagnetic radiation by chromophoric groups depends on the orientation between the electric vector of the light and the transition dipole moment of the chromophore. The orientation of the transition dipole moment in molecules is determined by the electronic structure of the chromophores. The direction of the electric vector is perpendicular to the propagation direction of the light. Polarization can be achieved using polarizers. Optical anisotropy can be characterized by combining polarized light and control of the orientation of the film with respect to the light's propagation. In principle, the two-dimensional character of nanosheets and layers do not allow a perfect preferential orientation of the dye molecules in all three space directions. However, three-dimensional anisotropy can be achieved using a monocrystal of layered host material with an ordered structure in all directions, such as $K_4Nb_6O_{17}$ [128].

There have been several attempts to characterize the molecular orientation of dye molecules in layered compounds. A parallel molecular orientation of dye molecules on the surfaces was most frequently considered, since it would contribute to the highest interaction area between the particle surface and dye molecules (see references in [12]). However, the Coulombic interaction between the surface and dye ions controlling dye molecular orientation depends greatly on the distribution of electron density in the molecule. Optical anisotropy obtained with X-ray photoelectron spectroscopy on well-defined systems based on mica and MB [129] and triphenylmethane dyes, crystal violet, and malachite green [130] determined an

inclined, almost perpendicular orientation of the molecules. The molecular orientation significantly depends on dye loading [126]: At low dye loadings the dye molecules lay flat on the surface. With increasing concentration there was a continuous change in the average molecular tilt angles to larger values. The perpendicular orientation of cationic laser dyes Rh 6G and oxazine 4, incorporated in an oriented film of synthetic fluoromica, was observed by polarized IR and UV-VIS absorption spectra [32]. A significant proportion of the dye cations assigned to aggregates were tilted, with the longest axis of the heteroaromatic ring nearly perpendicular to the host layer, and exhibited a positive optical dichroism. The spectral properties of ionic phthalocyanines intercalated into Hec and LDHs using various synthetic routes were compared [53]. The dye molecules were oriented parallel to the surface of Hec but exhibited a perpendicular orientation in LDH hybrid materials. The different orientation was assigned to the much higher layer charge of LDH, and higher density of intercalated dye anions in the interlayer spaces [53]. The orientation of tetracationic porphyrins in α-zirconium hydrogen phosphate with high layer charge was relatively inclined [131], although the parallel orientation was observed for the same dyes in the hybrids with LSil [132]. Large planar Cu^{II}-phthalocyanine tetraanions intercalated in layered $Cu_2(OH)_3CH_3CO_2$ were arranged with the orientation of the molecular planes perpendicular to the surface of $Cu_2(OH)_3^+$ layers [133]. The effect of the layer charge on dye molecular orientation was proved for Rh 6G cations in the films of RCMs: [29]. In contrast to the H-aggregates, the molecules forming J-aggregates were oriented more or less in parallel and had no tendency for perpendicular orientation [107]. On the other hand, the J-aggregates formed on layered particles exhibit negative dichroism [106–108, 117, 134]. Several studies found the hybrid systems to exhibit fluorescence anisotropy [15, 135, 136], although fluorescence cannot detect inactive species, such as H-aggregates. No significant depolarization due to the rotational relaxation of the fluorophores was observed in the solid hybrid films. Fluorescence anisotropy of the material proved a rigid association of the fluorophore molecules with the host surface [137–140]. However, some phenomena such as resonance energy transfer can lead to a partial or complete light depolarization [117, 140].

Whereby the orientation of layered particles in the films is achievable relatively easily, colloids are relatively isotropic systems with a random orientation of particles. On the other hand, the orientation of the chromophores in colloids can sensitively reflect the properties of the solvents, which can be important in various applications, such as for optical sensors or switches [141]. Electric linear dichroism is a phenomenon characterized by the anisotropic absorption of light under an externally applied electric field. The effect of the electric field is to induce a preferential orientation of the colloidal particles with respect to the direction of the field. Electro-optical properties have only been described for a few hybrid colloids [135, 142].

Optical anisotropy, birefringence, and linear dichroism are very important optical parameters. However, in some cases they can influence other properties.

One of the most interesting examples is the light-induced deformation of poly-(*N*-isopropylacrylamide) gels, which was mediated by LSil particles with adsorbed porphyrin molecules [143]. The alignment of the nanosheets in the gel was achieved by an electric field applied during polymerization to form optically anisotropic materials. When the gel was irradiated with light, only the colored part was photothermally deformed, which was followed by anisotropic shrinkage. The direction of the shrinkage was dependent on the orientation of the layered particles [143].

18.5.2 Structural Changes and Photochromic Properties

Conformational changes in molecules are realized by rotations around single bonds and do not require much energy. Dye molecules in the adsorbed state may have geometries different from those in solution. A typical example is the adsorption of porphyrin derivatives having cationic *N*-methylpyridinium substituents [104]. In solutions, the pyridinium groups in the molecules are inclined with respect to the plane of porphyrin ring. However, the inclined groups would not efficiently bind to the surface in the adsorbed state. Therefore, rotation of the pyridinium groups often occurs depending on the location of the methyl substituent and positive charge. Porphyrin with *N*-methyl-4-pyridinium groups (*ortho* substitution) have to rotate to an almost completely parallel orientation. Such conformational change leads to an overall flattening of the porphyrin molecule [144]. The extended conjugation of the π electron system in the planar molecule contributes to a reduction in the energies of both light absorption and emission. Spectral changes are significant and comparable to those induced by molecular aggregation. The combination of chemical modification, reaction conditions, molecular aggregation and conformational changes together can be applied to design materials with variable optical properties, but based on a single porphyrin dye [145–147]. The possible applications of such systems have been demonstrated in several papers [100, 148–150]. Recently, conformational changes were also described for the natural, luminescent dye berberine [151]. A positively charged, quaternary ammonium group is part of the dye's molecular skeleton. Partial planarization of the skeleton takes place upon dye adsorption to arrive at a more efficient electrostatic bonding, as has been proven by the systems with Sap [151].

Photochromism is the phenomenon of a reversible photochemical transformation between two isomers. The hybrid materials exhibiting photochromic properties are based on spirooxazines, spiropyrans, diarylethene, and azo dyes [14]. Photochromic materials can be used for various types of devices and industrial applications, such as optical switches, filters, light protection and photoresponsive coatings, optical data storage materials, etc. Photochromism has a reversible character; its limitations are related to the slow decomposition of the photochromic dye with the number of

applied cycles. Dye stabilization can be achieved using surfactant molecules. However, the chemical environment of the hydrophobic phase of surfactant chains can play a role in the chromophore response to photoactivation as well as in thermal relaxation of the excited molecules. Dye molecular aggregation significantly affects photochromic properties. It alters the parameters of photoactivation, but also new deactivation pathways may occur in the aggregated state. The effect of the molecular aggregation on reaction kinetics was also observed. An example is the slower formation of merocyanin from spiropyran intercalated in $MnPS_3$, due to the formation of spiropyran J-aggregates [152]. However, there are some cases where the aggregation does not significantly influence photochromic reactions. Examples are the aggregates of azo dyes exhibiting highly efficient and reversible trans-cis isomerization in hybrid materials [153–155]. The variable impact of molecular aggregation could be due to a large variation in the activation energies of photochromic reactions. For example, the formation of new constitutional isomers with new bonds and functional groups has much higher activation energies than stereoisomerization. In the former, the reactants can be stabilized in the form of molecular aggregates. On the other hand, stereoizomerization keeping bonds and functional groups unchanged have lower activation energies and could be easier to achieve regardless the occurrence of molecular aggregation. There are several reports on highly reversible photochromic hybrid materials based on nanosheets or nanolayered materials and photochromic dyes. For example, films of diarylethene/LSil hybrid materials exhibited a highly reversible decoloration of the dye. In contrast, the reaction of a dicationic derivative of azobenzene was effectively suppressed in both the colloids and films of LSil [155, 156]. Probably ionic fixation of the two cationic groups prevented dye photoisomerization. Anchoring ionic groups onto molecules and binding them on negatively charged surfaces could be utilized for the stabilization of some photolabile compounds [155]. In some cases, photochromic reactions also affect other properties. Small changes in basal spacing detected by X-ray diffraction were assigned to different arrangements and spaces occupied by different photoisomers [152, 153, 157, 158]. Another example is the reaction of spiropyran affecting the magnetic properties of the $MnPS_3$ host [152]. Interesting phenomena relate to the influence on the properties of other molecules coexisting in hybrid material. For example, the photoisomerization of diarylethene affected the molecular aggregation of cyanine dye co-intercalated into the same material [159]. The photoisomerization of azobenzene dye molecules in zirconium phosphonate, $ZrF(O_3PCH_2)_2NHC_8H_{17}$, led to their irreversible deintercalation [160]. Selective adsorption induced by the photoisomerization of azo dyes was also reported [161, 162]. The reversible cycles of adsorption or release of phenol substances could be controlled by repeated photoreaction applying UV and visible light irradiation cycles. Such materials can be used as recoverable substances for the purification of chemical wastes.

18.5.3 Nonlinear Optics

NLO properties strongly depend not only on the structure of dye molecules, but also on their bonding in the matrix of the inorganic host [163–165]. A random molecular orientation is not favorable. Optical anisotropy and preferential orientation may play a significant role in the improvement of NLO properties [166–170]. The stabilization of dye molecules in a hybrid system can also play a positive role. An essential role of dye molecular aggregation in NLO properties has also been reported. Concentration and orientation are the key factors affecting dipole-dipole interactions. For example, stilbazolium dye intercalated into layered chalkogenide MPS_3 exhibited second harmonic generation; however, this was only when in the form of J-aggregates [171]. In some cases, the structural changes to dye molecules contribute to the improvement of NLO properties in hybrid systems [168]. For example, increased molecular planarity upon the intercalation of some cationic porphyrins (see Sect. 18.5.2) can improve NLO properties [167]. An increasing concentration of hemicyanine dye in the hybrid materials with Lap altered the mechanism of the photoinduced charge-transfer process. The intramolecular mechanism taking place at low concentrations changed to the intermolecular pathway, which was reflected in a change in the NLO properties of the dye [170]. For practical use, NLO materials for optical devices must be in the form of either a single crystal or thin film. For the solid materials in the form of thin films, low light scattering is a crucial condition for successful applications [168, 172]. There are numerous examples of the construction of hybrid materials exhibiting second harmonic generation [171, 173] or two-photon absorption [62, 169]. Besides these, there are also other types, such as Langmuir monolayers or LB films [173, 174], LbL assemblies [166, 175] and nanocomposites with polymers [176, 177].

18.5.4 Resonance Energy Transfer

FRET is a phenomenon of light energy transfer taking place between two dye molecules. It can be described in two steps: 1. The dye molecule acting as the energy donor (ED) absorbs a photon and is lifted into its electronic excited state. 2. The excited molecule of ED transfers its energy to the second dye molecule, which plays the role of energy acceptor (EA). FRET is a nonradiative deactivation process, which is based on resonant electrostatic coupling between the transition dipole moments of the interacting molecules. The spectral overlap of the ED emission and EA absorption spectra is a basic condition for the resonance to take place. FRET efficiency is extremely sensitive to the intermolecular distance (1–10 nm), but also

depends on molecular orientation. Highly efficient FRET occurs in photosynthetic systems in green plants, and this phenomenon will likely play a key role in future solar cells performing at a molecular level.

Various hybrid systems exhibiting efficient FRET have been developed. The chief role of the layered particles is to concentrate the dye molecules to reach resonance. Unfortunately, an enhanced concentration of dye molecules often leads to a concurrent phenomenon - the loss of photoactivity due to molecular aggregation (see Sect. 18.4). Examples of hybrid systems exhibiting efficient FRET are LDH systems with anionic porphyrin and pyrene dye [178], or hybrids with cationic porphyrins and LSil [179]. In numerous cases, FRET efficiency achieved almost 100% [101, 150, 180]. High efficiencies were observed even with a large excess of ED molecules [180, 181]. Whereas the formation of H-aggregates is not desired, photoactive J-aggregates may play a positive role in FRET [68]. Exciton delocalization in the molecular aggregate would favor energy migration and very efficient excitation energy delivery to the EA molecules. An interesting type of molecular aggregates are mixed J-aggregates based on different dye molecules of similar structure. In such systems, very efficient *superquenchers* can accept the energy from a severalfold larger number of ED molecules. Such systems with layered nanoparticles have been only rarely investigated [182]. FRET is significantly more efficient in solid films than in colloids. In the solid phase, the process proceeds in all three dimensions, whereby in the colloids with dispersed individual layered particles, FRET is limited to two dimensions. [180]. The segregation of dye molecules can significantly reduce FRET efficiency [99]. The effect of molecular orientation has also been observed. The orientation of some porphyrin molecules intercalated in LSil responds to the solvent type. The changes in the molecular orientation responding to the presence of specific solvents makes it possible to control the FRET process by changing the chemical environment. Such systems can be used as sensors or in photofunctional devices [101, 183]. FRET in hybrid systems does not need to be limited to a single-step process. Energy migration, or two-step FRET in systems with three different dyes [140] or a multistep FRET [117] have already been reported. Besides the most common systems based on simple colloids or solid films, FRET in other types of materials have also been observed. Noteworthy examples are LB films [184–186], LbL assemblies [67, 68, 187] and others [188]. Besides the possible applications described above, FRET was found to be an extremely sensitive tool for the characterization of competitive dye adsorption on the surface of layered nanoparticles [180]. Some materials exhibiting FRET sensitively respond to pH or concentrations of various analytes [187, 189, 190]. Another type of application, which has been widely investigated, is the photoprotection of sensitive agricultural chemicals such as pesticides or insecticides. Photolabile compounds undergo easy and rapid photochemical decomposition upon solar irradiation, but FRET has been applied to slow down these processes [191–193].

18.5.5 Dye Reactions and Photosensitization

One of the major problems occurring with the applications of some organic dyes is their low photochemical stability. The stabilization of organic chromophores by the formation of hybrid systems was successfully achieved a long time ago: It was Maya blue which inspired the development of similar materials [1]. The stabilization of natural dyes can be very important in their use in the food industry and cosmetics [194]. However, the adsorption of organic dyes on layered nanoparticles does not always lead to their stabilization. For example, MB is stabilized on particles of some silicates, such as palygorskite and Mmt, but others, such as sepiolite, vermiculite and zeolite, accelerated its photodegradation [195]. It is sometimes difficult to determine which properties play a dominant role in a dye's stabilization. The stabilizing effects have been assigned to polar and ionic interactions [196], π-π interactions [194] and molecular aggregation [195]. Examples of stabilized organic dyes in hybrid systems include anthocyanin in Mmt [197], beta-carotene, and annatto dye in organically modified LDHs [194], natural anionic dyes, carmine yellow, and carthamus yellow in LDHs [196], 1,1′-diethyl-2,2′-cyanine and tris (2,2′-bipyridine)ruthenium(II)) in Sap [198], etc.

The photodecomposition of some organic dyes catalyzed by inorganic hosts has also been observed. Lap induced only a de-ethylation reaction of Rh cations, whereas the reaction with Mmt continued with the decomposition of the chromophore [199]. Photosensitization with Fe^{III} present in Mmt particles can play a role. Different pH of the colloids, layer charge, formation of reactive oxygen species (ROS), efficiency of light source; all these factors can influence dye decomposition [103, 200]. Labile dyes can be stabilized in more complex systems. For example, Rh B was unstable in polypropylene, but was stabilized in the polymer nanocomposites with Mmt particles [201]. Larger reactivity of the dyes is expected in the systems with layered semiconductors. For example, LNb played a role in the electron transfer from photoexcited Rh molecules, thus catalyzing their decomposition [202]. Therefore, using inert layered nanomaterials can be advantageous in dye stabilization.

Various dyes exhibiting properties of photosensitizers form stable triplet states upon their excitation with visible light. They are able to efficiently activate O_2 to its singlet form ($^1\Delta_g$), which can secondarily convert to other ROS. Their formation was observed in the systems based on LDH [203]. Formed $^1\Delta_g$ and ROS can efficiently accelerate the oxidative decomposition of organic compounds. The involvement of ROS in the fading of triphenylmethane dyes was observed [204]. The stabilizing effect of molecular aggregation can relate to the lower activity of dye aggregates to form triplet states [195, 205]. Another effect could be reduced diffusion rates of O_2 molecules in intercalated compounds. The hybrids with photosensitizers can be applied as disinfection materials due to their harmful activity to microorganisms. MB in the colloids of LSil exhibited high antimicrobial

activity, although dye photoactivity was significantly reduced [205]. Layered particles improved the antimicrobial effect by concentrating the photosensitizer on their surface and delivering active molecules to microbe cells. Similar materials based on LDH with porphyrin dyes were also investigated, and the formation of $^1\Delta_g$ was proven [110, 206–208]. $^1\Delta_g$ can be used as a specific oxidation agent in organic synthesis. The light-induced oxidation of electron-rich compounds, such as quinol, 1-naphthol and anthracene were mediated by hybrids with MB and Rose Bengal [209]. Some organic dyes are also reactive compounds under dark conditions, and their reactions can be initiated or catalyzed upon adsorption onto layered particles [98, 210, 211]. The bleaching of cyanine dyes in colloids was very fast with LSil with a high layer charge. The same dyes were stabilized at the surfaces of LSil with a low layer charge.

In a few cases, the reactions of organic dyes can lead to novel materials. For example, anionic azo dyes adsorbed on LDH formed highly luminescent and photostable compounds [212]. It was assumed that the reaction led to the breaking of –N=N– bond and a reactive product was chemisorbed onto the LDH surface [212]. In a similar way, UV irradiation was applied to initiate the reaction of 2-hydroxychalcones, yielding colored flavylium compounds. The products were stabilized in the matrix of Mmt modified with cationic surfactants [213]. Unique reactions of excimers or exciplex formation can be suppressed in hybrid systems [214]. Organic radicals are another type of interesting substances, having unpaired valence electrons. They are mostly unstable, but the stabilizing effect of inorganic layered hosts has been observed in numerous cases. Most often radicals or ion-radicals derived from viologen ions have been investigated. The hosts can initiate radical formation by the intercalation of reactant molecules. The inorganic matrix may also play a protective role to prevent the diffusion of O_2, which would reoxidize the formed radicals. Semiconductors such as LNb or LTi can play the role of electron donors. For example, viologen in hybrids with LTi changed to a blue radical product [215]. In other system, $Na_2Ti_3O_7$ modified with alkylammonium cations and intercalated with two cyanine dyes exhibited an electron transfer reaction. Electron spin resonance proved the formation of radical dications exhibiting high stability [216]. However, chemically inert particles of LSil were also able to promote and stabilize radical formation. Methylviologen intercalated in Lap samples converted to radicals, which initiated dimethylaniline polymerization. The polymeric product of a purple color was formed on the samples with low layer charge, whereas only oligomers occurred on the surface of high-charge Lap nanoparticles [217]. Another example is radical formation from the cationic dye safranin and its involvement in radical polymerization [218]. The photoinduced electron transfer between different organic dye molecules can be potentially applied in organic solar cells. Such reactions were reported between pyronine and Sb^V-porphyrine dye in hybrid films with Sap [219] or between $[Ru(2,2\text{-bipy})_2]^{2+}$ and methylviologen [220].

18.6 Applications in Research and Industry

18.6.1 Sensors

Numerous hybrid materials are based on organic molecules with sensing properties, which can be applied in various branches of analytical chemistry. They include sensors for pH, solvents, photochemical, and redox properties. The involvement of molecular probes and sensors in hybrid systems offers various advantages. They are relatively easy to prepare and the dye properties can be slightly tuned via the effect of host particles. Hybrid materials often provide improved stability and thermal resistance of the molecular probes. The photoactive molecules anchored on nanoparticles can be manipulated in similar ways, as pure nanoparticle systems, which can be easier than isolating or manipulating dye molecules in solutions. For example, hybrid colloids can undergo cyclic flocculation/peptization, could be isolated or purified by filtration, centrifugation, or dialysis. Layered particles can be incorporated into multicomponent films with well-defined molecular layers, such as LB films and LbL assemblies. MB and other phenothiazine dyes are well-known redox indicators changing to their colorless (leuco) form under reductive conditions. Electrochemistry of MB in the hybrid films with Mmt has been studied in detail [221]. MB performs in a similar way as in solutions. Furthermore, the electrochemistry of intercalated MB cations retains similar parameters at variable pH [222]. There are several examples of using MB as a sensor: The electrodes or sensors based on MB intercalated in layered compounds were developed for the analysis of ascorbic acid in commercial samples [223]. An MB hybrid with barium phosphate was used for the detection of the reduced form of nicotinamide adenine dinucleotide, NADH [224]. Sap modified with cationic surfactant and intercalated with the mixture of MB and reducing agent (either ascorbic acid or sugar) exhibited the properties of a sensitive O_2 sensor under anoxic conditions (<0.1% O_2) [225]. An amperometric biosensor using similar phenothiazine dye, azure B, intercalated in Lap was used for the detection of phenolic compounds. The dye acted as an electron shuttle with polyphenol oxidase reaching the detection limits in the range of nM concentrations [226]. Also other types of dyes were used as probes and sensors performing on various chemical reactions and phenomena. An interesting example is the solvatochromic properties of intercalated porphyrin dyes [101] (see Sect. 18.5.4). Another example is the detection of methanol, a highly toxic substance, which is very difficult to differentiate from other alcohols. It could be selectively detected by a composite film sensor prepared from oxoporphyrinogen and LDH [227]. Another example is sensing permanent water hardness based on FRET between two laser dyes, acriflavine and Rh B. The sensitivity was significantly increased when the dyes were incorporated in a Lap film [228]. The fluorescence quenching of photosensitizers with O_2 is another phenomenon which has been frequently applied in oxygen sensing [110]. The hybrid materials for multianalyte detection have not been significantly developed yet. In particular LbL assembly formation would be highly suitable for this purpose. Relatively new

applications use dye molecules as *in situ* probes of the processes occurring in the manufacture of polymers and their nanocomposites. Mmt modified with surfactants was doped with various fluorescent dyes for the real-time monitoring of polymer intercalation during nanocomposite processing [229]. In a similar study, Nile blue probe was used to monitor the compounding of nylon nanocomposites. The hybrid precursor was inactive due to the formation of dye aggregates, and luminescence appeared with the exfoliation of the layered particles in the polymer phase [230]. In another work, dye sensors were also used to inspect the morphology of polypropylene nanocomposites [231]. Dyes can also be used as *in situ* sensors for detecting the processes in colloids, to monitor transport in subsoils and aquifers [232].

18.6.2 Hybrids with Natural Dyes

Natural dyes have found their applications in various industrial fields. They are easily available, mostly at an affordable price, harmless enough to be used as food industry additives, in medicine or in cosmetics. Some natural dyes exhibit very interesting properties, such as biological activity, photosensitization, radical scavengers, luminescence, etc. There are several interesting examples of hybrid systems with natural dyes. Phycoerythrin, a natural pigment extracted from seaweed, was used for the synthesis of hybrid materials with Hec and Mmt. Bright fluorescence and higher stability against bleaching were achieved for the hybrid materials [51]. New hybrid materials were synthesized using a series of LDH samples and the natural pigment chlorophyll a. The extent of dye adsorption and the stability of the hybrid pigments depended on the type of inorganic host. The hybrid materials were more stable if LDH of Mg/Al-type were used, while catalytic decomposition occurred on the surface of Ni/Al-type LDH [233]. Low stability of carotenoids under irradiation limits their broader application in industry. An improvement in their stability was reported for beta-carotene and annatto dye intercalated in LDH. The host material had to be premodified with anionic surfactants to match the lipophilic properties of these dyes [194]. An improvement in thermal stability was reported for the hybrids of anthocyanins extracted from the acai fruit *Euterpe oleracea.* These dyes intercalated in Mmt or Sap exhibited the properties of efficient radical scavengers [234]. Nanohybrids with edible dyes used in the food industry were also investigated [235]. Natural red cabbage dye was used in electrodes combining Mmt and TiO_2 particles and tested in *natural dye solar cells* [236]. Abiogenic flavin and riboflavin-type chromophores prepared via the thermolysis of amino acid mixtures were adsorbed onto the particles of LSil. In this type of dyes, the adsorption significantly reduced their photosensitization properties [237]. Intercalation of the luminescent alkaloid berberine in Sap, altered its optical properties but did not reduce its photoactivity [151].

18.6.3 Hybrids Used in Biology, Medicine, and Agriculture

There is a limited number of hybrid systems applied in biology or medicine. Active dyes in the hybrid materials can actively participate in the interaction with living cells or play the role of biocides and photosensitizers. In some cases, antimicrobial properties can be reduced by the incorporation of active species into the hybrid material. An example is cationic p-phenylene ethynylenes intercalated in Lap [83]. On the other hand, the antimicrobial properties of MB adsorbed on Mmt colloid particles were significantly improved. The hybrid colloids were efficient against the sporulation of *Aspergilus niger* and *Penicillium sp.*, reduced the growth of the bacteria *Escherichia coli* and *Streptococus aureus*, and the yeast *Candida albicans*. The role of LSil particles was most likely to mediate the interaction between the microorganism cells and the photoactive MB [205, 238].

Staining is a technique using organic dyes to enhance contrast and highlight structures in microscopic images. In a few cases hybrid nanomaterials have been used for this purpose. The hybrids composed from quaternary tetraphenylethene probe intercalated in layered α-zirconium phosphate was developed as an effective fluorescence label for HeLa cells [239]. In another study, LDH nanoparticles were used as carriers to transport various organic biologically active substances to specific targets. In order to control their distribution, a near-infrared fluorescent probe (Cy5.5) was also incorporated. The functionalized particles acted as highly efficient contrast agents, since Cy5.5 probe molecules were stabilized by layered particles [240]. Nile red is a polarity probe, which is almost insoluble and non-emissive in water. It was stabilized and became photoactive in the hybrids with Lap. The hybrid materials have potential as optical probes for tumor imaging [90].

There are numerous examples of applying of dye/LSil hybrid systems in the stabilization of photolabile pesticides. The mechanism of the stabilization was assigned to FRET (see Sect. 18.5.4). The dye molecules playing the role of EA were carefully selected to match the energies of the excited states of the photolabile pesticide. Examples are bioresmethrin in Mmt co-adsorbed with cationic dye, methyl green [191], insecticide tetrahydro-2-(nitromethylene)-2H-1,3-thiazine with acriflavine [191] or 3,6-diamino-10-methylacridinium [241], microbial insecticides, such as the *Bacillus thuringiensis* toxin with various types of chromophores [191], insecticide tetrahydro-2-(nitromethylene)-2H-1,3-thiazine with cationic dye 3,6-diamino-10-methylacridinium [241], insecticide quinalphos with crystal violet [242], etc. In some cases other phenomena also played roles. For example, the steric stabilization of organic molecules on the particle surface, or photoquenching by Fe^{III} occurring in the matrix of some LSil [191].

18.6.4 Polymer Nanocomposites and Other Applications

Photofunctional materials based on industrial polymers can be prepared by the chemical modificiation of polymers with photoactive groups or directly during polymerization by incorporating the chromophoric units in polymer chains. The strategy via polymer nanocomposites is another, alternative way. Nanoparticles dispersed in the polymer matrix can play the role of carriers of photoactive dye molecules. Inorganic layered nanomaterials are not compatible with the hydrophobic nature of most industrial polymers, and their chemical premodification is mostly required. The most common way is based on modification with ionic surfactants. The organically modified layered particles are excellent sorbents forming stable colloids in organic solvents. Their complexes with organic dyes often exhibit high photoactivity [39]. The organically modified layered materials with adsorbed organic dyes are suitable precursors for polymer nanocomposites. Processing the polymer composite often requires an enhanced temperature and thermal stability of the hybrid precursors. There are a few works reporting an improvement in dye thermal stability in hybrid materials (see Sect. 18.5.5). One example is a nanopigment based on Basic Blue 41 intercalated in Na^+-Mmt [243]. The nanocomposites based on MB, Mmt, and poly(ethylene vinyl acetate) exhibited superior optical as well as mechanical properties [244]. Similar nanocomposites were reported in other studies [245, 246]. The superior properties of organically modified LSil were confirmed in the studies using laser dyes. An example is Rh B/organically modified Mmt composites with polypropylene [247]. Complexes of Rh 6G and nonmodified Mmt were also incorporated into polyethylene [248]. UV-exposure tests on colored Rh B/Mmt/polypropylene composites showed significant improvements in dye photostability [201]. LDH and hydroxide nanosheets bearing organic dyes were also applied: Layered $Zn(OH)_2$ with anionic orange azo dyes (methyl orange or methyl orange II) were used as the fillers for high-density polyethylene [249]. Composites of poly(vinyl alcohol) containing LDH particles with adsorbed anionic azo dyes were also investigated [250, 251]. Nanocomposites exhibiting nonlinear optical properties were prepared from dibenzilidene acetone-type chromophores intercalated in LSil. Active J-aggregates were preserved in the composite with poly(propylene) [176]. Nanoparticles can significantly affect the optical properties of polymers with chromophoric groups. LSil nanocomposites with poly(styrene) carrying fluorescent terfluorene side chains were used for the fabrication of transparent films with a controlled morphology. The films exhibited the properties of efficient emitters which has potential for their application in light-emitting devices [252]. Polyurethane with azo dye moieties was used for the preparation of nanocomposites containing various amounts of organically modified Mmt. Mmt layers were completely exfoliated in the polymer matrix, and the nanocomposites exhibited some mechanical properties that were superior to the pure polymer [253].

Besides the polymer industry, there are further technical branches of potential hybrid material applications which are worth mentioning. Some hybrid systems

have been tested as an alternative approach for dyeing industrial textiles [254, 255]. Another example are pigments applied for thermal dye transfer printing. The studied systems included organically modified LSil with fluoran [256], Rh 6G [257], and other dyes [258]. The adsorption improved dye stability in some cases [259]. The hybrids with triphenylmethane dyes were investigated for their application in commercial carbonless copying paper [204]. Fluoran dye intercalated in organically modified LSil exhibited the properties of a reversible color change via electrochemical activation. Such materials could be used in rewritable recording media controlled by electrostatic potential [260]. Rather chemical properties of MB immobilized in LSil was used for an efficient extraction of Hg^{2+} from waste waters. The sorbent could be quantitatively recovered by a controlled Hg^{2+}release via treatment with NH_3 [261].

18.7 Conclusions

Knowledge on hybrid materials has increased significantly over the last few decades. Numerous applications in the field have emerged by the combination of various constituents including molecules, polymeric substances, nanoparticles, compounds of biological origin into a single material. The combination of various substances at a molecular level provides extraordinary properties and various functionalities, and quantitatively an almost infinite number of new material types. With the development of novel fields in nanosciences, there are new demands in terms of material properties. The development of hybrids of layered nanoparticles with organic dyes has also spread into new areas of materials science. Interest in old types of materials has decreased and the emphasis is aimed on bioactive, biocompatible, electronic, optical, optoelectronic, and magnetic materials. These novel hybrid materials could be used in biochemistry, medicine, environmental sciences, electronics, optics, etc. The rapid development of these hybrid materials is being accelerated by modern research methods, such as high resolution microscopy or single-molecule spectroscopy methods. Modern technologies have developed new techniques for precisely organizing nanoscale building blocks and other constituents and to precisely tuning the material's structure to achieve the formation of the desired complex and multifunctional systems. Modern physicochemical methods combined with the latest knowledge are opening up new prospects in chemistry, such as the field of molecular and nanomaterial engineering for configuring novel material designs.

Acknowledgments This work was supported by the Slovak Research and Development Agency under the contract No. APVV-0291-11, APVV-15-0347. Support from Grant Agency VEGA (1/0278/16) is also acknowledged.

References

1. Zhang Y, Fan L, Chen H, Zhang J, Zhang Y, Wang A (2015) Learning from ancient Maya: preparation of stable palygorskite/methylene blue@SiO2 Maya Blue-like pigment. Microporous Mesoporous Mater 211:124–133. doi:10.1016/j.micromeso.2015.03.002
2. Giustetto R, Vitillo JG, Corazzari I, Turci F (2014) Evolution and reversibility of host/guest interactions with temperature changes in a Methyl Red@Palygorskite polyfunctional hybrid nanocomposite. J Phys Chem C 118(33):19322–19337. doi:10.1021/jp4091238
3. Domenech-Carbo A, Domenech-Carbo MT, Osete-Cortina L, Valle-Algarra FM, Buti D (2014) Isomerization and redox tuning in 'Maya yellow' hybrids from flavonoid dyes plus palygorskite and kaolinite clays. Microporous Mesoporous Mater 194:135–145. doi:10.1016/j.micromeso.2014.03.046
4. Ogawa M, Kuroda K (1995) Photofunctions of intercalation compounds. Chem Rev 95 (2):399–438. doi:10.1021/cr00034a005
5. Schulz-Ekloff G, Wohrle D, van Duffel B, Schoonheydt RA (2002) Chromophores in porous silicas and minerals: preparation and optical properties. Microporous Mesoporous Mater 51 (2):91–138
6. Lezhnina MM, Kynast UH (2010) Optical properties of matrix confined species. Opt Mater 33(1):4–13. doi:10.1016/j.optmat.2010.07.005
7. Latterini L, Nocchetti M, Aloisi GG, Costantino U, Elisei F (2007) Organized chromophores in layered inorganic matrices. Inorg Chim Acta 360(3):728–740. doi:10.1016/j.ica.2006.07.048
8. Demel J, Lang K (2012) Layered hydroxide-porphyrin hybrid materials: synthesis, structure, and properties. Eur J Inorg Chem 32:5154–5164. doi:10.1002/ejic.201200400
9. Takagi S, Eguchi M, Tryk DA, Inoue H (2006) Porphyrin photochemistry in inorganic/organic hybrid materials: clays, layered semiconductors, nanotubes, and mesoporous materials. J Photochem Photobiol, C 7(2–3):104–126. doi:10.1016/j.jphotochemrev.2006.04.002
10. Liu P, Zhang L (2007) Adsorption of dyes from aqueous solutions or suspensions with clay nano-adsorbents. Sep Purif Technol 58 (1):32–39. doi:http://dx.doi.org/10.1016/j.seppur.2007.07.007
11. Zhou CH, Shen ZF, Liu LH, Liu SM (2011) Preparation and functionality of clay-containing films. J Mater Chem 21(39):15132–15153
12. Bujdák J (2006) Effect of the layer charge of clay minerals on optical properties of organic dyes. A review. Appl Clay Sci 34(1–4):58–73. doi:10.1016/j.clay.2006.02.011
13. Schoonheydt RA (2002) Smectite-type clay minerals as nanomaterials. Clays Clay Miner 50(4):411–420
14. Okada T, Sohmiya M, Ogawa M (2015) Photochromic intercalation compounds. Struct Bond 166:177–211. doi:10.1007/978-3-319-16991-0-5
15. Arbeloa FL, Martinez V, Arbeloa T, Arbeloa IL (2010) Fluorescence anisotropy to study the preferential orientation of fluorophores in ordered bi-dimensional systems: rhodamine 6G/Laponite layered films. In: Geddes CD (ed) Reviews in fluorescence 2008, vol 5. Reviews in fluorescence. Kluwer Academic/Plenum Publ, New York, pp 1–35. doi:10.1007/978-1-4419-1260-2_1
16. Neumann MG, Gessner F (2002) Adsorption of Dyes on Clay Surfaces. In: Hubbard AT (ed) Encyclopedia of surface and colloid science, vol 1. Marcel Dekker A.G, New York, pp 307–320
17. Yariv S (2002) Staining of clay minerals and visible absorption spectroscopy of dye-clay complexes. In: Yariv S, Cross H (eds) Organo-clay complexes and interactions. Marcel Dekker, New York, pp 463–566
18. Lagaly G, Ogawa M, Dekany I (2013) Clay mineral-organic interactions. In: Bergaya F, Lagaly G (eds) Handbook of clay science, 2nd edn. Elsevier, Amsterdam, pp 435–505
19. Stewart TA, Nyman M, Deboer MP (2011) Delaminated titanate and peroxotitanate photocatalysts. Appl Catal B 105(1–2):69–76. doi:10.1016/j.apcatb.2011.03.036

20. Nakato T, Inoue S, Hiraragi Y, Sugawara J, Mouri E, Aritani H (2014) Decomposition of a cyanine dye in binary nanosheet colloids of photocatalytically active niobate and inert clay. J Mater Sci 49(2):915–922. doi:10.1007/s10853-013-7777-8
21. Miyamoto N, Nakato T (2003) Liquid crystalline colloidal system obtained by mixing niobate and aluminosilicate nanosheets: a spectroscopic study using a probe dye. Langmuir 19(19):8057–8064. doi:10.1021/la0268449
22. Nakato T, Yamashita Y, Kuroda K (2006) Mesophase of colloidally dispersed nanosheets prepared by exfoliation of layered titanate and niobate. Thin Solid Films 495(1–2):24–28. doi:10.1016/j.tsf.2005.08.301
23. Rytwo G, Nir S, Margulies L (1995) Interactions of monovalent organic cations with montmorillonite—adsorption studies and model-calculations. Soil Sci Soc Am J 59(2):554–564
24. Chen Y (2015) Nanotubes and nanosheets: functionalization and applications of boron nitride and other nanomaterials. CRC Press, New York
25. Rives V (2001) Layered double hydroxides: present and future. Nova Science Publishers, New York
26. Auerbach SM, Carrado KA, Dutta PK (2004) Handbook of layered materials. CRC Press, New York
27. Bujdák J, Komadel P (1997) Interaction of methylene blue with reduced charge montmorillonite. J Phys Chem B 101(44):9065–9068
28. Bujdák J, Janek M, Madejová J, Komadel P (1998) Influence of the layer charge density of smectites on the interaction with methylene blue. J Chem Soc, Faraday Trans 94(23):3487–3492
29. Bujdák J, Iyi N, Kaneko Y, Czímerová A, Sasai R (2003) Molecular arrangement of rhodamine 6G cations in the films of layered silicates: the effect of the layer charge. Phys Chem Chem Phys 5(20):4680–4685. doi:10.1039/b305699f
30. Bujdák J, Iyi N (2006) Molecular aggregation of rhodamine dyes in dispersions of layered silicates: influence of dye molecular structure and silicate properties. J Phys Chem B 110 (5):2180–2186. doi:10.1021/jp0553378
31. Chen GM, Iyi NB, Sasai R, Fujita T, Kitamura K (2002) Intercalation of rhodamine 6G and oxazine 4 into oriented clay films and their alignment. J Mater Res 17(5):1035–1040
32. Iyi N, Sasai R, Fujita T, Deguchi T, Sota T, Arbeloa FL, Kitamura K (2002) Orientation and aggregation of cationic laser dyes in a fluoromica: polarized spectrometry studies. Appl Clay Sci 22(3):125–136
33. Bujdák J, Iyi N (2006) Spectral and structural characteristics of oxazine 4/hexadecyltrimethylammonium montmorillonite films. Chem Mater 18(10):2618–2624. doi:10.1021/cm052715c
34. Miyamoto N, Nakato T (2002) Liquid crystalline nature of K4Nb6O17 nanosheet sols and their macroscopic alignment. Adv Mater 14(18):1267–1270
35. Hibino T, Jones W (2001) New approach to the delamination of layered double hydroxides. J Mater Chem 11(5):1321–1323. doi:10.1039/b101135i
36. Li L, Ma RZ, Ebina Y, Iyi N, Sasaki T (2005) Positively charged nanosheets derived via total delamination of layered double hydroxides. Chem Mater 17(17):4386–4391. doi:10.1021/cm0510460
37. Iyi N, Yamada H (2012) Efficient decarbonation of carbonate-type layered double hydroxide (CO32-LDH) by ammonium salts in alcohol medium. Appl Clay Sci 65–66:121–127. doi:10.1016/j.clay.2012.05.001
38. Iyi N, Yamada H, Sasaki T (2011) Deintercalation of carbonate ions from carbonate-type layered double hydroxides (LDHs) using acid-alcohol mixed solutions. Appl Clay Sci 54 (2):132–137. doi:10.1016/j.clay.2011.07.017
39. Bujdák J, Iyi N (2012) Highly fluorescent colloids based on rhodamine 6G, modified layered silicate, and organic solvent. J Colloid Interface Sci 388(1):15–20. doi:10.1016/j.jcis.2012.08.020
40. Eyama T, Yogo Y, Fujimura T, Tsukamoto T, Masui D, Shimada T, Tachibana H, Inoue H, Takagi S (2012) Adsorption and stacking behaviour of zwitterionic porphyrin on the clay surface. Clay Miner 47(2):243–250. doi:10.1180/claymin.2012.047.2.07

41. Luo ZX, Gao ML, Ye YG, Yang SF (2015) Modification of reduced-charge montmorillonites by a series of Gemini surfactants: characterization and application in methyl orange removal. Appl Surf Sci 324:807–816. doi:10.1016/j.apsusc.2014.11.043
42. Hata H, Kobayashi Y, Mallouk TE (2007) Encapsulation of anionic dye molecules by a swelling fluoromica through intercalation of cationic polyelectrolytes. Chem Mater 19(1):79–87. doi:10.1021/cm061908c
43. Gunister E, Bozkurt AM, Catalgil-Giz H (2013) Poly (diallyldimethylammoniumchloride)/sodium-montmorillonite composite; structure, and adsorption properties. J Appl Polym Sci 129(3):1232–1237. doi:10.1002/app.38792
44. Hao YF, Yan LG, Yu HQ, Yang K, Yu SJ, Shan RR, Du B (2014) Comparative study on adsorption of basic and acid dyes by hydroxy-aluminum pillared bentonite. J Mol Liq 199:202–207. doi:10.1016/j.molliq.2014.09.005
45. Qin ZH, Yuan P, Yang SQ, Liu D, He HP, Zhu JX (2014) Silylation of Al-13-intercalated montmorillonite with trimethylchlorosilane and their adsorption for Orange II. Appl Clay Sci 99:229–236. doi:10.1016/j.clay.2014.06.038
46. Tireli AA, Marcos FCF, Oliveira LF, Guimaraes ID, Guerreiro MC, Silva JP (2014) Influence of magnetic field on the adsorption of organic compound by clays modified with iron. Appl Clay Sci 97–98:1–7. doi:10.1016/j.clay.2014.05.014
47. Wlodarczyk P, Komarneni S, Roy R, White WB (1996) Enhanced fluorescence of coumarin laser dye in the restricted geometry of a porous nanocomposite. J Mater Chem 6(12):1967–1969
48. Felbeck T, Mundinger S, Lezhnina MM, Staniford M, Resch-Genger U, Kynast UH (2015) Multifold fluorescence enhancement in nanoscopic fluorophore-clay hybrids in transparent aqueous media. Chem Eur J 21(20):7582–7587. doi:10.1002/chem.201406416
49. Giustetto R, Seenivasan K, Bonino F, Ricchiardi G, Bordiga S, Chierotti MR, Gobetto R (2011) Host/guest interactions in a sepiolite-based maya blue pigment: a spectroscopic study. J Phys Chem C 115(34):16764–16776. doi:10.1021/jp203270c
50. Zhang YJ, Fan L, Zhang JP, Wang AQ (2015) Water-dispersible and stable fluorescent Maya Blue-like pigments. RSC Adv 5(44):35010–35016. doi:10.1039/c5ra01863c
51. Lin YH, Hori Y, Hoshino S, Miyazawa C, Kohno Y, Shibata M (2014) Fluorescent colored material made of clay mineral and phycoerythrin pigment derived from seaweed. Dyes Pigm 100:97–103. doi:10.1016/j.dyepig.2013.08.022
52. Lezhnina MM, Grewe T, Stoehr H, Kynast U (2012) Laponite blue: dissolving the insoluble. Angew Chem Int Ed 51(42):10652–10655. doi:10.1002/anie.201203236
53. Carrado KA, Forman JE, Botto RE, Winans RE (1993) Incorporation of phthalocyanines by cationic and anionic clays via ion-exchange and direct synthesis. Chem Mater 5(4):472–478
54. Fujii K, Hayashi S (eds) (2003) Syntheses of smectite-analogue/coumarin composites. 2001—a Clay Odyssey. Elsevier Science B.V., Amsterdam, Netherlands
55. Xue AL, Zhou SY, Zhao YJ, Lu XP, Han PF (2010) Adsorption of reactive dyes from aqueous solution by silylated palygorskite. Appl Clay Sci 48(4):638–640. doi:10.1016/j.clay.2010.03.011
56. Fujii K, Kuroda T, Sakoda K, Iyi N (2011) Fluorescence resonance energy transfer and arrangements of fluorophores in integrated coumarin/cyanine systems within solid-state two-dimensional nanospace. J Photochem Photobiol, A 225(1):125–134. doi:10.1016/j.jphotochem.2011.10.009
57. Fujii K, Iyi N, Sasai R, Hayashi S (2008) Preparation of a novel luminous heterogeneous system: rhodamine/coumarin/phyllosilicate hybrid and blue shift in fluorescence emission. Chem Mater 20(9):2994–3002. doi:10.1021/cm0716452
58. Bujdák J, Danko M, Chorvát D Jr, Czímerová A, Sýkora J, Lang K (2012) Selective modification of layered silicate nanoparticle edges with fluorophores. Appl Clay Sci 65–66:152–157. doi:10.1016/j.clay.2012.04.029
59. Al Bakain RZ, Al-Degs YS, Issa AA, Jawad SA, Abu Safieh KA, Al-Ghouti MA (2014) Activation of kaolin with minimum solvent consumption by microwave heating. Clay Miner 49(5):667–681. doi:10.1180/claymin.2014.049.5.04

60. Sas S, Danko M, Lang K, Bujdák J (2015) Photoactive hybrid material based on kaolinite intercalated with a reactive fluorescent silane. Appl Clay Sci 108:208–214. doi:10.1016/j.clay.2015.02.031
61. Okada T, Yoshido S, Miura H, Yamakami T, Sakai T, Mishima S (2012) Swellable microsphere of a layered silicate produced by using monodispersed silica particles. J Phys Chem C 116(41):21864–21869. doi:10.1021/jp307108t
62. Suzuki Y, Hirakawa S, Sakamoto Y, Kawamata J, Kamada K, Ohta K (2008) Hybrid films consisting of a clay and a diacetylenic two-photon absorptive dye. Clays Clay Miner 56(5):487–493. doi:10.1346/ccmn.2008.0560501
63. Shil A, Hussain SA, Bhattacharjee D (2015) Adsorption of a water soluble cationic dye into a cationic Langmuir monolayer. J Phys Chem Solids 80:98–104. doi:10.1016/j.jpcs.2015.01.005
64. Ras RHA, Nemeth J, Johnston CT, DiMasi E, Dekany I, Schoonheydt RA (2004) Hybrid Langmuir-Blodgett monolayers containing clay minerals: effect of clay concentration and surface charge density on the film formation. Phys Chem Chem Phys 6(16):4174–4184. doi:10.1039/b405862c
65. Ras RHA, Nemeth J, Johnston CT, Dekany I, Schoonheydt RA (2004) Orientation and conformation of octadecyl rhodamine B in hybrid Langmuir-Blodgett monolayers containing clay minerals. Phys Chem Chem Phys 6(23):5347–5352. doi:10.1039/b411339j
66. Bhattacharjee J, Hussain SA, Bhattacharjee D (2013) Control of H-dimer formation of acridine orange using nano clay platelets. Spectrochim Acta A Mol Biomol Spectrosc 116:148–153. doi:10.1016/j.saa.2013.07.018
67. Bujdák J (2014) Layer-by-layer assemblies composed of polycationic electrolyte, organic dyes, and layered silicates. J Phys Chem C 118(13):7152–7162. doi:10.1021/jp411155x
68. Place I, Penner TL, McBranch DW, Whitten DG (2003) Layered nanocomposites of aggregated dyes and inorganic scaffolding. J Phys Chem A 107(18):3169–3177. doi:10.1021/jp026048b
69. Leone G, Giovanella U, Bertini F, Porzio W, Meinardi F, Botta C, Ricci G (2013) Poly (styrene)-graft-/rhodamine 6G-fluoromica hybrids: synthesis, characterization and photophysical properties. J Mater Chem C 1(7):1450–1460. doi:10.1039/c2tc00533f
70. Nakamura T, Ogawa M (2013) Adsorption of cationic dyes within spherical particles of poly (N-isopropylacrylamide) hydrogel containing smectite. Appl Clay Sci 83–84:469–473. doi:10.1016/j.clay.2013.05.005
71. Olivero F, Carniato F, Bisio C, Marchese L (2012) A novel stable and efficient light-emitting solid based on saponite and luminescent POSS. J Mater Chem 22(48):25254–25261. doi:10.1039/c2jm34230h
72. Suchithra PS, Vazhayal L, Mohamed AP, Ananthakumar S (2012) Mesoporous organic-inorganic hybrid aerogels through ultrasonic assisted sol-gel intercalation of silica-PEG in bentonite for effective removal of dyes, volatile organic pollutants and petroleum products from aqueous solution. Chem Eng J 200:589–600. doi:10.1016/j.cej.2012.06.083
73. Zhang YX, Hao XD, Kuang M, Zhao H, Wen ZQ (2013) Preparation, characterization and dye adsorption of Au nanoparticles/ZnAl layered double oxides nanocomposites. Appl Surf Sci 283:505–512. doi:10.1016/j.apsusc.2013.06.136
74. Kobayashi T (2012) J-Aggregates, vol 2. World Scientific, Signapore
75. Bergmann K, O'Konski CT (1963) A spectroscopic study of methylene blue monomer, dimer, and complexes with montmorillonite. J Phys Chem 67(10):2169–2177
76. Bujdák J, Iyi N, Fujita T (2002) The aggregation of methylene blue in montmorillonite dispersions. Clay Miner 37(1):121–133. doi:10.1180/0009855023710022
77. Breen C, Loughlin H (1994) The competitive adsorption of methylene-blue on to Na-montmorillonite from binary-solution with N-alkylytrimethylammonium surfactants. Clay Miner 29(5):775–783
78. Gessner F, Schmitt CC, Neumann MG (1994) Time-dependent spectrophotometric study of the interaction of basic-dyes with clays. 1. Methylene-blue and neutral red on Montmorrillonite and Hectorite. Langmuir 10(10):3749–3753

79. Lofaj M, Valent I, Bujdák J (2013) Mechanism of rhodamine 6G molecular aggregation in montmorillonite colloid. Cent Eur J Chem 11(10):1606–1619. doi:10.2478/s11532-013-0289-1
80. Arbeloa FL, Martinez VM, Arbeloa T, Arbeloa IL (2007) Photoresponse and anisotropy of rhodamine dye intercalated in ordered clay layered films. J Photochem Photobiol, C 8:85–108. doi:10.1016/j.jphotochemrev.2007.03.003
81. Tsurumachi N, Okamoto H, Ishii K, Kohkami H, Nakanishi S, Ishii T, Takahashi N, Dou CS, Wen PH, Feng Q (2012) Formation of aggregates in nanohybrid material of dye molecules-titanate nanosheets. J Photochem Photobiol, A 243:1–6. doi:10.1016/j.jphotochem.2012.05.022
82. Tsukamoto T, Shimada T, Takagi S (2013) Photochemical properties of mono-, Tr-, and penta-cationic antimony(V) metalloporphyrin derivatives on a clay layer surface. J Phys Chem A 117(33):7823–7832. doi:10.1021/jp405767s
83. Hill EH, Zhang Y, Whitten DG (2015) Aggregation of cationic p-phenylene ethynylenes on Laponite clay in aqueous dispersions and solid films. J Colloid Interface Sci 449:347–356. doi:10.1016/j.jcis.2014.12.006
84. Ishida Y, Shimada T, Tachibana H, Inoue H, Takagi S (2013) Regulation of the collisional self-quenching of fluorescence in clay/porphyrin complex by strong host-guest interaction. J Phys Chem A 116(49):12065–12072. doi:10.1021/jp309502j
85. Ishida Y, Shimada T, Takagi S (2014) Surface-fixation induced emission of porphyrazine dye by a complexation with inorganic nanosheets. J Phys Chem C 118(35):20466–20471. doi:10.1021/jp506766t
86. Ferreira AUC, Poli AL, Gessner F, Neumann MG, Cavalheiro CCS (2013) Interaction of Auramine O with montmorillonite clays. J Lumin 136:63–67. doi:10.1016/j.jlumin.2012.11.022
87. Valandro SR, Poli AL, Neumann MG, Schmitt CC (2015) Photophysics of Auramine O adsorbed on solid clays. J Lumin 161:209–213. doi:10.1016/j.jlumin.2015.01.023
88. Sun ZZ, Wang J, Wei HY, Wang GQ, Jian Y, Luo SZ, Zhou ZJ (2014) Spectroscopic investigation of a synthetic cyanine amine derivative upon various scaffolds. Anal Lett 47 (16):2722–2730. doi:10.1080/00032719.2014.919505
89. Chakraborty S, Debnath P, Dey D, Bhattacharjee D, Hussain SA (2014) Formation of fluorescent H-aggregates of a cyanine dye in ultrathin film and its effect on energy transfer. J Photochem Photobiol, A 293:57–64. doi:10.1016/j.jphotochem.2014.07.018
90. Felbeck T, Behnke T, Hoffmann K, Grabolle M, Lezhnina MM, Kynast UH, Resch-Genger U (2013) Nile-red-nanoclay hybrids: red emissive optical probes for use in aqueous dispersion. Langmuir 29(36):11489–11497. doi:10.1021/la402165q
91. Costa AL, Gomes AC, Pillinger M, Gonçalves IS, De melo JSS (2015) An indigo carmine-based hybrid nanocomposite with supramolecular control of dye aggregation and photobehavior. Chem Eur J 21 (34):12069–12078. doi:10.1002/chem.201501344
92. Bujdák J, Iyi N (2002) Visible spectroscopy of cationic dyes in dispersions with reduced-charge montmorillonites. Clays Clay Miner 50(4):446–454
93. Bujdák J, Iyi N, Sasai R (2004) Spectral properties, formation of dye molecular aggregates, and reactions in rhodamine 6G/layered silicate dispersions. J Phys Chem B 108(14):4470–4477. doi:10.1021/jp037607x
94. Cione APP, Schmitt CC, Neumann MG, Gessner F (2000) The effect of added salt on the aggregation of clay particles. J Colloid Interface Sci 226(2):205–209
95. Czímerová A, Bujdák J, Gáplovský A (2004) The aggregation of thionine and methylene blue dye in smectite dispersion. Colloids Surf A 243(1–3):89–96. doi:10.1016/j.solsurfa.2004.05.002
96. Czímerová A, Bujdák J, Dohrmann R (2006) Traditional and novel methods for estimating the layer charge of smectites. Appl Clay Sci 34(1–4):2–13. doi:10.1016/j.clay.2006.02.008
97. Bujdák J, Janek M, Madejová J, Komadel P (2001) Methylene blue interactions with reduced-charge smectites. Clays Clay Miner 49(3):244–254

98. Bujdák J, Iyi N, Hrobáriková J, Fujita T (2002) Aggregation and decomposition of a pseudoisocyanine dye in dispersions of layered silicates. J Colloid Interface Sci 247(2):494–503. doi:10.1006/jcis.2001.8140
99. Ishida Y, Masui D, Tachibana H, Inoue H, Shimada T, Takagi S (2012) Controlling the microadsorption structure of porphyrin dye assembly on clay surfaces using the "size-matching rule" for constructing an efficient energy transfer system. ACS Appl Mater Interfaces 4(2):811–816. doi:10.1021/am201465a
100. Fujimura T, Shimada T, Hamatani S, Onodera S, Sasai R, Inoue H, Takagi S (2013) High density intercalation of porphyrin into transparent clay membrane without aggregation. Langmuir 29(16):5060–5065. doi:10.1021/la4003737
101. Takagi S, Shimada T, Ishida Y, Fujimura T, Masui D, Tachibana H, Eguchi M, Inoue H (2013) Size-matching effect on inorganic nanosheets: control of distance, alignment, and orientation of molecular adsorption as a bottom-up methodology for nanomaterials. Langmuir 29(7):2108–2119. doi:10.1021/la3034808
102. Chakraborty C, Dana K, Malik S (2011) Intercalation of perylenediimide dye into LDH clays: enhancement of photostability. J Phys Chem C 115(5):1996–2004. doi:10.1021/jp110486r
103. Tani S, Yamaki H, Sumiyoshi A, Suzuki Y, Hasegawa S, Yamazaki S, Kawamata J (2009) Enhanced photodegradation of organic dyes adsorbed on a clay. J Nanosci Nanotechnol 9 (1):658–661. doi:10.1166/jnn.2009.J081
104. Chernia Z, Gill D (1999) Flattening of TMPyP adsorbed on laponite. Evidence in observed and calculated UV-vis spectra. Langmuir 15(5):1625–1633
105. Miyamoto N, Kawai R, Kuroda K, Ogawa M (2000) Adsorption and aggregation of a cationic cyanine dye on layered clay minerals. Appl Clay Sci 16(3–4):161–170
106. Miyamoto N, Kuroda K, Ogawa M (2004) Exfoliation and film preparation of a layered titanate, $Na_2Ti_3O_7$, and intercalation of pseudoisocyanine dye. J Mater Chem 14(2):165–170. doi:10.1039/b308800f
107. Bujdák J, Iyi N (2008) Spectral properties and structure of the J-aggregates of pseudoisocyanine dye in layered silicate films. J Colloid Interface Sci 326(2):426–432. doi:10.1016/j.jcis.2008.06.036
108. Leone G, Giovanella U, Porzio W, Botta C, Ricci G (2011) In situ synthesis of fluorescent poly(norbornene)/oxazine-1 dye loaded fluoromica hybrids: supramolecular control over dye arrangement. J Mater Chem 21(34):12901–12909. doi:10.1039/c1jm11281c
109. Sasai R, Iyi N, Fujita TH, Takagi K, Itoh H (2003) Synthesis of rhodamine 6G/cationic surfactant/clay hybrid materials and its luminescent characterization. Chem Lett 32(6):550–551
110. Lang K, Kubat P, Mosinger J, Bujdak J, Hof M, Janda P, Sykora J, Iyi N (2008) Photoactive oriented films of layered double hydroxides. Phys Chem Chem Phys 10(30):4429–4434. doi:10.1039/b805081c
111. Sun ZY, Jin L, Shi WY, Wei M, Evans DG, Duan X (2011) Controllable photoluminescence properties of an anion-dye-intercalated layered double hydroxide by adjusting the confined environment. Langmuir 27(11):7113–7120. doi:10.1021/la200846j
112. Sasai R, Itoh T, Ohmori W, Itoh H, Kusunoki M (2009) Preparation and characterization of rhodamine 6G/Alkyltrimethylammonium/laponite hybrid solid materials with higher emission quantum yield. J Phys Chem C 113(1):415–421. doi:10.1021/jp805201n
113. Sasai R, Itoh T, Iyi N, Takagi K, Itoh H (2005) Preparation of hybrid organic/inorganic luminescent thin solid films with highly concentrated laser-dye cations. Chem Lett 34 (11):1490–1491. doi:10.1246/cl.2005.1490
114. Salleres S, Arbeloa FL, Martinez V, Corcostegui C, Arbeloa IL (2009) Effect of surfactant C12TMA molecules on the self-association of R6G dye in thin films of laponite clay. Mater Chem Phys 116(2–3):550–556. doi:10.1016/j.matchemphys.2009.04.030
115. Sasai R, Iyi N, Fujita T, Arbeloa FL, Martinez VM, Takagi K, Itoh H (2004) Luminescence properties of rhodamine 6G intercalated in surfactant/clay hybrid thin solid films. Langmuir 20(11):4715–4719. doi:10.1021/la049584z

116. Kaya M, Meral K, Onganer Y (2015) Molecular aggregates of Merocyanine 540 in aqueous suspensions containing natural and CTAB-modified bentonite. J Mol Struct 1083:101–105. doi:10.1016/j.molstruc.2014.11.046
117. Belušáková S, Lang K, Bujdák J (2015) Hybrid systems based on layered silicate and organic dyes for cascade energy transfer. J Phys Chem C 119:21784–21794. doi:10.1021/acs.jpcc.5b04982
118. Salleres S, Arbeloa FL, Martinez VM, Arbeloa T, Arbeloa IL (2010) On the arrangements of R6G molecules in organophilic C12TMA/lap clay films for low dye loadings. Langmuir 26 (2):930–937. doi:10.1021/la902414n
119. Konno S, Fujimura T, Otani Y, Shimada T, Inoue H, Takagi S (2014) Microstructures of the porphyrin/viologen mono layer on the clay surface: segregation or integration? J Phys Chem C 118(35):20504–20510. doi:10.1021/jp5076274
120. Sasai R, Iyi N, Kusumoto H (2011) Luminous change of rhodamine 3B incorporated into titanate nanosheet/decyltrimethylammonium hybrids under humid atmosphere. Bull Chem Soc Jpn 84(5):562–568. doi:10.1246/bcsj.20100343
121. Ishida Y, Kulasekharan R, Shimada T, Ramamurthy V, Takagi S (2014) Supramolecular-surface photochemistry: supramolecular assembly organized on a clay surface facilitates energy transfer between an encapsulated donor and a free acceptor. J Phys Chem C 118(19):10198–10203. doi:10.1021/jp502816j
122. Matejdes M, Czímerová A, Janek M (2015) Fluorescence tuning of 2D montmorillonite optically active layers with beta-cyclodextrine/dye supramolecular complexes. Appl Clay Sci 114:9–19. doi:10.1016/j.clay.2015.05.002
123. Yurekli K, Conley E, Krishnamoorti R (2005) Effect of laponite and a nonionic polymer on the absorption character of cationic dye solutions. Langmuir 21(13):5825–5830. doi:10.1021/la047540k
124. Vanamudan A, Pamidimukkala P (2015) Chitosan, nanoclay and chitosan-nanoclay composite as adsorbents for Rhodamine-6G and the resulting optical properties. Int J Biol Macromol 74:127–135. doi:10.1016/j.ijbiomac.2014.11.009
125. Czimerová A, Jankovič L, Madejová J, Čeklovský A (2013) Unique photoactive nanocomposites based on rhodamine 6G/polymer/montmorillonite hybrid systems. J Polym Sci, Part B: Polym Phys 51(23):1672–1679. doi:10.1002/polb.23382
126. Holzheu S, Hoffmann H (2002) Adsorption study of cationic dyes having a trimethylammonium anchor group on hectorite using electrooptic and spectroscopic methods. J Colloid Interface Sci 245(1):16–23. doi:10.1006/jcis.2001.7978
127. Bujdák J, Iyi N (2005) Molecular orientation of rhodamine dyes on surfaces of layered silicates. J Phys Chem B 109(10):4608–4615
128. Miyamoto N, Kuroda K, Ogawa M (2001) Uni-directional orientation of cyanine dye aggregates on a K4Nb6O17 single crystal: toward novel supramolecular assemblies with three-dimensional anisotropy. J Am Chem Soc 123(28):6949–6950. doi:10.1021/ja015541i
129. Hähner G, Marti A, Spencer ND, Caseri WR (1996) Orientation and electronic structure of methylene blue on mica: A near edge x-ray absorption fine structure spectroscopy study. J Chem Phys 104(19):7749–7757
130. Fischer D, Caseri WR, Hahner G (1998) Orientation and electronic structure of ion exchanged dye molecules on mica: an X-ray absorption study. J Colloid Interface Sci 198 (2):337–346
131. Wang HH, Han DX, Li N, Li KE (2005) Study on the intercalation and interlayer state of porphyrins into alpha-zirconium phosphate. J Incl Phenom Macrocycl Chem 52(3–4):247–252. doi:10.1007/s10847-004-7597-1
132. Čeklovský A, Bujdák J, Czímerová A, Iyi N (2007) Spectral study on the molecular orientation of a tetracationic porphyrin dye on the surface of layered silicates. Cent Eur J Phys 5(2):236–243. doi:10.2478/s11534-007-0010-0
133. Hayashi H, Hudson MJ (1995) Intercalation of the Copper(II) phthalocyanine Tetrasulfonate Anion ($CuPcTs^{4-}$) into basic Copper(II) salts. J Mater Chem 5(5):781–783. doi:10.1039/jm9950500781

134. Yan D, Lu J, Ma J, Wei M, Li S, Evans DG, Duan X (2011) Near-infrared absorption and polarized luminescent ultrathin films based on sulfonated cyanines and layered double hydroxide. J Phys Chem C 115(16):7939–7946. doi:10.1021/jp2002029
135. Windsor SA, Tinker MH (1999) Electro-fluorescence polarization studies of the interaction of fluorescent dyes with clay minerals in suspensions. Colloids Surf A 148(1–2):61–73
136. Salleres S, Arbeloa FL, Martinez VM, Arbeloa T, Arbeloa IL (2009) Improving the fluorescence polarization method to evaluate the orientation of fluorescent systems adsorbed in ordered layered materials. J Lumin 129(11):1336–1340. doi:10.1016/j.jlumin.2009.06.022
137. López Arbeloa F, Martínez Martínez V (2006) New fluorescent polarization method to evaluate the orientation of adsorbed molecules in uniaxial 2D layered materials. J Photochem Photobiol, A 181(1):44–49
138. López Arbeloa F, Martínez Martínez V (2006) Orientation of adsorbed dyes in the interlayer space of clays. 2 fluorescence polarization of rhodamine 6G in laponite films. Chem Mater 18 (6):1407–1416
139. Martinez V, Salleres S, Banuelos J, Arbeloa FL (2006) Application of fluorescence with polarized light to evaluate the orientation of dyes adsorbed in layered materials. J Fluoresc 16(2):233–240. doi:10.1007/s10895-005-0042-z
140. Bujdák J, Czímerová A, Arbeloa FL (2011) Two-step resonance energy transfer between dyes in layered silicate films. J Colloid Interface Sci 364(2):497–504. doi:10.1016/j.jcis.2011.08.042
141. Eguchi M, Tachibana H, Takagi S, Tryk DA, Inoue H (2007) Dichroic measurements on dicationic and tetracationic porphyrins on clay surfaces with visible-light-attenuated total reflectance. Bull Chem Soc Jpn 80:1350–1356. doi:10.1246/bcsj.80.1350
142. Yamaoka K, Sasai R, Takata N (2000) Electric linear dichroism. A powerful method for the ionic chromophore-colloid system as exemplified by dye and montmorillonite suspensions. Colloids Surf, A 175 (1–2):23-39
143. Inadomi T, Ikeda S, Okumura Y, Kikuchi H, Miyamoto N (2014) Photo-induced anomalous deformation of poly(N-Isopropylacrylamide) gel hybridized with an inorganic nanosheet liquid crystal aligned by electric field. Macromol Rapid Commun 35(20):1741–1746. doi:10.1002/marc.201400333
144. Egawa T, Watanabe H, Fujimura T, Ishida Y, Yamato M, Masui D, Shimada T, Tachibana H, Yoshida H, Inoue H, Takagi S (2011) Novel methodology to control the adsorption structure of cationic porphyrins on the clay surface using the “size-matching rule”. Langmuir 27(17):10722–10729. doi:10.1021/la202231k
145. Čeklovský A, Takagi S, Bujdák J (2011) Study of spectral behaviour and optical properties of cis/trans-bis (N-methylpyridinium-4-yl)diphenyl porphyrin adsorbed on layered silicates. J Colloid Interface Sci 360(1):26–30. doi:10.1016/j.jcis.2011.04.010
146. Čeklovský A, Czímerová A, Lang K, Bujdák J (2009) Effect of the layer charge on the interaction of porphyrin dyes in layered silicates dispersions. J Lumin 129(9):912–918. doi:10.1016/j.jlumin.2009.03.032
147. Čeklovský A, Czímerová A, Lang K, Bujdák J (2009) Layered silicate films with photochemically active porphyrin cations. Pure Appl Chem 81(8):1385–1396. doi:10.1351/pac-con-08-08-35
148. Hattori T, Tong ZW, Kasuga Y, Sugito Y, Yui T, Takagi K (2006) Hybridization of layered niobates with cationic dyes. Res Chem Intermed 32(7):653–669
149. Yui T, Kobayashi Y, Yamada Y, Tsuchino T, Yano K, Kajino T, Fukushima Y, Torimoto T, Inoue H, Takagi K (2006) Photochemical electron transfer though the interface of hybrid films of titania nano-sheets and mono-dispersed spherical mesoporous silica particles. Phys Chem Chem Phys 8(39):4585–4590. doi:10.1039/b609779k
150. Ishida Y, Shimada T, Masui D, Tachibana H, Inoue H, Takagi S (2011) Efficient excited energy transfer reaction in clay/porphyrin complex toward an artificial light-harvesting system. J Am Chem Soc 133(36):14280–14286. doi:10.1021/ja204425u
151. Bujdák J, Ratulovská J, Donauerová A, Bujdáková H (2016) Hybrid materials based on luminescent alkaloid berberine and saponite. J Nanosci Nanotechnol 16(8):7801–7804

152. Benard S, Leaustic A, Riviere E, Yu P, Clement R (2001) Interplay between magnetism and photochromism in spiropyran-$MnPS_3$ intercalation compounds. Chem Mater 13(10):3709–3716. doi:10.1021/cm011019j
153. Ogawa M, Yamamoto M, Kuroda K (2001) Intercalation of an amphiphilic azobenzene derivative into the interlayer space of a layered silicate, magadiite. Clay Miner 36(2):263–266
154. Ogawa M, Ishii T, Miyamoto N, Kuroda K (2003) Intercalation of a cationic azobenzene into montmorillonite. Appl Clay Sci 22(4):179–185. doi:10.1016/s0169-1317(02)00157-6
155. Bujdák J, Iyi N, Fujita T (2003) Isomerization of cationic azobenzene derivatives in dispersions and films of layered silicates. J Colloid Interface Sci 262(1):282–289. doi:10.1016/s0021-9797(03)00235-2
156. Umemoto T, Ohtani Y, Tsukamoto T, Shimada T, Takagi S (2014) Pinning effect for photoisomerization of a dicationic azobenzene derivative by anionic sites of the clay surface. Chem Commun 50(3):314–316. doi:10.1039/c3cc47353h
157. Ogawa M, Ishii T, Miyamoto N, Kuroda K (2001) Photocontrol of the basal spacing of azobenzene-magadiite intercalation compound. Adv Mater 13(14):1107–1109. doi:10.1002/1521-4095(200107)13:14<1107:AID-ADMA1107>3.0.CO;2-O
158. Ogawa M (2002) Photoisomerization of azobenzene in the interlayer space of magadiite. J Mater Chem 12(11):3304–3307. doi:10.1039/b204031j
159. Ishihara M, Hirase R, Mori M, Yoshioka H, Ueda Y (2009) Photoinduced spectral changes in hybrid thin films of functional dyes and inorganic layered material. Thin Solid Films 518 (2):857–860. doi:10.1016/j.tsf.2009.07.103
160. Gentili PL, Costantino U, Vivani R, Latterini L, Nocchetti M, Aloisi GG (2004) Preparation and characterization of zirconium phosphonate azobenzene intercalation compounds. A structural, photophysical and photochemical study. J Mater Chem 14 (10):1656–1662. doi:10.1039/b313828c
161. Okada T, Sakai H, Ogawa M (2008) The effect of the molecular structure of a cationic azo dye on the photoinduced intercalation of phenol in a montmorillonite. Appl Clay Sci 40(1–4):187–192. doi:10.1016/j.clay.2007.09.001
162. Okada T, Watanabe Y, Ogawa M (2005) Photoregulation of the intercalation behavior of phenol for azobenzene-clay intercalation compounds. J Mater Chem 15(9):987–992. doi:10.1039/b412707b
163. Boutton C, Kauranen M, Persoons A, Keung MP, Jacobs KY, Schoonheydt RA (1997) Enhanced second-order optical nonlinearity of dye molecules adsorbed onto Laponite particles. Clays Clay Miner 45(3):483–485
164. Ghofraniha N, Conti C, Ruocco G, Zamponi F (2009) Time-dependent nonlinear optical susceptibility of an out-of-equilibrium soft material. Phys Rev Lett 102 (3). doi:10.1103/PhysRevLett.102.038303
165. Ghofraniha N, Conti C, Ruocco G (2007) Aging of the nonlinear optical susceptibility in doped colloidal suspensions. Phys Rev B 75 (22). doi:10.1103/PhysRevB.75.224203
166. Laschewsky A, Wischerhoff E, Kauranen M, Persoons A (1997) Polyelectrolyte multilayer assemblies containing nonlinear optical dyes. Macromolecules 30(26):8304–8309
167. Suzuki Y, Tenma Y, Nishioka Y, Kamada K, Ohta K, Kawamata J (2011) Efficient two-photon absorption materials consisting of cationic dyes and clay minerals. J Phys Chem C 115(42):20653–20661. doi:10.1021/jp203809b
168. Suzuki Y, Tenma Y, Nishioka Y, Kawamata J (2012) Efficient nonlinear optical properties of dyes confined in interlayer nanospaces of clay minerals. Chem Asian J 7(6):1170–1179. doi:10.1002/asia.201200049
169. Suzuki Y, Sugihara H, Satomi K, Tominaga M, Mochida S, Kawamata J (2014) Two-photon absorption properties of an acetylene derivative confined in the interlayer space of a smectite. Appl Clay Sci 96:116–119. doi:10.1016/j.clay.2014.01.014
170. Epelde-Elezcano N, Duque-Redondo E, Martínez-Martínez V, Manzano H, López-Arbeloa I (2014) Preparation, photophysical characterization, and modeling of LDS722/Laponite 2D-Ordered hybrid films. Langmuir 30(33):10112–10117. doi:10.1021/la502081c

171. Coradin T, Clement R, Lacroix PG, Nakatani K (1996) From intercalation to aggregation: nonlinear optical properties of stilbazolium chromophores-MPS_3 layered hybrid materials. Chem Mater 8(8):2153–2158. doi:10.1021/cm960060x
172. Kawamata J, Suzuki Y, Tenma Y (2010) Fabrication of clay mineral-dye composites as nonlinear optical materials. Philos Mag 90(17–18):2519–2527. doi:10.1080/14786430903581304
173. Chakraborty S, Bhattacharjee D, Soda H, Tominaga M, Suzuki Y, Kawamata J, Hussain SA (2015) Temperature and concentration dependence of J-aggregate of a cyanine dye in a Laponite film fabricated by Langmuir-Blodgett technique. Appl Clay Sci 104:245–251. doi:10.1016/j.clay.2014.11.039
174. Kawamata J, Hasegawa S (2006) Clay-assisted disaggregation and stabilization in hemicyanine Langmuir-Blodgett films. J Nanosci Nanotechnol 6(6):1620–1624. doi:10.1166/jnn.2006.235
175. van Duffel B, Verbiest T, Van Elshocht S, Persoons A, De Schryver FC, Schoonheydt RA (2001) Fuzzy assembly and second harmonic generation of clay/polymer/dye monolayer films. Langmuir 17(4):1243–1249
176. Dudkina MM, Tenkovtsev AV, Pospiech D, Jehnichen D, Häußler L, Leuteritz A (2005) Nanocomposites of NLO chromophore-modified layered silicates and polypropylene. J Polym Sci, Part B: Polym Phys 43(18):2493–2502. doi:10.1002/polb.20532
177. Chao TY, Chang HL, Su WC, Wu JY, Jeng RJ (2008) Nonlinear optical polyimide/montmorillonite nanocomposites consisting of azobenzene dyes. Dyes Pigm 77(3):515–524. doi:10.1016/j.dyepig.2007.08.001
178. Yui T, Kameyama T, Sasaki T, Torimoto T, Takagi K (2007) Pyrene-to-porphyrin excited singlet energy transfer in LBL-deposited LDH nanosheets. J Porphyrins Phthalocyanines 11(5–6):428–433
179. Takagi S, Eguchi M, Shimada T, Hamatani S, Inoue H (2007) Energy transfer reaction of cationic porphyrin complexes on the clay surface: effect of sample preparation method. Res Chem Intermed 33(1–2):177–189
180. Bujdák J, Chorvát D, Iyi N (2010) Resonance energy transfer between rhodamine molecules adsorbed on layered silicate particles. J Phys Chem C 114(2):1246–1252. doi:10.1021/jp9098107
181. Ishida Y, Shimada T, Takagi S (2013) Artificial light-harvesting model in a self-assembly composed of cationic dyes and inorganic nanosheet. J Phys Chem C 117(18):9154–9163. doi:10.1021/jp4022757
182. Lu LD, Jones RM, McBranch D, Whitten D (2002) Surface-enhanced superquenching of cyanine dyes as J-aggregates on Laponite clay nanoparticles. Langmuir 18(20):7706–7713. doi:10.1021/la0259306
183. Eguchi M, Watanabe Y, Ohtani Y, Shimada T, Takagi S (2014) Switching of energy transfer reaction by the control of orientation factor between porphyrin derivatives on the clay surface. Tetrahedron Lett 55(16):2662–2666. doi:10.1016/j.tetlet.2014.03.027
184. Ras RHA, van Duffel B, Van der Auweraer M, De Schryver FC, Schoonheydt RA (2003) Molecular and particulate organisation in dye-clay films prepared by the Langmuir-Blodgett method. 2001—a Clay Odyssey:473–480
185. Hussain SA, Schoonheydt RA (2010) Langmuir-blodgett monolayers of cationic dyes in the presence and absence of clay mineral layers: N, N′-Dioctadecyl thiacyanine. Octadecyl Rhodamine B and Laponite Langmuir 26(14):11870–11877. doi:10.1021/la101078f
186. Hussain SA, Chakraborty S, Bhattacharjee D, Schoonheydt RA (2010) Fluorescence resonance energy transfer between organic dyes adsorbed onto nano-clay and langmuir-blodgett (LB) films. Spectrochim Acta A Mol Biomol Spectrosc 75(2):664–670. doi:10.1016/j.saa.2009.11.037
187. Dey D, Bhattacharjee D, Chakraborty S, Hussain SA (2013) Effect of nanoclay laponite and pH on the energy transfer between fluorescent dyes. J Photochem Photobiol, A 252:174–182

188. Olivero F, Carniato F, Bisio C, Marchese L (2014) Promotion of forster resonance energy transfer in a saponite clay containing luminescent polyhedral oligomeric silsesquioxane and rhodamine dye. Chem Asian J 9(1):158–165. doi:10.1002/asia.201300936
189. Dey D, Saha J, Roy AD, Bhattacharjee D, Hussain SA (2014) Development of an ion-sensor using fluorescence resonance energy transfer. Sens Actuators, B 195:382–388. doi:10.1016/j.snb.2014.01.065
190. Saha J, Datta Roy A, Dey D, Chakraborty S, Bhattacharjee D, Paul PK, Hussain SA (2015) Investigation of fluorescence resonance energy transfer between fluorescein and rhodamine 6G. Spectrochim Acta A Mol Biomol Spectrosc 149. doi:10.1016/j.saa.2015.04.027
191. Margulies L, Rozen H, Stern T, Rytwo G, Rubin B, Ruzo LO, Nir S, Cohen E (1993) Photostabilization of pesticides by clays and chromophores. Arch Insect Biochem Physiol 22 (3–4):467–486
192. Undabeytia T, Nir S, Tel-Or E, Rubin B (2000) Photostabilization of the herbicide norflurazon by using organoclays. J Agric Food Chem 48(10):4774–4779. doi:10.1021/jf9912405
193. Si YB, Zhou J, Chen HM, Zhou DM (2004) Photo stabilization of the herbicide bensulfuron-methyl by using organoclays. Chemosphere 54(7):943–950. doi:10.1016/j.chemosphere.2003.09.033
194. Kohno Y, Asai S, Shibata M, Fukuhara C, Maeda Y, Tomita Y, Kobayashi K (2014) Improved photostability of hydrophobic natural dye incorporated in organo-modified hydrotalcite. J Phys Chem Solids 75(8):945–950. doi:10.1016/j.jpcs.2014.04.010
195. Samuels M, Mor O, Rytwo G (2013) Metachromasy as an indicator of photostabilization of methylene blue adsorbed to clays and minerals. J Photochem Photobiol, B 121:23–26. doi:10.1016/j.jphotobiol.2013.02.004
196. Kohno Y, Totsuka K, Ikoma S, Yoda K, Shibata M, Matsushima R, Tomita Y, Maeda Y, Kobayashi K (2009) Photostability enhancement of anionic natural dye by intercalation into hydrotalcite. J Colloid Interface Sci 337(1):117–121. doi:10.1016/j.jcis.2009.04.065
197. Kohno Y, Kinoshita R, Ikoma S, Yoda K, Shibata M, Matsushima R, Tomita Y, Maeda Y, Kobayashi K (2009) Stabilization of natural anthocyanin by intercalation into montmorillonite. Appl Clay Sci 42(3–4):519–523. doi:10.1016/j.clay.2008.06.012
198. Ogawa M, Sohmiya M, Watase Y (2011) Stabilization of photosensitizing dyes by complexation with clay. Chem Commun 47(30):8602–8604. doi:10.1039/c1cc12392k
199. Shinozaki R, Nakato T (2008) Photochemical behavior of rhodamine 6G dye intercalated in photocatalytically active layered hexaniobate. Microporous Mesoporous Mater 113(1–3):81–89. doi:10.1016/j.micromeso.2007.11.005
200. Wang P, Cheng MM, Zhang ZH (2014) On different photodecomposition behaviors of rhodamine B on laponite and montmorillonite clay under visible light irradiation. J Saudi Chem Soc 18(4):308–316. doi:10.1016/j.jscs.2013.11.006
201. Raha S, Ivanov I, Quazi NH, Bhattacharya SN (2009) Photo-stability of rhodamine-B/montmorillonite nanopigments in polypropylene matrix. Appl Clay Sci 42 (3–4):661–666. doi:10.1016/j.clay.2008.06.008
202. Shinozaki R, Nakato T (2008) Photoelectrochemical behavior of a rhodamine dye intercalated in a photocatalytically active layered niobate and photochemically inert clay. J Ceram Soc Jpn 116(1352):555–560
203. Morimoto K, Tamura K, Iyi N, Ye JH, Yamada H (2011) Adsorption and photodegradation properties of anionic dyes by layered double hydroxides. J Phys Chem Solids 72(9):1037–1045. doi:10.1016/j.jpcs.2011.05.018
204. Caine MA, McCabe RW, Wang LC, Brown RG, Hepworth JD (2001) The influence of singlet oxygen in the fading of carbonless copy paper primary dyes on clays. Dyes Pigm 49 (3):135–143
205. Bujdák J, Jurečeková J, Bujdáková H, Lang K, Šeršeň F (2009) Clay mineral particles as efficient carriers of methylene blue used for antimicrobial treatment. Environ Sci Technol 43 (16):6202–6207. doi:10.1021/es900967g

206. Demel J, Kubat P, Jirka I, Kovar P, Pospisil M, Lang K (2010) Inorganic-organic hybrid materials: layered zinc hydroxide salts with intercalated porphyrin sensitizers. J Phys Chem C 114(39):16321–16328. doi:10.1021/jp106116n
207. Kafunkova E, Taviot-Gueho C, Bezdicka P, Klementova M, Kovar P, Kubat P, Mosinger J, Pospisil M, Lang K (2010) Porphyrins intercalated in Zn/Al and Mg/Al layered double hydroxides: properties and structural arrangement. Chem Mater 22(8):2481–2490. doi:10.1021/cm903125v
208. Jirickova M, Demel J, Kubat P, Hostomsky J, Kovanda F, Lang K (2011) Photoactive self-standing films made of layered double hydroxides with arranged porphyrin molecules. J Phys Chem C 115(44):21700–21706. doi:10.1021/jp207505n
209. Madhavan D, Pitchumani K (2002) Photoreactions in clay media: singlet oxygen oxidation of electron-rich substrates mediated by clay-bound dyes. J Photochem Photobiol, A 153(1–3):205–210
210. Bujdák J, Iyi N, Fujita T (2002) Aggregation and stability of 1,1′-diethyl-4,4′-cyanine dye on the surface of layered silicates with different charge densities. Colloids Surf A 207(1–3):207–214
211. Bujdák J, Iyi N, Fujita T (2003) Control of optical properties of adsorbed cyanine dyes via negative charge distribution on layered silicates. Solid State Chemistry V 90–91:463–468
212. Liu PF, Liu P, Zhao KC, Li L (2015) Photostability enhancement of azoic dyes adsorbed and intercalated into Mg-Al-layered double hydroxide. Opt Laser Technol 74:23–28
213. Kohno Y, Ito M, Kurata M, Ikoma S, Shibata M, Matsushima R, Tomita Y, Maeda Y, Kobayashi K (2011) Photo-induced coloration of 2-hydroxychalcone in the clay interlayer. J Photochem Photobiol, A 218(1):87–92. doi:10.1016/j.jphotochem.2010.12.007
214. Chakraborty S, Bhattacharjee D, Hussain SA (2014) Formation and control of excimer of a coumarin derivative in Langmuir-Blodgett films. J Lumin 145:824–831. doi:10.1016/j.jlumin.2013.09.001
215. Miyata H, Sugahara Y, Kuroda K, Kato C (1988) Synthesis of a viologen-tetratitanate intercalation. compound and its photochemical behaviour. J Chem Soc, Faraday Trans 84:2677–2682. doi:10.1039/f19888402677
216. Miyamoto N, Kuroda K, Ogawa M (2004) Visible light induced electron transfer and long-lived charge separated state in cyanine dye/layered titanate intercalation compounds. J Phys Chem B 108(14):4268–4274. doi:10.1021/jp035617s
217. Okada T, Matsutomo T, Ogawa M (2010) Nanospace engineering of methylviologen modified hectorite-like layered silicates with varied layer charge density for the adsorbents design. J Phys Chem C 114(1):539–545. doi:10.1021/jp9089886
218. Batista T, Chiorcea-Paquim AM, Brett AMO, Schmitt CC, Neumann MG (2011) Laponite RD/polystyrenesulfonate nanocomposites obtained by photopolymerization. Appl Clay Sci 53(1):27–32. doi:10.1016/j.clay.2011.04.007
219. Shiragami T, Mori Y, Matsumoto J, Takagi S, Inoue H, Yasuda M (2006) Non-aggregated adsorption of cationic metalloporphyrin dyes onto nano-clay sheets films. Colloids Surf A 284:284–289. doi:10.1016/j.colsurfa.2005.11.102
220. Kakegawa N, Ogawa M (2004) Effective luminescence quenching of tris(2,2-bipyridine) ruthenium(II) by methylviologen on clay by the aid of poly(vinylpyrrolidone). Langmuir 20(17):7004–7009. doi:10.1021/la036213u
221. de Souza GR, Fertonani FL, Pastre IA (2003) Espectroelectrochemical behavior of clay-dye structured systems. Ecletica Quim 28(1):77–83
222. Lazarin AM, Airoldi C (2008) Methylene blue intercalated into calcium phosphate—electrochemical properties and an ascorbic acid oxidation study. Solid State Sci 10(9):1139–1144. doi:10.1016/j.solidstatesciences.2007.11.023
223. Dilgin Y, Nisli G (2006) Flow injection photoamperometric investigation of ascorbic acid using methylene blue immobilized on titanium phosphate. Anal Lett 39(3):451–465. doi:10.1080/000032710500536053

224. Lazarin AM, Airoldi C (2004) Intercalation of methylene blue into barium phosphate-synthesis and electrochemical investigation. Anal Chim Acta 523(1):89–95. doi:10.1016/j.aca.2004.05.063
225. Sumitani M, Takagi S, Tanamura Y, Inoue H (2004) Oxygen indicator composed of an organic/inorganic hybrid compound of methylene blue, reductant, surfactant and saponite. Anal Sci 20(8):1153–1157
226. Shan D, Mousty C, Cosnier S, Mu SL (2003) A new Polyphenol oxidase biosensor mediated by azure B in laponite clay matrix. Electroanalysis 15(19):1506–1512. doi:10.1002/elan.200302740
227. Ishihara S, Iyi N, Labuta J, Deguchi K, Ohki S, Tansho M, Shimizu T, Yamauchi Y, Sahoo P, Naito M, Abe H, Hill JP, Ariga K (2013) Naked-eye discrimination of methanol from ethanol using composite film of oxoporphyrinogen and layered double hydroxide. ACS Appl Mater Interfaces 5(13):5927–5930. doi:10.1021/am401956s
228. Dey D, Bhattacharjee D, Chakraborty S, Hussain SA (2013) Development of hard water sensor using fluorescence resonance energy transfer. Sens Actuators, B 184:268–273. doi:10.1016/j.snb.2013.04.077
229. Esposito A, Raccurt O, Charmeau JY, Duchet-Rumeau J (2010) Functionalization of cloisite 30B with fluorescent dyes. Appl Clay Sci 50(4):525–532. doi:10.1016/j.clay.2010.10.007
230. Bur AJ, Roth SC, Start PR, Lee YH, Maupin PH (2007) Monitoring clay exfoliation during polymer/clay compounding using fluorescence spectroscopy. Trans Inst Measur Control 29 (5):403–416. doi:10.1177/0142331207073486
231. Banerjee S, Joshi M, Ghosh AK (2010) A spectroscopic approach for structural characterization of polypropylene/clay nanocomposite. Polym Compos 31(12):2007–2016. doi:10.1002/pc.20998
232. Gitis V, Dlugy C, Ziskind G, Sladkevich S, Lev O (2011) Fluorescent clays-similar transfer with sensitive detection. Chem Eng J 174(1):482–488. doi:10.1016/j.cej.2011.08.063
233. Marquez AES, Lerner DA, Fetter G, Bosch P, Tichit D, Palomares E (2014) Preparation of layered double hydroxide/chlorophyll a hybrid nano-antennae: a key step. Dalton Trans 43 (27):10521–10528. doi:10.1039/c4dt00113c
234. Teixeira-Neto ÃA, Izumi CMS, Temperini MLA, Ferreira AMDC, Constantino VRL (2012) Hybrid materials based on smectite clays and nutraceutical anthocyanins from the Açaí fruit. Eur J Inorg Chem 32:5411–5420. doi:10.1002/ejic.201200702
235. Choy JH, Kim YK, Son YH, Bin Choy Y, Oh JM, Jung H, Hwang SJ (2008) Nanohybrids of edible dyes intercalated in ZnAl layered double hydroxides. J Phys Chem Solids 69(5–6):1547–1551. doi:10.1016/j.jpcs.2007.11.009
236. Saelim NO, Magaraphan R, Sreethawong T (2011) Preparation of sol-gel TiO2/purified Na-bentonite composites and their photovoltaic application for natural dye-sensitized solar cells. Energy Convers Manage 52(8–9):2815–2818. doi:10.1016/j.enconman.2011.02.016
237. Kolesnikov MP, Kritsky MS (2001) Study of chemical structure and of photochemical activity of abiogenic flavin pigment. J Evol Biochem Physiol 37(5):507–514
238. Donauerová A, Bujdák J, Smolinská M, Bujdáková H (2015) Photophysical and antibacterial properties of complex systems based on smectite, a cationic surfactant and methylene blue. J Photochem Photobiol, B 151:135–141. doi:10.1016/j.jphotobiol.2015.07.018
239. Li DD, Miao CL, Wang XD, Yu XH, Yu JH, Xu RR (2013) AIE cation functionalized layered zirconium phosphate nanoplatelets: ion-exchange intercalation and cell imaging. Chem Commun 49(83):9549–9551. doi:10.1039/c3cc45041d
240. Kuo YM, Kuthati Y, Kankala RK, Wei PR, Weng CF, Liu CL, Sung PJ, Mou CY, Lee CH (2015) Layered double hydroxide nanoparticles to enhance organ-specific targeting and the anti-proliferative effect of cisplatin. J Mater Chem B 3(17):3447–3458. doi:10.1039/c4tb01989j
241. Rozen H, Margulies L (1991) Photostabilization of tetrahydro-2-(nitromethylene)-2H-1,3-thiazine adsorbed on clays. J Agric Food Chem 39(7):1320–1325
242. Banerjee K, Dureja P (1995) Photostabilization of quinalphos by crystal violet on the surface of kaolinite and palygorskite. Pestic Sci 43(4):333–337

243. Kievani MB, Edraki M (2015) Synthesis, characterization and assessment thermal properties of clay based nanopigments. Front Chem Sci Eng 9(1):40–45. doi:10.1007/s11705-015-1505-7
244. Beltran MI, Benavente V, Marchante V, Dema H, Marcilla A (2014) Characterisation of montmorillonites simultaneously modified with an organic dye and an ammonium salt at different dye/salt ratios. Properties of these modified montmorillonites EVA nanocomposites. Appl Clay Sci 97–98:43–52. doi:10.1016/j.clay.2014.06.001
245. Marchante V, Benavente V, Marcilla A, Martinez-Verdu FM, Beltran MI (2013) Ethylene vinyl acetate/nanoclay-based pigment composites: morphology, rheology, and mechanical, thermal, and colorimetric properties. J Appl Polym Sci 130(4):2987–2994. doi:10.1002/app.39422
246. Marchante V, Marcilla A, Benavente V, Martinez-Verdu FM, Beltran MI (2013) Linear low-density polyethylene colored with a nanoclay-based pigment: morphology and mechanical, thermal, and colorimetric properties. J Appl Polym Sci 129(5):2716–2726. doi:10.1002/app.38903
247. Aloisi GG, Costantino U, Latterini L, Nocchetti M, Camino G, Frache A (2006) Preparation and spectroscopic characterisation of intercalation products of clay and of clay-polypropylene composites with rhodamine B. J Phys Chem Solids 67(5–6):909–914. doi:10.1016/j.jpcs.2006.01.003
248. Smitha VS, Manjumol KA, Ghosh S, Brahmakumar M, Pavithran C, Perumal P, Warrier KG (2011) Rhodamine 6G intercalated montmorillonite nanopigments-polyethylene composites: facile synthesis and ultravioletstability study. J Am Ceram Soc 94(6):1731–1736. doi:10.1111/j.1551-2916.2010.04326.x
249. Zimmermann A, Jaerger S, Zawadzki SF, Wypych F (2013) Synthetic zinc layered hydroxide salts intercalated with anionic azo dyes as fillers into high-density polyethylene composites: first insights. J Polym Res 20(9). doi:10.1007/s10965-013-0224-3
250. da Silva MLN, Marangoni R, da Silva AH, Wypych F, Schreiner WH (2013) Poly(vinyl alcohol) composites containing layered hydroxide salts, intercalated with anionic azo dyes (Tropaeolin 0 and Tropaeolin 0). Polimeros 23(2):248–256. doi:10.1590/s0104-14282013005000026
251. Marangoni R, Gardolinski J, Mikowski A, Wypych F (2011) PVA nanocomposites reinforced with Zn2Al LDHs, intercalated with orange dyes. J Solid State Electrochem 15 (2):303–311. doi:10.1007/s10008-010-1056-2
252. Giovanella U, Leone G, Galeotti F, Mroz W, Meinardi F, Botta C (2014) FRET-assisted deep-blue electroluminescence in intercalated polymer hybrids. Chem Mater 26(15):4572–4578. doi:10.1021/cm501870e
253. Rafiemanzelat F, Adli V, Mallakpour S (2015) Effective preparation of clay/waterborne Azo-containing polyurethane nanocomposite dispersions incorporated anionic groups in the chain termini. Des Monomers Polym 18(4):303–314. doi:10.1080/15685551.2014.999459
254. Monteiro A, Jarrais B, Rocha IM, Pereira C, Pereira MFR, Freire C (2014) Efficient immobilization of montmorillonite onto cotton textiles through their functionalization with organosilanes. Appl Clay Sci 101:304–314. doi:10.1016/j.clay.2014.08.019
255. Zavodchikova AA, Safonov VV, Solina EV, Ivanov VB (2014) Ultraviolet paints based on nanopigments for printing on textile materials. Text Res J 84(13):1400–1410. doi:10.1177/0040517514523177
256. Ito K, Kuwabara M, Fukunishi K, Fujiwara Y (1997) Thermal recording media using clay-fluoran dye intercalation as a stable colour former. Dyes Pigm 34(4):297–306
257. Ito K, Zhou N, Fukunishi K, Fujiwara Y (1994) Potential use of clay-cationic dye complex for dye fixation in thermal dye-transfer printing. J Imaging Sci Technol 38(6):575–579
258. Ito K, Kuwabara M, Fukunishi K, Fujiwara Y (1996) Application of clay-cationic dye intercalation to image fixation in thermal dye transfer printing. J Imaging Sci Technol 40(3):275–280
259. Takashima M, Sano S, Ohara S (1993) Improved fastness of carbonless paper color images with a new trimethine leuco dye. J Imaging Sci Technol 37(2):163–166

260. Ito K, Fukunishi K (1997) Alternate intercalation of fluoran dye and tetra-n-decylammonium ion induced by electrolysis in acetone-clay suspension. Chem Lett 4:357–358
261. Hassanien MM, Abou-El-Sherbini KS, Al-Muaikel NS (2010) Immobilization of methylene blue onto bentonite and its application in the extraction of mercury (II). J Hazard Mater 178(1–3):94–100. doi:10.1016/j.jhazmat.2010.01.048

Chapter 19
Optical Materials

Yasutaka Suzuki and Jun Kawamata

19.1 Nanosheets and Nanosheet-Based Materials for Optoelectronic Applications

In the last two decades, assemblies of nanosheets or nanosheet-based materials have been fabricated for the development of excellent optical materials. Electrons in nanosheets are confined in the 2D in-plane direction. This anisotropic quantum confinement of electrons is expected to obtain efficient optical responses, especially nonlinear optical (NLO) responses, from nanosheets. Optical materials comprising nanosheet-based hybrid systems have also been developed. In such hybrid materials, nanosheets are used as the host materials of outstanding opto and photofunctional chemical species.

The thickness of a nanosheet is typically smaller than that of an exciton Bohr radius. Thus, a nanosheet is a potential building block of a superlattice so-called quantum well structure. In the quantum wells, the effects of the quantum confinement take place, as described in Sect. 19.4. Owing to the quantum confinement, such materials exhibit prominent and/or unique optoelectronic properties [1–8]. Quantum wells are typically grown by molecular beam epitaxy or chemical vapor deposition with control of the layer thickness down to monolayers. However, the employment of nanosheets makes the fabrication of quantum wells possible without the requirement of a complicated protocol. Actually, several prototypical superlattice structures, using nanosheets as the building blocks, have already been constructed by using the layer-by-layer (LBL) deposition or Langmuir–Blodgett (LB) techniques [9].

Y. Suzuki · J. Kawamata (✉)
Graduate School of Science and Technology for Innovation, Yamaguchi University,
1677-1, Yoshida, Yamaguchi 753-8512, Japan
e-mail: j_kawa@yamaguchi-u.ac.jp

T. Nakato et al. (eds.), *Inorganic Nanosheets and Nanosheet-Based Materials*,
Nanostructure Science and Technology, DOI 10.1007/978-4-431-56496-6_19

Nanosheet-based hybrid materials obtained by intercalation or ion-exchange reactions of opto and photofunctional chemical species exhibit specific optoelectronic functionalities which are not observed in the solution, polymer dispersed, or pure crystalline states, as described in other chapters. In these hybrid materials, the intercalated chemical species are confined in a 2D nanospace. Owing to the confinement, control of the orientation and/or aggregation state of the confined functional chemical species is possible and results in maximizing the functionality. In fact, several hybrid materials, exhibiting an excellent nonlinear optical property [10–18], high luminescence quantum yields [17, 19], and so forth, have been fabricated.

To use the prominent optoelectronic features of nanosheets and nanosheet-based materials as practical devices, the fabrication of low light-scattering solid materials consisting of nanosheet assemblies is an essential requirement. In the first part of this chapter, promising protocols for the fabrication of low light-scattering nanosheet assemblies are described. Then, several nanosheets or nanosheet-based materials exhibiting excellent optical properties will be reviewed.

19.2 Fabrication of Low Light-Scattering Nanosheet Materials

Light scattering from a particle can be categorized as follows. For a particle larger than the wavelength of light, geometric scattering is dominant. This scattering is typically observed in an opaque glass. When a particle size is on the same order as the wavelength of light, Mie scattering occurs, which is the phenomenon causing the white color of clouds. Rayleigh scattering occurs from a particle with a size smaller than the wavelength of light. The white turbidity of milk is a result of Rayleigh scattering of casein micelles with sizes of 20–150 nm. According to the particle size dependence of light scattering, geometric, and Mie scattering are not observed for particles with a size sufficiently smaller than the wavelength of light. In addition, the intensity of the Rayleigh scattering is proportional to the sixth power of the particle size. Therefore, Rayleigh scattering can also be suppressed by decreasing the size of the particle.

Actually, low light-scattering nanosheet materials can be prepared when a small lateral-sized exfoliated nanosheet has been dispersed in water. For example, the transparency of a water dispersion of exfoliated nanosheets with a size smaller than 50 nm is almost the same as that of pure water.

However, for nanosheets in the solid state, light scattering is not always suppressed even when small sized nanosheets are assembled. In a solid nanosheet assembly, a discontinuous point in the refractive index, namely where the particle behaves as an origin of light scattering, occurs at the gap between nanosheets. Therefore, the magnitude of light scattering is strongly related to the size of the gap rather than the size of the nanosheet itself. Considerable light scattering occurs if

the size of the gap is larger than the wavelength of light even when the size of the nanosheet itself is sufficiently smaller than the wavelength of light. Thus, a solid nanosheet assembly in the powder form is a strong light-scattering media. For suppressing such light scattering, decreasing the discontinuity of the refractive index, namely the gap, is important.

Light scattering of solid nanosheet materials can be suppressed for use as optical materials if the size of the discontinuous point of the refractive index can be decreased to be approximately one-tenth that of the wavelength of light. To achieve this, minimization of the size of the gap, namely the preparation of a densely stacked nanosheet assembly, is an effective method. Such an assembly can be constructed through a restacking of the nanosheet followed by exfoliation. Another strategy for minimizing the light scattering from a nanosheet assembly is to fill the gap with an organic compound whose refractive index is almost the same as that of the nanosheet. This strategy is termed index matching.

19.2.1 Restacking Technique

Langmuir–Blodgett (LB)-based and filtration-based techniques can be used with the promising restacking procedures for obtaining low light-scattering nanosheet-based solid materials. For films fabricated by both techniques, exfoliated nanosheets are restacked in a parallel orientation. As a result, the obtained nanosheet assembly possesses 2D anisotropy. Thus, these techniques are useful for the fabrication of nanosheet materials for which anisotropy is an essential requirement. Another feature of the nanosheet assembly obtained by these techniques is that the size of the assembly in the in-plane direction can easily be extended to be in the order of tens of centimeters. This lateral size is sufficient for their practical application as optical materials.

19.2.1.1 Langmuir–Blodgett-Based Technique

The LB technique was originally a fabrication process of a single-layered film of an amphiphilic organic molecule [20]. As already described in detail in Sect. 2.3, a hybrid film consisting of a nanosheet and an organic compound can also be obtained [21, 22] based on the LB technique. Multilayered films can also be constructed to repeat the deposition procedure. During the repetitive deposition, another type of nanosheet can also be inserted by using a trough filled with a dispersion of another type of nanosheet. The thickness of a single-layered LB film is approximately 1 nm and therefore a film of several hundred nanometers can be obtained by several hundred depositions. The LB-based technique is effective to obtain nanosheet-based thin layer films with precise nanosheet orientation or a precisely controlled heterostructure.

The hybrid LB film can be categorized into two groups. The first group is a film consisting of a nanosheet modified by a surfactant [23]. As for the surfactant, a tetraalkylammonium, such as tetramethylammonium (TMA) or tetrabutylammonium (TBA), is typically used. When dispersed in water, part of such an alkylammonium-modified nanosheet can float on water. The floating nanosheets can be collected by mechanical compression of the surface of the subphase to obtain a single-layered nanosheet film. The single-layered nanosheet film can be deposited on a substrate by a vertical dipping or horizontal lifting method. The former film is called a LB film and the latter is a Langmuir–Schaefer film.

Another type of hybrid LB film consists of nanosheets and a functional cationic molecule. For fabricating such films, a water dispersion of an anionic nanosheet exfoliated into a single layer is employed as the subphase. A cationic molecule dissolved in a volatile and nonpolar solvent, such as chloroform, benzene, or so on, is spread onto the subphase. After evaporation of the solvent, the cationic molecule is adsorbed onto a nanosheet near the air–water interface by an ion-exchange reaction. Since the obtained hybrid is hydrophobic, the hybrid floats on water. The resulting floating hybrid is collected and then deposited on a substrate, as is the case for the surfactant-modified nanosheet LB film. In this type of LB film, the molecule spread onto the subphase does not always need to be an amphiphile. The dominant attractive force determining the molecular orientation in the hybrid LB film is an electrostatic interaction between the anionic nanosheet and the cationic molecule. Therefore, oriented molecular alignment can be realized even when a non-amphiphilic molecule is employed as the cationic molecule [24].

An atomic force microscope image of a hybrid LB film, consisting of synthetic saponite (SSA) and tris(4,7-diphenyl-1,10-phenanthroline)ruthenium(II) perchlorate, is shown in Fig. 19.1 [25]. As can be seen from this figure, the gaps between the clay layers are smaller than one-tenth of the wavelength of light and, thus, light scattering from the film is considerably suppressed.

Hybrid LB films thus obtained have been employed for detailed analysis of the properties of a single-layer nanosheet [26], emergence of an electronic property caused by the stacking structure of nanosheet [27] and highly sensitive molecular sensing by using the interlayer space of the stacking structure of the nanosheet [28].

19.2.1.2 Filtration-Based Technique

Nanosheet films with a thickness greater than those obtained by the LB technique can be obtained by filtration of a dispersion of the nanosheet. When the particle size of the nanosheet is larger than the pore size of the filter, the nanosheet will be trapped by the filter. The resulting deposit can be peeled off from the filter to obtain a self-standing film consisting of the nanosheet. This technique can be applied for the fabrication of both a pure nanosheet and a hybrid film. This technique was used for obtaining films where the light-scattering quality of the sample is unimportant, such as for infrared and nucleus magnetic resonance spectroscopies [29].

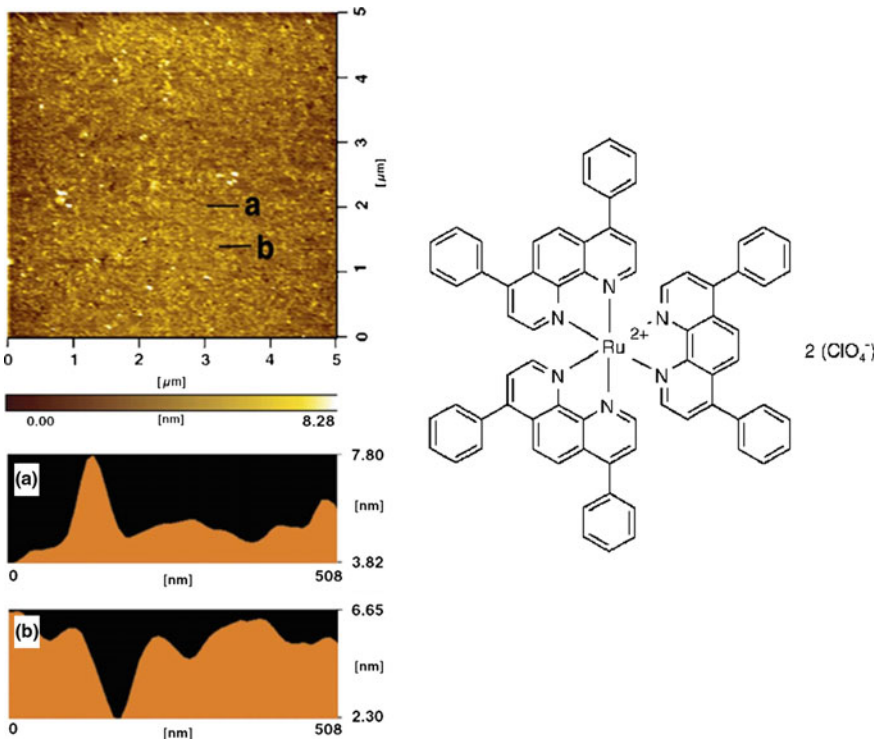

Fig. 19.1 AFM image of a hybrid LB film consisting of synthetic saponite and a ruthenium complex. Reprinted from Ref. [25], Copyright 2006, with permission from Elsevier

A relatively low light-scattering film, suitable for ultraviolet–visible spectroscopic measurements, has been fabricated by Professor S. Takagi's group using the filtration-based technique employing a highly purified synthetic nanosheet [28]. The light scattering of the film fabricated by the filtration-based technique can be further suppressed by careful treatment of the hybrid dispersion [30, 31]. The fabrication protocol of a low light-scattering hybrid film is shown in Fig. 19.2. A cationic molecule dissolved in a water-miscible solvent is added to exfoliate the nanosheet dispersion to obtain a hybrid dispersion. This hybrid dispersion is slowly filtrated using a membrane filter to obtain a low light-scattering film deposited on the membrane filter. The slow filtration also facilitates a parallel stacking of the nanosheets and results in a large anisotropy.

When fabricating a hybrid film with a cationic organic molecule, aggregation (partial stacking) of the hybrid occurs in the dispersion owing to an increase of the hydrophobicity of the nanosheet by hybridization with an organic species [31]. The size of the gap in the film is strongly influenced by the size of the aggregate. Decreasing the particle size of the aggregate results in a decrease in the size of the

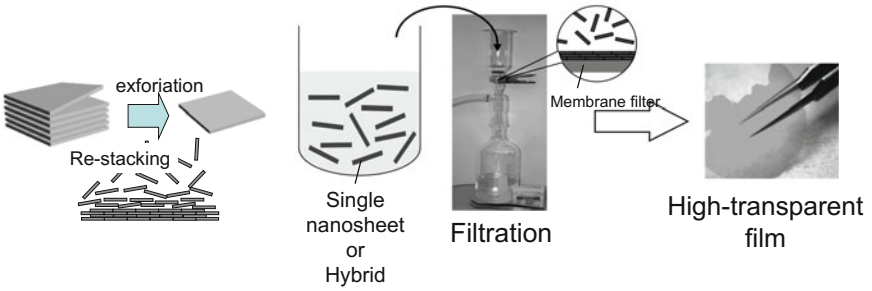

Fig. 19.2 Schematic representation of the fabrication of a hybrid film by the filtration-based technique

gap and thus a low light-scattering film can be obtained. However, the hybrid film cannot be obtained by using smaller-sized particles of the aggregate than that of the pores of the membrane. Therefore, to obtain a low light-scattering hybrid film, control of the aggregate size is crucial. The size of the aggregate is influenced not only by the original particle size of the nanosheet but also by the layer charge, concentration of the nanosheet in the dispersion, hydrophobicity of the employed organic molecule, and the loading level of the hybridized organic molecule. In addition, if an organic solvent is used as a solvent for dissolving the organic molecule, the amount of solvent also influences the size of the aggregate. By optimizing these parameters, a low light-scattering hybrid solid with a haze value of approximately 6% can be obtained. For such a low haze value hybrid film, a laser mode pattern can be retained after passing through the sample. Such materials are suitable as optical devices in terms of the light scattering.

19.2.2 Index Matching by Composition

When two substances with the same refractive index are next to each other, light passes from one to the other without reflection or refraction, and thus, no incoherent light scattering is observed. Such a situation can be realized when the gap between nanosheet particles is filled by a gel or liquid possessing a refractive index close to that of the nanosheet. In optics, such a means is called index matching. Index matching is often used for obtaining optical devices consisting of a heterostructure of different substances.

A schematic representation of an index-matched nanosheet composite is shown in Fig. 19.3. An organic polymer was typically used in early studies as a filler in between the nanosheets [32]. Recently, a small molecular weight molecule, comparable to that of benzene, has also been employed as the filler [33, 34]. Index-matched nanosheet-based materials can be fabricated through the following procedure. The nanosheet is mixed with a polymer or a molecule, which exhibits a

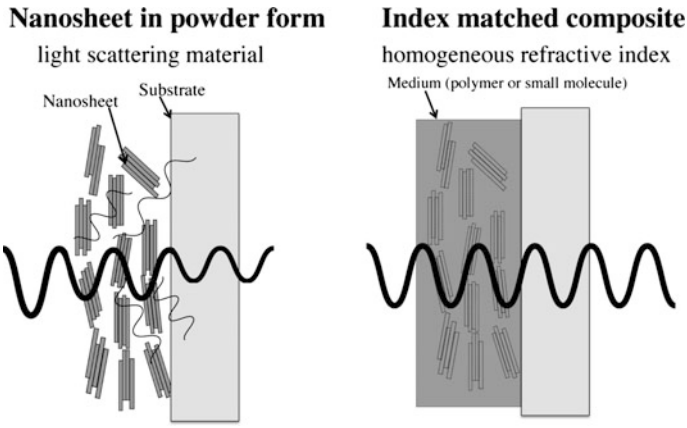

Fig. 19.3 Schematic representation of an index-matched hybrid composite based on a nanosheet. The wave schematically represents the propagation of a laser beam

refractive index close to that of the nanosheet, to obtain a homogeneous gel. The prepared mixed gel is coated on a substrate to obtain a homogeneous composite film. By using this technique, a film, which is thicker than that of a sample fabricated by an LB- or filtration-based technique, can easily be obtained. However, it is difficult to obtain a homogeneous gel by employing functional molecules with a large molecular weight. Most of the functional molecules are hydrophobic. However, nanosheets are typically dispersed in an aqueous media. The preparation of a homogeneous gel consisting of both hydrophilic and hydrophobic components is not easy. Composite films fabricated from an inhomogeneous gel typically exhibit considerable light scattering.

Here, let us demonstrate several index-matched films. A film consisting of SSA and polyacrylic acid is known to exhibit low light-scattering characteristics with a haze value of approximately 6%. The refractive index of SSA has often been considered to be approximately 1.5, though the value has not yet strictly been determined. The refractive index of polyacrylic acid is known to be 1.53, which is comparable with that of SSA. Owing to the similar refractive indices of polyacrylic acid and SSA, the light scattering of a carefully fabricated composite consisting of SSA and polyacrylic acid is very small [32]. A composite employing nanocellulose [35] or poly(*N*-isopropylacrylamide) [36] as the filler has been reported as another example to polyacrylic acid. These composites are expected to be used as a substrate for optoelectronic devices because they are not only low light scattering but also exhibit high flexibility and a gas barrier property.

A homogeneous gel was prepared by mixing sodium hectorite and a small molecule, a fluorescent stilbazolium derivative, in a water and ethanol mixed solvent. A relatively low light-scattering film was obtained by coating the resulting gel to a substrate [34]. According to polarized spectroscopy, each nanosheet was found

to be oriented parallel to the substrate and thus the composite exhibited anisotropy. A low light-scattering composite film employing imidazolium instead of stilbazolium has also been reported [33].

19.3 Nanosheet-Based Optical Material

As briefly described in Sect. 19.1, a nanosheet is expected to possess excellent NLO properties owing to their characteristic form. Therefore, a nanosheet or nanosheet-based optical materials developed to date are mainly NLO materials.

A surface plasmon is an intense nano-sized local electric field that occurs at the surface of metals or semiconductors. This effect is known to induce large NLO responses from a material [37]. Because of the large surface area and nano-sized thickness of the nanosheet, a surface plasmon enhancement and thus a strong NLO response can be effectively induced from semiconducting nanosheets.

Materials possessing quantum well structures have recently received a lot of attention as efficient NLO materials [38–41]. As illustrated in Fig. 19.4, the quantum well is a nanostructure in which a layered semiconductor is sandwiched by another layered substance with a larger energy gap. When the thickness of the sandwiched layer is smaller than the exciton Bohr radius (few to several tens of nm), quantum effects can result. In an appropriately designed quantum well, the exciton can be stabilized owing to the large boundary energy of the exciton. This stable exciton induces a large transition dipole moment, and therefore, a material with a quantum well structure exhibits a large NLO response. A GaAs/AlGaAs quantum well, which is a typical example of an efficient quantum well structured NLO material, was first demonstrated in the 1980 s [42]. Quantum well-structured NLO materials are now widely applied as high-speed optical switches or laser media. A quantum well structure is typically constructed by crystal growth techniques such as molecular beam epitaxy or chemical vapor deposition. Recently, the fabrication of a quantum well has been demonstrated by the stacking of semiconductor nanosheets [9]. It should be noted that a structure can be constructed under ambient pressure and temperature by employing semiconductor nanosheets. Thus, the use of nanosheets has enabled the low-cost construction of a quantum well structure.

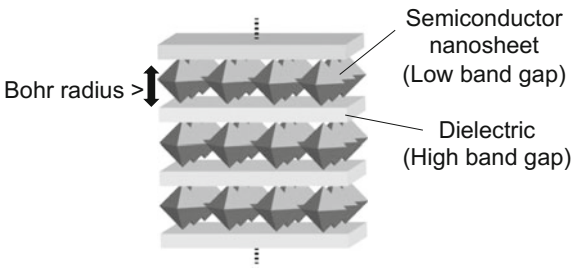

Fig. 19.4 Schematic representation of a nanosheet-based quantum well

Nanosheets have also been used as host materials for excellent opto and photofunctional chemical species. Several organic compounds exhibit considerably larger NLO responses than those of inorganic crystals. However, the growth of organic single crystals required for practical devices, namely sufficient size, lack of defects, and so on, is still not practical [41]. This restricts the application of organic compounds as practical devices. To overcome this problem, several low light-scattering hybrid materials consisting of nanosheets and organic molecules with efficient NLO responses have been fabricated. In such materials, both an excellent NLO response and the requirements for practical devices are realized.

19.3.1 Modulation of Coherent Light by Using a Single-Layer Magnetic Nanosheet [37]

A large magneto-optic response is known to occur by the combination of a magnetic material and a metal nanoparticle owing to the surface plasmon enhancement. A layered magnetic nanosheet, $Ti_{0.8}Co_{0.2}O_2$, was deposited on 50 nm of Au nanoparticles immobilized on a substrate to create a plasmonic nanostructure. This plasmonic nanostructure exhibited an efficient magneto-optical Kerr effect. The magnitude of the Kerr effect was found to be three orders of magnitude greater than that of a single-layered $Ti_{0.8}Co_{0.2}O_2$ nanosheet.

19.3.2 Buildup and Nonlinear Optical Property of Multi-quantum Well Structure

A quantum well structure, consisting of a protonated 4-fluorophenethylamine sandwiched by a semiconductor nanosheet, which is a two-dimensional $(PbI_6)^{4-}$ octahedral sheet was reported by Papagiannouli. The structure of this quantum well was repetitive, alternatively stacking organic and semiconductor layers, namely a multi-quantum well. A third-order NLO response of the multi-quantum well was five orders of magnitude greater than that of quantum dots of PbI_6 [1].

Ishihara reported a $(C_{10}H_{21}NH_3)_2PbI_4$ quantum well that possesses a large boundary energy of the exciton [2]. Owing to the resulting large transition dipole moment, this material is expected to be a good candidate for an NLO material. The $(R–NH_3)_2MX_4$ (R = alkyl chain; M=Pb^{2+}, Sn^{2+}, Ge^{2+}, Cu^{2+}, Ni^{2+}, Mn^{2+}, Fe^{2+}, Co^{2+}, Eu^{2+}; X=Cl^-, Br^-, I^-) type multi-quantum wells were reported as other kinds of nanosheet-based quantum wells [3–8]. They are expected to be used as future electro-optical devices.

19.3.3 Graphene Nanosheet-Based Optical Limiting Materials

Optical limiting devices work as an absorber only when an intense light is irradiated, while it maintains a high transmittance at a low input power. By using this characteristic, protection for optical devices or sensors to the hot spot occurring in a laser system can be realized. A laser with a large output power is typically equipped with an optical limiter. Graphene and graphene oxide nanosheets are known to exhibit an excellent optical limiting property for a pulsed laser [43–45].

Anand reported that the optical limiting property of reduced graphene oxide (rGO) can be increased by increasing the defects of rGO by means of acid post-treatment. Graphene, which is obtained by exfoliation of graphite or graphite oxide in the liquid phase, is known to exhibit an efficient optical limiting property [46, 47]. Graphene with many defects obtained by chemical vapor deposition was also reported to exhibit efficient optical limiting behavior [48, 49].

The optical limiting property of metal nanoparticle modified rGO is further increased compared with that of unmodified rGO. This arises from their charge transfer between the metal and rGO. Modified rGOs with silver [50], copper oxide [51], zinc oxide [52] or all of these metals exhibit efficient optical limiting properties.

19.3.4 Nanosheet–Organic Compound Hybrid Materials for Wavelength Conversion

A π-conjugated molecule, equipped with strong electron donor (D) and strong acceptor (A) groups at both ends of the π-electron system, exhibits a large NLO constant at the molecular level [53]. A typical example of such a molecule is *p*-nitroaniline, which is a so-called D–π–A type molecule. However, most of the D–π–A type molecules crystallized in a centrosymmetric way for the canceling out of their large permanent dipole moment. Given that the centrosymmetric system is second-order NLO forbidden, such centrosymmetric crystals never exhibit second-order NLO effects, even though the NLO constant in the molecular level is large.

Kuroda and coworkers constructed a non-centrosymmetric assembly of *p*-nitroaniline by using the non-centrosymmetric interlayer space of kaolinite, a kind of layered inorganic compound. A schematic representation of the molecular assembly is shown in Fig. 19.5 [10]. The obtained assembly was optical second-harmonic generation (SHG) active, which is a typical second-order NLO effect.

Even when a centrosymmetric interlayer space is employed, an SHG-active hybrid solid is obtained. A hybrid solid obtained by employing SSA and chiral [Ru(1,10-phenanthroline)$_3$]$^{2+}$ was reported to exhibit SHG activity [11]. A model of the

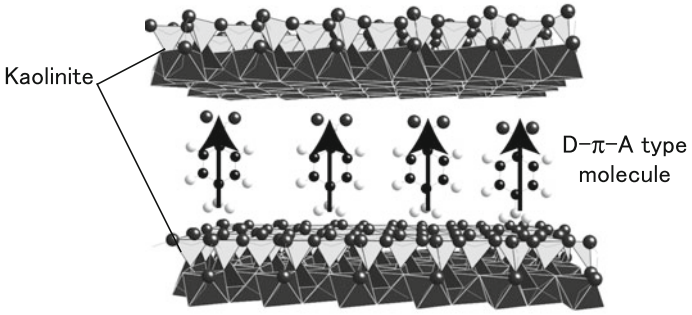

Fig. 19.5 Schematic representation of the interlayer space of the kaolinite–organic hybrid material

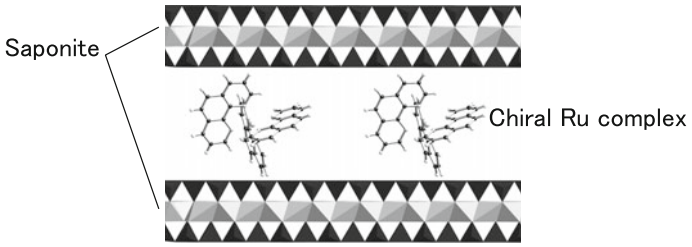

Fig. 19.6 Schematic representation of the interlayer space of a smectite–chiral ruthenium complex hybrid material

molecular alignment of this system is illustrated in Fig. 19.6. In principle, the molecular arrangement of a chiral molecule is non-centrosymmetric. In this system, the nature of the chiral molecule has been ingeniously used.

As for other SHG-active nanosheet–organic molecule hybrids, layered chalcogenophosphates (MPS_3) mixed with stilbazolium derivatives have been reported [12–15]. However, the molecular arrangement and thus the origin of SHG activity in this system is not yet clearly revealed.

19.3.5 Nanosheet–Organic Compound Hybrids with Efficient Two-Photon Absorption Properties

As a strategy for increasing the two-photon absorption (TPA) cross-section (efficiency of TPA) of organic molecules, increasing their transition dipole moment is well established means [54]. For increasing the transition dipole moments of organic molecules, the interlayer space of nanosheets can be used.

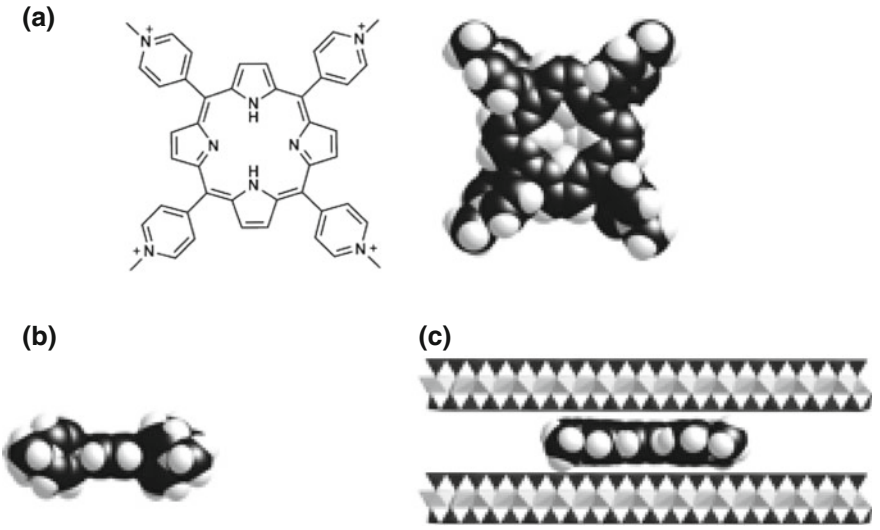

Fig. 19.7 Molecular structure (**a**) and stereo-structures of TMPyP in solution (**b**) and in interlayer space (**c**)

The TPA cross-section of tetrakis(1-methylpyridinium-4-yl)porphyrin (TMPyP; Fig. 19.7a) or 1,4-bis(2,5-dimethoxy-4-{2-[4-(*N*-methyl)pyridinum]ethenyl}-phenyl)butadiyne (MPPBT; Fig. 19.8a) intercalated in a clay mineral were enhanced 13 or 5 times, respectively, compared with those in their solution state [16, 17]. As shown in Fig. 19.7b, in the solution state, the pyridinium groups of TMPyP are not coplanar with respect to the porphyrin ring owing to the steric hindrance. Additionally, in the solution state, the diacetylenic moiety of MPPBT is rotating at room temperature, as can be seen from Fig. 19.8b. However, by confining the interlayer space of a clay mineral, the molecular stereo-structure of these molecules become planar to enhance the π-conjugation, as seen in Figs. 19.7c and 19.8c. As a result, significant enhancement of the TPA cross-sections occur by increasing the transition dipole moments. A direct means for obtaining a molecule with a large transition dipole moment is the design of a molecule with a planar and extended π-electron system. However, the synthesis and treatment of such a molecule is very difficult owing to the strong π–π interaction and thus low solubility. However, the synthesis and treatment of a distorted molecule is relatively easy even when a large π-electron system is involved. Intercalation of distorted molecules into an interlayer space of nanosheets results in a planar molecular stereo-structure. When a molecule with a large but distorted π-electron system is intercalated, the fully π-electron system can be flattened. This results in an extension of the π-electron system and enhanced NLO responses. Design of the NLO materials based on the present strategy is a very effective means for obtaining excellent TPA materials [18].

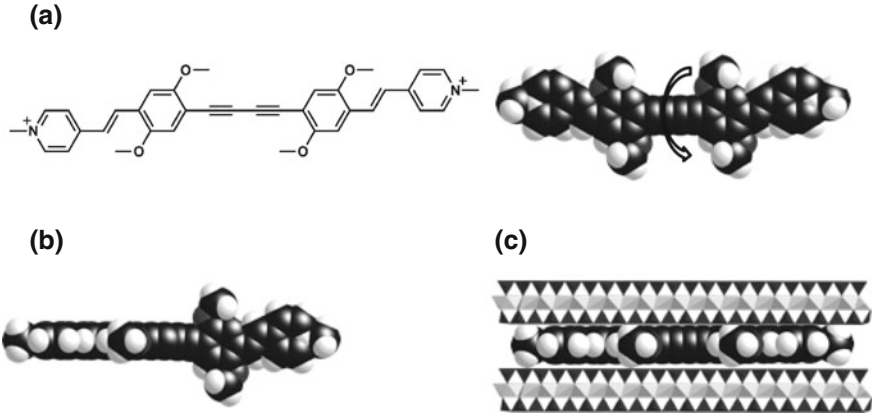

Fig. 19.8 Molecular structure (**a**) and stereo-structures of MPPBT in solution (**b**) and in interlayer space (**c**)

19.4 Conclusions

As discussed in this chapter, various types of nanosheet or nanosheet-based optoelectronic materials can be constructed through soft-chemical processes. The building block, which is the nanosheet itself, possesses various physical properties. The specific characteristics of the nanosheets have ingeniously been used especially for fabricating nanosheet-based plasmonic nanostructures or superlattice devices. Nanosheet-based hybrid materials are also promising candidates for future optoelectronic devices. In such hybrid materials, the potential functionalities of confined molecules can be fully withdrawn.

The key process for creating these materials is the stacking of the nanosheets. A suitable method for constructing (stacking) the nanosheet-based optical materials has not yet been fully developed. Especially, exploration of the available methods for the industrial process remains an important issue for using nanosheet-based optical materials for various practical optical applications.

References

1. Papaginnouli I, Maratou E, Koutselas I, Couris S (2014) J Phys Chem C 118:2766–2775
2. Ishihara T, Takahashi J, Goto T (1989) Solid State Commun 69:933–936
3. Kato Y, Ichii D, Ohashi K, Kungita H, Ema K, Tanaka K, Takahashi T, Kondo T (2003) Solid State Commun 128:15–18
4. Zhang S, Audebert P, Wei Y, Lauret JS, Galmiche L, Deleporte E (2011) J Mater Chem 21:466–476
5. Calabrese J, Jones NL, Harlow RL, Herron N, Thorn DL, Wang Y (1991) J Am Chem Soc 113:2328–2330

6. Dammak T, Koubaa M, Boukheddaden K, Bougzhala H, Mlayah A, Abid Y (2009) J Phys Chem 113:19305–19309
7. Papavassiliou GC, Mousdis GA, Koutselas IB (1999) Adv Mater Opt Electron 9:265–271
8. Xu C, Kondo T, Sakakura H, Kumata K, Takahashi Y, Ito R (1991) Solid State Commun 79:245–248
9. Li BW, Osada M, Ozawa TC, Ebina Y, Akatsuka K, Ma R, Funakubo H, Sasaki T (2010) ACS Nano 4:6673–6680
10. Takenawa R, Komori Y, Hayashi S, Kawamata J, Kuroda K (2001) Chem Mater 13:3741–3746
11. Suzuki Y, Matsunaga R, Sato H, Kogure T, Yamagishi A, Kawamata J (2009) Chem Commun 45:6964–6966
12. Lacroix PG, Clement R, Nakatani K, Zyss J, Ledoux I (1994) Science 263:658–660
13. Bénard S, Yu P, Coradin T, Rivière E, Nakatani K, Clément R (1997) Adv Mater 9:981–984
14. Van der Boom ME, Zhu P, Evmenenko G, Malinsky JE, Lin W, Dutta P, Marks TJ (2002) Langmuir 18:3704–3707
15. Cariati E, Macchi R, Roberto D, Ugo R, Galli S, Casati N, Macchi P, Sironi A, Bogani L, Caneschi A, Gatteschi D (2007) J Am Chem Soc 129:9410–9420
16. Suzuki Y, Tenma Y, Nishioka Y, Kamada K, Ohta K, Kawamata J (2011) J Phys Chem C 115:20653–20661
17. Kamada K, Tanamura Y, Ueno K, Ohta K, Misawa H (2007) J Phys Chem C 111:11193–11198
18. Suzuki Y, Tenma Y, Nishioka Y, Kawamata J (2012) Chem Asian J 7:1170–1179
19. Ishida Y, Shimada T, Takagi S (2014) J Phys Chem C 118:20466–20471
20. Petty MC (ed) (1996) Langmuir-Blodgett films an introduction. Cambridge University Press, Cambridge
21. Inukai K, Hotta Y, Taniguchi M, Tomura S, Yamagishi A (1994) J Chem Soc Chem Commun 959
22. Kotov NA, Meldrum FC, Fendler JH, Tombacz E, Dekany I (1994) Langmuir 10:3797–3804
23. Osada M, Sasaki T (2015) Polymer J 47:89–98
24. Higashi T, Yasui R, Tani S, Ogata Y, Yamagushi A, Kawamata J (2006) Clay Sci 12:42–45
25. Kawamata J, Seike R, Higashi T, Inada Y, Sasaki J, Ogata Y, Tani S, Yamagishi A (2006) Coll Surf A 284–285:135–139
26. Kim HJ, Osada M, Ebina Y, Sugimoto W, Tsukagoshi K, Sasaki T (2016) Sci Rep 6:19402
27. Shibata T, Takano H, Ebina Y, Kim DS, Ozawa TC, Sasaki T (2014) J Mater Chem C 2:441–449
28. Sato H, Tamura K, Taniguchi M, Yamagishi A (2010) New J Chem 34:617–622
29. Kuang W, Facey GA, Detellir C, Casal B, Serratosa JM, Ruiz-Hitzky E (2003) Chem Mater 15:4956–4967
30. Suzuki Y, Hirakawa S, Sakamoto Y, Kawamata J, Kamada K, Ohta K (2008) Clay Clay Mineral 56:487–493
31. Kawamata J, Suzuki Y, Tenma Y (2010) Phil Mag 90:2519–2527
32. Ebina T, Mizukami F (2007) Adv Mater 19:2450–2453
33. Kawasaki K, Ebina T, Mizukami F, Tsuda H, Motegi K (2010) Appl Clay Sci 48:111–116
34. Stöter M, Biersack B, Rosenfeldt S, Leitl MJ, Kalo Schobert H R, Yersin H, Ozin GA, Förster S, Breu J (2015) Angew. Chem Int Ed 54:4963–4967
35. Wu CN, Yang Q, Takeuchi M, Saito T, Isogai A (2014) Nanoscale 6:392–399
36. Haraguchi K, Takehisa T, Fan S (2002) Macromolecules 35:10162–10171
37. Osada M, Hajduková-Smídová N, Akatsuka K, Yoguchi S, Sasaki T (2013) J Mater Chem C 1:2520–2524
38. Arakawa Y, Sasaki H (1982) Appl Phys Lett 40:939–941
39. Schultheis L, Sturge MD, Hegarty J (1985) Appl Phys Lett 47:995–997
40. Faist J, Capasso F, Sivco DL, Sirtori C, Hutchinson AL, Cho AY (1994) Science 264:553–556

41. Zhang S, Lanty G, Lauret JS, Deleporte E, Audebert P, Galmiche L (2009) Acta Mater 57:3301–3309
42. Jovanovic VD, Indjin D, Vukmirovic N, Iknic Z, Harrison P, Linfield EH, Page H, Marcadet X, Sirtori C, Worrall C, Beere HE, Ritchie DA (2005) Appl Phys Lett 86:211117
43. Feng M, Zhan H, Chen Y (2010) Appl Phys Lett 96:033107
44. Song W, He C, Dong Y, Zhang W, Gao Y, Wu Y, Chen Z (2015) Phys Chem Chem Phys 17:7149–7157
45. Tan D, Liu X, Dai Y, Ma G, Menuier M, Qiu J (2015) Adv Optical Mater 3:836–841
46. Anand B, Kaniyoor A, Sai SSS, Philip R, Ramaprabhu S (2013) J Mater Chem C 1:2773–2780
47. Ma F, Zhou ZJJ, Liu YT, Zhang YZ, Miao TF, Li ZR (2011) Chem Phys Lett 504:211–215
48. Hernandez Y, Nicolosi V, Lotya M, Blighe FM, Sun Z, De S, McGovern IT, Holland B, Byrne M, Gun'Ko YK, Boland JJ, Niraj P, Duesberg G, Krishnamurthy S, Goodhue R, Hutchison J, Scardaci V, Ferrari A C, Coleman J N (2008) Nat Nanotechnol 3:563–568
49. Murugan AV, Muraliganth T, Manthiram A (2009) Chem Mater 21:5004–5006
50. Kalanoor BS, Bisht PB, Ali SA, Baby TT (2012) Ramaprabhu S (2012). J Opt Soc Am B 29:669–675
51. Anand B, Kaniyoor A, Swain D, Baby TT, Venugopal Rao S, Sai SSS, Ramaprabhu S, Philip R (2014) J Mater Chem C 2:10116–10123
52. Kavitha MK, John H, Gopinath P, Philip R (2013) J Mater Chem C 1:3669–3676
53. Günter P (ed) (2002) Nonlinear Optical Effects and Materials. Springer, Berlin
54. Rumi M, Ehrlich JE, Heikal AS, Perry JW, Barlow S, Hu Z, McCord-Maughon D, Parker TC, Röckel H, Thayumanavan S, Marder SR, Beljonne D, Brédas JL (2000) J Am Chem Soc 122:9500–9510
55. Takagi S, Shimada T, Eguchi M, Yui T, Yoshida H, Tryk DA, Inoue H (2002) Langmuir 18:2265–2272

Chapter 20
Chirality and Its Application

Hisako Sato and Akihiko Yamagishi

20.1 Introduction

"Molecular recognition" is one of the most extensively studied topics in chemistry. A number of biomimetic systems such as crown ethers, cryptands, and cyclodextrins are designed as artificial sites to activate an appropriate substrate in a specific way. In comparison to the molecular systems in homogenous phases, the surface of a solid provides another possibility for molecular recognition. The clean surface of a metal single crystal, for example, provides information on an atomic scale how a molecule interacts with a surface or with its neighbors. In this chapter, the works on the chiral aspects of smectite clays were reviewed. In comparison to metals or bulk metal oxides, smectite clays are characterized by the following unique features from the view point of molecular recognition: (1) two-dimensional network structures of a phyllosilicate sheet, (2) high cation exchange capacity, and (3) exfoliation into inorganic nanosheets.

In the following, the works on the use of smectite clays for optical resolution, asymmetric syntheses, and electrochemical and photochemical reactions are reviewed. An attention is focused on how the above structural characters contributed to the recognition of molecular chirality on a clay surface.

H. Sato (✉)
Graduate School of Science and Engineering, Ehime University,
2-5, Bunkyo-Cho, Matsuyama 790-8577, Japan
e-mail: sato.hisako.my@ehime-u.ac.jp

A. Yamagishi
Faculty of Medicine, Toho University, 5-21-16, Omori-Nishi,
Ota-Ku, Tokyo 143-8540, Japan

T. Nakato et al. (eds.), *Inorganic Nanosheets and Nanosheet-Based Materials*,
Nanostructure Science and Technology, DOI 10.1007/978-4-431-56496-6_20

20.2 Structural Studies on the Chiral Crystal of Kaolinite

Kaolinite ($Al_4[Si_4O_{10}](OH)_8$) is a 1:1 dioctahedral phyllosilicate (layered aluminosilicate) with little isomorphous substitution. Each layer consists of a sheet of SiO_4 tetrahedra forming six-membered silicate rings connected via a common apical oxygen atom to a sheet of edge-sharing [AlO_6] octahedra. Three polytypes are found in nature: kaolinite, dickite, and nacrite. These minerals are stacked with different positions of octahedral vacancies in successive layers. The crystal structure of kaolinite (non-H atoms) was first reported using powder X-ray diffraction. Bailey demonstrated that both kaolinite and dickite are based on a 1*M* stacking sequence of layers [1]. It has been shown that octahedral site vacancies alternate in dickite, whereas in kaolinite the location of the vacancy is the same in repeating layers. In the 1*M* structure, there are three possible locations of the vacant octahedral site, denoted as A-, B-, or C-site vacancies. If the vacant site occurs at the B- or C-site, the structures are chiral; in the case of the A-vacant site, the structure is achiral. In nature, the vacant site of kaolinite occurs in the C (or B) position resulting in a chiral structure.

The first-principles calculations of kaolinite are performed using density functional theory (DFT) [2]. The lattice parameters and structures of the three 1*M* polytypes of kaolinite (vacancies in the A, B, and C positions) were optimized using the exchange-correlation functional (PBE functional). The cell shape and internal atomic coordinates were systematically optimized to search the minimum of total energy. For such calculation, space group *P1* was used as a reduced cell in order to reduce the number of atoms to half of that for the ordinary cell (*C1*). The optimized structures of kaolinite modeled with A-, B-, and C-site vacancies, using *C1* and *P1* unit cells, respectively, are shown in Fig. 20.1. The calculated values of bond lengths for the C-site polytype are in good agreement with experimental data based on the kaolinite structure. It is interesting to see whether the chiral structure is preferred from the energetic point of view. Comparing the formation energies, the chiral polymorphs of kaolinite (B- or C-site vacancy) have similar formation energies as dickite and nacrite, while achiral kaolinite with A-site vacancy is only slightly less stable than the other polytypes (Table 20.1).

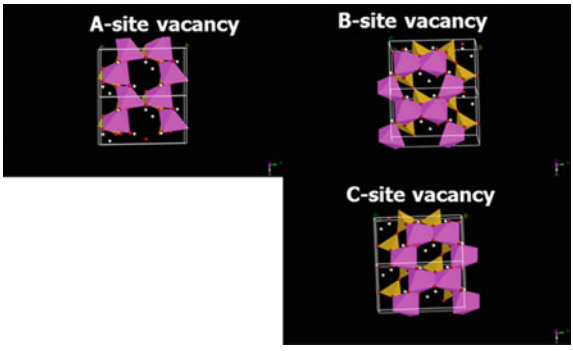

Fig. 20.1 Optimized structures of kaolinite polytypes

Table 20.1 Optimized energy of kaolin polytypes

Polytype	Kaolinite with A-site	Kaolinite with B-site	Kaolinite with C-site
ΔE (kJ/mol)	−1.671	−1.858	−2.050

Note $\Delta E = E–E$(kaolinite single layer)

Kogure and Inoue [3] reported the stacking defect structures in kaolin minerals by applying TEM imaging technique on near-atomic resolution. Electron diffraction and high-resolution imaging of dickite showed that few stacking defects exist in this polytype. On the other hand, kaolinite crystals contain high density of stacking defects. Disorder by the coexistence of B layer and C layer, or dickite-like stacking sequence was never observed. These results provided not only an unambiguous settlement for the long controversy of the defect structures in kaolinite, but also a new clue to understanding kaolinite-to-dickite transformation mechanism. They also reported the chiral structure of a single crystal of kaolinite. By means of back-scattered electron diffraction, it was elucidated that a single crystal of kaolinite itself was chiral [4].

20.3 Stereochemistry Related to the Two-Dimensional Network of a Smectite Clay Surface

There have been extensive efforts to apply a solid surface as a site providing chiral substances on a preparative scale [5, 6]. The finding described in this section opened a possibility of developing such a method on the basis of clay minerals.

20.3.1 Spectroscopic Studies on the Adsorption of Metal Complexes by a Smectite Clay

It was reported that some biological substances such as amino acids and glucoses were adsorbed stereoselectively by natural montmorillonite or vermiculite clay [7–9]. If it was the case, the fact might have profound significance in chiral selection during the period of the chemical evolution. Motivated by the work, the adsorption of chiral molecules was studied by colloidally dispersed sodium montmorillonite. As an adsorbate, tris(1,10-phenanthroline)metal(II) ($[M(phen)_3]^{2+}$) (phen = 1,10-phenanthroline) was chosen [10]. The complex was known to be adsorbed strongly by clay minerals. Moreover, its rigid and highly symmetric properties were expected to be helpful in detecting the subtle difference of adsorption structures between optical antipodes rather than flexible bioorganic molecules.

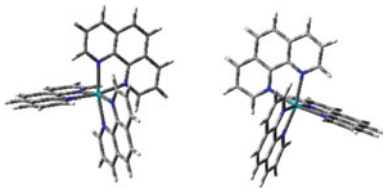

Fig. 20.2 Chiral structures of a tris-chelated metal complex: (*left*) Δ-isomer and (*right*) Λ-isomer

The enantiomers of $[M(phen)_3]^{2+}$ are denoted as Δ- and Λ-isomers, depending on the direction of helical twisting (Fig. 20.2). The adsorption of enantiomeric $[Ru(phen)_3]^{2+}$ by a clay was studied by measuring the electronic absorption spectrum of a colloidal dispersion. When Δ-$[Ru(phen)_3]Cl_2$ was added to an aqueous dispersion of sodium montmorillonite, the metal-to-ligand charge-transfer (MLCT) transition band around 450 nm increased its intensity and shifted toward the longer wavelength with the simultaneous decrease of the π–π* transition band localized in the ligands around 270 nm. These spectroscopic changes were caused by the adsorption of the chelate by a clay particle. No effect of molecular chirality was detected, when the spectral change was compared between the Δ- and Λ-enantiomers of $[Ru(phen)_3]^{2+}$.

When the same experiments were performed for a racemic mixture of $[Ru(phen)_3]^{2+}$, the change of the electronic spectrum was distinctly different from the enantiomeric case. The bathochromic shift of the MLCT transition band was more enhanced and the π–π* transition band split into two composites. In addition to the spectroscopic differences, a remarkable difference was observed in the adsorption amounts. The chelates were adsorbed so strongly that the amount of adsorption increased linearly with the increase of an added clay amount. In case of the enantiomer, the adsorption was saturated when the ratio of clay-to-metal chelate (denoted as [clay]/[chelate]) attained the value of 2, where [clay] and [chelate] were measured in terms of the CEC equivalent/L and mole/L, respectively. The results were reasonable since $[Ru(phen)_3]^{2+}$ carried two positive charges and neutralized two negative charges on adsorption by a clay. Contrary to this, in case of the racemic mixture, the adsorption was saturated already at [clay]/[chelate] = 1. In other words, the chelate was adsorbed to two times excess over the CEC, including external anions for electric neutrality.

The above facts indicated that the chelates interacted with each other on a clay surface in a stereoselective way. Here "stereoselective way" means that the situations are different whether the interacting two molecules are a Δ–Δ (or Λ–Λ) pair or a Δ–Λ pair. If the interaction was indifferent to such chirality effects, no difference would have appeared whether the chelates were added as a pure enantiomer or as a racemic mixture. The fact that the racemic mixture was adsorbed to two times excess of the enantiomers suggested that the chelates preferred to form a racemic pair on a clay surface. This type of adsorption is denoted as "racemic adsorption by clays."

The adsorption by sodium montmorillonite was investigated over the wide range of chiral chelates [11–13]. Table 20.2 lists the classification of investigated chelates

Table 20.2 Classification of metal chelates according to the stereochemical effects on adsorption by a clay

Chelates showing racemic adsorption
$[M(phen)_3]^{2+}$ (M = Ni, Fe, Ru and Os) (phen = 1,10-phenanthroline)
$[Fe(phen)_2(CN)_2]$
$[Co(PAN)_2]^{2+}$ (PAN = pyridylazoresorcinol)
$[Co(PAN)_2]^{+}$
Chelates showing enantiomeric adsorption
$[Ru(bpy)_3]^{2+}$ (bpy = 2,2′-bipyridine)
Chelates showing no stereochemical effect
$[Co(phen)_3]^{3+}$
$[Co(en)_3]^{3+}$ (en = ethylenediamine)
cis-$[Co(en)_2Cl_2]^{+}$

according to the stereochemical effects on adsorption behavior. As deduced from the table, the chelate that shows either racemic or enantiomeric adsorption is coordinated with two or three bulky planar ligands and carries an electric charge of less than two. These facts are consistent with a view that the discrimination of chirality of an adsorbed molecule is performed by the stereochemical interaction between the adjacent molecules on a clay surface. Such interaction might be low for metal complexes with small ligands such as ethylenediamine. Electrostatic repulsion is too large to have chelates stacked, if they are too positive like $[Co(phen)_3]^{3+}$.

No stereochemical effect was observed when $[M(phen)_3]^{2+}$ was adsorbed by other ion exchangers such as cation-exchanging resins, zirconium phosphates, and layered niobates. Thus the phenomena are particular to smectite clays. The structural origin of racemic adsorption was investigated by applying a number of spectroscopic methods such as XRD [14], electric dichroism [15], ESR [16], photoelectron spectroscopy [17], and AFM [18] together with the theoretical calculation [19].

When the thin film of an ion-exchange adduct of racemic $[Os(phen)_3]^{2+}$/montmorillonite was analyzed by in-plane XRD measurements, the two-dimensional regularity existed with the periodicity of 0.95 nm [20]. Scanning tunneling microscopy (STM) was successful only for highly crystalline clay minerals like hydrotalcite [21].

The basal spacing (d_{001}) was determined by XRD measurements for the adducts of sodium montmorillonite and $[M(phen)_3]^{2+}$. The value of d_{001} was 1.78 nm when the chelate was adsorbed to the CEC of a clay. Subtracting the thickness of one layer (0.95 nm) from the basal spacing, the height of the interlayer space was estimated to be 0.83 nm. This height was nearly equal to that of $[M(phen)_3]^{2+}$ along its C_3 axis. The basal spacing of a clay–chelate adduct was expanded to 2.90 nm when the chelate was adsorbed to two times excess of CEC. Accordingly the height of the interlayer space was estimated to be 1.95 nm. The Fourier analyses for a sample of a 2:1 adduct of a clay and racemic $[Fe(phen)_3]^{2+}$ showed that the adsorbates formed a double-molecular layer in the interlayer space. The peak of

electron density in the middle of the space was ascribed to the external anion, SO_4^{2-}, which compensated the excess positive charge [14].

Electro-optical measurements were applied to determine the orientation of $[Ru(phen)_3]^{2+}$ bound on the surface of a colloidal clay particle. According to the method, an electric field pulse was applied to a dispersion containing a colloidal clay and the chelate. The anisotropy in optical absorption (dichroism) was induced by the alignment of an exfoliated clay platelet in the direction of electric field. The electric dichroism was monitored by linearly polarized light. The rise and decay of the signals corresponded to the orientation and de-orientation processes of clay particles in the presence and absence of electric field, respectively. The magnitude of the dichroism is related to the angle, θ, between the electric field and the polarization of the monitoring light as below:

$$\Delta A/A = (\rho/6)(1 + 3\ \cos\ 2\theta). \tag{1}$$

At the limit of complete orientation, ρ, the reduced linear dichroism, is expressed by

$$\rho = (-3/8)(1-3\ \cos\ 2\phi) \tag{2}$$

in which ϕ is the angle between the C_3 axis of the chelate and the direction normal to a clay surface. The angle, ϕ, was obtained to be close to zero or the chelate was adsorbed with its C_3 axis perpendicularly to a clay surface as shown in Fig. 20.3.

The adsorption of a cationic metal complex, $[Ru(phen)_3]^{2+}$, onto a mica surface from its aqueous solution was investigated with atomic force microscopy (AFM). An attention was focused on the effect of molecular chirality on the structures of adsorption layers. AFM observation showed that the surface remained smooth when a mica surface was in contact with an aqueous solution of racemic $[Ru(phen)_3](ClO_4)_2$, while the surface was rough in contact with an Δ-enantiomeric solution. The difference was interpreted in terms of the formation of the compact bimolecular layer for the racemic mixture, while a rough multilayer adsorption layer was formed for the enantiomer [22]. The results were interpreted by the assumption that the racemic adsorption layer was composed of the unit of closely packed

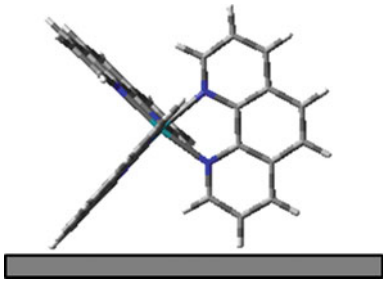

Fig. 20.3 The orientation of $[M(phen)_3]^{2+}$ adsorbed on a smectite clay surface

racemic pairs, while the enantiomeric adsorption layer was composed of two domains or double-molecular and monomolecular layers.

The kinetic formation of the adsorption layer of racemic chelates was studied by means of a stopped-flow electric dichroism apparatus [14]. The rate was compared between the following two cases: (a) a dispersion of a Δ-$[Ru(phen)_3]^{2+}$/clay (denoting a clay particle adsorbing the chelate to CEC) was mixed with a solution of Λ-$[Ru(phen)_3]Cl_2$ and (b) a dispersion of a racemic $[Ru(phen)_3]^{2+}$/clay was mixed with a solution of racemic $[Ru(phen)_3]Cl_2$. For both cases, electric dichroism amplitude ($\Delta A/A$) and absorbance (A) increased on mixing, indicating the occurrence of adsorption in excess over the CEC. The rates of increases were higher for (a) than for (b). The results were rationalized in terms of the mechanism that, in case of (a), the racemic layer was formed simply by pairing a pre-adsorbed Δ-$[Ru(phen)_3]^{2+}$ with an incoming Λ-$[Ru(phen)_3]^{2+}$, while, in case of (b), the process of molecular rearrangement was required among the pre-adsorbed racemic chelates before a racemic pair was formed.

Breu et al. also performed the experiments on the intercalation of metal complexes by a smectite clay. In case of the intercalation compounds of natural smectites, no 2D long-range order of the interlamellar space was observed. To this contrary, the in-plane order was detected using a homogeneously charged synthetic fluorohectorite as a host material. With these intercalates, the distinct 2D structures for enantiopure and racemic $[Ru(bpy)_3]^{2+}$ interlayers as previously predicted by atomistic simulations could be proven experimentally [23].

Villemure [13] reported the absorption of enantiomeric $[Ru(bpy)_3]^{2+}$ by several different kinds of smectite samples. The absorption of racemic mixture was lower than that of pure enantiomer. The enantiomer was absorbed in excess over CEC.

20.3.2 *Theoretical Studies of Racemic Adsorption and Its Significance for Chiral Recognition*

The adsorption behavior was simulated theoretically by use of Monte Carlo technique [19]. The calculation showed the predicted bound states of a pair of racemic and enantiomeric $[M(phen)_3]^{2+}$ molecules at the minimum binding energy, respectively. As was expected, a racemic pair forms an associate with their ligands interlocked closely, while an enantiomeric pair forms a loose associate due to the steric repulsion between the facing ligands. When the free energy was calculated statistically using a Metropolis algorism, the racemic and enantiomeric pairs took the sharp minima of free energy at the intermolecular distances of 0.95 and 1.42 nm, respectively. One important deduction of the above model is that there exists a vacant space surrounded by the bound chelates when a clay surface is covered with enantiomeric $[M(phen)_3]^{2+}$. Such a space is stereoselective toward further adsorption, since it accepts exclusively its optical antipode. Based on this hypothesis, an ion-exchange adduct of enantiomeric $[M(phen)_3]^{2+}$ (M = Ni,

Ru)/clay was used as a chiral adsorbent for optical resolution and asymmetric syntheses. A number of examples have been accumulated to demonstrate the capability of such a surface in discriminating molecular chirality.

Breu et al. also simulated the metal complexes on a clay surface. Lattice energy minimization techniques were used to study the 2D molecular organization of $[Ru(bpy)_3]^{2+}$ and $[Ru(phen)_3]^{2+}$ confined in the interlamellar space of low-charged smectites. With racemic pillars, favorable π stacking lead to the clustering of pillars even with homogeneously charged smectites. Long-range and/or short-range ordering of the isomorphous substitution within the silicate layer strongly influence the interlayer structure, since host–guest interactions are dominated by electrostatics [24].

20.4 Chirality Recognition by a Clay Modified with Metal Complexes

20.4.1 Anti-racemization of Labile Metal Complexes

One example was shown to show how chirality was recognized by the adsorbed molecules on the surface of a smectite clay [25]. A labile complex, $[Fe(phen)_3]^{2+}$, racemizes with a half-life time ($t_{1/2}$) of 25 min in water at 25 °C, while $[Ni(phen)_3]^{2+}$ is less labile with $t_{1/2}$ = 3 h under the same conditions. Racemic $[Fe(phen)_3]Cl_2$ was added to an aqueous dispersion of a Δ-$[Ni(phen)_3]^{2+}$/clay. The amount of added $[Fe(phen)_3]^{2+}$ was below the CEC. When the dispersion was monitored by the circular dichroism (CD) spectrum, no CD activity was observed initially in the wavelength region of 350–700 nm. This was because Δ-$[Ni(phen)_3]^{2+}$ was nearly transparent in this wavelength region. The CD band appeared in several minutes and developed in hours until it nearly coincided with the CD spectrum of Λ-$[Fe(phen)_3]^{2+}$. The results were rationalized in terms of the mechanism: (i) Λ-$[Fe(phen)_3]^{2+}$, half of added $[Fe(phen)_3]^{2+}$, was adsorbed instantly by a Δ-$[Ni(phen)_3]^{2+}$/clay; (ii) the remaining Δ-$[Fe(phen)_3]^{2+}$ racemized gradually in water to Λ-$[Fe(phen)_3]^{2+}$ and was adsorbed by a Δ-$[Ni(phen)_3]^{2+}$/clay; and finally (iii) the whole of added $[Fe(phen)_3]^{2+}$ ions was stabilized as the Λ-form by pairing with Δ-$[Ni(phen)_3]^{2+}$ on a smectite clay surface.

20.4.2 Clay Column Chromatography for Optical Resolution

The chiral recognition by the modified surface of a smectite clay lead to the development of chromatographic resolution [26, 27]. A spherically shaped aggregate was prepared by spray drying an aqueous dispersion of synthetic hetorite.

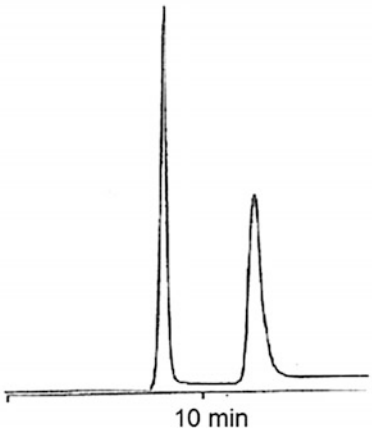

Fig. 20.4 The chromatogram when a racemic mixture of 1,1′-bi-2-naphthol was eluted on a column packed with Λ-$[Ru(phen)_3]^{2+}$/synthetic hectorite with methanol. The *first* and *second peaks* are *R*- and *S*-enantiomers, respectively

Particles of a size of c.a. 5 μm were soaked in a methanol solution containing Λ-$[Ru(phen)_3]Cl_2$. The ion exchanging of Λ-$[Ru(phen)_3]^{2+}$ into a clay took place in seconds to produce a yellow-colored solid. The material was packed into a stainless steel tube and used as a column for high-performance liquid chromatography (HPLC) [28, 29].

Figure 20.4 shows the chromatogram when a racemic mixture of 1,1′-bi-2-naphthol was eluted on the column (4 mm (i.d.) × 250 mm) with methanol. Two peaks with the equal area were obtained on the base-line separation. From the CD spectra, the less and more retaining peaks contained the pure *R*- and *S*-enantiomers of 1,1′-bi-2-naphthol, respectively. The separation factor was calculated to be 1.78, which was quite large in comparison to the known chiral columns. The enthalpy change ($-\Delta H$) of adsorption was determined from the temperature dependence of the retention times: $-\Delta H$ = 3.1 and 5.7 kJ mol^{-1} for the *R*- and *S*-1,1′-bi-2-naphthol, respectively. Thus the high separation capability of the present column was ascribed to the large difference of adsorption enthalpy (∼2.6 kJ mol^{-1}). From the XRD measurements, the basal spacings of ternary adducts of a clay, Δ-$[Ru(phen)_3]^{2+}$ and *R*- or *S*-1,1′-bi-2-naphthol was obtained to be 2.78 or 2.45 nm, respectively. The more strongly adsorbed *S*-enantiomer gave the narrower spacing, or it was located closer to a clay surface, probably forming a side-by-side associate with Λ-$[Ru(phen)_3]$.

The clay column exhibited the following characteristics from the practical point of view:

1. Performance is stable and reproducible for a long time against the change of temperature or eluting solvents (except for water).
2. Resolution capacity is high (e.g., 400 mg of $[Ru(acac)_3]$ was resolved for a single run on a 20 mm (i.d.) × 250 mm column).

3. Antipodal columns, or Δ-$[Ru(phen)_3]^{2+}$/clay and Λ-$[Ru(phen)_3]^{2+}$/clay are both available. This is particularly useful in separating a mixture of diastereomeric species [30].
4. The systematic modification of a packing material is possible to tune resolution capability by changing the structure of a pre-adsorbed chelate (e.g., $[Ru(bpy)_3]^{2+}$/clay) [25].

A column packed with Δ-$[Ru(phen)_3]^{2+}$/synthetic hectorite is commercially available and is used for separating wide range of organic and inorganic compounds [Ceramosphere Ru-1, Shiseido (Japan)]. As one of the recent applications, all of the four diastereomers of a star-burst type tetranuclear ruthenium(III) complex was resolved. The diastereomers were differentiated by the parts connecting the core and periphery regions. Thus the column discriminated local chirality within a large molecule [31, 32].

20.4.3 Photochemistry on a Modified Surface

Asymmetric catalysis driven by visible light is regarded as one of the most promising environmentally friendly methods [33]. One promising attempt to enhance chiral selectivity is the immobilization of a chiral catalyst onto a solid surface [34]. Such heterogeneous photochemistry has been explored using organic and inorganic hosts. For practical uses, the immobilization of a chiral species in a solid leads to an advantage of the versatile separation of a catalyst from a solution as well as the avoiding of effluxes of poisonous metals. Only a few heterogeneous asymmetric catalysis has been reported in photochemistry probably because of the difficulties in the preparations of suitable solid supports [35]. In the following, the photochemical reactions of clay minerals have been reviewed by Shichi and Takagi [36].

20.4.3.1 Asymmetric Syntheses

The ion-exchange adducts of a clay and a metal chelate was utilized as an adsorbent to produce chiral molecules. Figure 20.5 shows the basic principle for it. A prochiral molecule is adsorbed on a void space surrounded by chiral chelates. When the bound molecule undergoes a chemical change, it might transform to an optically active molecule under the steric control of the surrounding chelates.

As an example, phenyl alkyl sulfide was adsorbed by an adduct of sodium montmorillonite ion exchanged with either chiral $[Ru(phen)_3]^{2+}$ or $[Ru(bpy)_3]^{2+}$. The adsorbed sulfide was photooxidized to a sulfoxide under the illumination of visible right. The reaction was driven by the photosensitizing action by Ru(II) complexes. The sulfoxide was produced in the chiral form at the enantioselectivity (e. e.) of about 43% [37]. The observed stereoselectivity was ascribed to the

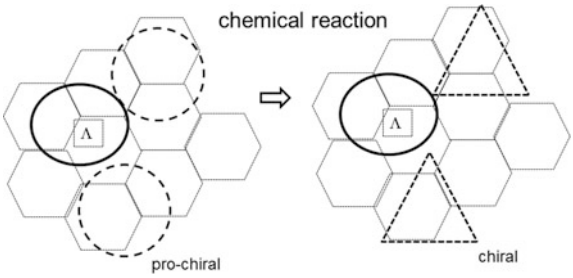

Fig. 20.5 A schematic model for the transformation of a prochiral molecule to chiral one under the steric control of chelates bound on the surface of a smectite clay

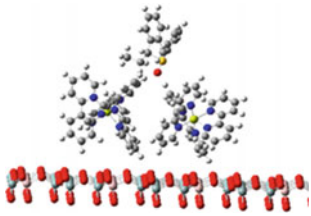

Fig. 20.6 Schematic drawing of the possible reaction paths on a clay surface

selection of reaction paths on a clay surface as shown in Fig. 20.6. The chirality of a sulfoxide molecule was determined under the steric control by pre-adsorbed Ru(II) complexes. It was noted that no chiral induction was attained for the homogenous system (water/methanol medium), even if the same chiral chelates were used as a photosensitizer. Thus the fixation of a substrate on the surface of a smectite clay was essential to chiral recognition.

The above method was applied to the auto-catalytic systems [38]. A prochiral aldehyde was transformed to chiral pyrimidyl alkanol by the catalytic reaction of i-Pr_2Zn. The reaction was performed in the presence of Δ-$[Ru(phen)_3]^{2+}$/clay or Λ-$[Ru(phen)_3]^{2+}$/clay. The enantiomer excess of the product attained as high as 80–90%. Again chiral selectivity was determined by the absolute configuration of the adsorbed chelates.

20.4.3.2 Chiral Ru(II) Metal Complexes on a Clay Surface

Thomas et al. reported the studies on the photophysical processes of tris(2,2′ bipyridine)ruthenium(II) ($[Ru(bpy)_3]^{2+}$) bound to colloidal kaolinite and montmorillonite particles [39–41]. The absorption and emission spectroscopy at room temperature and 77 K were found to be effective in probing the environmental difference between the external surface and internal layers of these minerals. The significant quenching of $[Ru(bpy)_3]^{2+}$ was observed on a montmorillonite containing 4% iron. Hydrazine was used to reduce Fe(III) to Fe(II) in a lattice. This conversion resulted in the decrease in the quenching effect of $[Ru(bpy)_3]^{2+}$. The rate data of fluorescence quenching showed that both cationic and uncharged molecules moved quite freely on a clay surface.

Ghosh and Bard [42, 43] reported the spontaneous racemic and pseudo-racemic interactions between optically active poly(pyridyl) metal chelates ($[Ru(bpy)_3]^{2+}$) which were adsorbed on a smectite clay. The results highlighted differences in the binding modes of these two forms at low loading levels (1–4%). The optical purity, loading level, mode of addition of the complex, and the type of clay minerals had an effect on the observed differences in binding states. Their results revealed that the absorption spectra of an enantiomer and a racemate were different even at low loading and that the spectrum of the latter was understood in terms of two effects: clay–chelate and spontaneous antipode–antipode (or racemic) interactions. These effects were additive for the metal-to-ligand charge-transfer (MLCT) transition. The adsorption of pure enantiomers raised the energy of the emission maximum, while racemic interactions produced a bathochromic shift. The contrasting nature of the absorption (MLCT) and emission trends was rationalized in terms of the assumption that the observed shifts in peak positions were exclusively due to perturbations in the energies of ligand-centered orbital.

Kamat et al. [44] studied the photophysical behavior of enantiomeric and racemic $[Ru(bpy)_3]^{2+}$ on a layered clay. The decrease in the luminescence yield of a racemate on increasing the loading was mainly associated with an attenuation in the peak emission intensity as found from time-resolved measurements. The intensity of luminescence differed nearly two times between enantiomeric and racemic $[Ru(bpy)_3]^{2+}$ even at the low loading level. Besides there existed a definite difference in the peak position of luminescence between the racemic (605 nm) and enantiomeric (586 nm) $[Ru(bpy)_3]^{2+}$. The emission of the racemate falls off rapidly with increased loading from 0 to 50%, whereas the emission from the enantiomeric adsorbate remained almost constant. These results were rationalized in terms of a model that the racemates were clustered locally while the enantiomeric ions were more randomly distributed on a clay surface.

The orientation of a metal complex was tuned by attaching alkyl chains at the different positions of a bpy ligand [45]. It was shown that the orientation of adsorbed polypyridyl Ru(II) complexes ($[Ru(bpy)_2X]^{2+}$ with X = 2,2′-bipyridine, 4,4′-diundecyl-2,2′-bipyridine, and 5,5′-diundecyl-2,2′-bipyridine) had a decisive effect on their chiral discrimination in an energy transfer reaction. The quenching rate of phosphorescence due to an adsorbed Ru(II) chelate was measured for the energy transfer between excited polypyridyl Ru(II) complexes and chiral $[Ru(acac)_3]$ (acac = acetylacetonato). As a results, at the loading of 10% of cation exchange capacity (CEC), the quenching rate constant was nearly equal between the Δ- and Λ-enantiomers of $[Ru(acac)_3]$ within the experimental error (c.a. 5%). Thus no stereoselectivity appeared at this loading level for all three complexes. At the loading of 40% of CEC, however, there was a distinctive difference between the enantiomer of the quencher for all three kinds of Ru(II) chelates. In other words, Δ-$[Ru(acac)_3]$ is more effective than Λ-$[Ru(acac)_3]$ in quenching excited Λ-$[Ru(bpy)_2X]^{2+}$ on a clay surface. Notably such stereoselective effect was largest for the case of $[Ru(bpy)_2$(5,5′-diundecyl-2,2′-bipyridine)$]^{2+}$.

20.4.3.3 Ir(III) Complexes Applied as a Luminescent Modifier on a Clay Surface

Iridium(III) complexes are known to be strongly emissive under the irradiation of visible light. This property was used to prepare photoreactive clay hybrid materials [46–49]. In addition to the emitting properties, some chelated iridium(III) complexes are chiral and stable against racemization at higher temperature. The optical resolution of a cationic iridium(III) complex, $[Ir(ppy)_2dmbpy]^+$ (ppy = 2-phenylpyridine and dmbpy = 4,4′-dimethyl-2,2′-bipyridine), was achieved by means of liquid chromatography on a chiral column [48].

The quenching of excited $[Ir(ppy)_2dmbpy]^+$ (denoted as Ir(III)) was studied in an aqueous dispersion of synthetic saponite [48]. Chiral $[Ru(acac)_3]$ was used as a quencher. The emission intensity at 650 nm was compared between the following two pairs, clay/Δ-Ir(III)/Δ-$[Ru(acac)_3]$ (pseudo-enantiomeric combination) and clay/Δ-Ir(III)/Λ-$[Ru(acac)_3]$ (pseudo-racemic combination), in 3:1 (v/v) water–methanol. In both cases, the intensity of emission decreased on adding $[Ru(acac)_3]$, indicating that Ru(III) complex acted as an efficient quencher. The quenching effect was analyzed in terms of the Stern–Volmer plots. It was revealed that luminescence quenching was more efficient for the clay/Δ-Ir(III)/Δ-$[Ru(acac)_3]$ system than for the clay/Δ-Ir(III)/Λ-$[Ru(acac)_3]$. From the analyses of the plots, the rate of quenching was much higher than the diffusion processes. Therefore, it was suggested that the quenching reaction was not a simple collisional process, but it might involve the process of molecular association on a clay surface. Notably, no stereoselectivity was detected in methanol for the same emitter/quencher pairs. Thus the fixation of the iridium(III) complex on a clay surface was concluded to be a crucial step for chiral recognition.

Sato et al. [49] investigated the energy transfer between two types of iridium(III) complexes, $[Ir(dfppy)_2(C_n\text{-bpy})]^+$ (dfppyH = 2-(2′,4′-difluorophenyl)pyridine; C_n-bpy = 4,4′-dialkyl-2,2′-bipyridine; dialkyl = dimethyl (C_1), didodecyl (C_{12}), and dinonyldecyl (C_{19})) and $[Ir(piq)_2(C_n\text{-bpy})]^+$ (piqH = 1-phenyisoquinoline) as a donor and an acceptor, respectively (Fig. 20.7). The complexes were co-adsorbed by colloidally dispersed synthetic saponite. The efficiency of energy transfer (η_{ET}) was obtained from the emission spectra at various donor-to-acceptor ratios (D/A). The results were analyzed on the basis of the Förster-type energy transfer mechanism. For C_1-bpy, η_{ET} was as high as 0.5 with a D/A of ca. 20. The results implied

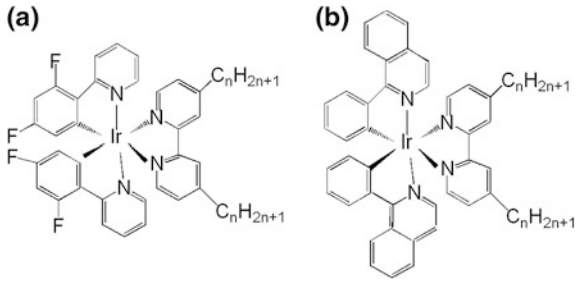

Fig. 20.7 Structures of the Ir(III) complexes, Δ-$[Ir(dfppy)_2(C_n\text{-bpy})]^+$ (dfppyH = 2-(4′,6′-difluorophenyl)pyridine; C_n-bpy = 4,4′-dialkyl-2,2′-bipyridine) (donor) (**a**) and Δ-$[Ir(piq)_2(C_n\text{-bpy})]^+$ (piqH = 1-phenyisoquinoline) (acceptor) (**b**)

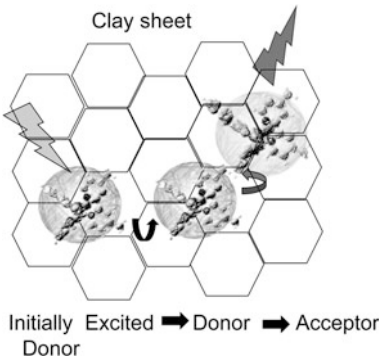

Fig. 20.8 Light-harvesting model on a clay surface

that the photon energy captured by several donor molecules was collected by a single acceptor molecule (i.e., the harvesting of light energy). The harvesting of light energy was considered to occur on a clay surface according to the mechanism as shown in Fig. 20.8. Enantioselectivity was observed in the present type of energy transfer of C_1-bpy, which indicated the participation of a contact pair of donor and acceptor molecules. For C_{12}-bpy and C_{19}-bpy, η_{ET} was low and exhibited no enantioselectivity, because their long alkyl chains inhibited close contact between the donor and acceptor molecules.

20.4.4 Construction of Clay Nano-Sheet Films for Gas Sensing

The Langmuir–Blodgett method preparing a single-layered clay film (denoted as clay-LB) was first reported by two groups (Yamagishi et al. and Kotov et al.) in 1994 [50, 51]. Yamagishi et al. extended their study to the photophysical application of the multilayer films [52]. For preparing a clay-LB film, cationic amphiphiles such as alkylammonium in chloroform was spread over the surface of an aqueous suspension of a clay mineral. Photoreactive metal complexes are replaced with alkylammonium ions simply by immersing a prepared electrode in their aqueous or methanol solution. This is the combination of the Langmuir–Blodgett (LB) method and self-assembly (SA).

The photophysical studies on a clay-modified electrode revealed that a single clay layer acted as an efficient barrier for the occurrence of electron transfer from an amphiphilic polypyridyl Ru(II) complex (electron donor) to an amphiphilic acetylacetonato-Ru(III) complex (electron acceptor). Multi-layered films were prepared, in which an emitter/clay and a quencher/clay were deposited in an alternative way. In such a film, it was revealed that a single clay layer acted as a barrier for the transfer of photon energy [53].

Recently luminescent films have been applied for chemo- and bio-sensing [54–56]. A hybrid film of a clay and iridium(III) complex as described in the previous section was applied for the oxygen sensing [57–60].

20.4.5 Chiral Sensing on an Electrode Modified with a Thin Film of Clay/Chelate Hybrid

The sensing of molecular chirality through the reaction of electron transfer was attempted by use of clay-modified electrodes as described above [61, 62]. As one example, an ITO electrode was modified with a thin film of $[Os(phen)_3]^{2+}$/clay. UV light was irradiated on such an electrode. When Λ-$[Os(phen)_3]^{2+}$/clay was used, the oxidation photocurrent was enhanced in the presence of *R*- (or *S*-1,1′-bi-2-naphthol) in an electrolyte solution. The results indicated that Os(II) complex acted as a mediator catalyzing the oxidation of binaphthol. Notably, the catalytic current was higher for *S*-1,1′-bi-2-naphthol than for *R*-1,1′-bi-2-naphthol by about 1.8 times at 700 mV. This provides a possibility of electrochemical sensing of a chiral molecule.

The current increases linearly with the increase of the concentration up to 0.11 mM of 1,1′-2-binaphthol. Λ-$[Os(phen)_3]^{3+}$ was first generated by photoinduced electron transfer from photoexcited Λ-$[Os(phen)_3]^{2+}$. The oxidized Λ-$[Os(phen)_3]^{3+}$ was reduced to Λ-$[Os(phen)_3]^{2+}$ by 1,1'-2-binaphthol. Stereoselectivity arose from the difference of adsorption strength of the substrate toward a clay surface modified with Λ-$[Os(phen)_3]^{2+}$ complexes. Photocurrent was also measured for other kinds of binaphthyl derivatives. As a result, chiral sensing was successful in case of 1,1′-2-binaphthol and 1,1′-2-binaphthyl amine. These compounds were possible to be oxidized by Λ-$[Os(phen)_3]^{3+}$. Other compounds were not detected because they were resistant to oxidation under the mediating action of adsorbed Os (II) complexes. Thus it was concluded that the present chiral electrode was applicable by the action of oxidation mediator by a photo-responsive molecule adsorbed on an electrode surface.

20.5 Summary and Future Development

Smectite clays were used as an adsorbent for molecular recognition. The surface of a clay was modified with chiral metal complexes. In case of using an enantiopure molecule, either Δ- or Λ-$[Ru(phen)_3]^{2+}$, a microscopic vacant space was generated on such a surface. The space acted as a binding site with stereoselectivity. Since clay minerals are ubiquitous and friendly to the environment, the present method sheds a light on the utility of such a material for the finely controlled chemical reactions.

As for the future development of the present approach, the following possibilities are proposed:

1. To pursue a possibility of obtaining a chiral single crystal of kaolinite [4]. Such an attempt has a significance in both fundamental (as a possible role in generating chiral molecules during the chemical evolution) and practical fields (as a material for chiral support for heterogeneous asymmetric syntheses)
2. To improve the clay column chromatography by selecting metal complexes as a chiral modifier [63]. One target might be to resolve directly non-derivatized aliphatic compounds like amino acids with no aromatic group.
3. To construct a single-layered film of clay nanosheets with high quality. Such a film might be used as an electronic device such as an insulating film with high dielectric constant [64, 65].
4. To manipulate the molecular aggregate on a clay film in which several components such as donor, mediator, and acceptor are arranged in an organized order [49, 59, 66]. Such a system might present an inorganic model for light harvesting in biological photosyntheses.

References

1. Bailey SW (1988) Polytypism of 1:1 layer silicates, Chap. 2 In: Bailey SW(ed) Hydrous phyllosilicates (exclusive of mica). Reviews in mineralogy, vol 19. Mineralogical Society of America, Washington, D.C., pp 9–27
2. Sato H, Ono K, Johnston CT, Yamagishi A (2004) Am Mineral 89:1581–1585
3. Kogure T, Inoue A (2005) Am Mineral 90:85–89
4. Kameda J, Yamagishi A, Kogure T (2005) Am Mineral 90:1462–1465
5. Mallouk TE, Gavin JA (1998) Acc Chem Res 31:209–217
6. Yamagishi A, Sato H (2012) Clays Clay Miner 60:411–419
7. Bondy SC, Harrington M (1979) Science 203:1243–1244
8. Fraser DG, Greenwell HC, Skipper NT, Smalley MV, Wilkinson MV, Demé B, Heenan RK (2011) Phys Chem Chem Phys 13:825–830
9. Fraser DG, Fitz D, Jakschitz T, Rode BM (2011) Phys Chem Chem Phys 13:831–838
10. Yamagishi A, Soma M (1981) J Am Chem Soc 103:4640–4642
11. Yamagishi A (1982) J Phys Chem 86:2474–2479
12. Yamagishi A, Fujita N (1984) J Colloidal Interface Sci 100:136–142
13. Villemure G (1990) Clays Clay Miner 38:622–630
14. Taniguchi M, Yamagishi A, Iwamoto T (1991) J Phys Chem 30:2462–2467
15. Yamagishi A, Taniguchi M, Takahashi M, Asada C, Matsushita N, Sato H (1994) J Phys Chem 98:7555–7561
16. Yano Y, Watanabe T, Taniguchi M, Yamagishi A (1992) Clay Sci 8:381–391
17. Yamagishi A, Tanaka K, Toyoshima I (1982) Chem Commun 343–345
18. Takahashi S, Tanaka R, Wakabayashi N, Taniguchi M, Yamagishi A (2003) Langmuir 19:6122–6125
19. Sato H, Yamagishi A, Kato S (1992) J Am Chem Soc 114:10933–10940
20. Umemura Y, Shinohara E (2004) Chem Commun 42:1110–1111
21. Yao Y, Taniguchi M, Nakata M, Takahashi M, Yamagishi A (1998) Langmuir 14:2890–2895

22. Wakabayashi N, Nishimura SI, Kakegawa N, Sato H, Yamagishi A (2004) Clay Sci 12:259–266
23. Breu J, Stoll A, Lange KG, Probst T (2001) Phys Chem Chem Phys 3:1232–1235
24. Breu J, Nilesh RN, Catlow CRA (1999) J Chem Soc Dalton Trans 835–845
25. Yamagishi A (1985) Inorg Chem 24:1689–1695
26. Yamagishi A (1985) J Am Chem Soc 107:732–733
27. Yamagishi A, Taniguchi M, Imamura Y, Sato H (1996) Appl Clay Sci 11:1–10
28. Nakamura Y, Yamagishi A, Matsumoto A, Tohkubo K, Ohtsu Y (1988) J Chromatogr 482:165–167
29. Kakegawa N, Yamagishi A (2005) Chem Mater 17:2997–3003
30. Sato H, Mori Y, Fukuda Y, Yamagishi A (2009) Inorg Chem 48:4353–4361
31. Fujimoto N, Mori Y, Yamagishi A, Sato H (2010) Chem Commun 46:5473–5474
32. Sato H, Sato F, Taniguchi M, Yamagishi A (2012) Dalton Trans 41:1709–1712
33. Huo H, Shen X, Wang C, Zhang L, Röse P, Chen LA, Harms K, Marsch M, Hilt G, Meggers E (2014) Nature 515:100–103
34. Yamagishi A (1987) J Coord Chem 16:131–211
35. Sato H, Yamagishi A (2007) J Photochem Photobiol, C 8:67–84
36. Shichi T, Takagi K (2000) J Photochem Photobiol, C 1:113–130
37. Fujita S, Sato H, Kakegawa N, Yamagishi A (2006) J Phys Chem B 110:2533–2540
38. Kawasaki T, Omine T, Suzuki K, Sato H, Yamagishi A, Soai K (2009) Org Biomol Chem 7:1073–1075
39. Thomas JK (1988) Acc Chem Res 21:275–280
40. Dellaguardia RA, Thomas JK (1983) J Phys Chem 87:990–998
41. Chu DY, Thomas JK (1985) J Phys Chem 89:4065–4070
42. Ghosh PK, Bard AJ (1984) J Phys Chem 88:5519–5526
43. Ghosh PK, Bard AJ (1983) J Am Chem Soc 105:5691–5693
44. Kamat PV, Gopidas KR, Mukherjee T, Joshi V, Kotkar D, Pathak VS, Ghosh PK (1991) J Phys Chem 95:10009–10018
45. Sato H, Hiroe Y, Tamura K, Yamagishi A (2005) J Phys Chem B 109:18935–18941
46. Sato H, Tamura K, Taniguchi M, Yamagishi A (2009) Chem Lett 38:14–15
47. Sato H, Tamura K, Taniguchi M, Yamagishi A (2014) Appl Clay Sci 97–98:84–90
48. Sato H, Tamura K, Aoki R, Kato M, Yamagishi A (2011) Chem Lett 40:65–67
49. Tamura K, Yamagishi A, Kitazawa T, Sato H (2015) Phys Chem Chem Phys 17:18288–18293
50. Inukai K, Hotta Y, Taniguchi M, Tomura S, Yamagishi A (1994) J Chem Soc Chem Commun 959–960
51. Kotov NA, Meldrum FC, Fendler JH, Tombacz E, Dekany I (1994) Langmuir 10:3797–3804
52. Tamura K, Setsuda H, Taniguchi M, Yamagishi A (1999) Langmuir 15:6915–6920
53. Inukai K, Hotta Y, Tomura S, Takahashi M, Yamagishi A (2000) Langmuir 16:7679–7684
54. Umemura Y, Koura A, Nishioka T, Tanaka D, Shinohara E, Suzuki T, Sasaki T (2010) J Phys Chem C 114:19697–19703
55. Guan W, Zhou W, Lu J, Lu C (2015) Chem Soc Rev 44:6981–7009
56. Sato H, Tamura K, Taniguchi M, Yamagishi A (2010) New J Chem 34:617–622
57. Sato H, Tamura K, Ohara K, Nagaoka S, Yamagishi A (2011) New J Chem 35:394–399
58. Morimoto K, Nakae T, Ohara K, Tamura K, Nagaoka S, Sato H (2012) New J Chem 36:2467–2471
59. Sato H, Tamura K, Ohara K, Nagaoka S (2014) New J Chem 38:132–138
60. Sato H, Ochi M, Kato M, Tamura K, Yamagishi A (2014) New J Chem 38:5715–5720
61. He J, Sato H, Umemura Y, Yamagishi A (2005) J Phys Chem B 109:4679–4683
62. Yoshida J, Saruwatari K, Kameda J, Sato H, Yamagishi A, Sun L, Corriea M, Villemure G (2006) Langmuir 22:9591–9597
63. Okada T, Kumasaki A, Shimizu K, Yamagishi A, Sato H (2016) J Chromatogr Sci 54: 1238–1243

64. Sato H, Okamoto K, Tamura K, Yamada H, Saruwatari K, Kogure T, Yamagishi A (2008) Appl Phys Expr 1:035001–035003
65. Kim SS, Khai TV, Kulish V, Kim Y-H, Na HG, Katoch A, Osada M, Wu P, Kim HW (2015) Chem Mater 27:4222–4228
66. Ohtani Y, Nishinaka H, Hoshino S, Shimada T, Takagi S (2015) J Photochem Photobiol, A 313:15–18

Chapter 21
Applications of Nanoclay-Containing Polymer Nanocomposites

Jayita Bandyopadhyay and Suprakas Sinha Ray

21.1 Introduction

In 1989, a report from the Toyota Central Research and Development Laboratory on the synthesis of nanoclay-containing polyamide nanocomposites using in situ polymerization opened a new era for polymer nanocomposites (PNCs) [1]. PNCs provide several significant advantages over traditional polymer composites. To impart the desired mechanical or thermal properties, conventional composites usually require a high filler loading (usually 10–50 wt%), whereas the same or even better performance can be achieved with PNCs at a much lower nanoclay loading (usually 3–5 wt%) [2]. Hence, it is possible to develop high-performance and lightweight polymeric materials using PNC technology. Over the last two decades, several journal articles, conference proceedings and patents have been published on the preparation, characterization and properties of PNCs covering almost all polymer matrices; however, the commercialization of PNCs was harder than initially anticipated. In the early 1990s, a first attempt was made to introduce PNC-based components in Japan. The idea was soon abandoned due to cost-competitiveness [2]. However, the past few years have provided key breakthroughs in nanocomposite technology. The announcement by General Motors (GM) that they were introducing polypropylene (PP)/clay nanocomposites to fabricate the step assist in two of their 2002 mid-size vans was a milestone in the commercialization of PNC technology. The PP/clay nanocomposite part used in GM vans was the first commercial product resulting from fundamental developments [2].

J. Bandyopadhyay · S.S. Ray (✉)
DST-CSIR National Centre for Nanostructured Materials,
Council for Scientific and Industrial Research, Pretoria 0001, South Africa
e-mail: rsuprakas@csir.co.za

S.S. Ray
Applied Chemistry Department, University of Johanneburg,
Doornfontein 2028, Johanneburg, South Africa

T. Nakato et al. (eds.), *Inorganic Nanosheets and Nanosheet-Based Materials*,
Nanostructure Science and Technology, DOI 10.1007/978-4-431-56496-6_21

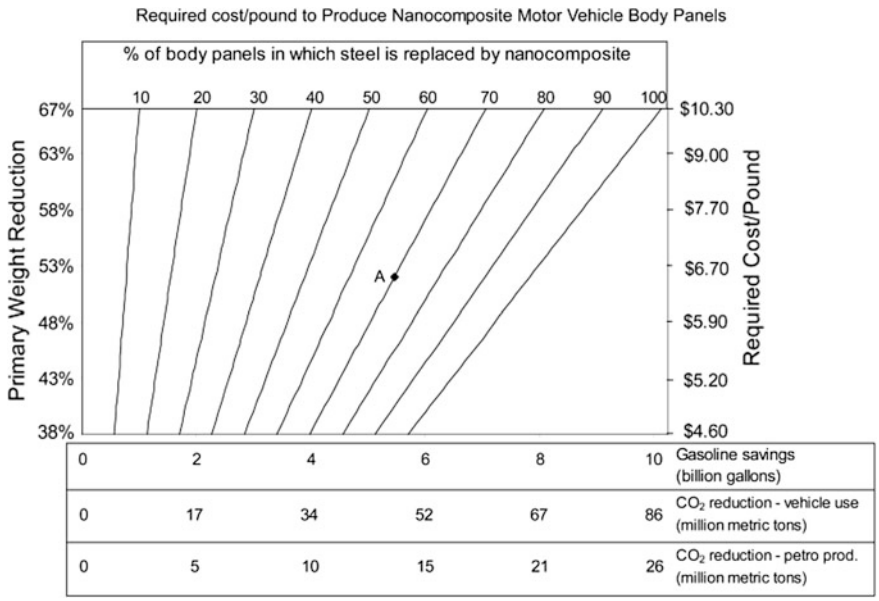

Fig. 21.1 Required cost/pound for wide-scale commercialization of nanocomposite motor vehicle body panels (includes materials, processing, and production costs) [3]

Lloyd and Lave reported that the demand for new and advanced materials in automotive applications continued afterwards for vehicle safety, performance and fuel efficiency [3]. The authors also mentioned other applications using nanoclays including underground piping and packaging.

Figure 21.1 demonstrates that the substitution of metals by PNCs will enable the production of cost-effective and lightweight car panels alongside a better fuel efficiency and lower CO_2 production. On one hand, repairing composite-based parts will be a challenge, but the nanoclay-based composites can be reused further for different applications. It is expected that due to the lower filler concentrations, the nanocomposite materials will be more recyclable than conventional composites [2].

Besides GM/Basell, Honeywell also announced the commercial availability of its "Aegis" line of Nylon 6 (N6)-based nanocomposites in 2001 [2]. The Aegis products targeted packaging applications. In addition, the nanocomposites were injection moulded to produce rigid parts for automotive, industrial, and consumer applications. The commercially available PNCs and their applications are summarized in Table 21.1.

According to a BCC research, in 2010, the main applications of the PNCs were automotive parts, packaging, and coatings with a market share of 41, 32 and 16%, respectively [2, 4]. However, this market research predicts a decrease in automotive parts and coatings share by 2016, whereas an increase in the packaging share is expected. PNCs market share is expected to increase to approximately 58% in 2016 and 60.2% in 2019. Meanwhile, carbon nanotube-containing composites and metal/metal oxide nanocomposites shares are expected to decrease to 16 and around

Table 21.1 Principal applications of nanoclay-containing nanocomposites

Applications	Type of nanocomposites	Commercial status	Company	Developed product with specific applications
Automotive	Nylon/montmorillonite	Commercial		
	TPO/montmorillonite	Commercial		
	PP/montmorillonite	Commercial	PolyOne Corp. Noble Polymers	Nanoblend used for auto interior and exterior Seat back of car, office furniture
	Acetal/montmorillonite	Commercial		
	Nylon/mica fluoride	Commercial	Unitika, Ltd.	Nylon 6 nanocomposite (Nylon M1030DH) used by Mitsubishi Motors to make engine covers for its GDI models
	Butyl rubber/montmorillonite	Developmental		
	PE/montmorillonite	Developmental	PolyOne Corp.	Auto interior and exterior
Packaging	Nylon/montmorillonite	Commercial	Alcoa Closure Systems International, Inc. Honeywell Bayer AG in collaboration with Nanocor Mitsubishi Chemical Corp. RTP Showa Denko Ube Industries	Nanocomposite based liners for the plastic bottle caps for beer, juice, carbonated soft drinks etc. Barrier application (mainly for alcohol and carbonated beverages) under the brand name 'Aegis' Barrier film under the brand name 'Durethan' Imperm N is used as a barrier layer for multilayer PET bottles, multilayer thermoformed containers for deli meats and cheeses, as well as flexible multilayer films for potato chips and ketchup Film and sheet applications Nylon66/clay nanocomposite Nylon6/66 coplymer nanocomposite (Ecobesta) for structural applications

(continued)

Table 21.1 (continued)

Applications	Type of nanocomposites	Commercial status	Company	Developed product with specific applications
	HDPE/montmorillonite	Commercial	LG Chem	Rigid packaging for handling toluene and light hydrocarbon fluids
	PP/montmorillonite	Developmental	Clariant International in collaboration with Nanocor	Nanoclay-based masterbatches for the packaging application
	PET/montmorillonite	Developmental		
	EVOH/montmorillonite	Developmental	Triton	Barrier film
Life Science	Nylon12/montmorillonite	Commercial	Foster Corp.	Medical device applications such as intravascular or balloon-type catheters
Consumer products	Butyl rubber/vermiculite	Commercial	InMat, LLC and Hoechst Research and Technology	sporting goods e.g. flotation equipments, air cushions and running shoes
	PE/clay	Commercial	InMat, LLC	Gas barrier application
	Neoprene/clay	Commercial	InMat, LLC	Tires
	Chloroprene/clay	Commercial	InMat, LLC	Chemical protective rubber gloves
	PP/montmorillonite	Developmental		
Flame retardant material	EVA/montmorillonite	Commercial	Kabelwerk Eupen in cooperation with Süd-Chemie AG	Nanoclay-filled EVA/LDPE cables
	PP/montmorillonite	Developmental		

9%, respectively. New types of nanocomposites, such as nanobiocomposites, fuel cell membranes and photonic band-gap nanocomposites are in the development stage. The main applications and commercial status of PNCs are tabulated in Table 21.1. Although some of the nanocomposites have been already commercialized, a detailed understanding of the nanoclay-dispersion chemistry and structure-property correlation are still required for further development and commercialization of PNCs.

21.2 Keys for the Design and Application of PNCs

The PNC is a promising and fascinating research area, but both processing and successful development of nanocomposites are quite challenging. The addition of nanoclays to a polymer matrix is not a "drop-in" solution. A careful selection of the materials for targeted applications is the most important step. Depending on the application, it is essential to choose the correct polymer as well as the nanoclay. In most cases, it is necessary to use a organically modified nanoclay to improve the wettability of the nanoclay with the polymer matrix. Interaction parameters for the polymer and the surfactant present in the organoclay determined by the group contribution method developed by Fedors are a good indicator to assess the compatibility between the matrix and the nanoclay. The properties of the nanocomposite depend not only on the polymer-nanoclay interaction, but also on the processing techniques and conditions. From a commercialization point of view, the development path should be iterative with proper understanding of the cost-performance indices associated with the technology.

21.3 Application of PNCs

PNCs provide some significant advantages over the traditional polymer composites. Conventional composites usually contain a high percentage of inorganic fillers. Usually, filler concentration varies from 10 to 50 wt% in order to achieve the desired mechanical or thermal properties. On the other hand, nanocomposites with typically 3–5 wt% of filler can exhibit almost the same properties (e.g., increased tensile strength, improved heat deflection temperature, and flame retardancy). In nanocomposites, a substantial reduction in the filler concentration enables the production of materials with lower density and higher processability than traditional reinforcements [2]. Earlier, it used to be expensive and difficult to produce nanocomposites from large volume commodity plastics (such as PP, polyethylene (PE), etc.). The PP part used in GM vans was the first commercial automotive exterior application of a polymer nanocomposite [2]. This improved the confidence in the commercialization of polymer nanocomposites, which have been at the development stage for more than a decade. Nowadays, several low-cost and

high-performance nanocomposites are moving towards commercialization. The principal applications of nanoclay-containing polymer nanocomposites are summarized in Table 21.1.

21.4 Commodity Polymer/Clay Nanocomposites

21.4.1 PP/Clay Nanocomposites

PP is one of the most widely used commodity polymers. PP has a moderate toughness and modulus of elasticity that is situated between high density PE (HDPE) and low density PE (LDPE). The melting temperature of PP is usually in the range of 160–168 °C. This makes PP containers dishwasher safe and suitable for industrial hot filling processes. Most plastic hinges are made of PP due to its high resistance of fatigue. Nanocor in collaboration with Clariant developed PP/montmorillonite (MMt) masterbatches for packaging film applications [2]. Nanoclay-based PP composites can be used as heavy-duty electrical enclosures provided the material presents various fire ratings, low-temperature toughness, and weatherability [5]. In 2003, Noble Polymers introduced PP nanocomposites commercially known as "Forte". It was used in the seat backs of 2004 Acura TL. PP nanocomposites are also used in the centre consoles of cars [2]. Other applications involve office furniture, appliances, pipes and other construction materials. It has a potential to replace 20% of the glass-filled PP. For example, a thermoplastic polyolefin nanocomposite containing 2.5% of nanofiller has almost the same stiffness as that with ten times the amount of conventional talc filler. This enables a weight saving of 20%, depending on the part and the material that is being replaced by the thermoplastic polyolefin nanocomposite [2]. The properties and the applications of the commercially available nanoclay-containing PP composites are summarized in Table 21.2. According to this table, commercially available nanoclay-containing PP composites are designed for rigid packaging applications. However, other applications of PP nanocomposites are still in the developmental phase. The application range of PP nanocomposites can be widened by proper selection of filler material, processing method and conditions. The optimized processing methods and conditions allow improvement in several properties in the PP nanocomposites when compared with the neat resin. This in turn widens the range of application of PP nanocomposites for textile, outdoor, and even flexible multilayer barrier films as mentioned in the Table 21.3. In addition, Onder et al. reported that PP-organoclay nanocomposite filaments are also suitable for textile applications [6].

In recent years, the wood–plastic composite market has expanded as a replacement for solid wood, mainly for outdoor applications. Moisture absorption is one of the main challenges with such composites. The addition of organically modified nanoclays (for example, Cloisite®15A, C15A) reduces the water absorption and thickness swelling of PP-wood-fibre composites [7]. This will

enable the production of long-term hygroscopic wood-fibres and nanoclay-based PP composites. For outdoor applications, another important aspect is UV-resistance properties. Komatsu et al. (2014) studied the effect of environmental ageing on the mechanical properties of high melt strength PP (HMSPP)-Cloisite®20A (C20A) nanocomposites [8]. They reported that the composite showed intense surface cracks after 3 months of environmental aging, but not as deep as HMSPP. Moreover, the composite with 0.1% C20A exhibited an increased stability during the aging process [8]. This indicates that the composite might prolong the lifetime of HMSPP. However, it may not be a suitable candidate for long-term outdoor appliances. Therefore, for the selection of a material for outdoor application it is important to study the aging effect under UV radiation.

The most important aspects of composite-based product development are the design of high-performance materials, weight reduction of the parts, and finally the cost-benefit ratio. The weight reduction is highly desirable especially in the automotive, aerospace, and aircraft industries. Compared to several commercially available types of fillers, nanoclays have lower density. Thus, organically modified nanoclay-based PP nanocomposites enable the fabrication of lighter parts with better thermal and mechanical properties [9].

It is possible to design a high-performance polymeric material with tailored properties using nanotechnology. This requires a proper choice of matrix polymers and fillers as well as understanding the interfacial interactions between the matrix and the fillers. The corresponding improvement of the matrix polymer properties depends on features such as proper dispersion, delamination and orientation of the nanoclay platelets, orientation of the polymer chain itself, crystal structure of the crystalline or semi-crystalline polymer, and interaction between the polymer and the dispersed nanoclay platelets. To enhance the interaction between the polymer matrix and the nanoclay, occasionally it is necessary to use a compatibilizer. In PP/clay

Table 21.2 Properties and applications of commercially available clay-based PP—nanocomposites

Matrix	Type of clay	Chief properties	Applications	Commercial name	Supplier
PP	MMT	High flexural modulus High impact resistance Low bulk density High resistance to fatigue Scratch resistance Fire-retardant	Automotive parts: seat backs and centre consoles	Forte	Noble polymers
			Furniture	Forte	Noble polymers
			Rigid packaging: plastic hinges		
			Flexible packaging: film	40–50% clay concentrate PP	Nanocor (in collaboration of Clariant)
			Appliances: heavy-duty electrical enclosures	Forte	Noble polymers

Table 21.3 Processing and possible applications of nanoclay-based PP—nanocomposites

Matrix	Compatibilizers	Fillers	Processing	Improvement w.r.t neat PP	Possible application
PP homopolymer	PPgMA	3 wt% SC24 OMMT	Nanocomposite monofilament produced via melt spinning in a micro-compounder. The process involves two steps of mixing and compounding, extrusion and finally drawing	High breaking strain/tenacity of nanocomposite monofilament	Textile
Recycled PP or virgin PP	PPgMA	3% Cloisite 15A, 40% wood flour	Compounded in a Haake internal mixer at 175 °C with a rotation speed of 60 rpm	Nanoclay reduces the water absorption and thickness swelling of wood flour-based PP composite	Outdoor furniture
PP homopolymer	PPgMA (1 wt %MA)	3% Na-based bentonite EB grade	Master batch dilution method. Masterbatch was produced in a single screw extruder and the dilution was carried out in a twin screw extruder.	HDT: 5.1% Stiffness: 4% Strength: 18.5% T_c: 3.7%	Structural
PP homopolymer	PPgMA	Intumescent flame retardant and organically modified Fe-MMT	Extruded at 180 °C using an internal mixer at 60 rpm for 10 min	Composite achieved V-0 grade along with higher thermal stability, flame retardancy, and smoke suppression while the neat PP burned and dripped	Electrical and electronic appliances
PP random copolymer and Poly-β-pinene (commercial name: Piccolyte S115)		MMT modified with high content of dimethyldihydrogenated tallow quartenary ammonium salt		OTR: 24% WVTR: 31% Poly-β-pinene has antibacterial effect on *Escherichia coli* 25922 bacteria	Shelf-life of salami and pastrami packed under vacuum with this film (thickness ~100 μm) is quite comparable with commercial multilayer film

nanocomposites, the most widely used compatibilizer is maleic anhydride-grafted PP (PPgMA). This PPgMA also plays an important role in the photooxidation of the nanocomposites [10]. The clay-based nanocomposites showed a reduced formation of photooxidation products in the carbonyl region, while calcium carbonate composites exhibited a strong reduction in the formation of photooxidation products related to carboxylic acid salts, due to the interaction between the basic filler and the photooxidation products from the PP. In a recent study, we have noticed that nanoclays could act as UV blockers. This means that if one uses the nanocomposite as a packaging material for UV-sensitive substances, the composite film will first undergo photooxidation and, hence, delay the photooxidation of UV-sensitive substances. To understand the UV-blocking properties of the nanocomposite film, beakers containing a methylene blue solution were covered with a PP film and a nanocomposite film. The photodegradation of methylene blue in the presence of titanium dioxide (TiO_2) was studied.

The initial absorbance value recorded for the methylene blue solution before UV exposure was 0.07. After 1 h of exposure, the absorbance value recorded for the methylene blue solution protected with the PP film was 0.0025, whereas that for the nanocomposite-protected film was 0.00033. This indicates that the photodegradation is less effective in the methylene blue solution protected with the nanocomposite film. In this case, the photo-catalytic activity of TiO_2 is less pronounced. As a result, the degradation of the methylene blue molecules slows down and the solution maintains its bluish coloration. The methylene blue solution covered with the PP film undergoes a complete photodegradation and, hence, decolourization.

It is well known that the inherent flammability of PP restricts its application in fields like electrical and electronic appliances. This issue can be solved to a certain extent by the incorporation of organically modified nanoclays with and without intumescent flame retardant properties in the PP matrix. Such composites exhibit improved thermal stability and fire retardant behaviour compared to the PP matrix [11–13]. Liu et al. reported that the thermal stability, flame retardancy, and smoke suppression performance of a PP/intumescent flame retardant/organically modified Fe-MMt composite are better compared to those of a PP/intumescent flame retardant/organically modified MMt composite [14]. Organically modified Fe-MMt can be used as an effective synergistic flame retardant material with an intumescent flame retardant. Fe-MMt retards the flame spread speed by forming a much more compact char compared to Na-MMt. The authors reported that UL-94 achieves a V-0 grade for the composite containing 6% of the organically modified Fe-MMt. Given its superior flame retardant properties, ethyl vinyl acetate (EVA)/MMt wires are used in electrical cables. Nanocor has developed a PP/MMt concentrate for heavy-duty electrical enclosures [2]. Therefore, improved flame retardant PP composites have the potential to extend the application range of PP.

Another drawback of PP is its poor dyeing and coating ability. Incorporation of nanoclays (e.g. C20A) improves the adhesion between the surface of the composite and the applied paint or coating [15]. Therefore, PNC technology has the potential to improve the quality of printed labels. On one hand, the application of nanotechnology can improve the printability, and on the other hand, it can improve the

packaging performance, such as a gas and volatile barrier, heat resistance, mechanical strength, etc.

Rigid or flexible packaging materials with improved barrier properties and heat deflection temperature are highly desired for microwavable packaging materials. With a fast-paced modern life style, the demand for flexible packaging for food is growing rapidly [16]. Since 2002, the U.S. Army Natick Soldier Center has been conducting extensive research on the packaging material for military food rations. The main criteria for such packaging materials are that they should be no-foil composite structures, lightweight and air-droppable, and they should have a minimum of three-year shelf-life at 80 °C and six months at 100 °C [16]. Several studies have already been reported in this direction. Recently, Ayhan et al. [17] reported that a film comprising a PP random copolymer, poly-β-pinene, and MMt could improve the shelf-life of salami and pastrami packed under vacuum. The film thickness is $\sim$100 μm, which is comparable to a commercial multilayer film. Poly-β-pinene has an antibacterial effect on *Escherichia coli* 25922 bacteria. Agarwal et al. [18] developed a packaging material for potato chips and bread with a high O_2 transmission rate (OTR) and a moderate improvement in water vapour transmission rate (WVTR). They used an electrospinning technique to prepare N6-MMt composite fibres over PP films. According to the authors, the OTR and WVTR of PP improved by 98.7 and 27.6%, respectively [18]. Nanocor reported a 20% reduction in the OTR for a PP/Nanomer composite when compared to a neat PP [19]. The improvement in barrier properties are not only related with the dispersion and the orientation of the nanoclay platelets, but also depend on the aspect ratio and, hence, the volume fraction of the nanoclay platelets. The high aspect ratio of nanoclay dispersed in the polymer matrix along with a good delamination and orientation leads to the creation of tortuous paths. A long tortuous path slows the progression of the gas molecules through the polymer matrix and, hence, the nanocomposite exhibits improved gas barrier properties [2, 4].

Generally, PP is chemically resistant to organic solvents as well as acids and alkalis, except strong oxidizing acids, chlorinated hydrocarbons and aromatics. Moreover, PP has a design stress of 1000 psi at 22.7 °C (73 °F). Hence, PP can be considered as an excellent material for laboratory and industrial drainage pipes, where mixtures of acids, bases, and solvents are involved [2, 4]. Yusof et al. [20] prepared a PPgMA-based composite containing two fillers—bentonite clay and multi-walled carbon nanotubes for bioreactor liner applications. This material showed stable mechanical properties after exposure to certain chemicals.

21.4.2 PE/Clay Nanocomposites

Like PP, PE is also a widely used polyolefin. Depending on the density and branching, PE can be classified into four different categories: ultra-high molecular weight PE, HDPE, LDPE, and linear low density PE (LLDPE). PE is resistant to

water, acids, alkalis and most of the solvents. Generally, PE acts as a good barrier to moisture vapour transmission. However, the drawback is its high OTR. Since the oxidation of food or microbial growth can be accelerated in the presence of O_2, a low OTR is also preferable for packaging films along with a low WVTR. The general approaches to enhance the barrier properties are: application of an extra coating on the flexible film or rigid container using an ultrathin layer of material that provides a high intrinsic barrier [21], blending a high barrier polymer with medium barrier ones [22], construction of multilayer structures containing barrier layers [23], and incorporation of barrier-enhancing additives to the matrix polymer.

A barrier-enhancing additive can be either active (e.g., scavenger) or passive (e.g., nanoclay). Therefore, one way to improve the barrier performance of the polymer is the preparation of nanocomposites. The proper dispersion of nanoclay platelets in the polymer matrix creates tortuous paths and delays gas permeation. Because of their high barrier and good mechanical properties, PE/clay nanocomposites have been used in the packaging industry. HDPE/MMt nanocomposites have already been commercialised (refer to Table 21.1) and used to produce containers for handling toluene and other hydrocarbons. It is also suitable for automotive interior and exterior parts (refer to Table 21.1). Kubisova and Merinska [24] reported that a Nanofil (organically modified MMt)-containing PE nanocomposite improved the CO_2 barrier property, but not the O_2 one.

Since the key to property improvement of nanocomposites is the matrix-filler interaction, several studies have been conducted to understand the role of the compatibilizer [25] and the surfactant used to modify the nanoclay [26]. A detailed understanding of the effect of chain branching, processing technique and conditions, clay/polymer surface chemistry on the dispersion and finally on the barrier and mechanical properties of PE, may extend the application of PE/clay nanocomposites to other fields.

21.4.3 Polyvinyl Chloride (PVC)/Nanoclay Nanocomposites

PVC is the third most widely used thermoplastic polymer after PE and PP. According to a BCC market research, large-diameter pipes and other construction applications (e.g. windows and doors) are expected to become the key market for PVC nanocomposites [2]. The incorporation of nanoclays in the PVC matrix can improve the fracture resistance, corrosion resistance, watertight joints and provide a high load-bearing capability. The flame retardancy properties of PVC/clay nanocomposites might have the potential for wire and cable jacketing. Although the nanoclay can have a negative effect on the plasticizers used in flexible PVC, researchers have developed a plasticizer based on coated nanoclay particles to overcome this issue [2].

21.4.4 EVA/Clay Nanocomposites

EVA is a copolymer of ethylene hydrocarbon with vinyl acetate groups distributed randomly throughout the polymer chain. EVA has good clarity and gloss, barrier properties, toughness at low temperatures, stress-crack resistance and resistance to UV radiation [2].

EVA/MMt nanocomposites provide enhanced flame resistance without the use of halogen-based flame retardant materials. EVA/MMt nanocomposites provide a further advantage in terms of processing simplicity. The main commercial application of EVA/MMt nanocomposites to date has been in electrical wire and cable sheathing materials. Calorimeter tests reveal a strong decline in heat release at relatively low (3–5%) loadings. EVA nanocomposites also exhibit superior mechanical properties, chemical resistance and thermal stability. The predicted market size for EVA/MMt nanocomposites as a halogen-free fire retardant material is 27 million USD by 2019 [2]. In addition to the EVA/clay nanocomposites being commercialised, blend nanocomposites comprising EVA and PE have been commercialized as well. The wire and cables developed by Kabelwerk Eupen in cooperation with Süd-Chemie consist of an EVA/PE blend nanocomposite (refer to Table 21.1).

21.4.5 Engineering Polymer/Clay Nanocomposites

21.4.5.1 Polyethylene Terephthalate (PET)/Clay Nanocomposites

PET is a saturated thermoplastic polyester resin widely used in packaging (e.g., bottles and packaging films for foods), automotive (e.g. mirror backs, grille supports, head lamp reflectors and alternator housings), electrical (e.g. motor housings, electrical connector relays, microvan interiors and switches), and structural applications (e.g. pump housings and hand tools) due to its high transparency, dimensional stability, good barrier properties against CO_2 and O_2, good thermal and mechanical properties and recyclability [2]. Several studies have been conducted to improve further its properties using nanotechnology. Eastman, Dow Chemicals and Honeywell took the initiative to commercialize PET/MMt nanocomposites as barrier applications. However, according to a BCC market research [5], there is a low probability of success for the commercialization of such nanocomposites within the next couple of years. One of the main drawbacks of PET is its high melting and processing temperatures (usually around 265–280 °C) [2]. Several alkyl ammonium-modified nanoclays lead to polymer degradation since the ammonium modifier faces the Hoffmann elimination reaction at 200–300 °C and produces additional Brønsted acid sites [2]. Hence, for the preparation of PET/nanoclay nanocomposites, it is important to modify the clay surface with high thermally stable surfactants (e.g. alkyl imidazolium) [27]. The properties of the nanocomposite not

only depend on the thermal stability of the nanoclay, but also depend on the interaction between the PET and nanoclay, orientation (uniaxial and biaxial stretching), crystal thickness, crystal defects, etc. For example, crystal thickness can be increased by annealing, the defects can be minimized, and the boundary between the amorphous and crystalline regions sharpened. Consequently, the gas permeability can be improved. However, for commercialization it is important to meet the cost-performance index criterion. PET/clay nanocomposites are still in the development phase and have not yet entered the commercial market probably due to its cost-performance index criterion.

21.4.5.2 Ethyl(vinyl alcohol) (EVOH)/Nanoclay Nanocomposites

EVOH is a copolymer barrier resin with good processability characteristics. It is used to make strong, flexible, and transparent films with good O_2 barrier properties. The U.S. military and NASA, in conjugation with Triton Systems, Inc., Chelmsford, Mass., are researching nanoclays as barrier enhancers for EVOH in long-shelf-life packaging [28]. An experimental thermoformed food tray made from a EVOH/nanoclay nanocomposite (containing 3% of C20A) layer sandwiched between two PP layers imparts a three- to five-year shelf-life without refrigeration, in addition to good clarity, processability, and recyclability. Researchers are also studying possible applications of EVOH nanocomposites in future "meal, ready to eat" (MRE) packaging. Their target is to reduce the cost of MRE packaging and replace the aluminium foil barrier layer used in current MRE packages by nanocomposite films. This will reduce the amount of waste generated from the disposal of MRE packages. In tests, the EVOH nanocomposite achieved the O_2 barrier requirement for the MRE, but these properties depend on temperature and humidity. One potential solution to this issue is to sandwich the EVOH nanocomposite layers between LDPE layers. It is unknown when or whether the Army will initiate large-scale procurements of EVOH nanocomposite-wrapped MREs.

Since EVOH contains both organophilic repeating units of ethylene and hydrophilic repeating units of vinyl alcohol (refer to Scheme 21.1), it is quite challenging to determine the exact type and amount of surfactant to treat the clay. The following discussion highlights the variety of organically modified clays used to prepare EVOH nanocomposite films for barrier properties. Somwangthanaroj et al. reported that a nanocomposite containing a single alkyl tail with two repeating units of oxyethylene surfactants showed better tensile properties [29].

Kim and Cha prepared EVOH/Cloisite®30B (C30B) nanocomposites by a solvent casting method [30]. The gas barrier properties of the C30B-based EVOH

Scheme 21.1 Molecular structure of EVOH

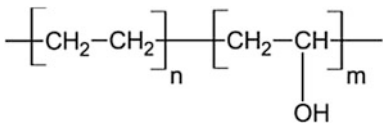

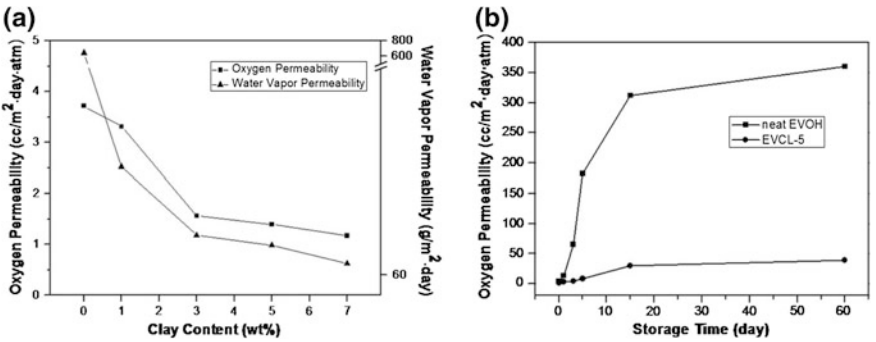

Fig. 21.2 **a** Oxygen and water vapour permeabilities of the EVOH/clay nanocomposite films as a function of clay content and **b** Oxygen permeabilities of neat EVOH and EVCL nanocomposite (containing 5 wt% C30B) films as a function of storage time under humid atmosphere of 100% [30]

nanocomposites and the effect of storage time on the OTR are presented in Fig. 21.2. As evidenced from Fig. 21.2a, a 5 wt% C30B loading exhibits the best barrier properties. Figure 21.2b shows that the dispersed clay layers delay the O_2 permeability in the nanocomposite film [30]. Seethamraju et al. reported an improvement in the gas barrier properties using a poly(ethylene-co-methacrylic acid)/EVOH blend nanocomposite [29]. For this purpose, three authors modified MMt with 15–35 wt% of octadecylamine together with 0.5–5 wt% of aminopropyltrimethoxysilane.

Besides the proper choice of clay, the ethylene content in EVOH also plays an important role on the gas barrier properties. The H-bonding depends on the ethylene content of EVOH [31]. OH groups in EVOH produce strong intermolecular and intramolecular forces. As a result, EVOH has a high cohesive energy. The H-bond strength decreases with increasing ethylene content. This property is important to select the appropriate organically modified clay for the nanocomposite preparation. The other parameter that affects the barrier properties of EVOH is the degree of crystallinity. A higher crystallinity provides a lower OTR. EVOH is currently used in multilayer films for packaging food and beverages. However, EVOH nanocomposite films are not yet commercially available. The barrier properties of a three-layered film consisting of a EVOH-Cloisite®25A composite as the middle layer and a Huntsman 1031S grade PE as outer layers are reported in the patent US8784978 B2 [32]. However, there was no noticeable improvement in the barrier properties. Another patent, US 20060094811 A1, reveals that PET/EVOH and PET/Nylon nanocomposite blends provide better OTR than PET/EVOH and PET/Nylon blends [33]. Despite the two patents on EVOH/clay nanocomposite films (as mentioned above), they have not yet been commercialized. Therefore, there is a possibility for improvement in this field.

21.4.6 Nylon/Clay Nanocomposites

In the family of engineering thermoplastics, Nylon is the most versatile one with an excellent balance of strength, ductility, impact resistance, abrasion resistance and heat resistance. For example, N6 exhibits a high impact resistance at 50% relative humidity, and Nylon 12 exhibits flexibility in dry conditions but becomes stiffer and more rigid at normal humidity conditions or when saturated in water. Nylon also provides better gas barrier properties when compared to polyolefins. Even though Nylon already has excellent properties, a further improvement can be achieved through PNC technology. The first major breakthrough on the in situ polymerisation of N6/clay nanocomposites was reported by Okada et al. [1]. Toyota then licenced this technology to several companies including Nanocor (U.S.) and Ube Industries (Japan). Since then, N6/mica fluoride has been commercialized for the production of automotive parts due to its heat and impact resistance, tensile strength and barrier properties. N6/MMt composites have been used in under-the-bonnet automotive parts (e.g., timing belt), medical devices (from Foster Corp.) such as catheters, food packaging (both film and rigid containers), etc. The N6/clay nanocomposites for packaging applications are now commercially available from Alcoa CSI and Lanxess. Honeywell produces Aegis (N6/clay nanocomposites) for automotive painted parts. N6/clay nanocomposites (nanoTuff and nanoSeal) used in the cold weather automotive industry are the commercial product of Nylon Corporation of America. NanoSeal is commonly used for the fuel system (tanks and hoses) to meet the CARB fuel emission standard. The N6-based blend nanocomposites (N6/acetal/clay) have also been commercialized by Showa Denko for flame retardancy applications [5]. The detailed information regarding the commercially available Nylon/clay nanocomposites and their applications are tabulated in Table 21.1.

Although some nanocomposites are already available in the market, researchers are still trying to develop Nylon/clay-based materials with better barrier properties [34–36]. It is well known that the tortuous path created by the dispersed nanoclay platelets can reduce the permeation rate of gases by acting as a passive barrier material. However, other models such as shape and size of the constrained polymer regions, and magnitude of the diffusion coefficient in the constrained regions might influence the water uptake [37].

It has been revealed that the fabrication of multi-layered films using Nylon/clay nanocomposites as a middle layer provides a significant improvement in the gas barrier properties. For example, the OTR for a PET monolayer, a MXD6 (aromatic Nylon) multilayer, and an Imperm multilayer is 0.025, 0.013 and 0.004 cm^3/bottle day 0.21 atm, respectively. Similarly, the CO_2 shelf-life (10% loss) for the PET monolayer, MXD6 (aromatic Nylon) multilayer and Imperm multilayer is 7, 14 and 23 weeks, respectively. A paper-coated N6 nanocomposite (Durethan KU2-2601) can be used for medium barrier applications. The Nylon/clay nanocomposite

(Aegis^{TM} OX)-based beer bottles available in the market is a commercial product of Honeywell Polymers, which also contain O_2 scavengers to improve the beer shelf-life.

Both in situ intercalation and melt compounding can be used to prepare Nylon/clay nanocomposites at an industrial scale. However, the selection of a proper molecular weight for Nylon, choice of surfactant used to modify the nanoclay, and concentration of the nanoclay are important for the melt compounding process [38, 39]. A high molecular weight grade leads to a high level of delamination of the nanoclay platelets in the N6 matrix [38].

21.4.7 Poly(Ether Ether Ketone) (PEEK)/Clay Nanocomposites

PEEK is a semi-crystalline thermoplastic with excellent mechanical and chemical resistance properties even at a high temperature. Because of its robustness, PEEK is used to fabricate bearings, piston parts, compressor plate valves, as insulation for cables, and ultra-high vacuum devices. It is also used for medical applications, such as spinal fusion devices and reinforcing rods. It is extensively used in the aerospace, automotive and chemical process industries. In the field of clay-based PEEK nanocomposites, few reports are available on the application of PEEK/clay nanocomposites for fuel cells [40]. Sulfonated PEEK/C20A/triaminopyrimidine nanocomposite membranes have the potential to be an alternative polymer electrolyte for direct methanol fuel cell applications [41]. Doğan et al. reported that the addition of dimethyl dioctadecyl ammonium to a modified MMt clay improved the proton conductivity of the composite membrane designed for fuel cell applications [42]. However, to the best of our knowledge, these nanocomposites have not yet been commercialized.

21.4.8 Acetal/Clay Nanocomposites

Acetal, also known as polyacetal, polyoxymethylene, or polyformaldehyde, is a high-performance engineering polymer. Because of its high strength, elasticity and resistance to impact and fatigue, it is used as a weight-saving metal replacement. The negative aspect of acetals is that they degrade in acid and base solutions and are not readily available in a flame retardant grade.

Acetal/MMt nanocomposites were introduced in automotive and electronics applications in the late 1990s. Compared to unfilled acetal copolymers, acetal nanocomposites provide a 40% higher flexural modulus and 45 °F higher heat resistance. Several Japanese manufacturers currently sell acetal/clay nanocomposites. Showa Denko is aiming to use acetal nanocomposites for under-the-bonnet parts [43].

21.4.9 Butyl/Clay Nanocomposites

Butyl is a synthetic rubber formed by copolymerizing isobutene and small amounts of isoprene. Butyl shows an impermeability to gases, flexibility, resistance to weathering and to ozone, vibration dampening and biocompatibility.

At present, butyl/vermiculite nanocomposites are used mainly in sporting goods applications. Vermiculite has a high aspect ratio ($\sim$10,000). Hence, the vermiculite platelets dispersed in the butyl/vermiculite nanocomposite can inhibit gas permeation through the composite by increasing the path length. Therefore, the vermiculite clay platelets also act as a passive gas barrier material in the butyl/vermiculite nanocomposite. Yilmaz et al. [44] studied the effect of different cationic surfactants used to modify MMt on the preparation of nanocomposites based on acrylic (butyl acrylate-co-methyl methacrylate-co-acrylamide) terpolymers via an emulsion polymerization method. The authors reported that a lower amount of emulsifier was required for the emulsion polymerization in the presence of octadecyl amine or a modifier with one methyl group (e.g., Cloisite®93A). These nanocomposites showed good mechanical and thermal properties [44].

21.4.10 Biopolymer/Clay Nanocomposites

Biopolymer (bio-based and biodegradable)-based nanocomposites are an emerging field of research. Usually, biopolymers are more expensive than petroleum-derived polymers. However, the price of some biopolymers is being reduced due to the scaling-up in production [4]. Since the commodity-product markets are price sensitive, the clay-based nanobiocomposites might find an application in high-end products. For example, poly(N-isopropylacrylamide)/C30B, chitosan/polyethyleneimine/halloysite, MMt and halloysite clay-based chitosan/poloxamer 407 can be used for drug delivery applications [45]. Nanobiocomposites can also be used in tissue engineering and as drug/gene delivery carriers. Liu et al. [45] reported that chitosan/halloysite nanocomposites are cytocompatible event at high halloysite loadings and have potential for applications in tissue engineering and as drug/gene delivery carriers [45]. Poly(ethylene glycol)diacrylate/laponite nanocomposite hydrogels can support two- and three-dimensional cell cultures [46]. The authors claimed that it was a minimally invasive injectable system for in vivo applications.

Other developing research areas consist of cotton/clay nanocomposite fibres, such as polyhydroxyalkanoate/clay/cellulose nanocomposites, and nanoreinforced polylactic acids [4]. The cotton/clay nanocomposite fibres have a heat tolerance 20–30 °C higher than the unbleached cotton. In addition, the clay also improves the flame retardant properties, softness, and printability of cotton. Therefore, such fibres can be used in heat-resistant clothing for fire fighters. Other possible applications include low-cost disposable point-of-use water filtration devices. Nanobiocomposites are still in the development phase.

21.4.11 Conducting Polymer/Clay Nanocomposites

In this family, the two most important polymers are polyaniline (PANI) and poly (ethylene oxide) (PEO). PANI/clay nanocomposites are used as corrosion protective coatings [47, 48]. According to Navarchain et al. [47] the corrosion of a steel panel can be prevented by coating the panel with an epoxy/PANI/organically modified MMt. The epoxy/PANI/organically modified MMt coating performs better than the epoxy, epoxy/PANI, and even epoxy/PANI/MMt coatings [47]. On the other hand, studies are taking place using PEO/clay nanocomposites for solid polymer electrolyte membrane applications [49, 50].

21.5 Future of Clay-Based Polymer Nanocomposites

Some nanocomposites have already been commercialized through the advances in nanotechnology research over the past few years. The most important aspect for commercialization is the cost/performance index and the market demand. Evidently, from the above discussion, polymer nanocomposites are already being used in different industries, and the market for these materials is expanding. Venture capitalists and companies are trying to explore and expand the range of novel properties and new applications for polymer nanocomposites. For example, in Europe, the automotive industry invests over 5% of its annual turnover for further research and development. Consequently, the application of nanocomposites has increased in the automotive sector in the past few years. Lloyd and Lave summarized the required cost per pound and resulting environmental implications for various nanocomposite substitution scenarios [3]. Interestingly, the substitution of 70% of the steel present on the vehicle body panels by nanocomposites can reduce the primary weight by 52%, with a reduction of the annual petroleum production by 5.5 billion gallons, and an annual CO_2 production during vehicle use by 47 million tons.

The largest market (according to the sales rank) of PNCs is Nylon/MMt nanocomposites. The main application domains of Nylon/MMt nanocomposites are food packaging and automotive parts. The market forecast until 2019 predicts that Nylon/MMt nanocomposites will continue to dominate the market. Besides the main stream of polymer nanocomposites, nanobiocomposites are another emerging research area. It is a fascinating interdisciplinary area that unites biology, nanotechnology, and material science. Nanobiocomposites are usually prepared by mixing biopolymers with nanobio-reinforcements. Besides nanoclay, different nanobio-reinforcements (e.g., cellulose) are also being used for this purpose. The application-oriented research on nanobiocomposites is still in the development phase. However, according to a BCC market research, there is a possibility for commercialization of such nanocomposites before 2019.

21.6 Conclusion

The field of nanoclay-containing polymer nanocomposites is growing rapidly, and such nanocomposites provide several significant advantages. However, it is also important to consider the value chain from the product development to the commercialization and finally the recyclability, reusability and biodegradation of nanobiocomposites. One of the main challenges of polyolefin or engineering polymer-based nanocomposites is their recyclability. It has been reported that clay-based nanocomposites can be recycled without a significant variation in the properties, since the probability of an aspect ratio variation with the dispersed MMt clay is lower compared to long glass fibres [3]. However, it should be pointed out that in order to improve the interaction between the nanoclay and the polymer matrix, it is necessary to modify the natural hydrophilic MMt to an organophilic one. The thermal stability of the matrix and organically modified nanoclay play an important role during recycling of the nanocomposite material. Instead of recycling, nanocomposites can also be reused to produce different products, such as plastic fences, etc.

Acknowledgements The authors thank the Department of Science and Technology and the Council for Scientific and Industrial Research, South Africa for their financial support.

References

1. Okada A, Kawasumi M, Usuki A et al (1989) Nylon 6–clay hybrid. MRS Proc 45–50
2. Ray SS (2013) Clay containing polymer nanocomposites: from fundamentals to real applications. Elsevier. ISBN 978-0-444-59437-2
3. Lloyd SM, Lave LB (2003) Life cycle economic and environmental implications of using nanocomposites in automobiles. Environ Sci Technol 37:3458–3466
4. Ray SS (2013) Environmentally friendly polymer nanocomposites. Woodhead Publishing, England. ISBN 0 85709 777 6
5. McWilliams A, BCC research, global markets for global markets for nanocomposites, nanoparticles, nanoclays, and nanotubes. NANO21F, ISBN 1-56965-807-2
6. Onder E, Sarier N, MS Ersoy (2012) The manufacturing of polyamide- and polypropylene-organoclay nanocomposites filaments and their suitability for textile applications. Thermochim Acta 543:37–58
7. Khanjanzadeh H, Pirayesh H, Salari A (2013) Long term hygroscopic characteristics of polypropylene based hybrid composites with and without organo-modified clay. Eur J Wood Prod 71:211–218
8. Komatsu LGH, Wl Oliani, Lugao AB et al (2014) Environmental ageing of irradiated polypropylene/montmorillonite nanocomposites obtained in molten state. Rad Phys Chem 97:233–238
9. Kulshreshtha AK, Maiti AK, Choudhuri MS et al (2006) Nano-addition of raw bentonite enhances polypropylene (PP) properties. J Appl Polym Sci 99:1004–1009
10. Morreale M, Dintcheva NT (2013) Accelerated weathering of PP based nanocomposites: effect of the presence of maleic anhydride grafted polypropylene. eXPRESS Polym Lett 7:703–715

11. He A, Wang L, Yao W et al (2010) Structural design of imidazolium and its application in PP/montmorillonite nanocomposites. Polym Degrad Stabil 95:651–655
12. Dahiya JB, Kumer N, Bockhorn H (2014) Fire performance and thermal stability of polypropylene nanocomposites containing organic phosphinate and ammonium polyphosphate additives. Fire Mater 38:1–12
13. Yi D, Yang R, Wilkie CA (2014) Full scale nanocomposites: clay in fire retardant and polymer. Polym Degrad Stabil 105:31–41
14. Liu H, Zhong Q, Kong Q et al (2014) Synergistic effect of organophilic Fe-montmorillonite on flammability in polypropylene/intumescent flame retardant system. J Therm Anal Calorim 117:693–699
15. Sari MG, Shahbazi M, Pakdel AS (2014) Developing a novel hyperbranched polymer-modified PP/clay nanocomposite: characteristic investigation. Polym-Plast Technol Eng 53:1561–1573
16. Downing-Perrault A (2005) Polymer nanocomposites are the future. Downloaded on 18 Jan 2016
17. Ayhan Z, Cimmino S, Esturk O et al (2015) Development of films of novel polypropylene based nanomaterials for food packaging application. Packag Technol Sci 28:589–602
18. Agarwal A, Raheja A, Natarajan TS et al (2014) Effect of electrospun montmorillonite-nylon 6 nanofibrous membrane coated packaging on potato chips and bread. Innovat Food Sci Emer Technol 26:424–430
19. Lan T (2009) Nanocomposite materials for packaging film applications, symposium on nanomaterials for flexible packaging. Downloaded on 18 Jan 2016
20. Yusof F, Olalekan ST, Shah QH et al (2011) Chemical resistance tests on PP-ternary nanocomposite for its application in bioreactor liner fabrication. Sci China 54:2217–2223
21. Maul P (2005) Barrier enhancement using additives. Fillers, pigments and additives for plastics in packaging applications. Pira international conference Brussels, Belgium, 5–6 Dec
22. Siró I, Plackett D, Sommer-Larsen P (2010) A comparative study of oxygen transmission rates through polymer films based on fluorescence quenching. Packag Technol Sci 23: 301–315
23. Di Maio L, Scarfato P, Galdi MR (2015) Development and oxygen scavenging performance of three-layer active PET films for food packaging. J Appl Polym Sci 132:41465 (10 pages)
24. Kubisova H, Merinska D (2008) Polyolefin/clay nanocomposites: comparing mechanical and barrier properties. In: Aciemo D, D'Amore A, Grassia L (eds) CP1042, IVth international conference on times of polymers (TOP) and composites. American Institute of Physics, ISBN 978-0-7354-0570-7/08
25. Sánchez-Valdes S, Méndez-Nonell J, Madellín-Rodríguez FJ et al (2010) Evaluation of different amine-functionalized polyethylenes as compatibilizers for polyethylene film nanocomposites. Polym Int 59:704–711
26. Olewnik E, Garman K, Peichota G et al (2012) Thermal properties of nanocomposites based on polyethylene and *n*-heptaquinolium modified montmorillonite. J Therm Anal Calorim 110:479–484
27. Manias E, Heidecker MJ, Nakazima H, Costache MC et al (2011) Poly(ethylene terephthalate) nanocomposites using nanoclays modified with thermally stable surfactants, Chap. 4. Cambridge University Press, Cambridge
28. Sherman LM (2004) Chasing nanocomposites. Plast Technol, November Issue. Downloaded on 9 Feb 2016
29. Somwangthanaroj A, Photyotin K, Limpanart S, et al (2012) Effect of type of surfactants and organoclay loading on the mechanical properties of EVOH/clay nanocomposite blown films. Polym Plast Technol Eng 51:1173–1180
30. Kim SW, Cha S-H (2014) Thermal, mechanical, and gas barrier properties of ethylene-vinyl alcohol copolymer-based nanocomposites for food packaging films: effects of nanoclay loading. J Appl Polym Sci 131:40289 (8 pages)
31. Mokwena KK, Tang J (2012) Ethylene (vinyl alcohol): a review of barrier properties for packaging shelf stable foods. Crit Rev Food Sci Nutr 52:640–650

32. Apoorva S, Arjan G, Yoojeong K (2014) Multilayer flame retardant barrier films and fabrics. US Patent 8784978 B2
33. Kim M (2006) Nanocomposite composition having barrier property. US Patent 20060094811 A1
34. Cho JW, Paul DR (2001) Nylon 6 nanocomposites by melt compounding. Polymer 42: 1083–1094
35. Turner SR, Connell GW, Gilmer JW et al (2002) High barrier amorphous polyamide-clay nanocomposite and a process for preparing same. US Patents 6417262 B1
36. García A, Eceolaza S, Iriarte M et al (2007) Barrier character improvement of an amorphous polyamide (trogamid) by the addition of a nanoclay. J Memb Sci 301:190–199
37. Adame D, Beall GW (2009) Direct measurement of the constrained polymer region in polyamide/clay nanocomposites and the implications for gas diffusion. Appl Clay Sci 42: 545–552
38. Shah RK, Paul DR (2004) Nylon 6 nanocomposites prepared by a melt mixing Masterbatch process. Polymer 45:2991–3000
39. Fornes TD, Yoon PJ, Paul DR (2003) Polymer matrix degradation and color formation in melt processed nylon 6/clay nanocomposites. Polymer 44:7545–7556
40. Hasani-Sadrabadi MM, Ghaffarian SR, Mokarram-Dorri N et al (2009) Characterization of nanohybrid membranes for direct methanol fuel cell applications. Solid State Ion 180: 1497–1504
41. Ilbeygi H, Ismali AF, Mayahi A et al (2013) Transport properties and direct methanol fuel cell performance of sulfonated poly (ether ether ketone)/cloisite/triaminopyrimidine nanocomposite polymer electrolyte membrane at moderate temperature. Sep Purif Technol 118: 567–575
42. Doğan H, Inan TY, Koral M et al (2011) Organo-montmorillonites and sulfonated PEEK nanocomposite membranes for fuel cell applications. Appl Clay Sci 52:285–294
43. Plastic in European cars (2000–2008) A Rapra Industry Analysis Report, IG Helps, Febrary 2001
44. Yilmaz O, Cheaburu CN, Durraccio D et al (2010) Preparation of stable acrylate/ montmorillonite nanocomposite latex via in situ batch emulsion polymerization: effect of clay types. Appl Clay Sci 49:288–297
45. Liu M, Wu C, Jiao Y et al (2013) Chitosan-Halloysite nanotubes nanocomposite scaffolds for tissue engineering. J Matter Chem B 1:2078–2089
46. Chang C-W, van Spreeuwel A, Zhang C et al (2010) PEG/clay nanocomposite hydrogel: a mechanically robust tissue engineering scaffold. Soft Mat 6:5157–5164
47. Navarchain AH, Joulazadeh M, Karimi F (2014) Investigation of corrosion protection performance of epoxy coatings modified by polyaniline/clay nanocomposites on steel surfaces. Prog Org Coat 77:347–353
48. Akbarinezhad E, Ebrahimi M, Sharif F et al (2011) Synthesis and evaluating corrosion protection effects of emeraldine base PAni/clay nanocomposite as a barrier pigment in zinc-rich ethyl silicate primer. Prog Org Coat 70:39–44
49. Loyens W, Maurer FHJ, Jannasch P (2005) Melt-compounded salt-containing poly(ethylene oxide)/clay nanocomposites for polymer electrolyte membranes. Polymer 46:7334–7345
50. Ratna D, Divekar S, Patchaiappan S et al (2007) Poly(ethylene oxide)/clay nanocomposites for solid polymer electrolyte applications. Polym Int 56:900–904

Chapter 22
Biological Materials

Challa Vijaya Kumar

22.1 Accumulation of Man-Made Materials in the Environment

Recent advances in our use of man-made materials and our high standard of living have increased the environmental burden of our civilization. For example, the plastic items that we use in our daily life are ending up in the oceans. Currently, there are estimates of nearly 110 million tons of plastic floating on our oceans, as very large man-made islands of the size of Texas or larger (Fig. 22.1a) [1]. These islands are causing havoc on the wild life and they will continue to cause damage for several hundreds of years to come and resulting in irreparable damage [2]. Therefore, we are changing the planet and its habitat in a large and negative manner. There are several such large islands of plastic on our world oceans [3]. Imagine their impact on the fish, birds, aquatic plants, and the invisible microorganisms that live in these waters.

This kind of mega change to the planet on very large scale is not sustainable nor it is acceptable. For example, a surfer surfing on the ocean encounters large amounts debris around is not only unpleasant but such waste can also have devastating effect [4]. Therefore, everyday activities of humans continue to release plastic items that do not degrade for very long time and continue to pollute our land, air, and water. If these items were to be made of biodegradable materials, on the other hand, then these would degrade in the natural environment and not persist for long. The persistence timescales of specific materials can be programed while

C.V. Kumar (✉)
Department of Chemistry, Department of Molecular and Cell Biology, University of Connecticut, Storrs, CT 06269, USA
e-mail: Challa.Kumar@uconn.edu

C.V. Kumar
Inorganic and Physical Chemistry Department, Indian Institute of Science, Bengaluru 500016, India

T. Nakato et al. (eds.), *Inorganic Nanosheets and Nanosheet-Based Materials*, Nanostructure Science and Technology, DOI 10.1007/978-4-431-56496-6_22

Fig. 22.1 Six large islands of plastic articles floating on our world oceans, which may continue to exist for hundreds of years, reproduced with permission from Am Dienstag (www.Strangesounds.org)

making the biological materials, as required by their usage, disposal, and degradation. There has been a major overall transformation that has been occurring on this planet, which is responsible for the accumulation of these nonbiodegradable materials on our oceans, land, and in the atmosphere in the form of visible or invisible particulate material. Examples of some of these transformations of major concern are illustrated below.

22.2 Man-Made Materials that Are Replacing Natural Materials that Were Used by Humans for Millennia: Transformations of Immense Proportions on a Global Scale

There are a number of transformations that are occurring on this planet in immense proportions over the past several decades (Fig. 22.2, top), and these have contributed to the accumulation of waste that does not seem to degrade over reasonable timescales or release toxic products. For example, the use of cloth bags is being discontinued and replaced with plastic bags by millions of people around the globe, and this simple change can contribute to millions of tons of plastic waste, which may or may not be recycled.

It is not clear how much of plastic from these objects is being recycled or simply discarded in waste landfills across the globe. Similarly, the humble pottery utensils previously made of clay are now being replaced by the corresponding plastic items, particularly in the developing world, on a very large scale (Fig. 22.2, second from top).

Few other major transformations that are causing severe concern may include our means of transportation and housing. For example, the major mode of transportation of people, goods, and other items in New York City, a century ago, has

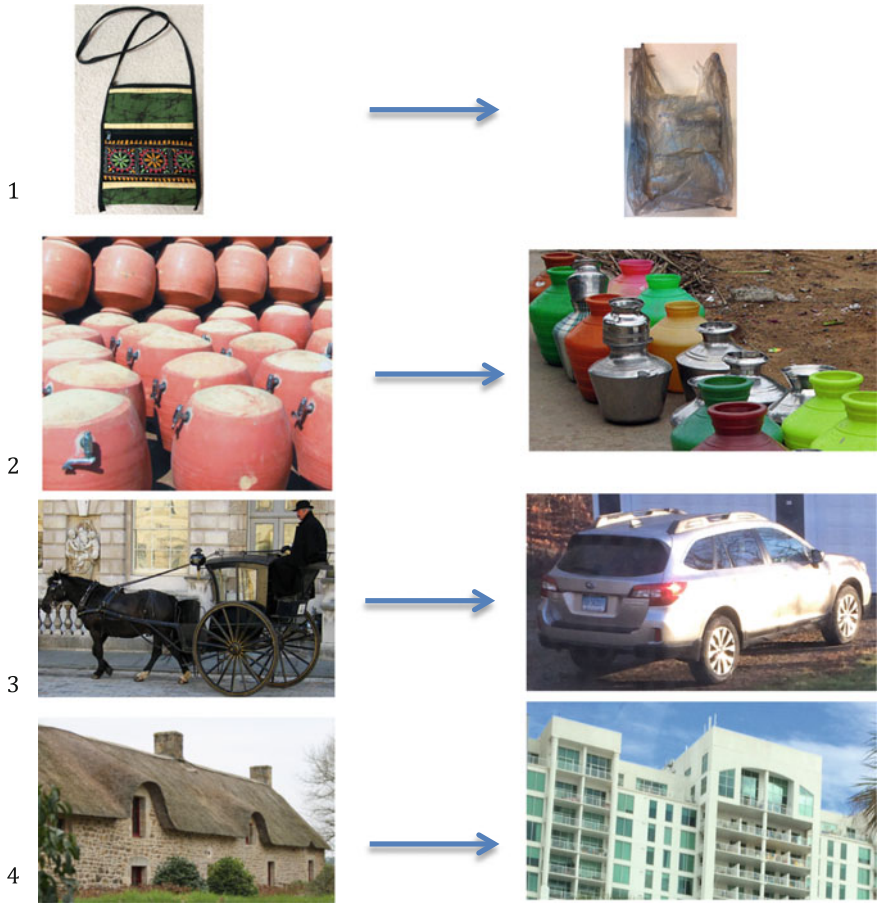

Fig. 22.2 Some interesting transformations of immense scale on this planet that are changing the type of materials that are being used to support our current standards of living with dangerous consequences over the next several decades to come, unless urgent appropriate steps are taken. (By Pottery reproduced with permission from CC BY-SA 3.0, https://commons.wikimedia.org/w/index.php?curid=7174223; plastic pots by Mckay Savage UK was reproduced with permission from Creative Commons Attribution 2.0 Generic license; horse cart reproduced with permission from By Andrew Dunn—English Wikipedia, original upload 20 September 2004 by Solipsist, CC BY-SA 2.0, https://commons.wikimedia.org/w/index.php?curid=326412; thatched hut reproduced with permission by By Stéphane Batigne—Own work, CC BY-SA 3.0, https://commons.wikimedia.org/w/index.php?curid=18331885)

been the humble horse wagon. Everything in the vehicle, wheels, the motor (horse), including the driver, is biodegradable. Several such examples can be cited over the entire globe where the traditional mode of transportation, be it bullock cart or horse buggy or camel cart, had little are no impact on the planet over thousands of years of use. Now, these humble modes of transportation are being replaced gradually by

automobiles or trucks with devastating consequences which are directly or indirectly responsible for the current status of pollution, accumulation of toxic waste, and ultimately leading to the climate change [5]. A question can be asked, can these modern methods of transportation be sustained over the next several millennia without severe impact on our environment, and the answer is simple. The consumer society can be sustained long term only if the materials used are recyclable or degradable to nontoxic components over reasonable timescale with no toxic release. While the metal and glass used in our goods are recycled with high efficiency to make tangible, functional goods, the same cannot be said about the plastic that is often used. Another example of immense proportions where the traditional natural materials are being replaced by nondegradable materials on a very very large scale is the housing industry (Fig. 22.2, bottom) [6]. Traditional materials such as bamboo, straw, palm leaves, and stone have been extensively used in our traditional cultures over millennia as building materials with no serious consequences to the environment. These natural materials degrade over sufficiently long timescales such that they are functional, inexpensive, and disposable at the end. However, these are now being replaced by steel, concrete, plastic, and glass in many modern construction dwellings, but most of it ends up in landfill when the building is demolished, except for glass and metal which can be recycled efficiently. While we continue to enjoy these modern amenities and replacing traditional natural materials by nonbiodegradable materials in these various large-scale transformations on this planet; this is already having substantial impact on the environment and will continue in the next few to several decades unless serious changes are made. While we cannot go back to the traditional ways of transportation, housing and communication, we need to find acceptable alternative materials that can be highly functional, yet do not accumulate in the environment after their use over their intended usage life span.

22.3 Molecules to Materials to Devices (MMD): How Nature Does It?

Biological materials come to mind as reasonable alternatives to replace the nonbiodegradable or nonrecyclable materials we use on a daily basis without compromising on the function, cost, utility, and feasibility for a sustainable green society to flourish over the next several millennia. At first, this may appear impossible and may be thought of as ‘pie in the sky’ dream. However, a number of examples can be found in nature that would guarantee success in achieving the above dream if major breakthroughs are made at fundamental level, in chemistry, biology, materials science, and engineering. A few examples may be necessary to convince the enormous potential of the natural materials in the making of future biodegradable functional devices. Nature’s materials are fully biodegradable and do not persist in the environment longer than necessary. A few examples may be


Biodegradable Solar Cell


Biodegradable Stereo-Camera


Biodegradable Gas Sensor

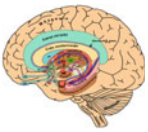
Biodegradable Supercomputer

Fig. 22.3 Proteins are nature's materials and nature uses these materials to make functional devices which are completely biodegradable. Thus, natural solutions to the problems of interest discussed in this chapter are already known, and now it is the grand challenge for the chemists and engineers to devise similar solutions that fit to our everyday needs. Eagle eye was reproduced with permission from Woodwalker, under the Creative Commons Attribution-Share Alike 3.0 Unported license. Fox nose was reproduced with permission from Wikimedia, by Harlequeen from Cambridge, United Kingdom [CC BY 2.0 (http://creativecommons.org/licenses/by/2.0)], via Wikimedia Commons. Human brain by John Taylor—File: The Limbic System and Nearby Structures—John Taylor.jpg; Taylor, John. General Science. Taylor Electronics. Archived from the original on June 9, 2013. Retrieved on March 27, 2014, Public Domain, https://commons.wikimedia.org/w/index.php?curid=52350239)

recalled from our everyday experiences, as shown in Fig. 22.3, which clearly illustrates the sophisticated devices that nature produces under ordinary conditions.

The very first example in Fig. 22.3 (left) is the biodegradable solar cell that we are familiar with, such as the green leaf. These are all solar cells and they are converting Sun's energy into fuels. These fuels are then being used by plants, or animals and organisms that eat the plant materials. Therefore, these solar cells are fully functional, inexpensive, biodegradable, green, sustainable and do not leave a footprint even after billions of years of their existence on this planet. Therefore, the challenge is to produce that kind of solar cells in the laboratory where light is converted into liquid or gas fuels that we can readily use in our daily life. However, there are no such devices in existence as of now, and this is one of the greatest challenges for chemists and engineers.

Moving on to the next example above, we find the eye, a biodegradable, fully functional, color-sensitive, autofocusing camera with essentially infinite memory, instant image processing and permanent color fastness, etc. How to create such a functional high-fidelity camera that would also biodegrade? This is another challenge of immense proportions, but it is not essential to duplicate such a device but build devices based on biodegradable components and materials. Along these lines, the nose of a bear is said to be 100 times more sensitive than that of human nose, highly selective, rapid in analyzing thousands of molecules very quickly and identifying them immediately or instantaneously. All this may sound altruistic but one final example to cap off this discussion would be the supercomputer, human brain. This device is built out of fully biodegradable components and modules, and runs on 10 mM glucose while consuming only 20 watts of power. It has built-in software that can be trained and it uses advanced genetic algorithms, which we do not even understand yet, to process immense amounts of data very rapidly with

essentially infinite memory and instant recall depending on the model.[1] Mainframe computers equivalent in power to that of the human brain has been estimated to consume about hundred megawatts of power.[2]

The above examples from nature demonstrate the feasibility of using biological materials to prepare a diverse set of devices to produce complex functions, yet fully biodegradable when discarded into the environment. Therefore, we can see a road map in fully delivering functional devices by mimicking nature's materials and combining them with modern science to design disposable and biodegradable devices. Perhaps, one day we might be able to make iPhones or iPads that can be composted after their use, without significant impact on the environment. Thus, being green is not enough and biodegradability should also be considered as an important criterion for sustainable living of humans on this planet over the current and coming millennia.

22.4 Basics of Protein Chemical Modification as a General Strategy for Biological Material Synthesis by Rational Methods

Here are few examples of biodegradable materials made in my lab, which are also functional with respect to their intended use or they could be starting points for routes to make functional biological materials that could also biodegrade. Some examples include polyamides [7], polyesters, polyalcohols, artificial lipoproteins, artificial glycoproteins, polymer–protein conjugates [8], protein nanoparticles [9], and protein-derived 2-Dimensional materials [10]. These materials are anticipated to undergo biodegradation due to the ways they have been prepared using amide or ester chemistry. Because of the amide or the ester bonds introduced into these natural substances during the chemical modification, these bonds are susceptible to hydrolysis by proteases, which are ubiquitous in our environment [11]. When these materials are released into the environment, therefore, they are expected to be degraded on a reasonable timescale and they are unlikely to accumulate in the environment for hundreds of years. The resulting molecular fragments from these biological materials are mostly amino acids which serve as nutrients for bacteria, fungi, and other life forms on this planet. In our view, biological materials such as these should not generate toxic waste during the production, use, and disposal as much as possible.

Chemical modification of proteins can be a powerful strategy to manipulate their physical, chemical, biochemical and engineering characteristics in a significant

[1]For fun facts, go to https://faculty.washington.edu/chudler/bvc.html.

[2]Millions of times faster than the IBM Watson and thousand times faster than the fastest supercomputer, K of Fujitsu. T. Pearson, IBM Watson—How to build your own "Watson Jr." in your basement, Inside System Storage.

manner. Understanding the structure–function relationships of such modified proteins can be useful in the rational design of chemistries needed to make tailored molecules, and this could lead to novel materials and biodegradable devices. Since chemical modification is not restricted to the use of amino acids, the protein modification by any suitable chemical entity can be designed, and hence a variety of modifications can be achieved. The chemistry will not be limited to the use of natural amino acids, and hence one of the major limitations of the popular molecular biology approaches which can substitute one natural amino acid by another has been overcome [12]. The use of non-natural amino acids is also known in the molecular biology techniques but this task is quite challenging. Therefore, the protein chemistry described here is not limited to using natural amino acids and it is being extended to a variety of organic molecules, lipids, sugars, and inorganic molecules as well as synthetic polymers [13].

Given in Fig. 22.4 are the chemical transformations carried out on proteins, in our laboratory, over the past several years. For example, amidation of the carboxyl groups of the protein results in polyamides (right center), while modification with

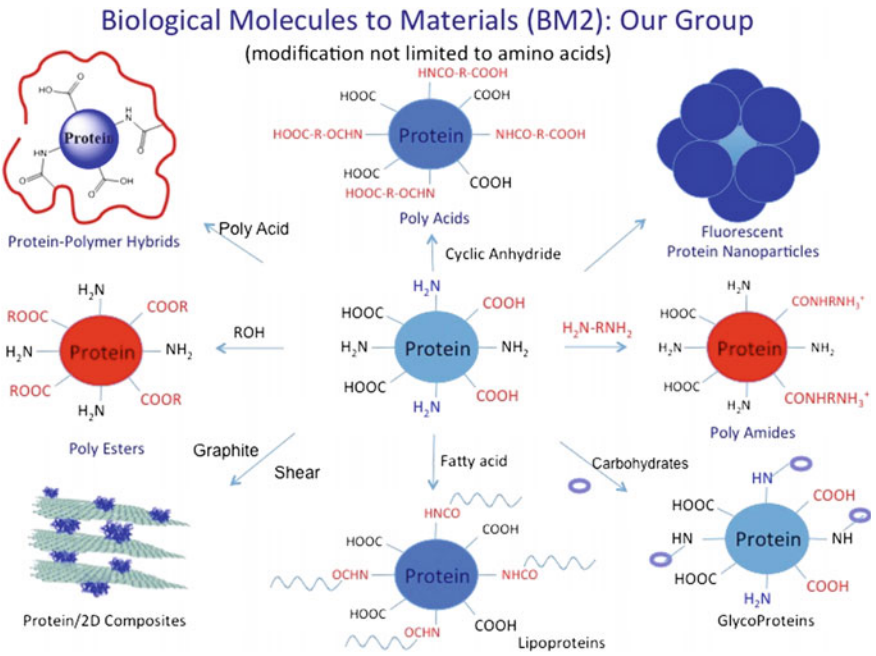

Fig. 22.4 Proteins are nature's materials and they can be modified with specific chemical transformations to produce potentially functional materials through standard transformations. For example, amidation of the carboxylic acid groups of proteins can produce polyamides, esterification could produce polyesters, conjugation with polymers produce protein–polymer covalent conjugates, etc., to make a variety of materials with controlled properties in a rational manner. This idea has not been fully explored by chemists and poses a significant promise to generate biodegradable functional materials from proteins, as one possibility, among many others

alcohols gives rise to polyesters (left center). Modification with lipids gave us artificial lipoproteins (center bottom) and modification with succinic anhydride resulted in polyacids (center top). These various chemical derivatives are potentially good materials whose properties can be controlled systematically by choosing the appropriate modification reagent and the extent of modification carried out. In addition to these simple transformations, we are also conjugating specific proteins and enzymes with poly(acrylic) acid to produce the corresponding nanogels of the protein–polymer covalent conjugates. These are another set of novel materials where the biological properties of proteins are coupled with the material properties of the synthetic polymers and the resulting materials are being evaluated as sensors, biocatalysts, or drug delivery systems. Thus, a variety of novel materials are being generated by logical combination of traditional organic molecules and proteins, as examples of rational design.

In another set of experiments, we have used proteins to produce 2–4 layer graphene using a simple kitchen blender (Fig. 22.4, lower left) and the resulting graphene–water dispersions are then coated onto regular printing paper to make nonmetallic conducting materials [10]. Along these lines, we have used amide chemistry to link protein molecules together to make well-defined protein-based nanoparticles (top right). Upon labeling with appropriate fluorescent dyes, these protein nanoparticles are strongly fluorescent and they are competing with quantum dots for practical applications. Since each particle contains 100–150 dye molecules, the particles are very bright, and fluorescence quantum yields of the dyes are increased in selected cases, with respect to free dyes [9]. Thus, simple chemical reactions performed on proteins can be profitable in making interesting molecules, materials and may ultimately lead to functional devices [8]. Thus, systematic investigations of protein chemical modification might lead to tangible biodegradable materials that could substitute at least some of the materials that are being used now in practical applications. Further progress in this area of chemistry where biodegradable, biocompatible chemistries, proposed here as edible chemistry, could be useful in addressing some of the concerns raised earlier. We will provide one specific example, where the protein modification chemistry is used extensively to make novel, functional, biodegradable, edible nanomaterials. These will be edible to some organisms, bacteria, fungi or animals, but not intended for human consumption because these particles are made from edible proteins and dyes that are harmless to most organisms.

Three specific examples of biodegradable materials have been developed in our laboratory (Fig. 22.5). These clearly indicate the potential of chemical modification of proteins in a rational manner, and provide preliminary proof for the concepts proposed above. For example, the nanoparticles made by cross-linking proteins, under controlled conditions, resulted in 10–100 nm particles where the size and size distributions are under chemical control [9]. Similarly, wrapping of enzymes with synthetic polymers gave corresponding covalent conjugates, which are more robust than the corresponding free enzymes, in many respects, while retaining full enzymatic activities. These are being explored to construct ‘Wash and Wear’ biosensors which can be washed several times without significant loss of activity [8]. As a third

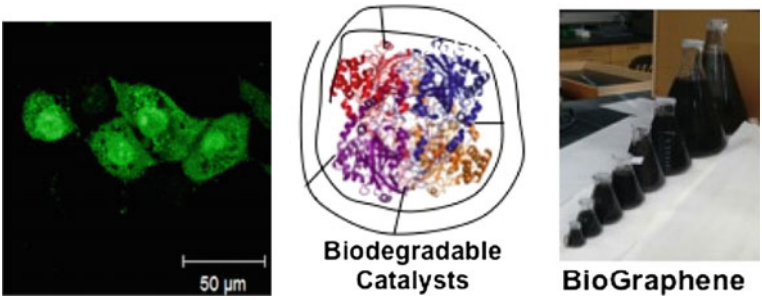

Fig. 22.5 Three examples of biodegradable functional materials. Protein fluorescent nanoparticles that rival quantum dots for cellular imaging (*left*), enzyme–polymer conjugates for the construction of 'Wash & Wear' biosensors (*middle*), and protein-assisted, large-scale production of biographene (*right*)

example, we demonstrate the solvating power of proteins to produce few-layer graphene as water dispersions, using a kitchen blender with high efficiency and fast production rate [10]. Out of these three examples, one will be described in detail to further the scientific argument regarding the production and utility of biodegradable functional materials, even under resource-limited laboratory conditions. These functional products can replace corresponding toxic analogs, if the community is willing.

22.5 Synthesis, Characterization, and Evaluation of Protein Fluorescent Nanoparticles

The very first examples of edible, biodegradable, functional, protein, fluorescent nanoparticles of controlled size and size distribution from a variety of proteins and enzymes by a general method are described here [9]. These are made from a variety of proteins such as bovine serum albumin (BSA), glucose oxidase (GOx), Horseradish peroxidase (HRP), lipase and catalase, as few examples to illustrate the feasibility of the concept.

Our initial studies focused on BSA (Fig. 22.6) as the edible protein and fluorescein as the biocompatible dye, which is often used by ophthalmologists on humans, and then we developed general methods for the control of particle size and size distribution, as well as labeling with this dye. Several drugs and dyes are known to bind to particular locations on BSA as shown in Fig. 22.6. For example, Coumarin 450C, Fluorescein, and Rhodamine B have specific sites to bind, and reactive versions of these dyes such as isothiocyanates, succinimidyl esters, squaraines, or other suitable reactive derivatives are expected to bind to the corresponding sites on the protein and react at these sites. Alternatively, they might also react at other sites on the protein where they may bind with a weaker affinity

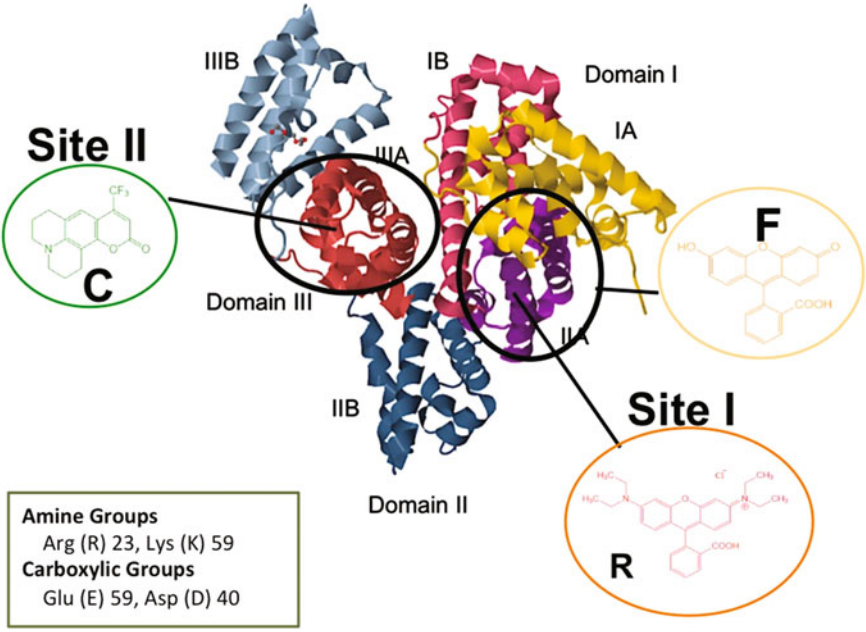

Fig. 22.6 Structure of bovine serum albumin and the location of specific ligand-binding sites on it. The known binding sites of Coumarin 450C, Fluorescein, and Rhodamine B on the protein as documented in the literature, and labeling of the protein particles by these dyes are expected to occur at these corresponding binding sites. In addition, this protein also binds a variety of biological ligands such as amino acids, fatty acids, hormones, and metal ions at specific locations on the protein, and the resulting protein particle may be used in drug delivery applications

but the exact location of ligand on the protein is to be determined experimentally. We have previously developed extensive photochemical foot printing methods to locate the binding sites of small organic or inorganic dyes on BSA [14–16].

In addition to the nanoparticels from BSA, we also prepared nanoparticles from other proteins and enzymes such as glucose oxidase (GO), Horseradish peroxidase (HRP), Lipase and Catalase (Fig. 22.7). GO is often used in glucose biosensors, while HRP is very widely used in signal conversion and quantification in biosensing. Lipase is extensively used in biofuel production as well as in biosensing applications and catalase is attractive for environmental remediation of hydrogen peroxide [17]. The choice of these enzymes or proteins is not limited to this particular set, and any protein with sufficient numbers of cross-linkable groups which are accessible on its surface is amenable to the approach described here. The proteins shown in Fig. 22.7, for example, have a number of amine and carboxyl groups on their surfaces that are amenable for cross-linking chemistry with standard carbodiimide reagents and they have been used to produce the corresponding nanoparticles of well-defined size and size distributions. Details of these studies are presented next.

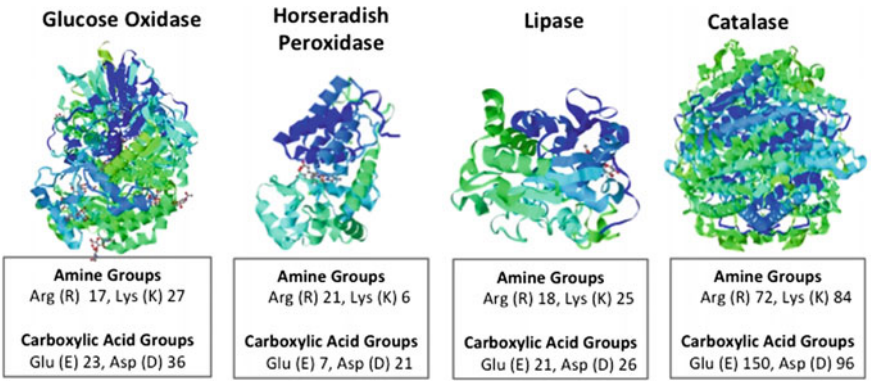

Fig. 22.7 Additional proteins/enzymes used in the nanoparticle synthesis and these have sufficient numbers of amine/carboxy functions for cross-linking of the proteins by standard organic chemistry methods

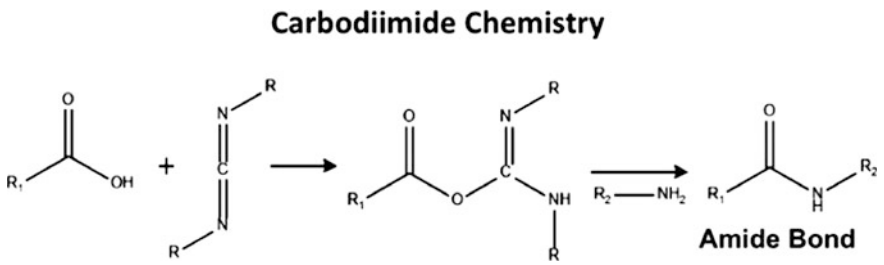

Fig. 22.8 Standard coupling chemistry with a water-soluble carbodiimide was used to make the protein nanoparticles where the carboxyl groups are activated and reacted with the amine groups on another protein molecule. The amide bond thus formed is amenable to biodegradation in the environment by the ubiquitous peptidases, enzymes which hydrolyze peptide bonds efficiently into their constituent amine and carboxyl components. Thus, the particles formed with this method are susceptible to biodegradation, unlike quantum dots, which are not readily biodegraded

22.5.1 Nanoparticles of Controlled Size from Bovine Serum Albumin

Activation of the carboxyl groups on BSA with water-soluble carbodiimide (Fig. 22.8) gives rise to the acyl intermediate, which can react with suitable amine groups on another protein molecule [18]. This type of conjugation between the carboxyl groups on one protein with the amine groups of another molecule of BSA, for example, generates BSA dimer. This dimer in turn may be linked to another BSA molecule or another dimer to produce larger aggregates, finally producing protein nanoparticles where the resulting particle size depends upon the extent of reaction. Nanoparticle growth, therefore, was controlled by adjusting the protein concentration, carbodiimide concentration, time of reaction and reaction

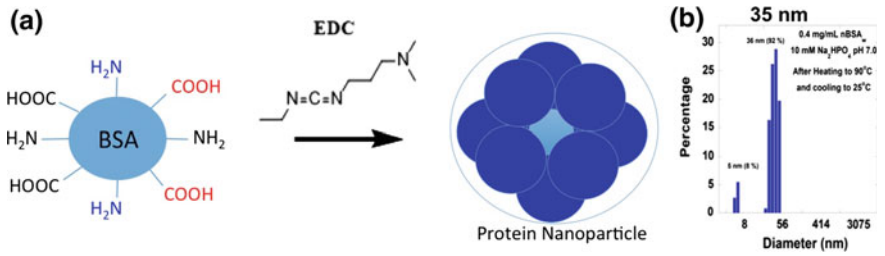

Fig. 22.9 **a** Synthesis of BSA nanoparticles (nBSA) by cross-linking the protein units with each other by carbodiimide (EDC), and **b** the resulting nanoparticles were annealed at elevated temperatures to give particles of 35 nm in average diameter as the major fraction (>90%)

temperature, as in any general chemical reaction where the rate of reaction is proportional to key variables of the reaction that is taking place.

Under controlled conditions, the particle size increased with protein concentration and prolonged annealing of the samples, after synthesis, at elevated temperatures for extended periods of time sharpened size distribution, through Ostwald ripening [19]. Thus, smaller particles of BSA aggregate to make larger, more stable nanoparticles. BSA nanoparticles of 35 nm in diameter with a full width at half height of the size distribution curve of about 5 nm were readily obtained by this annealing method. A small peak corresponding to 8 nm diameter (<10%) was also present, but the major size fraction was of >% weightage with a diameter of 35 nm. This meant that the larger particles are made of aggregation of the smaller 8 nm particles. This hypothesis was supported by the sodium dodecyl sulfate polyacrylamide gel electrophoresis (SDS PAGE) studies of the BSA nanoparticles (nBSA). Even when the nBSA samples indicated the absence of any free BSA in the agarose gels, discussed below, SDS PAGE data showed substantial amounts of a band whose molecular weight matched with that of BSA. Therefore, annealing is a major step in controlling the particle size as desired. The particle size and size distribution, ultimately, depended on the annealing conditions used for particle growth, and this approach provided a rational handle for the control of particle size over a range of 30–170 nm (Fig. 22.9).

22.5.2 Characterization of Nanoparticles and Labeling with FITC

The nBSA particles are visualized in agarose gels for purity, uniformity and charge characterization, and this was facilitated by labeling the particles with fluorescein isothiocyanate (FITC) as shown in Fig. 22.10. Fluorescent dye labeling of the protein particles where the isothiocyanate function of FITC reacted with the amine groups on the protein, give rise to intense emission from the particles, characteristic of fluorescein when excited at a suitable wavelength.

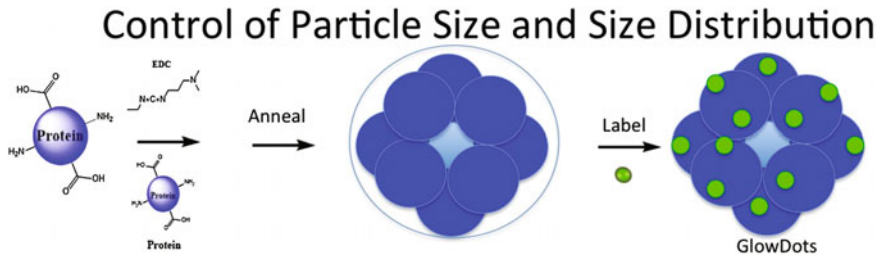

Fig. 22.10 Labeling of the protein nanoparticles (nBSA) with fluorescein isothiocyanate (FITC) to give strongly fluorescent nBSA particles

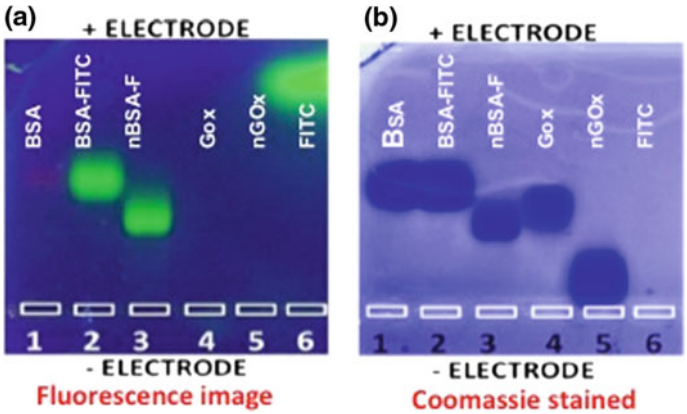

Fig. 22.11 Agarose gels of nBSA particles demonstrating the purity of the sample, where BSA (*lane 1*) and FITC-labeled BSA (*lane 2*) separated well from that of the dye labeled BSA nanoparticles (nBSA-F, *lane 3*). These data clearly indicate high purity of the sample. **a** The gel photographed under UV illumination to visualize the presence of the dye in the samples, and **b** gel stained with Coomassie Blue to identify the presence of protein in the corresponding lanes of the gel in panel (**a**)

Fluorescent dye labeling facilitated the characterization of the particles in agarose gels, where the samples are subjected to an electric field, under conditions that are suitable for the separation of the free protein and free dye from the nanoparticles (Fig. 22.11).

The agarose gel viewed under UV light clearly indicated the presence of FITC-labeled BSA (BSA-F) in lane 2 (Fig. 22.11a), FITC-labeled nBSA (nBSA-F) in lane 3, and free FITC in lane 6. The data clearly show that the samples migrated toward the positive electrode and their mobilities are quite distinct. The mobility of nBSA-F, for example, is much less than that of BSA-FITC, and FITC itself moved much more rapidly than the protein due to its small size. The larger size of nBSA particles had slow migration in the gel and this lane did not show any BSA-FITC or free FITC, thus providing evidence for its high purity. This conclusion was also

supported by Coomassie Blue staining of the same gel to visualize protein bands in the corresponding lanes (Fig. 22.11b). For example, BSA (lane 1) and BSA-FITC (lane 2) and nBSA-F contained the protein as indicated by the blue stain, while the FITC lane did not. Thus, the EDC coupling, followed by FITC labeling provided excellent evidence for the proposed synthesis of the protein nanoparticles while the dynamic light scattering (DLS) data shown in Fig. 22.9 confirmed the particle size. Encouraged by the above data, we proceeded to test if the current methodology is appropriate to make nanoparticle from several other proteins and enzymes. We named these as GlowDots which are now commercially available from Kerafast, a biological product company.

22.5.3 *Nanoparticle Synthesis from Other Proteins and Enzymes*

Nanoparticles produced by the cross-linking of the amine and carboxyl groups on the enzyme surfaces or protein surfaces shown in Fig. 22.7 with carbodiimide (EDC) coupling also resulted in the corresponding nanoparticles, under similar reaction conditions as above. The sizes of the particles as obtained prior to any annealing treatment are shown in Fig. 22.12. The transmission electron micrographs of the nanoparticles obtained from Glucose Oxidase, Horseradish Peroxidase, and Lipase are shown as examples.

The insets depict the expanded views of single particles from each of the sample, which clearly show the formation of nearly spherical particles, and the sample is of fairly uniform size, and the particle sizes of these enzymes ranged from 10 to 20 nm depending on the enzyme used for the particle synthesis. Due to the small sizes obtained here, there was no need for annealing of the samples and proceeded to check some applications of these protein fluorescent nanoparticles for cell imaging studies.

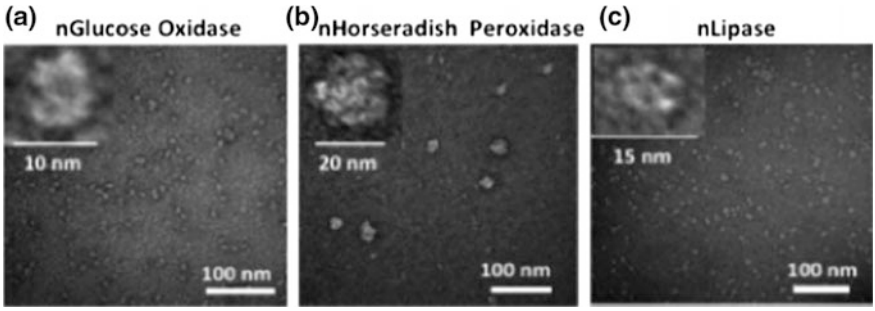

Fig. 22.12 Transmission electron micrographs (TEM) of the enzyme nanoparticles obtained from the cross-linking of the amine and carboxyl groups of **a** Glucose Oxidase, **b** Horseradish Peroxidase, and **c** Lipase by carbodiimide coupling chemistry. The *insets* in each panel show the expanded views of single particles

22.5.4 *Live Cell Imaging with Protein Fluorescent Nanoparticles*

The utility of these protein fluorescent nanoparticles for live cell imaging was examined using HN12 oral cancer cell lines in collaboration with Dr. Gutkind at the National Institutes of Health and his research team. Incubation of these cells with nGO-FITC led to quick uptake of the fluorescent nanoparticles and imaging of the cells after washing allowed the visualization of green emission of the particles from inside the cells in a confocal optical microscope (Fig. 22.13).

As the cells are exposed to the fluorescent nanoparticles nGO-FITC, the intensity of the emission in each of the cells was monitored as a function of time, and increase in the fluorescence intensity has been monitored as a function of time. Each cell behaved slightly differently from that of its neighbor, and this is not unexpected because cancer cells are heterogeneous, nonidentical populations. Some cells did not show any uptake while others have indicated rapid uptake of the nGO-FITC GlowDots (Fig. 22.14) and the uptake of nGO-FITC was complete in roughly >3 h. nGO-FITC catalyzes the oxidation of glucose present in the media by atmospheric oxygen with hydrogen peroxide as the by-product. Exposure of cells to hydrogen peroxide is well known to make the cell membranes permeable.

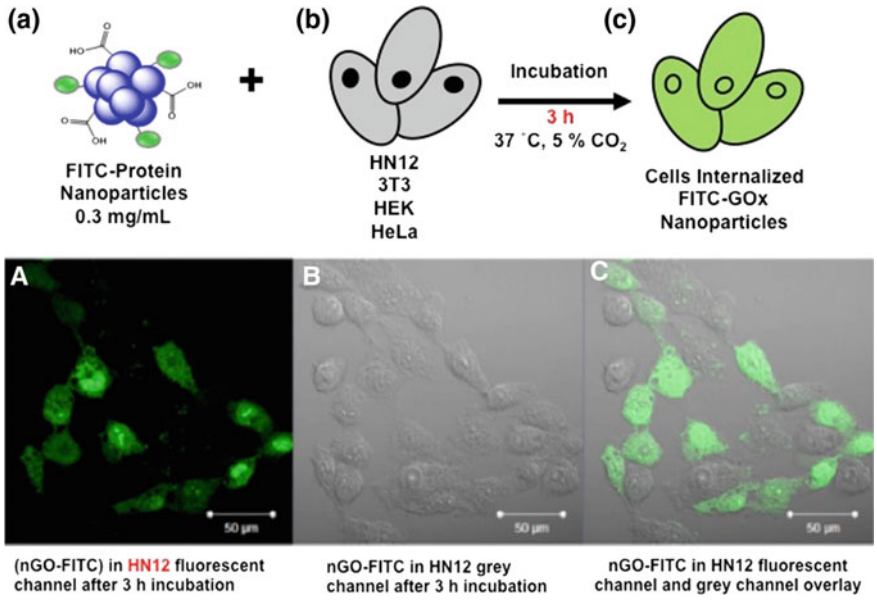

Fig. 22.13 Cellular uptake of nGO-FITC by HN12 cells. **a** Cellular uptake was complete in about 2 h and the green fluorescence seen from within the cells, **b** the corresponding phase contrast image, and **c** superposition of panels *A* and *B* which indicated that some cells did not have any uptake of nGO-FITC

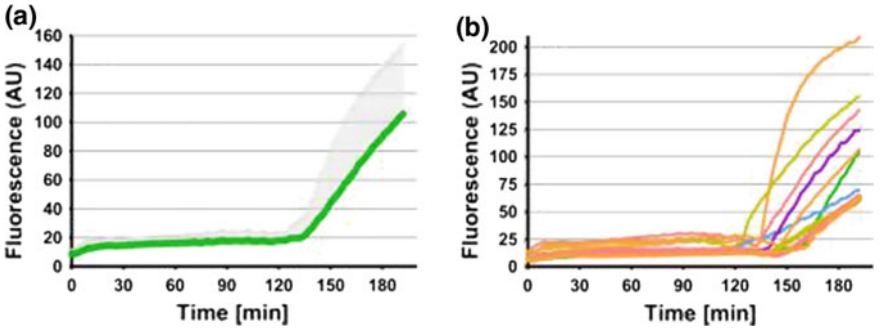

Fig. 22.14 Cellular uptake of nGO-FITC particles into HN12 cells as a function of time. **a** The *green line* on the *left* is the average of uptake traces from 10 different cells, and **b** the traces on the *right show* the uptake by individual cells

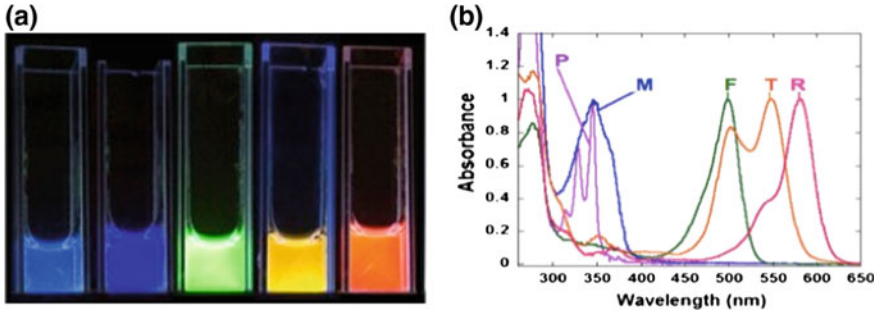

Fig. 22.15 **a** nBSA GlowDots labeled with a variety of fluorescent dyes *P*, *M*, *F*, *T*, and *R*; and **b** their corresponding absorption and emission spectra (not shown)

We postulate that cell membrane damage by hydrogen peroxide may be facilitating the uptake of GlowDots into the cells. This hypothesis was supported by the fact that in the presence of nGO and glucose, the cells rapidly internalized dextran Texas Red (Mol. Wt., 10,000). In the absence of nGO, there has been no uptake under otherwise identical conditions. Therefore, GlowDots are highly promising for cellular uptake by these and other cell lines and kinetics of uptake.

In another study, the HN12 cells were incubated with a mixture of Alexa555-Transferrin and nGO-FITC for 3 h, and the release of the particles examined after the cells have been washed with fresh media. Both Alexa555-Transferrin and nGO-FITC were released simultaneously from the cells but nGO-FITC release was complete within an hour. In these studies, and over these timescales, none of the cells were killed which could be due to the biocompatibility of the GlowDots. Therefore, the above data are highly promising and competitive with Quantum Dots for imaging applications. GlowDots are also now commercially available with a variety of dyes attached to the protein nanoparticles in multiple colors with a variety of excitation and emission wavelengths (Fig. 22.15).

22.5.5 GlowDots of Multiple Colors

The protein nanoparticles prepared in the above method have been labeled with several specific fluorescent dyes to produce the corresponding GlowDots (Fig. 22.15), enabling the tuning of their color and emission. Since the particle stock solution used for labeling was the same for all the dyes, particles of different color have the same size. Thus, the particle size does not have to be changed to tune the color and all particles have essentially the same size, surface features and surface chemistry, except for the presence of different dyes used. Therefore, highly uniform set of GlowDots of tunable absorption and emission colors are readily obtained, quickly, efficiently and by inexpensive methods. These reactions can be readily undertaken in a resource-limited laboratory with commonly available instrumentation and few selected reagents.

22.5.6 Comparisons of GlowDots with Quantum Dots

It will be fair to compare the progress made with GlowDots with other competing approaches to evaluate the pros and cons of the above approach. Such a discussion would raise some interesting possibilities and also point out the challenges that lay ahead. For example, the comparisons in Table 22.1 show that the two approaches are comparable initially with similar characteristics. For example, the spectral tuning, size tuning, extinction coefficients of the particles at their corresponding peak absorption wavelengths, quantum yields of fluorescence are all comparable between GlowDots and QDots. Further comparisons illustrate key differences. For example, GlowDots are nontoxic and depending on the application, one could choose dog albumin, cat albumin, cow albumin, human albumin, or porcine which are all very likely to produce the corresponding protein nanoparticles in a similar

Table 22.1 GlowDots versus QDots

	GlowDots	QDots
Toxicity	Low to none	High
Size	Controlled	Controlled
Extinction/Abs (# of dyes)	High	High
Emission	Tunable	Tunable
QY	High	High
Stability	Biodegradable	Toxic
Price	Low	High
Making	Easy	Challenging
Surface groups	Variety	Limited
Biocompatibility	High	Low
Blinking	None	Major issue
Biorecognition	Yes	None

manner. This way, the biological applications of the particles can be tailored to a particular species of mammals, and such versatility is lacking with QDots. Another major advantage of GlowDots is their biocompatibility without further chemical manipulation of their surface chemistry, since most albumins are of low immune response across the species, and well tolerated. This is not the case with QDots, which need extensive surface modification and even then their universal adaptation for biological applications is questionable. While GlowDots are made of nature's elements such as carbon, hydrogen, oxygen, nitrogen and sulfur, QDots require highly toxic, sometimes rare elements.

As GlowDots are made via the amide chemistry, these new amide bonds can be readily processed and hydrolyzed by proteases, thus releasing the nutrients back into the environment to sustain different forms of life. Thus, GlowDots do not persist in the environment for long times and they can be 'edible' for some organisms, animals, or plants. While QDots could be highly toxic and biological methods of remediation is just not possible, as the elements currently used in the synthesis of these particles are highly unfriendly to biological systems, and some of them could also be limited in amounts. Another comparison to be made is their synthesis, while GlowDots are made efficiently with carbodiimide or other suitable chemistries to link proteins together even by high school students after minimal laboratory training in a resource-limited context, QDots require elaborate methods by well-trained personnel with high-tech resources. This could be another major difference between them which could drive the sustainable, large-scale adoption of GlowDots.

Because GlowDots are made from proteins, the surfaces of these particles have a rich chemistry and display a variety of functions for ligation of ligands, biorecognition elements, or further chemical modification. No additional surface functionalization is often needed due to this richness of chemical groups present on them. On the other hand, QDots need expensive chemical transformations and coatings for further manipulation of their surfaces and raise their expense. GlowDots are also much superior to simple use of organic dyes [20]. In addition, another major advantage of GlowDots is their inherent biocompatibility depending on the protein chosen to make the particles. As discussed above, different albumins are currently available to tailor the biological nature of the particles and the proteins used are already bioactive, which is not the case with QDots.

Two other major points to be made are the size/color dependence and blinking of QDots [21]. The color of QDots is inherently related to their size, and hence color is tuned by changing the size of the particles or by changing their composition. This can be a serious drawback when one requires to keep the size the same but needs different colored particles for imaging or other applications. As indicated here, size of GlowDots is kept essentially the same but particles with vastly different colors and emission maxima quickly generated. Thus, GlowDots have a significant advantage. This major difference is to be kept in mind while choosing the type of nanoparticles for particular applications.

The last but not least important issue is 'Blinking'. Since GlowDots may have 100–150 emitters per particle, they do not blink, for all practical purposes. On the

other hand, blinking is a major issue with QDots and some progress has been made to alleviate this problem with limited success. Because most QDots reported at present are single source emitters, it is said that blinking is an inherent problem with them. The presence of multiple chromophores in a GlowDot, on the other hand, make it nearly impossible for blinking. Thus, there are significant major advantages for GlowDot technology platform described here over the existing alternatives.

22.6 Conclusions

The above discussion of protein chemical modification and experimental demonstration of the synthesis of benign protein nanoparticles of particular size, size distribution (after annealing) clearly demonstrate the potential of current strategy of using biological molecules and bio-friendly chemistry to make functional materials that could replace toxic alternatives. GlowDots are the most recent developments that could replace QDots and they are promising for most applications while being biodegradable. This endeavor of replacing nonbiodegradable substances such as QDots is a strong possibility. The large-scale use of biological materials support our current standard of living needs to be nurtured and developed to support future generations without creating additional environmental burden. Chemists and engineers have great challenges that lay ahead of them in this exciting new form of biological materials chemistry and technology.

Acknowledgements Author thanks the Fulbright Foundation for a fellowship, and the National Science Foundation for partial financial support of this work (DMR-1401879).

References

1. Dautel SL (2009) Transoceanic trash: international and United States strategies for the great Pacific Garbage Patch. Golden Gate U. Environ L J 3:181
2. Young LC, Vanderlip C, Duffy DC, Afanasyev V, Shaffer SA (2009) In: Ropert-Coudert Y (ed) Bringing home the trash: do colony-based differences in foraging distribution lead to increased plastic ingestion in Laysan Albatrosses? PLoS ONE 4(10):e7623
3. Ryan PG, Moore CJ, Van Franeker JA, Moloney CL (2009) Monitoring the abundance of plastic debris in the marine environment. Philos Tran R Soc B Biol Sci 364(1526):1999–2012. doi:10.1098/rstb.2008.0207
4. Rios LM, Moore C, Jones PR (2007) Persistent organic pollutants carried by synthetic polymers in the ocean environment. Mar Pollut Bull 54:1230–1237. doi:10.1016/j.marpolbul.2007.03.022
5. Joshi S (2000) Product environmental life-cycle assessment using input-output techniques. J Ind Ecol 3:95
6. Mahasenan N, Smith S, Humphreys K, Kaya Y (2003) The cement industry and global climate change: current and potential future cement industry CO_2 emissions. In: 6th international conference on greenhouse gas control technologies. Pergamon, Oxford, pp 995–1000. doi:10.1016/B978-008044276-1/50157-4

7. Novak MJ, Pattammattel A, Koshmerl B, Puglia M, Williams C, Kumar CV (2015) 'Stable-on-the-table' enzymes: engineering enzyme-graphene oxide interface for unprecedented stability of the biocatalysts. ACS Catal 6:339–447
8. Riccardi CM, Mistri D, Hart O, Anuganti M, Lin Y, Kasi RM, Kumar CV (2016) Covalent interlocking of glucose oxidase and peroxidase in the voids of paper: enzyme-polymer 'spider-webs". Chem Comm. doi:10.1039/c6cc00037a (5 Jan 16)
9. Deshapriya I, Stromer BS, Kim CS, Patel V, Gutkind JS, Kumar CV (2015) Novel, protein-based nanoparticles: improved half-lives, retention of protein structure and activities. Bioconj Chem 26:396–404
10. Pattammattel A, Kumar CV (2015) Kitchen chemistry 101: efficient exfoliation of high quality graphene with a blender and edible proteins. Adv Funct Mater, Oct 15/15 (in press)
11. Vranova V, Rejsek K, Formanek P (2013) Proteolytic activity in soil: a review. Appl Soil Ecol 70:23–32
12. Emery AEH (1984) An introduction to recombinant DNA. Taylor and Francis, Routledge
13. Thilakarathne VK, Briand VA, Ghimere A, Zore OV, Lenehan PJ, Kasi RM, Kumar CV (2015) Ultra-stable, hemoglobin-poly(acrylic) acid "Nanogels". Chem Sci J Sept 29/15; Kumar CV, Benson KB, Baveghems C, Stromer BS, Thilakarathne VK, Novac MJ, Rossi (2015) Toward the design of bio-solar cells: high efficiency cascade energy transfer among four donor-acceptor dyes self assembled in highly ordered protein-DNA matrix. RSC Adv 5:72416–72422; Zore O, Pattamattel A, Gnanaguru S, Kumar CV, Kasi R (2015) Bienzyme-polymer-graphene oxide quaternary hybrid biocatalysts: efficient substrate channeling at chemically and thermally denaturing conditions. ACS Catal 5:4979–4988; Pattammattel A, Williams CL, Pande P, Tsui WG, Basu AK, Kumar CV (2015) Biological relevance of oxidative debris present in as-prepared graphene oxide. RSC Adv 5:59364–59372; Deshapriya I, Stromer BS, Kim CS, Patel V, Gutkind JS, Kumar CV (2015) Novel, protein-based nanoparticles: improved half-lives, retention of protein structure and activities. Bioconj Chem 26:396–404; Sun X, Ma X, Kumar CV, Lei Y (2014) Protein-based sensitive, selective and rapid fluorescence detection of picric acid. Anal Methods 6:8464–8468; Riccardi CM, Cole KS, Benson KR, Ward J, Bassett K, Zhang Y, Zore O, Stromer B, Kasi RM, Kumar CV (2014) Toward 'stable-on-the-table' enzymes: improving key properties of catalase by simple covalent conjugation with poly(acrylic acid). Bioconj Chem 25:1501–1510; Zore OV, Lenehan PJ, Kumar CV, Kasi RM (2014) Efficient biocatalysis in organic media with hemoglobin and poly(acrylic acid) nanogels. Langmuir 30:5176–5184
14. Duff MR Jr, Kumar, CV (2009) The metallomics approach: use of Fe(II) and Cu(II) footprinting to examine metal binding sites on serum albumins. Metallomics 1:518–523
15. Kumar CV, Buranaprapuk A (1999) Tuning the selectivity of protein photocleavage: spectroscopic and photochemical studies. J Am Chem Soc 121:4202–4210
16. Kumar CV, Buranaprapuk A (1997) Site specific photocleavage of proteins. Angew Chem Int Ed Engl 36:2085
17. Schmid A, Dordick JS, Hauer B, Kiener A, Wubbolts M, Witholt B (2001) Industrial biocatalysis today and tomorrow. Nature 409:258–268
18. Baldwin AD, Kiick KL (2010) Polysaccharide-modified synthetic polymeric biomaterials. Pept Sci Biopolymers 94:128–140
19. Ostwald W (1889) Lehrbuch der Allgemeinen Chemie. Part 1. Leipzig, Germany
20. Resch-Genger U, Grabolle M, Cavaliere-Jaricot S, Nitschke R, Nann T (2008) Quantum dots versus organic dyes as fluorescent labels. Nat Methods 5:763–775
21. Medintz IL, Uyeda T, Goldman ER, Mattoussi H (2005) Quantum dot bioconjugates for imaging, labeling and sensing. Nat Mater 4:435–446